UNIVERSITÀ DEGLI STUDI DI NAPOLI FEDERICO II



Department of Civil, Building and Environmental Engineering

Ph.D. program in Civil Systems Engineering

XXXVII Cycle

SEISMIC PERFORMANCE AND FRAGILITY OF A CONCRETE FACE ROCKFILL DAM

by

JUAN MANUEL BARBAGELATA

A dissertation submitted in partial fulfillment of the requirements for the degree of

Doctor of Philosophy in Civil Systems Engineering

2025

Coordinator
Andrea Papola

Advisors
Francesco Silvestri
Anna d'Onofrio
Luca Pagano

"Deterministic analyses give an impression of certainty.
Probabilistic analyses complete the picture
by making explicit the uncertainties and their effects.
For improved geotechnical practice, we need both."

S. Lacasse
55th Rankine Lecture (2016)

Abstract

The methodologies for evaluating the safety of embankment dams under seismic actions have evolved, and regulatory agencies increasingly require risk assessments and probabilistic evaluations of seismic performance as part of dam safety evaluations. In this context, fragility functions play an essential role, as their ability to represent dam behavior can significantly influence performance and risk assessments. The need for reliable fragility functions is therefore imperative. This dissertation presents the application of a novel methodological framework for deriving case-specific fragility functions, exemplified through its implementation for Potrerillos Dam, a Concrete Face Rockfill Dam (CFRD) located in northern Mendoza Province, the most seismically active region of Argentina.

The framework highlights the importance of each step and the opportunities to incorporate variability and uncertainty throughout the process. A detailed characterization of the dam and site conditions is first provided, supported by a rigorous evaluation of geotechnical laboratory and in-situ tests, and the analysis of static and seismic monitoring records. A preliminary identification of Potential Failure Modes (PFMs) is then performed to link the fragility functions with the main seismically induced damage mechanisms of the system. The definition of seismic hazard is established through a primer Probabilistic Seismic Hazard Analysis (PSHA) for the site, followed by the selection of hazard-consistent records to be used as input motion in the numerical analyses. Advanced numerical models are subsequently constructed and calibrated, and then employed to perform a large number of Nonlinear Dynamic Analyses (NDAs). The results of the NDAs support the calibration of fragility functions through different fitting methods, damage criteria, and ground motion intensity measures, all of them carefully described.

The resulting fragility functions describe the vulnerability of the dam to different PFMs while also revealing the influence of damage criteria and intensity measures on seismic fragility across damage states. The derived functions, linked to PFMs and consistent with the seismic hazard, provide a robust representation of the system's fragility. The use of the fragility functions derived within an Earthquake Early Warning System for embankment dams was also explored as a novel application of the fragility functions. The application of this framework to generate reliable case-specific fragility functions constitutes a significant advancement that enhances performance-based evaluations and seismic risk assessments.

Acknowledgments

The acknowledgements are be available only in the printed version of the dissertation.

Table of Contents

1. Introduction 17
1.1 Scope of the research 19
1.2 Dissertation outline 20
2. Background 22
2.1 General characteristics of embankment dams 22
2.2 Evaluation of seismic performance of embankment dams 26
2.3 Seismic hazard assessment 26
2.4 Case histories of embankment dam response during earthquakes 33
2.5 Damage mechanisms of embankment dams under seismic actions 37
2.6 Dynamic analysis of embankment dams 40
2.7 Seismic performance and fragility of embankment dams 44
2.8 Earthquake Early Warning Systems 64
3. Case-specific fragility functions for Potrerillos CFRD 65
3.1 Methodological framework for deriving case-specific seismic fragility 65
3.2 Main features of Potrerillos Dam 72
3.3 Geotechnical in-situ and laboratory tests 80
3.4 Dam past behavior and monitoring data interpretation 100
4. Preliminary identification of potential failure modes 135
4.1 Exploratory assessment of potential failure modes for Potrerillos CFRD 136
4.2 Seismically driven PFMs identified for seismic fragility analysis 139
5. Site-specific seismic hazard assessment 142
5.1 Tectonic setting and regional seismicity 142
5.2 Seismic sources characterization 146
5.3 PSHA calculations 160
5.4 Seismic hazard results 171
5.5 Selecting and adjusting earthquake ground motions 174
6. Numerical model definition 179
6.1 Geometry for numerical analysis 179
6.2 Selection and calibration of soil constitutive models 182
6.3 Numerical model construction and static analysis 200

7. Nonlinear dynamic analyses 207
7.1 Evaluation of seismic performance 208
7.2 Influence of the modeling decisions 213
8. Derivation of seismic fragility functions 214
8.1 Intensity measures of the ground motion 215
8.2 Engineering demand parameters and damage measures 216
8.3 Calibration of seismic fragility functions 232
8.4 Integration of Fragility Curves into Earthquake Early Warning Systems 273
9. Discussion and conclusion 284
9.1 General discussion 284
9.2 Closing remarks 287
9.3 Future developments 289
10. References 293
11. Appendixes 325
11.1 Appendix I 325
11.2 Appendix II 347

List of Figures

Fig. 2.1: Typical cross-section of several types of embankment dams (Pells & Fell, 2002). 22

Fig. 2.2: a) typical cross section and zoning of a CFRD dam (Fell et al., 2014), and b) connection between slab and cut-off-wall, example from Puclaro CFRD (ICOLD, 2010)). 25

Fig. 2.3: PBEE framework illustrating all its components (Kramer, 2024) 26

Fig. 2.4: Illustrative hazard curve for peak ground acceleration (PGA) (Somerville & Moriwaki, 2003) 29

Fig. 2.5: Illustration of the steps involved in PSHA (Bommer, 2022; USNRC, 2018). Where a) diverse geometrical definitions of seismic sources; b) definition of the different sources-to-site distances; c) Gutenberg-Richter model of seismicity; d) Characteristics model of seismicity; e) GMMs for different magnitudes; and f) resulting hazard curve. 30

Fig. 2.6: Example of a UHS, indicating a) derivation from hazard curves of Sa at different periods, and b) the UHSs for two exceedance rates related to T_R = 475 and 2475 y (Baker et al., 2021). 31

Fig. 2.7: Example of a disaggregation chart for Sa (0.5 s) and T_R = 475 y (Chioccarelli et al., 2019). 32

Fig. 2.8: a) aerial picture of the dam after the earthquake (USGS Archive), b) cross-section with the reconstruction of the cinematic mechanism of the sliding and the zoning (Seed et al., 1989) 34

Fig. 2.9: Plan view of the areas with transverse and longitudinal cracks of Austrian dam after the 1989 Loma Prieta earthquake (Harder et al., 1998). It is evident how the longitudinal cracks are concentrated close to the crest of the dam, whereas the transverse cracks are close to the abutments. 35

Fig. 2.10: a) dislocated slabs of Zipingpu CFRD after the 2008 Wenchuan earthquake (Zou et al., 2012), b) dislocation detail and its "Z" shape, showing kinked rebars and detached concrete (Zou et al., 2012). 37

Fig. 2.11: Typical damage mechanisms induced by earthquakes in embankment dams (Pagano & Sica, 2013)..... 38

Fig. 2.12: double integration procedure of the sliding block method (Kramer & Stewart, 2004) 42

Fig. 2.13: Typical output of a nonlinear dynamic analysis, in this case, the contour of maximum shear strains (Paull et al., 2022). 44

Fig. 2.14: illustrative performance matrix for the case of a building (Moehle, 2024) 45

Fig. 2.15: PBEE framework illustrating the roles of response, damage, and loss models (Kramer, 2024) 45

Fig. 2.16: Graphical representation of a fragility function (Baker et al., 2021). 48

Fig. 2.17: Illustrative IDA curves and vertical statistics for the derivation of fragility functions, for a building structure (Baltzopoulos et al., 2017) 50

Fig. 2.18: a) IDA curves and vertical statistics for different IM levels, and b) IDA-based lognormal fragility function fitted with data for every IM level (Bakalis & Vamvatsikos, 2018). 51

Fig. 2.19: a) EDP (peak story drift ratio) values for every IM stripe, observing the DM = 0.08 and the number of numerical collapses. b) MSA-based lognormal fragility function fitted (Baker, 2015). 52

Fig. 2.20: a) IM-DCR point cloud (including collapses) and the cloud linear regression in log-log space. b) CA-based lognormal fragility function fitted considering or not collapses, and its complementary cumulative distribution function (CCDF). Modified from Jalayer et al. (2017). 53

Fig. 3.1: Methodological framework for deriving case-specific fragility functions for embankment dams. 66

Fig. 3.2: a) Location of Potrerillos CFRD, and b) upper basin of Mendoza River, and their main tributaries: Las Cuevas, Vacas, and Tupungato Rivers. 72

Fig. 3.3: Upper view of Potrerillos dam and reservoir. Courtesy of Eng. Julieta Fajardo. 73

Fig. 3.4: Upper view of the downstream of the dam during construction. Archive Prof. A. Barchiesi. 74

Fig. 3.5: a) Downstream stabilizing embankment during its construction. In the bottom left corner is possible to see the gallery built to collect the discharge from the drainage system, and b) a photograph from the downstream showing the embankment with its final geometry. Archive Prof. A. Barchiesi. 75

Fig. 3.6: a) Typical cross section of the dam with the main dimensions and zoning, and b) section perpendicular to the stream direction, across the dam axis. 76

Fig. 3.7: Aerial pictures of the dam and appurtenances during the construction, with its most relevant components: a) downstream view, and b) upstream view. Archive Prof. A. Barchiesi. 77

Fig. 3.8: a) Cavern housing the control valves of the bottom outlet, and b) gallery over the roof of the cavern to control the infiltration and improve its stability. 78

Fig. 3.9: Contours of alluvium thickness in the dam site, reconstructed from boreholes and geophysics. 79

Fig. 3.10: Section of the cut-off wall parallel to the dam axis, from upstream. The four distinct materials used in its construction are highlighted using different colors. 80

Fig. 3.11: Systematic methodology for site characterization of gravelly alluvium (DeJong et al., 2016) 80

Fig. 3.12: Summary of the geotechnical tests available for every soil and rock type of the dam. TX refers to static triaxial test, CTX to cyclic triaxial tests, CD stands for consolidated and drained, CU for consolidated and undrained, ∅ is the sample diameter and d_{max} the maximum particle size. 82

Fig. 3.13: Location of the drillings where the RQD was performed, together with the alluvium thickness contours 83

Fig. 3.14: a) RQD vs. elevation, b) RQD histogram and extreme value distribution, and c) RQD CDF. 83

Fig. 3.15: a) Location of the drillings where Lugeon tests were performed, b) distribution of Lugeon units vs. elevation, and c) distribution of estimated hydraulic conductivity vs. elevation. 84

Fig. 3.16: Plan view of the dam with the location of the alluvial zone and the boreholes (BH) with logging. Those associated with Section C in a buffer zone of 20 m are highlighted. 86

Fig. 3.17: Cross-section of the dam with the selected boreholes, and their identified lithology. 86

Fig. 3.18: Picture of the coring corresponding to the borehole SPCD-8. Archive Prof. A. Barchiesi. 87

Fig. 3.19: Uncorrected or raw blow count of the SPT tests performed in the boreholes, a) P3A, and b) P5A. 88

Fig. 3.20: Granulometric curves for the soils contained in the sampler during the SPT performed in the borehole P5A, overlapped with the limits for “Easily” and “Very Easily” liquefiable by Iai et al. (1989). 89

Fig. 3.21: Granulometric curves for the soils contained in the sampler during the SPT performed in the borehole P3A, overlapped with the limits for “Easily” and “Very Easily” liquefiable by Iai et al. (1989). 90

Fig. 3.22: a) Location of the cross-hole tests, and b) profile of Vs from all the cross-hole tests. 91

Fig. 3.23: Location of the surficial tests-pits where the samples for the laboratory tests were taken. 92

Fig. 3.24: Granulometric curves for the soils of the test pits a) CP6, b) CP8, c) CP9, and d) CP10. 92

Fig. 3.25: q-p’ plots of the results from the TX-CD tests on the alluvial soils, and the linear fitting used for the derivation of the friction angle for a) peak values, and b) large-strain values. 93

Fig. 3.26: Cyclic resistance curve (CRR) from CTX tests over sample CP9 (D_R = 50%), and the sample CP6 (D_R = 60%), where the cyclic stress ratio CSR = τ_{cyc}/σ'_{v_0} , the ratio of cyclic shear stress and consolidation vertical effective stress. 94

Fig. 3.27: Quarries for soils 2B, 3A & 3B, in the alluvium of Cacheuta and Mendoza rivers, respectively. 94

Fig. 3.28: Soil representative from the quarry used for 3A. Archive Prof. A. Barchiesi. 95

Fig. 3.29: Granulometric curves for the soils of the dam body, with black thin lines representing the Old tests, colored lines for the New tests, and black thick dashed lines identifying the admissible limits for the soils a) 3A, and b) 3B. 96

Fig. 3.30: q-p’ plots of the results from the TX-CD tests on the 3A, and the linear fitting used for the derivation of the friction angle for a) peak values, and b) large strain values. 97

Fig. 3.31: q-p’ plots of the results from the TX-CD tests on the 3B, and the linear fitting used for the derivation of the friction angle for a) peak values, and b) large strain values. 97

Fig. 3.32: Coefficient of uniformity C_u for the soils a) 3A, and b) 3B. 98

Fig. 3.33: Dry unit weight γ_d from the compaction control during construction, for a) 3A, and b) 3B. 99

Fig. 3.34: Load plate tests performed on a trial embankment made of 2B material. 100

Fig. 3.35: Cross-sections and given color scheme used to identify buried instruments. 102

Fig. 3.36: In-plant view of dam features and distribution of surficial monitoring instruments. 103

Fig. 3.37: In-plant view of the distribution of buried sensors in the dam and foundation. 104

Fig. 3.38: Location of the inclinometers, piezometers, and triaxial joint opening gauges along the cut-off wall, a) upstream view, b) Isometric view, and c) detail of the instruments in the floating plinth. 104

Fig. 3.39: Section E1-i a) location of the piezometers in cross-section, b) location of the piezometers in plan view, and c) records of pore water pressure of the selected instruments, together with the elevation of the instruments, and the impoundment level of the reservoir. 106

Fig. 3.40: Section E1-ii a) location of the piezometers in cross-section, b) location of the piezometers in plan view, and c) records of pore water pressure of the selected instruments, together with the elevation of the instruments, and the impoundment level of the reservoir. 107

Fig. 3.41: Location of piezometers that present large steps in pore pressure records, together with the contours of alluvium thickness beneath the dam. 108

Fig. 3.42: Location of the Cacheuta meteorological station and Guido hydrological station, close to the dam. 109

Fig. 3.43: Records of pore water pressure at Section E1-ii overlapped with daily precipitation time series at Cacheuta station. 109

Fig. 3.44: Records of pore water pressure at Section E1-ii plot together with the daily fluid discharge at Guido hydrological station..... 110

Fig. 3.45: Records of pore water pressure at Section E1-ii superimposed with weekly solid discharge at Guido hydrological station..... 110

Fig. 3.46: Plot with the combined records of pore water pressure at Section E1-ii, impoundment level, solid discharge at Guido station, and fluid discharge 112

Fig. 3.47: Fixed point measurements and contours of the cumulated settlements at the surface of the dam since the end of the construction of the dam in 2002, up to 2022. 114

Fig. 3.48: a) installation of vibrating wire settlement gauge before filling the cube with concrete, from Made et al. (2002), and b) distribution of settlement gauges along Section D. 115

Fig. 3.49: Relative settlements of the dam at the end of the construction of the embankment. 115

Fig. 3.50: Parameters from the shear beam model, modified from Dakoulas & Gazetas (1985). 117

Fig. 3.51: a) Partial cross-section with the distribution of settlement gauges considered in this analysis, b) experimental points and analytical profile of relative settlements, and c) distribution of shear stiffness along the dam height based on Eq. 3.6 (E_{oed}), Eq. 3.7 (E), and Eq. 3.8 (shear beam). 118

Fig. 3.52: Downstream view of the dam with the location of the seismic stations. 119

Fig. 3.53: a) Plan view and main features of the dam with the location of all accelerometric stations, and accelerometer component orientation; b) location of the accelerometric stations along the dam central transverse section; c) dam longitudinal section 120

Fig. 3.54: a) Downstream slope of the dam with the monitoring booths, with C9 and C7 highlighted, and b) data transfer system for all four accelerometers. 121

Fig. 3.55: a) Distribution of seismic events recorded at the dam site, with the location of the dam and the events reported in Table 3.4 emphasized (white ring), and b) East-West cross section with surface topography (out of scale) and distribution of recorded seismic events in depth. 124

Fig. 3.56: Focal mechanism of the events with an available moment tensor solution, highlighting the events from Table 3.4..... 125

Fig. 3.57: Plots clustering the seismic events with respect to their focal mechanism, for a) crustal events (CR), b) intraslab events (IS), c) subduction interface events (SD), and d) a reference for the identification of the regions where every focal mechanism prevails (Álvarez-Gómez, 2019)..... 126

Fig. 3.58: a) Number of records at every station, and b) the number of records at all the stations, just the stations of the dam body (C1, C7, and C9), or the two uppermost stations (C7 and C9). 127

Fig. 3.59: Ratio of PGA at the crest (C9) with respect to mid-height (C7) over the years of operation. 128

Fig. 3.60: SSR for the three types of seismic sources identified: a) crustal (CR), b) intraslab (IS), and c) subduction (SD). The fundamental frequency of the dam-foundation system is highlighted in red. 129

Fig. 3.61: RSA and Sa(f) for the C9 and GMD motion (event CR-01, TRA component) 130

Fig. 5.1: Pampean flat subduction segment, with contours of the subducted plate or Benioff zone, and related mountain ranges (Ramos & Folguera, 2009). 143

Fig. 5.2: Reference location map and an east-west crustal cross-section of the Pampean Flat subduction, with its various geological structures and related faults. After Capaldi et al. (2020). 144

Fig. 5.3: Historical crustal earthquakes in the north of Mendoza, along with the trace of a few geological active structures, and surface velocity vectors from geodetic GPS (Salomon et al., 2013). 145

Fig. 5.4: a) Block diagram of the Pampean flat subduction; and b) intraslab seismicity in the Pampean flat subduction range (Jordan et al., 1983). 146

Fig. 5.5: Plan view showing the projection of the crustal faults considered in the PSHA, with the identification of the fault scarp and an arrow illustrating the rake direction. 149

Fig. 5.6: Illustrative example of the magnitude-frequency distribution using the combination of the Characteristic Model (uniform) and Gutenberg-Richter (exponential) models (blue thick line), in contrast with just using the G-R model (thin light blue line) (Baker et al., 2021)..... 151

Fig. 5.7: Crustal seismic events from a combined catalog (instrumental + historical) in the northern part of the Cuyo basin and the southern portion of the Western Precordillera. These seismic events were used for the fitting of the Gutenberg-Richter model and evaluation of the regional b-value. 153

Fig. 5.8: Adjusted G-R distribution based on the best combination of b-value and M_C for crustal events. ... 154

Fig. 5.9: Dam location, surface projection of the intraslab source, and the contours of the top of the subducted slab reproduced from those reported by Alvarado et al. (2009). 156

Fig. 5.10: a) plan view of the seismicity at the dam site for depths larger than 60 km (ISC, 2022), proposed intraslab source, profile, and the buffer considered for the cross-section; b) cross-section showing the topography (out of scale), dam site, seismicity and location of the intraslab source..... 157

Fig. 5.11: Selected events from the reviewed ISC catalog of seismicity to calibrate the G-R for the intraslab source. 159

Fig. 5.12: Adjusted G-R model based on the best combination of b-value and M_C for intraslab events. 160

Fig. 5.13: a) the user interface of R-CRISIS to introduce the geometrical definition of the crustal sources and the option of considering the fault as b) Stirling fault, or c) Frankel fault. Case: El Totoral. 162

Fig. 5.14: User interface for the definition of the parameters of the Characteristic Model in R-CRISIS. Case: La Cal. 164

Fig. 5.15: Definition of the parameters of the G-R model in R-CRISIS. Case: SW Precordillera. 165

Fig. 5.16: Combined CM + G-R distribution used to define the seismicity of crustal sources. Case: La Cal. 166

Fig. 5.17: G-R distribution used to define the seismicity of the intraslab source. 167

Fig. 5.18: Global parameters to be defined before carrying out the PSHA using R-CRISIS. 169

Fig. 5.19: Logic tree combination for the PSHA, considering the variability of activity rates and GMMs. ... 171

Fig. 5.20: Hazard curves for crustal sources, intraslab source, and their combination (Total hazard), highlighting the annual rate of exceedance in correspondence to the established return periods. 172

Fig. 5.21: Uniform hazard spectra for the five selected return periods: 144, 475, 975, 2475, and 4975 y. 173

Fig. 5.22: Disaggregation chart for Sa(0.5s) and T_R 2475 y. Can be observed the influence on the seismic hazard of two types of sources characterized by different magnitudes and distances. 173

Fig. 5.23: Searching engine of the database of the NGA West 2 project, with three well-defined sections for defining the parameters for searching records, selecting the component, and scaling. The shaded portion corresponds to the definition of a multi-period scaling not used in this work. 176

Fig. 5.24: Response spectra for the records selected and scaled for T_R = 2475 y, together with their mean spectrum and respective UHS. 177

Fig. 6.1: Plan view and central cross sections of the dam, evidencing the variability in geometry of the bedrock. 179

Fig. 6.2: Model of the dam representing Section C, with the identification of the principal dimensions and the color scheme identifying different blocks of the model. 181

Fig. 6.3: Contours of the zone condition of each element, showing an average good quality of the mesh. 182

Fig. 6.4: Color scheme to differentiate among different soils considered in the numerical analyses. 182

Fig. 6.5: Comparison between the calibrated interface model and the experimental results from Zhang & Zhang (2008) for the interface between concrete slab and soil. 187

Fig. 6.6: Single element response for the calibration of PM4Sand for AL_L in terms of a) cyclic resistance curve, b) CSR vs. shear strain, c) normalized stress path, and d) r_u vs. number of cycles. 192

Fig. 6.7: Single element response for the calibration of PM4Sand for AL_S in terms of a) cyclic resistance curve, b) CSR vs. shear strain, c) normalized stress path, and d) r_u vs. number of cycles. 193

Fig. 6.8: Single element response for the calibration of PM4Sand for 3_AS in terms of a) G/G_0 vs. γ, and b) D vs. γ, for two levels of confinement (200 and 600 MPa), and comparison with the curves from literature for gravel from Rollins et al. (2020). 194

Fig. 6.9: Modulus reduction and damping curves from Rollins et al. (2020) for different levels of confinement. a) G/G_0 vs. γ for 3A, b) D vs. γ for 3A, c) G/G_0 vs. γ for 3B, d) D vs. γ for 3B. 197

Fig. 6.10: Modulus reduction and damping curves from the calibration 3A using UBCHyst. The curves from the driver are compared with Rollins et al. (2020) for two different confinements. a) G/G_0 vs. γ for 3A, b) D vs. γ for 3A, c) τ_{xy} vs. γ curve for σ'_0 = 250 MPa, d) τ_{xy} vs. γ curve for σ'_0 = 750 MPa. 198

Fig. 6.11: Profile of shear wave velocity into the alluvium, comparing the adjusted model with the Vs profiles obtained from the cross-hole tests, except for the soil AL_L, which adopts the Vs estimated from SPT. 201

Fig. 6.12: Contours of shear wave velocity for the alluvium and bedrock, before the construction of the dam. 201

Fig. 6.13: Profile of shear wave velocities at the center of the dam, with the half-section to give the dimension of the height of the dam and show the layering. 202

Fig. 6.14: Contours of shear wave velocity after the construction of the dam. 202

Fig. 6.15: Contours of vertical effective stress after construction, empty reservoir. 203

Fig. 6.16: Contour of horizontal effective stress after the construction, empty reservoir. 203

Fig. 6.17: Contours of mean effective stress after the construction, empty reservoir. 204

Fig. 6.18: Coefficient of earth pressure at rest K_0 after the construction, empty reservoir. 204

Fig. 6.19: Alpha coefficient α after the construction, empty reservoir. 204

Fig. 6.20: Contours of vertical displacements after the construction, empty reservoir. 204

Fig. 6.21: Contours of horizontal displacements after the construction, empty reservoir. 205

Fig. 6.22: Contours of pore water pressure after the rise of the reservoir. 205

Fig. 6.23: Compliant base and free-field boundary conditions, modified from Itasca software guides (Itasca Consulting Group, Inc., 2023) 207

Fig. 7.1: Acceleration time history of the record RSN_4231_H2_TR475. 208

Fig. 7.2: Contour of displacement magnitude for the ground motion RSN_4231_H2_TR475. 209

Fig. 7.3: Contour of shear strains for the ground motion RSN_4231_H2_TR475. 209

Fig. 7.4: Time history of crest settlements for the ground motion RSN_4231_H2_TR475. 209

Fig. 7.5: Location of the four points where the pore water pressure was measured, in the soil AL_L. 210

Fig. 7.6: Time history of pore water pressure ratio r_u, for the ground motion RSN_4231_H2_TR475. 210

Fig. 7.7: Acceleration time history of the record RSN_5618_H2_TR4975. 211

Fig. 7.8: Contour of displacement magnitude for the ground motion RSN_5618_H2_TR4975. 211

Fig. 7.9: Contour of shear strains for the ground motion RSN_5618_H2_TR4975. 211

Fig. 7.10 Time history of crest settlements for the ground motion RSN_5618_H2_TR4975. 212

Fig. 7.11: Time history of pore water pressure ratio r_u, for the ground motion RSN_5618_H2_TR4975. 213

Fig. 8.1: Scheme showing the parameters involved in the calculation of NCS_{DH+AT}, the settlement Δ, dam height DH, and alluvium thickness AT (Swaisgood, 2014). 218

Fig. 8.2: Comparison between the probabilistic and deterministic definitions of DMs, considering the probabilistic models of He & Rathje (2024), and the deterministic limits of Pells & Fell (2003). 224

Fig. 8.3: Backward erosion after a flooding episode during the construction of Tokwe-Mukorsi CFRD, Zimbabwe (Fry, 2016). 228

Fig. 8.4: Graphic to set the damage state of a concrete slab element based on the demand over capacity ratio (DCR_S) and the cumulative overstress duration (COD_S) (Pang et al., 2019). 230

Fig. 8.5: Options for the variation of the damage factor di based on DCR_S-COD_S, a) variation parallel to the limit between severe and moderate damage, and b) variation independent of COD_S. 231

Fig. 8.6: Spectral acceleration at T = 0.5 s, Sa(0.5s), vs. permanent crest settlement for the five initial levels of the intensity measure. 234

Fig. 8.7: Sa(0.5s) vs. permanent crest settlement, with the DMs from Swaisgood (2014), in semilogarithmic scale. 235

Fig. 8.8: Example of the fragility function fitting using maximum likelihood estimation, showing the points which represent P(EDP >DM | IM = im) vs im, and the adjusted lognormal CDF for the "Minor" damage level of the criterion from Swaisgood (2014). 236

Fig. 8.9: First set of fragility functions for PFM overtopping and DMs set by Swaisgood (2014). It is evident the change in shape and apparent lower dispersion in the curve for the "Serious" damage level. 236

Fig. 8.10: Response spectra for the records selected and scaled for T_R = 9975 y, together with their mean spectrum and respective UHS. 238

Fig. 8.11: Sa(0.5s) vs. permanent crest settlements including the results from the intensity level corresponding to T_R= 9975 y, together with the DMs from Swaisgood (2014), in semilogarithmic scale. 239

Fig. 8.12: Second group of fragility functions for the DMs proposed by Swaisgood (2014) for the PFM of overtopping, including the results of the new intensity level corresponding to T_R = 9975 y. 240

Fig. 8.13: Sa(0.5s) vs. permanent crest settlements, together with the DMs from Pells & Fell (2003), in semilogarithmic scale. 241

Fig. 8.14: Fragility functions for the DMs proposed by Pells & Fell (2003), for the PFM of overtopping. The "Collapse" damage set by this criterion was not achieved by any ground motion; that is the reason why there is no fragility function defined for this damage state. 241

Fig. 8.15: Sa(0.5s) vs. permanent crest settlements, together with the DMs from Pang et al. (2018), in semilogarithmic scale. 243

Fig. 8.16: Fragility functions for the DMs proposed by Pang et al. (2018), for the PFM of overtopping. 243

Fig. 8.17: Sa(0.5s) vs. permanent crest settlements, and the DMs set by Pang et al. (2019), in semilogarithmic scale. 244

Fig. 8.18: Fragility functions for the DMs proposed by Pang et al. (2019), PFM of overtopping. 245

Fig. 8.19: Sa(0.5s) vs. permanent crest settlements, and DMs set by Aliberti et al. (2019), in semilogarithmic scale. 246

Fig. 8.20: Fragility functions for the DMs given by Aliberti et al. (2019), for the PFM of overtopping. 247

Fig. 8.21: Sa(0.5s) vs. permanent crest settlement, the DMs defined in terms of freeboard reduction, in semilogarithmic scale. 248

Fig. 8.22: Fragility functions for the DMs based on freeboard reduction, for the PFM of overtopping. 249

Fig. 8.23: Fragility functions for the "Moderate" damage level, for all the criteria corresponding to the PFM of overtopping. 250

Fig. 8.24: Sa(0.5s) vs. displacement of a well-defined sliding mass, together with the DMs defined in terms of the criteria adopted by Regina (2021), in semilogarithmic scale. 251

Fig. 8.25: Fragility functions for the DMs based on the criterion adopted by Regina (2021), for the PFM of global instability. 252

Fig. 8.26: Sa(0.5s) vs. displacement of a well-defined sliding mass, together with the DMs defined in terms of the criteria defined by Idriss (1985), in semilogarithmic scale. 253

Fig. 8.27: Fragility functions for the DMs defined by Idriss (1985), for the PFM of global instability. 253

Fig. 8.28: Fragility functions for the two sets of DMs corresponding to the PFM of global instability. "R" stands for Regina (2021) criterion, whereas "I" stands for Idriss (1985) criterion. 254

Fig. 8.29: Sa(0.5s) vs. slab damage index (SDI), together with the DMs defined by Pang et al. (2018). 255

Fig. 8.30: Fragility functions for the PFM of slab damage followed by internal erosion, considering the DMs established by Pang et al. (2018). 256

Fig. 8.31: Fragility functions for the "Severe" damage level, for three PFM considering the criteria of Swaisgood (2014) for overtopping, Regina (2021) for global instability, and Pang et al. (2018) for slab damage. 257

Fig. 8.32: Linear regression in logarithmic space to obtain the fragility function using CA, for the "Moderate" damage level of the criterion of Swaisgood (2014), PFM of overtopping, and PGA as intensity measure. LR stands for Linear Regression, whereas β is the logarithmic standard deviation. 260

Fig. 8.33: Fragility function via CA for the "Moderate" damage level defined by Swaisgood (2014), PFM of overtopping, and the PGA as intensity measure. 260

Fig. 8.34: Fragility functions via CA for the PFM of overtopping and DMs defined by Swaisgood (2014), considering two peak intensity measures: a) PGA, and b) PGV. 261

Fig. 8.35: Fragility functions via CA for the PFM of overtopping and the DMs defined by Swaisgood (2014), considering three integral intensity measures: a) I_A, b) CAV, and c) I_H. 262

Fig. 8.36: Fragility functions via CA for the PFM of global instability and DMs set by Regina (2021), considering two peak intensity measures: a) PGA, and b) PGV. 264

Fig. 8.37: Fragility functions via CA for the PFM of overtopping and the DMs defined by Regina (2021), considering three integral intensity measures: a) I_A, b) CAV, and c) I_H. 265

Fig. 8.38: Comparison of fragility function via CA, for the PFM of global instability (GI) and overtopping (O), in terms of PGV. 266

Fig. 8.39: Fragility functions for the PFM of overtopping using the probabilistic capacity model from He & Rathje (2024), considering two peak intensity measures: a) PGA, and b) PGV. 269

Fig. 8.40: Fragility functions for the PFM of overtopping using the probabilistic capacity model from He & Rathje (2024), considering three integral intensity measures: a) I_A, b) CAV, and c) I_H. 270

Fig. 8.41: Comparison of fragility functions for the PFM of overtopping using the deterministic definition of the DMs from Swaisgood (2014) and the probabilistic capacity model of He & Rathje (2024), considering two intensity measures: a) PGA, and b) I_H. 272

Fig. 8.42: Criteria based on magnitude-distance to start a post-event inspection on dams (Tani, 1999; MIT, 2002; ICOLD, 2016b; MIT, 2017). 274

Fig. 8.43: Schematic diagram of the proposed EEWS for an embankment dam with all its components (Barbagelata et al., 2024). 277

Fig. 8.44: Array of seismic stations for the local dam monitoring, with the minimum (solid) and the recommended (dashed) locations (Barbagelata et al., 2024). 278

Fig. 8.45: Schematic view of a regional seismic network for the ground motion estimation at the dam (Barbagelata et al., 2024). 279

Fig. 8.46: Schematic illustration of the process to obtain the DSP from the fragility functions, knowing the measured value of the intensity measure (im), and comparing it to the respective thresholds. 282

Fig. 11.1: Labeling used for the identification of the instruments. 325

Fig. 11.2: Location and records of piezometers of Section A-i. 326

Fig. 11.3: Location and records of piezometers of Section A-ii. 327

Fig. 11.4: Location and records of piezometers of Section B-i. 328

Fig. 11.5: Location and records of piezometers of Section B-ii. 329

Fig. 11.6: Location and records of piezometers of Section B-iIi. 330

Fig. 11.7: Location and records of piezometers of Section C-i. 331

Fig. 11.8: Location and records of piezometers of Section C-ii. 332

Fig. 11.9: Location and records of piezometers of Section C-iii. 333

Fig. 11.10: Location and records of piezometers of Section D. 334

Fig. 11.11: Location and records of piezometers of Section E-i. 335

Fig. 11.12: Location and records of piezometers of Section E-ii. 336

Fig. 11.13: Location and records of piezometers of Section E-iii. 337

Fig. 11.14: Location and records of piezometers of Section E1-i. 338

Fig. 11.15: Location and records of piezometers of Section E1-ii. 339

Fig. 11.16: Location and records of piezometers of Section F. 340

Fig. 11.17: Location and records of piezometers of Section G-i. 341

Fig. 11.18: Location and records of piezometers of Section G-ii. 342

Fig. 11.19: Location and records of piezometers of Section G-iii. 343

Fig. 11.20: Location and records of standpipe piezometers (freatimeters) of the downstream foot -i. 344

Fig. 11.21: Location and records of standpipe piezometers (freatimeters) of the downstream foot -ii. 345

Fig. 11.22: Location and records of standpipe piezometers (freatimeters) of the downstream foot -iii. 346

Fig. 11.23: Hazard curves in terms of PGA for all the seismic sources, and their combination (Total Hazard). Evidenced the return periods for every level of the ground shaking selected. 348

Fig. 11.24: Hazard curves in terms of Sa(0.5s) for all the seismic sources, and their combination (Total Hazard). Evidenced the return periods for every level of the ground shaking selected. 348

Fig. 11.25: Hazard curves in terms of Sa(1.0s) for all the seismic sources, and their combination (Total Hazard). Evidenced the return periods for every level of the ground shaking selected. 349

Fig. 11.26: Uniform hazard spectra (UHSs) for the six return periods considered. 350

Fig. 11.27: Disaggregation charts for T_R = 144 y, for a) PGA, and b) Sa(0.5s). 351

Fig. 11.28: Disaggregation charts for T_R = 475 y, for a) PGA, and b) Sa(0.5s). 351

Fig. 11.29: Disaggregation charts for T_R = 975 y, for a) PGA, and b) Sa(0.5s). 351

Fig. 11.30: Disaggregation charts for T_R = 2475 y, for a) PGA, and b) Sa(0.5s). 352

Fig. 11.31: Disaggregation charts for T_R = 4975 y, for a) PGA, and b) Sa(0.5s). 352

Fig. 11.32: Disaggregation charts for T_R = 9975 y, for a) PGA, and b) Sa(0.5s). 352

Fig. 11.33: Response spectra for the records selected and scaled for T_R = 144 y, together with their mean spectrum and respective UHS. 353

Fig. 11.34: Response spectra for the records selected and scaled for T_R = 475 y, together with their mean spectrum and respective UHS. 355

Fig. 11.35: Response spectra for the records selected and scaled for T_R = 975 y, together with their mean spectrum and respective UHS. 357

Fig. 11.36: Response spectra for the records selected and scaled for T_R = 2475 y, together with their mean spectrum and respective UHS. 359

Fig. 11.37: Response spectra for the records selected and scaled for T_R = 4975 y, together with their mean spectrum and respective UHS. 361

Fig. 11.38: Response spectra for the records selected and scaled for T_R = 9975 y, together with their mean spectrum and respective UHS. 363

List of Tables

Table 2.1: Main characteristics of common types of embankment dams. 23

Table 2.2: Research works with examples of fragility functions for embankment dams found in the literature (in English). 63

Table 3.1: Results from ultrasonic tests and unconfined compression tests done over three rock samples, where ρ_R is the rock matrix density, f_u is the unconfined compression strength, E_s is the static elastic modulus and E_d is the dynamic elastic modulus, while G_d is the dynamic shear modulus and v the Poisson ratio. 85

Table 3.2: Young modulus for the monotonic and the unload-reload obtained from load plate tests made of 2B material. 100

Table 3.3: Summary of the monitoring system of Potrerillos CFRD, listing the type, number of installed instruments, and frequency of readings for each kind of sensor, adapted from Espinosa et al. (2010). 101

Table 3.4: Properties of the selected events and reference weak motion records. 122

Table 5.1: Crustal sources geometrical definitions and MCE (Mingorance, 2024). 150

Table 5.2: Average slip rate for all the crustal sources, and the methodology used for their estimation (Mingorance, 2024). 152

Table 5.3: Comparison of b-values for crustal events in the Cuyo region available in literature, and the one calculated in the present work. 155

Table 5.4: Geometry of the intraslab source, based on the geometry of the subducted slab and seismicity. .. 158

Table 5.5: Comparison of b-values for intraslab events available in literature and the present work. 160

Table 5.6: Return periods, related time windows, and related probabilities of exceedance. 169

Table 5.7: Event and site characteristics, and the scaling factor for the records corresponding to the return period T_R = 2475 y. 177

Table 5.8: Selected intensity measures of the scaled ground motions, for T_R = 2475 y. 178

Table 6.1: Constitutive models considered for every soil and stage, and the code to distinguish them. 183

Table 6.2: Parameters adopted for the Mohr-Coulomb model for BR, GC, and COW. 184

Table 6.3: Parameters from the calibration of the Plastic Hardening model for alluvial soils. 185

Table 6.4: Parameters from the calibration of the Plastic Hardening model for the soils of the dam body. ... 186

Table 6.5: Parameters from the calibration for the elastic reinforced concrete slab and interface. 187

Table 6.6: Parameters from the calibration of the soils that use the PM4Sand constitutive model. 195

Table 6.7: Parameters from the calibration of the soils that use the UBCHyst constitutive model. 199

Table 6.8: Hydraulic conductivity (permeability) and porosity for all the soils considered in the model. 199

Table 8.1: Damage levels in terms of NCS_{DH+AT} and permanent crest settlement adopting DH+AT=147m, using the criterion from Swaisgood (2014). 219

Table 8.2: Damage levels in terms of NCS_{DH}, and permanent crest settlement adopting DH =109.4m, using the criterion from Pells & Fell (2003). 220

Table 8.3: Damage levels in terms of NCS_{DH+AT}, and permanent crest settlement adopting DH+AT=147m, established by the criterion from Pang et al. (2018). 221

Table 8.4: Damage levels in terms of NCS_{DH+AT}, and permanent crest settlement adopting DH+AT=147m, established by the criterion from Pang et al. (2019). 221

Table 8.5: Damage levels in terms of NCS_{DH+AT} and permanent crest settlement adopting DH+AT=147 m, using the criterion from Aliberti et al. (2019). 222

Table 8.6: Damage levels in terms of freeboard reduction and permanent crest settlement considering a minimum freeboard of 7 m. 223

Table 8.7: Parameters of the lognormal distribution defined in Eq. 8.3 to describe the capacity models for the permanent crest settlement of embankment dams, together with the median value for the three damage levels established by He & Rathje (2024). 224

Table 8.8: Damage levels considering the displacements of well-defined sliding mass as a damage measure, as adopted by Regina (2021). 226

Table 8.9: Damage levels for the displacement of a well-defined sliding mass, adopted by Vecchietti et al. (2022) from Idriss (1985). 227

Table 8.10: Damage levels proposed by Pang et al. (2018) for the slab damage index (SDI). 229

Table 8.11: Values of Sa(0.5s) for the five stripes considered for the derivation of fragility functions using the MSA approach, coinciding with the initial five T_R of the PSHA. 233

Table 8.12: Return period, time window, probability of exceedance, and Sa(0.5s) for T_R = 9975 y. 238

Table 8.13: Parameters of the lognormal fragility functions, for the damage levels using the criterion of Swaisgood (2014), for the PFM of overtopping. 240

Table 8.14: Parameters of the lognormal fragility functions, for all the damage levels established by the criterion of Pells & Fell (2003), PFM of overtopping. 242

Table 8.15: Parameters of the lognormal fragility functions, for the damage levels set by Pang et al. (2018), PFM of overtopping. 244

Table 8.16: Parameters of the lognormal fragility functions, for the damage levels following the criterion of Pang et al. (2019), PFM of overtopping. 245

Table 8.17: Parameters of the lognormal fragility function, for all the damage levels using the criterion of Aliberti et al. (2019), PFM of overtopping. 247

Table 8.18: Parameters of the lognormal fragility function, for all the damage levels using the criterion based on freeboard reduction, for the PFM of overtopping. 249

Table 8.19: Parameters of the lognormal fragility function, for all the damage levels using the criterion adopted by Regina (2021), PFM of global instability. 252

Table 8.20: Parameters of the lognormal fragility function, for all the damage levels using the criterion defined by Idriss (1985), for the PFM of global instability. 254

Table 8.21: Parameters of the lognormal fragility functions, for the PFM slab damage followed by internal erosion, using the DMs set by Pang et al. (2018). 256

Table 8.22: Parameters of the lognormal fragility functions derived using CA, using the DMs proposed by Swaisgood (2014) for the PFM of overtopping, and several intensity measures (PGA, PGV, I_A, CAV, I_H).. 263

Table 8.23: Parameters of the lognormal fragility functions derived using CA, using the DMs adopted by Regina (2021) for the PFM of global instability, and several intensity measures (PGA, PGV, I_A, CAV, I_H). 266

Table 8.24: Parameters of the adjusted PSDM for the five selected IM (PGA, PGV, I_A, CAV, I_H)..... 268

Table 8.25: Parameters of the fragility functions derived using the probabilistic capacity model developed by He & Rathje (2024), for the PFM of overtopping and several IMs (PGA, PGV, I_A, CAV, I_H)..... 271

Table 11.1: Table with the values of spectral acceleration Sa(T) of the UHSs. 350

Table 11.2: Event and site characteristics, and the scaling factor of the records for T_R = 144 y..... 353

Table 11.3: Selected intensity measures of the scaled ground motions, for T_R = 144 y..... 354

Table 11.4: Event and site characteristics, and the scaling factor of the records for T_R = 475 y..... 355

Table 11.5: Selected intensity measures of the scaled ground motions, for T_R = 475 y..... 356

Table 11.6: Event and site characteristics, and the scaling factor of the records for T_R = 975 y..... 357

Table 11.7: Selected intensity measures of the scaled ground motions, for T_R = 975 y..... 358

Table 11.8: Event and site characteristics, and the scaling factor for the records corresponding to the return period T_R = 2475 y..... 359

Table 11.9: Selected intensity measures of the scaled ground motions, for T_R = 2475 y..... 360

Table 11.10: Event and site characteristics, and the scaling factor of the records for T_R = 4975 y..... 361

Table 11.11: Selected intensity measures of the scaled ground motions, for T_R = 4975 y..... 362

Table 11.12: Event and site characteristics, and the scaling factor of the records for T_R = 9975 y..... 363

Table 11.13: Selected intensity measures of the scaled ground motions, for T_R = 9975 y..... 364

1. Introduction

Embankment dams are among the largest infrastructure projects ever constructed, and their multiple purposes make them vital assets for the regions in which they are situated. This is especially true in arid regions such as northern Mendoza, Argentina, where effective water resource management is essential for its use in agricultural production. The relevance of the wine industry in the economy and the history of the province makes water management a topic of paramount importance. In this context, large dams and reservoirs like the Potrerillos Dam play a critical role in regulating river flows and administrating water discharge, guaranteeing its availability along the period when artificial irrigation is essential.

When large dams are constructed in areas of high seismic activity, concerns arise not only for the potential interruptions to their operation but also about their structural integrity. The stability of the dam and appurtenances could be severely compromised during a strong earthquake and, in extreme cases, lead to collapse. Over the years, numerous tools have been developed to evaluate the seismic performance of embankment dams, accompanied by rigorous safety requirements aimed at preventing structural collapse and uncontrolled release of the reservoir. In this context, fragility functions could be introduced to provide a new perspective for assessing the seismic safety of embankment dams.

Performance-based earthquake engineering (PBEE) and seismic risk assessments are not new concepts to the earthquake engineering and dam engineering communities; however, their scope and applications have expanded in recent years as the field shifts toward more reliable methods that account for uncertainty and evaluate performance in terms of risk or loss metrics.

In this context, the adoption of quantitative risk evaluations in the field of dam engineering by several agencies worldwide (ICOLD, 2005; SPANCOLD, 2012; FERC, 2016; USBR & USACE, 2019) represents a significant progress in dam safety evaluation. The adoption of risk-based approaches, not only to assess the safety condition of existing dams but also to support better decision making through risk informed approaches, is a major enhancement towards a more reliable evaluation of the seismic performance of large dams. Fragility functions are a key component of quantitative risk assessments and probabilistic PBEE evaluations, as they provide the link between the intensity of seismic ground shaking and the probability of reaching specific damage states, related to a particular failure mode.

Few studies on the development of fragility functions for embankment dams have explored some of the various aspects involved in their formulation. For instance, Regina et al. (2023) examined the influence of both simple and advanced constitutive models while also investigating the selection of an optimal intensity measure for ground shaking. On the other hand, Pang et al. (2018) developed fragility functions for concrete face rockfill dams, and McCann et al. (2023) explicitly incorporated both epistemic and aleatoric uncertainties, relying on expert judgment at each stage of the derivation process for use in seismic risk assessments.

However, a framework that brings transparency to the process of deriving case specific fragility functions for embankment dams is still missing. Examples found in literature show considerable variation in the approaches utilized, not only in the final calibration of the fragility functions but throughout the entire process, from the definition of input motions to the modeling techniques to capture the seismic response. This variability often makes it difficult to assess the quality of the resulting outputs in the context of their intended application. Furthermore, the connection between fragility functions and the potential failure modes that a given dam could experience during strong earthquakes is often overlooked, and there is frequently a lack of alignment between the seismic hazard at the dam site and the ground motions used for fragility derivation.

In this work, a methodological framework for deriving case-specific fragility functions for embankment dams is presented. The framework is illustrated through the calibration of fragility functions for Potrerillos Dam, a Concrete Face Rockfill Dam (CFRD) located in the north of Mendoza Province, the most seismically active region of Argentina.

Central to the framework is the emphasis on considering the specific characteristics of the dam and site conditions, ensuring that the resulting fragility functions remain case-specific, and highlighting the importance of this consideration for future applications. The treatment of uncertainty at each step of the calibration process is discussed and addressed when feasible, along with alternative methods that could be applied. A reasoned evaluation of the results is finally provided, concluding with an example of how fragility functions can be used as part of an earthquake early warning system.

The results obtained show that diverse aspects of the process can significantly influence the final fragility functions, and how the proposed framework helps to systematically identify and handle these critical aspects in a consistent manner. The integration of fragility functions into

an earthquake early warning system is also presented as a promising application of the developed curves, contributing to ongoing efforts to mitigate the seismic risk of large dams. Additionally, the need for improved tools to define damage in embankment dams following earthquakes, as well as the implications of deriving case-specific fragility functions instead of generic fragility functions is discussed.

The application of the proposed framework to other dams offers an opportunity to improve the traceability of the results and to develop more reliable fragility functions for their use in seismic risk assessments, performance-based evaluations, emergency management through their integration into Earthquake Early Warning Systems (EEWS), and progress toward Risk Informed Decision Making (RIDM) in the management of embankment dams in seismically active regions.

1.1 Scope of the research

This work aims to present a methodological framework for the derivation of case-specific fragility functions for embankment dams, illustrated throughout the assessment of seismic performance and fragility of Potrerillos Dam, a CFRD located in northwestern Mendoza Province, Argentina. Characterizing the seismic response of the dam within the unified environment provided by fragility functions offers an opportunity to better identify the most critical failure modes according to the adopted performance criteria. The characteristics of dam and foundation, and the tools used to evaluate seismic performance across a wide range of ground motion intensities and levels of seismic damage also played a key role in the seismic safety assessment. The integration of the case-specific fragility functions into an EEWS is also explored as an alternative application, with potential benefits for seismic risk mitigation and post-earthquake emergency management in a Risk Informed Decision Making (RIDM) framework. Some specific objectives are:

- A rational interpretation of site conditions and soil characteristics of the dam and foundation with the information available from the project and construction stages, exploring the variability of the geological conditions and characterizing the geomaterials based on the number and quality of the existing data.
- Comprehension of the past hydraulic and loading history of the dam by interpreting the monitoring records of the surveying system, to establish the long-term static conditions of the dam and obtain useful information for calibration purposes.

- Forecasting of the seismic actions at the dam site through a site-specific probabilistic seismic hazard analysis (PSHA), followed by an adequate selection and scaling of strong motion records oriented to the derivation of seismic fragility curves.
- Building a reliable numerical model able to reproduce the complex response of the dam under seismic actions, and a further evaluation of the results from several Nonlinear Dynamic Analyses (NDAs), analyzing their ability to describe the dynamic response of the dam, capturing the identified Potential Failure Modes (PFMs).
- Calibration of parametric seismic fragility functions for the main seismically driven failure modes identified for the dam-foundation system, the description of their applications, and a proposal for using the fragility functions in post-event safety evaluations.

The integration of procedures from diverse scientific disciplines also implies an improvement in the understanding of the processes necessary to describe the seismic performance of such a complex and critical infrastructure as the large dams. In addition, this work could be used to inform better monitoring practices for embankment dams, particularly regarding how monitoring data could be integrated in the evaluation of the dam response and validation of advanced numerical models.

Moreover, a careful description of the procedure here implemented to derive fragility functions, starting from the geological and geotechnical information until the fitting procedures and applications of fragility curves, discussing the benefits of the selected approaches and possible alternatives, tracking the sources of uncertainty and managing their impact along the process, and identifying where improvements could be made are the main goals of this dissertation.

Across the text, alternatives to certain approaches or assumptions will be briefly discussed and referenced, aiming to point out the variety of feasible methodologies to handle each problem. Ending up with a well-documented case study able to be reproduced in other dams is also a scope of this work.

1.2 Dissertation outline

Chapter 2 introduces the reader to the main topics covered by the dissertation, briefly describing some helpful concepts to enhance the understanding of the remaining chapters.

The dissertation comprises twelve chapters, of which Chapter 1 introduced the work and presents the scope and the main purposes of the research.

In the first part of Chapter 3, a description of the methodology proposed to derive seismic fragility is presented, together with a brief depiction of the dam and appurtenances. Then, a summary of the geological and geotechnical information available and the analysis of the monitoring data since the construction of the dam is presented.

Chapter 4 presents a preliminary identification of the potential failure modes of the dam to support the development of case-specific fragility functions. While this is not intended to serve as a formal potential failure mode analysis, the preliminary description of a cluster of feasible failure modes that could occur in the dam is essential to enhance the validity of the derived fragility functions in the context of risk assessments.

Chapter 5 is completely devoted to the seismic hazard and record selection, with a first description of the seismotectonic environment and seismic history of the region, followed by a site-specific PSHA and ending with the selection and scaling of records to be used as input motion in the numerical analyses.

Chapters 6 and 7 include all the activities related to the numerical models. Chapter 6 presents the building of the numerical model, describing the several modeling stages and the procedures adopted for the calibration of the constitutive models. Then, Chapter 7 summarizes some characteristic results of numerical analyses, and a first assessment of seismic performance is done based on the output of the numerical analyses.

The calibration of the fragility functions is carried out in Chapter 8 based on the results from numerical analyses, using different approaches, thresholds, and intensity measures to derive fragility functions for every PFM. The chapter concludes with an application of fragility functions as a component of an EEWS.

Finally, Chapter 9 discusses the outputs of the work, presents the main conclusions of the dissertation, and outlines the ideas that emerged during the development of the research and would be prospects for future work.

The final two chapters present the cited bibliography and appendices, which contain useful information referenced but not included in the main body of the text.

2. Background

2.1 General characteristics of embankment dams

Large dams are among the most extensive and complex infrastructure projects worldwide, and geotechnical engineering plays a crucial role in their design and construction. In addition, every dam is itself a prototype as the site conditions, materials, dam usages, and the state of knowledge at the moment of construction are different between projects, and all of them could have a great impact on the project and further seismic performance of the dam.

Embankment dams are characterized by using soils and/or rocks as their primary structural material, often comprising the entire volume of the dam body. The geometry of this type of dam results from the mechanical behavior of the geomaterials conforming the dam body and the loads to which are subjected, and has evolved since the construction of ancient dams (Fahlbusch, 2009). Their cross-section typically consists of a trapezoidal shape which at the bottom adapts to the valley topography when follows the dam axis, building up in this way the dam body. The dam axis is ideally straight and perpendicular to the mainstream direction, but it may also be inclined, polygonal, or curved depending on the site conditions. Berms can be included on the upstream and downstream dam faces to enhance its stability. Several cross-sections for different types of embankment dams are presented in Fig. 2.1.

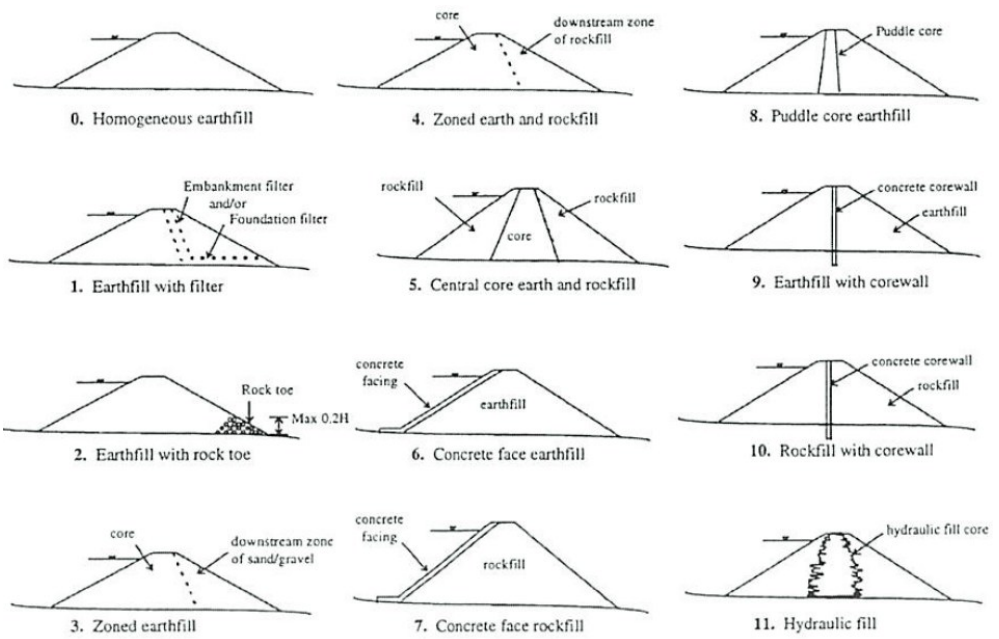


Fig. 2.1: Typical cross-section of several types of embankment dams (Pells & Fell, 2002).

Embankment dams can be grouped with respect to the materials used for the construction of cores and shells, and how they control the seepage, as presented in Table 2.1.

Type	Core/face material	Shell material	Seepage control
Homogeneous earthfill	Same as shell	Low permeability fines-gravel mixtures	Long seepage path and low permeability
Zoned earthfill	Fine-grained soils	Sand-gravel mixtures	Central impervious core
Rockfill with central core	Fine soil or concrete	Rockfill	Low-permeability core
Rockfill with upstream face	Concrete or asphalt concrete	Rockfill or sand-gravel mixtures	Impervious upstream face
Hydraulic fill	Fine-grained soil	Coarse-grained soils	Low-permeability core

Table 2.1: Main characteristics of common types of embankment dams.

A common feature of embankment dams, as seen in Table 2.1, is their zoning, which seeks to optimize the characteristics of every geomaterial used in construction. In addition, the zoning try to enhance the overall hydraulic and mechanical response of the dam with the available materials. Homogeneous dams without upstream facing used in the past, are now limited to small dams or levees, as they are less convenient in comparison with other alternatives for large dams. This is mainly because of the difficulty of finding a unique material that has both good hydraulic and mechanical characteristics.

Zoned dams have in general a central core of fine-grained soils that work as an impervious barrier, surrounded by clean sand-gravel filters followed by an upstream and a downstream gravel shell. The filters should have a specific gradation to limit the migration of core material and reduce the susceptibility to internal erosion (FEMA, 2011), while shells must provide mechanical stability to the assembly.

Because of this configuration, the upstream shell and core are typically saturated when the downstream shell is the most of the time unsaturated. Shells are mainly constructed with sand-gravel mixtures (SGM) coming from the river alluvium or quarries close to the construction site, and they are densified by different compaction techniques to improve their mechanical behavior (Tatsuoka & Gomes Correia, 2018). The zoning can vary in shape and size, resulting in different configurations with their respective pros and cons, which should be captured through a proper analysis and design.

In contrast, in rockfill dams the dam body is composed of dumped or compacted rockfill material, with rock blocks of different gradation coming from blasting or natural deposits. The impervious barrier can be composed of a fine-grain soil core, or an upstream face or core of a manufactured material (e.g., asphalt concrete, regular concrete, geosynthetics, etc.). The interaction between the impervious barrier and the rockfill is a critical aspect in design to guarantee the integrity of the assembly, as well as the union between the impervious barrier and the abutments or cut-off walls in the case of dams placed over alluvial material. Both aspects have led to the inclusion of a cushion (o transition) layers between the rockfill and the concrete/asphalt face (Fig. 2.2a), and the construction of lateral plinths to join the rock abutments and the impervious barrier, two key components in modern concrete face rockfill dams (ICOLD, 2010).

The use of dumped rockfill had led in past to large settlements and deflection of the impervious barrier during the first full impoundment, as densification continues with the increase of the hydrostatic forces (Clements, 1984). This aspect promoted the use of compacted geomaterials in the dam body to reduce volumetric deformation of the dam body and control the settlements. In some cases, the large volume of high-quality rockfill needed for the dam body could restrict the choice of this type of dam, but rockfill can be replaced by compacted alluvial sand-gravel mixtures without loss of performance (Cruz et al., 2009). The use of sand-gravel mixtures requires the inclusion of clean gravel drains within the dam body to compensate for the lower permeability of the alluvial material in contrast with the highly permeable rockfill, and it is necessary to control the seepage in case the impervious barriers are damaged. Special attention should be given as well to the design of the drainage system and the contact between the dam body and the rock abutments, to ensure good hydraulic performance of the dam in wide-ranging load conditions (Choo et al., 2013).

In the same way as compaction plays an important role in the response of rockfill dams, old earth dams constructed using hydraulic filling techniques were deprecated as their deficiencies in material densification make them susceptible to liquefaction during earthquakes, as occurred in famous case histories as the Lower San Fernando dam (ICOLD, 2001). However, this is still a concern for the retrofit of old hydraulic fill dams and some particular types of tailing dams (Valenzuela, 2015).

One of the major advantages of embankment dams, besides their flexibility in design and the use of locally available geomaterials, is their adaptability to a wide range of foundation conditions. Embankment dams can be safely built over deep alluvial deposits with a correct

design (Wen et al., 2022), incorporating cut-off walls linked to the impervious element in the dam to control the seepage along all the impervious barriers (Sainov, 2020).

In the case of CFRD over deep alluvial deposits, the cut-off wall upstream of the dam should be connected with the concrete slab of the dam to secure the watertightness, but allowing some relative movement between both independent elements. A feasible solution is linking the valley (or floating) plinth and the cut-off wall with a couple of slabs furnished with water stop joints (Fig. 2.2b), getting a flexible yet impervious solution.

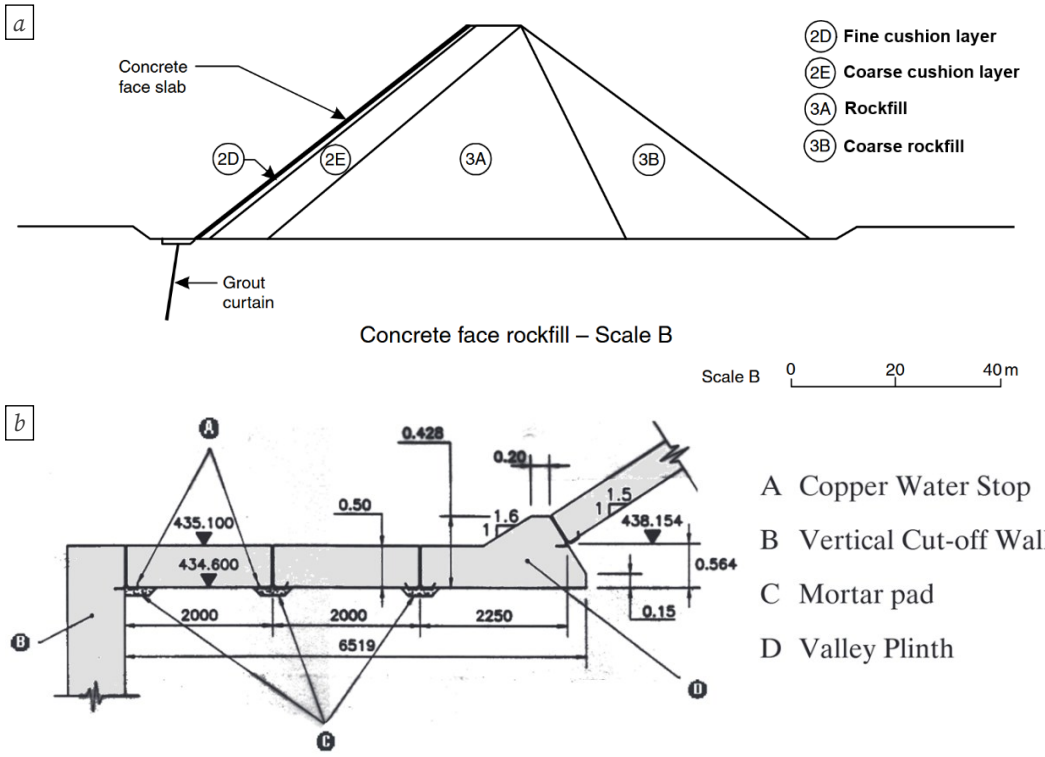


Fig. 2.2: a) typical cross section and zoning of a CFRD dam (Fell et al., 2014), and b) connection between slab and cut-off-wall, example from Puclaro CFRD (ICOLD, 2010)).

This brief description does not intend to be extensive and highlights only a few useful aspects of embankment dams, with many important details omitted for the sake of brevity and because they are beyond the scope of this introduction. More advanced aspects related to embankment dam analysis, design, and construction can be explored in specific literature of each topic (Fell et al., 2014).

2.2 Evaluation of seismic performance of embankment dams

The definition of the seismic performance of an embankment dam involves many aspects from diverse branches of civil engineering. Furthermore, knowledge related to each topic has evolved through the years with experiences from the experience of case histories and advances in research and professional practice, all of them driving the development of advanced tools for analysis and design. Following the performance-based earthquake engineering workflow presented in Fig. 2.3, it is evident that the evaluation of seismic performance involves many different components, some of which will be briefly described in the next sections.



Fig. 2.3: PBEE framework illustrating all its components (Kramer, 2024)

2.3 Seismic hazard assessment

The forecasting of the ground shaking during earthquakes can be approached by several strategies and entails a requirement for the design and analysis of any civil infrastructure sited in a seismically active region.

For large dams in general and embankment dams in specific, guaranteeing safety during and after a seismic event usually requires the characterization of the seismic hazard through site-specific seismic hazard studies. The complexity of these analyses increases with the consequences of a possible dam failure, often requiring the intervention of specialists to ensure reliable results (ICOLD, 2016a).

Approaches such as Deterministic Seismic Hazard Analysis (DSHA) (Kramer, 1996), Probabilistic Seismic Hazard Analysis (PSHA) (Baker et al., 2021), or physics-based ground motion simulations (Taborda & Roten, 2015), and others methodologies derived from these three are the most common procedures currently used in engineering practice and research to estimate earthquake strong motions, briefly described next.

DSHA identifies an individual earthquake scenario, defined by a magnitude (M) and a particular source-to-site distance (R), for each relevant seismic source. Then, a probability level set as an entire number of standard deviations above the median (0, 1, or 2) is specified to obtain the magnitude of the ground shaking in terms of a given Intensity Measure (IM) using specific Ground Motion Models (GMM), where IMs are quantitative parameters that

summarize key characteristics of seismic ground shaking, while GMMs are statistical models developed from empirical data and or simulations that relate seismic source and site parameters to the expected level of ground shaking.

The larger ground motion from any single scenario is used as the design ground motion (Abrahamson, 2006). Other relevant characteristics that could influence the ground shaking as site conditions, fault type, and seismotectonic environment, among others, are also introduced as part of the seismic scenario during the calculations.

This method is appropriate for regions where sufficient data is available for the key parameters that characterize the earthquake scenario, guaranteeing not to fall in excessively conservative bounding values for such parameters that could lead to a grossly excessive prediction of the seismic hazard (IAEA, 2022). However, some authors have opposite opinions about its applicability and use (Bommer, 2002; Krinitzsky, 2002; McGuire, 2001) as far as this method does not present a straightforward approach to account for the inherent variability in the characteristics of the seismic scenario.

Instead, PSHA can consider several earthquake scenarios at once and explore the probability of exceeding a particular ground motion intensity for a given time window, including the uncertainty in the definition of the seismic scenario. However, it is precise to define only physically possible earthquake scenarios and set the range of variation of the seismic source parameters to accurately manage the uncertainty in the calculations, being this approach is more suitable when the earthquake scenario characteristics are not clearly defined (Abrahamson & Bommer, 2005). On the other hand, even if the seismic hazard is not presented as straightforward as in the DSHA, the results from a PSHA can give a clear overview of the seismic hazard as a whole, bringing useful information for the selection of strong ground motion records, such as the Uniform Hazard Spectra (UHS) and the disaggregation of the seismic hazard.

Lastly, the physics-based ground motion simulations attempt to predict the ground motion generated by an earthquake using numerical models that explicitly incorporate the physics of rupture dynamics and seismic wave propagation throughout the Earth's crust, being able to capture topographic or stratigraphic effects at upper layers. The results obtained are the most complete among all the methodologies as they can directly record the ground motion at any point of the modeling domain, capturing the time and space variability of the seismic wave propagation. However, the complex definition of the rupture process, calibration of

parameters, model validation, and the computational resources required for every run limit their application (Rosti et al., 2023). Still, its use for engineering purposes is increasing with the current computational capabilities and new information about earthquake sources (Baker et al., 2014).

Extending the description of the PSHA, as will be used in this work, this method was introduced during the late sixties in parallel by the working groups of Allin Cornell and Luis Esteva (McGuire, 2008). The most frequent version of this method (Cornell, 1968) uses the total probability theorem to evaluate the probability of exceedance of a certain level of shaking intensity given an earthquake scenario, $P(IM > im \mid EQ_j)$, where im is a particular value of intensity measure IM, and EQ_j is a particular seismic scenario usually described by its specific magnitude m, sources-to-site distance r, site conditions, etc.

Under the hypothesis of a Poisson distribution for the occurrence of seismic events, considered a good approach for engineering purposes (Cornell & Winterstein, 1988) and the small probability level of interest, the probability of exceedance can be converted to the mean annual frequency or rate of exceedance (Baker et al., 2021). This approach also makes it possible to relate the results to the reciprocal value of this rate, known as the mean return period (or simply return period), T_R (Eq. 2.1).

$$T_R = \frac{1}{\lambda} \qquad \textit{Eq. 2.1}$$

Hence, it is necessary to define the earthquake scenarios and seismicity for each source in terms of probability distributions, and set them all together in the so-called hazard integral, presented in general form in Eq. 2.2 for several seismic sources (Baker, 2013):

$$\underbrace{\lambda\left(IM > im\right)}_{\substack{\text{Rate of}\\ \text{exceedance}}} = \sum_{i=1}^{n_{sources}} \underbrace{\lambda\left(M_i > m_{\min}\right)}_{\text{Earthquake rate}} \left(\int_{m_{\min}}^{m_{\max}} \int_{0}^{r_{\max}} \underbrace{P\left(IM > im \mid m,r\right)}_{\text{Ground Motion Model}} \underbrace{f_{M,R}\left(m,r\right)}_{\substack{\text{M-R joint probability}\\ \text{distribution}}} dr\, dm \right)_i \qquad \textit{Eq. 2.2}$$

The explicit introduction of uncertainty in seismic hazard calculations constitutes a major advantage regarding the arbitrary and subjective nature of the definitions of the earthquake sources, the characterization of the seismicity based on incomplete catalogs, variability in ground motion models, etc. The main result of a PSHA is the so-called hazard curve (Fig. 2.4) that relates the mean annual rate of exceedance of several intensity levels of a specific IM, for a single earthquake scenario or a combination of them.

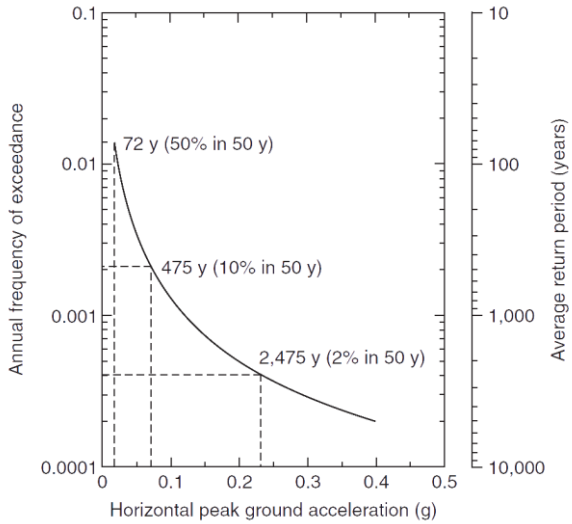


Fig. 2.4: Illustrative hazard curve for peak ground acceleration (PGA) (Somerville & Moriwaki, 2003)

At a basic level, PSHA can be split into five steps (Baker et al., 2021):

i. Specify the ground-motion intensity measure of interest.
ii. Specify the site properties that help to predict ground-motion intensity.
iii. Compute the locations, characteristics, and occurrence rates of all rupture (or earthquake) scenarios capable of producing damaging ground motions.
iv. Predict the resulting distribution of ground-motion intensity as a function of the site characteristics and each rupture scenario's properties.
v. Consider all possible ruptures and uncertainty in the resulting ground-motion intensity.

This procedure can also be grouped into three major steps: source characterization, ground motion definition, and hazard calculations, as shown in Fig. 2.5. Each step can grow in complexity concerning the site conditions, importance of the asset, and risk targets.

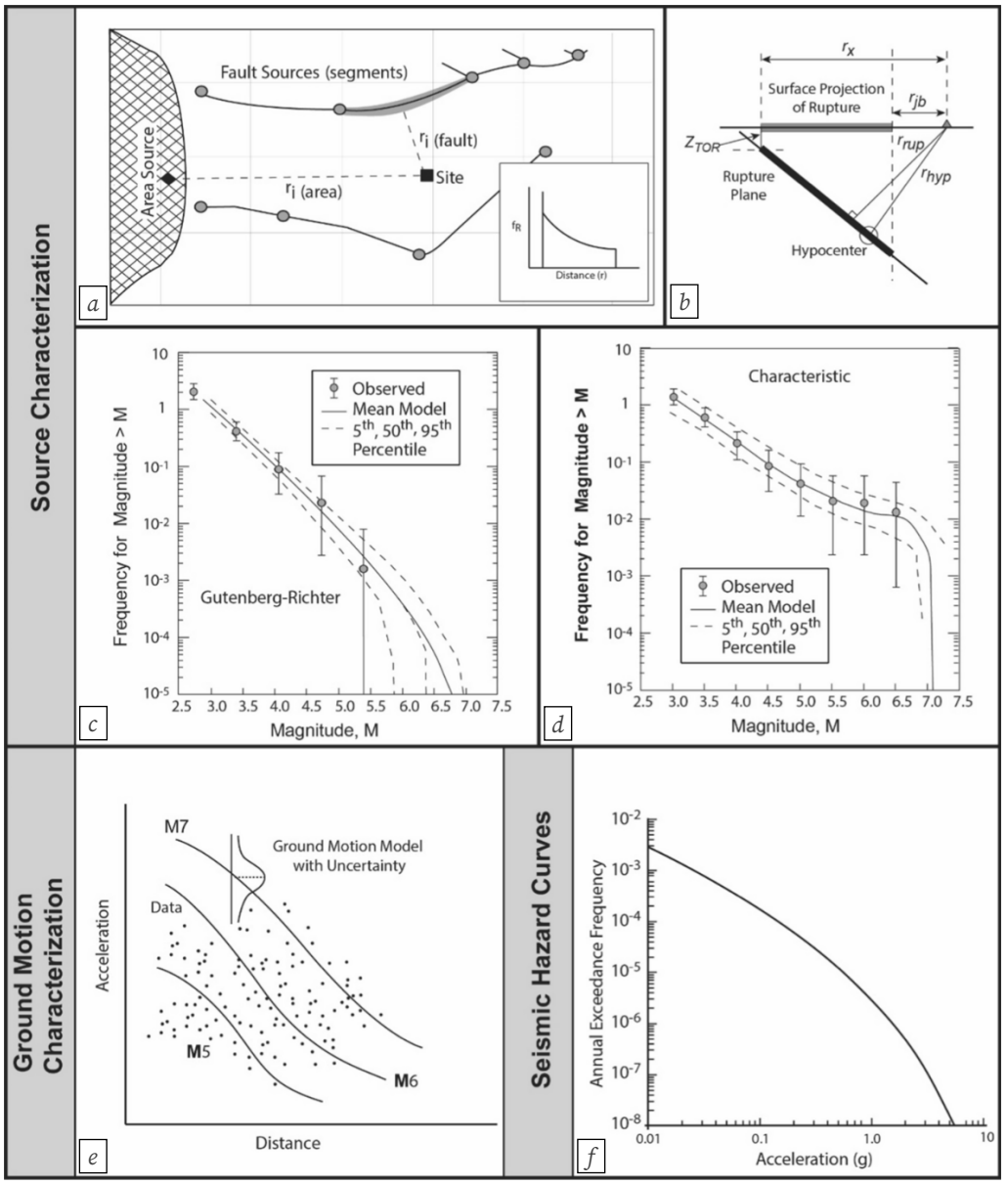


Fig. 2.5: Illustration of the steps involved in PSHA (Bommer, 2022; USNRC, 2018). Where a) diverse geometrical definitions of seismic sources; b) definition of the different sources-to-site distances; c) Gutenberg-Richter model of seismicity; d) Characteristics model of seismicity; e) GMMs for different magnitudes; and f) resulting hazard curve.

Once the site location and the characteristics related to seismic site response are set (i.e. equivalent shear wave velocity, topography, etc.), the seismic sources in the vicinity of the site need to be identified. This involves not only their geometrical definition but also their seismic activity, source mechanism, and any other information useful for better characterizing the seismic scenarios associated with each source A seismic scenario is understood as the combination of magnitude, source-to-site distance, and site conditions related to a specific

seismic event. These characteristics are then used to adjust specific mathematical models, like the Gutenberg-Richter model for the magnitude-frequency distribution (Gutenberg & Richter, 1944), which are expressed in terms of probabilities and introduced into the hazard integral to perform the hazard calculations.

Under Poissonian hypothesis, it is necessary to set a particular probability of exceedance and a time frame to interpret the results of the PSHA in terms of a given *IM*. Both parameters are closely related to the expected performance level and importance of the infrastructure under study. As an example, the design actions of many standards for buildings around the world correspond to a probability of exceedance of 10 % in 50 years, equivalent to a mean return period of $T_R = 475$ years.

The results of PSHA can also be analyzed in terms of the Uniform Hazard Spectrum (UHS), which is the result of combining the hazard curves for *IM* equal to the spectral accelerations at different structural periods (or periods), *T*. Then, for a given rate of exceedance (or return period) it is possible to have a spectrum that is representative of the selected hazard level.

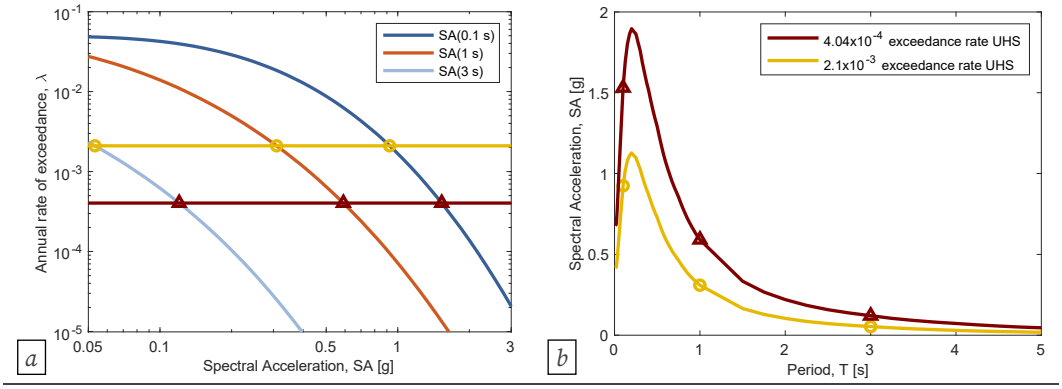


Fig. 2.6: Example of a UHS, indicating a) derivation from hazard curves of Sa at different periods, and b) the UHSs for two exceedance rates related to T_R = 475 and 2475 y (Baker et al., 2021).

Another product of the PSHA that provides useful information for the definition of seismic hazard is the disaggregation charts (Bazzurro & Cornell, 1999).

These charts, as shown in Fig. 2.7, aim to identify which of the seismic scenarios (or related sources) provide the largest contribution to the hazard condition $IM>im$. Formally, they represent the conditional probability distribution of *M*, *R*, and ε given that $IM>im$, where ε is the variable reflecting the relation between the value of *IM* relative to the median prediction using a GMM. The identification of the dominant mean causal magnitude and mean causal

distance in the disaggregation charts is crucial for the hazard-consistent strong-motion record selection for dynamic analyses and fragility evaluation (Sousa et al., 2017).

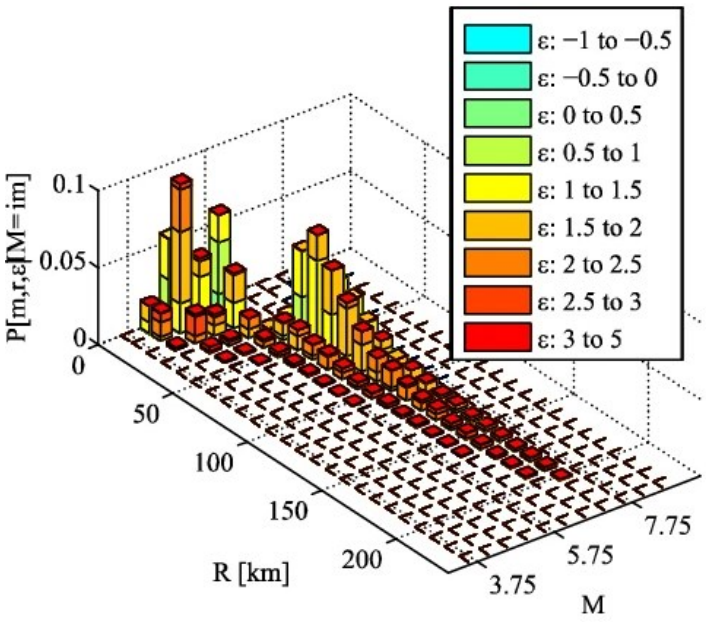


Fig. 2.7: Example of a disaggregation chart for Sa (0.5 s) and T_R = 475 y (Chioccarelli et al., 2019).

As a matter of fact, the acceleration time histories to be used as input motion in the dynamic analyses should be representative of the probable earthquakes that could occur at the site of interest. This condition has two requirements: the records must be consistent with the seismic hazard, and the signals should have similar characteristics to those expected at the site.

These requirements could be addressed using diverse approaches. One of the most widespread begins with the definition of the hazard level to be matched, in terms of an *IM* as the spectral acceleration at the first mode of vibration, $Sa(T_1)$, or the peak ground acceleration, *PGA*.

Then, a search for real strong motion records is performed in worldwide repositories, following a criterion that attempts to match the seismic scenario that, according to the disaggregation chart, contributes the most to the hazard expressed in terms of the given *IM*. This search should consider not just the pair M-R defined by the disaggregation chart, but also the faulting type, site conditions, seismotectonic environment, and the quality of the records (Watson-Lamprey & Abrahamson, 2006). In addition, the strong motion records must be processed using proper methodologies to avoid issues when used as input motion in numerical analyses (Boore & Bommer, 2005).

The recorded ground motions can also be significantly influenced by the local site conditions at the recording station (Williams et al., 1999). Therefore, the selection process should aim to match site characteristics as closely as possible to those at the location of interest. Tools such as seismic deconvolution can be used to retrieve motions at the bedrock level or the base of a numerical model from surface recordings, being known the subsurface conditions at the station (Pretell et al., 2019; Chowdhury et al., 2024).

Once the candidate records are identified, they must be modified to match the hazard condition established by the seismic hazard analysis. To achieve it, several strategies can be used, among which can be mentioned: linear scaling of the ground motions in the time domain (Bommer & Acevedo, 2004), in such a way that their average response spectrum match that representative of the seismic hazard at the site (e.g. UHS) at least within a range of periods that contains the natural period of the structure (Hancock et al., 2006), or use a Conditional Mean Spectrum (CMS) (Baker, 2011) or a combination of UHS and CMS (Kwong & Chopra, 2017) to scale the records at one particular period or a range that include the natural periods of the structure.

Once the scaling is performed, the acceleration time histories can be used as input motions in numerical analyses. More details regarding the approaches used in this work will be presented in Chapter 5.

2.4 Case histories of embankment dam response during earthquakes

Embankment dams are among the most damaged types of dams during earthquakes, but also the ones considered to have a good performance when they are correctly designed, being capable of withstanding substantial earthquake shaking with no detrimental effects (USSD, 2014). Site conditions, materials, and construction techniques can all play a big role in defining whether the seismic response of this type of dam will be satisfactory or not.

Case studies of both good and bad performances have contributed to understanding the response of embankment dams during earthquakes, but also helped to develop better tools for their seismic analysis and design, together with setting the thresholds of what is considered a bad or a good performance. As every case is itself a lesson, only a few notable examples are presented here to illustrate a specific aspect of the seismic response of this type of dam.

2.4.1 Lower San Fernando Dam - San Fernando earthquake, US (1971)

Probably one of the most noteworthy and better studied cases of the performance of a hydraulic fill dam under strong shaking, the nearly overtopping of the Lower San Fernando dam during the 1971 M_w 6.6 San Fernando earthquake was a clear proof of their susceptibility to liquefaction under strong ground motions. During the earthquake, a portion of the upstream shell liquefied (Seed et al., 1975), triggering a complex instability mechanism of the upstream slope that left the dam with a minimum freeboard concerning the reservoir level, as can be shown in Fig. 2.8.

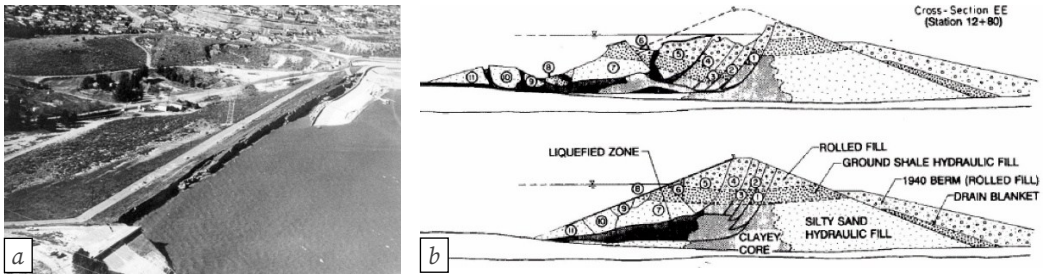


Fig. 2.8: a) aerial picture of the dam after the earthquake (USGS Archive), b) cross-section with the reconstruction of the cinematic mechanism of the sliding and the zoning (Seed et al., 1989)

Being also a well-documented case history of partial collapse of a dam, this case has allowed testing diverse approaches for assessing the response and reproducing the damage mechanism of the dam after the earthquake, as the works done by Seed et al., (1975), Castro et al., (1992) and Talbot et al., (2024), among others. This case sets a precedent in how the evaluation of the seismic safety of embankment dams is done.

2.4.2 Austrian and Lexington dams – Loma Prieta earthquake, US (1989)

During the 1989 M_W 6.93 Loma Prieta earthquake, more than 100 dams were affected within an 80 km radius of the epicenter. Although more than half were 18 m high or less, a number of large dams were strongly shaken and presented moderate damage (USSD, 1992). One of them was the Austrian dam, a 55 m high earth dam located above the projected northern segment of the fault. The dam was subjected to an estimated PGA of about 0.55-0.6 g and exhibited a permanent crest settlement of 0.76 m, presenting several longitudinal and transverse cracks in the crest, abutments, and spillway (Fig. 2.9).

Even if the dam was conceived as zoned with an upstream impervious zone and a downstream pervious zone, the mechanical and hydraulic properties of the material composing the dam

were roughly uniform. Being built using low plasticity clayey sand and clayey gravels, the dam behaves as a homogeneous dam, and the excess of pore water pressure generated by ground shaking dissipated relatively slowly, according to the piezometric levels, which took days after the event (Boulanger, 2019).

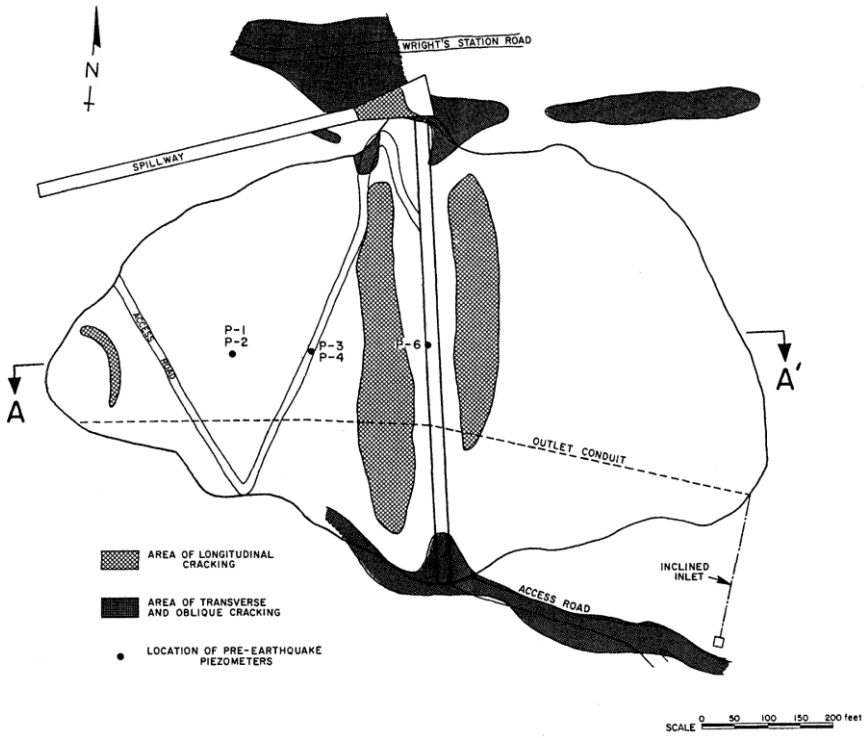


Fig. 2.9: Plan view of the areas with transverse and longitudinal cracks of Austrian dam after the 1989 Loma Prieta earthquake (Harder et al., 1998). It is evident how the longitudinal cracks are concentrated close to the crest of the dam, whereas the transverse cracks are close to the abutments.

Lexington dam was located at the north of the fault's projection and subjected to a PGA of 0.45 g according to the seismic instruments present at the dam. The dam presented mild cracking, with longitudinal cracks at the crest and transverse cracks close to the abutments, and a permanent crest settlement of about 0.25 m (Harder et al., 1998).

Both dams show how the cracking should be considered as a parameter to describe the damage of embankment dams produced by earthquakes.

2.4.3 Chang, Shivlakha, and other small dams - Bhuj earthquake, India (2001)

Many small and moderate size dams built for agricultural purposes were severely affected during the 2001 M_W 7.7 Bhuj earthquake (USSD, 2014). Many of these dams were

constructed directly on loose alluvial deposits, and evident liquefaction manifestations were observed in the post-event recognition campaigns. The most severe damage in moderate size dams was observed in the 15.5 m high Chang dam and the 18.0 m Shivlankha dam, both earth dams with a central masonry wall covered by an impervious soil core and gravel shells. The dams were placed over natural sand and silt mixtures which liquefied during the event, producing severe cracking and slope failure in both dams (Singh et al., 2005). Other dams affected by this event presented similar but less severe damage, with longitudinal cracks close to the crest and liquefaction manifestations (Krinitzsky & Hynes, 2002). The case of the Bhuj earthquake highlighted the critical importance of thorough site investigations for identifying potentially liquefiable soils in dam foundations.

2.4.4 Zipingpu Dam – Wenchuan Earthquake, China (2008)

One of the very few cases of a modern CFRD subjected to strong ground motions, the Zipingpu 156 m high dam was just 17 km far from the epicenter of the M_s 8.0 Wenchuan earthquake. An acceleration spike of approximately 2 g was recorded at the crest, evidencing the intensity of ground motion experienced by the dam (Zhang et al., 2015). Despite the large acceleration, the dam performed well, exhibiting a permanent crest settlement of approximately 0.74 m, with some damage in the parapet walls and the concrete slab, as commented below. The low reservoir level at the moment of the earthquake likely contributed to this favorable response.

As illustrated in Fig. 2.10, the reinforced concrete slabs suffered a dislocation of about 0.17 m in coincidence with the uppermost horizontal construction joint. The dislocation extended approximately 340 m along the center part of the dam, exhibiting a “Z” shape, which suggests the effects of the inertial forces in the upstream direction (Zou et al., 2012). This singular aspect, together with the fact that the reservoir level was just below the dislocation, indicates that the submerged part of the slab was supported by the counterweight of the impounded water, whereas the upper part was more susceptible to horizontal movements (Ishihara, 2010). This particular response denotes that the influence of dam-reservoir interaction can be significant for the response of the slabs of CFRD dams.

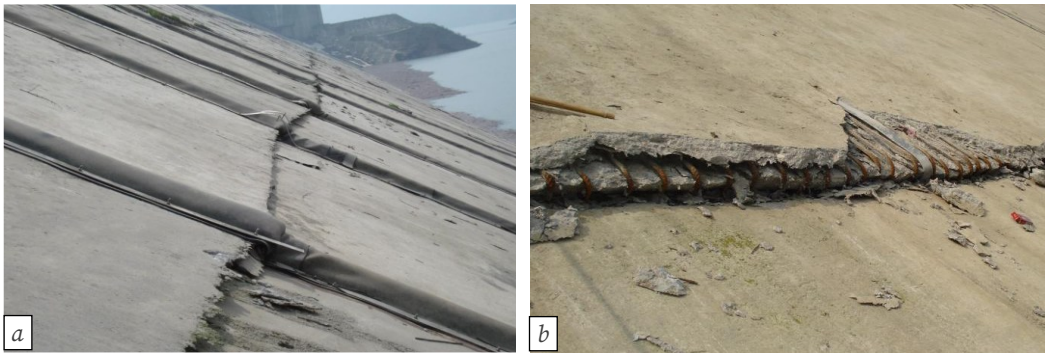


Fig. 2.10: a) dislocated slabs of Zipingpu CFRD after the 2008 Wenchuan earthquake (Zou et al., 2012), b) dislocation detail and its "Z" shape, showing kinked rebars and detached concrete (Zou et al., 2012).

Other cases as the collapse of Fujinuma Dam after the 2011 Tohoku earthquake in Japan (Ishihara, 2010), the seismic records of La Villita and El Infiernillo dams in Mexico (Elgamal et al., 1990), or the damage observed in several dams during the Turkish-Syrian earthquakes of 2023 (Cetin et al., 2024) have also contributed to the understanding of the seismic performance of embankment dams during large earthquakes.

2.5 Damage mechanisms of embankment dams under seismic actions

Some of the damage mechanisms that embankment dams can develop during earthquakes were already mentioned throughout the case studies, and this section will just provide a brief description of each one and how they can affect dam safety.

Based on the description made by Pagano et al. (2019), the main damage mechanisms on embankment dams are slope instability, crest settlement or freeboard reduction, cracking, internal erosion, and liquefaction (Fig. 2.11). Certain mechanisms can work as the trigger of a second one (Barbagelata & Barchiesi, 2024), like liquefaction inducing slope instability, or transverse cracking causing internal erosion. Moreover, some damage mechanisms could affect a certain type of dam more than others.

Slope instability refers to seismically induced sliding masses, as a direct effect of inertial forces on the soils of embankment and foundation, or as a consequence of the post-event redistribution of pore water pressure. This last effect can be induced by a rapid drawdown of the reservoir (Sica et al., 2019), the lack of pore water pressure dissipation in liquefiable soils, or the excess of pore pressure induced by aftershocks. If the extension of the sliding mass is large enough, this can jeopardize the global stability of the whole dam.

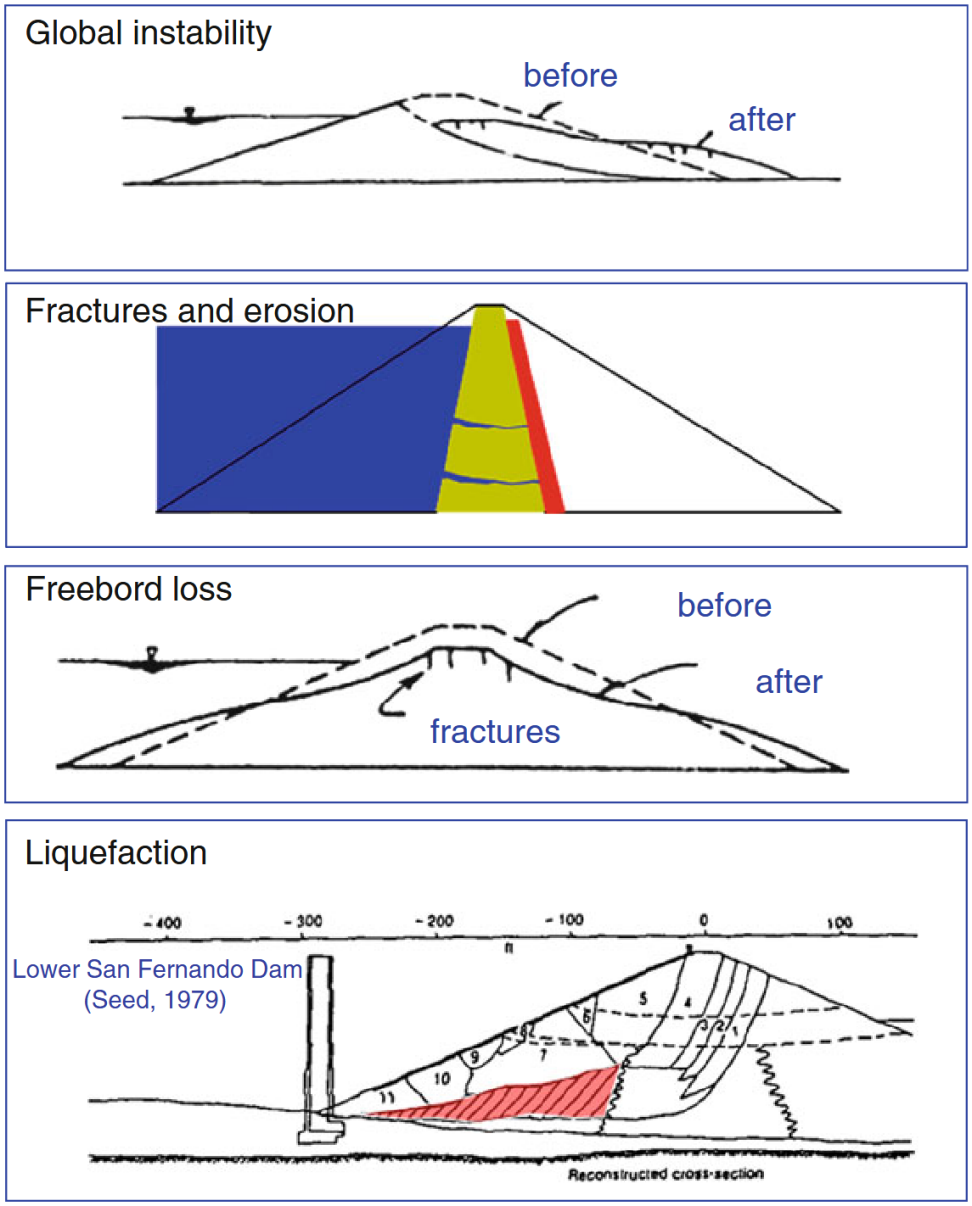


Fig. 2.11: Typical damage mechanisms induced by earthquakes in embankment dams (Pagano & Sica, 2013)

Permanent crest settlements may result from a complex post-earthquake distribution of deformations, likely driven by the distribution of plastic strains within the embankment and the partial sliding of unstable masses on the upstream and downstream slopes. However, in cases where rockfill dams are built with dumped rockfill, these settlements can be the consequence of a densification induced by the ground shaking (Verdugo & Peters, 2009). Less common, some crest settlement can be produced by the post-seismic reconsolidation of low-permeability fine-grained materials present in homogeneous dams or the core of zoned dams,

which accumulated pore pressure during shaking and dissipate it after the event (Costigliola, 2017).

The crest settlement is closely related to one of the most dangerous failure modes an embankment dam can be subjected to, the overtopping. If after the earthquake, the available freeboard is reduced to a minimal value, the water from the reservoir can easily overtop the damaged dam crest, initiating a breach that expands as scour progresses and the flow discharge increases, ultimately leading to dam failure and the uncontrolled unsafe release of reservoir water.

The cracking induced by earthquakes is one of the most common damage mechanisms and yet one of the most challenging to capture by conventional analysis tools (He et al., 2021). This is essentially because crack propagation in soil is controlled by the principles of fracture mechanics (Mejia, 2024). Cracking is the manifestation of large tension stresses in the soil mass, and the origins of these cracks during and after earthquakes are diverse: enlargement of existing cracks originated in static conditions by arching effects in cores (Fontanella et al., 2020), wet-dry conditions and desiccation of plastic soils, or abrupt change of stiffness (He et al., 2022), driven by the settlement of the embankment; the scarps or the sliding masses along the embankment, or more extraordinary by differential tectonic settlements or surface fault displacement (Mejia & Dawson, 2019).

Cracks can also appear in concrete/asphalt cores or slabs as a consequence of the interaction between the embankment, plinths, slabs or cores, and the reservoir during shaking. These cracks evidently affect the efficiency of the impervious barrier, but most importantly they are preferential paths for the water flow through the dam that can induce large hydraulic gradients and trigger internal erosion mechanisms. Modern dams are built with filters that should prevent the generation of large hydraulic gradients in soil that can be eroded, but depending on the extent of the damage, these drains can be overwhelmed and soil migration triggered.

Next, internal erosion is a damage mechanism that covers several phenomena related to the migration of soils from the dam and/or foundations due to excessive seepage. Scouring, suffusion, and piping can be related to internal erosion, even if the physical processes that take place are essentially different. In the context of earthquake engineering, the internal erosion can be triggered after the damage/cracking of soils or impervious barriers leading to the creation of preferential flow paths in the dam body and/or foundation, that in turn can cause

the migration of soils outside the system and eventually the subsidence and partial collapse the dam (Pells & Fell, 2003). Like most erosion processes, once soil migration begins, the flow section typically enlarges, which increases both the hydraulic gradient and the erosive potential. This process tends to propagate in the upstream direction, moving toward the water source. It continues until either the hydraulic head is sufficiently reduced or the self-formed conduit within the soil collapses.

Internal erosion can also be verified in static conditions, and it is itself a complex damage mechanism to be modelled (Fell & Fry, 2007). In addition, it is a mechanism that gives no clear signals of development at the dam surface until the scouring is advanced, requiring tools based on real-time monitoring of pore water pressure or other physical quantities for an early identification of its triggering.

Finally, the liquefaction of susceptible dam or foundation soils could lead to dam collapse if the extent and severity of the phenomenon are significant. The loss of strength and stiffness caused by the increase in pore water pressure because of the contractive behavior of saturated loose granular soils during ground shaking could produce weak zones within the dam and/or foundation, leading to the sliding of large soil masses. The identification and characterization of potentially liquefiable soils in dam and foundation, together with an accurate evaluation of their impact on the dam behavior using adequate tools, is crucial to accurately evaluate the extent and severity of this damage mechanism (Boulanger et al., 2015). It is worth remembering that this phenomenon was responsible for the extensive damage or collapse of several dams in the past (Hinks et al., 2012).

2.6 Dynamic analysis of embankment dams

The tools used to evaluate the response of embankment dams during earthquakes have evolved since the first works presented by Mononobe et al. (1936), and improved years later by the contributions of Ambraseys (1959), Newmark (1965), Seed (1979), Gazetas (1987) and many others researchers concerned about the seismic analysis and design of this type of dams. The following section provides a concise description of the most relevant methodologies.

The pseudo-static approach, one of the first methods used to analyze the seismic response of dams and slopes, basically introduces into the limit equilibrium analyses an extra driving force related to the inertial effects induced by the seismic actions. This force is decomposed into its horizontal and vertical components for convenience, and oriented outwards the slope.

The magnitude of both components of the inertial force is established as proportional to the weight of the sliding mass through a seismic coefficient, which multiplied by the acceleration of gravity can be interpreted as the average seismic acceleration affecting the unstable mass. This coefficient can be affected by factors that account for the effects of amplification, asynchronism, and ductility in a simplified manner. Being yet a limit equilibrium method, if the factor of safety between driving and resisting forces is less than 1.0 the slope is unstable; otherwise can be considered stable (Fell et al., 2014).

The pseudo-static approach was the standard method for stability assessment of embankment dams under earthquake loading until the 1970s. However, the method presents several limitations since it is essentially a static method that ignores the dynamic nature of the problem, but also neglects other phenomena related to the seismic response, such as the buildup of pore water pressure, cyclic degradation, etc. Currently, improved versions of this method are used for preliminary stability assessments, screening analyses, or in cases where structural collapse does not pose a significant risk (Bray & Travasarou, 2009; Papadimitriou et al., 2014; Andrianopoulos et al., 2014).

The explicit inclusion of acceleration time histories arrived with the sliding block analysis proposed by Newmark (1965), which computes the permanent displacements of a rigid sliding mass during shaking. The basic concept behind this method is that for a given slope exists a critical or yield acceleration (and pseudo-static coefficient) associated with a global factor of safety equal to 1.0, and only the accelerations of the sliding mass that exceed this critical value can produce permanent displacements. The relative acceleration, defined as the difference between the acceleration of the sliding mass and the critical acceleration, is integrated with respect to the time to evaluate the relative velocity, and then another time to finally obtain the permanent relative displacements of the soil mass, as presented in Fig. 2.12 (Kramer & Stewart, 2004). To capture the influence of asymmetries in the input motion selected, both direct and inverse directions of the acceleration time history should be used during calculations.

The sliding block method was further improved, introducing the deformability of the system, degradation of the strength, buildup of pore pressure, etc., and the decoupled and coupled approaches were born as better alternatives for the evaluation of permanent displacements (Kramer & Stewart, 2024). This method is also the base of many predictive models used to evaluate the displacement of slopes under seismic actions, due to its easy implementation with reliable results for shear-type sliding (Tropeano et al., 2017; Bray & Macedo, 2019).

Nonetheless, the method still presents limitations in capturing complex plastic deformations and cyclic soil behavior; hence, when this behavior is expected, a more complex procedure should be preferred over the sliding block analysis.

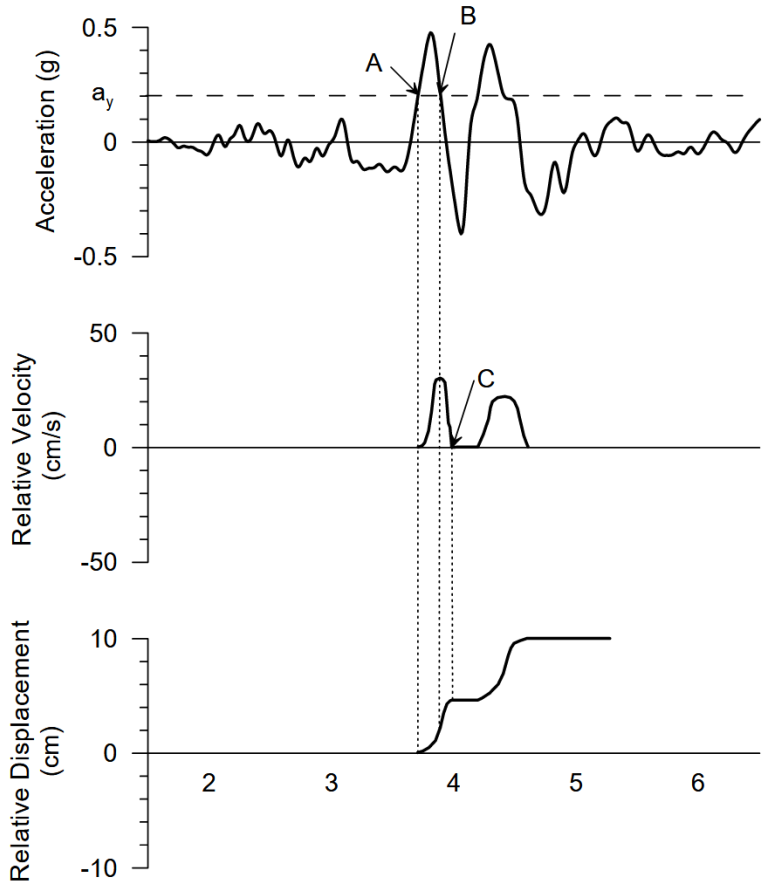


Fig. 2.12: double integration procedure of the sliding block method (Kramer & Stewart, 2004)

Another approach used for analyzing embankment dams under seismic actions is the so-called shear beam model, widespread after the solution proposed by Gazetas (1981). This method assumes the 2D cross-section of the dam as a 1D shear column with variable properties along height, subjected to seismic actions at the base. The model allows for the use of elastic (Dakoulas & Gazetas, 1985) but also for elastoplastic materials (Elgamal et al., 1987), and typically adopts a parabolic distribution of stiffness along height as is expected to be found in real dams (Park & Kishida, 2018).

This model is particularly useful for the estimation of the natural periods of vibration of the dam, since using basic information about geometry and stiffness provides a reasonable estimation of the natural frequencies of vibration (Zimmaro & Ausilio, 2020). In the same

manner, the inverse process could be done, and based in an estimation of the natural frequency of the dam furnished by the analysis of weak-motion monitoring records (Sica, Pagano, & Vinale, 2008) or direct measurements of microtremors and operative modal analysis (Verret et al., 2021) an first estimate of the average wave velocity of the dam can be obtained in absence of in situ measurements (Barbagelata et al., 2024). However, the method furnishes consistent estimations for the fundamental frequency of vibration, but less reliable results for the frequencies of higher modes (Lo & Pelecanos, 2018).

The estimations of the natural periods of vibration obtained using the shear beam model or any other 1D/2D approach can be adjusted to consider the impact of the shape of the valley through empirical relationships (Dakoulas & Gazetas, 1986, 1987). These relationships associate the natural frequency of the 1D model with the 3D conditions, depending on the geometry of the valley where the dam is placed, considering not just their overall shape (squared, cylindrical, trapezoidal, etc.) but also the aspect ratio (length/height) of the valley.

The modern approaches used for the evaluation of the seismic response of embankment dams are based on numerical models, and diverse methodologies as Finite Element Method (FEM), Finite Difference Method (FDM), or Material Point Method (MPM), etc., have been used in the characterization of seismic performance of this type of dams (Chowdhury et al., 2020). The flexibility of these approaches and the opportunities that they bring for the definition of complex geometries, use of advanced material models, variety of outputs, etc., make it possible to reproduce with a reasonable degree of confidence the seismic response of the dam when appropriately built, calibrated, and validated.

In order to obtain reliable results, the model should be comparable in geometry and characteristics to the real dam but still be able to have a predictable response. The level of detail should be aligned with the pursued objectives, avoiding excessively complex models unless strongly justified. A set of general rules for the development or control of nonlinear dynamic analyses for embankment dams can be consulted in Boulanger & Beaty (2016).

The reproduction of the history of stresses and hydraulic conditions during construction stages and first impoundment, the comparison of the static response with the records from the monitoring system (Sica et al., 2008), the calibration of material models based on a combination of laboratory test, site conditions and expected behavior (Boulanger, 2022), and the validation of the system response are all recommended steps to be followed during the construction of the numerical model as their impact in the dynamic stage of the analyses can

be noteworthy. Particularly in cases with complex site conditions, it is important to combine numerical models into the design of the monitoring system. In this way, monitoring records can be supportive for development of digital twins and the continuous evaluation of the behavior of the dam.

The outputs from numerical analysis vary with the methodology and software used, but commonly the results are given in the form of contours (Fig. 2.13), time histories, vector fields, etc., of any static or kinematic magnitude involved in the calculation, or derived from them.

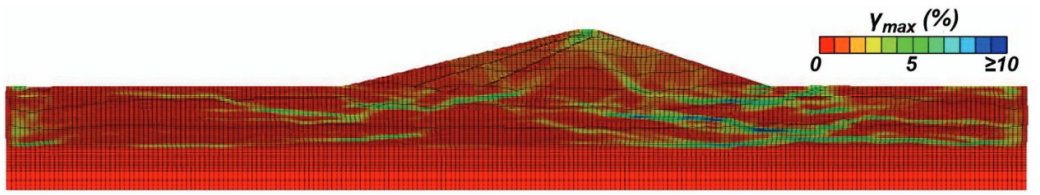


Fig. 2.13: Typical output of a nonlinear dynamic analysis, in this case, the contour of maximum shear strains (Paull et al., 2022).

Nonlinear Dynamic Analyses (NDAs) became a standard tool not just for the regular evaluation of seismic response of dams (Costigliola et al., 2022), but also to capture the response of complex phenomena as liquefaction or cyclic softening of susceptible soils (Boulanger & Ziotopoulou, 2018), dam-reservoir interaction (Pelecanos et al., 2020), spatial variability of foundation conditions (Paull et al., 2022), concrete slab response in CFRD dams (Saberi et al., 2022), and other critical aspects of dam behavior during seismic events.

A final comment is given about simplified methods, which can be used in screening analyses or as a reference for controlling the results of more advanced methodologies. Numerous interesting proposals have been made over time based on different approaches and hypotheses, such as simple or complex regression analyses over case histories or results of numerical analyses (Swaisgood, 2014; Papadimitriou et al., 2014; Ghaemi & Konrad, 2023; Nardo et al., 2024).

2.7 Seismic performance and fragility of embankment dams

The use of performance-based concepts in seismic engineering practice has increased over the past 30 years, based on the idea that structures and facilities can be designed and constructed in such a manner that their performance under diverse levels of seismic loading can be predicted with reasonable accuracy (Kramer, 2024).

The fundamental concept behind performance-based earthquake engineering (PBEE) is that structures are expected to exhibit different performance levels as seismic intensity increases, and an appropriate design should ensure that these performance objectives are met under specified seismic demands. In other words, for a given level of seismic actions, the structure should achieve a corresponding performance level to be considered adequately designed. This concept can be simply represented by a performance matrix, as in the example of Fig. 2.14 for a building structure (Moehle, 2024).

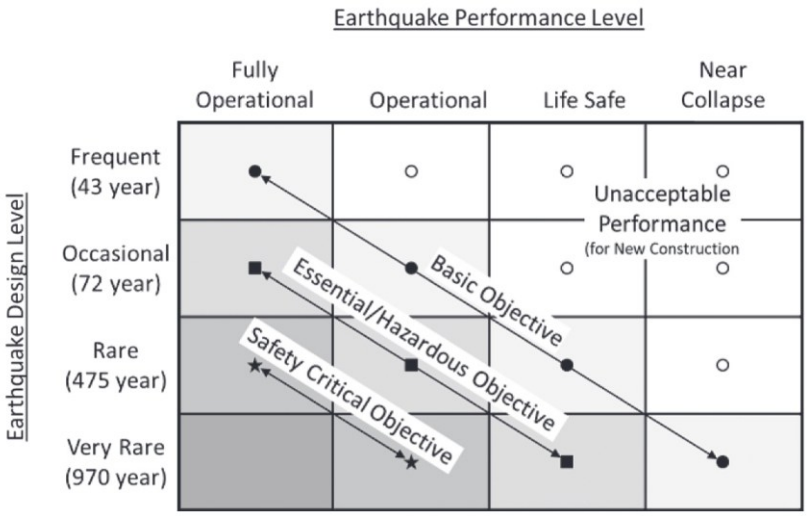


Fig. 2.14: illustrative performance matrix for the case of a building (Moehle, 2024)

To consider the uncertainties present in the definition of both seismic actions and earthquake performance, the Pacific Earthquake Engineering Research Center (PEER) framework for the PBEE also presents a probabilistic procedure where fragility functions play a crucial role, linking seismic actions with the probability of exceeding certain damage levels. The framework can be related to the progression that leads to earthquake losses, as shown in Fig. 2.15, where the models that link components and variables are displayed.

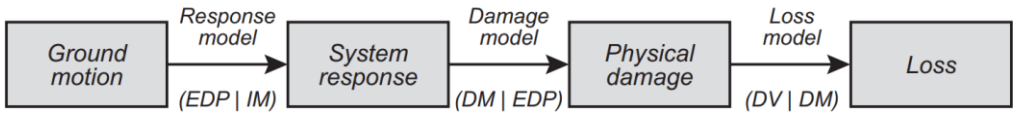


Fig. 2.15: PBEE framework illustrating the roles of response, damage, and loss models (Kramer, 2024)

Following the notation proposed by the PEER framework and described in Kramer (2024), *IM* corresponds to the intensity measure used to describe the seismic hazard, while the Engineering Demand parameter (*EDP*) is a physical magnitude able to represent the seismic

response of the whole system. Instead, the Damage Measure (*DM*) relates the physical damage attained by the structure to a given damage state, and the Decision Variable (*DV*) is linked to the losses produced by an earthquake of a certain damage level in terms of a risk metric. The terms *im, edp, dm,* and *dv*, as the common practices in statistics, correspond to a particular but not specific value of every parameter when they are considered as random variables.

At this point, it is important to establish the differences between "damage state", "damage level", and "limit state". Damage states describe the observed or expected physical damage of a structure after an extraordinary event, in this case, an earthquake. These states are often described in levels such as minor, moderate, or severe damage, and can be established in a qualitative or semi-quantitative manner (e.g., few small cracks, etc.).

Damage levels instead refer to quantitative thresholds, usually based on case histories and expert judgment, that define the boundaries between damage states (Jalayer et al., 2023). They relate not only to the observed damage but also connect that damage to a measurable physical parameter, such as deformations. Ideally, damage levels should also be related to evident changes in the structural response or performance, in terms of measurable physical quantities.

On the other hand, a limit state refers to a threshold beyond which a structure no longer meets a specific performance requirement, establishing itself as a performance criterion such as serviceability or damage control. Limit states are often set by guidelines or standards for use in design (e.g., NTC, 2018). Aliberti et al. (2019) proposed a correlation between damage states and limit states based on crest settlement for embankment dams, although this approach is not commonly adopted in practice.

In many geotechnical systems, such as embankment dams, it can be challenging to establish a statistical relationship between physical damage and system response in an equivalent manner to what is commonly done for building structures, where the damage of a single structural component can be statistically related to the response of the whole structure in a relatively simple manner.

In such cases, *DMs* for different damage levels are assigned deterministically based on threshold levels of the engineering demand parameter; that is, a particular damage level is verified once a given *EDP* value is exceeded (He & Rathje, 2024). For this reason, in this thesis, *EDP* and *DM* will represent the same physical quantity. The term *DM* will be used when

referring to *EDP* thresholds, as a compromise to maintain consistency with the nomenclature adopted by Kramer (2024) and the PEER framework.

These thresholds are commonly established based on case histories, but their definition heavily depends on the criteria and experience of the developers (Pells & Fell, 2003; Swaisgood, 2014). When available, the use of probabilistic capacity models is suggested. This is due to the fact that, even when based on the same data and criteria as the deterministic models, probabilistic models can explicitly account for the uncertainty in the relationship between *EDP* and *DM* (Rathje & He, 2022).

Following, the PEER framework can be formulated in its integral form using the total probability theorem as presented in Eq. 2.3 (Baker et al., 2021).

$$\lambda(DV > dv) = \int_{DM}\int_{EDP}\int_{IM} P(DV > dv \mid DM)\underbrace{f(DM \mid EDP)\, f(EDP \mid IM)}_{\text{Fragility}} \left|d\lambda(IM)\right| dEPD\ dDM \qquad \textit{Eq. 2.3}$$

The central role that fragility plays in the probabilistic definition of performance is evident, and the same happens in the evaluation of risk (McCann & Rix, 2023). Graphically, fragility functions are represented as a probability Cumulative Distribution Function (CDF) with *IM* on the x-axis, and the probability of having a failure given a particular value of *IM* on the y-axis (Fig. 2.16).

It is important as well to set the difference between fragility and vulnerability in the domain of seismic engineering, as they are often erroneously used as synonyms. While both are tools used in risk assessments to relate ground-motion intensity to resulting impacts or damage, fragility functions represent the probability of a binary outcome (e.g., failure or no failure), whereas vulnerability functions describe a continuous outcome, as the probability distribution of a consequence (e.g., loss, repair costs, etc.) as a function of the intensity measure (Baker et al., 2021). The applications of both curves are also different, and fragility functions can be used to derive vulnerability functions when the relationship between the damage measure and the decision variable is available.

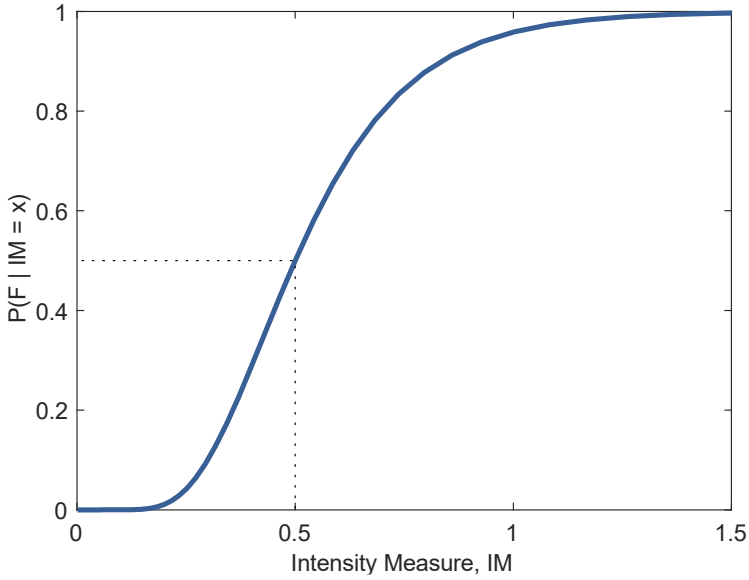


Fig. 2.16: Graphical representation of a fragility function (Baker et al., 2021).

Lastly, fragility curves are not a tool exclusive to seismic engineering and are also used to estimate the probability of an undesired outcome given an intensity of any other hazard, as in the case of embankment scouring (McKenna et al., 2021) or levee flooding (Vahedifard et al., 2020). However, in this work, the term fragility functions will always be related to seismic fragility.

Fragility functions can be estimated with enough information using general probabilistic concepts, but more practical procedures based on the application of these concepts in a more general framework are currently preferred to derive fragility curves. Some of these methods are described below.

2.7.1 Approaches to derive fragility functions

Fragility functions can be estimated using various methods, and a first distinction among methodologies is made upon the type of data used. If the data from the structural response comes directly from surveys after a real earthquake, the ground shaking intensity can be measured or estimated to develop empirical fragility curves using appropriate statistical methods. This approach not only relies on a reasonable amount of data to produce reliable results, but also for efficient post-event surveys, adequate discrimination among structural types, accurate estimation of the ground motion at every site, etc. (Rosti et al., 2021). If accurately obtained, empirical fragilities give valuable information as the real response of the structure carries on many sources of uncertainty often missed by analytical approaches.

Another approach uses the results from numerical analyses to derive analytical fragility functions. This approach is the most widely adopted, as it provides the flexibility of numerical analyses that can reasonably replicate the response of any structure when properly developed and calibrated. The numerical models used to predict the response should be able to capture the inelastic behavior of the structure during ground shaking, and special attention must be given to the number and characteristics of the selected strong motion records used in the analyses (Bakalis & Vamvatsikos, 2018). After, suitable statistical techniques can be used to calculate the probability of failure in correspondence with every ground shaking intensity considered. These approaches will be briefly explained later in this section.

A third kind of fragility can be obtained by synthesizing the opinion of a group of experts who, in absence of empirical observations or results from analytical models, try to fill the gaps in knowledge where other methods have not yet provided fragility estimations (Baker et al., 2021). This is particularly useful when dealing with a general set of fragility functions for a wide range of structural types. Finally, hybrid fragility functions can be developed by combining the curves derived from the previously described methods.

Focused in analytical methods, they evolved along the years from the frequentist approaches (Kennedy & Ravindra, 1984), response surface (Franchin et al., 2004; Iervolino et al., 2004), to the more practical methodologies from HAZUS (FEMA, 2019) or SYNER-G (Pitilakis et al., 2014), to end up in the three statistical methodologies used nowadays: Incremental Dynamic Analysis (IDA) (Vamvatsikos & Cornell, 2002, 2004), Multiple Stripes Analysis (MSA) (Jalayer & Cornell, 2003, 2009), and Cloud Analysis (CA) (Jalayer et al., 2015, 2017), alongside their updates and variations.

Most of these methods furnish parametric fragility functions, as they fit a probabilistic distribution and set the best-fitting parameters based on the data coming from numerical analyses. The lognormal CDF (Eq. 2.4) has been the preferred distribution for at least two reasons: first, it fits a variety of structural failure data well requiring only two parameters; and second, it has zero probability density at and below zero (Porter et al., 2007).

$$P\left(\text{Failure} \mid IM = im\right) = \Phi\left(\frac{\ln\left(im/\theta\right)}{\beta}\right) \qquad \textit{Eq. 2.4}$$

In Eq. 2.4, Φ() correspond to the standard normal cumulative distribution function, θ is the median of the fragility function (the IM level with a 50% probability of failure), and β is the

standard deviation of the ln(*IM)* level at which failure will occur (often referred as the dispersion of *IM*). However, the use of lognormal distribution is not mandatory, and other distributions can be used, or even no distribution if the amount and quality of data consent for the development of nonparametric fragilities (Hu et al., 2023).

The main difference among the IDA, MSA, and CA procedures lies in three aspects: the statistical approach used for fitting the curves, how they deal with collapses, and the selection and scaling of ground motion records. This latter aspect makes it challenging to use the same set of results across different fitting procedures. However, with a careful selection of input motions, it is possible to obtain suitable results using a second approach based on different intensity measures, as will be discussed in Chapter 8.

In the IDA method, as the name suggests, a big number of nonlinear dynamic analyses are carried out based on an initial set of ground motions, which are progressively scaled a given number of times. The results are then presented in the form of the so-called IDA curves that links the pairs *EDP-IM* for all the scaled input motions of the same original record (Fig. 2.17). Whit the IDA curves from several ground motions, the probability of exceeding a given *EDP* value is derived by identifying the *DM* in correspondence of a stablished damage level, and calculating the probability below a particular *IM* considering the distribution of the *IMs* given by such IDA curves, following the concept of "vertical statistics" proposed by H. Krawinkler (Zareian et al., 2004), and illustrated in Fig. 2.17 and Fig. 2.18.

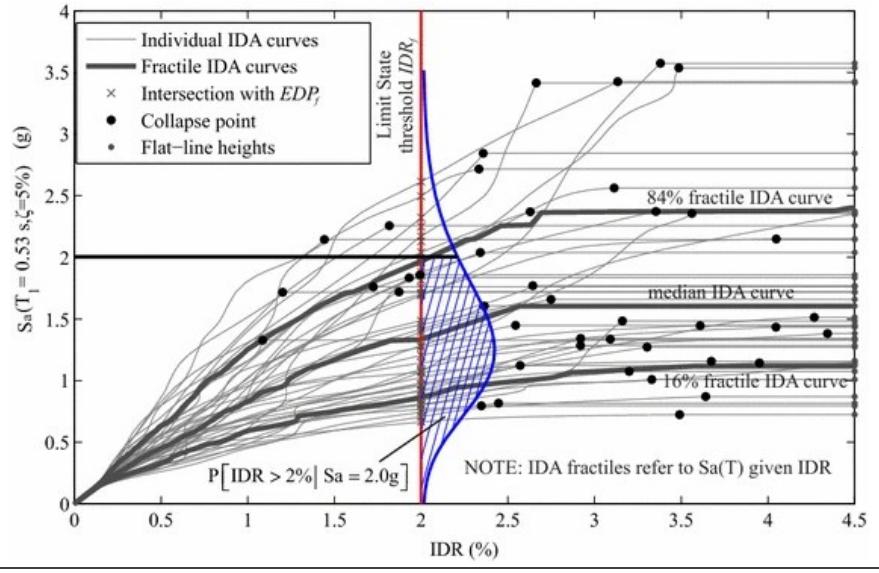


Fig. 2.17: Illustrative IDA curves and vertical statistics for the derivation of fragility functions, for a building structure (Baltzopoulos et al., 2017)

This last step yields a value of $P(EDP > DM \mid IM = im)$. Repeating the procedure for several *im* is possible to have many points to fit the fragility functions using a lognormal distribution (Fig. 2.18). As the *edp* is chosen and the statistics done in terms of *IM* values, this approach can also be referred to as *IM*-based or given-*EDP*. (Bakalis & Vamvatsikos, 2018).

To deal with collapses, intending collapses as the impossibility of continuing the numerical analysis due to loss of stability or excessive mesh deformations, the IDA method is pragmatic and continues the IDA curve horizontally until a large value of the *EDP* without incurring any methodological issue.

This method has a few drawbacks: the large number of analyses needed to deliver reliable results, the scaling of the ground motions by large scaling factors could lead to unrealistic input signals, and the hazard consistency of the input motions is not always defensible. Moreover, the application of IDA is preferred when the numerical models are simple, and the number of analyses does not represent a concern.

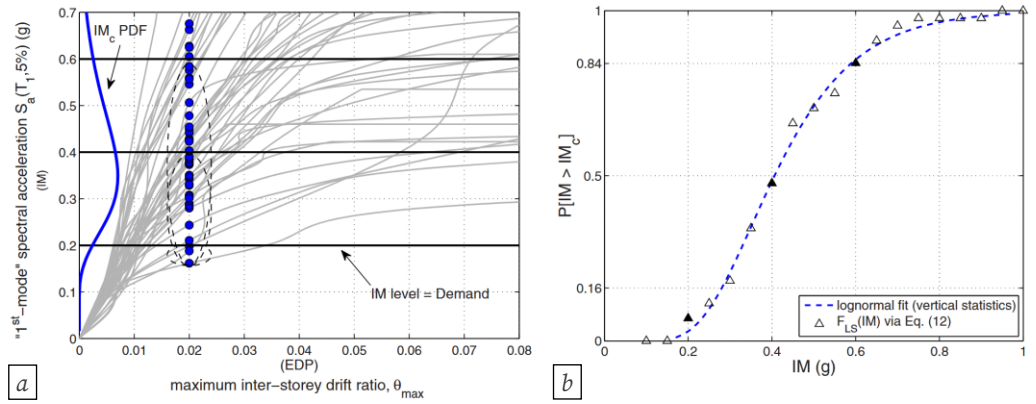


Fig. 2.18: a) IDA curves and vertical statistics for different IM levels, and b) IDA-based lognormal fragility function fitted with data for every IM level (Bakalis & Vamvatsikos, 2018).

MSA approach is slightly different: nonlinear dynamic analyses are done with a set of hazard-consistent ground motions that are all characterized by the same *IM* value, and the probability of exceeding a given value of *EDP* is directly stablished by identifying the number cases that exceed this *DM* (referred as failures or collapses) and compare them to the total of cases of the same stripe to establish the probability of exceede the given *DM*. Then, this probability can be calculated by a simple frequentist approach (Bakalis & Vamvatsikos, 2018) or using a binomial distribution (Baker, 2015), and referred to as the characteristic *IM* of the ground motions represent a point to be used for the calibration of a lognormal fragility curve, through a reliable fitting procedure (e.g. least squares, maximum likelihood, etc.). Analogously to IDA,

this method is often named *EDP*-based or given-*IM,* as the *IM* of every stripe must be the same. An example of an MSA fragility function is illustrated in Fig. 2.19.

The hazard-consistency is verified when the records are initially chosen based on the mean causal magnitude and distance coming from disaggregation charts, and then are scaled/matched to agree with the hazard magnitude defined by the UHS, CMS, or alternative representations of the hazard.

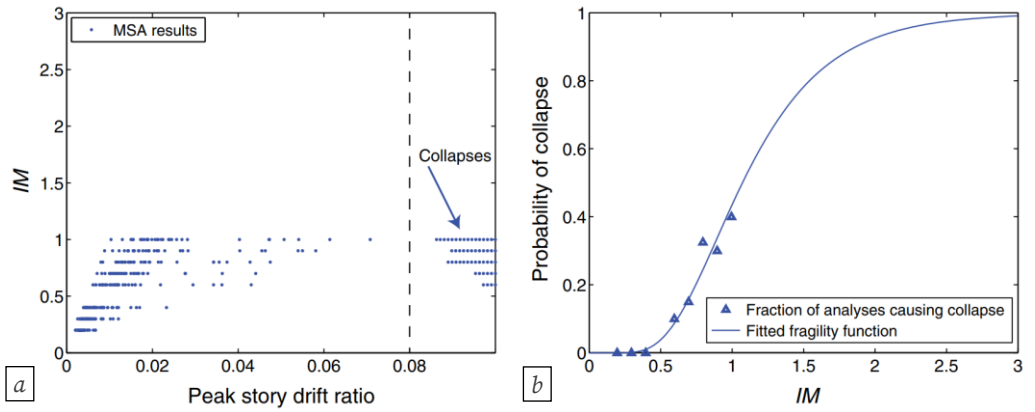


Fig. 2.19: a) EDP (peak story drift ratio) values for every IM stripe, observing the DM = 0.08 and the number of numerical collapses. b) MSA-based lognormal fragility function fitted (Baker, 2015).

The method provides a straightforward approach to managing numerical collapses by considering all such cases exceeding the *DM* threshold in the probability calculations. The main drawback of this method is the need for hazard-consistent and uniformly scaled ground motions, but it is possible to obtain good results with fewer analyses than other methodologies (Miano et al., 2024). Moreover, among the three approaches, the MSA-based procedure for deriving fragility functions is arguably the most intuitive of the three methods.

While IDA and MSA approaches show similarities, Cloud Analysis (CA) is based on a different approach. Simpler than the precedent methods, for using CA it is necessary to carry out a moderate number of nonlinear dynamic analyses using unscaled ground motions, with the only condition that the *IM* of these records should cover a broad range of magnitudes to guarantee the representativeness of the results. Then, the computed *EDP* values are divided by the *DM* values of a given damage level to obtain the Demand over Capacity Ratio (*DCR*), which paired with their corresponding *IM,* produces an *IM-DCR* point cloud. A linear regression in log-log space is carried out with the data of the point cloud to obtain the fragility function, as presented in Fig. 2.20 (Jalayer et al., 2015).

The hazard consistency of the ground motions could be partially considered by selecting ground motions which seismic scenarios respect the disaggregation from a seismic hazard analysis, but given the need for unscaled records, these could not strictly correspond to the hazard level established by the same seismic hazard analysis.

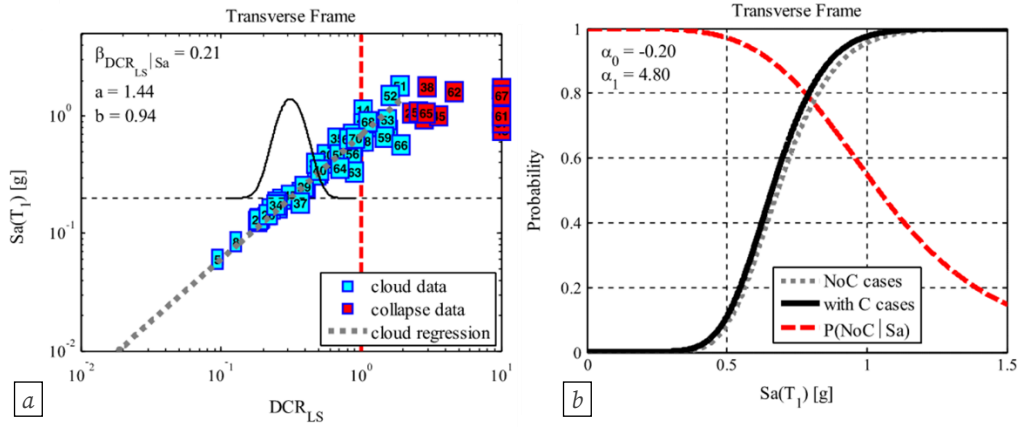


Fig. 2.20: a) IM-DCR point cloud (including collapses) and the cloud linear regression in log-log space. b) CA-based lognormal fragility function fitted considering or not collapses, and its complementary cumulative distribution function (CCDF). Modified from Jalayer et al. (2017).

The major advantages of the method lie in not requiring input motion scaling and being based on a simple linear regression to derive the fragility parameters. Nonetheless, the treatment of the uncertainty as a uniform value along the full range of *IMs*, the possible bias in the linear regression if a scattered point cloud (without linear trend) is used, or the non-intuitive inclusion of the numerical collapses are alerting points to have in mind when using this approach. This latter aspect can be solved by using a modified CA (Jalayer et al., 2017) that explicitly considers the collapse cases.

In recent years, the use of machine learning techniques in earthquake engineering applications has extended to the evaluation of fragility functions, with applications in different stages of their calibration. Some applications include the use of advanced machine learning methods to fit fragility functions (Li & Ni, 2025), the use of pre-trained machine learning-based predictive models to capture the nonlinear response of the system (Ni et al., 2018), or in the case of a large portfolio of parametric fragility functions, the training of a machine learning algorithm to estimate the parameters of the lognormal CDF based on the characteristics of the system under study, among others possible applications. Advances in this field are expected to further enhance the flexibility and effectiveness of fragility function development.

2.7.2 Seismic fragility functions for geotechnical systems

Fragility functions have been widely used in structural engineering as an efficient tool for estimating the probability of collapse across a wide range of structures. Since the pioneering work in the nuclear field (Kennedy et al., 1980) methodologies for deriving fragility functions have evolved significantly and their application in seismic engineering has expanded, becoming a key component in probabilistic performance-based earthquake engineering evaluations (Moehle & Deierlein, 2004), seismic risk assessments (Fabbrocino et al., 2005), and earthquake early warning systems (Wald et al., 2008), among others. The computation capabilities and progress of numerical modelling tools to capture the inelastic response of the structures under seismic actions have made possible to derive more reliable fragility functions, considering the uncertainty of model configuration and ground motions (Iervolino, 2022).

Their application to geotechnical earthquake engineering problems began to gain interest in the late 2000s (Lagaros et al., 2009), and nowadays, there are still many topics to be addressed for the development and use of fragility functions for geotechnical systems. Some examples of the use of this functions for describing the performance of geotechnical systems can be named as the case of tunnels (Andreotti & Lai, 2019; Tsinidis et al., 2024), slopes (Hu et al., 2025; W. Wang et al., 2023), retaining walls (Argyroudis et al., 2013; Cosentini & Bozzoni, 2022; Amendola et al., 2024), embankments (Shinoda et al., 2022; Petala et al., 2024), levees (Kwak et al., 2016a, 2016b) and liquefaction problems (Bullock et al., 2021). The inclusion of dynamic soil-structure interaction effects in the derivation of fragilities has gained more recognition as being related to structural response, as reflected in (Amendola & Pitilakis, 2023).

2.7.3 Fragility functions for embankment dams

Even if fragility curves have been part of seismic engineering for more than 40 years, the field of dams has just adopted them in the past decades as their applications started to be functional to the modern methodologies of dam safety assessment. The quantitative evaluation of dam risk (Rix et al., 2023), risk screening of embankment dam portfolios (Donahue et al., 2018; Hunt et al., 2018), or their introduction into earthquake early warning systems (Barbagelata et al., 2024) looks to be the most promising fields of application of fragility functions for embankment dams.

Table 2.2 presents an extensive list of the works in the literature (in English) with examples of fragility functions for embankment dams. The summarizing table shows that notable progress has been made in this field over the past 3–4 years. However, the heterogeneity in methodologies used to derive fragility, along with the variability in dam typologies adopted as references across studies, impedes both a direct comparison of the resulting curves and the development of a robust, type-specific portfolio of fragility functions.

These concerns reveal two aspects that this work will try to cover: the necessity of a well-defined procedure for the deriving of reliable fragility functions for embankment dams and set the discussion about when case-specific fragility functions are needed and when a more generic definition of fragility can be sufficient, individualizing the differences between the approaches that can be used to obtain each one. This discussion will be covered in Chapter 8.

Reference	Dam Type (height)	Real case?	PFMs or damage mechanisms	*EDPs*	*IMs*	Remarkable aspect considered
Lizarraga & Lai (2012)	Zoned dam (25.0 m)	Yes	Overtopping	Crest settlement	*PGA*	Considering random variability in materials from the dam body.
Nishimura et al. (2016) Nishimura et al. (2021)	Small zoned dam	No	Overtopping	Shear stress	*PGA*	Combination of earthquake and rainfall risk evaluations.
Donahue et al. (2018) Hunt et al. (2018)	Earthfill & rockfill dams (15.2-61.0 m)	No	Overtopping, sliding	Crest settlement	*Sa*	Introduction of fragility functions in a risk screening framework.
Pang et al. (2018) Pang et al. (2019)	CFRD (250 m)	No	Overtopping, concrete slab damage	Crest settlement, slab damage index	*PGA*	Introducing the slab damage index as *EDP*.
Jin & Chi (2019)	Earth core rockfill dam (261.5 m)	Yes	Overtopping	Crest settlement	*PGA*	Evaluation of the number of ground motions to have reliable fragility functions.
Marquez & Kamalzare (2019) Kamalzare & Marquez (2020)	Homogenous dam (45.1 m)	Yes	Overtopping	Crest settlement	*PGA*	Evaluation of the design criteria based on the results of fragility.
Rix et al. (2019)	Earthfill dams (6.0-129.0 m)	Yes	Undetermined	Crest settlement	-	Basic capacity model based on case histories in literature.
Figura (2020)	Homogeneous earthfill (10.8 m)	Yes	Overtopping, sliding	Crest settlement, horizontal displacement	*PGA, PGV, EDA, ASI,* A_{RMS}	Evaluation of the optimal intensity measures for different failure modes

Continues on next page...

Reference	Dam Type (height)	Real case?	PFMs or damage mechanisms	*EDPs*	*IMs*	Remarkable aspect considered
Pang et al. (2020)	CFRD (200 m)	No	Overtopping, concrete slab damage	Crest settlement, slab damage index	*PGA*	Influence of mainshock-aftershock sequence on fragility.
Phalen et al. (2021)	Zoned dam (15.25 m)	No	Overtopping, cracking	Crest settlement	*PGA*	Process for deriving fragility with a framework to evaluate reliability, materials variability with Latin Hypercube Sampling.
Regina (2021) Regina et al. (2022) Regina et al. (2023)	Zoned earth dams (27.75 m and 30.0 m)	Yes	Overtopping, global instability, filter damage, liquefaction in foundation soils	Crest settlement, loss of freeboard, sliding mass displacement, filter dislocation, excess pore water pressure ratio	*PGA, PGV,* I_A*,* CAV*,* CAV_5	Comparison between two different constitutive models (simple and advanced), and evaluation of the quality of diverse IM.
Zhou et al. (2021)	CFRD (200 m)	No	Overtopping, concrete slab damage	Crest settlement, slab damage index	*PGA*	Introduction of support vector machine techniques to make calculations more efficient.
Chowdhury et al. (2022)	Zoned dam (16.5 m)	Yes	Overtopping, liquefaction	Crest settlement, dam stretching, maximum shear strain, maximum hardfill strain	T_R	Evaluation of fragility before and after a dam retrofit.

Continues on next page...

Reference	Dam Type (height)	Real case?	PFMs or damage mechanisms	*EDPs*	*IMs*	Remarkable aspect considered
Rathje & He (2022) He & Rathje (2024)	Embankment dams	Yes	Overtopping	Crest settlement	*PGA, PGV*	Derivation of capacity models based on case histories and a framework for their use in deriving fragility functions.
Vecchietti et al. (2022)	Bituminous faced rockfill dam (90.0 m)	Yes	Global instability	Sliding mass displacement	*PGA*	Comparison of predictive models and a simplified direct-displacement-based approach for evaluating the dam fragility.
Ayati Ahmadi et al. (2023)	Asphalt core rockfill dam (110 m)	Yes	Overtopping	Crest settlement	*PGA*	Calibration of numerical models based on 1G physical models.
Chen et al. (2023)	CFRD (250 m)	No	Overtopping, concrete slab damage	Crest settlement, slab damage index	*PGA*	Introduction of uncertainty in the model by using stochastic ground motion and randomness in material properties.
Gibson & Bensi (2023)	Embankment dams	Yes	Overtopping, liquefaction	Loss or freeboard, liquefaction FS	*PGA*	The work proposes a Bayesian Network approach to evaluate the fragility using simple models for both damage mechanisms.

Continues on next page...

Reference	Dam Type (height)	Real case?	PFMs or damage mechanisms	*EDPs*	*IMs*	Remarkable aspect considered
Hu et al. (2023)	Small homogeneous dam (15.0 m)	No	Global instability	Factor of Safety	*PGA*	Comparison between homogeneous, random variable, and random field properties for the embankment, and calculating fragility using a nonparametric approach.
Khalid et al. (2023) Khalid et al. (2024)	CFRD (60.0 m)	No	Overtopping	Crest settlement	*PGA, PGV, PGD, PGV/PGA,* A_{RMS}, V_{RMS}, D_{RMS}, I_A, I_C, *SED, CAV, ASI, VSI,* I_H, *SMA, SMV, EPA,* A_{95}, T_P, T_m.	Evaluation of the optimum intensity measure for the evaluation of the fragility of the dam in analysis, and derivation of fragility surfaces considering vector-valued intensities.
McCann et al. (2023) McCann & Rix (2023)	Zoned dam (56.0 m)	Yes	Overtopping	Crest settlement	*Sa*	Use of an expert committee to deal with the characterization of the uncertainty.
Rix et al. (2023)	Zoned dam (53.3 m)	Yes	Overtopping	Crest settlement	*Sa*	Introduction to a real case quantitative risk analysis.

Continues on next page...

Reference	Dam Type (height)	Real case?	PFMs or damage mechanisms	*EDPs*	*IMs*	Remarkable aspect considered
Tretola & Sica (2023)	Zoned dam (13.0 m)	No	Overtopping, global instability, damage to the impervious barrier	Crest settlement, loss of freeboard, sliding mass displacement, maximum strain in clay core	*PGA, PGV,* I_A	Comparison among diverse *EDPs* and *IMs* for this specific kind of dam.
Xu et al. (2023)	CFRD (200 m)	No	Overtopping	Crest settlement	*PGA*	Evaluation of the influence of multi-component ground motion in the derivation of seismic fragility.
Baziar & Alavi (2024)	Zoned dams (63.0 m and 72.0 m)	Yes	Overtopping	Crest settlement	*PGA, SED,* I_A	Model calibration on case history information, flow chart with a procedure to evaluate fragility and threshold definitions based on international standards.
Lashgari & Moss (2024)	Embankment dams	Yes	Overtopping	Crest settlement, horizontal crest displacement	$k_y g/PGA$ $k_y g/CAV$ $k_y g/I_A$	Empirical fragility from dams affected by the 2023 Turkish earthquake events.

Continues on next page...

Reference	Dam Type (height)	Real case?	PFMs or damage mechanism	*EDPs*	*IMs*	Remarkable aspect considered
Pang et al. (2024) Xu & Pang (2025)	CFRD (250 m)	No	Global instability	Sliding mass displacement, cumulative time with FS < 1.0	*PGA*	Introduction of the cumulative time with FS minor than 1.0 as *EDP*.
Derakhshan & Alielahi (2025)	CFRD (85 m)	Yes	Overtopping	Crest settlement	*PGA, PGV, PGD, PGV/PGA,* A_{RMS}, V_{RMS}, D_{RMS}, I_A, I_C, *SED, CAV, ASI,* VSI, I_H, *SMA, SMV, EDA,* A_{95}, T_p, T_m, *Sa*	Model validation on monitoring data, randomly chosen ground motions, evaluation of the optimal *IM,* fragility surfaces considering vector-valued intensities, and resilience curves and surfaces.
Wang et al. (2025)	CFRD (160 m)	No	Overtopping, concrete face damage, cut-off wall damage	Crest settlement, embankment settlement and horizontal displacement, concrete face stress, cut-off displacements	*PGA, PGV, PGD, CAV,* I_A,$D_{5\text{-}PGA}$	Evaluation in terms of fragility functions of the efficiency of a reinforcement, considering several *IM* and *EDP*

Continues on next page...

Reference	Dam Type (height)	Real case?	PFMs or damage mechanism	*EDPs*	*IMs*	Remarkable aspect considered
Su et al. (2025)	Earth core rockfill dam (295.0 m)	Yes	Overtopping	Crest settlement	Deep learning-aided *IM*	Introduction of a deep learning-aided *IM* which combines several traditional intensity measures of the ground motion
Ahmed et al. (2025)	Zoned earth dam (13.0 m)	Yes	Global instability	Horizontal displacement of a sliding mass	*PGA*	Use Newmark analysis to derive fragility functions of a small dam
Qiu et al. (2025)	Rockfill dam (225.0 m)	No	Overtopping	Crest settlement	*SED*	Use different scenarios of upstream and downstream berms for stabilizing. Also explores the effects of horizontal and horizontal + vertical ground motions
Ahmadi & Noorzad (2025)	Asphaltic concrete core rockfill dam (84.0 m)	Yes	Overtopping	Crest settlement	*PGA*	Explore different hypotheses about the inclination of the core, and validate the numerical model with a centrifuge test. Used IDA to calibrate fragility.

Continues on next page...

Reference	Dam Type (height)	Real case?	PFMs or damage mechanism	*EDPs*	*IMs*	Remarkable aspect considered
Ahmadi et al. (2025)	Asphaltic concrete core rockfill dam (53.3 m)	Yes	Overtopping	Crest settlement	*PGA*	Use IDA as the method for deriving fragility functions

Acronyms: Concrete face rockfill dam (CFRD), peak ground acceleration (*PGA*), peak ground velocity (*PGV*), peak ground displacement (*PGD*), spectral acceleration (*Sa*), Arias intensity (I_A), cumulative absolute velocity (*CAV*), cumulative absolute velocity for a(t) > 0.05 g (CAV_5), return period (T_R), peak velocity/acceleration ratio (*PGV/PGA*), root mean square acceleration (A_{RMS}), root mean square velocity (V_{RMS}), root mean square displacement (D_{RMS}), characteristic intensity (I_C), specific energy density (*SED*), acceleration spectrum intensity (*ASI*), velocity spectrum intensity (*VSI*), Housner intensity (I_H), sustained maximum acceleration (*SMA*), sustained maximum velocity (*SMV*), effective design acceleration (*EDA*), A95 parameter (A_{95}), predominant period (T_p), mean period (T_m), duration for acceleration greater than 0.05 *PGA* ($D_{5\text{-}PGA}$), engineering demand parameter (*EDP*), intensity measure (*IM*).

Table 2.2: Research works with examples of fragility functions for embankment dams found in the literature (in English).

2.8 Earthquake Early Warning Systems

Earthquake Early Warning (EEW) is a modern strategy for reducing seismic risk and enhancing the resilience of the built environment and infrastructure systems (Satriano et al., 2011). Earthquake Early Warning Systems (EEWS) utilize strong-motion networks to deliver real-time information on ongoing earthquakes. When properly calibrated, these systems can provide rapid, first-order estimates of the performance of critical buildings and infrastructure immediately following an event (Iervolino, 2014; Cremen & Galasso, 2021). This timely information is essential for effective seismic risk mitigation and post-disaster response, and management.

In the field of dams, some approaches for concrete dams have been developed using a combination of seismic monitoring systems deployed at the dam and numerical models (El-Idrissi et al., 2023), while a general framework for embankment dams was proposed by Pagano & Sica (2013). On the other hand, generic fragility functions were adopted in EEW frameworks for bridges (Lin et al., 2022) or roadway retaining walls (Cosentini & Bozzoni, 2022).

Due to the strategic importance of large embankment dams in post-earthquake emergency management and the potentially catastrophic cascading effects of their failure (Tosun, 2024), the development and implementation of case-specific fragility functions for their use within an EEWS is essential. An accurate definition of its behavior during earthquakes is essential to ensure a reliable near-real-time assessment of the dam's seismic safety.

The prediction should aim at identifying the triggering of potential damage mechanisms activated during the shaking phase and provide an initial estimate of structural performance. This, in turn, enables dam operators to enhance standard post-earthquake inspections, prioritizing the monitoring of key physical parameters that can effectively capture the progression of these mechanisms during the post-seismic phase.

A proposal for the use of fragility functions as an interpretative model within an EEWS for embankment dams will be covered in Section 8.4, as an extended version of the work presented in Barbagelata et al. (2024).

3. Case-specific fragility functions for Potrerillos CFRD

This chapter contains two important parts of the dissertation. The first is the presentation of the methodological framework proposed for deriving case-specific fragility functions, and the second is the presentation of the case study and its main characteristics. Both aspects remain crucial for the ultimate objective of the thesis, which is the derivation of case-specific fragility functions for the Potrerillos CFRD.

3.1 Methodological framework for deriving case-specific seismic fragility

Fragility functions developed for building structures or bridges often include a generic component in their formulation, allowing their application to groups of structures with comparable characteristics within a portfolio. A similar approach could be considered for some geotechnical structures, such as small roadway retaining walls, which can be characterized by a few geotechnical and geometrical features, have a seismic response that is relatively simple to evaluate, and whose failure rarely poses an extremely hazardous situation for the population.

These assumptions cannot be extended to large embankment dams, as each one is inherently a prototype with unique features (design, geometry, site conditions, materials, construction technologies used). Moreover, given the critical role of large dams and the severe consequences associated with their failure or collapse, relying on generic fragility functions is inadvisable for seismic risk or performance assessments.

For these reasons, a framework for deriving fragility functions that account for the unique conditions of a given embankment dam is proposed here, establishing the procedure to be applied in calibrating the fragility functions for Potrerillos CFRD.

Similar frameworks have been proposed in a general manner for dam risk evaluation (McCann & Rix, 2023) and for dam resilience assessment (Derakhshan & Alielahi, 2025), but they omit some aspects that could significantly influence the resulting fragility functions, which this procedure aims to address.

In the evaluation of the seismic performance of a complex structure such as an embankment dam, each decision must be carefully weighed to achieve the most reliable results, while also relying on reasonable assumptions that realistically capture the dam's characteristics and conditions throughout the entire evaluation process (Boulanger & Beaty, 2016). The

underlying idea is that every step involved in deriving case-specific fragility functions must be well suited to the final objective, starting from the very outset of the process.

Therefore, the proposed framework for deriving case-specific fragility functions is summarized in Fig. 3.1, and its components are described in the following sections.

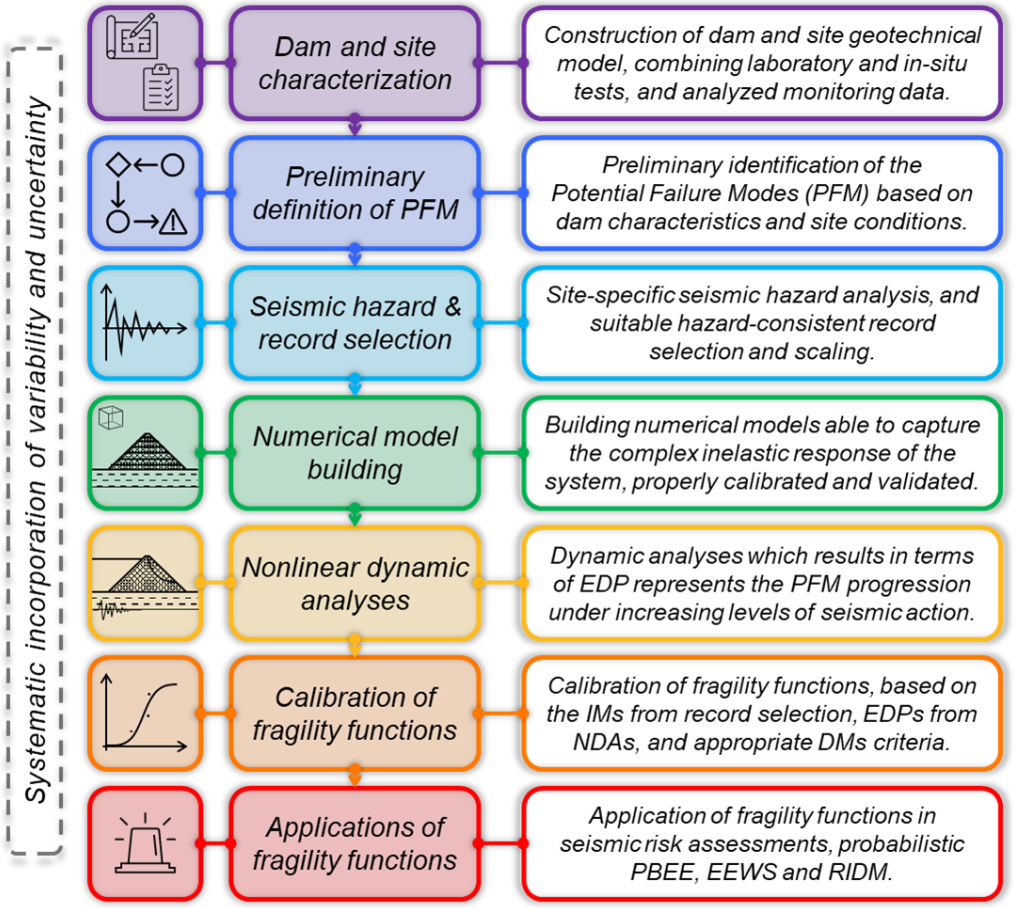


Fig. 3.1: Methodological framework for deriving case-specific fragility functions for embankment dams.

3.1.1 Dam and site characterization

The characterization of dam materials and site conditions is fundamental for any evaluation of seismic performance. Identifying the geomechanical properties of the soils and rocks in the embankment and foundation, and building trustable geological and geotechnical models is critical for accurate seismic response calculations (Chowdhury et al., 2022). Then, it is essential to determine the scope and extent of geological and geotechnical investigations, as well as the number and types of in-situ and laboratory tests required to reasonably characterize

the material properties of the geomaterials, recalling that these properties will subsequently be used to calibrate constitutive models for seismic performance evaluations (Amorosi, 2020).

Dam body soils generally exhibit relatively uniform material properties because modern construction techniques involve placing and compacting processed soils in layers to minimize large variations in their hydraulic and mechanical characteristics. This makes it possible to characterize them with a modest number of tests during the project and construction stages. However, since soil properties can vary over time due to dam aging, and because site conditions, operational circumstances, or natural events may alter the characteristics of the dam materials, some testing should be carried out periodically throughout the life of the asset to evaluate these potential variations and its impact in the seismic response (Chowdhury et al., 2023).

The situation is significantly different in the case of foundation soils, where geological and fluvial processes govern the deposition of soil particles, leading to considerable spatial variability in the characteristics of different lithological and stratigraphical units (Nichols, 2010). The evolution of the fluvial erosion and deposition processes in a tectonically active environment can further accentuate the variability of the alluvium characteristics (Schumm et al., 2002). This makes an adequate characterization of the spatial variability of alluvial soils crucial, combining geological, geophysical, and geotechnical surveys with laboratory tests to set the database for the building of subsurface geological-geotechnical models. These models can be built by an expert who combines them in a unique harmonized model (Fookes, 1997), or using statistical tools (Remy et al., 2009) or data-driven approaches (Shuku & Phoon, 2023) which can explicitly include the uncertainty. Several realizations could be included within a logic tree to carry with the uncertainty in the definition of the geotechnical model of the foundation soils.

In the case of dams equipped with an active monitoring system, the evaluation of records from physical variables captured by sensors installed in the dam and its foundation during normal operation and extraordinary events can provide valuable information. This includes insights into long-term static and hydraulic conditions, as well as the response of the system to extreme hydrological events or weak and strong seismic motions, among other possibilities. Moreover, the information obtained from monitoring records can be processed to extract relevant data to support the calibration and validation of numerical models of the dam.

3.1.2 Preliminary definition of Potential Failure Modes (PFM)

The identification of potential failure modes (PFMs) that could develop in the dam, based on its specific characteristics, is a critical step to focus efforts on deriving fragility functions for those seismically induced damage mechanisms that could compromise the safety of the dam and potentially lead to its collapse.

A formal potential failure mode analysis in the context of dam risk assessment is actually a multidisciplinary process that involves professionals from several fields related to dam engineering. The objective of the analysis is not only to define the sequences of events that could lead to dam failure but also to establish a hierarchy of PFMs, giving greater importance to the evaluation of those considered more feasible.

The need for at least a preliminary identification of the seismically induced PFMs of the dam before proceeding with the subsequent steps in the derivation of fragility functions ensures that those functions represent feasible damage mechanisms that the dam could develop during strong earthquakes. Moreover, the process of defining the PFMs also aids in identifying the physical quantities or damage indices later used as engineering demand parameters (*EDPs*), aiming to capture and condense the dam's response associated with the development of each failure mode.

3.1.3 Seismic hazard and record selection

Evaluating the seismic hazard at the dam site should establish both the intensity and the characteristics of ground shaking expected during future earthquakes. Given the uncertainties in defining seismic sources and their activity, probabilistic seismic hazard analysis (PSHA) is one of the most comprehensive tools available for forecasting the intensity of potential ground motions. In PSHA, seismic hazard is expressed in terms of probabilities of exceedance, which also allows for the definition of different levels of seismic intensity by relating these probabilities to the mean return period of events capable of producing the corresponding ground motion.

The results of seismic hazard forecasting help not only in determining the expected ground shaking intensity using various intensity measures (such as *PGA*, *Sa(T)*, etc.), but also in identifying the ranges of earthquake magnitudes and source-to-site distances that contribute most significantly to the hazard, typically through disaggregation charts. These two outputs, together with additional information about faulting style and site conditions, further support

the selection and scaling of real earthquake records, ensuring consistency with the seismic hazard and compliance with the criteria established by the procedure used to calibrate the fragility functions. Guaranteeing the hazard consistency of the input motions used in numerical analyses remains crucial, as it contributes to reducing epistemic uncertainty in defining the expected seismic actions, a factor often overlooked in the development of generic fragility functions.

In addition, expressing the intensity of ground shaking in terms of various intensity measures (*IMs*) is highly valuable, as they reflect different characteristics of the ground motion, such as amplitude, frequency content, or energy release, which may be more suitable for describing the dam's seismic performance. The use of optimal *IMs* based on metrics like the "efficiency" or "sufficiency" of the *IM* could genuinely improve the quality of the obtained fragility functions.

Finally, this step is not limited to defining the ground shaking associated with earthquakes but can also be extended to other seismic-related hazards such as surface fault displacement. If the dam is located at a site that could be affected by primary or secondary co-seismic deformations, there are available methodologies to estimate the magnitude of such deformations in a manner analogous to PSHA, known as probabilistic fault displacement hazard assessment (PFDHA) (Valentini et al., 2025). These displacements can then be introduced as input in numerical analyses to evaluate the response of the dam to surface fault displacements (Mejia, 2024).

3.1.4 Numerical model building

Using numerical tools to reproduce the evolution of seismically induced PFM of the dam is also an important step in developing case-specific fragility functions. Although simplified methodologies can be used if they can capture the inelastic response of the dam, the use of advanced numerical methods such as the finite element method (FEM) or the finite difference method (FDM) is encouraged, as they are better suited to represent the complex behavior of the dam under seismic loading, including phenomena such as liquefaction and cyclic softening (Boulanger & Ziotopoulou, 2018).

The numerical models should be constructed according to the geometry of the dam and its foundation, even more so in cases in which the bedrock has a complex shape (Wen et al., 2022). The reproduction of the construction sequence and the gradual rise of the reservoir

level are also aspects that should be taken into account as closely as practicable, given their influence on the modeling of the static conditions (Potts & Zdravković, 2001) before the dynamic stage of the analysis.

The protocols used to calibrate the constitutive models for both static and dynamic stages should focus on selecting input parameters that enable the model to produce the desired response, rather than strictly attempting to reproduce the laboratory tests from which the soil properties are derived (Boulanger, 2022). Moreover, using parameters derived from monitoring records can enrich the calibration process by relating the response of the numerical model to the current state of stresses, deformations, and hydraulic conditions of the dam (Sica et al., 2008). Understanding the limitations of the available data used during the calibration process, preventing inconsistencies between information from different sources, and accounting for the inherent variability in every part of the process are crucial to obtaining a reliable numerical model capable of reproducing the expected dynamic response of the dam. Different calibration sets, or even alternative constitutive models, can also be incorporated into a logic tree to better capture the variability that these components may introduce into the evaluation process.

3.1.5 Nonlinear dynamic analyses

A reliable numerical model makes it possible to carry out nonlinear dynamic analyses (NDAs) using the previously selected and scaled hazard-consistent ground motion records. These NDAs should reproduce in a reliable manner the cyclic behavior of the embankment and foundation soils, and capture the development of the damage mechanism in agreement with the assumed potential failure modes.

The results of the NDAs, beyond their practical role in assessing the seismic performance of the dam, to be useful at deriving fragility functions have to be expressed in terms of the engineering demand parameters (*EDPs*), which were initially identified during the definition of the PFMs but had to be confirmed at this stage as representative of the dam's seismic response and damage progression.

Finally, confirming that the outcomes of the NDAs are reasonable and consistent with the hypotheses made during the development of the numerical model serves as evidence of an adequate calibration of the constitutive models and appropriate modeling assumptions.

3.1.6 Calibration of fragility functions

Once the NDAs are performed and having their results expressed in terms of *EDPs*, and the input motions are described in terms of their respective *IMs*, only one piece of information is missing to calibrate the fragility functions, which is the definition of the damage measures (*DMs*) related to diverse damage levels.

The criteria for defining *DMs* for different damage levels, often established through threshold values of *EDPs*, are typically derived from the evaluation of case histories. Their selection should therefore depend on the quality of the underlying database and the assumptions used in their derivation. Moreover, due to the limited number of *DMs* in the literature, the choice of *EDPs* is frequently constrained by the available *DMs*.

Having established the *DMs* for each *EDP*, it is possible to calibrate the parameters of the probability distribution that defines the fragility curve using appropriate statistical methods. When a lognormal CDF is selected as the probability model, the fragility functions are fully characterized by calibrating the parameters θ and β from Eq. 3.1 to fit the data obtained from the numerical analyses.

$$P\left(EDP \geq DM \mid IM = im\right) = \Phi\left(\frac{\ln\left(im/\theta\right)}{\beta}\right) \qquad \textit{Eq. 3.1}$$

Methods like Multiple Stripe Analysis (MSA) or Cloud Analysis (CA) are feasible options for the derivation of case-specific fragility functions.

3.1.7 Applications for fragility functions

Fragility functions have many applications. The most important include their use in quantitative risk analyses, vulnerability assessments, and probabilistic evaluations of seismic performance. They can also be incorporated into earthquake early warning systems as interpretative models and support risk-informed decision making for emergency management of dams after earthquakes.

This framework could be further improved by explicitly including uncertainty at every step of the process. Using appropriate statistical tools, it is possible to develop a probabilistic model that describes the dam's fragility not only in terms of a median value but also by accounting for the dispersion in the results.

To conclude, the use in the field of large dams of generic fragility functions or those based on simplified analysis techniques should be limited to screening processes or preliminary assessments of seismic performance, as they cannot fully capture the complexity that characterizes the seismic response of large embankment dams.

3.2 Main features of Potrerillos Dam

Located in the north of Mendoza Province, western Argentina, and 29 km from Mendoza Urban Area (Fig. 3.2a), Potrerillos dam and reservoir constitute the main hydroelectric complex and the only large dam of the Mendoza River. The discharge regime of the Mendoza River is controlled by snowmelt in the upper part of its basin (Toum et al., 2024), where its tributaries (Tupungato, Las Cuevas, and Vacas Rivers) supply the meltwater coming from the tallest section of the Andes Cordillera Mountain chain (Fig. 3.2b).

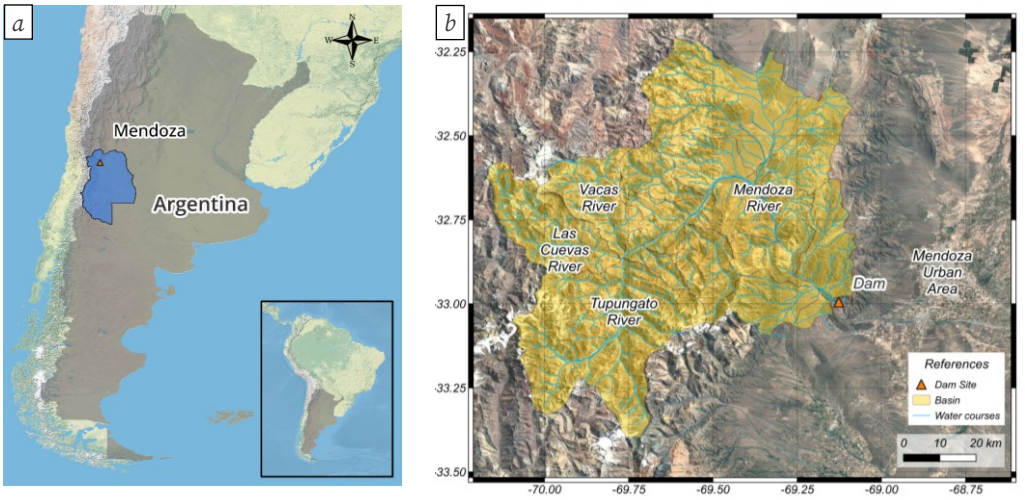


Fig. 3.2: a) Location of Potrerillos CFRD, and b) upper basin of Mendoza River, and their main tributaries: Las Cuevas, Vacas, and Tupungato Rivers.

Alongside the production of hydroelectricity and the promotion of recreational activities on the coast of the water body (Fig. 3.3), the primary usages of the complex are the supply of water for human consumption, and the regulation of the river discharges with the aim of covering the demand of water for agricultural purposes.



Fig. 3.3: Upper view of Potrerillos dam and reservoir. Courtesy of Eng. Julieta Fajardo.

The role of Potrerillos in the supply of water for artificial irrigation is essential, given that the northern part of Mendoza Province is characterized by a desert climate, yet its main economic activities (agriculture, vineyards, and wine production) strongly depend on artificial irrigation. For this reason, since the colonial age, the conscientious management of water resources has been a priority in Mendoza, leading to the construction of hydraulic infrastructure as a strategic measure for the development of the Cuyo region (Martin et al., 2010).

3.2.1 Brief history of the project

In the early 20th century, the first studies conducted in the region by the Italian engineer Cesare Cipolletti identified a suitable location for a dam and reservoir to regulate the water discharge of the Mendoza River, upstream of the small diversion dam he constructed, now named in his honor. Since 1923, several proposals for the dam were projected considering diverse typologies, heights, and financial resources; all of them surrounded by diverse political interests. The debate ended with the final project developed by the consortium of Coyne et Bellier (France), Geotécnica Consultora (Chile) & THYA (Argentina) in 1996-1998 and built

by Consorcio de Empresas Mendocinas Para Potrerillos S.A. (CEMPPSA) between 1999 and 2002 (M. E. Espinosa et al., 2010).



Fig. 3.4: Upper view of the downstream of the dam during construction. Archive Prof. A. Barchiesi.

The construction followed the scheduled program, and the first full impoundment was set for the end of 2003. However, due to interpretative discrepancies between the design/construction teams and project inspectors regarding the influence of a group of sand-like alluvial materials, identified during the construction phase in some exploratory boreholes and excavations, on the dynamic response of the dam, additional investigations and analyses were carried out to try to clarify the situation (Carmona et al., 2004; Geomatrix, 2004; Barchiesi et al., 2006; Núñez, 2010; Núñez & Sfriso, 2013).

Even when most of these studies yielded results in agreement with the original assumptions about the impact of these materials in the global response of the dam, the inspection compelled the construction of a 18 m tall stabilizing embankment downstream the dam (Fig. 3.5) over the natural alluvium as a countermeasure to the claimed negative impact of the sand-like materials on the dam's seismic response. This requirement initiated a lawsuit between the parties involved that ended with an outcome in favor of the design and construction consortium (Núñez, 2012; Toso & Barchiesi, 2013).



Fig. 3.5: a) Downstream stabilizing embankment during its construction. In the bottom left corner is possible to see the gallery built to collect the discharge from the drainage system, and b) a photograph from the downstream showing the embankment with its final geometry. Archive Prof. A. Barchiesi.

The Potrerillos Dam system comprises two hydroelectric power stations. The primary facility, Cacheuta, is situated approximately 4 km downstream of the dam. The discharge from the Cacheuta plant is conveyed via an open-channel system to the Álvarez Condarco power station, which was originally designed as a run-of-river facility and subsequently retrofitted and integrated into the Potrerillos hydroelectric scheme. A particular condition of this dam is that, since it does not have another compensating dam downstream, hydroelectric production is most of the time subject to the demand for water for artificial irrigation, more than the demand for electric energy production.

3.2.2 Embankment dam and appurtenant structures

Potrerillos dam is a Concrete Face Rockfill Dam (CFRD) 120 m tall over the riverbed and 490 m long at the crest (Fig. 3.6). The upstream and downstream slopes are respectively 1.5:1.0 and 1.8:1.0, and it is almost 400 m long between the downstream and upstream toe. The zoning respects the criteria of increasing the permeability and particle size towards downstream, and the characteristics of each material will be described in detail during the characterization.

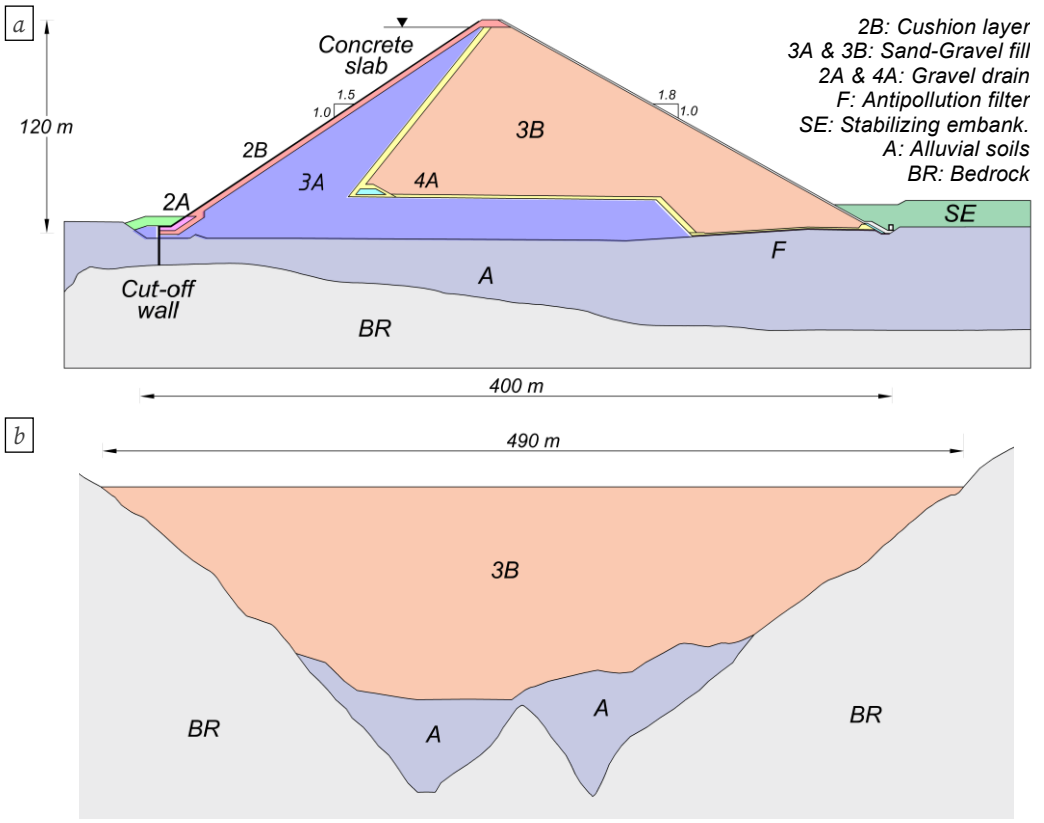


Fig. 3.6: a) Typical cross section of the dam with the main dimensions and zoning, and b) section perpendicular to the stream direction, across the dam axis.

The control of seepage through the dam and its foundation is ensured by several interconnected elements (Fig. 3.7): a reinforced concrete slab with variable thickness placed along the upstream face of the dam, a 1 m thickness cut-off wall within the alluvium which will be described in detail later, lateral plinths that link the concrete slab with the rock abutments, a floating plinth connecting the cut-off wall to the concrete face, and a grout curtain located in the rock beneath the plinths and the cut-off wall.

The cofferdam used for river diversion during construction is also shown in Fig. 3.7b. With a total height of about 30 m over the riverbed, it can itself be considered a large dam.

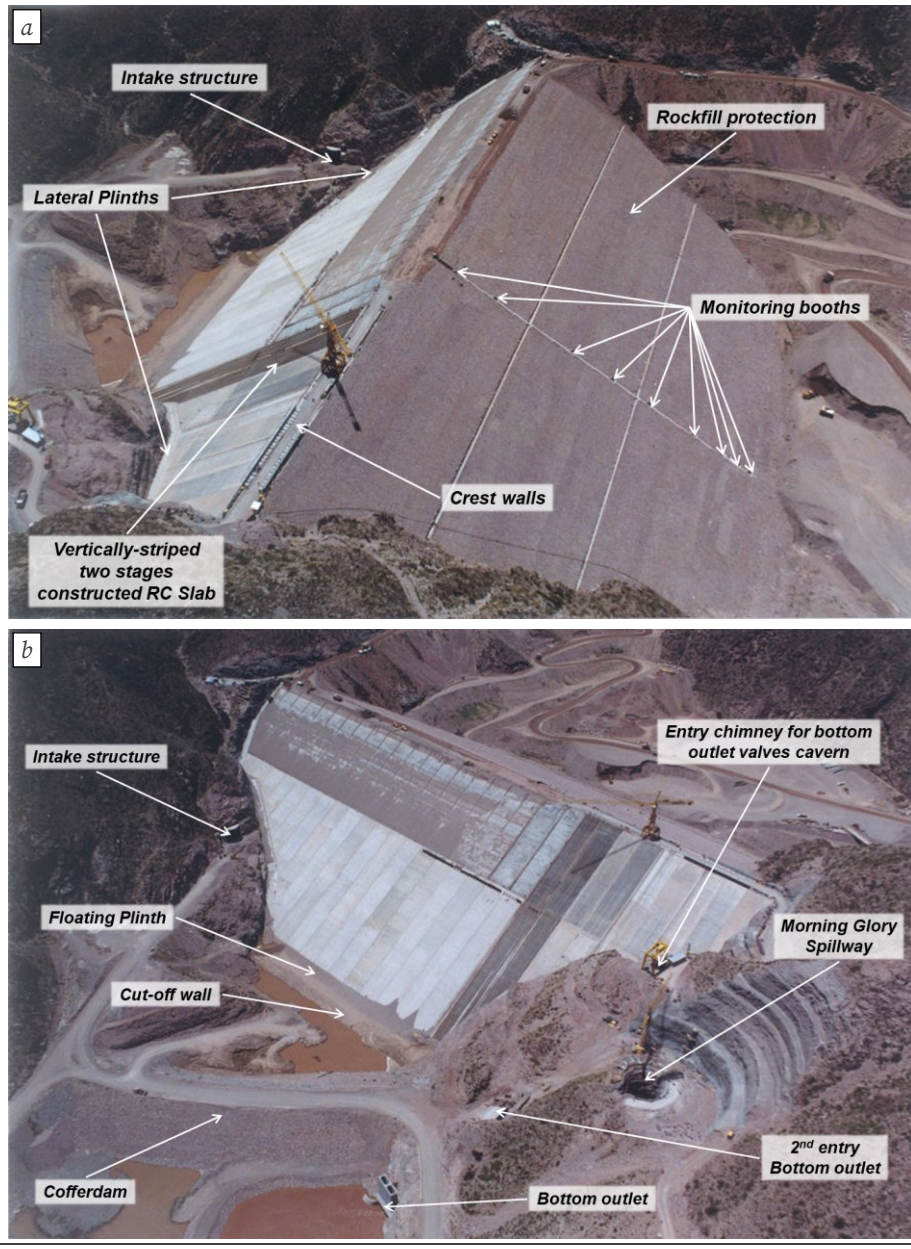


Fig. 3.7: Aerial pictures of the dam and appurtenances during the construction, with its most relevant components: a) downstream view, and b) upstream view. Archive Prof. A. Barchiesi.

As illustrated in Fig. 3.7, the dam is equipped with appurtenant structures distributed along both the right and left abutments. All these structures are embedded within the surrounding rock mass and are physically independent from the dam body itself. On the left abutment are located the intake structures, which connect the reservoir to the Cacheuta hydropower station through a 4.3 km long tunnel of 5 m diameter (Espinosa et al., 2002).

On the right abutment, the hydraulic control structures are situated. These include a morning glory spillway with a maximum discharge capacity of 2200 m^3/s, and a bottom outlet system comprising two intake points: a primary intake for regular operation and a secondary intake designed to be used when sediment accumulation obstructs the primary. Also on the right abutment, within the rock mass, there is a cavern (Fig. 3.8a) housing the valve system that controls the bottom outlet, connected to the surface via a vertical shaft (Lara et al., 2008). The cavern is built within a fractured rock mass, and to improve its stability, a gallery forming a ring above the cavern roof was constructed to control infiltrations (Fig. 3.8b).



Fig. 3.8: a) Cavern housing the control valves of the bottom outlet, and b) gallery over the roof of the cavern to control the infiltration and improve its stability.

One of the most remarkable features of the dam, at least from a geotechnical perspective, is its foundation on alluvial material of variable thickness, overlying a Triassic granite bedrock with a complex geometry. This complexity is evident in Fig. 3.9, which shows the contours of the alluvium thickness reconstructed from exploratory boreholes and geophysical surveys.

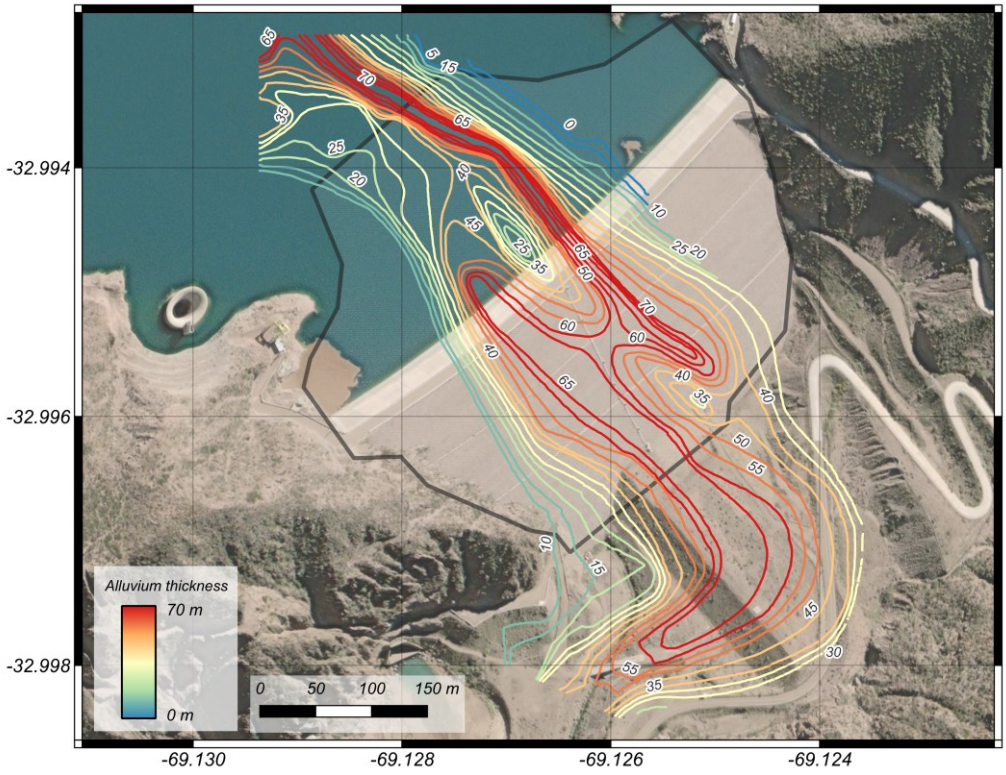


Fig. 3.9: Contours of alluvium thickness in the dam site, reconstructed from boreholes and geophysics.

The complex shape of the bedrock is likely the result of the tectonic history combined with fluvial processes that have occurred over thousands of years. This irregular geometry required a specially designed cut-off wall, incorporating four different materials to form the impervious barrier, as illustrated in Fig. 3.10. The base of the cut-off wall consists of a mixture of concrete and bentonite slurry, followed by a section of plain concrete, and topped with reinforced concrete (Barchiesi et al., 2005). In the sections where the bedrock surface was too irregular or steep to allow excavation, the alluvial soils were treated with jet grouting to reduce their permeability. The influence of the foundation on the response of the dam will be contemplated during the performance evaluations.

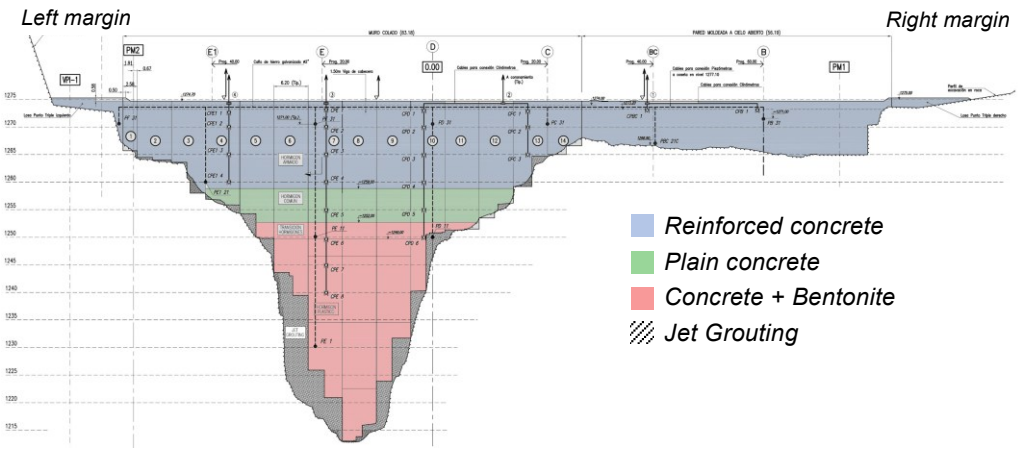


Fig. 3.10: Section of the cut-off wall parallel to the dam axis, from upstream. The four distinct materials used in its construction are highlighted using different colors.

Finally, the dam is equipped with a monitoring system with more than 200 instruments, which will be object of a detailed description and analysis in the final part of this chapter.

3.3 Geotechnical in-situ and laboratory tests

As with any large-scale project, the design and construction of an embankment dam typically involve a wide range of geotechnical investigations, including both in situ and laboratory tests, to characterize the soils and rocks involved in the project. A feasible methodology for the characterization of a gravelly alluvium proposed by DeJong et al. (2016) is shown in Fig. 3.11 to illustrate the steps that should be involved in the process.

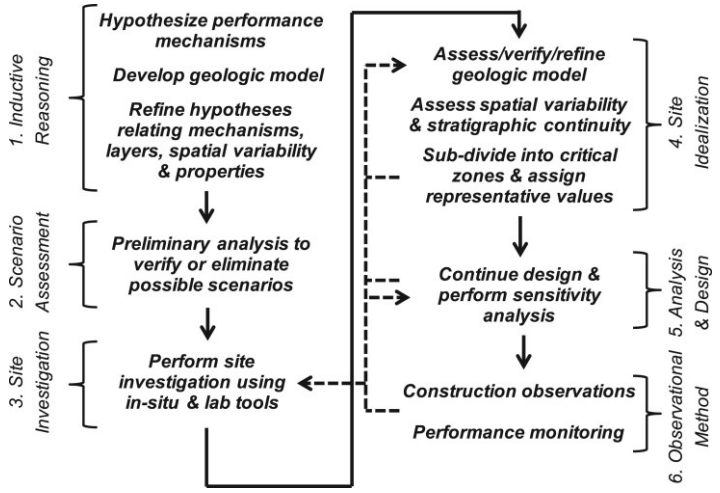


Fig. 3.11: Systematic methodology for site characterization of gravelly alluvium (DeJong et al., 2016)

The planning of the geotechnical investigation campaign and the selection of the laboratory tests to be performed should be carried out with careful consideration of the intended use of the results, as well as the extent and representativeness of each characterization (Chowdhury et al., 2022). Moreover, the characterization techniques or laboratory tests have to be suitable for the type of soil under study, selecting those methods with the ability to accurately identify the mechanical or hydraulic properties of the specific soil under investigation.

The characterization of the soils and rocks involved in the design of the Potrerillos Dam is described below, focused on both in-situ and laboratory tests that will be later used for the calibration of constitutive models. Recognizing the potential inconsistencies that could arise between tests, a critical evaluation will be conducted to assess the representativeness of the samples concerning the actual materials they aim to characterize, and to try to harmonize the characterization. Additionally, any issues identified in the outcomes of the in-situ and laboratory tests will be analyzed to determine their reliability and relevance for use in the calibration of numerical models.

The geological and geotechnical campaigns for the Potrerillos project were developed in four different periods:

- In 1986-1988, concerning a former project (Consorcio Potrerillos, 1988).
- In 1998-1999, to support the development of the dam project (GCPP, 1998).
- In 1999-2002, with test embankments and construction control (GCPP, 1999).
- In 2003-2005, evaluations after construction (THYA & Coyne et Bellier, 2005).

The information for all the periods was evaluated and considered, keeping in mind that the objectives of each campaign were different and not explicitly related to the modeling of the dynamic response of the dam. A summary of the available tests of the soils and rocks from the dam and foundation is reported in Fig. 3.12, together with the cross section of the dam. The presentation of the characterization will focus on the soils considered in the subsequent chapters, and will present only those tests used for the further calibrations.

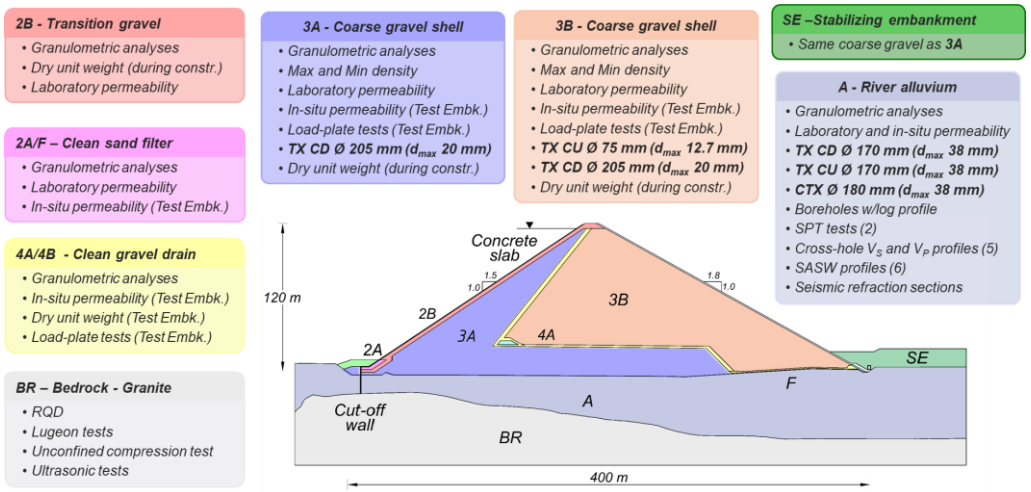


Fig. 3.12: Summary of the geotechnical tests available for every soil and rock type of the dam. TX refers to static triaxial test, CTX to cyclic triaxial tests, CD stands for consolidated and drained, CU for consolidated and undrained, ∅ is the sample diameter and d_{max} the maximum particle size.

3.3.1 Bedrock characterization

The rock mass beneath the dam foundation corresponds to a Triassic granite, part of the Potrerillos Formation, with the outcropping sections of this rock mass revealing moderate fracturing. The geometry of the bedrock was delineated through a combination of geophysical surveys and borehole data distributed across the dam site (GCPP, 1998).

From the drillings with core recovery that penetrated the bedrock, shown in Fig. xx, the Rock Quality Designation (RQD) (Deere & Deere, 1988) was determined at every meter of coring. The RQD values are plotted with respect to elevation in Fig. 3.14a to try to identify any trends in the distribution. In addition, a basic statistical analysis of the RQD data is also provided through a histogram and a cumulative distribution function (CDF), in Fig. 3.14b and Fig. 3.14c, respectively. Also, an extreme value distribution was fitted to the data to facilitate graphical identification of the mean and median values. The mean and median RQD values were found to be 68 and 60, respectively, presented in Fig. 3.14a together with all the points. Such values of RQD can be further correlated with the Geological Strength Index (GSI) (Marinos & Hoek, 2000), adopting a condition for the discontinuities using the parameter $JCond_{89}$ (Bieniawski, 1989), equal to 20, corresponding to an intermediate condition, it is possible to obtain the GSI using Eq. 3.4.

$$GSI = 1.5 \cdot JCond_{89} + RQD/2 \qquad \text{Eq. 3.2}$$

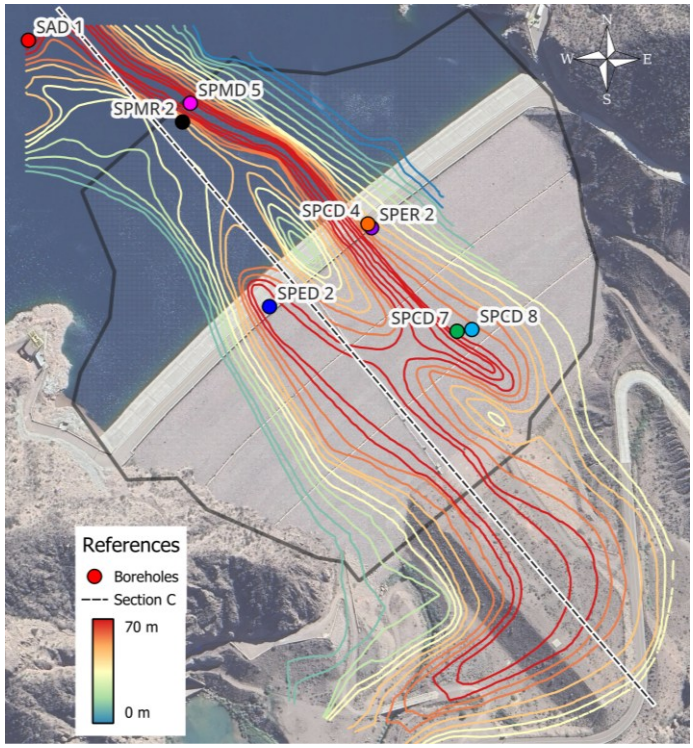


Fig. 3.13: Location of the drillings where the RQD was performed, together with the alluvium thickness contours

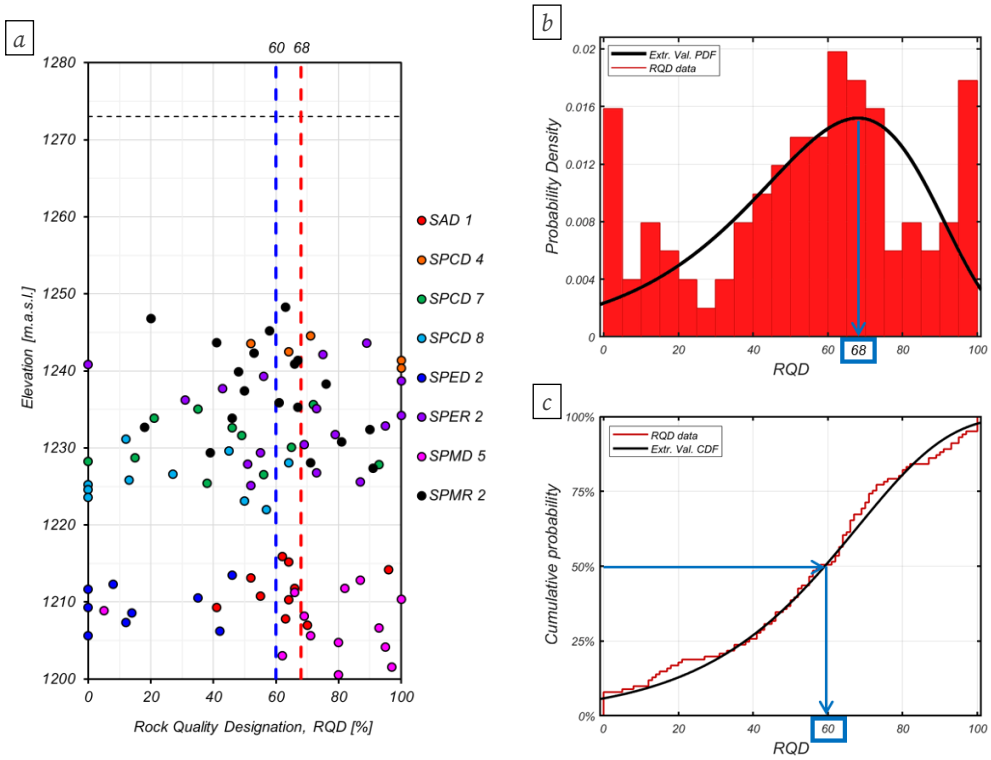


Fig. 3.14: a) RQD vs. elevation, b) RQD histogram and extreme value distribution, and c) RQD CDF.

The GSI oscillates between 60-64, depending on the RQD value adopted was the median or mean value. All these indices will be considered in the evaluation of the stiffness and strength of the rock mass in Chapter 6.

The hydraulic properties of the rock mass are evaluated using the results from Lugeon tests (Vaskou et al., 2019) performed on the drillings presented in Fig. 3.15a. A Lugeon unit (LU) is defined as the loss of one litre of water per minute per metre of the borehole test section, at an excess injection pressure of 1 MPa in the center of the test interval, and can be correlated with the hydraulic conductivity of the rock mass in a simplified manner by considering 1 LU $\equiv 1.0 \times 10^{-7}$m/s (USBR, 2014). In this way, it is possible to plot the distribution of LU vs. the elevation (Fig. 3.15b), and also the hydraulic conductivity k vs. elevation (Fig. 3.15c), and estimate an average hydraulic conductivity $k = 1.7 \times 10^{-6}$m/s for the rock mass.

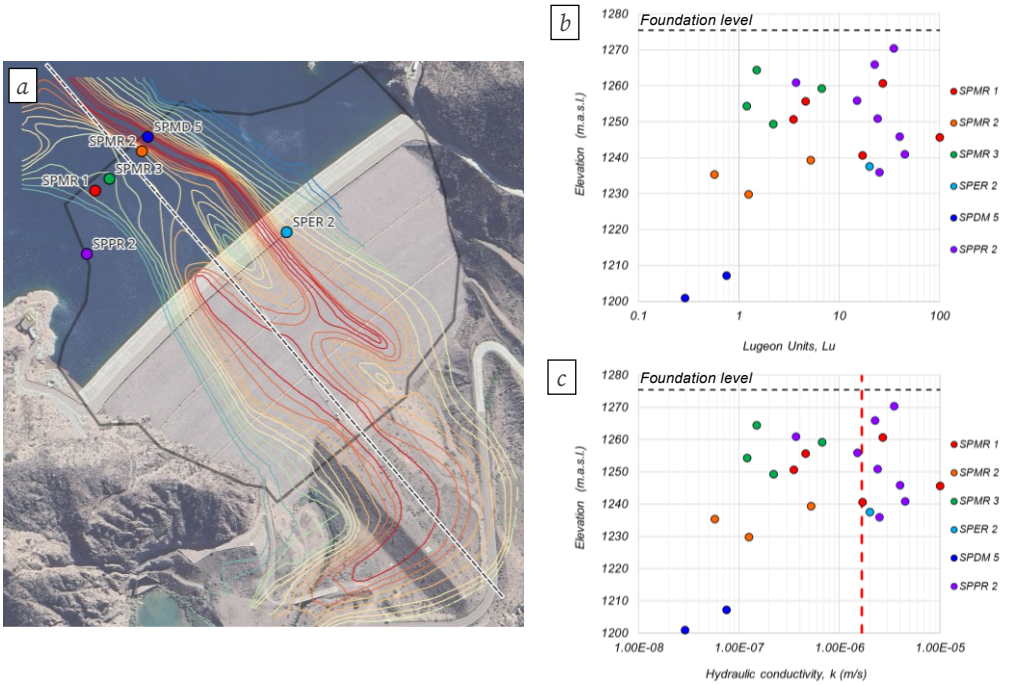


Fig. 3.15: a) Location of the drillings where Lugeon tests were performed, b) distribution of Lugeon units vs. elevation, and c) distribution of estimated hydraulic conductivity vs. elevation.

The last tests performed on the rock were done on samples representative of the core extracted during the drilling. The results from three unconfined compression tests and three ultrasonic tests are presented in Table 3.1.

BH	ρ_R (kg/m^3)	f_u (MPa)	E_s (MPa)	E_d (MPa)	E_s/E_d	G_d (MPa)	ν
SPMR-3	2613	129	29226	56175	0.52	21329	0.32
SPMR-4	2603	114	28423	53041	0.54	19981	0.33
SPMR-5	2601	98	28060	42790	0.66	16204	0.32

Table 3.1: Results from ultrasonic tests and unconfined compression tests done over three rock samples, where ρ_R is the rock matrix density, f_u is the unconfined compression strength, E_s is the static elastic modulus and E_d is the dynamic elastic modulus, while G_d is the dynamic shear modulus and ν the Poisson ratio.

3.3.2 Alluvium characterization

The characterization of the alluvial soils is done considering the results from triaxial tests and cross-hole tests done in different places along the alluvium. In addition, two standard penetration tests (SPT) are available downstream of the dam and will support the characterization of the sandy soils in the foundation, the same soils that promoted the construction of the stabilizing embankment.

But first, and focused on a central cross-section (Section C), it is possible to present in a cross-section the boreholes in the vicinity of this section, aiming at identifying different lithologies or stratigraphic sequences that could help in defining the geotechnical model of the alluvium. The location of the boreholes in plan and the cross section are presented in Fig. 3.16 and Fig. 3.17, respectively. In addition, in Fig. 3.16 are also evidenced the boreholes P5A and SPCD-8, which will be referred to the SPT tests and soil characterization, respectively.

From the first evaluation of the figures and solely based on the information of the eight boreholes selected, there is a tendency for the presence of sand and silty sand around 30-35 m below the surface level. Even if this tendency does not confirm the presence of a continuous layer given the number of boreholes considered and the distance among them, it is evident that the soils present between those depths are going to contain an important percentage of sand and behave like sand-like soils. This will be further considered at the moment of the modeling, when calibrating the constitutive models.

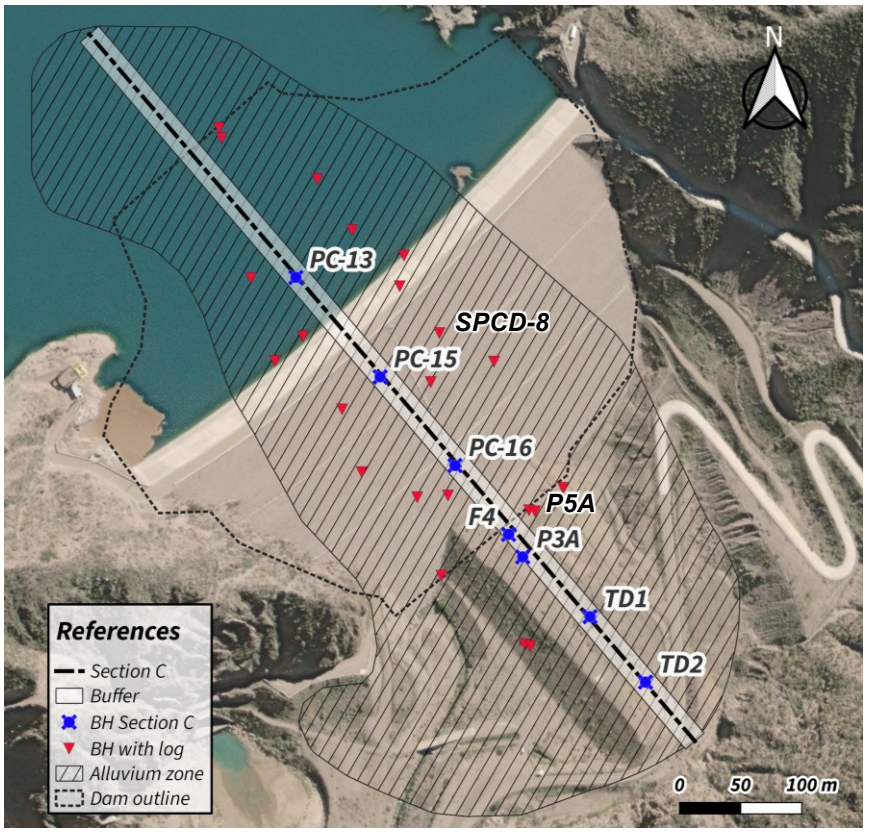


Fig. 3.16: Plan view of the dam with the location of the alluvial zone and the boreholes (BH) with logging. Those associated with Section C in a buffer zone of 20 m are highlighted.

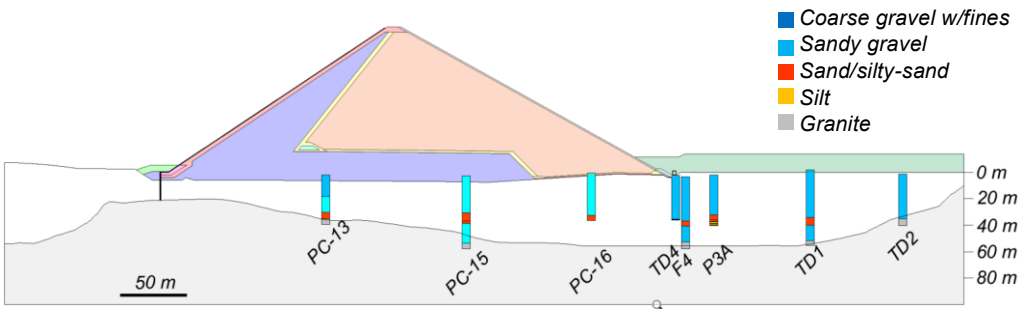


Fig. 3.17: Cross-section of the dam with the selected boreholes, and their identified lithology.

To visualize the variability of the soil, the core obtained from borehole SPCD-8 is presented in Fig. 3.25. It can be observed that the particle sizes range from sand and finer soils to large boulders exceeding 1 meter in diameter. This wide variability poses significant challenges in characterizing the mechanical properties of the alluvial soils, as conventional in situ and laboratory testing methods developed for sands and fine-grained soils often encounter limitations when applied to soils containing large particles.

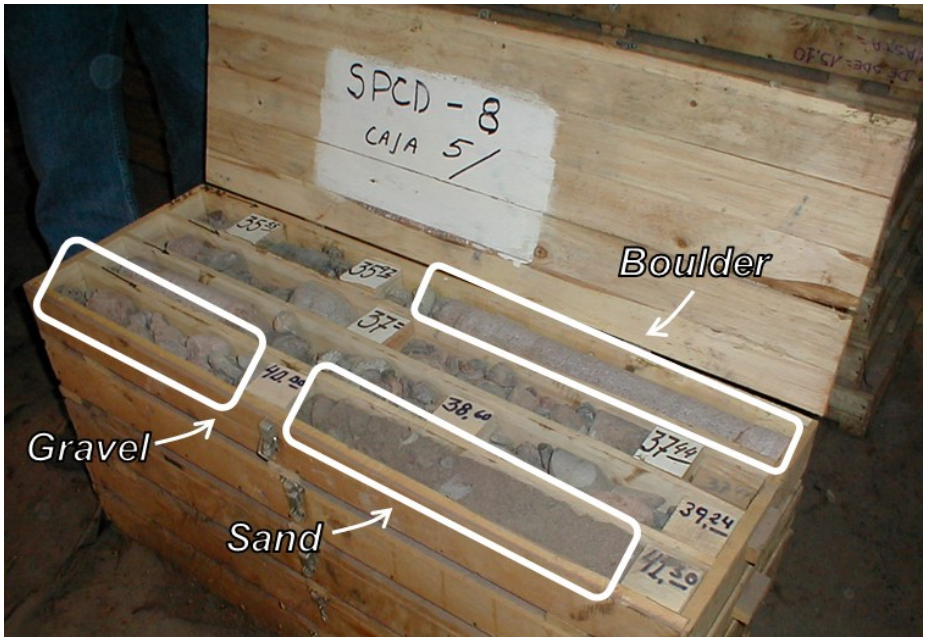


Fig. 3.18: Picture of the coring corresponding to the borehole SPCD-8. Archive Prof. A. Barchiesi.

This limitation can be further evidenced in the analysis of the results from the two SPT tests performed in the alluvial soils, in the boreholes P3A and P5A. The results from both tests are presented in Fig. 3.23.

From the first evaluation is clear that the tests were performed focused on characterizing only the portion with sand and silts, between 30-35 m depth. The second thing that can be observed in Fig. 3.23 is that, on average, the raw blow counts are large except for a few layers that exhibit values even under 20 blows. Given that information on the number of blows per unit of penetration was not available, it remains unclear whether the high blow counts were due to densified soil or the presence of cobbles.

When considering how the test is conducted in this type of soil, a high blow count may result from either a densified soil or the impact with a cobble or boulder during testing. This distinction can sometimes be clarified after the test by inspecting the equipment for signs of damage to the sampler or by analyzing the blow count per unit of penetration. In contrast, a low blow count is generally considered a more reliable indicator, as the influence of drilling disturbance is typically minimized by excluding the first 15 cm of penetration. Hence, a low blow count is likely a consequence of a less dense soil.

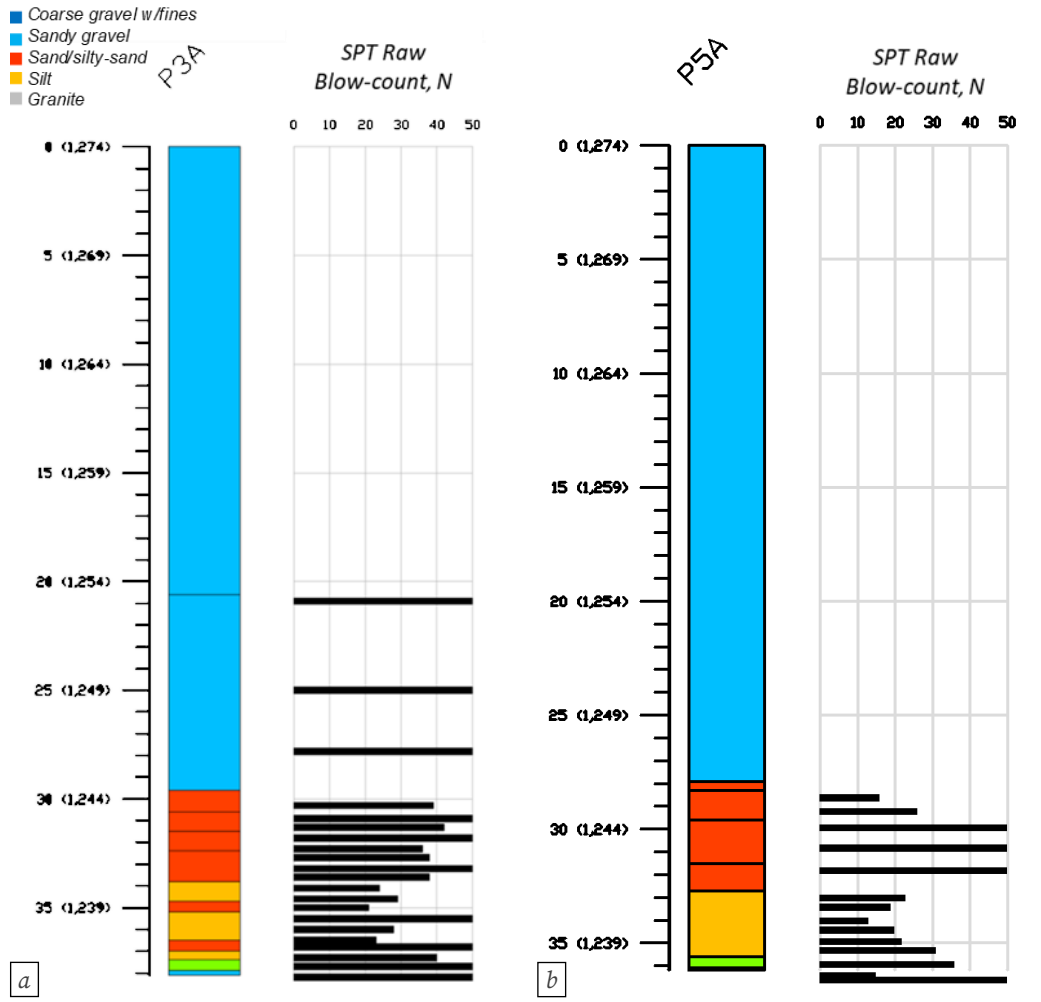


Fig. 3.19: Uncorrected or raw blow count of the SPT tests performed in the boreholes, a) P3A, and b) P5A.

Another two SPTs were performed in shallow test pits over deposits mostly removed during the excavation before dam construction, using a non-standardized solid cone tip instead of the Terzaghi sampler, with mostly large values of blow count.

Granulometric analyses from the material obtained from the sampler of the SPT are presented in Fig. 3.20 and Fig. 3.21 for the boreholes P5A and P3A, respectively. As a first screening criterion for the identification of the liquefaction susceptibility of the abovementioned soils, overlapping the granulometric curves with the limits for “Easily” or “Very Easily” liquefiable material for both uniform and well-graded soils (Iai et al., 1989), it could be an interesting first evaluation to combine with the SPT values.

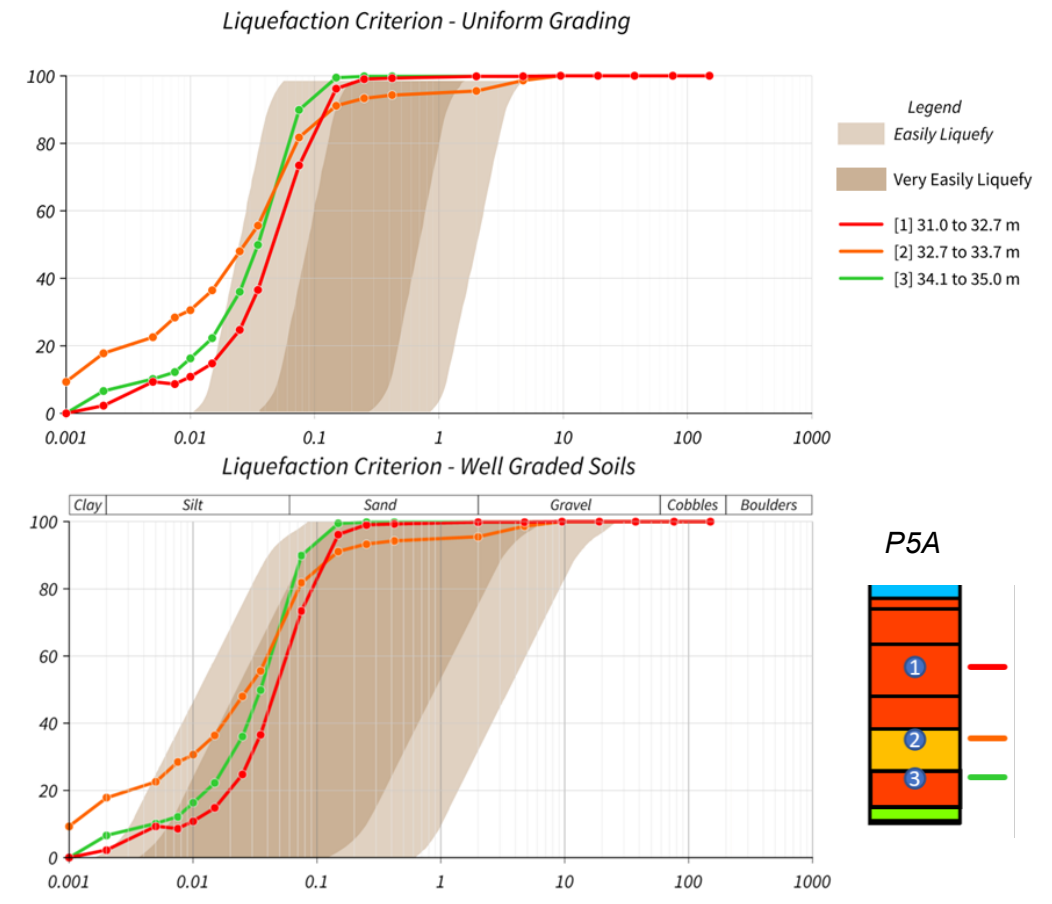


Fig. 3.20: Granulometric curves for the soils contained in the sampler during the SPT performed in the borehole P5A, overlapped with the limits for "Easily" and "Very Easily" liquefiable by Iai et al. (1989).

It is evident from the first analysis of the figures that many of the soils from the last part of both boreholes, at least based on the selected screening criteria, have the potential of being liquefiable under strong ground shaking. However, the stress conditions and relative density of the soil could play a more important role than just the particle size distribution in the triggering of liquefaction and will be considered when calibrating the constitutive models in Chapter 6.

The lowest blow count related to a material described in the logging as a fine sand without fines is N = 16 from the borehole P5A at 28 m below the riverbed. In a conservative approach, this value will be used for the calibration of the models related to this part of the alluvium.

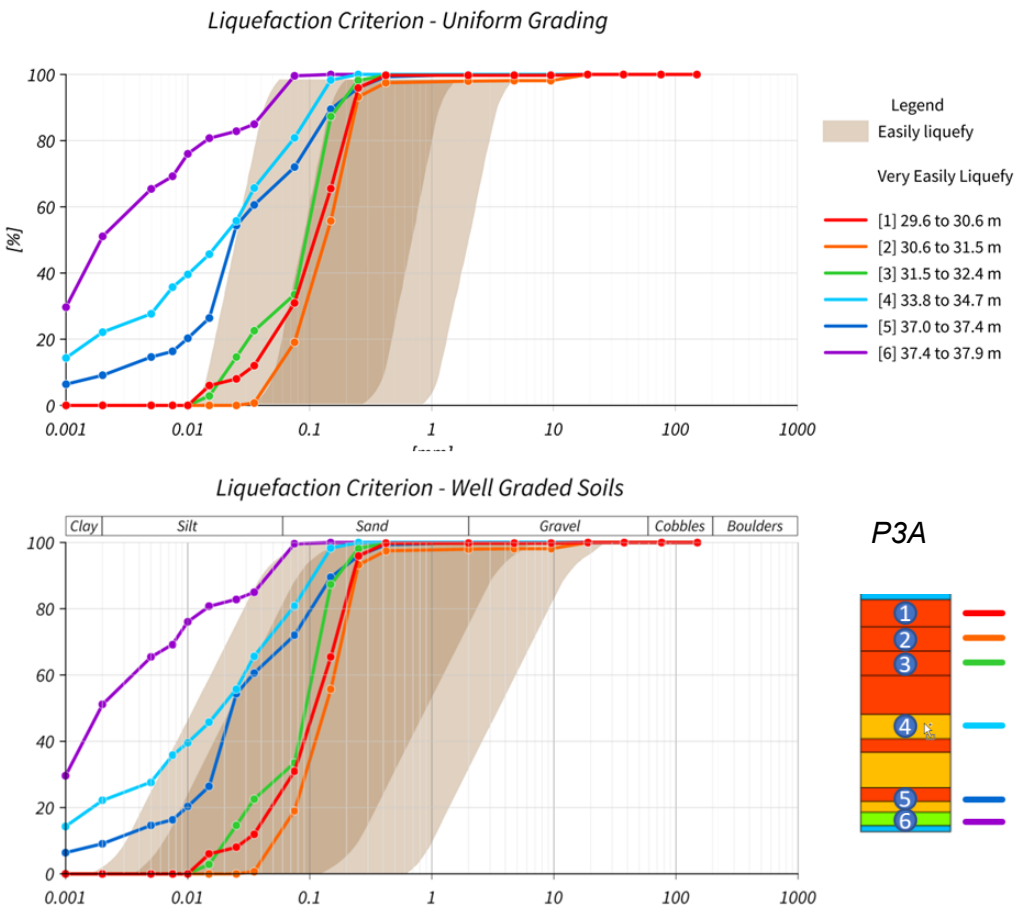


Fig. 3.21: Granulometric curves for the soils contained in the sampler during the SPT performed in the borehole P3A, overlapped with the limits for "Easily" and "Very Easily" liquefiable by Iai et al. (1989).

The SPTs were performed using the most widespread variation of SPT used in Argentina, called pin-weight free-fall, with an energy efficiency of about 90% (Leoni et al., 2011).

Following with the characterization of the alluvium, a total of five cross-hole tests were done in the alluvium, three of them (CH-1, CH-2, and CH-3) before the construction of the dam, and the two remaining (CH-4, and CH-5) focused on the depths where the sand and silty-sand soils were found. The location in plan view of these tests and the profile of shear wave velocity (Vs) vs. depth are presented in Fig. 3.22. What is noticeable from the profiles of shear wave velocity is that the first 10 m show an almost constant value of Vs around 300 m/s, after which it starts to increase following a parabolic distribution in depth.

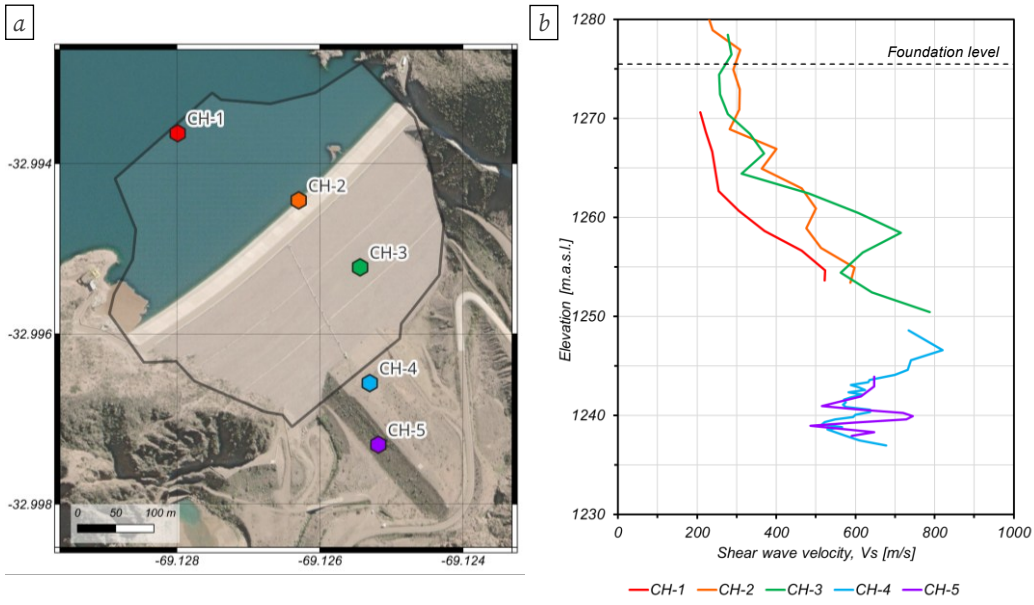


Fig. 3.22: a) Location of the cross-hole tests, and b) profile of Vs from all the cross-hole tests.

The second peculiarity is that the values of Vs from CH-4 and CH-5 do not suggest the same level of densification as the SPTs for the sand and silty-sand soils. This could be the consequence of many factors, among which the cementation of the soils, but also could be that being the distance between boreholes more than 4 m and the sandy soils surrounded by gravelly soils, the direct waves arrived after those that travelled through the stiffer gravelly soils, ending with an evaluated shear wave velocity larger than the real (Butler & Curro, 1981).

The last tests considered for the characterization of the alluvial soil are laboratory tests, performed over reconstructed samples obtained from a few shallow test pits at the dam site. A total of 10 consolidated drained monotonic triaxial tests (TX-CD) and four cyclic triaxial tests (CTX) were done with soils coming from the test pits presented in Fig. 3.23. The samples used in these tests were reconstructed considering a scalped granulometric distribution, limited by the maximum particle size (d_{max}) presented in Fig. 3.12, and considering a relative density closer to the in-situ relative density of the alluvial soils.

To evidence the kind of soils that these tests are trying to represent, the granulometric curves for the test pits CP6, CP8, CP9, and CP10 are reported in Fig. 3.24. The range of grain size observed in the curves gives an idea of the type of soils involved, mostly coarse gravels with a variable percentage of sand that in some cases could be over 30% in weight of the sample, limits beyond which the sand fraction become influential in the cyclic response of sand-gravel mixtures (Pokhrel et al., 2024).

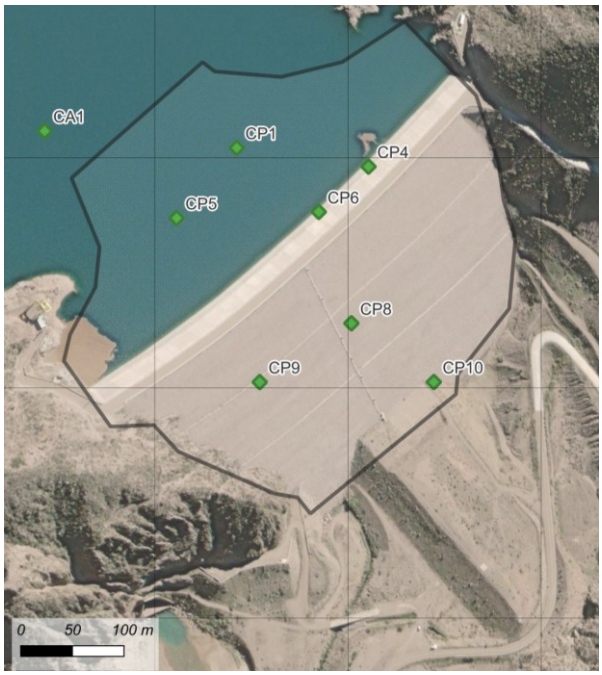


Fig. 3.23: Location of the surficial tests-pits where the samples for the laboratory tests were taken.

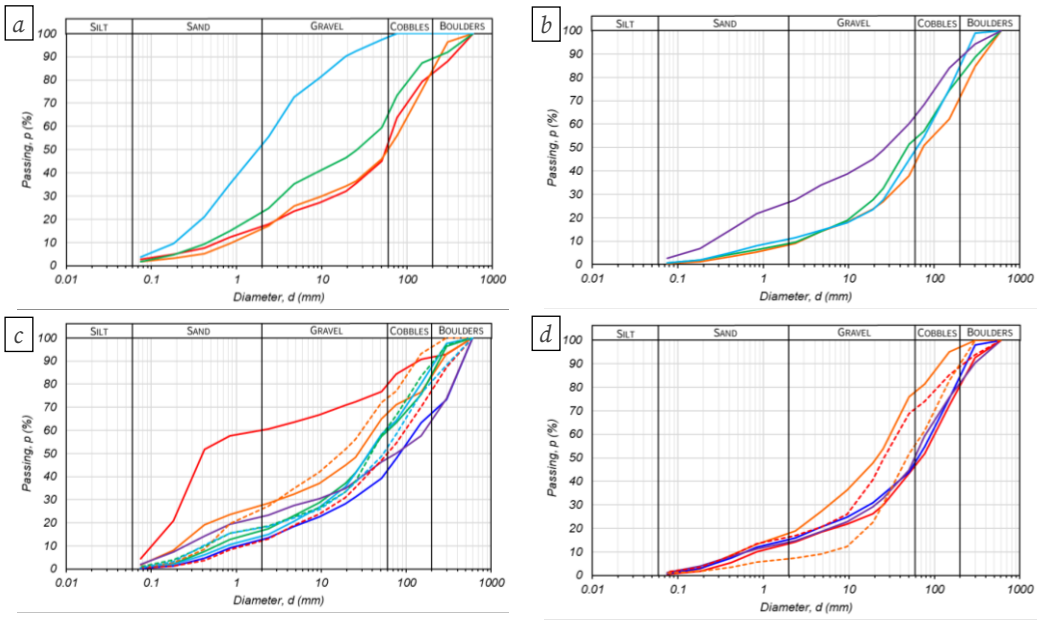


Fig. 3.24: Granulometric curves for the soils of the test pits a) CP6, b) CP8, c) CP9, and d) CP10.

The samples for the TX-CD tests had a diameter of 170 mm and a maximum particle size d_{max} = 38 mm, being the samples obtained by scalping the particles larger than this size and not maintaining the values of the coefficient of uniformity (C_u). This approach could condition the representativity of the tests (Flora & Modoni, 1997).

The results from the tests used for deriving a unique value of friction angle based on a linear fitting over the results for peak and large strain *q-p'* values, are presented in Fig. 3.25.

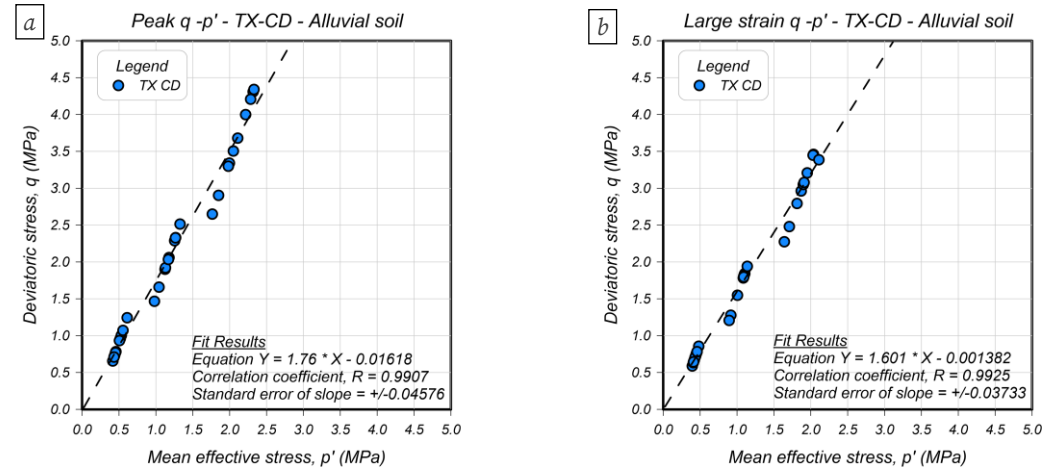


Fig. 3.25: q-p' plots of the results from the TX-CD tests on the alluvial soils, and the linear fitting used for the derivation of the friction angle for a) peak values, and b) large-strain values.

The first impression raises doubt about the quality of the information, as it seems to be following a stress path before reaching the failure, but the data points were verified and come from different tests. Using the parameters of the linear fitting, it is possible to obtain the friction angle using Eq. 3.3, where M is the slope of the linear fitting.

$$\sin(\phi) = \frac{3 \cdot M}{6 + M} \qquad \text{Eq. 3.3}$$

The resulting peak friction angle is $\phi_P = 42.9°$, and the large strain friction angle is $\phi_{LS} = 39.2°$. The latter is not reported as a 'critical state' friction angle due to the absence of volumetric strain (ε_V) data to prove it.

Following, only two out of the four CTX tests will be considered for the calibration of the constitutive models, as they are more suitable in terms of soil types and the relative density reported for the test pits. These tests were performed on a sample with a 180 mm diameter and d_{max} = 38 mm. Fig. 3.26 presents the cyclic resistance ratio (CRR) curves for the soils at 4 to 5 m depth in test pits CP9 and CP6, corresponding to relative densities of D_R = 50% and D_R = 60%, respectively.

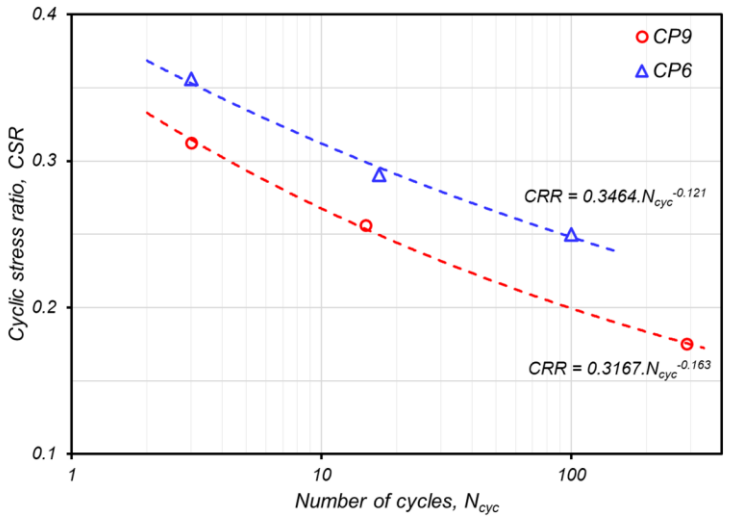


*Fig. 3.26: Cyclic resistance curve (*CRR*) from CTX tests over sample CP9 (D_R = 50%), and the sample CP6 (D_R = 60%), where the cyclic stress ratio* CSR = τ_{cyc}/σ'_{v_0} *, the ratio of cyclic shear stress and consolidation vertical effective stress.*

3.3.3 Dam embankment soils characterization

The soils 2B, 3A, and 3B, which compose more than 98% of the volume of the dam body, come from two quarries located upstream of the dam (Fig. 3.27).

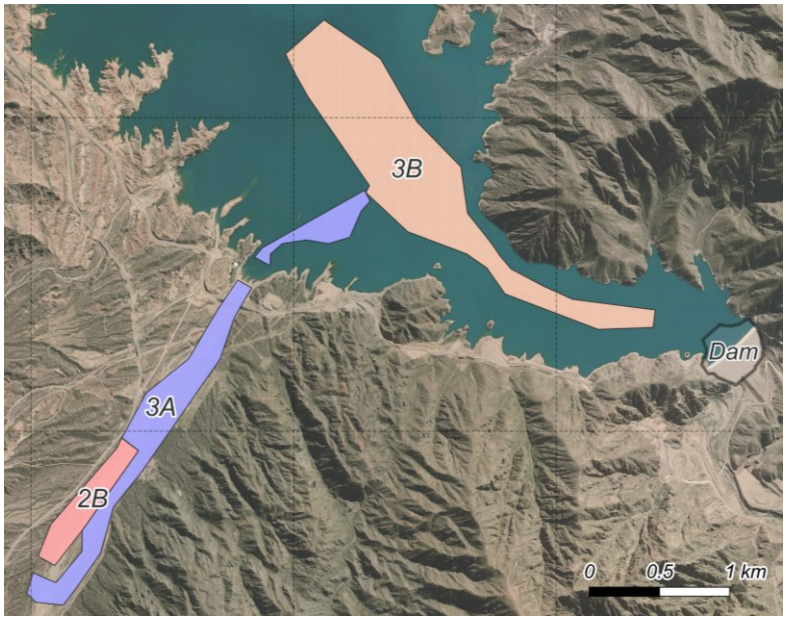


Fig. 3.27: Quarries for soils 2B, 3A & 3B, in the alluvium of Cacheuta and Mendoza rivers, respectively.

The quarries were located in the alluvium of the Mendoza River for 3B and the dry river Chacheuta for 3A. Soils from 3B are similar to those found beneath the dam, whereas soils from 2B and 3A tend to have more fines, as shown in the photography of Fig. 3.28.



Fig. 3.28: Soil representative from the quarry used for 3A. Archive Prof. A. Barchiesi.

This description is relevant as most of the laboratory tests were made over the natural material taken from the quarries as found, and not over the material homogenized and processed before being placed and compacted in the embankment. A few other tests were performed over trial embankments built at the dam site, as the load plate tests.

The first step is to present the granulometric distribution of these soils, overlapping the old tests coming from the campaign of geotechnical surveys of 1988 (Old tests) with those made in 1999 (New tests), and the limits set for the material effectively used in the dam body. The plots for the 3A and 3B soils are presented in Fig. 3.35.

It is evident from the figures and was a condition pursued during the design of the dam, that the material from 3B is coarser than the corresponding to 3A, which is located in the upstream portion of the dam body. This is evident as well from the evaluation of the limit curves. This was not only with the idea that a material with larger particles could be stiffer and stronger than one without them, but also to allow the presence of more fines in the upstream part of the dam body in case of damage to the concrete face.

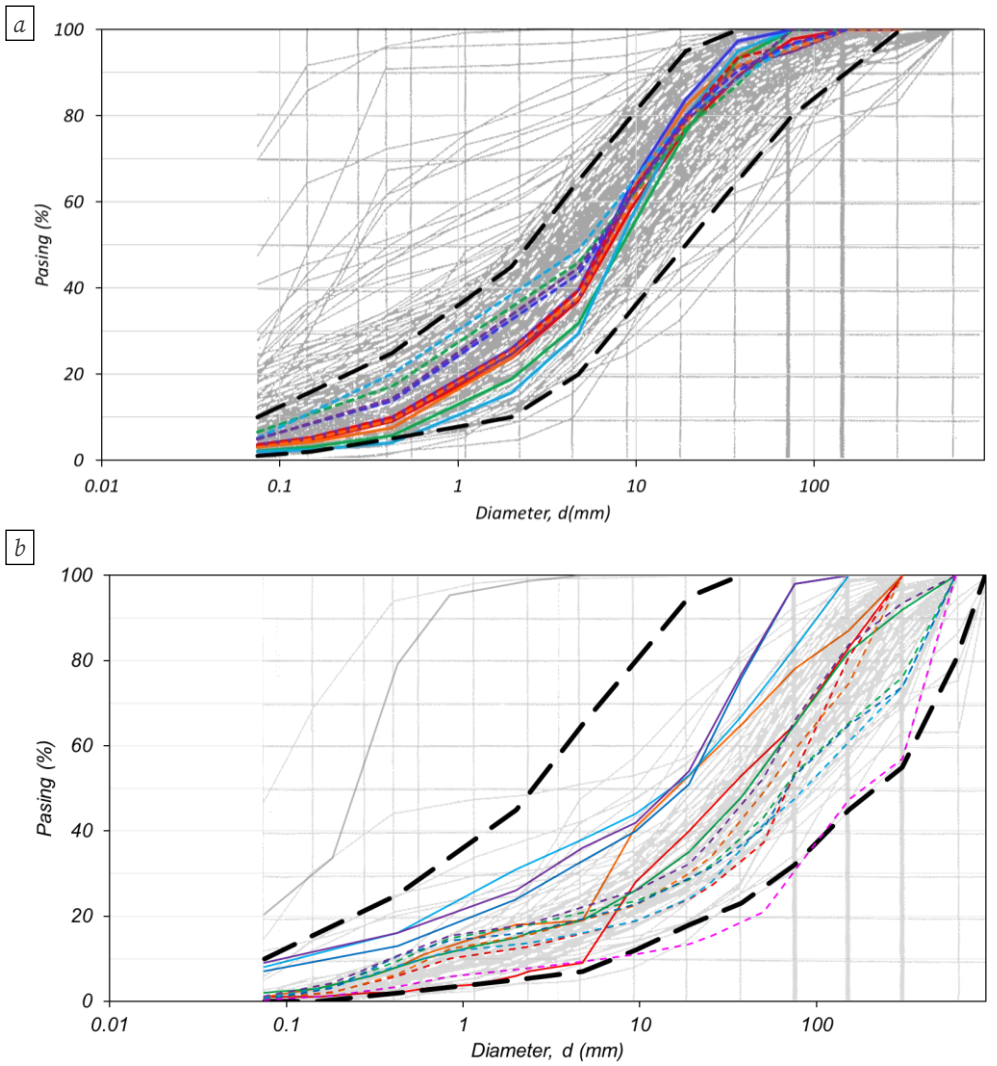


Fig. 3.29: Granulometric curves for the soils of the dam body, with black thin lines representing the Old tests, colored lines for the New tests, and black thick dashed lines identifying the admissible limits for the soils a) 3A, and b) 3B.

The data from the TX-CD test available for these soils are also from the geotechnical campaigns of 1988 and 1999, and the test was performed with a sample of 205 mm in diameter and d_{max} = 20 mm, at a dry unit weight γ_d = 22 kN/m^3. By using the same procedure used for the alluvial soils, the friction angle will be evaluated by carrying out a linear fitting over the *q-p'* values for the peak and large-strain conditions. Fig. 3.30 and Fig. 3.31 contain the referred points and parameters of the linear fitting for the soils of 3A and 3B, respectively.

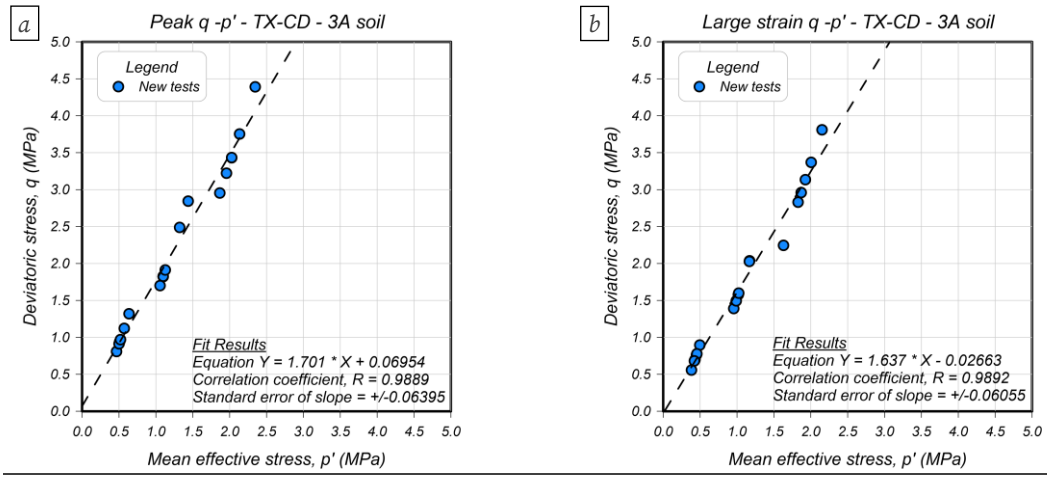


Fig. 3.30: q-p' plots of the results from the TX-CD tests on the 3A, and the linear fitting used for the derivation of the friction angle for a) peak values, and b) large strain values.

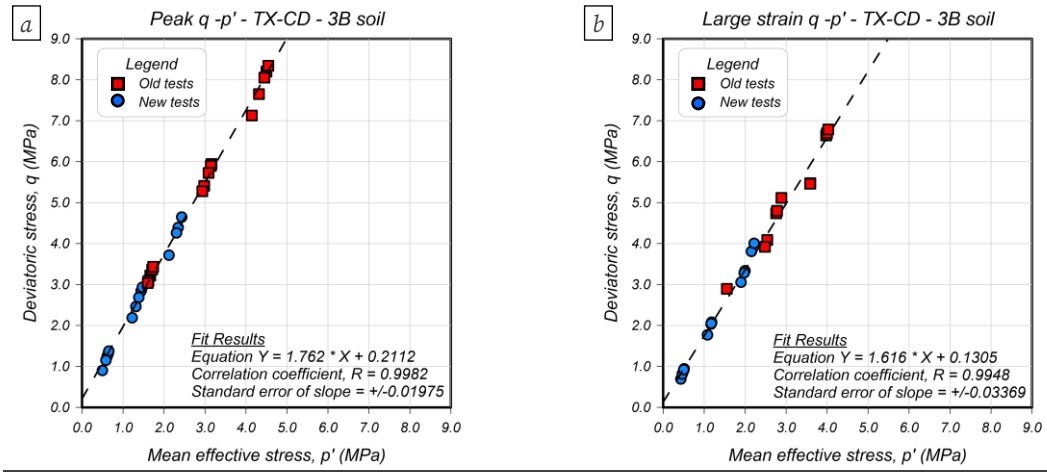


Fig. 3.31: q-p' plots of the results from the TX-CD tests on the 3B, and the linear fitting used for the derivation of the friction angle for a) peak values, and b) large strain values.

Using the Eq. 3.3 it is possible again to obtain the values for the peak and large strains friction angles, that for the soil 3A result equal to $\phi_P = 41.5°$ and $\phi_{LS} = 39.2°$, whereas for the soil 3B are $\phi_P = 42.9°$ and $\phi_{LS} = 39.5°$. From the comparison among these values and the ones obtained for the alluvial soils, it is evident that there are no significant differences among them, and this is detrimental for the characterization of the alluvial soils, as the reconstruction of the sample disregards the fabric of the naturally deposited soils. Moreover, it is again a compromise to consider tests with a d_{max} far smaller than the real d_{max} of the soil representative of their response, but the technology for realizing tests with large particles was unavailable at the moment of the dam construction, and the better estimates are provided by the test previously presented.

A further characterization of the soils of the dam body is the coefficient of uniformity C_u, which will be used during the calibration processes for adjusting literature curves for the variation of the normalized shear modulus G/G_0 vs. γ and damping D vs. γ. The values of C_u from the granulometric analysis of 1999 are presented as a histogram in Fig. 3.32, for 3A and 3B soils.

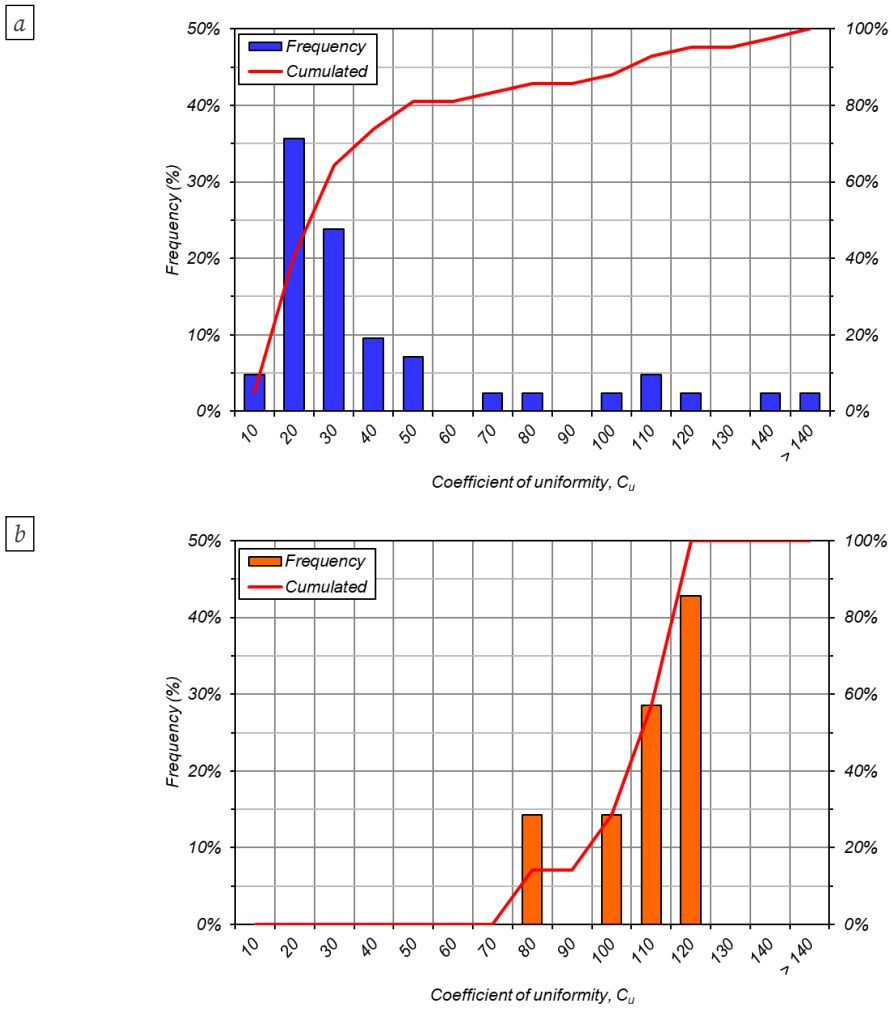


Fig. 3.32: Coefficient of uniformity C_u for the soils a) 3A, and b) 3B.

In terms of C_u, the difference between 3A and 3B soils is more evident, even if both can be classified as well-graded soils.

The same representation can be furnished for the dry unit weight γ_d, which was controlled during the construction to verify the compaction of the soils. The plot presenting the histograms of the distribution of γ_d for 3A and 3B is presented in Fig. 3.33.

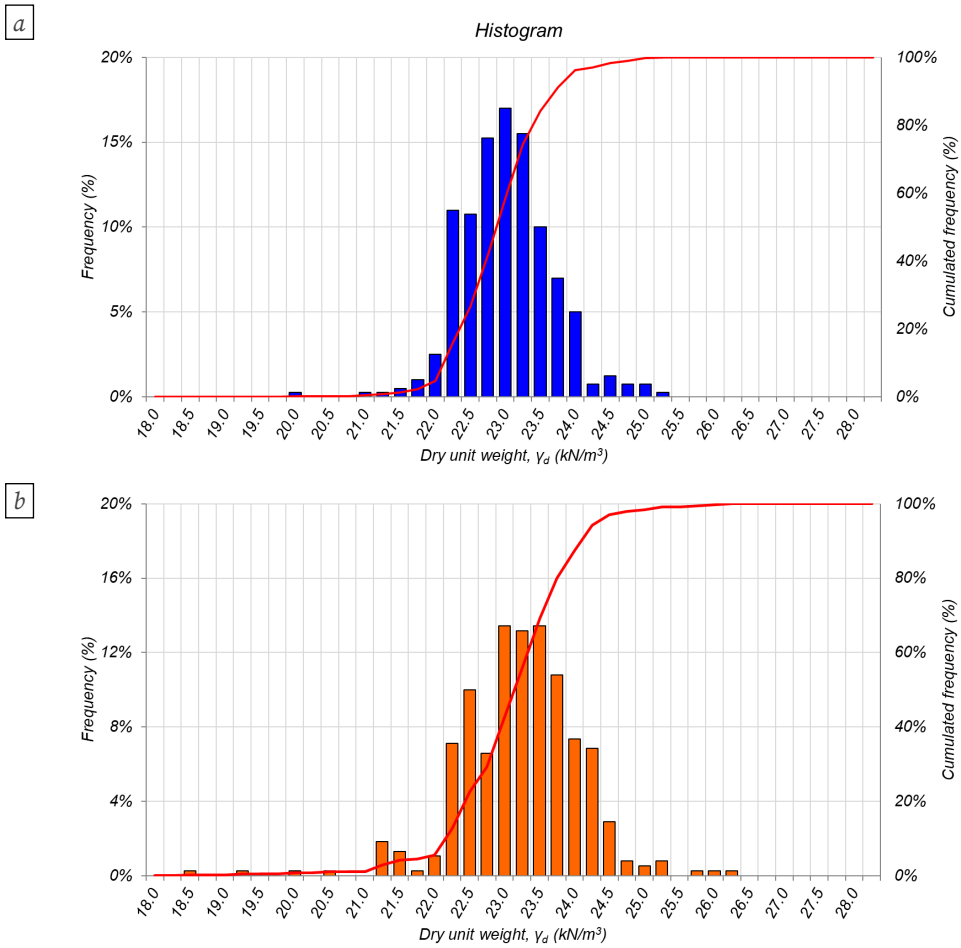


Fig. 3.33: Dry unit weight γ_d from the compaction control during construction, for a) 3A, and b) 3B.

The last test presented for the soils of the dam body will be the plate load tests performed on trial embankments at the dam site, in specific the one done using the cushion material beneath the concrete slab 2B. The plot with the curves of normal stress vs. vertical displacement is presented in Fig. 3.34. The results were further processed using the procedure of the standard DIN-18134 (DIN, 1993) to obtain the values of young modulus for the monotonic and the unload-reload paths, which average values for the three load cycles of every test are summarized in Table 3.2.

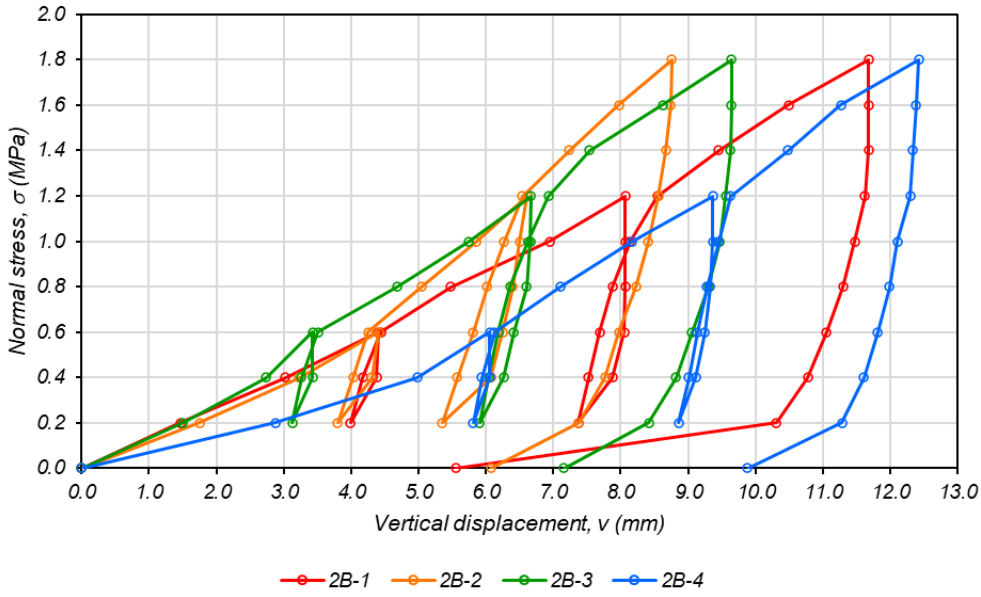


Fig. 3.34: Load plate tests performed on a trial embankment made of 2B material.

Test number	E (MPa)	E_{UR} (MPa)
2B-1	112	265
2B-2	138	241
2B-3	131	331
2B-4	133	412

Table 3.2: Young modulus for the monotonic and the unload-reload obtained from load plate tests made of 2B material.

3.4 Dam past behavior and monitoring data interpretation

An important step in the assessment of the seismic performance of a dam is to establish the baseline of the existing hydraulic and mechanical conditions before the next earthquake. To set this initial state, a well-rounded tool is the evaluation of the static and long-term hydraulic response of the dam throughout the analysis of monitoring records (Penman et al., 2018). Potrerillos Dam has more than 200 different instruments (Table 3.3) distributed all along the dam and foundation. These sensors monitor diverse physical magnitudes representative of the state of stress and hydraulic conditions of the system, bringing valuable information for dam surveillance during normal operation and extraordinary events.

Instrument	Type	Number	Reading frequency in normal operation
Piezometer	Vibrating wire	92	Continuous
Standpipe freatimeter	Water level sounder	10	Weekly
Total pressure cell	Hydraulic-electric transductor	14	Monthly
Settlement gauges	Vibrating wire	22	Monthly
Electric Limnimeter	Vibrating wire	1	Continuous
Uniaxial joint opening gauges	Vibrating wire	15	Weekly
Triaxial joint opening gauges	Vibrating wire	15	Weekly
Inclinometer (cut-off wall)	Electronic level	23	Monthly
Accelerometer	Micro-Electro-Mechanical System (MEMS)	4	Continuous
Open channel flow meter	Thin-walled triangular wire with a level sensor	4	Weekly
Thermometer	Vibrating wire	4	Weekly
Topography fix points	Concrete monoliths	28	Six-months

Table 3.3: Summary of the monitoring system of Potrerillos CFRD, listing the type, number of installed instruments, and frequency of readings for each kind of sensor, adapted from Espinosa et al. (2010).

Instruments can be classified as either surficial or buried. Most of the buried instruments are arranged along cross-sections designated alphabetically from left (Section A) to right margin (Section G), with an additional unaligned group located downstream. A color scheme is used to differentiate the buried instruments by section, as shown in Fig. 3.35.

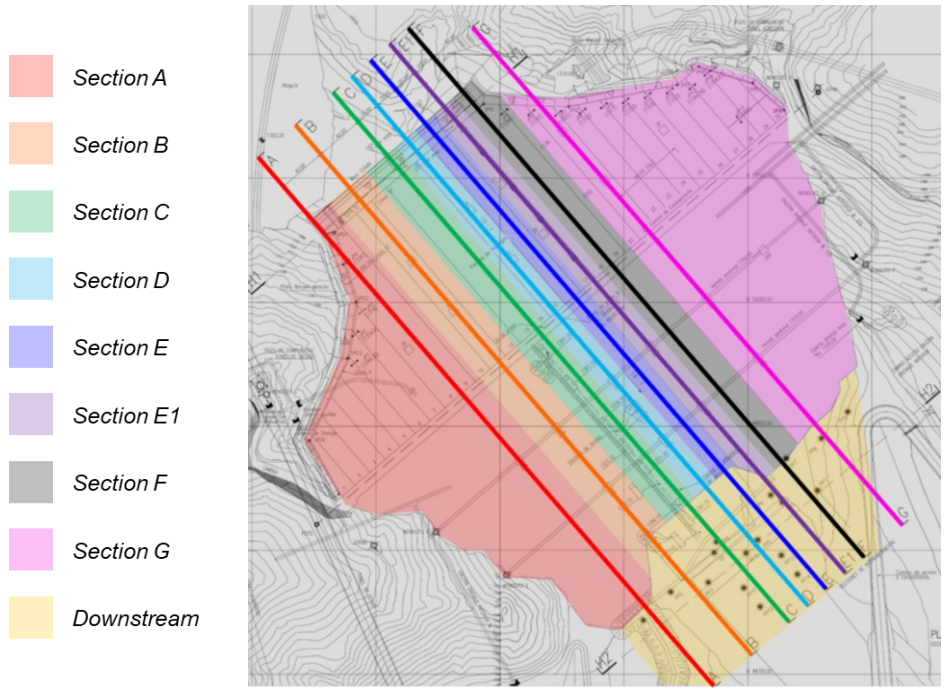


Fig. 3.35: Cross-sections and given color scheme used to identify buried instruments.

The spatial distribution of both surficial and buried instruments is presented in Fig. 3.36 and Fig. 3.37, respectively. The thermometers are not presented in Fig. 3.37 as they are installed together with some settlement gauges and are only used for calibration purposes. The instruments embedded in the cut-off wall and floating plinth are shown in Fig. 3.38.

Since the construction of the dam, the vast majority of the sensors have been in operation, and records of more than 20 years of monitoring are available for the analysis. The reliability of the monitoring records will be discussed, as circumstances like improper calibration, malfunction of the instrument, incorrect installation, or inaccurate processing of the information could lead to an erroneous valuation of the physical magnitude and a flawed interpretation of the response of the structure.

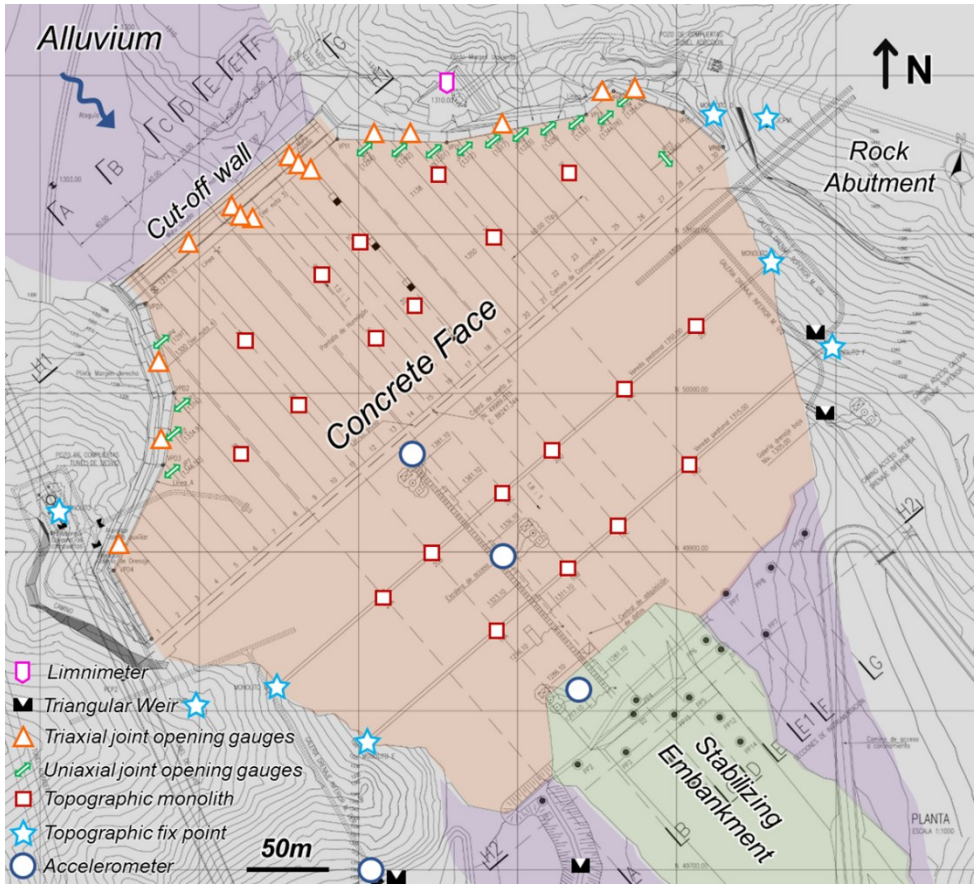


Fig. 3.36: In-plant view of dam features and distribution of surficial monitoring instruments.

Monitoring records will be analyzed using an integrated approach (Fontanella et al., 2020). Wherever possible, data from multiple sensor types will be combined and interpreted in relation to significant dam features. Hydrological information, including fluctuations in reservoir level and river water and solid discharge, will also be incorporated as these variables influence the normal operation of the dam and are captured by the surveillance system.

Particular attention will be given to the analysis of the seismic monitoring records, as they bring valuable information about the dynamic response of the dam under weak motion events (Sica & Pagano, 2020), and also help characterize the seismicity in the vicinity of the dam, and to derive useful information for the calibration and validation of the numerical models, as will be described as well in Section 6.

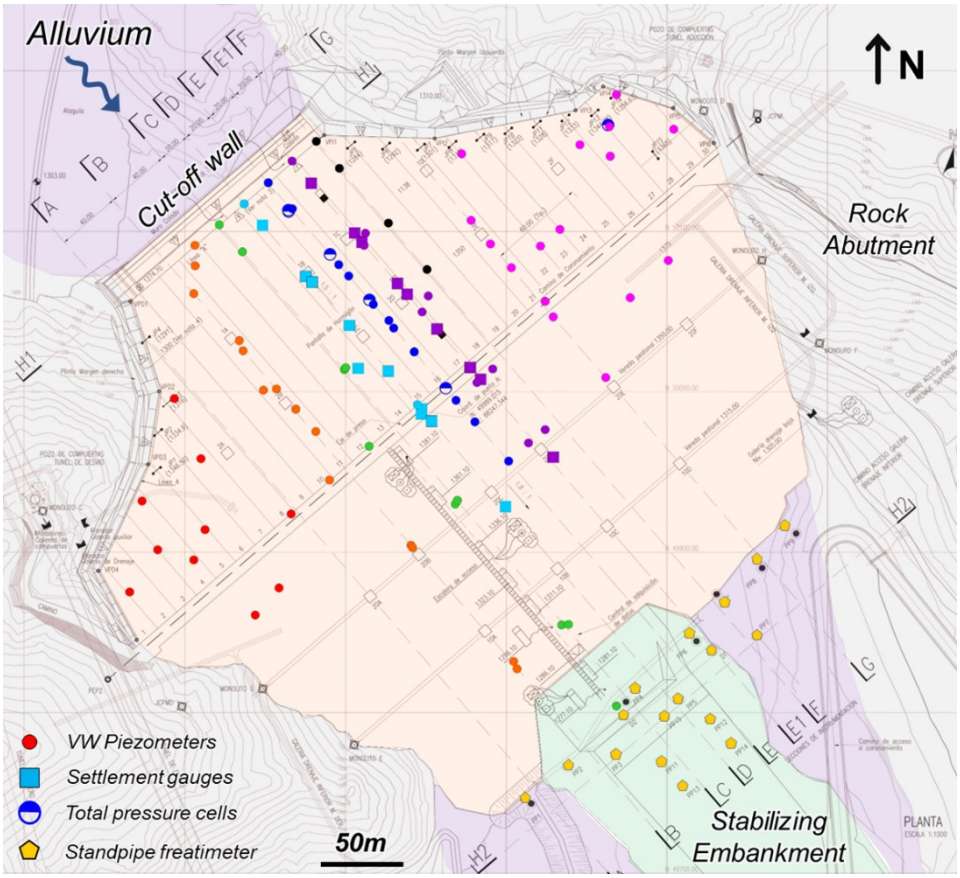


Fig. 3.37: In-plant view of the distribution of buried sensors in the dam and foundation.

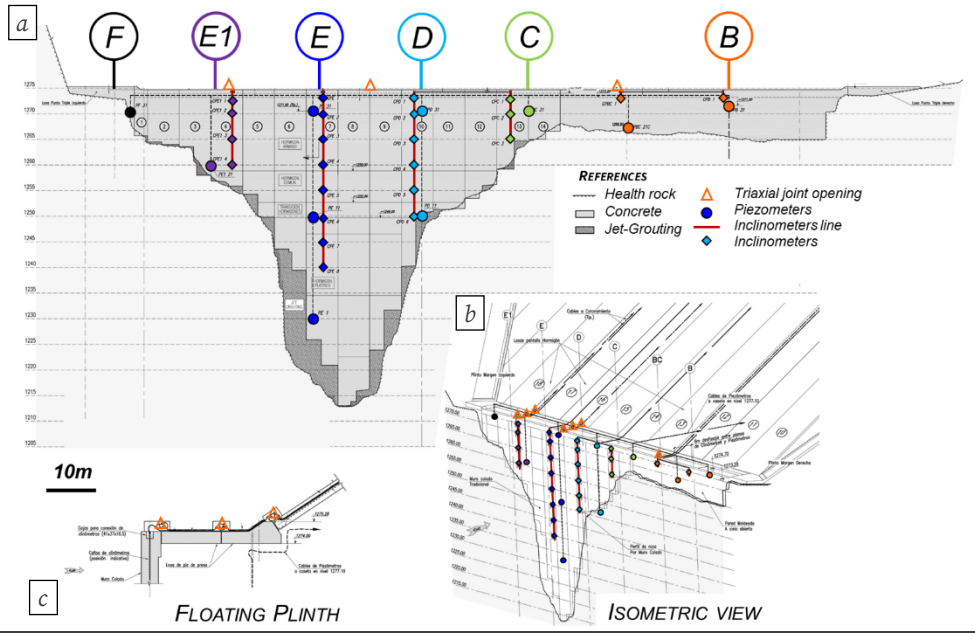


Fig. 3.38: Location of the inclinometers, piezometers, and triaxial joint opening gauges along the cut-off wall, a) upstream view, b) Isometric view, and c) detail of the instruments in the floating plinth.

For the sake of brevity and given that their analysis offers a minor contribution to the characterization of the dam response or calibration of numerical models for this study, some types of instruments will not be presented in further sections.

3.4.1 Piezometric and seepage records

As presented in Table 3.3, a total of 92 vibrating wire piezometers were installed in the Potrerillos Dam during its construction. These instruments were strategically distributed throughout the dam body and foundation to maximize the usefulness of their measurements in interpreting the dam's response. It can be noticed in Fig. 3.37 that most of the piezometers are placed towards the upstream part of the dam, which is reasonable as this portion of the dam is more likely to be saturated during normal operation or after an extraordinary event (e.g., damage of the concrete face).

A particular aspect to highlight is that the piezometers are installed in locations that are either expected to remain permanently saturated under normal operating conditions, occasionally saturated due to reservoir level fluctuations, or submerged only during extraordinary events. In the latter two cases, and considering the technology available at the time of installation, some instruments may experience difficulties with the resaturation of the filter surrounding the sensing membrane connected to the vibrating wire strain gauge (Penman, 2002; Thomann et al., 2003; Dunnicliff et al., 2003). As a result, both calibration and measurements may be compromised; hence, particular caution is taken when evaluating the records in instruments close to the water table.

It is worth noting a situation briefly mentioned in Section 3.2.1 before proceeding with the analyses. The first full impoundment was initially scheduled to start in 2002, following the completion of dam construction. However, disagreements among the parties involved in the project, along with the construction of the stabilizing embankment downstream of the dam, led to a delay that resulted in the first full impoundment occurring four years later. Since 2006, the dam has been in normal operation.

The analysis of the piezometers will be centered on a group of instruments that present an unusual response, taking as reference the monitoring records from Section E1 and presented for convenience in two groups (i & ii), in Fig. 3.39 and Fig. 3.40, respectively. The registrations from such instruments were also subject to analysis by the dam’s manager to evaluate if the hydraulic conditions verified, over the limits established for normal operation, could affect

the safety of the dam (Navarro, 2018; Barchiesi, 2019). The figures from the records of the remaining sections will be available in Appendix I.

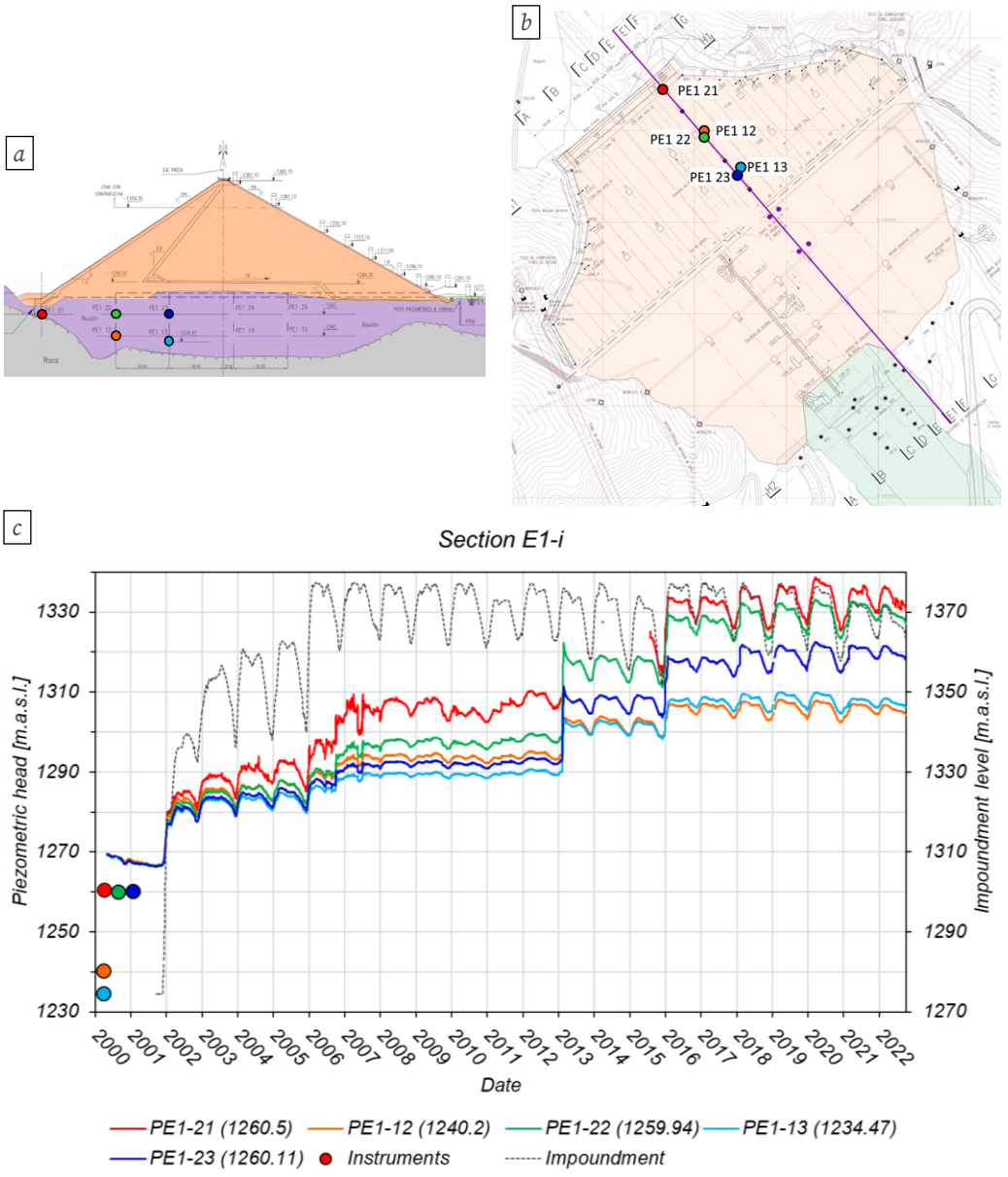


Fig. 3.39: Section E1-i a) location of the piezometers in cross-section, b) location of the piezometers in plan view, and c) records of pore water pressure of the selected instruments, together with the elevation of the instruments, and the impoundment level of the reservoir.

As can be observed in Fig. 3.39 and Fig. 3.40, several piezometers present a step in the pore water pressure records in the years 2013 and 2016. It is evident that this variation was not a consequence of reservoir level fluctuations, as those oscillations of the piezometric head are

nearly three times smaller. Moreover, this change represents a singular event that established a new average level of pore pressure in the dam foundation.

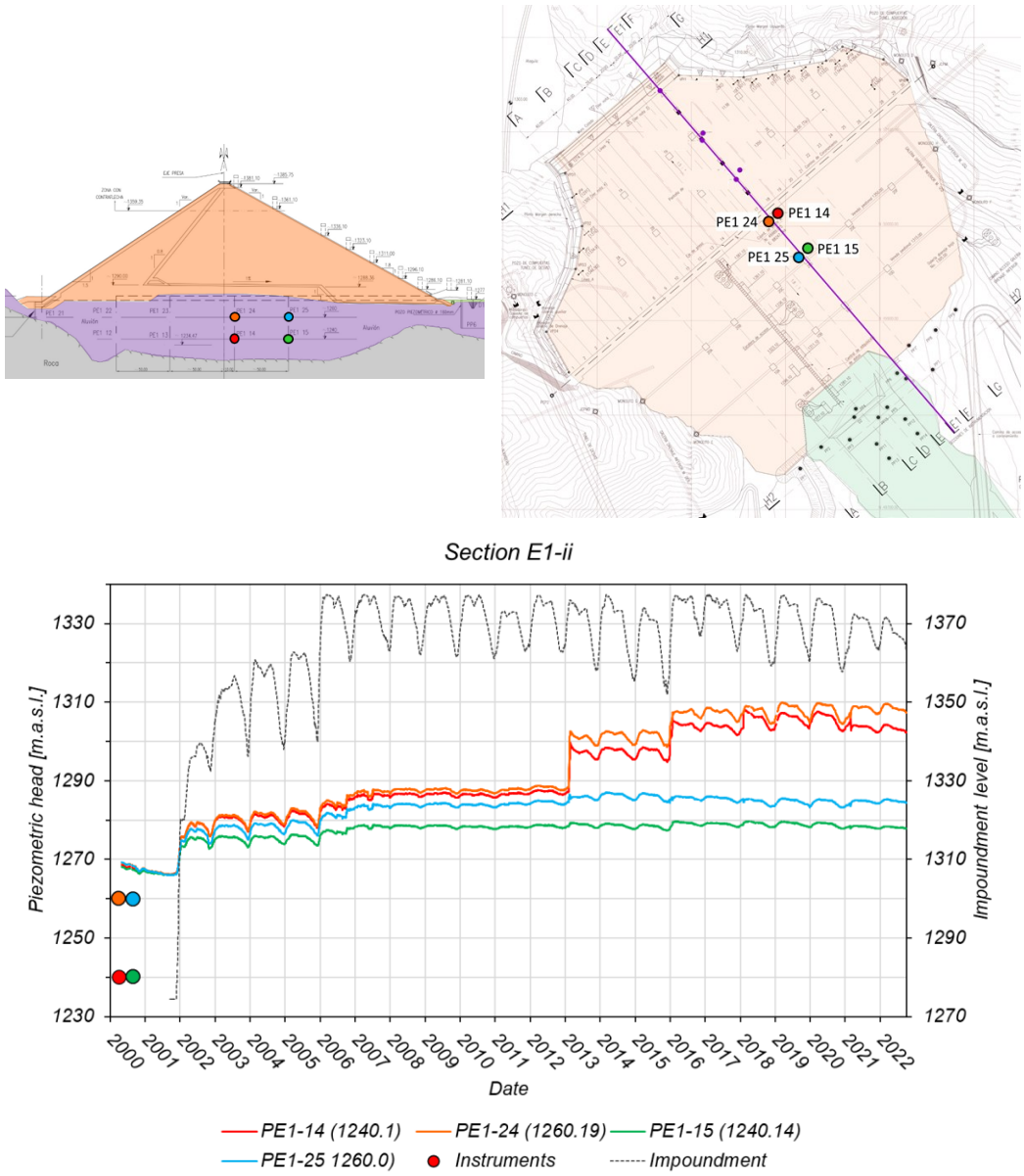


Fig. 3.40: Section E1-ii a) location of the piezometers in cross-section, b) location of the piezometers in plan view, and c) records of pore water pressure of the selected instruments, together with the elevation of the instruments, and the impoundment level of the reservoir.

The possibility of malfunctioning of the instruments does not seem feasible, as a similar behavior with varying magnitude was observed in several instruments distributed along the left margin side of the foundation (Fig. 3.41), where the alluvium thickness can reach up to

70 m. This tendency may also be associated with a preferential seepage path toward the left margin of the foundation, guided by the geometry of the bedrock

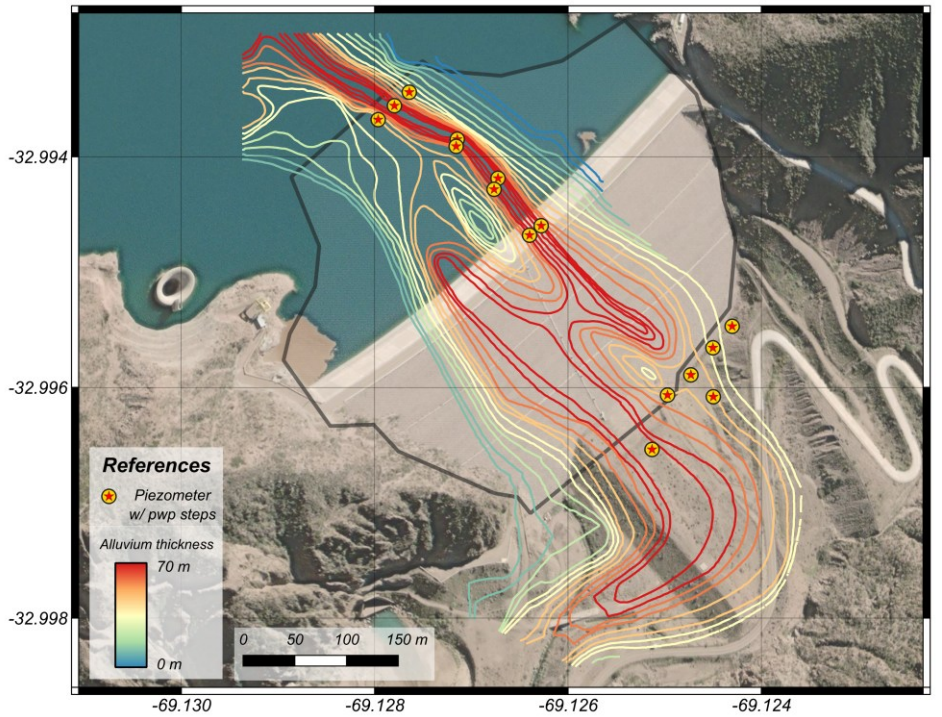


Fig. 3.41: Location of piezometers that present large steps in pore pressure records, together with the contours of alluvium thickness beneath the dam.

Dam managers and specialists consulted linked the occurrence of these steps in pore pressure with the occurrence of large storms in the basin of the Mendoza River. To verify this hypothesis, three different plots were done, overlapping the records of pore pressure of Section E1-ii with the time series of hydrological variables (Subsecretaría de Recursos Hídricos, 2022) from Cacheuta meteorological station and Guido hydrological station, both located close to the dam (Fig. 3.42). Then, the precipitation time series measured at Cacheuta station are plotted together with the pore water pressure records of Section E1-ii in Fig. 3.43, while the graphics combining pore pressures with daily fluid discharge and weekly solid discharge of the river are shown in Fig. 3.44 and Fig. 3.45, respectively.

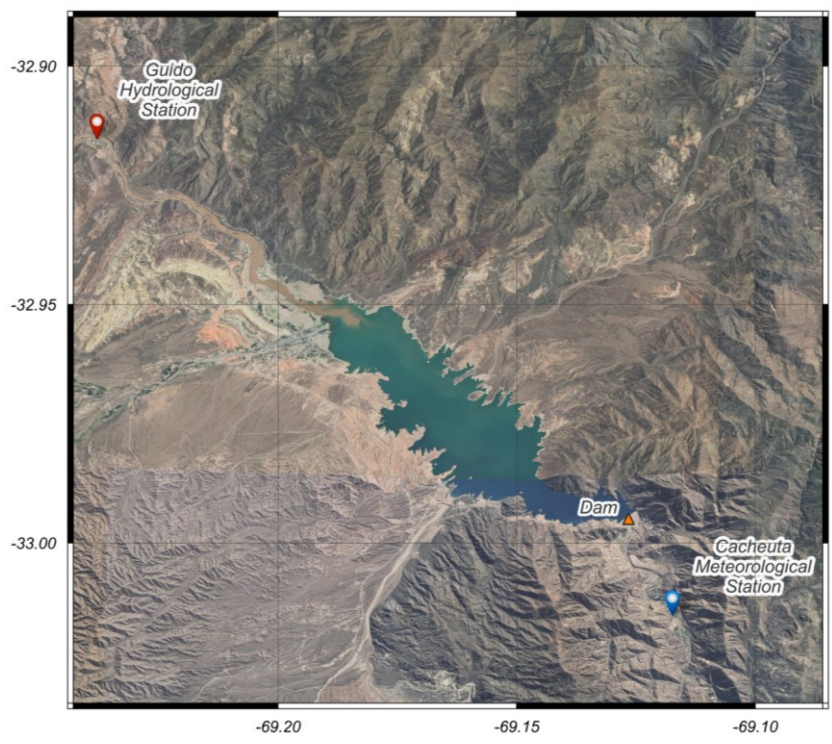


Fig. 3.42: Location of the Cacheuta meteorological station and Guido hydrological station, close to the dam.

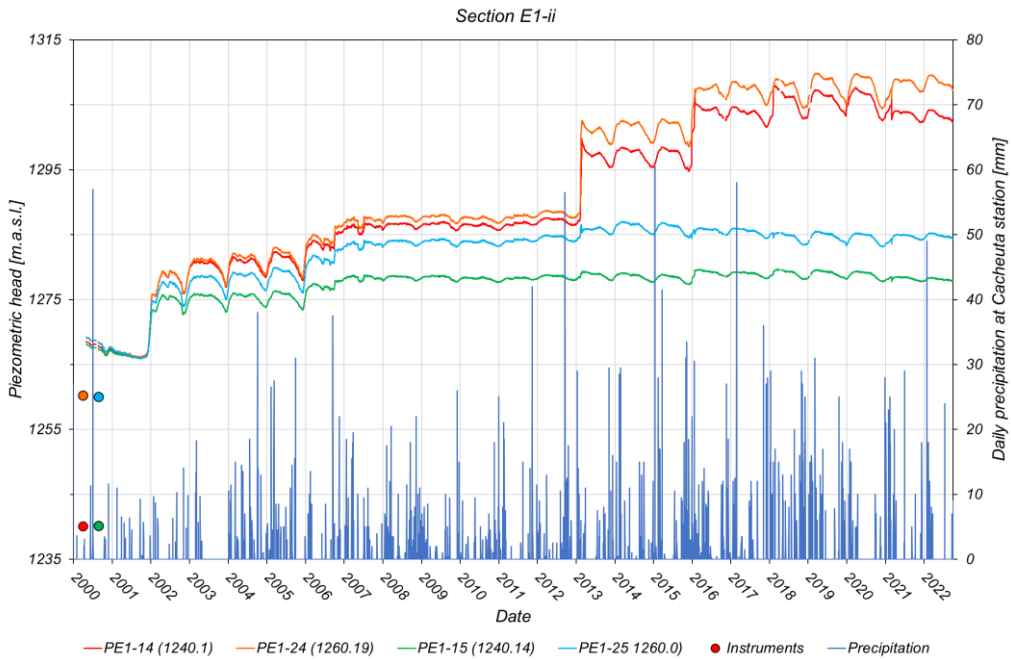


Fig. 3.43: Records of pore water pressure at Section E1-ii overlapped with daily precipitation time series at Cacheuta station.

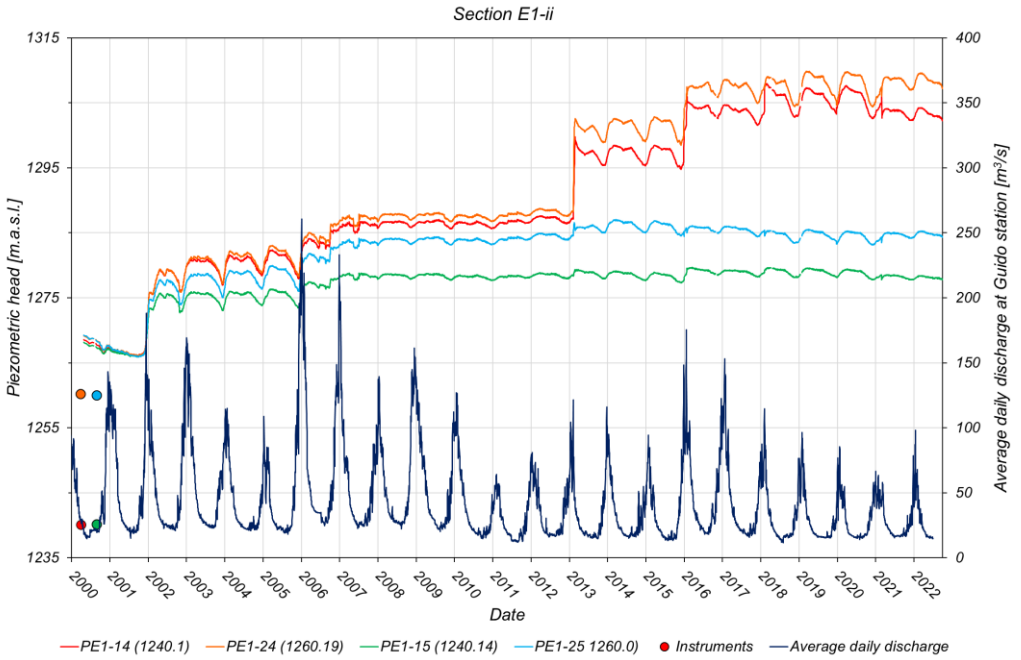


Fig. 3.44: Records of pore water pressure at Section E1-ii plot together with the daily fluid discharge at Guido hydrological station.

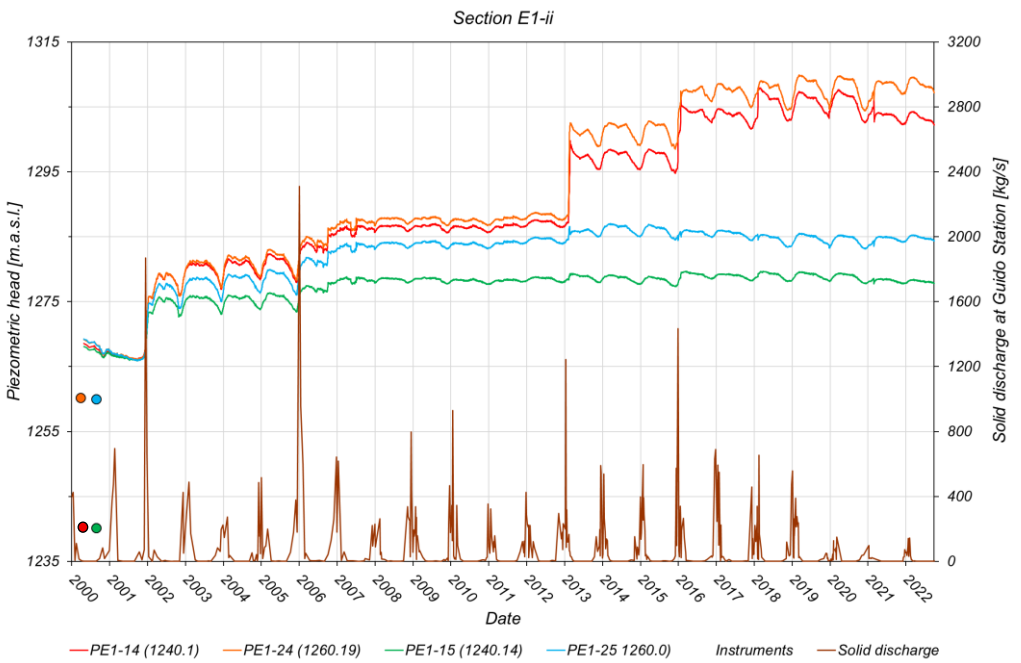


Fig. 3.45: Records of pore water pressure at Section E1-ii superimposed with weekly solid discharge at Guido hydrological station.

From the observation of Fig. 3.43 and Fig. 3.44, it is evident that there is no strong correlation between the pore pressure steps and precipitation time series, whereas a slight trend appears to be present with respect to the daily fluid discharge. By contrast, a more evident correlation is observed in Fig. 3.45, where the two larger fluctuations of pore water pressure in 2013 and 2016 occur at the same time as two important solid discharges are measured in the river upstream of the dam. These large solid discharges into the river can be attributed to high-intensity rainfall events occurring in the upper part of the basin, where erodible sedimentary rocks and fine-grained soil cover are prevalent. The resulting sediments are subsequently transported downstream to the dam reservoir.

The other two solid-discharge peaks shown in Fig. 3.45 coincide with two milestones in the life of the dam: the end of construction and beginning of reservoir filling in 2002, and the first full impoundment in 2006. The hydraulic conditions verified during the reservoir level rise are often unstable, as both hydraulic and static conditions not previously experienced in the dam and alluvium are reached; therefore, it is possible that the influence of the first two peaks in solid discharge was overlooked and attributed to the reservoir filling process.

Having set a link between the steps in pore pressure and the solid discharge in the river, a hypothesis can be set about the physical process that relates these two parameters regarding the characteristics of the dam.

As mentioned in Barchiesi et al. (2005), due to the irregular and steep slopes of the rock massif in the deeper portion of the cut-off wall, excavation using the hydromill trench cutter was not feasible near the bedrock. To ensure watertightness in the alluvium close to the rock, jet grouting was performed in the soil between the alluvium and the concrete cut-off wall.

The low efficiency of the sealing provided by the jet grouting, or breakage of the cut-off wall, could explain the migration of fine suspended solids from the reservoir water into the alluvium beneath the dam. These fine-grained materials, transported by seepage through the alluvium, tend to settle and accumulate, leading to a non-uniform distribution of permeability. These changes in the hydraulic conductivity of the alluvium could lead to new hydraulic conditions in the dam foundation and be the reason behind the steps in the pore water pressure records.

Assuming the previous hypothesis is feasible, the progressive clogging of voids in the foundation soil may lead to a gradual reduction in the surface water discharge collected by the

drainage gallery at the downstream foot of the dam. To prove this point, a unified graphic with the pore water pressure records at Section E1-ii, reservoir water level, solid discharge at Guido station, and water discharge from the drainage gallery at the downstream foot of the dam are presented in Fig. 3.46.

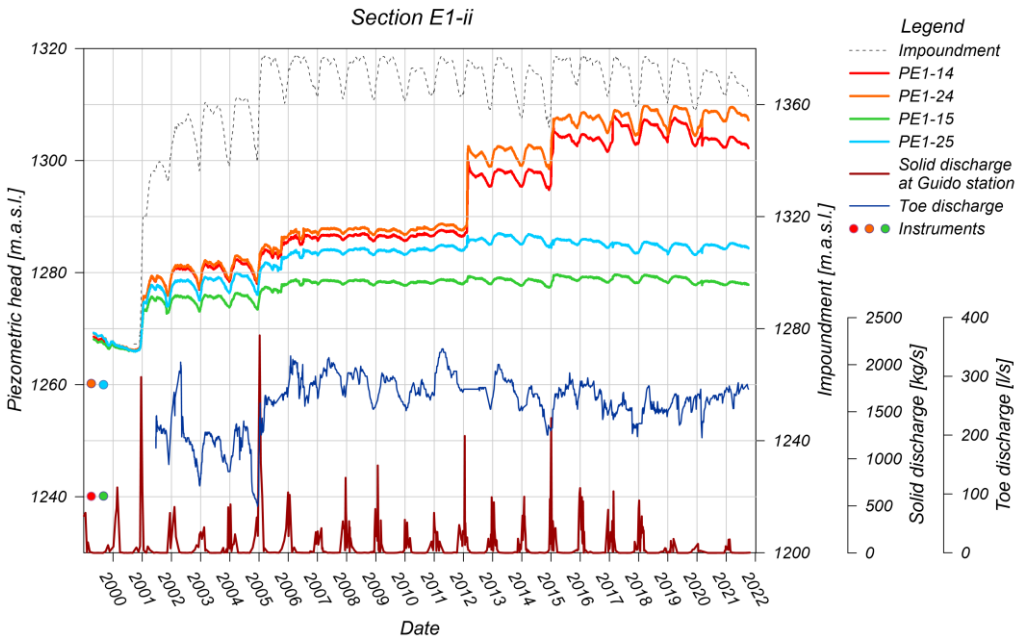


Fig. 3.46: Plot with the combined records of pore water pressure at Section E1-ii, impoundment level, solid discharge at Guido station, and fluid discharge

A decreasing trend in the discharge at the downstream gallery is evident after the peak in pore pressure of 2013, continuing until 2020. From that point onward, a tendency of decreasing pore pressure and increasing discharge is observed through the end of the available records in 2022.

A last singular aspect related to the pore pressure records can also be shown in Fig. 3.40, where the two piezometers located upstream (PE1-14 and PE1-24) present a noticeable step in pore pressure previously analyzed, while those located downstream (PE1-15 and PE1-25) just exhibit a small perturbation. This could be interpreted at least in two ways: the clogging process started to decay after the piezometers PE1-14/24 and was less evident in the sensors downstream of this point; or the main seepage flow changed direction in coincidence with the abovementioned sensors, following the geometry of the deeper part of the bedrock. Both conditions should be, however, verified with specific studies over the scope of this work.

The influence of the distribution of pore pressure in the foundation will be considered during the calculations, as the real distribution coming from piezometric records will be used to set the water table in static and dynamic phases.

3.4.2 Settlement gauges and topographic surveys

The dam is equipped with 22 settlement gauges equally distributed along Section D and Section E1 (Fig. 3.37), and 28 fixed points located on the dam and abutments for use during topographic surveys (Fig. 3.36). While the former is intended to provide information on the deformation pattern of the materials within the dam body, the latter aims to capture the resulting surface deformations.

Concerning the topographic surveys, only the fixed points located on the crest and downstream slope of the dam are accessible during normal operation, and measurements are conducted twice a year or following an extraordinary event. The cumulative settlements measured at these points since the end of construction are shown in Fig. 3.47, together with the contours of surface settlements evaluated from them.

Consistent with the behavior of embankment dams in narrow valleys (Sukkarak et al., 2019), the settlement pattern exhibits larger settlements at the central part of the dam, while the displacements of the flanks are restricted by the rock abutments. However, what is uncommon is that, along the center of the dam, the largest settlements are not verified at the crest but at the mid-height of the dam. This singular response could be attributed to the complexity of the shape of the bedrock, and the important thickness of the alluvial layer beneath the dam at this specific point (refer to Fig. 3.9). Moreover, this particular aspect of the behavior of the dam will be retrieved in the discussion about its dynamic response under weak motions, in the section about the seismic monitoring.

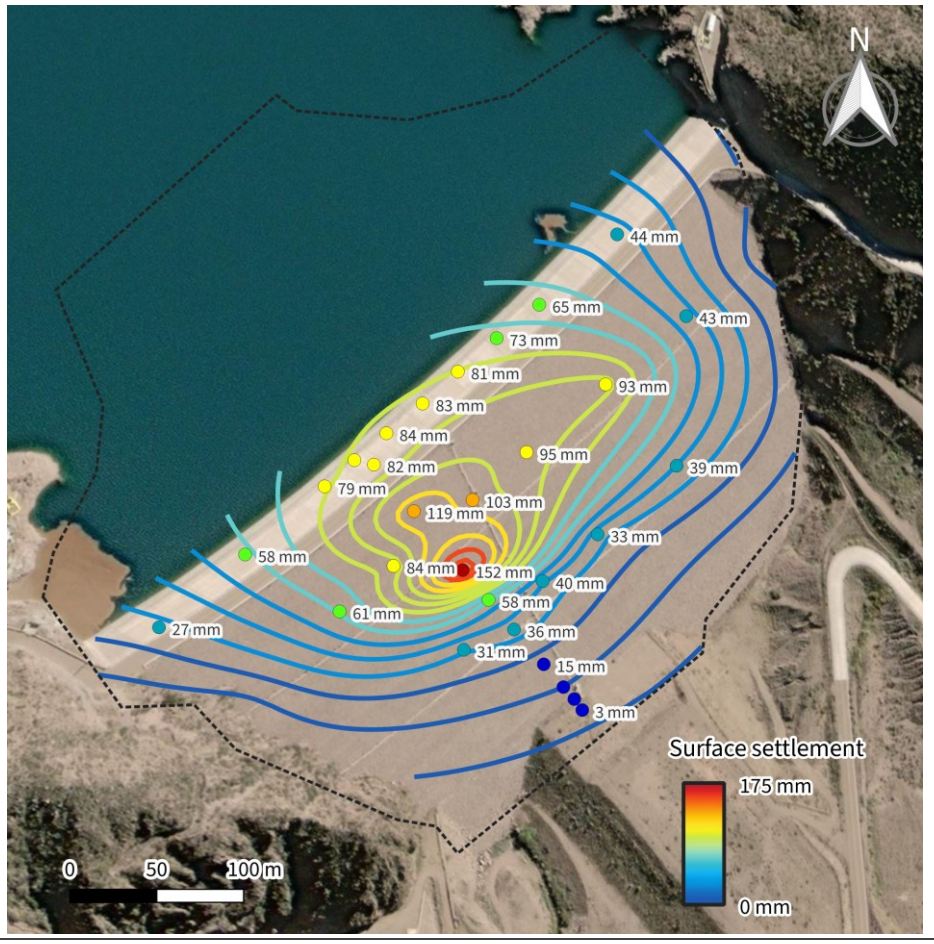


Fig. 3.47: Fixed point measurements and contours of the cumulated settlements at the surface of the dam since the end of the construction of the dam in 2002, up to 2022.

The vibrating wire settlement gauges were installed within concrete cubes embedded in the dam during embankment construction (Fig. 3.48a). They are distributed across two central sections, following the same layout shown in Fig. 3.48b for Section D.

The analysis of the settlement after construction can be exploited to evaluate the stiffness distribution at medium to large deformation through simplified methods (Marsal & Resendiz, 1983; Pagano et al., 1998), but also to estimate the fundamental frequency of the dam at large strains, as will be explained at the end of this section.

The records from the settlement gauges aligned with the dam axis, namely AD44, AD44b, AD54, and AD64 in Fig. 3.48b, will be used for the analyses as they could be considered representative of the average dam vertical deformation, due to the location of Section D in the center zone of the dam (Fig. 3.35).

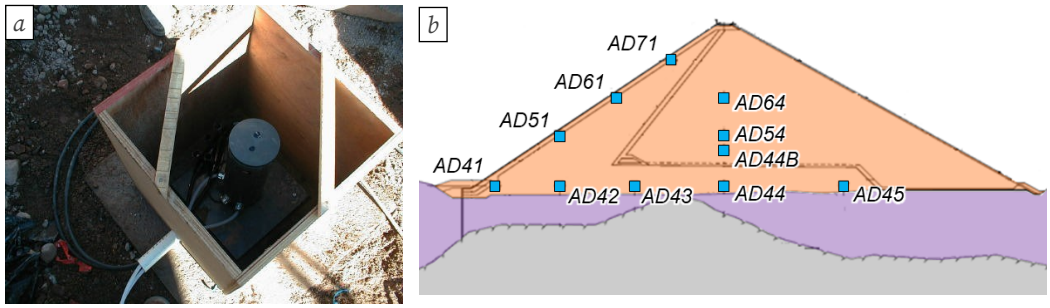


Fig. 3.48: a) installation of vibrating wire settlement gauge before filling the cube with concrete, from Made et al. (2002), and b) distribution of settlement gauges along Section D.

The records coming from the selected settlement gauges after the end of the fill construction were processed following the procedure of Poulos et al. (1972) to obtain only the permanent vertical displacements relative to the embankment (Fig. 3.49), even if it is expected that the foundation may have some influence on them. The records from the lowest sensor, AD44, are taken as the reference for the displacement at the base of the embankment. The differences between this reference settlement gauge and the records from the other sensors are representative of the relative displacements experienced solely by the dam body.

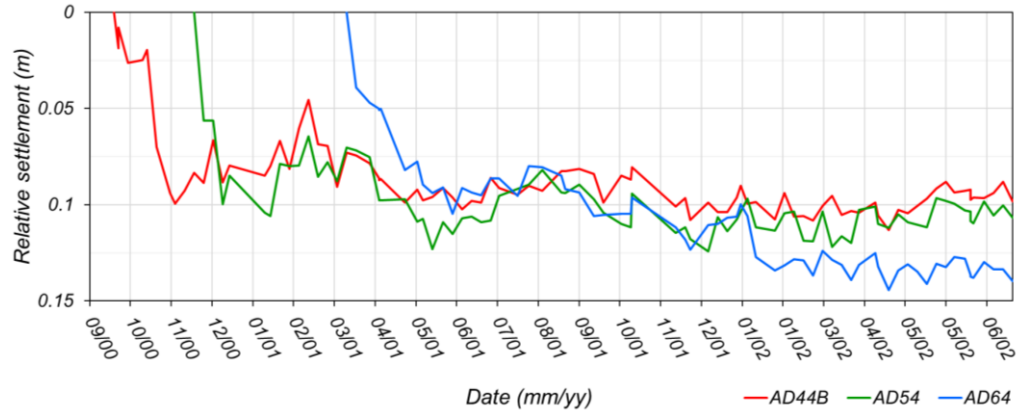


Fig. 3.49: Relative settlements of the dam at the end of the construction of the embankment.

Noticing that the deformation level developed during the construction of the embankment is expected to be in the range of medium to large deformations (Fell et al., 2014), and such deformations could be comparable with the deformation level of the embankment during a strong earthquake (Ghaemi & Konrad, 2022), the evaluation of the settlement after construction can be exploited to evaluate the stiffness distribution and further evaluation of the fundamental frequency of the dam at large strains.

The analytical model considered for the interpretation of the settlement is that developed by Pagano et al. (1998), which represents the dam as a one-dimensional non-homogeneous fill with a linearly variable stiffness *D(z)*. The profile of relative settlements and stiffness are defined by Eq. 3.4 and Eq. 3.5 respectively.

$$s(z) = \gamma \cdot \frac{H - z}{\eta} \cdot \ln\left(1 + \frac{\eta}{D_0} \cdot z\right) \qquad \text{Eq. 3.4}$$

$$D(z) = D_0 + \eta \cdot z \qquad \text{Eq. 3.5}$$

Where γ is the unit weight of the dam soil, H is the total height of the dam, z is the elevation from the foundation level, D_0 is the stiffness of the dam at the foundation level, and η the stiffness variation with the elevation. The values of D_0 and η should be adjusted until a reasonable agreement between the analytical profile and the average value of the measured settlements is reached.

Once the profile of stiffness *D(z)* is obtained, and having in mind the fact of dealing with a 1D model, there are two possible interpretations for the one-dimensional stiffness D:

- Assuming the lateral displacements are restricted, making D approach the oedometric modulus E_0. This hypothesis is more realistic in the middle-low zones of the embankment, as they are subject to the effects of the frictional restraint by the foundation, and the dam body is significantly wider.
- Consider free lateral displacements, which correspond to relating D to the elastic modulus E. This hypothesis would be more accurate in the upper zone of the dam, far from the foundation restraining effects and featuring a thinner dam body.

Using the relationships between elastic and shear modulus from the theory of elasticity, for a given constant Poisson ratio ν, the two above interpretations attributed to D result in two different shear modulus profiles. For the hypothesis of $D \cong E_0$ the shear modulus distribution is then represented by Eq. 3.6:

$$G_{s-E_0}(z) = \left(D_0 + \eta \cdot z\right) \cdot \frac{1 - 2\nu}{2\left(1 - \nu\right)} \qquad \text{Eq. 3.6}$$

Instead, for the case of $D \cong E$ the distribution of shear modulus can be defined by Eq. 3.7:

$$G_{s-E}(z)=\left(D_0+\eta\cdot z\right)\cdot\frac{1}{2\left(1+\nu\right)} \qquad \textit{Eq. 3.7}$$

These two profiles aim to establish the possible range of variation for G along the height of the embankment, under the assumptions of the previously stated 1D model.

A step forward can be taken by attempting to adjust the shear stiffness distribution to better match those observed in real dams (Park & Kishida, 2018), which can also be used to calibrate a shear beam model with a non-uniform stiffness distribution, such as that proposed by Dakoulas & Gazetas (1985).

This last model is then adopted to quantify the profile of shear modulus at medium to large strains, according to a calibration that may ensure that the profile of shear stiffness for the shear beam model G_{SB} does not fall beyond the range defined by Eq. 3.6 and Eq. 3.7. The variation of G_{SB} is expressed as a power function of the depth (Eq. 3.8).

$$G_{SB}(z)=G_b\cdot\left(\frac{\left(H+h\right)-z}{H+h}\right)^m \qquad \textit{Eq. 3.8}$$

Where G_b is the shear modulus at the base of the dam; H is the height of the dam; h is the height difference between the truncated and not truncated wedge that represents the dam 2D section; m is the power coefficient that controls the variation of the stiffness with height, between 0.4 and 0.75, according to Dakoulas & Gazetas (1985). The profile of G of Eq. 3.8 is slightly modified from the original to unify the parameters with the model of Pagano et al. (1998), and the respective parameters presented in Fig. 3.50.

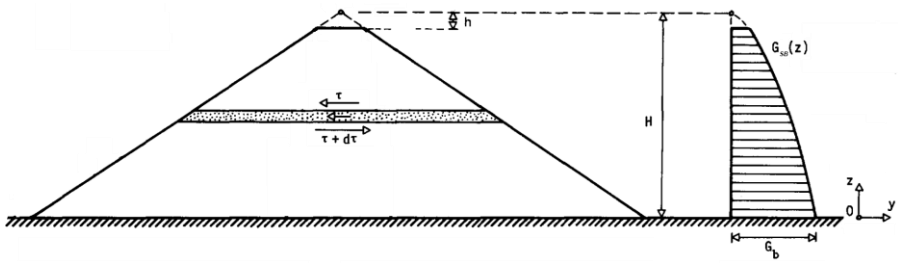


Fig. 3.50: Parameters from the shear beam model, modified from Dakoulas & Gazetas (1985).

The analytical settlement profile based on Eq. 3.4, fitting experimental points that represent the relative settlement of Fig. 3.49, is presented parallel to the distribution of settlement gauges in Fig. 3.51b and Fig. 3.51a. It was considered a dam height H = 120 m, and unit weight γ = 22 kN/m^3 corresponding to the values adopted by De Cicco et al. (2015).

The best fitting was obtained for D_0 = 700 MPa and η = - 4 MPa. Yet again, according to De Cicco et al. (2015), the Poisson ratio was set as ν = 0.26 for the dam body materials. These values provided the range of variation for the shear stiffness G under the two assumptions previously stated of $D \cong E_0$ (oedometric conditions, see Eq. 3.6) and $D \cong E$ (unconfined conditions, see Eq. 3.7), as presented in Fig. 3.51c with blue and green dashed lines respectively.

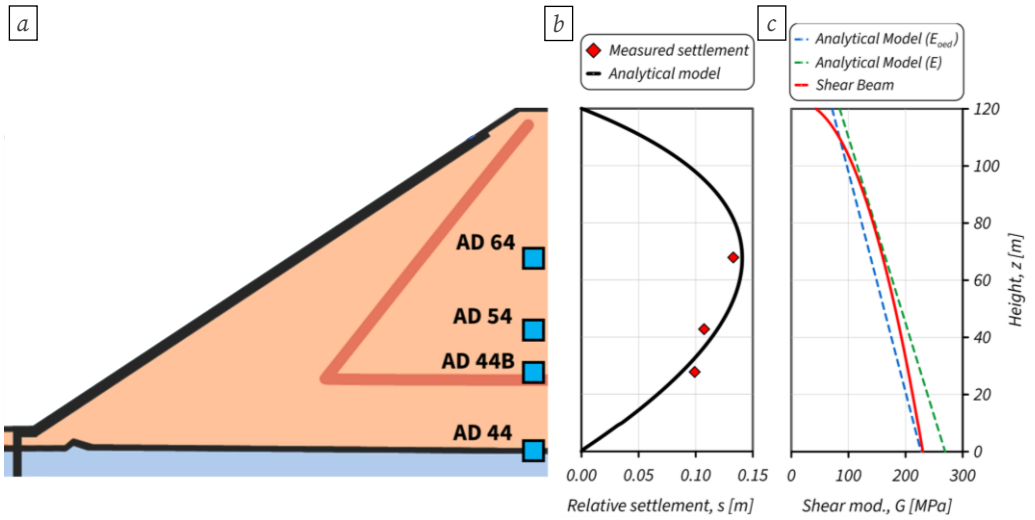


Fig. 3.51: a) Partial cross-section with the distribution of settlement gauges considered in this analysis, b) experimental points and analytical profile of relative settlements, and c) distribution of shear stiffness along the dam height based on Eq. 3.6 (E_{oed}), Eq. 3.7 (E), and Eq. 3.8 (shear beam).

The G_b and m parameters of the shear-beam model (see Eq. 3.8) were calibrated forcing the shear stiffness given by the model of Dakoulas & Gazetas (1985) to fall within the range of G previously stated, approaching the "oedometric" profile (dashed blue line of Fig. 3.51c) around the dam bottom, and the "unconfined" profile (dashed green line of Fig. 3.51c) near the crest. The calibration resulted in the curved profile (red line) of Fig. 3.51c for the parameters H = 120 m, h = 3 m, G_b = 230 MPa, and m = 0.45.

This profile is going to be considered during the calibration of the material models for the static analysis in Section 6.3, and also in the evaluation of the natural period of the dam at large strains at the end of this chapter.

3.4.3 Seismic monitoring

Since the end of the construction of the Potrerillos project, the dam has been equipped with a seismic monitoring system composed of four accelerometric stations. Three of these are

placed along the downstream slope in the central cross-section (Section C) of the dam body (Fig. 3.52 and Fig. 3.53): at the crest (C9), mid-height (C7), and toe (C1). The fourth station (GMD) is currently located on the right abutment.

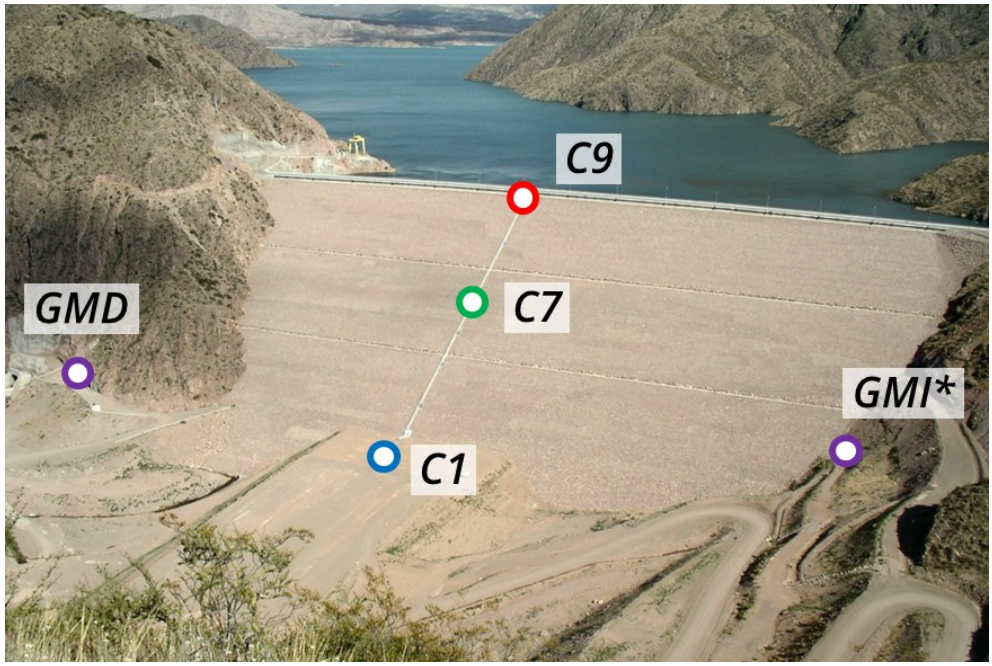


Fig. 3.52: Downstream view of the dam with the location of the seismic stations.

Since the completion of the dam, the monitoring system underwent two major changes. In 2004, the construction of a stabilizing embankment at the downstream toe of the dam led to the burial of C1 station under a 12 m layer of gravel (CEMPPSA, 2007). Later in 2007, the GMD station initially placed on the left abutment (GMI* in Fig. 3.53a), was repositioned to the entry of a gallery located in the right margin (GMD in Fig. 3.53a).

Each station (Fig. 3.54a) is equipped with a triaxial electronic accelerometer (GeoSIG AC-33) mounted on a reinforced concrete block independent of the monitoring booth structure, with the three components (TRA, LON, UP) oriented as shown in Fig. 3.53. Every instrument is equipped with a GPS to synchronize the recording time of the whole array. The accelerometers are connected through an intranet with the monitoring center (Fig. 3.54b), located about 4 km away from the dam, from where the instrument setting can be controlled and the signal logged and stored.

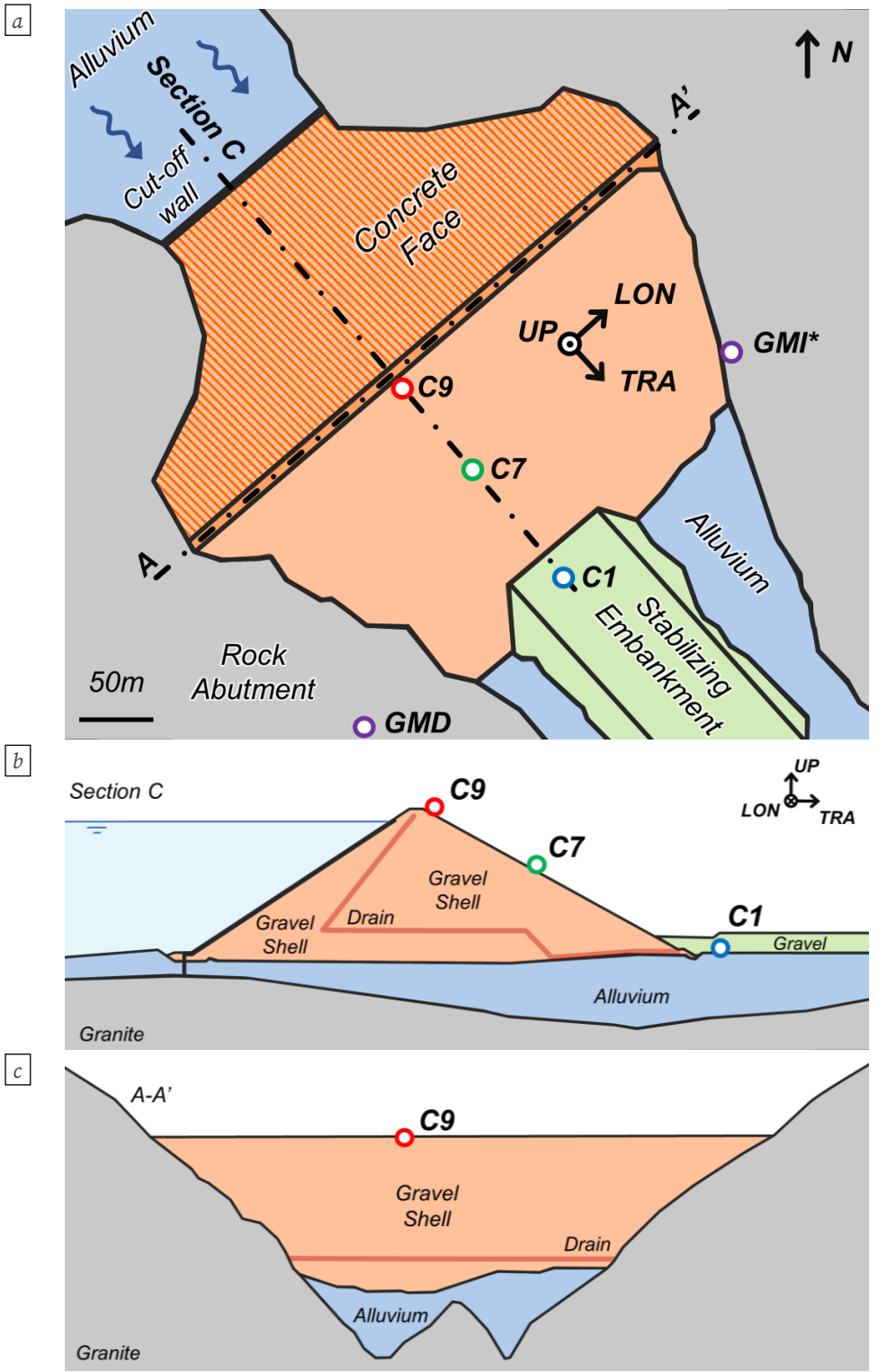


Fig. 3.53: a) Plan view and main features of the dam with the location of all accelerometric stations, and accelerometer component orientation; b) location of the accelerometric stations along the dam central transverse section; c) dam longitudinal section

The triggering threshold for all instruments is set to a_{tr} = 0.004 g, and the full-scale range to ± 2 g. The pre-and post-event buffer time lengths are set to 15 s and 25 s, respectively (Calderón & Cordone, 2019).

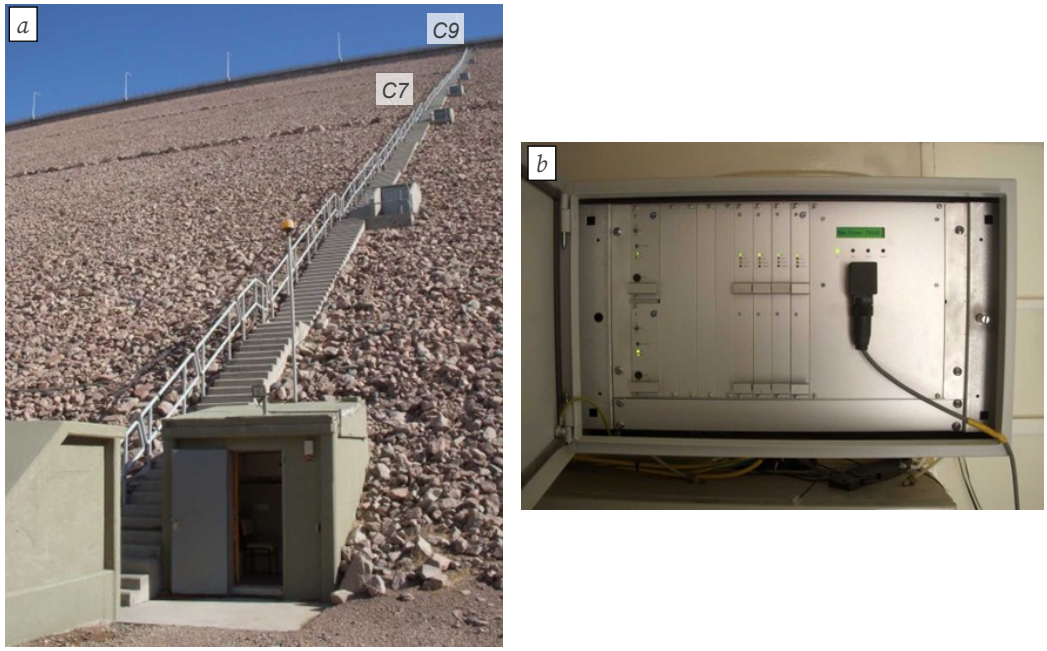


Fig. 3.54: a) Downstream slope of the dam with the monitoring booths, with C9 and C7 highlighted, and b) data transfer system for all four accelerometers.

The system has been in operation since the end of the construction of the dam, and the records of almost 20 years of recordings will be analyzed in the subsequent sections, extending the work already presented in Barbagelata et al. (2024).

3.4.3.a Spatial distribution and characteristics of the recorded events

From the records generated by the seismic monitoring system at the dam in the period between 2002 and 2021, it was possible to accurately establish the source for 119 out of the 129 earthquakes recorded by at least one station. Among them, 108 resulted in mainshocks and 11 aftershocks.

For all recorded signals, the earthquake source was identified by searching the ISC seismicity catalog (ISC, 2022) for a georeferenced event with a starting time matching that of the recorded signal. The local INPRES catalog (INPRES, 2022) was also consulted for small-magnitude events not covered by the ISC catalog.

Each event was associated with the main seismic sources that characterize the local seismotectonic setting (Ramos et al., 2002), distinguishing among shallow crustal (CR), subduction intraslab (IS), and subduction interface (SD) earthquakes. Out of the 119 identified records, 15 correspond to SD earthquakes, 31 are linked to IS sources, and the remaining 62 are attributed to CR events.

A few significant events were selected for each type of faulting mechanism, based on the highest peak ground acceleration (*PGA*). The signals were initially processed following the suggestions of Boore & Bommer (2005), applying baseline correction and bandpass filtering to reduce the influence of the noise on the subsequent interpretation of the dam's dynamic response from the seismic records.

For the transverse (TRA) component of the six selected events Table 3.4 lists the seismic scenario properties (magnitude, epicentral distance, and focal depth), the peak ground acceleration (*PGA)* and Arias Intensity (I_A) at the crest, and the dominant frequency (f_D) at the abutment, which is the reciprocal of the dominant period (T_D).

Event	Date	Magnitude M_w	Epicentral distance (km)	Depth (km)	*PGA* C9 (g)	I_A C9 (cm/s)	f_D GMD (Hz)
CR-01	5/8/2006	5.6	33.7	32.0	0.065	3.79	5.0
CR-02	23/6/2021	4.6	12.0	19.0	0.094	2.83	10.0
IS-01	26/4/2009	5.1	33.9	132.0	0.007	0.03	7.1
IS-02	18/1/2010	5.5	199.6	91.0	0.027	0.5	3.6
SD-01	27/2/2010	8.8	502.3	22.9	0.024	5.33	2.3
SD-02	16/9/2015	8.3	287.1	22.4	0.016	3.26	4.2

Table 3.4: Properties of the selected events and reference weak motion records.

The spatial distribution of the 119 seismic events identified in the catalogs is shown in Fig. 3.55. The different colors refer to different source faulting styles, while symbol sizes are related to the magnitude. In the same figure, the contours indicating the depth of the subducted plate are also reported in Fig. 3.55a, while the focal depths are plotted along a vertical West-East section across the dam site in Fig. 3.55b.

The subduction earthquakes selected in this study, the Maule 2010 M_W 8.8 and Illapel 2015 M_W 8.3 (refer to Table 3.4), correspond to the largest and most significant events in the past 15 years along the coastal Chilean subduction zone. They generated ground motions with a non-negligible energy content at the dam site, although their epicentral distance are considerably large (more than 500 km and almost 300 km, respectively).

The intraslab events, primarily located to the north of the dam, are characterized by greater focal depths. Their hypocenters align along a plane that reflects the geometry of the subducted plate (see Fig. 3.55). In contrast, the crustal events are concentrated near the dam site and show a shallower, nearly horizontal distribution of focal depths. This pattern results from the regional seismotectonic setting associated with the flat slab subduction regime, as described by Ramos et al. (2002) and illustrated by the depth contours of the subducted plate shown in Fig. 3.55a.

The focal mechanism was identified for 39 earthquakes, characterized by a moment tensor solution present in the catalogs CMT (Ekström et al., 2012), ANSS (USGS, 2017), and GFZ (Quinteros et al., 2021). These events with a well-identified focal mechanism are plotted in the map of Fig. 3.56, according to the same color code and symbol size previously assumed for Fig. 3.55.

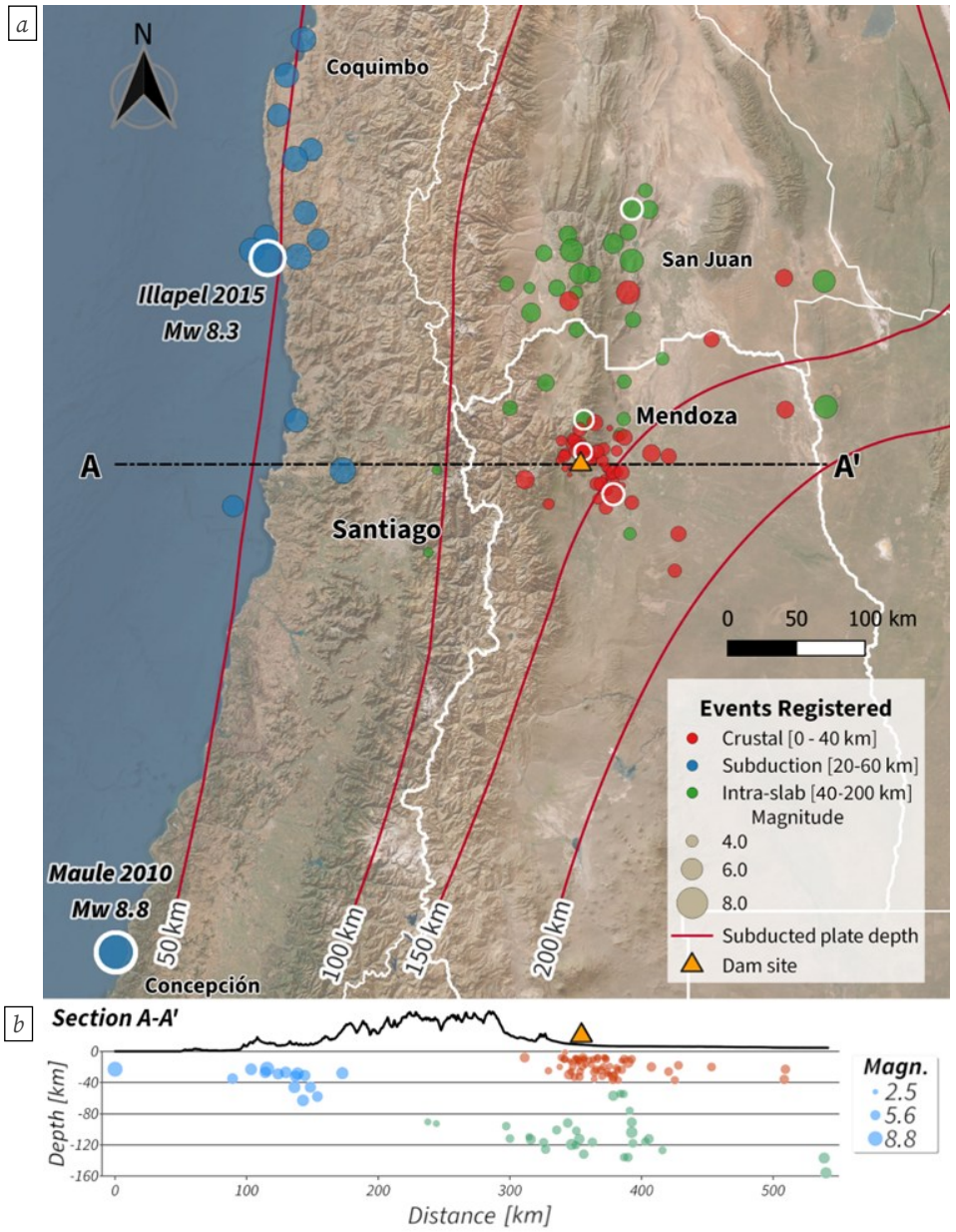


Fig. 3.55: a) Distribution of seismic events recorded at the dam site, with the location of the dam and the events reported in Table 3.4 emphasized (white ring), and b) East-West cross section with surface topography (out of scale) and distribution of recorded seismic events in depth.

It can be observed from Fig. 3.56 that each type of source can be associated with a characteristic focal (and fault) mechanism. This aspect becomes more evident using a plot that clusters the events based on their focal mechanisms, showing how closely they align with the three classical fault types (reverse, normal, and strike-slip) or a combination of them. Fig. 3.57, generated using the FMC code (Álvarez-Gómez, 2019), groups the events according to their moment tensor solutions and provides the corresponding classification diagram.

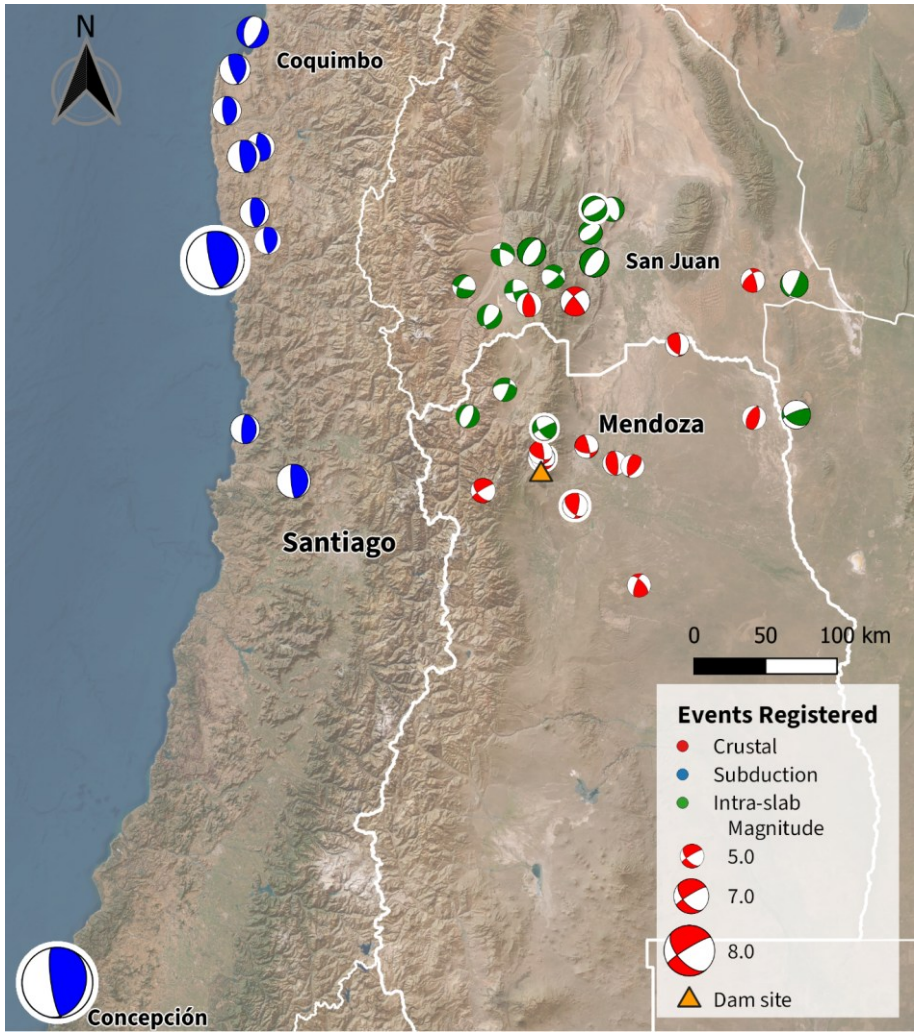


Fig. 3.56: Focal mechanism of the events with an available moment tensor solution, highlighting the events from Table 3.4.

Fig. 3.57 reveals that nearly all subduction interface events correspond to reverse faulting, intraslab events are distributed between normal or normal-strike-slip mechanisms, while the majority of crustal events are either oblique or reverse. This information will be useful during the evaluation of the seismic hazard in Section 5, not just to support the characterization of the seismotectonic environment, but also to set the faulting type of the seismic sources defined for the probabilistic seismic hazard analysis.

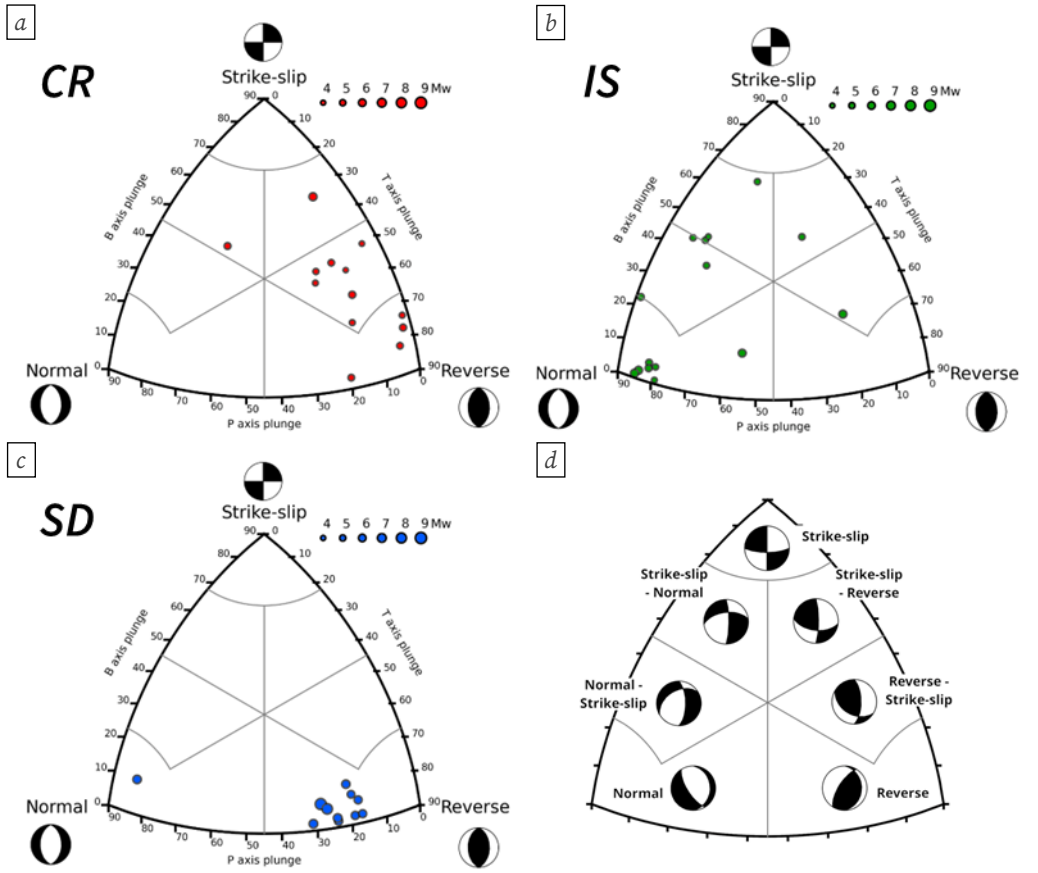


Fig. 3.57: Plots clustering the seismic events with respect to their focal mechanism, for a) crustal events (CR), b) intraslab events (IS), c) subduction interface events (SD), and d) a reference for the identification of the regions where every focal mechanism prevails (Álvarez-Gómez, 2019).

The ground motion records will be analyzed to identify features of the dam's response under seismic weak motions and to derive useful information about its dynamic characteristics.

3.4.3.b Dynamic characteristics of the dam under seismic weak motions

The first peculiarity observed from the records (Fig. 3.58) is that out of the 119 identified events, 28 were recorded by the GMD/GMI* station, 67 by C1, 117 by C7, and 95 by C9. Moreover, 21 events were recorded at all the stations; simultaneously at the embankment stations (C1, C7 & C9) only 47, and 65 at the same time at the two higher and more sensitive dam stations (C7 & C9). This singular response, considering that all sensors share the same acceleration trigger, suggests that the station at mid-height (C7) is more sensitive to triggering event recordings. This could also indicate that this station is more frequently subjected to larger accelerations than the crest station (C9), which has nearly 35% fewer recorded signals.

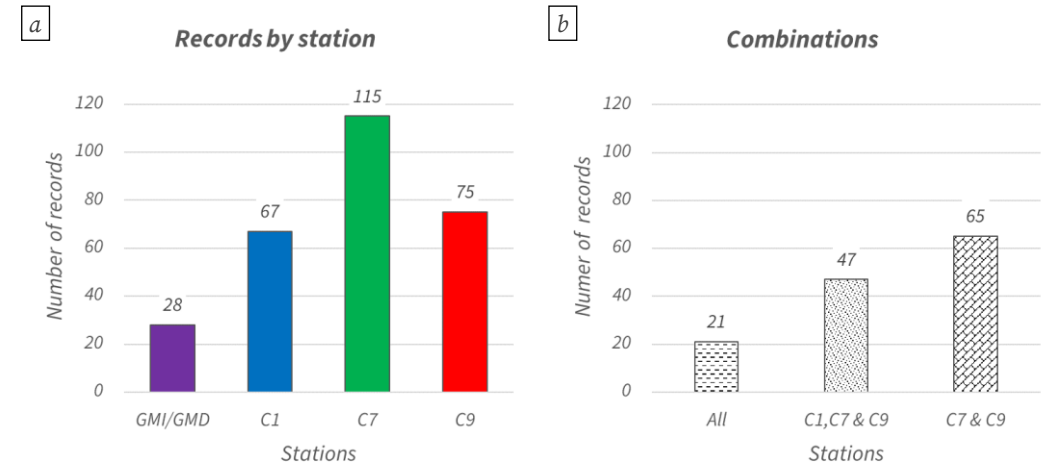


Fig. 3.58: a) Number of records at every station, and b) the number of records at all the stations, just the stations of the dam body (C1, C7, and C9), or the two uppermost stations (C7 and C9).

This aspect can be further explored by examining the ratio between the peak ground acceleration recorded at the dam crest (C9) and mid-height (C7) for the TRA and LON components. This ratio is plotted in Fig. 3.59 for all the 65 records simultaneously captured by these two stations, with the aim of verifying whether the tendency previously identified based on the number of triggered events can be confirmed.

Most data points presented in Fig. 3.59 fall in the green-shaded area, associated with a peak acceleration at the crest (PGA_{C9}) attenuated with respect to mid-height peak acceleration (PGA_{C7}). In detail, this happens for 70% of the records of the transversal component (TRA) parallel to the embankment cross-section, and for 60% of those of the longitudinal component (LON), parallel to the dam axis. This particular response seems to be not linked to a particular focal mechanism but more related to the dynamic response of the dam under seismic weak motions, and can also be associated with a larger deformability of the dam at this point identified in the analysis of the vertical settlements (Fig. 3.47).

Moreover, this apparent anomaly might depend on the combination of the dam-foundation 3D variable geometry and soil properties, leading to a response notably influenced by asynchronism (Bilotta et al., 2010) associated with higher vibration modes (see Fig. 3.60 and Fig. 3.61) which might induce maximum acceleration amplitudes around the middle zone of the dam's height. The presence of asynchronism for the cases where $PGA_{C9}/PGA_{C7} < 1.0$ is supported by the fact that the ratio between the predominant frequency of the reference motion recorded at the abutment (f_D) and the first natural frequency of the dam-subsoil

system (f_1) is greater than 1.0 (e.g. CR-01, IS-01 and SD-02 in Table 3.4), a condition identified in literature as a signature of asynchronism (Sica & Pagano, 2009).

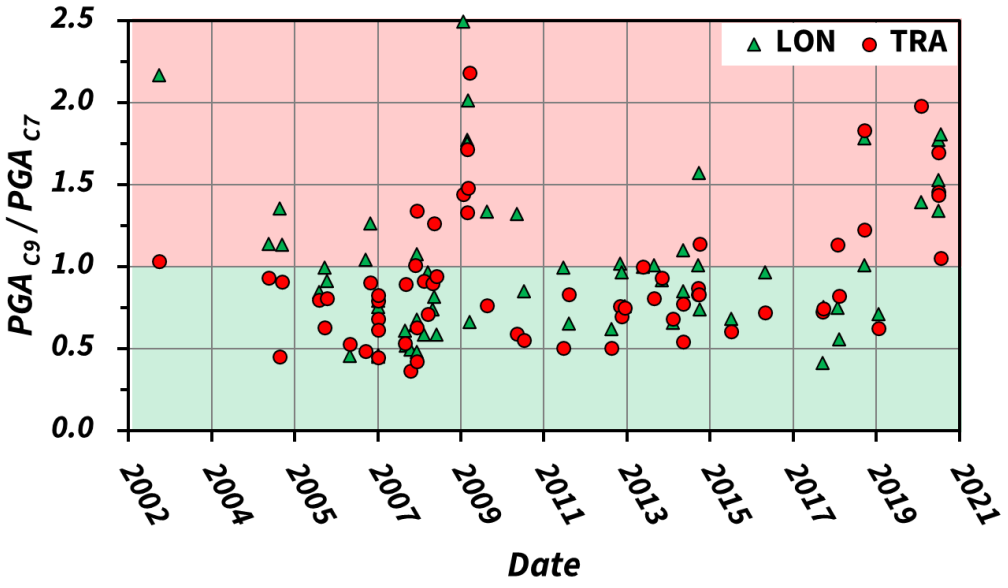


Fig. 3.59: Ratio of PGA at the crest (C9) with respect to mid-height (C7) over the years of operation.

Following the analyses, the six processed acceleration time histories with the largest *PGA* recorded at the dam crest, whose key properties are summarized in Table 3.4, are used to compute spectral ratios for their subsequent use in deriving some dynamic properties of the dam at small strains.

In particular, the Standard Spectral Ratio (*SSR*) and the Ratio of Spectral Acceleration (*RSA*) between the crest (C9) and the abutment (GMD) ground motions were determined according to the procedures adopted by Castro et al. (2000) and Armstrong et al. (2021), correspondingly:

$$SSR(f) = \frac{A(f)_{C9}}{A(f)_{GMD}} \qquad \text{Eq. 3.9}$$

$$RSA(f) = \frac{Sa(f)_{C9}}{Sa(f)_{GMD}} \qquad \text{Eq. 3.10}$$

Where *A(f) is the* Fourier amplitude and *Sa(f)* is the acceleration response spectra.

The computation of *SSR* was carried out following the time windowing recommended by Mikami et al. (2008) and adopting the moving average algorithm suggested by Konno & Ohmachi (1998) for the spectral smoothing, assuming a bandwidth coefficient $b = 40$ to avoid distortions in the peaks of the spectral ratios.

The *SSR* defined by Eq. 3.9 was used to identify some dynamic characteristics of the dam at small strains using weak motion records, as described in (Sica & Pagano, 2020). Fig. 3.60 shows the *SSR* between the TRA components relevant to the three couples of events (see Table 3.4), grouped according to the type of source mechanism.

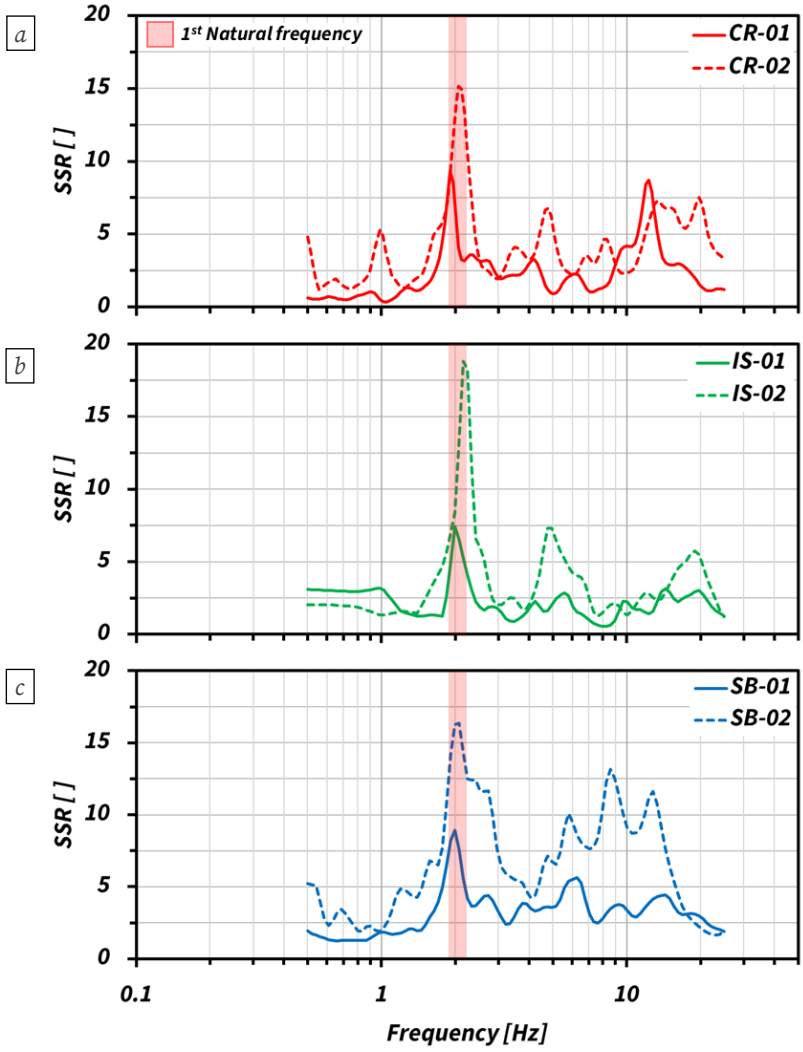


Fig. 3.60: SSR for the three types of seismic sources identified: a) crustal (CR), b) intraslab (IS), and c) subduction (SD). The fundamental frequency of the dam-foundation system is highlighted in red.

Spectral ratios derived from weak motion recordings are widely utilized to identify the fundamental period of dams under small-strain conditions (Sica, Pagano, & Vinale, 2008; Verret et al., 2021). In Fig. 3.60, the predominant *SSR* peak identifies the first natural frequency of the dam-foundation system. It results in around 2 Hz regardless of the faulting mechanism considered, exhibiting the robustness of the method. The remaining peaks could be identified as frequencies linked to higher modes of vibration, but the energy content of part of the signals made it impossible to have a clear identification across the types of sources for the fundamental frequency. The fundamental frequency of about 2 Hz also confirms the results reported by Calderón & Cordone (2019).

The plot in Fig. 3.61 illustrates in double scale *Sa* and *RSA* computed as defined in Eq. 3.10, for the TRA component of CR-01 motion, assuming a 5% viscous damping. The 2 Hz peak furnished by the *RSA* pertains to the dynamic response of the dam-foundation system rather than to the intrinsic features of the ground motion, as it is not present in the spectrum of the reference motion recorded at the abutment (purple spectrum), while it appears at the crest (red spectrum). This result confirms the results obtained in terms of *SSR* for the fundamental frequency of the dam-foundation system at small strains. In addition, a higher vibration mode of around 10.5 Hz can also be recognized.

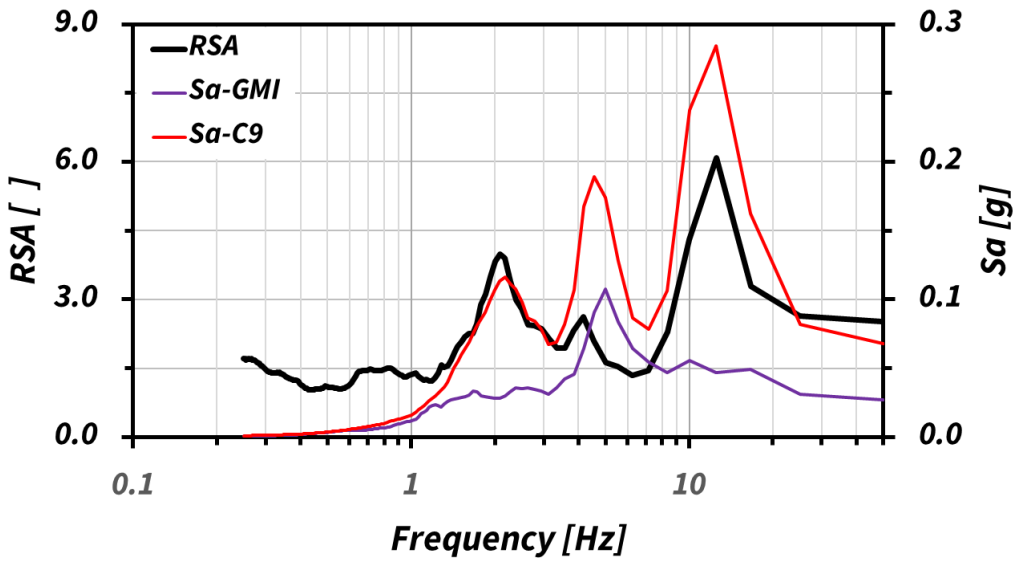


Fig. 3.61: RSA and Sa(f) for the C9 and GMD motion (event CR-01, TRA component)

The knowledge of the natural frequency of the dam at small strains can be used to back-figure an average shear wave velocity (Vs) of the gravelly soil constituting the embankment when

combined with some dam geometrical features. An estimation of *Vs* in the embankment is highly appreciated considering that it has never been measured in the embankment so far.

The calculations were carried out according to the expressions provided by Gazetas & Dakoulas (1992) for the case of a triangular-shaped dam lying on a foundation subsoil with comparable properties, both assumed as characterized by a parabolic stiffness profile:

$$f_1 = \frac{\overline{V}_s}{2.57 \times 0.9 \times H} \qquad \textit{Eq. 3.11}$$

In Eq. 3.11, the numerical coefficient 2.57 accounts for the 2D response of the dam body reproduced adopting an inhomogeneous 1D shear-beam scheme, considering a variation of the shear wave velocity proportional to the height to the power of 1/3 ($\overline{V}_s \propto z^{1/3}$). Furthermore, following the suggestions by Dakoulas & Gazetas (1987), the correcting factor of 0.9 accounts for the longitudinal foundation geometry approximated to a trapezoidal valley (see Fig. 3.53c).

By assuming a height of the dam H = 120 m, and the fundamental frequency at small strains f_1 = 2 Hz, the average shear wave velocity $\overline{V}_s$ resulted equal to 555 m/s. This value is higher than that estimated in previous studies (424 m/s) using seismic refraction surveys in trial embankments at the dam site (De Cicco et al., 2015). This inconsistency can be primarily attributed to the different states of confinement and magnitude of lithostatic stresses between the trial embankment and the real dam.

Using the stiffness distribution estimated from the dam settlement records after the end of construction, it is possible to infer a value for the fundamental frequency under large-strain conditions. This estimation is particularly useful for assessing the shift in natural periods resulting from the incursion of significant portions of the dam body into the inelastic domain during strong ground shaking. Accordingly, Eq. 3.12 from Dakoulas & Gazetas (1985) can be applied to estimate the fundamental frequency of the dam at large strains, considering that the properties from the derived stiffness profile set as reference correspond to medium to large deformation conditions.

$$f_{1_L} = \frac{a_n \cdot (2-m)}{4\pi} \cdot \frac{V_{S_b}}{H} \qquad \text{Eq. 3.12}$$

Where a_n is a tabulated coefficient depending on the power coefficient m and the truncation ratio h/H; V_{S_b} is the shear wave velocity at the base of the dam, evaluated as $V_{S_b} = \sqrt{G_b/\rho}$ where ρ = dam body soil density.

Introducing in Eq. 3.12 the evaluated value of G_b = 230 MPa and m = 0.45, and considering a_n = 2.910 as tabulated in Dakoulas & Gazetas (1985) for the first natural frequency, with the ratio h/H = 0.025 the value of the natural frequency at large deformations is equal to $f_{1_L} = 1.1\text{Hz}$, well below, as expected, of the estimated frequency under small strain conditions, f_1 = 2.0 Hz.

Ending with the estimation of the natural frequencies under diverse deformation levels utilizing monitoring information and analytical models, it is possible to affirm that the use of the *SSR* for identifying the natural frequencies of the dam (Fig. 3.60), demonstrated reliability after applying suitable signal processing procedures. The identified natural frequencies at small strains were checked to be independent of the choice of records with variable source mechanisms and distances (refer to Table 3.4). On the other hand, the use of the *RSA* as an alternative to the *SSR* is an attractive option to identify the natural frequencies of vibration, because it requires an easier procedure, is less sensitive to correction, filtering, and smoothing techniques.

A feasible value for the first natural frequency at large strains was estimated through the interpretation of the vertical settlement records. The evaluation of the vertical settlement profile using the methodology presented by Pagano et al. (1998) allowed to identification of the variation of shear stiffness along the dam's height, which, in turn, has been used to estimate the fundamental frequency at large strains after having opportunely adjusted the Dakoulas & Gazetas (1985) shear-beam model.

To validate the anticipated values for the fundamental frequency at small and large strains, it is possible to make use of a few empirical tools present in the literature. The first one, developed by Sasaki et al. (2018), provides the correlation between fundamental period and height for different typologies of dams, based on earthquake records from the seismic monitoring systems of a large portfolio of Japanese dams.

For the case of rockfill dams, the fundamental frequency in the stream direction considering H = 120 m falls between 1.25 Hz to 1.99 Hz. These values could be associated with weak motion events, as far as almost 80% of the records used in the correlation correspond to events with PGA < 0.1 g.

The second procedure was proposed by Ghaemi & Konrad (2022), which based on the ground motion database of the Japanese Committee of Large Dams and a consistent analytical framework, furnishes an expression that relates the ratio of natural frequencies at large and small strains, f_{1_L}/f_1, with the maximum shear strain $\gamma_{\max}$ sustained in the dam body. This shear strain is further linked with the maximum ratio of shear modulus degradation G/G_0, giving an idea of how degraded the dam stiffness should be to exhibit a fundamental frequency at large strains, as the one previously estimated. Therefore, for a ratio of fundamental frequencies $f_{1_L}/f_1 = 0.55$ as the one based on the results of this work, the larger shear modulus degradation is expected to be equal to $G/G_0 = 0.33$, which is a feasible value for a dam under strong ground motion excitation.

Finally, a third empirical correlation developed by Papadimitriou et al. (2014), originally used to obtain the nonlinear fundamental period given a magnitude of the PGA, was utilized by swapping the unknown variable to identify which value of PGA could correspond to the derived fundamental frequency ratio. Consequently, for the ratio $f_{1_L}/f_1 = 0.55$, the related peak ground acceleration results in $PGA \cong 0.4$ g when adopting the average shear wave velocity back-figured using Eq. 3.11. This value of PGA is consistent with the values that could arise in a seismically active region such as the one where the dam is located.

It must be mentioned that an empirical estimation of the fundamental frequency of the embankment-foundation system is not applicable in the design stage but is limited to existing dams with an installed seismic monitoring system, such as Potrerillos Dam. Moreover, the two approaches previously applied can represent an affordable, yet reliable, alternative with respect to the use of numerical simulations or simplified formulae, in order to define the appropriate constraints for the selection of reference input motions required for seismic hazard assessment (Zimmaro & Ausilio, 2020). Since both methods rely on monitoring records, local conditions difficult to cover with other empirical or numerical procedures are implicitly considered. This is a great advantage, even when simple interpretive models are used

as part of the procedure, standing out as reliable alternatives to identify the dynamic characteristics of the dam when monitoring records are available.

Finally, it is worth noting that the average shear wave velocity back-calculated using Eq. 3.11 resulted larger than the values used in previous seismic response studies and design analyses, which were based on geophysical investigations on a trial embankment but never supported by direct measurements in the actual dam body. Nevertheless, the information recorded after almost 20 years of seismic monitoring helped to better identify the dynamic characteristics of the system and provide information to calibrate the geotechnical model used for seismic safety assessments, whereas previous studies on the seismic response of the dam (De Cicco et al., 2015; Barbagelata et al., 2022) were carried out based only on geotechnical design parameters. The differences among shear wave velocity values could be related to the different stress distributions and confinement level in the trial embankment and the actual dam, influenced not only by the embankment self-weight but also by the reservoir loading along the upstream face.

The evaluation of the monitoring records brought out very interesting results concerning the overall response of the dam under static and seismic conditions, but also furnished information that will be used for the calibration of the numerical models in Section 6. Now, a preliminary evaluation of the potential failure modes of the dam will be carried out to support the evaluation of reliable case-specific fragility functions.

4. Preliminary identification of potential failure modes

Following the framework described in Section 3.1, the preliminary identification of potential failure modes to which the dam may be subjected is an important step in developing case-specific fragility functions. This step ensures consistency between the actual mechanisms that could lead to dam failure and fragility assessment, in a fashion similar to what is also recognized for risk analyses (McCann et al., 2022).

As defined by several dam safety guidelines (ICOLD, 2005; FERC, 2021), a Potential Failure Mode (PFM) represents a specific sequence of events that could cause failure or disrupt the operation of the dam-reservoir system, or part of it. Hence, a Potential Failure Mode Analysis (PFMA) is the process of identifying all such PFMs under various loading conditions (normal operation, flood, earthquake, sediment load, ice, etc.) and evaluating those significant enough to warrant ongoing awareness and attention to monitoring, visual observations, and where appropriate, further analysis and remediation measures.

These definitions highlight the inherently multi-hazard nature of dam risk assessment. The probabilistic tools used in such evaluations (SPANCOLD, 2012; USBR & USACE, 2019) can account for the recurrence, magnitude, and interaction of causes and consequences associated with each hazard, with varying levels of sophistication depending on the chosen approach. However, some experts remain skeptical, arguing that these methods are not yet fully reliable (Wieland, 2019) and instead support methodologies that analyze one hazard at a time using deterministic approaches, often neglecting or overly simplifying the treatment of variability and uncertainty in dam safety evaluations.

Every PFM can be described in more detail using an Event-Tree Analysis (ETA), which provides a graphical representation of the PFM and its possible consequences. ETA helps identify the logical progression of events that could lead to failure, starting with an initiating event and continuing through a sequence of conditional events to a range of possible outcomes. The logic of ETA is “downstream”, beginning with a trigger event and branching out toward potential failure scenarios, and for this reason, is particularly useful in the identification of PFMs. This contrasts with Fault Tree Analysis (FTA), which follows an “upstream” logic, starting from an observed failure and working backward to identify its possible causes, making it more suitable for analyzing actual failures rather than hypothetical ones (USBR & USACE, 2019).

Traditional dam safety evaluations have historically emphasized compliance with design codes, tending to focus on a reduced number of "standard-based" concerns, such as structural stability or hydraulic capacity under a set of predefined loading conditions. While important, this approach may not account for all the ways a dam could fail, and modern case histories have proven this point (McCann et al., 2022). PFMAs are intended to broaden the scope of the safety evaluations to include potential failure scenarios that may have been overlooked in past reviews and evaluations, through a rational procedure.

A formal PFMA in the context of dam risk assessment requires the compilation and analysis of a comprehensive body of information about the project. It also involves the engagement of a multidisciplinary panel of experts and the application of a structured and systematic procedure. The objective is not only to identify the potential failure modes of the dam but also to evaluate their feasibility and likelihood, and to establish a hierarchy of failure modes based on their contribution to the overall risk of the asset (SPANCOLD, 2012; USBR & USACE, 2019). This process helps prioritize attention and resources toward those failure modes that are most likely to control or dominate the dam's risk.

Although not intended to replicate the depth and rigor of a formal PFMA, a preliminary identification of PFMs is considered in this thesis a fundamental component in the formulation of case-specific fragility functions. In this context, a non-exhaustive list of credible PFMs applicable to the dam under consideration is provided below, along with a concise description of the event sequences that could plausibly lead to failure.

4.1 Exploratory assessment of potential failure modes for Potrerillos CFRD

This identification is informed by the available project data outlined in Section 3, the author's domain expertise, and existing literature on the subject. Accordingly, the outcomes of this assessment should be considered in light of these informational boundaries. Hence, the potential failure modes related to the failure of the dam are listed below, identifying the initiator, failure mechanism, and resulting impact on the dam:

- Instability of abutments after an earthquake: Abutment rock slope failures during a strong earthquake, mobilizing portions of the embankment material and/or concrete face slab as part of the sliding mass. The displacement of the sliding may lead to progressive global instability of the dam structure or initiate internal erosion processes.

- Instability of abutments due to rapid drawdown: Abutment rock slope failures induced by elevated pore water pressure in the fractured rock mass during rapid reservoir drawdown following a hazardous event. The resulting landslide may compromise the structural stability of the dam and initiate scouring processes at the flanks of the dam.
- Localized seepage along slab-plinth-abutment interface: Under seismic or static conditions, excessive opening of the slab-plinth or plinth-abutment joint may occur, compromising watertightness and allowing concentrated leakage along the opening. The resulting flow may overwhelm the blanket filter capacity, starting a progressive internal erosion process.
- Seismic liquefaction in alluvial deposits leading to a large downstream landslide: During a strong earthquake, zones of the foundation soils lose strength due to a reduction in effective stress from excess pore water pressure generated by ground shaking. This condition may trigger a slide involving both the dam body and its foundation, compromising the structural integrity of the dam and increasing the risk of overtopping.
- Excessive damage in the concrete face due to earthquake loading: During a large seismic event, high stresses induced in the concrete face slab may cause extensive cracking and joint opening. The resulting widespread damage allows significant seepage into the dam, triggering localized internal erosion processes that compromise the stability of the upstream slope and may lead to the formation of a breach.
- Transverse cracks in the dam body for combining settlements and a complex foundation: After an earthquake, the dam typically undergoes settlement, but the complex geometry of the bedrock locally restrains the movement in parts of the dam body and foundation. This differential settlement can induce transverse cracking, creating preferential flow paths and initiating erosion processes.
- Excessive pore pressure on the foundation: A breakage or construction defect in the cut-off wall may allow water carrying suspended solids, particularly after a large storm, to infiltrate the alluvium and alter the permeability distribution of the foundation soils. Preferential flow paths, resulting from the complex geometry of the foundation and the heterogeneous permeability of the materials, can lead to zones of concentrated seepage and elevated pore pressures. The resulting reduction in effective stress in these areas may escalate, potentially triggering suffusion or localized stability problems.

- Surface fault displacement in the dam zone after a strong earthquake: Unmapped faults crossing the dam may undergo tectonic displacement during a near-field earthquake. Such fault movements can induce large cracks in the dam body and foundation, initiating internal erosion processes. Additionally, dip-slip fault displacements may reduce freeboard, increasing the risk of overtopping.
- Piping through the alluvial foundation due to damage in the cut-off wall: during an earthquake event, the cut-off wall can suffer damage, and leakage of water from the reservoir could start an erosion process throughout the alluvial soils.
- Large seismically induced displacements of the drains interrupt the controlled seepage: The deformation of the dam body after a strong earthquake could generate large displacements of the clean gravel drains within the dam. The interruption of flow through these high-permeability regions can induce a rise in the pore water pressure, and depending on its position in the dam and the state of stresses, lead to an internal erosion process. This process can lead to significant scouring and, ultimately, result in stability issues.
- Large slope failures entering the reservoir generate overtopping waves: Static or seismically induced landslides along the reservoir coastline or underwater can generate large water waves that the spillway cannot immediately attenuate. The resulting wave run-up may exceed the available freeboard and initiate overtopping.
- Seismically induced deformation of the dam body: Seismic shaking may cause settlement due to shear and volumetric deformation, resulting in freeboard reduction, and potentially overtopping of the dam.
- Differential settlement of the dam induces slab joints opening: Due to large differential settlements after an earthquake, promoted by abrupt changes in geometry and stiffness within the dam and foundation system, dislocation of the concrete face slab joints may occur. Combined with the extent of the damage in the dam body, this condition can initiate an internal erosion process.
- Large opening of the joints in the floating plinth and excessive seepage: Under static or seismic conditions, differences in terms of horizontal displacement between the cut-off wall and the concrete slab or dam may exceed the accommodation capacity of the floating plinth and connection slabs. The rupture of the water stop allows uncontrolled water flow into the dam, potentially overwhelming the drainage system and initiating internal scouring processes.
- Damage to the bottom outlet impedes drawdown: after a strong earthquake, the bottom outlet gets severely damaged by seismic shaking or tectonic deformation, or

its entry is blocked by an underwater landslide of the reservoir sediments. This situation impedes a rapid drawdown of the reservoir and keeps large hydrostatic loads along the upstream slope of the dam, jeopardizing the structural stability of a likely damaged dam. Moreover, if the water level keeps rising, it could also result in the dam overtopping.

- Surface fault displacement in the reservoir decreases the effective freeboard: A near-field earthquake with a dip-slip mechanism produces surface fault displacement in the reservoir, close to the dam. The water level of a part of the reservoir suddenly changes and causes a water wave that runs up over the crest, starting a breach.
- Surface scouring after a large storm: During an extreme storm event, the surface runoff from the abutment slopes concentrates into flow channels that discharge onto the downstream slope of the dam. This concentrated flow induces erosion at the contact between the dam body and the abutment, potentially initiating a localized scouring process that may lead to the instability of a part of the dam body.

It is important to remember that all previously listed failure modes are feasible yet hypothetical, hence the term "potential", and should be subjected to expert panel screening based on the most exhaustive project information available. Although a few of them may appear unlikely, a discussion on the possibility of their occurrence must be carried out, and clear reasons should be provided to justify their exclusion.

A subset of the previously mentioned failure modes, potentially including those most critical during an earthquake, was selected to support the development of the seismic fragility functions, as described in the following section.

4.2 Seismically driven PFMs identified for seismic fragility analysis

Among the previously identified potential failure modes, three were selected for the derivation of seismic fragility functions. These failure modes were chosen based on the characteristics of the dam, the damage mechanism exhibited in the past by dams during strong earthquakes, the identification of reliable *EDP,* and the availability of truthful *DM* related to each PFM. This last concern is a conditioning factor and will be discussed in Section 8.1. The selected failure modes are described below.

4.2.1 Loss of freeboard after earthquake deformations

Plastic deformations and combined upstream and downstream sliding that occur in the dam after a strong earthquake can lead to significant settlements at the crest. Extensive damage to the soil and concrete face slabs near the top of the dam may reduce the effective freeboard, especially if transverse cracks are formed near the crest.

Additionally, the liquefaction or cyclic mobility of portions of the foundation soils may further increase crest settlements and reduce the available freeboard. As the water level approaches the dam crest, the risk of overtopping increases, potentially initiating a breach through the dam body and leading to an uncontrolled and unsafe release of reservoir water.

The presence of continuous reinforced concrete walls on both edges of the crest perpendicularly linked by beams and filled with compacted gravel, generates a semi-rigid body at the top of the dam that could be subjected to "whiplash" effects (Gazetas, 1987), worsening the damage that the top of the dam may exhibit.

This PFM is commonly considered in the seismic performance evaluation of embankment dams because it is associated with a recurrent damage mechanism, is linked to a physical parameter that can be easily measured after an earthquake such as the permanent crest settlement, and has clearly identifiable consequences: dam overtopping and the uncontrolled release of reservoir water.

The *EDPs* for this PFM are related to the permanent crest settlement, being normalized with respect to the height of the dam, the dam and the foundation, or the effective freeboard. More details about the definition of the *EDPs* and *DMs* for this failure mode will be given in Section 8.1.

4.2.2 Global instability due to strong ground-shaking

Following a strong earthquake, a large sliding mass that cuts across portions of the dam embankment and foundation compromises the global stability of the dam under normal loading conditions. The large size of the landslide could be promoted by the presence of weak zones within the dam foundation, resulting from the buildup of pore water pressure in coarse-grained saturated soils due to ground shaking. This increase in pore pressure reduces the effective stresses, leading to a loss of stiffness and strength, which depending on the susceptibility of the material could ultimately trigger soil liquefaction.

The global instability of the dam can result in structural collapse, loss of freeboard, followed by overtopping, or the initiation of backward erosion, depending on the location and magnitude of the sliding mass. The *EDP* for this potential failure mode should be related to the maximum displacement of a well-identified sliding mass comprising parts of the dam body and foundation, as this is a commonly adopted performance parameter in cases of earthquake-induced slope instability (Kramer & Stewart, 2024).

4.2.3 Internal erosion triggered by seismic damage in the concrete face

The concrete slabs on the upstream face of the dam become severely damaged after strong earthquakes, exhibiting excessive joint opening and the formation of large cracks in the concrete. These cracks permit reservoir water to flow into the dam body, which has also experienced significant deformation and cracking. Consequently, water infiltration into the dam becomes substantial in the most heavily affected areas of the upstream face.

The seepage through the highly deformed coarse soils initiates a scouring process. The concentrated flow, driven toward the damaged filters, exceeds their capacity, allowing the erosive process to extend along the most compromised sections of the dam. As the flow reaches the downstream slope, backward erosion develops and progressively undermines the stability of the entire system.

The *EDP* for this PFM will be focused on the damage to the concrete face, as having a forecast of scouring is still challenging using the regular tools of numerical modeling in geotechnical engineering. The proposed method to evaluate the damage to the concrete slab will be presented in Section 8.1.

A last comment related to the identification of the PFM, is that some seismically driven damage mechanisms could be correlated, for example when the genesis of both mechanisms is the large deformations in the soils of embankment and foundations. This situation could take place when significant crest settlements are followed by an instability issue. However, every PFM is characterized by a main damage mechanism which is the trigger of the most unsafe conditions and probable collapse. If a second damage mechanism is triggered by the conditions induced during the development of a precedent damage mechanism, and this second mechanism could lead to collapse conditions, it should be treated as another PFM.

5. Site-specific seismic hazard assessment

The proposed framework for the derivation of case-specific fragility functions requires a site-specific seismic hazard assessment and an appropriate record selection. This may seem to contradict the concept underlying the derivation of generic fragility functions. These latter should be as independent as possible from the ground motions used in their development, to avoid introducing biases when they are applied across different seismotectonic environments.

On the other hand, for deriving case-specific fragility functions it is advised to use input motions that are selected and scaled based on the results of a site-specific probabilistic seismic hazard analysis. Such a choice ensures hazard consistency, since it reduces the epistemic uncertainty by constraining the definition of the seismic scenarios used to select and scale the seismic records, introducing in the process information about the seismotectonic environment around the dam site.

In this study, a probabilistic seismic hazard analysis, the first ever conducted for Potrerillos dam, was carried out to support the selection and scaling of strong motion records to be used in the derivation of fragility functions, while also providing a clear description of the seismic hazard at the dam site.

5.1 Tectonic setting and regional seismicity

The seismicity of western South America is driven by the convergence of two tectonic plates: the oceanic Nazca plate subducting beneath the continental South American plate. The ongoing subduction of these plates along the Peru–Chile trench is largely responsible for the Andean orogeny and the current tectonic activity in the region (Jordan et al., 1983). With a convergence velocity of approximately 7 cm/y (Ruegg et al., 2009), this plate boundary has been responsible for the largest earthquake ever recorded, the 1960 M_w 9.5 Valdivia earthquake. Moreover, many other recent subduction interface megathrust events took place along the southern part of the trench, including the 2010 M_w 8.8 Maule earthquake, the 2014 M_w 8.2 Iquique earthquake, and the 2015 M_w 8.3 Illapel earthquake.

The tectonic activity of the zone is not restricted to the vicinity of the plate margin, and the influence or the subduction can extend significantly to both plates. Specifically, at a latitude of -32°, the presence of the Juan Fernández Ridge within the Nazca plate gives origin, between 18-12 million years ago, to the Pampean “flat subduction” or “flat slab” segment. The presence of this submarine mountain belt of volcanic origin significantly increased the

asperity in the subduction contact and altered the dynamics of the plate boundary, inducing a change in the angle of the plate contact between -33° and -27° (Ramos et al., 2002).

This condition extends the interaction between plates far under the South American plate, resulting in the significant tectonic activity of the Cuyo region. The Pampean flat slab is responsible for the orogeny of the highest pikes of the Andes Cordillera, and the formation of several parallel, south-north-oriented mountain ranges such as the Precordillera and Sierras Pampeanas (Fig. 5.1). As the influence of the plate boundary diminishes, tectonic activity decreases toward the east of the country.

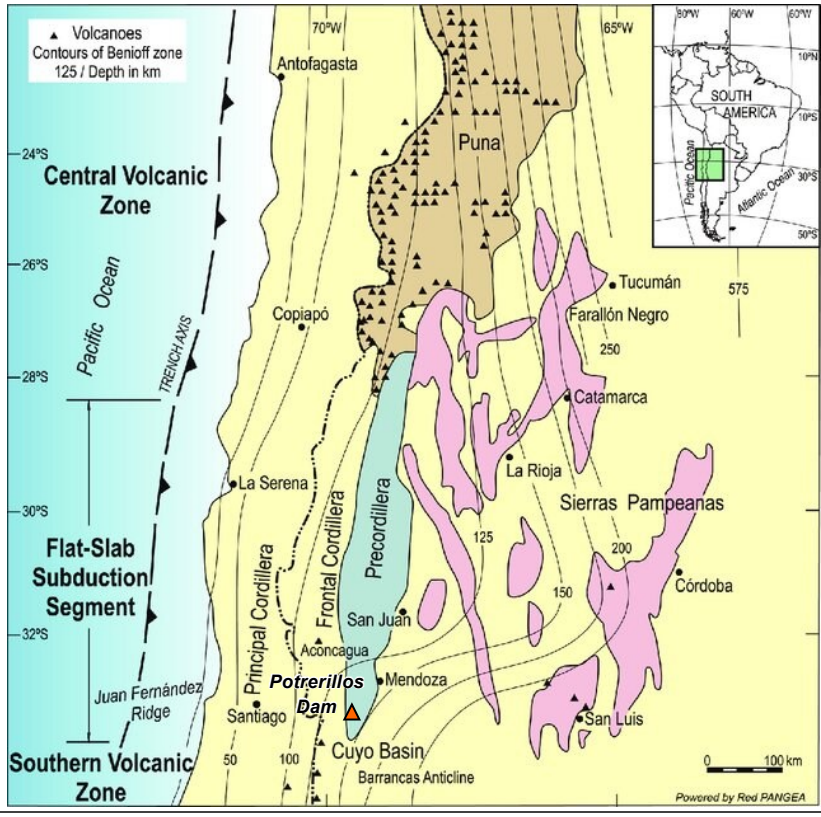


Fig. 5.1: Pampean flat subduction segment, with contours of the subducted plate or Benioff zone, and related mountain ranges (Ramos & Folguera, 2009).

The abovementioned change in the contact angle of the subduction (Fig. 5.2) induces a large compression in the upper part of the continental plate, giving origin to the active tectonic activity and faulting of the Cuyo region, largely responsible for the seismic activity of the south of San Juan and north of Mendoza provinces (Alvarado et al., 2009).

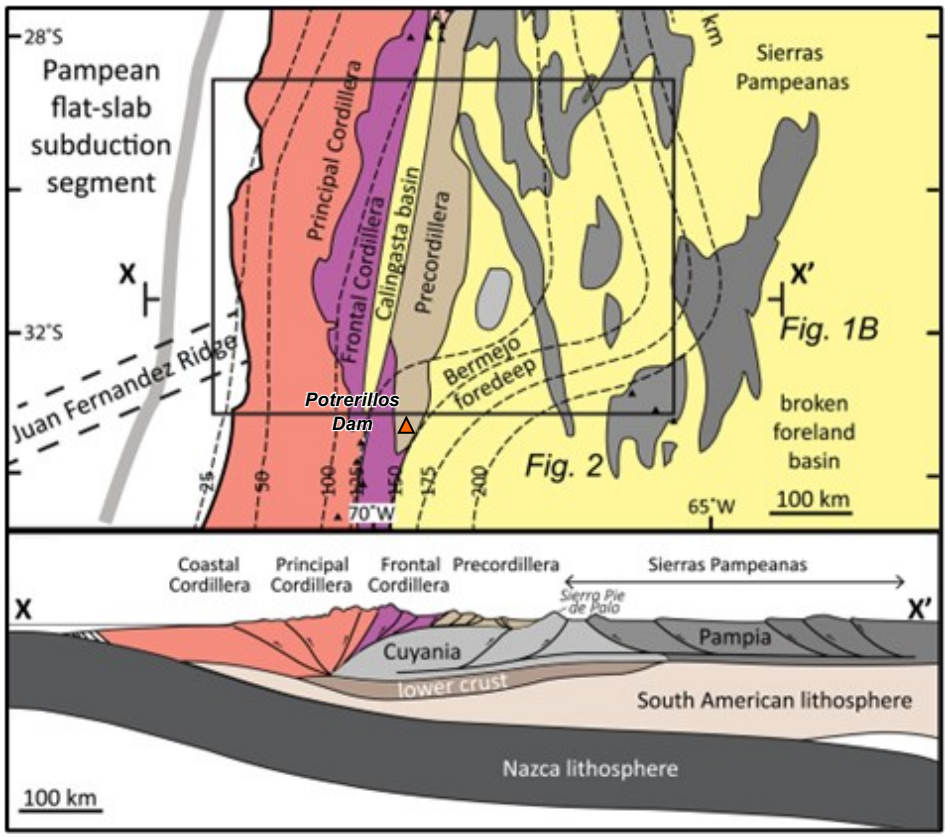


Fig. 5.2: Reference location map and an east-west crustal cross-section of the Pampean Flat subduction, with its various geological structures and related faults. After Capaldi et al. (2020).

This compressional tectonic regime results in most seismically active crustal faults in western Argentina being reverse or oblique-reverse, with only a few significant strike-slip events recorded. Evidence of this predominant faulting style is highlighted by the most damaging earthquakes in the historical record of the Cuyo Region, all of them associated with reverse faulting. These include the 1944 M_w 7.0 San Juan and the 1977 M_w 7.4 Caucete earthquakes, both of which severely affected the city of San Juan, as well as the 1861 M_w 7.0 Mendoza earthquake (Fig. 5.3), which destroyed the city of Mendoza and resulted in the death of approximately one-third of its population (Perucca & Moreiras, 2009).

The most important historical crustal earthquakes occurred in the north of Mendoza province are also related to compressive structures. They are presented in Fig. 5.3 together with the trace of some geological active structures and the vectors of surface velocity from geodetic GPS stations. The location of some historical earthquakes, such as that of 1782, is open to discussion, as many of them have not been linked with an active structure, and their location was inferred based on a limited number of evidences.

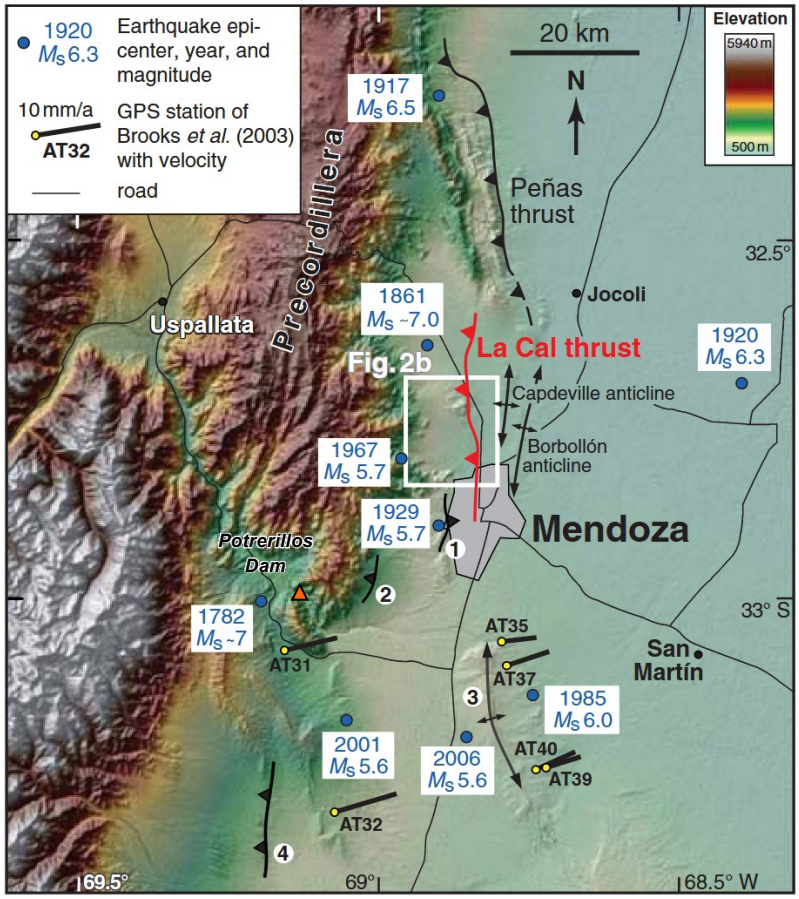


Fig. 5.3: Historical crustal earthquakes in the north of Mendoza, along with the trace of a few geological active structures, and surface velocity vectors from geodetic GPS (Salomon et al., 2013).

Even though crustal earthquakes have produced the largest damage in the natural and building environment along the seismic history of the Cuyo region (Moreiras & Páez, 2015), they were not the only ones perceived by the population. Large earthquakes can occur within the oceanic plate, both west (in the sea) and east (Benioff zone) the contact with the continental plate.

In the segment of the Pampean flat subduction (Fig. 5.4a), intraslab earthquakes take place beneath the South American plate with hypocenters in depths between 60 and 200 km, following the geometry of the subducting slab (Fig. 5.4b) until it melts into the mantle.

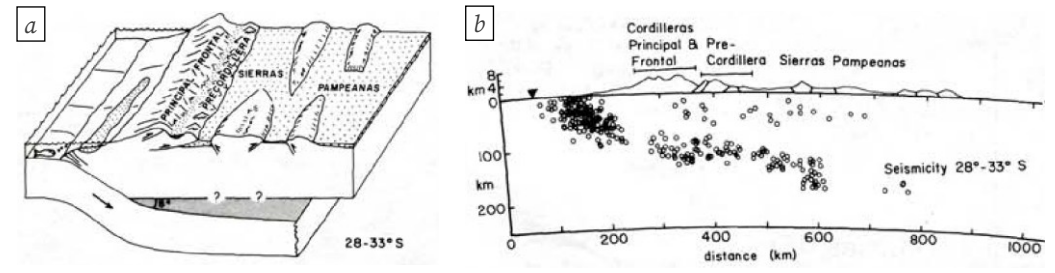


Fig. 5.4: a) Block diagram of the Pampean flat subduction; and b) intraslab seismicity in the Pampean flat subduction range (Jordan et al., 1983).

Due to the dynamics of asthenospheric convection near subduction margins, the mantle tends to drag the plate, generating pulling forces on the subducted slab. The resulting extension within this portion of the subducted plate leads to the occurrence of so-called "slab-pull" earthquakes, which can produce large-magnitude events and typically exhibit normal faulting mechanisms (Leyton et al., 2009). This kind of intraslab earthquake include some historical events in the north of Mendoza, such as the 1927 M_S 7.1 earthquake, with an estimated depth of 110 km and an epicenter just 50 km away from the dam site, close to the city of Uspallata. This event produced moderate damage to the structures of the region, but showed that intraslab earthquakes could significantly influence the seismic hazard of the whole area (Loos, 1928).

Large subduction interface (or interplate) earthquakes have been recorded in the north of Mendoza, but the amplitude of the registered ground shaking barely produced some slight damage. As a matter of fact, the seismic records from the monitoring system of Potrerillos dam presented in Barbagelata et al. (2024) show that during the 2010 Maule and 2015 Illapel earthquakes, accelerations with *PGA* below 0.025 g were measured at the dam crest.

The identification and description of the events recorded at the monitoring system of the dam, and presented in Section 3.4.3, are consistent with the previously described tectonic setting, supporting the established seismotectonic environment and the further assumptions considered in the characterization of the seismic sources.

5.2 Seismic sources characterization

In an analogous fashion to that considered in Section 3.4.3 to differentiate among the various faulting types of the recorded events, the sources considered in the seismic hazard assessment for Potrerillos dam can be initially classified into crustal, intraslab, and subduction interface mechanism.

Is worth to remember that the impact of subduction interface events at the dam site has proven to be minor, as acceleration records from large subduction earthquakes exhibited very low peak accelerations. This argument is further supported by the reconstructed Shakemap of the 1906 M_w 8.2 Valparaiso earthquake present in the USGS Shakemap Atlas (Marano et al., 2024), an event considered the largest subduction interface earthquake at the same latitude as Potrerillos dam. This Shakemap shows that the *PGA* estimated at the dam site does not exceed 0.05 g, a value that for a modern dam designed to sustain much larger accelerations can be considered negligible.

The two conditions mentioned above, together with the fact that the maximum source-to-site distance considered in the most commonly used ground motion models for subduction sources (Abrahamson et al., 2016) is smaller than the distance between the dam and the Chilean subduction trench (Fig. 5.1), provide sufficient justification to exclude subduction interface sources from the seismic hazard analysis.

The geometry and potential seismicity of the crustal and intraslab sources were characterized and introduced in the software R-CRISIS (Ordaz et al., 2017), used to evaluate the seismic hazard following the conventional probabilistic approach proposed by Cornell (1968), as briefly described in Section 2.3.

The sources considered in the analysis are all defined as fault sources, while background seismicity is not included to cover potential unknown structures. This decision is supported by two hypotheses. First, the seismicity catalogs present discrepancies due to the limited coverage and resolution of the regional seismological networks, which affects the reliability of the data used to define the characteristics of the background seismicity. Second, the available geological information indicates that the main active geological structures have been incorporated into the analysis, and any other potential sources either show no significant activity to be considered active or can be correlated with the identified faults.

However, future work could include background seismicity to identify potential sources related to reservoir-triggered seismicity or slow-deformation processes in the vicinity of the dam.

5.2.1 Crustal sources

The lack of a complete and reliable catalog of active faults in Argentina made the definition of the seismogenic sources to consider in the PSHA a challenging task. The identification and

characterization of the active seismic sources in the vicinity of the dam, were accomplished with the information coming from a few research works available in literature, integrated by the ad-hoc work done by Mingorance (2024).

Seven active crustal sources with potential impact on the seismic hazard of the dam were identified within a radius of 40 km around the dam site (Fig. 5.5). These sources are: La Cal fault (Mingorance, 2006), Barrancas monocline (Chiaramonte et al., 2000), Southwestern Precordillera (Mingorance, 2024), El Melocotón fault (Moreiras et al., 2021), La Carrera fault (Cortés et al., 2006), La Aguadita fault (Casa et al., 2010) and El Totoral fault (García & Casa, 2015).

Other geological structures presented in Moreiras et al. (2021) and Mingorance (2024) were not considered, as they do not show clear evidence of tectonic activity during the Quaternary or do not represent a significant contribution to the seismic hazard.

Among the abovementioned sources, La Cal and Barrancas are the only ones associated with historical earthquakes. La Cal is considered the source of the 1861 M_w 7.0 Mendoza earthquake (Mingorance, 2006), the seismic event that produced the most casualties in the history of Argentina (INPRES, 1986). Moreover, La Cal is the only structure of the group with paleoseismological studies (Salomon et al., 2013), having a more reliable estimate for the average slip rate than the other structures.

Barrancas folded structure was responsible for the last two moderate earthquakes of the region: the 1985 M_S 6.0 and the 2006 M_s 5.6 Barrancas earthquakes. The first produced extensive damage in adobe buildings (INPRES, 1985; Zamarbide & Castano, 1993), while the second just produced mild damage in a few sectors of the Gran Mendoza urban conurbation.

The tectonic activity of the remaining sources was evidenced based on the identification of geomorphological evidence of active tectonics (Burbank & Anderson, 2011) and the inference of tectonic deformation from borehole breakouts observed in drillings from the petroleum industry (Guzmán & Cristallini, 2009).

5.2.1.a Crustal sources geometry

The geometry of crustal sources (Fig. 5.5) was drawn based on literature works, deep geophysics from the petroleum industry, geomorphological evidence of active tectonics, and geological constraints, hence the magnitude of the Maximum Credible Earthquake (MCE)

was estimated based on the fault geometry using empirical equations (Mingorance, 2024). All the sources correspond to reverse faults with dipping towards the west, in agreement with the prevalent seismotectonic setting.

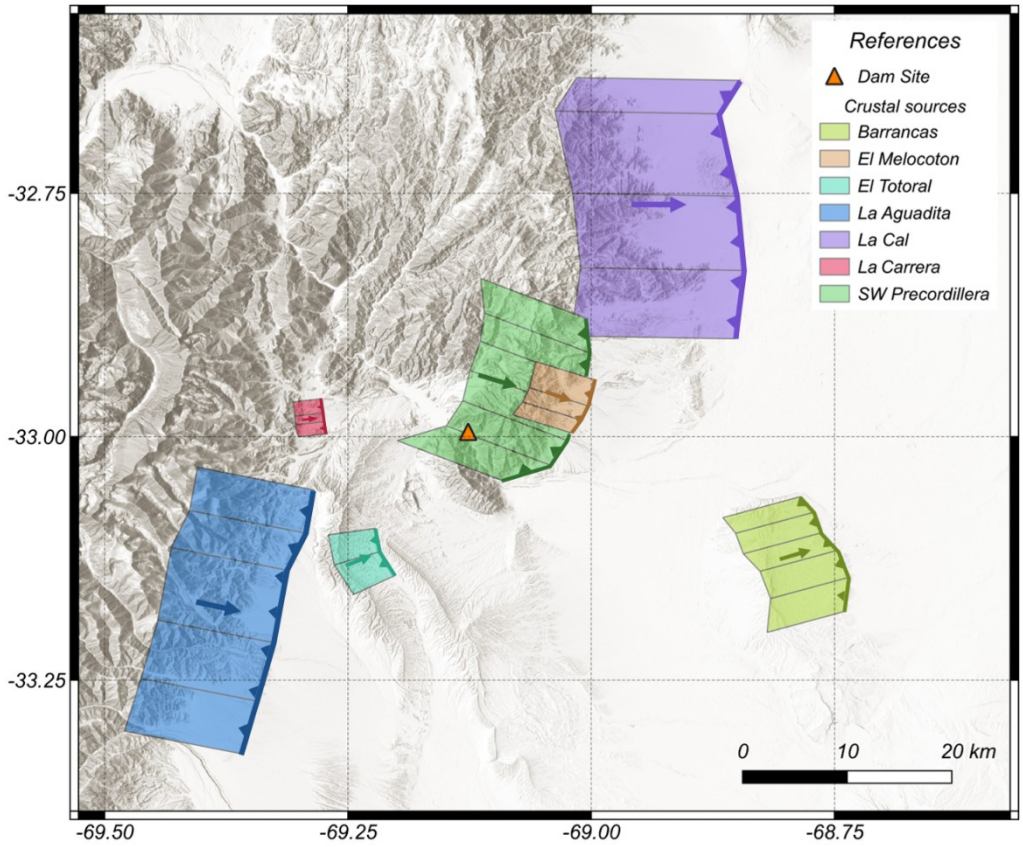


Fig. 5.5: Plan view showing the projection of the crustal faults considered in the PSHA, with the identification of the fault scarp and an arrow illustrating the rake direction.

As can be noted in Fig. 5.5, the dam is located on the hanging wall of the Southwestern Precordillera source; it is therefore expected that this source will be one of the most influential in the evaluation of the seismic hazard.

The fault length, dip angle and MCE with its range of variability for each crustal source are reported in Table 5.1. The MCE was estimated using the rupture area as reference geometry of the source, and the largest magnitude that came out from using the relationships of Wells & Coppersmith (1994) and Stirling et al. (2002). This information will be introduced in R-CRISIS to perform the PSHA calculations.

Source	Fault length (km)	Dip angle (°)	MCE (M_w)
La Cal	30.7	30	7.00 ± 0.25
SW Precordillera	22.0	40	6.75 ± 0.32
Barrancas	14.2	30	6.25 ± 0.25
El Melocotón	7.0	30	6.05 ± 0.30
La Carrera	4.0	60	5.75 ± 0.30
La Aguadita	31.0	40	6.80 ± 0.48
El Totoral	12.1	30	5.70 ± 0.30

Table 5.1: Crustal sources geometrical definitions and MCE (Mingorance, 2024).

5.2.1.b Seismicity of the crustal sources

The definition of the seismicity of the crustal sources will be conducted considering the hypothesis of a Poissonian distribution of the seismic events with time, a common and appropriate assumption for large tectonic earthquakes (Cornell & Winterstein, 1988). This model is further combined with the magnitude-frequency distribution models to establish the time distribution of seismic events with a given magnitude or earthquake recurrence rate.

The magnitude-frequency distribution of seismicity for the crustal sources will be a combination of two models: The characteristic earthquake model, or simply the Characteristic Model (CM) (Youngs & Coppersmith, 1985), and the Gutenberg-Richter model (G-R) (Gutenberg & Richter, 1944). This approach is presented in the manual of R-CRISIS (Ordaz et al., 2017) as the way to use the characteristic model within the software.

While the Characteristic Model (CM) assumes an uniform magnitude-frequency distribution, the Gutenberg-Richter (G-R) model is based on an exponential distribution derived from statistical analyses of global and regional seismicity. In its simpler version, the G-R distribution is represented by a linear equation in semi-log space (Eq. 5.1).

$$Log_{10} N\left(M > m\right) = a - b\,m \qquad \textit{Eq. 5.1}$$

where M and m are respectively a general and a particular value of the earthquake magnitude, N is the number of seismic events with $M > m$, while a-value and b-value are parameters of the model to be adjusted to fit the real seismicity of the region under analysis.

Modern versions of this distribution consider an upper and lower boundary for the magnitude, the first to avoid giving a finite number of occurrences to physically impossible seismic events, and the second to define the total activity rate only for magnitudes that are at least as large as the threshold level of completeness of the seismicity catalog.

The uniform CM is a suitable model for seismogenic sources identified with well-defined faults (Bommer, 2022), where the defined geometry allows for establishing the magnitude of the MCE, which is then considered as the characteristic earthquake of every source. The problem with this model is that it only focuses on the frequency of the characteristic earthquake, overlooking the small magnitudes associated with secondary structures or smaller rupture lengths. To solve this problem, the CM is combined with the exponential G-R model: the CM controls the frequency of the characteristic earthquake while accounting for its variability, and the G-R model defines the distribution of smaller magnitudes. An illustrative example of the combined model is shown in Fig. 5.6.

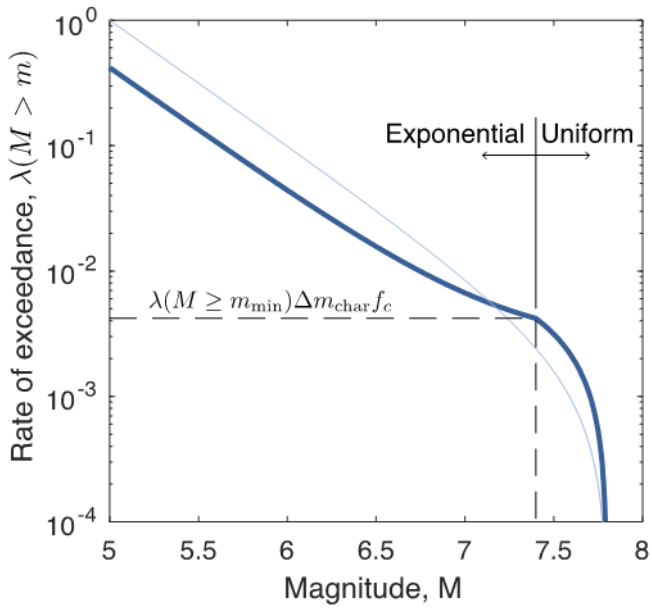


Fig. 5.6: Illustrative example of the magnitude-frequency distribution using the combination of the Characteristic Model (uniform) and Gutenberg-Richter (exponential) models (blue thick line), in contrast with just using the G-R model (thin light blue line) (Baker et al., 2021).

To define the characteristics of the CM and G-R models for every source, it is necessary to have an estimation of two parameters: the average slip rate of every fault and an estimate of the regional *b*-value of the Gutenberg-Richter distribution.

The average slip rate estimated by Mingorance (2024), except for La Cal fault, which counts with paleoseismological studies (Salomon et al., 2013), were supported by geomorphological evidence of active tectonics, or the borehole breakouts from drillings of the petroleum industry. When feasible, the estimations were related to the measurements of surface velocity from geodetic GPS from Brooks et al. (2003), already presented in Fig. 5.3. The estimated values are shown in Table 5.2 and represent the best estimates of the average slip rate given the available information. However, these values imply a large uncertainty in their estimation, and to cover this variability in the PSHA, they will be included in a logic tree to consider the impact of the variability of the average slip rates in seismic hazard predictions.

Source	Average slip rate (mm/y)	Methodology
La Cal	3.00	Paleoseismology
SW Precordillera	0.50	Tectonic geomorphology
Barrancas	0.48	Borehole breakout from petroleum drilling
El Melocotón	0.50	Tectonic geomorphology
La Carrera	0.50	Tectonic geomorphology
La Aguadita	0.21	Borehole breakout from petroleum drilling
El Totoral	0.23	Borehole breakout from petroleum drilling

Table 5.2: Average slip rate for all the crustal sources, and the methodology used for their estimation (Mingorance, 2024).

To estimate a regional *b*-value, an analysis of catalogs of instrumental and historical seismicity was carried out using the Matlab code ZMAP (Wiemer, 2001). The code has diverse tools useful for the processing of seismicity catalogs, among which several methodologies for the estimation of the minimum magnitude at which the catalog can be considered complete, known as corner magnitude (M_C). It also gives the possibility to fit a Gutenberg-Richter distribution combined with the previously calculated M_C (Woessner & Wiemer, 2005).

The catalog considered for the calculations was a combination of the reviewed catalog of instrumental seismicity from the International Seismological Center (ISC, 2022) for the events in the period of 1927-2022, merged with the catalogs of historical earthquakes reported by Mingorance (2006) and Moreiras et al. (2021), covering the period between 1782-1927.

The harmonized catalog was then declustered using the Reasenberg algorithm implemented in ZMAP (Reasenberg, 1985), considering the standard parameter values (Stiphout et al., 2012). The completeness of the catalog was accounted, as only events with magnitudes above M_C were considered in the calculations (Mignan & Woessner, 2012).

The events considered were restricted to earthquakes located in the southernmost segment of Western Precordillera and the northern part of the Cuyo basin (Fig. 5.7), with hypocentral depths up to 40 km. In this region, the tectonic setting and geological structures can be assumed as reasonably uniform, and a regional estimation of the *b*-value is feasible.

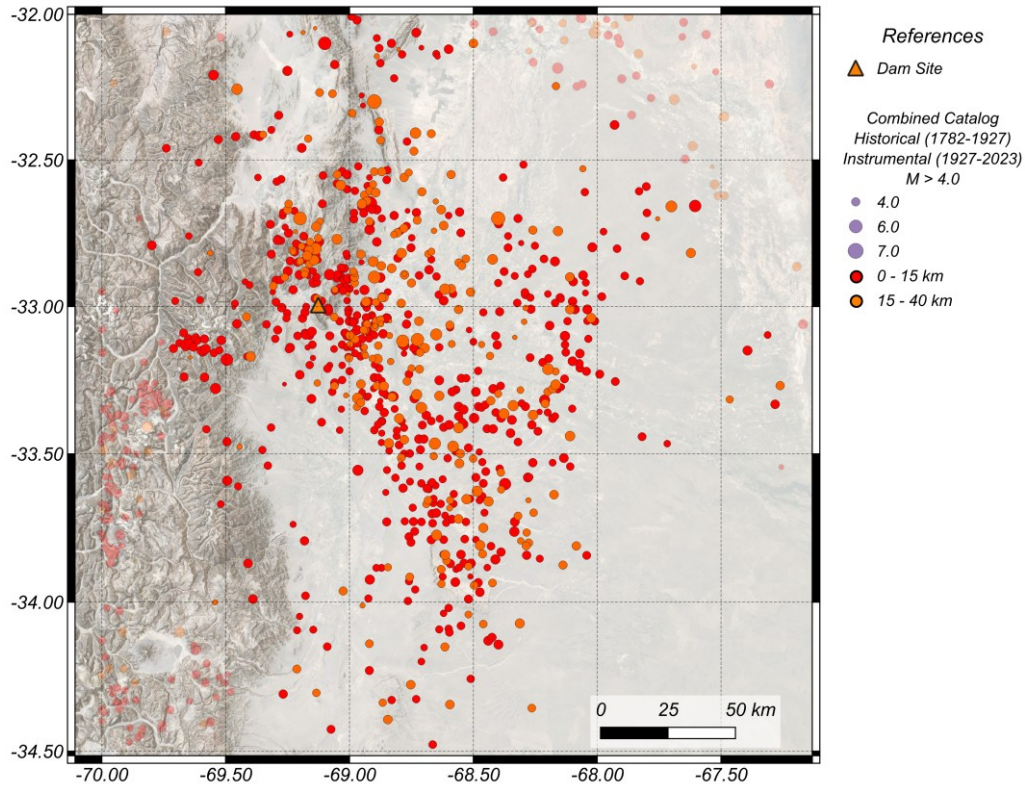


Fig. 5.7: Crustal seismic events from a combined catalog (instrumental + historical) in the northern part of the Cuyo basin and the southern portion of the Western Precordillera. These seismic events were used for the fitting of the Gutenberg-Richter model and evaluation of the regional b-value.

The fitting of the Gutenberg-Richter model was carried out using an approach that searches for the best combination of the *b*-value and corner magnitude at the same time, given the distribution of events. To account for the uncertainty in the sampling used during the calculations, a bootstrapping procedure available within the code was utilized.

The output of ZMAP with the fitted distribution is presented in Fig. 5.8, along with the points that represent the discrete or cumulative number of seismic events with $M>m$, considering magnitude bins of 0.1.

The adjusted model shows good agreement with the distribution of cumulative events in the whole range of magnitudes above M_C. The slight divergence observed at large magnitudes can be considered negligible, as the frequency of large magnitudes has to be evaluated by the CM model in the PSHA.

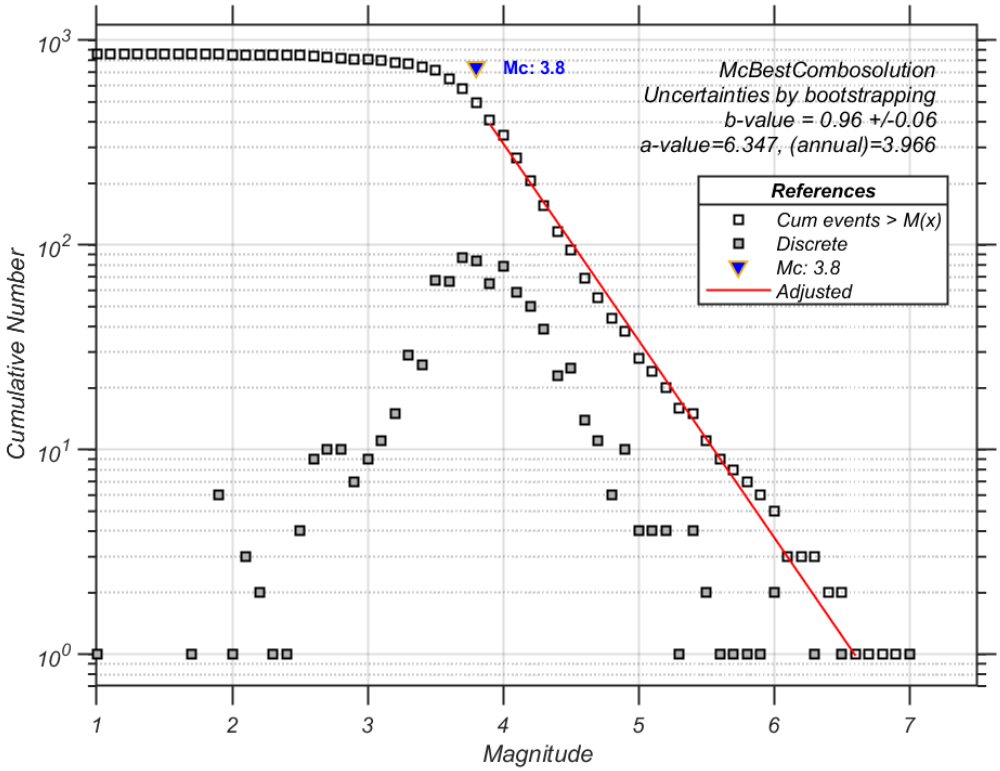


Fig. 5.8: Adjusted G-R distribution based on the best combination of b-value and M_C for crustal events.

A *b*-value around 1.0 is considered realistic for seismically active regions and tectonic earthquakes (Marzocchi & Sandri, 2003). A comparison of regional *b*-values reported in the literature for regions that cover all or part of the same area considered in this work is presented together with the calculated *b*-value in Table 5.3, along with their respective references.

Reference	*b*-value
INPRES (1985)	0.9753
INPRES (1986)	0.7
Gil et al. (1982)	0.78
Gregori & Christiansen (2018)	1.01
This work	0.96 ± 0.06

Table 5.3: Comparison of b-values for crustal events in the Cuyo region available in literature, and the one calculated in the present work.

The comparison indicates that the estimated value aligns with two out of the four values reported in the literature. The observed discrepancies may be attributed to the limited data availability in earlier studies and the use of broader magnitude bins (around 0.5), which likely resulted in linear regressions more susceptible to bias.

5.2.2 Intraslab source

As previously mentioned, the earthquakes that take place in the Benioff zone at the latitude of Potrerillos could be influential for the seismic hazard of the dam site.

The location of intraslab earthquakes at the same latitude as the dam has hypocenters with depths between 60 and 200 km beneath the surface, making the sources of this type of event particularly difficult to characterize (Smalley & Isacks, 1987). The tools available for the definition of the geometry and seismicity of this source rely solely on references from literature and instrumental seismicity, as will be discussed in the following sections.

5.2.2.a Intraslab source geometry

Given that intraslab earthquakes can occur throughout the entire subducted plate, the actual extent of the seismic source corresponds to the full slab, from the subduction interface to the point where the slab melts into the mantle. However, modeling the entire slab in a site-specific PSHA is not practical. For this reason, a plane with 125 km on each side and centered on the dam site is adopted to represent the geometry of the intraslab seismic source (Fig. 5.9). The extent of the plane was chosen to fall within the range of site-to-source distances considered by the ground motion models, around 300 km (Abrahamson et al., 2016).

The plane is oriented to approximate as closely as possible the geometry of the Benioff zone, represented in Fig. 5.9 with the contours of the top of the subducted slab reproduced from those reported by Alvarado et al. (2009). In this way, the variation in depth of the intraslab earthquakes close to the eastern edge of the subducted slab is accurately reproduced.

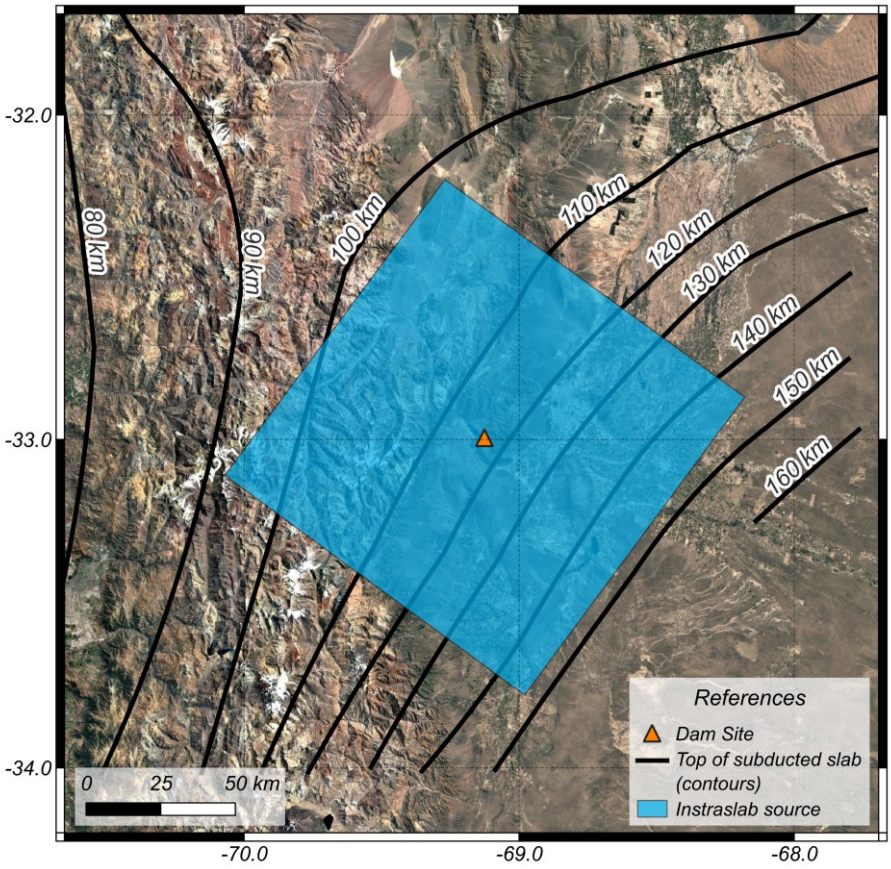


Fig. 5.9: Dam location, surface projection of the intraslab source, and the contours of the top of the subducted slab reproduced from those reported by Alvarado et al. (2009).

To confirm whether the proposed source is also related to the observed seismicity, Fig. 5.10 presents both in plan and cross-section the proposed plane source geometry along with the epicenters of the seismic events from the reviewed ISC catalog (ISC, 2022) occurring at depths greater than 60 km.

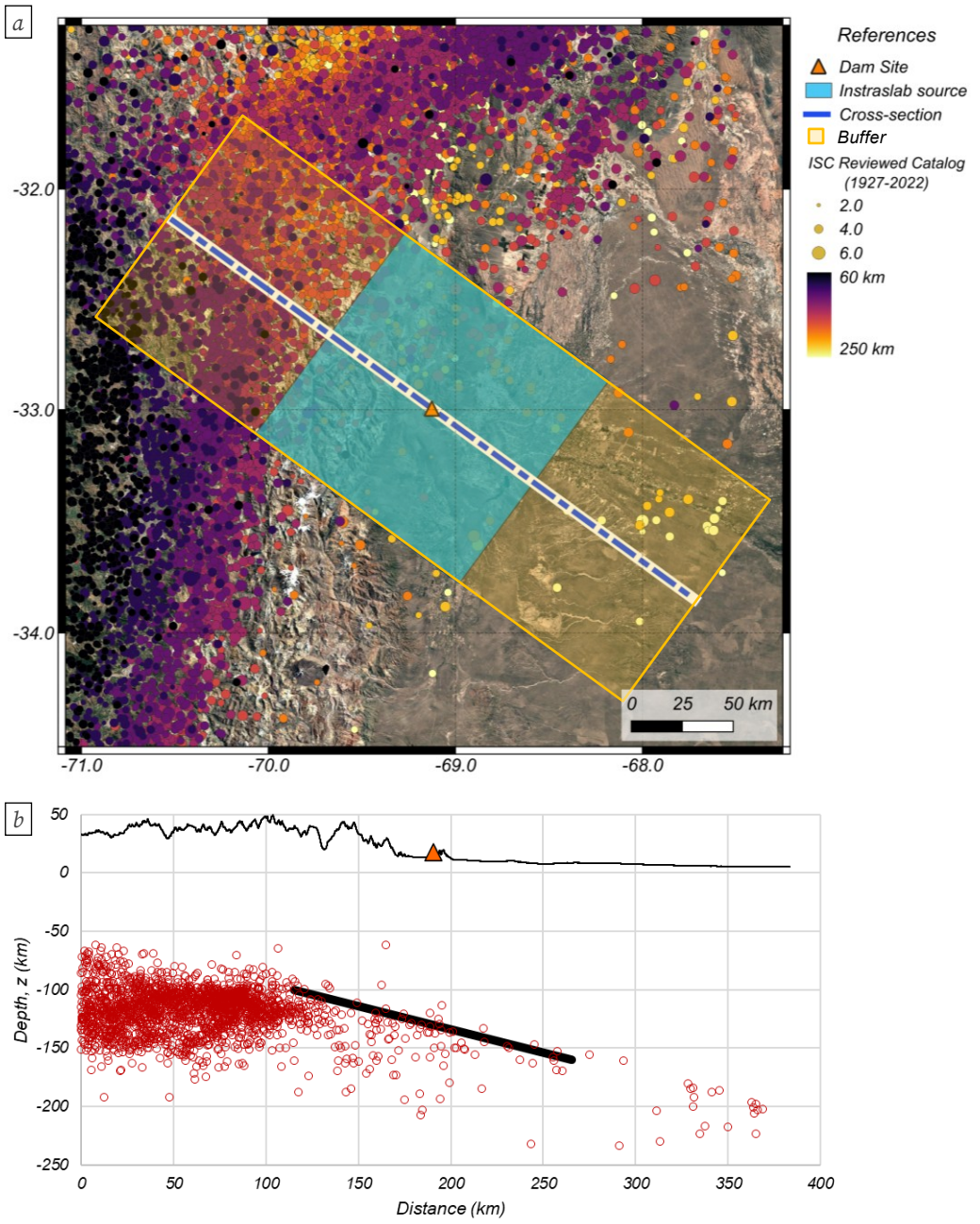


Fig. 5.10: a) plan view of the seismicity at the dam site for depths larger than 60 km (ISC, 2022), proposed intraslab source, profile, and the buffer considered for the cross-section; b) cross-section showing the topography (out of scale), dam site, seismicity and location of the intraslab source.

The proposed source geometry can be considered consistent with the seismicity enclosed within a buffer zone with the same width as the source. Furthermore, the purpose of positioning the source closer to the shallower hypocenters is motivated by the shorter source-to-site distances, which are likely to result in higher ground shaking at the dam site.

Nonetheless, the full range of earthquake depths will be covered in the PSHA calculations by contemplating multiple parallel planes along the thickness of the subducted slab.

It is worth noting that the proposed source geometry does not represent a single fault, as in the case of crustal sources, but rather an idealized representation intended for PSHA purposes. The assumption behind this approach is that earthquakes with different magnitudes can take place in any part of the plane, incorporating in this manner the uncertainty in the location of the actual faults.

Having established the geometry of the intraslab source, detailed in Table 5.4, it is necessary to identify the seismicity related to this segment of the subducted plate.

Coordinates (°)		Depth (km)
-70.07	-33.11	100.0
-69.27	-32.20	100.0
-68.18	-32.87	160.0
-68.98	-33.78	160.0

Table 5.4: Geometry of the intraslab source, based on the geometry of the subducted slab and seismicity.

5.2.2.b Intraslab source seismicity

The definition of the seismicity associated with the intraslab source, based on Poissonian assumptions, requires the fitting of a Gutenberg-Richter model to the magnitude-frequency distribution of seismic events. In this case, the Characteristic Model is not appropriate, as there is no clear identification of a specific fault.

The catalog used is again the reviewed catalog of the International Seismological Centre (ISC, 2022), covering the period from 1927 to 2022 and depths ranging from 60 to 250 km.

The spatiotemporal distribution of seismic events along the subducted plate is not uniform, and it would be incorrect to evaluate the seismicity of a region dominated by slab-pull events, where the source is located, using data from areas where different tectonic conditions prevail. For this reason, the seismic events used in the evaluation of the Gutenberg-Richter parameters are restricted to the region identified by the darker points in Fig. 5.11, where the events are believed to be a consequence of slab-pull mechanisms.

This area was defined by approximately following the 95-kilometer depth contour of the top of the subducted plate, which is slightly shallower than the minimum depth considered in the definition of the source geometry.

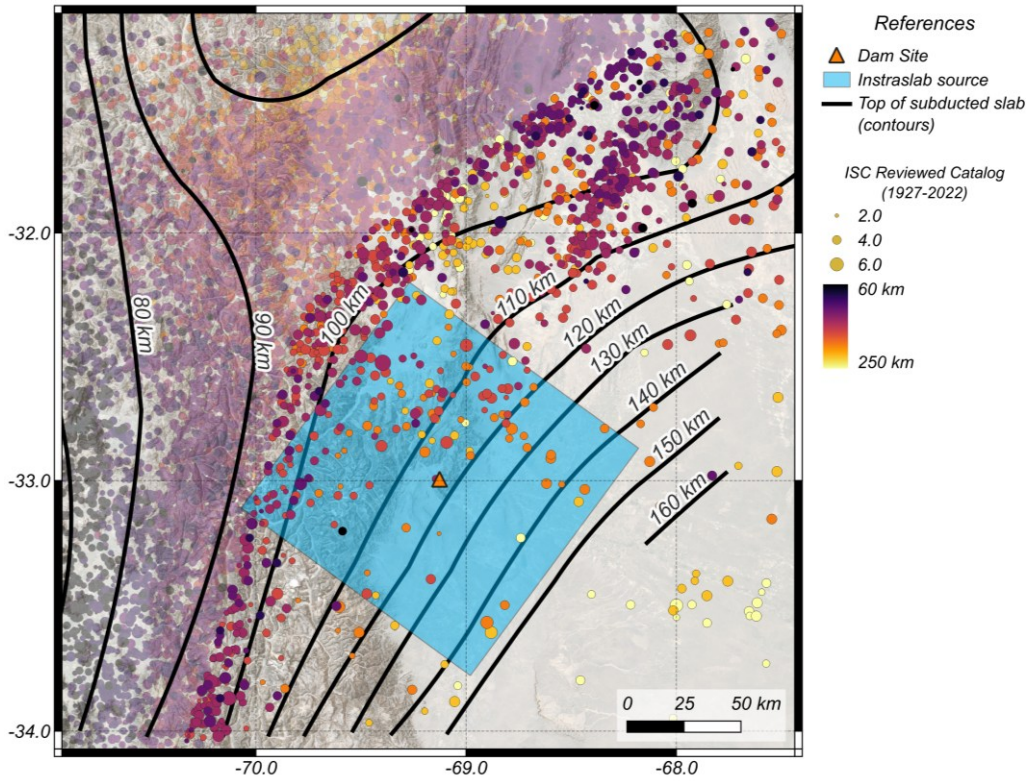


Fig. 5.11: Selected events from the reviewed ISC catalog of seismicity to calibrate the G-R for the intraslab source.

Using the ZMAP code once again, the catalog is declustered using the Reasenberg algorithm with standard parameters. To address issues related to catalog completeness, only events with magnitudes above the corner magnitude M_C are considered in the calculations. The estimated *a*-value and *b*-value of the Gutenberg–Richter distribution were then performed using the same approach applied to the crustal sources, selecting the best combination of M_C and *b*-value during the linear fitting process. The resulting adjusted model is presented together with the discrete and cumulative number of seismic events with $M>m$ in Fig. 5.12, adopting magnitude bins of 0.1.

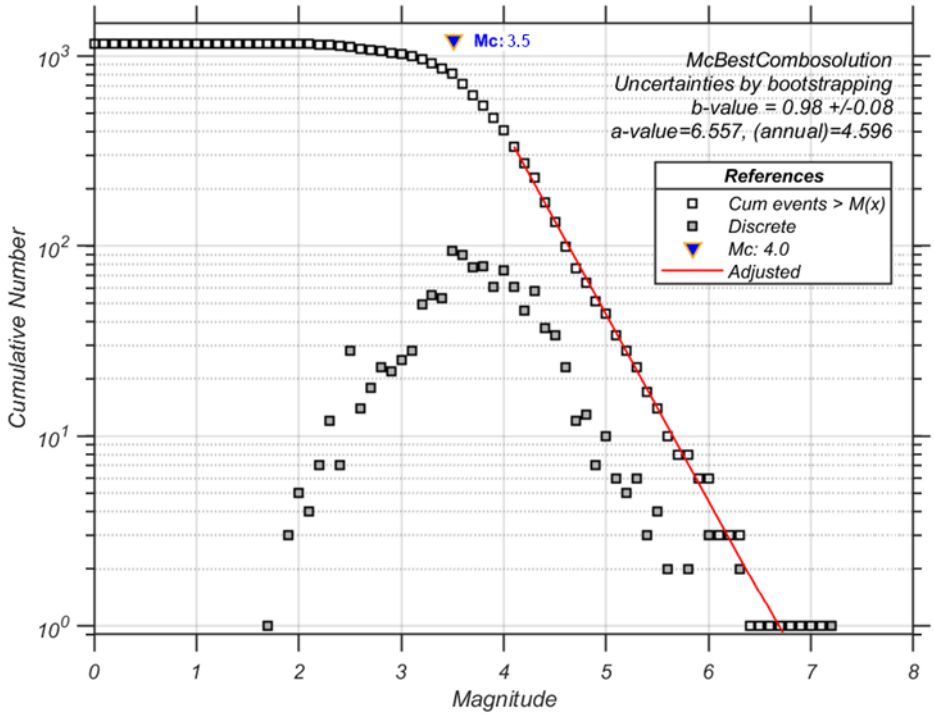


Fig. 5.12: Adjusted G-R model based on the best combination of b-value and Mc for intraslab events.

The adjusted *b*-value is compared with those available in literature in Table 5.5.

Reference	*b*-value
(Gil et al., 1982)	1.0
(Poulos et al., 2019)	0.98
This work	0.98 ± 0.08

Table 5.5: Comparison of b-values for intraslab events available in literature and the present work.

The proposed value is close to those in literature and can be considered reliable to be use in the PSHA calculations. Hence, having defined the geometry and seismicity of the seismic sources, it was possible to introduce them in the software and to carry out the probabilistic seismic hazard analysis.

5.3 PSHA calculations

As previously mentioned, the PSHA calculations will be performed using the freeware software R-CRISIS (Ordaz et al., 2017), which implements the conventional approach to evaluate the seismic hazard using the total probability theorem (Cornell, 1968). The steps necessary to carry out the analysis with R-CRISIS are:

- establish the dam site location and source geometry.
- define the seismicity of the sources.
- establish the ground motion models to be used.
- specify the global calculation parameters.

5.3.1 Site location and source geometry

The dam location is defined by its geographical coordinates (-32.99, -69.13), and to accurately calculate the site-to-source, a Digital Elevation Model (DEM) is uploaded to set the real elevation of the ground surface.

To define the geometry of the seismic sources, R-CRISIS offers several options depending on the spatial extension and characteristics of the source (point, line, area, etc.). For the study case, crustal sources (Fig. 5.5) will be defined using the Rectangular Fault source (Fig. 5.13a), which defines the geometry "as a fault" based on the coordinates of the fault trace, dipping angle, depth to the top of the seismogenic zone (Z_{TOR} in Fig. 2.5) and width of the fault.

The possibility of considering the source as a "Stirling fault" means that the geometry of the fault trace is replicated in the lower lip of the rupture area, and both are linked with straight segments to generate a corrugated surface that represents the fault (Fig. 5.13b). Instead, if this option is unticked, the fault is treated as a "Frankel fault" where the dip direction of each rectangle that conforms the fault is perpendicular to the strike of every individual segment (Fig. 5.13c) (Wei et al., 2025). The crustal sources in this work will be considered as "Stirling faults" as they are better suited for complex fault geometries.

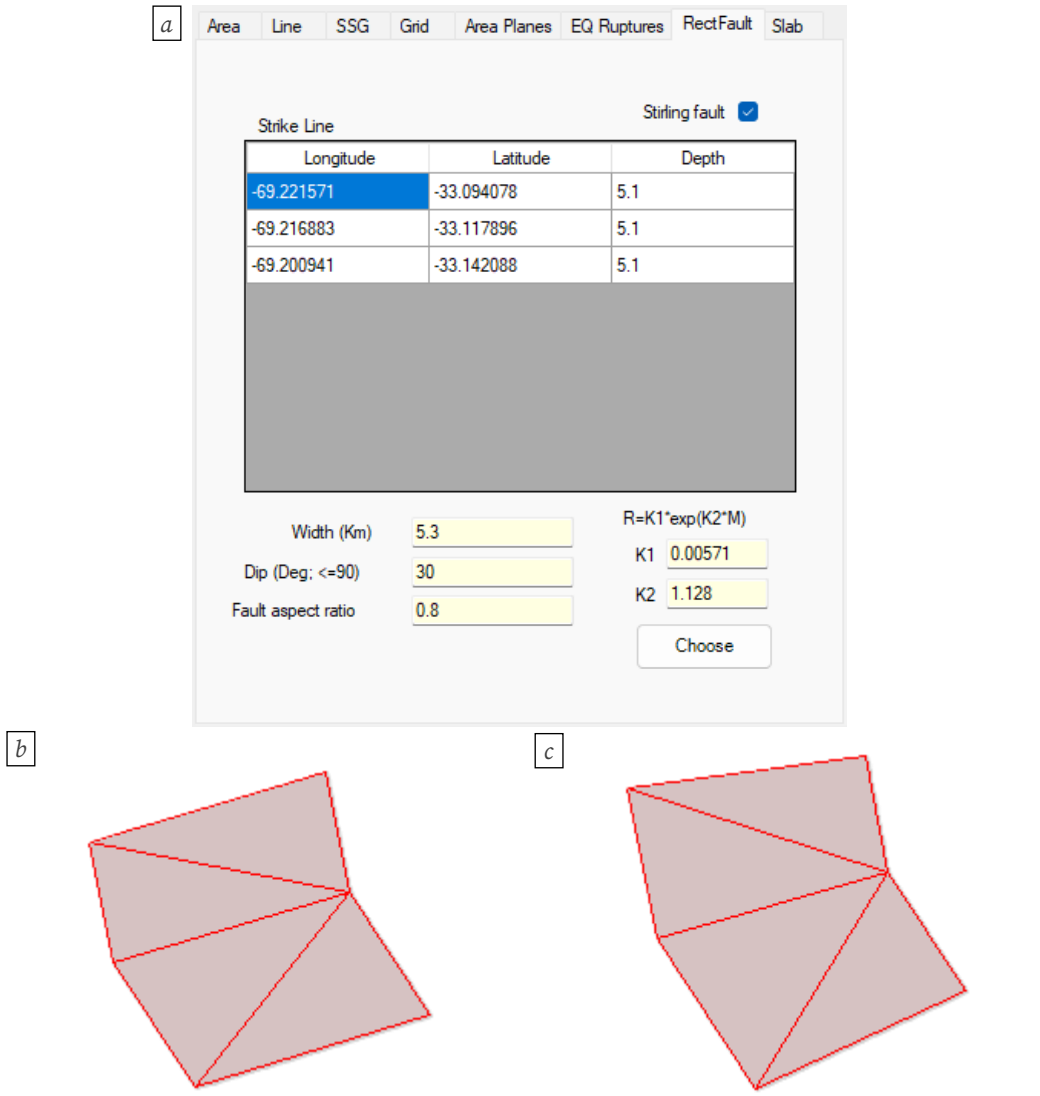


Fig. 5.13: a) the user interface of R-CRISIS to introduce the geometrical definition of the crustal sources and the option of considering the fault as b) Stirling fault, or c) Frankel fault. Case: El Totoral.

Two additional definitions related to the integration process must be established: the K1 and K2 parameters of the area–magnitude empirical relationships, which in this case correspond to the Wells & Coppersmith (1994) relation for reverse faults; and the fault aspect ratio, which governs the relationship between the dimensions of each rupture considered within the source typically ranging between 0.2 and 0.8.

The geometry of the intraslab source (Fig. 5.9) is set by using an Area source, that only needs the coordinates and depth of the four corners of the plane (Table 5.4), and to consider several parallel planes and reproduce better the seismicity of the subducted slab, an option is available

to set a total of three (3) parallel planes in a thickness of 10 km. The aspect ratio is set at 0.35, and the K1 and K2 factors follow the Wells & Coppersmith (1994) relation for normal faults.

5.3.2 Seismicity of the sources

For the definition of the seismic activity, as mentioned at the beginning of this section, the crustal sources will use a combination of the CM and G-R models, while for the intraslab sources, only the G-R model will be used.

To set the properties of the CM model for a particular fault (Fig. 5.14), it is necessary to know the magnitude of the characteristic earthquake, coincident with the MCE, and its expected variability (Table 5.1), in order to set minimum (M_0), maximum (M_U) and expected magnitude of the characteristic earthquake. The time rate of events is determined by the median value of years between characteristic earthquakes, adjusted to match the slip rate $\dot{s}$ ("S rate" in Fig. 5.14) with the average value estimated for the source (Table 5.2).

The slip rates are automatically computed by R-CRISIS following Eq. 5.2 based on the seismic moment rate $\dot{M}_0$ ("M rate" in Fig. 5.14) evaluated from the seismicity parameters, where μ is the crustal rigidity and A is the rupture area of the source.

$$\dot{M}_0 = \mu A \dot{s} \qquad \textit{Eq. 5.2}$$

Still looking at Fig. 5.14, the number of magnitudes defines the discretization of the magnitude interval over which the calculations are performed. The parameters F and T00 are not defined, as the time-dependent formulation of the expected magnitude is not considered in the analysis.

Setting the activity rate of a source based on average slip rates is appropriate under the assumption of a characteristic earthquake related to the source (Baker et al., 2021), an assumption also in agreement with the magnitude-frequency model adopted.

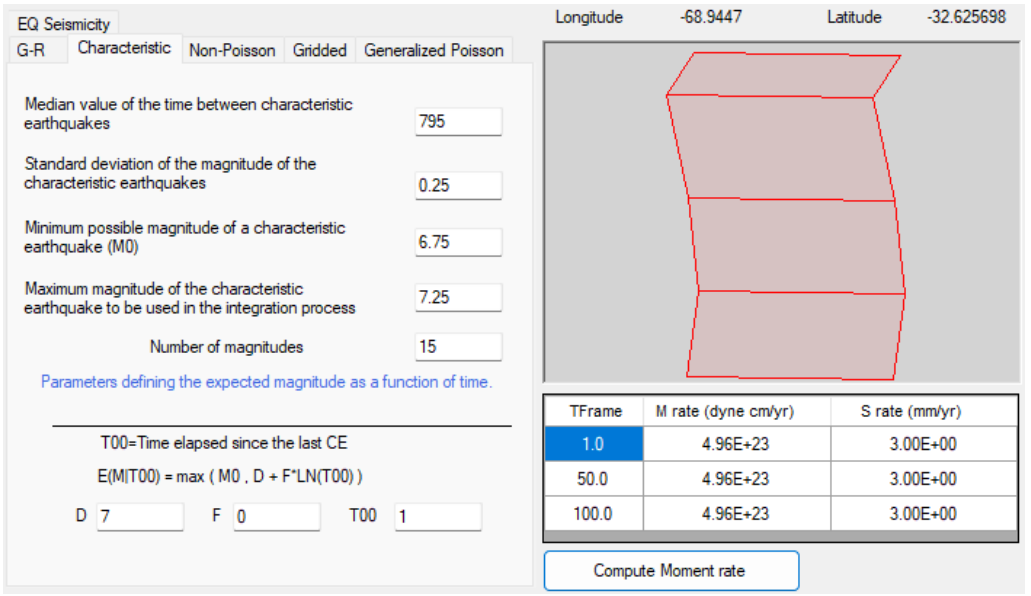


Fig. 5.14: User interface for the definition of the parameters of the Characteristic Model in R-CRISIS. Case: La Cal.

The variation of the Gutenberg-Richter model implemented in the software (Fig. 5.15) is the double-bounded established by Cornell & Vanmarcke (1969), defined in terms of the rate of earthquakes having the form of Eq. 5.3, with $\beta_{GR} = \ln(10)\, b$. Hence, it is precise not just to express the b-value in terms of β_{GR}, but also to define the maximum and minimum magnitudes.

$$f_M(m) = \frac{\beta_{GR} \cdot \exp\left(\beta_{GR}\left(m - M_0\right)\right)}{1 - \exp\left(\beta_{GR}\left(M_U - M_0\right)\right)} \qquad M_0 \le m \le M_U \qquad \textit{Eq. 5.3}$$

For crustal sources, the maximum magnitude expected value corresponds to the lowest magnitude considered in the Characteristic Model, that is, the minor magnitude expected for the characteristic earthquake. The minimum magnitude is instead defined as the lower one that still can produce any damage to civil structures, and for natural tectonic earthquakes, can be adopted as $M_{min} = 4.5$ (Bommer & Crowley, 2017).

The maximum magnitude for the intraslab source is set in coincidence with the largest historical earthquake related to the source, the 1927 M_W 7.0 earthquake (Loos, 1928), and adopting a feasible variability results $M_U = 7.0 \pm 0.2$. For the minimum magnitude is not possible to follow the principle used for crustal sources for a limitation in the ground motion model, reason why the minimum magnitude is set equal to the minimum usable magnitude of the GMM, $M_{min} = 5.0$ (Abrahamson et al., 2016).

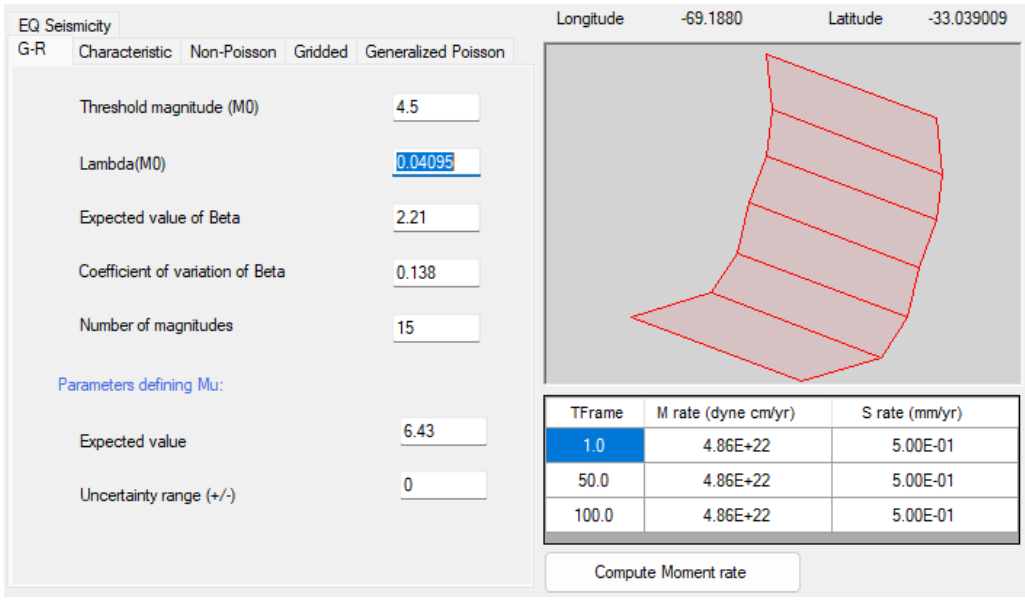


Fig. 5.15: Definition of the parameters of the G-R model in R-CRISIS. Case: SW Precordillera.

The *b*-value and its uncertainty, in Table 5.3 and Table 5.5 for crustal and intraslab sources, are introduced through the alternative G-R parameter β_{GR}, and the number of magnitudes is always the discretization considered for the interval of magnitudes.

Pertaining to the rate of earthquakes for the minimum magnitude $\lambda(M_0)$, the criteria adopted for the two types of sources differ as the approach followed for the definition of the seismicity and the available information differ for crustal and intraslab sources.

For crustal sources, the earthquake rate for the G-R part of the distribution is adjusted to produce a slip rate coincident with the average value presented in Table 5.2, as done for the CM part. The combined model using CM and G-R to estimate the annual rate of earthquakes is presented in Fig. 5.16 for a particular crustal source, exhibiting a shape similar to the literature example of Fig. 5.6.

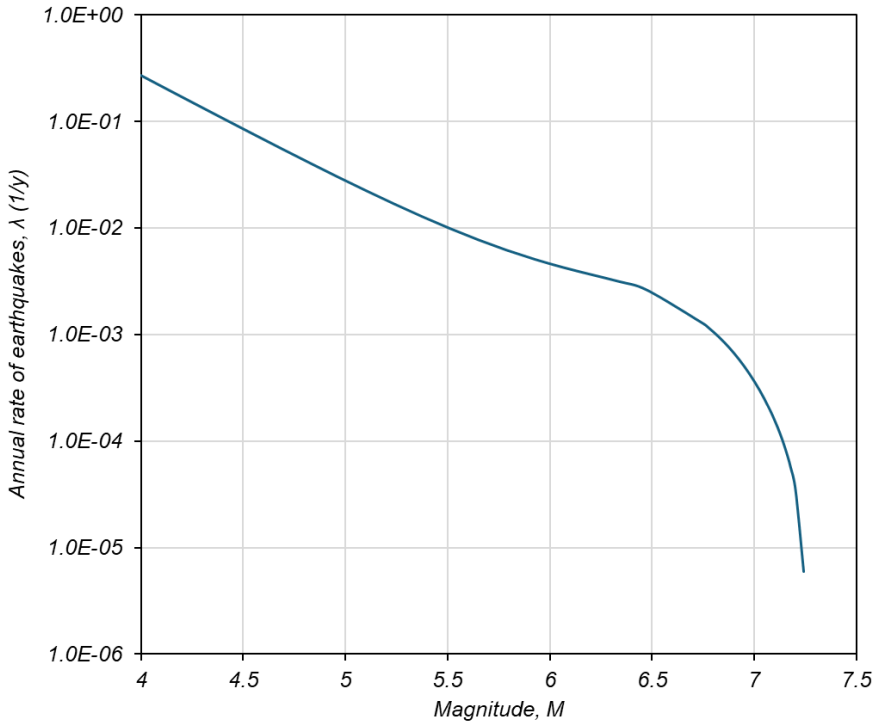


Fig. 5.16: Combined CM + G-R distribution used to define the seismicity of crustal sources. Case: La Cal.

The criteria for defining $\lambda(M_0)$ into the G-R model for the intraslab source are only based on seismicity, and can be approximated by applying logarithm rules to Eq. 5.1 to evaluate the mean annual number of earthquakes (Eq. 5.4), using the annual *a*-value from the G-R model shown in Fig. 5.12 and the corresponding *b*-value from Table 5.5.

$$\lambda\left(M_0\right) \cong 10^{a_{annual} - b\,M_0} \qquad \textit{Eq. 5.4}$$

The distribution for the rate of earthquakes of the intraslab sources is then presented in Fig. xx, exhibiting the usual shape of the double-bounded Gutenberg-Richter model.

Once the geometry and seismicity of the sources have been defined, the next step is to establish the relationship between the seismic scenarios and the expected ground shaking by means of the ground motion models.

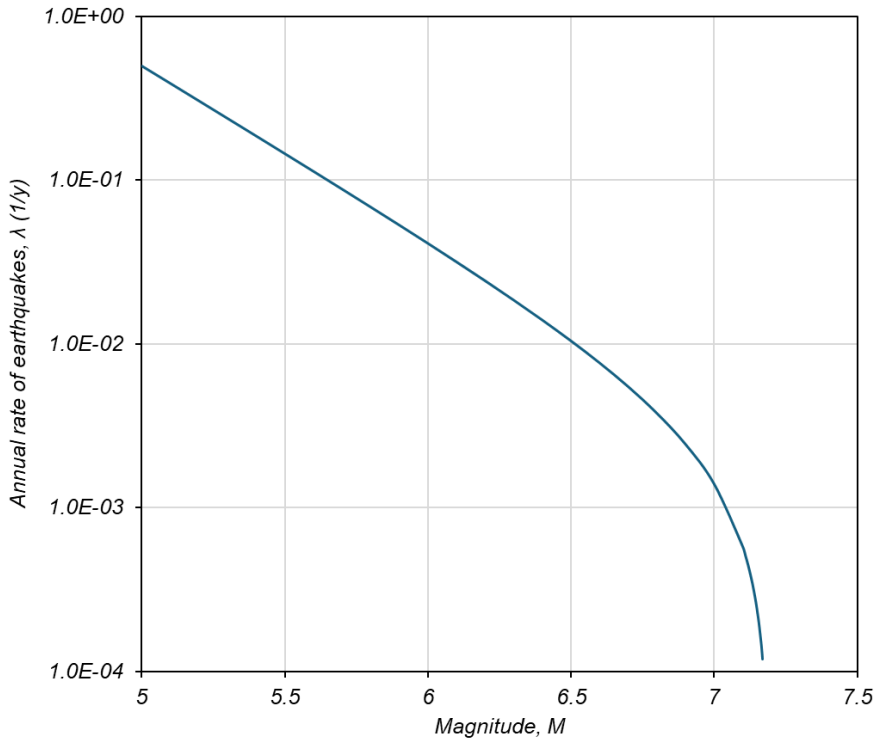


Fig. 5.17: G-R distribution used to define the seismicity of the intraslab source.

5.3.3 Ground motion models (GMM) utilized

The selection of ground motion models for each source type follows the recommendations made by Bommer et al. (2010) and Bommer & Stafford (2020), which advise that, in the absence of regional models, GMMs developed for seismotectonic environments similar to that of the site should be used. If several models meet this criterion, preference is given to those that are most widely recognized and thoroughly validated.

Due to the absence of modern ground motion models for crustal earthquakes in Western Argentina, mainly a consequence of the limited coverage of accelerometric networks and the lack of strong motion records, the GMMs adopted for crustal sources are those developed in the NGA West 2 project.

These models were based on a large dataset of earthquake records from events around the world and have been proven to bring reliable forecasts (Gregor et al., 2014). The selected models include:

- ASK14, by Abrahamson et al. (2014)
- BSSA14, by Boore et al. (2014)
- CB14, by Campbell & Bozorgnia (2014)
- CY14, by Chiou & Youngs (2014).

Although all these GMMs were calibrated using the same ground motion dataset, they are based on different assumptions and statistical approaches, which may result in variations in their predictions. To account for this variability, all models are incorporated into the calculations for each seismic source through a logic tree approach, as described in the following section.

For the intraslab earthquakes, the GMMs considered are two: the extensively used and validated BCH16 model developed by Abrahamson et al. (2016) for the Canadian BC Hydro, and the regional model based on Chilean records MBR17 from Montalva et al. (2017). Both models will also be considered in the logic tree to account for their variability. These models differentiate interface and intraslab events into their formulation, and only those parameters related to intraslab intermediate depth events will be considered in this application.

The site parameters to be introduced in the GMMs are set following the characteristics of the bedrock at the dam site, as the numerical model will include the modeling of the wave propagation through the soil beneath the dam. These parameters are set according to the evaluations of Section 3.3, defining a shear wave velocity of the bedrock Vs_{BR} = 1100.0 m/s.

Hence, the average shear wave velocity of the first 30 m is set equal to Vs_{30} = 1100.0 m/s, which is also the maximum available by most of the GMMs. The $Z_{1.0}$ and $Z_{2.5}$ parameters, used to represent basin effects and corresponding to the depth at which the shear wave velocity is respectively 1 km/s and 2.5 km/s, are set $Z_{1.0}$ = 0.0 km and $Z_{2.5}$ = 1.0 km, as these values are consistent with the absence of basin effects.

5.3.4 Global calculation parameters and Logic Tree Combination

The final step before running the PSHA involves defining global parameters that govern both the integration process and the outputs. The parameters related to the integration process are shown in the upper left corner of Fig. 5.18, where the selected maximum integration distance covers the source-to-site distance of all the sources, and the minimum triangle size and distance/triangle size ratio chosen generate a fit mesh and give results independent from the discretization.

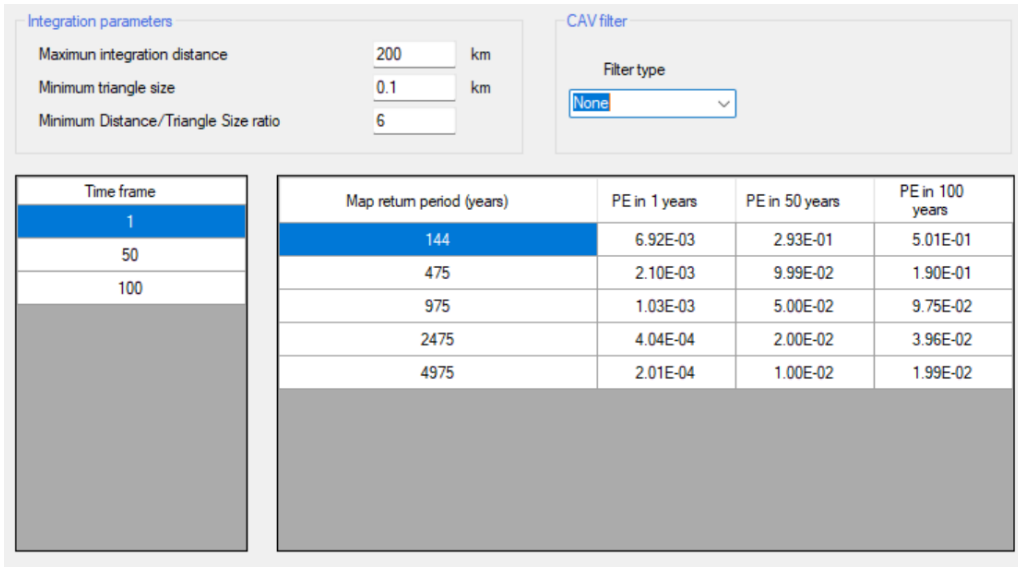


Fig. 5.18: Global parameters to be defined before carrying out the PSHA using R-CRISIS.

The time frames considered (1, 50, and 100 years) are functional for the definition of the outputs, as they can be related to annual rates and the time windows used by the diverse guidelines and standards to establish the return periods (Lee et al., 2025).

The chosen return periods (T_R) are related to different levels of seismic hazard, levels that will determine the stripes used for the derivation of fragility functions. Furthermore, these levels of hazard are related to different probabilities of exceedance in given time windows as presented in Table 5.6 and Fig. 5.18, and coincide with the levels contemplated in a few dam risk guidelines and seismic analysis standards (FERC, 2014; ICOLD, 2016a; USBR & USACE, 2019).

Return period (y)	Time window (y)	Probability of exceedance (%)
144	100	50.0
475	50	10.0
975	50	5.0
2475	50	2.0
4975	50	1.0

Table 5.6: Return periods, related time windows, and related probabilities of exceedance.

The T_R of 10000 years (or 9975) will be not initially considered as is reserved for dams which fail could lead to a large consequence in case of failure (ICOLD, 2016a), and its application in regions of high seismic activity may result in predictions that can exceed the worst scenario based estimates (Somerville et al., 2015).

As previously mentioned, a logic tree will be used to address the epistemic uncertainty (Bommer, 2005; Bommer & Scherbaum, 2008; Bommer, 2012). Two elements of the PSHA assessment are incorporated into the logic tree: the slip rate for crustal sources or the earthquake rate for intraslab sources as parameters that control the activity rate, and the GMMs.

The logic tree presented in Fig. 5.19 shows the weights considered for the two branches regarding the activity rate of the sources and the ground motion models. For the GMMs, there is no reason to consider any different weight for every option, so the distribution is uniform. In the case of the activity rates, a different criterion was considered.

For the activity of crustal faults, defined by their slip rates, a range ± 20 % was considered due to the uncertainties in estimating average slip rates based on geomorphology. An exception was made for the La Cal fault, for which the slip rate was determined through paleoseismological studies, allowing the uncertainty range to be reduced to ± 10 %. The assigned weights also consider that slip rates estimated from geomorphological features tend to be conservative, being more likely that the actual slip rate is exceeded rather than not exceeded.

The variation in the rate of earthquakes for the minimum magnitude $\lambda(M_0)$ of the intraslab source was considered with a variation of ± 10 %, considering that the input parameters used were based on the current seismicity of the source.

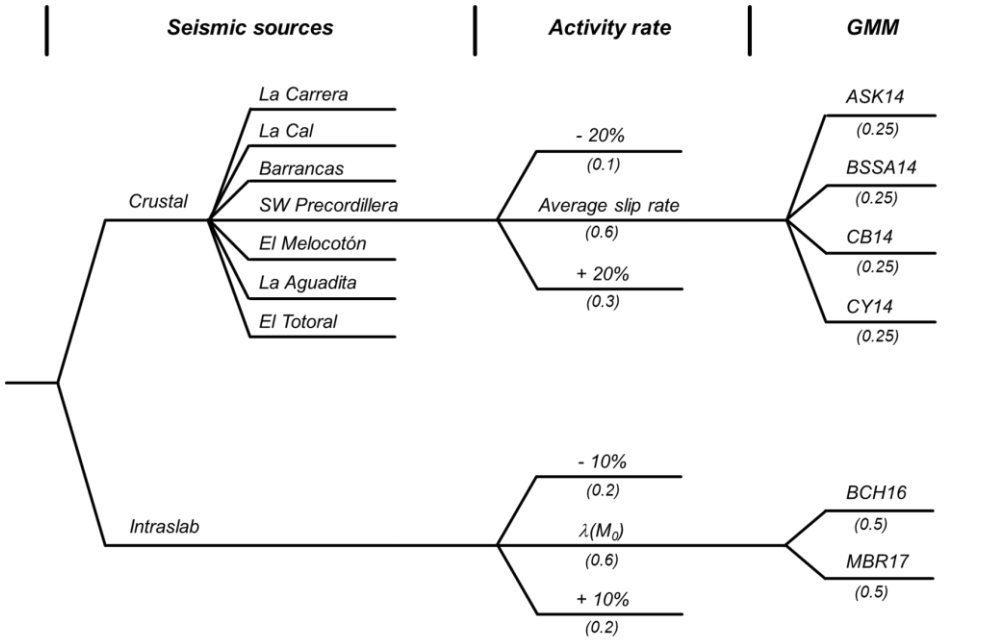


Fig. 5.19: Logic tree combination for the PSHA, considering the variability of activity rates and GMMs.

5.4 Seismic hazard results

The results of the probabilistic seismic hazard analysis are presented in terms of hazard curves, uniform hazard spectra (UHSs), and disaggregation charts, as the regular practice mentioned in Section 2.3.

The hazard curves for PGA in Fig. 5.20 correspond to those related to every individual seismic source and their combination. This figure presents a clear overview of the seismic hazard at the dam site, where the closer sources (SW Precordillera and El Melocotón) and the more active one (La Cal) are the most influential in the seismic hazard at all the return periods considered.

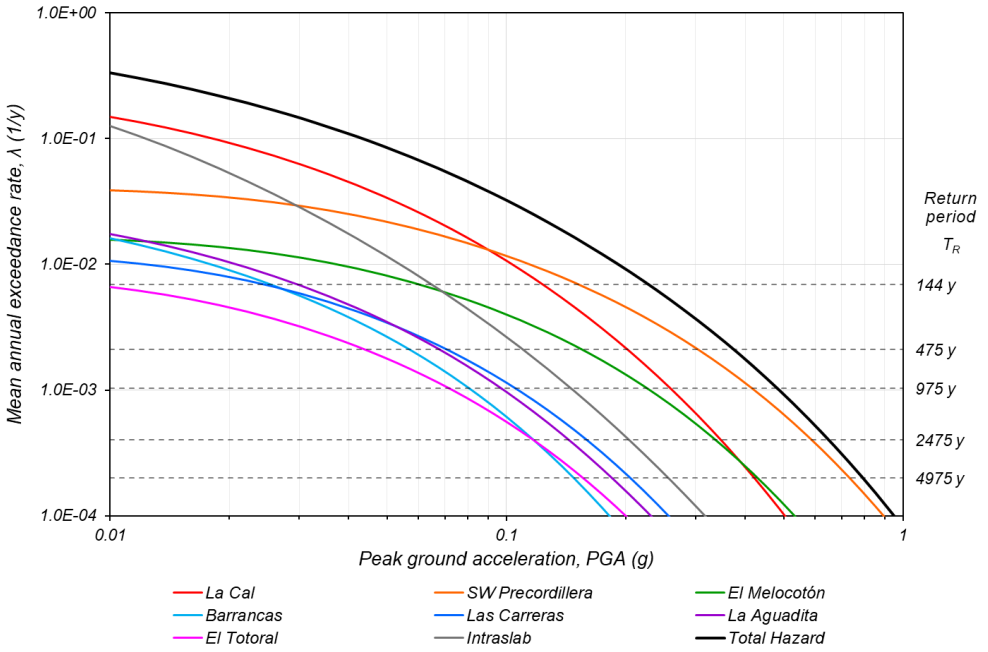


Fig. 5.20: Hazard curves for crustal sources, intraslab source, and their combination (Total hazard), highlighting the annual rate of exceedance in correspondence to the established return periods.

The intraslab source has some influence on low return periods due to its significant seismic activity at moderate magnitudes. However, the large source-to-site distances associated with depths over 90 km reduce their contribution at most of the other return periods.

The remaining sources, either because of their source-to-site distance or because of low seismic activity, contribute less to the seismic hazard of the dam than the previously mentioned sources.

The Uniform Hazard Spectra (UHSs) for the five selected return periods are presented in Fig. 5.21. The different hazard levels associated with each return period are distinguishable across the different spectra, and this even distribution will support the evaluation of fragility functions by MSA as the intensity measure levels of each stripe are uniformly distributed across the range of feasible ground motion amplitudes. The UHSs will be used to set the hazard level when scaling the ground motions used for dynamic analyses.

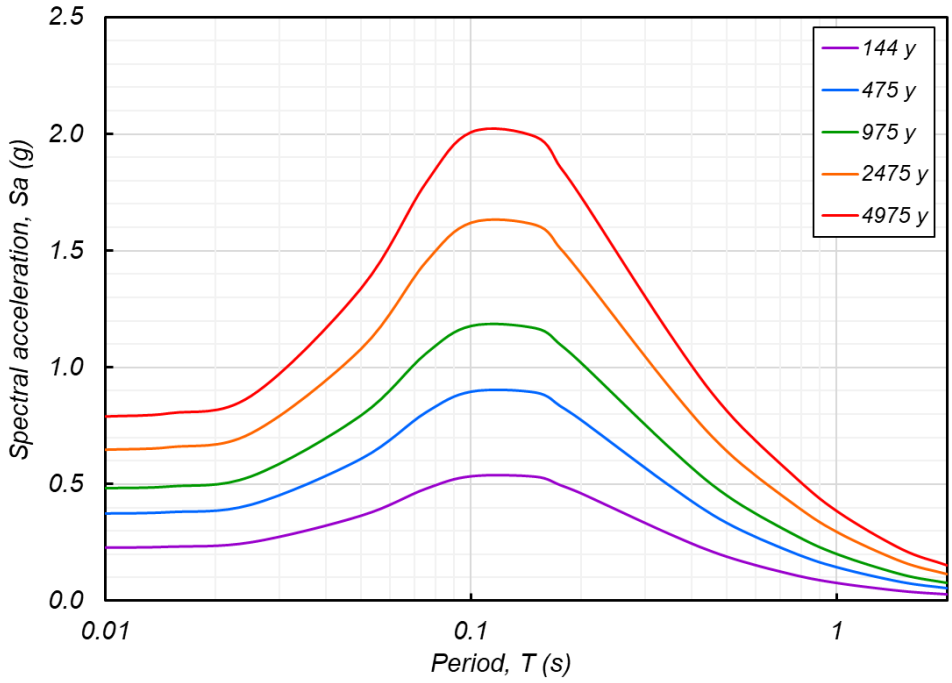


Fig. 5.21: Uniform hazard spectra for the five selected return periods: 144, 475, 975, 2475, and 4975 y.

Finally, the disaggregation chart for *Sa(0.5s)* and T_R = 2475 y is presented in Fig. 5.22.

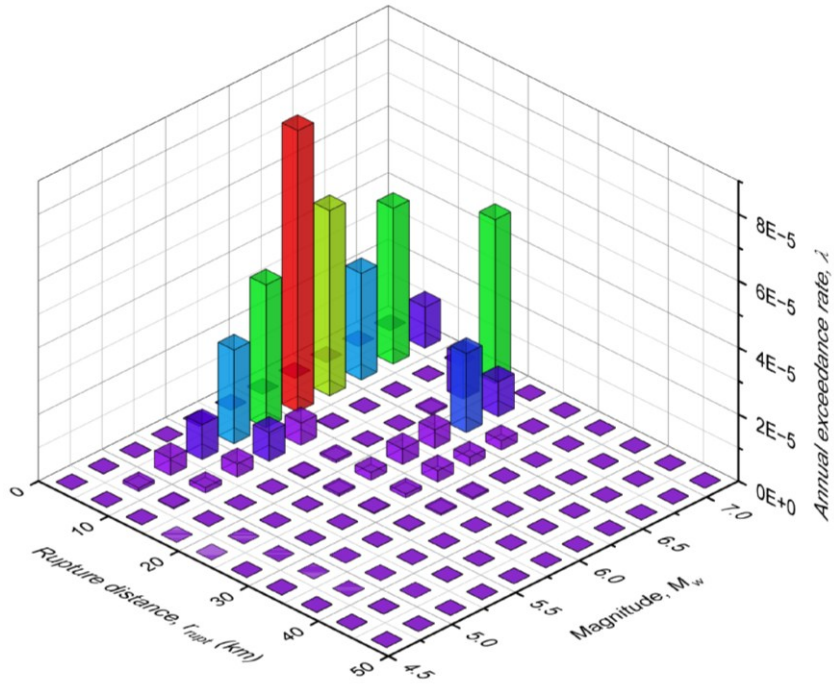


Fig. 5.22: Disaggregation chart for Sa(0.5s) and T_R 2475 y. Can be observed the influence on the seismic hazard of two types of sources characterized by different magnitudes and distances.

It is noteworthy that, for this particular case, even when the mean causal magnitudes and distances contributing most significantly to the seismic hazard are associated with the closer sources, there is a second group of seismic scenarios of larger but more distant events that also contribute to the hazard. This particular aspect will be considered during the record selection.

Other results from the PSHA will be presented in Appendix II, in particular the hazard curves for *Sa(0.5s)* and *Sa(1.0s)*, the table of values of the UHSs, and the disaggregation charts for different *IM* and T_R.

5.5 Selecting and adjusting earthquake ground motions

The input motions considered for the nonlinear dynamic analysis will come from the selection and adjustment of records from real earthquakes, as they correspond to a more accurate description of the ground shaking than artificial or synthetic records (Bommer & Acevedo, 2004). To achieve hazard consistency at the site of interest, the selected ground motion records should, at least, align with the seismic scenarios and the expected levels of ground shaking forecasted in the PSHA.

The seismic scenarios identified by the PSHA can be represented through disaggregation charts, which indicate the mean causal magnitudes and distances that contribute most significantly to a given hazard level. When combined with the expected faulting mechanism, this information provides a reference framework for selecting ground motion records from available databases, ensuring that the chosen records reflect the magnitude, distance, and faulting characteristics that control the seismic hazard at the site.

Several methods can be used to scale ground motions, as discussed in Section 2.3. In this case, linear scaling in the time domain is applied to match the spectral acceleration at the fundamental period of the dam $Sa(T_1)$ of each selected ground motion, with the corresponding value from the UHS.

Conditioning the scaling to a single structural period addresses the main limitation of using the UHS as a reference spectrum for ground motion selection and yields results that are only slightly more conservative than those obtained using more sophisticated methodologies (Baker et al., 2021).

This limitation arises from the fact that the UHS represents an envelope of contributions from multiple magnitude and distance scenarios (Bommer et al., 2000), something evident if

a comparison among disaggregation charts of *Sa(T)* at two different periods is made. Hence, if the match is performed over a range of periods instead of a single period, it implicitly assumes that the maximum response from various seismic scenarios occurs simultaneously within a single ground motion, which may lead to overly conservative or physically unrealistic inputs (Baker, 2011).

The ground motion selection and scaling are then carried out using the search engine of the database of the NGA West 2 project (Ancheta et al., 2014), introducing the information of the seismic scenarios, site conditions, scaling method, and component of the record considered (Fig. 5.23). The records are labeled in the database using a Record Sequence Number (RSN), nomenclature that will be combined with the name of the respective component considered (H1 or H2), and the return period for better identification of every ground motion.

The seismic scenarios are set by defining the fault type, reverse/reverse-oblique, as the most influential sources are only crustal, and the range of magnitude and distance will vary for every return period based on their particular disaggregation distribution.

Site conditions must be defined in terms of Vs_{30} and should approximate bedrock conditions. However, restricting the search to records from stations with Vs_{30} greater than 1100 m/s could significantly reduce the number of available records. For this reason, the threshold was relaxed to Vs_{30} > 600 m/s, as the influence of site response at these shear wave velocities can be considered still moderate. This compromise is justified by the need for a large number of ground motions to develop fragility functions.

The selected horizontal components of the ground motion are then scaled to match, with their respective spectral acceleration at the fundamental period of the dam, $Sa(T_1)$, the reference value of the UHS at the same period. The fundamental period of the dam was already established by the analysis of monitoring records in T_1 = 0.5 s (Section 3.4.3).

To keep the scaling factors in a reasonable range and avoid problems, they were limited to the range between 0.3-3.0 for all the return periods except T_R 4975, where it was extended to 0.2 - 4.0, limits still tolerable for a careful record selection (Watson-Lamprey & Abrahamson, 2006; Luco & Bazzurro, 2007).

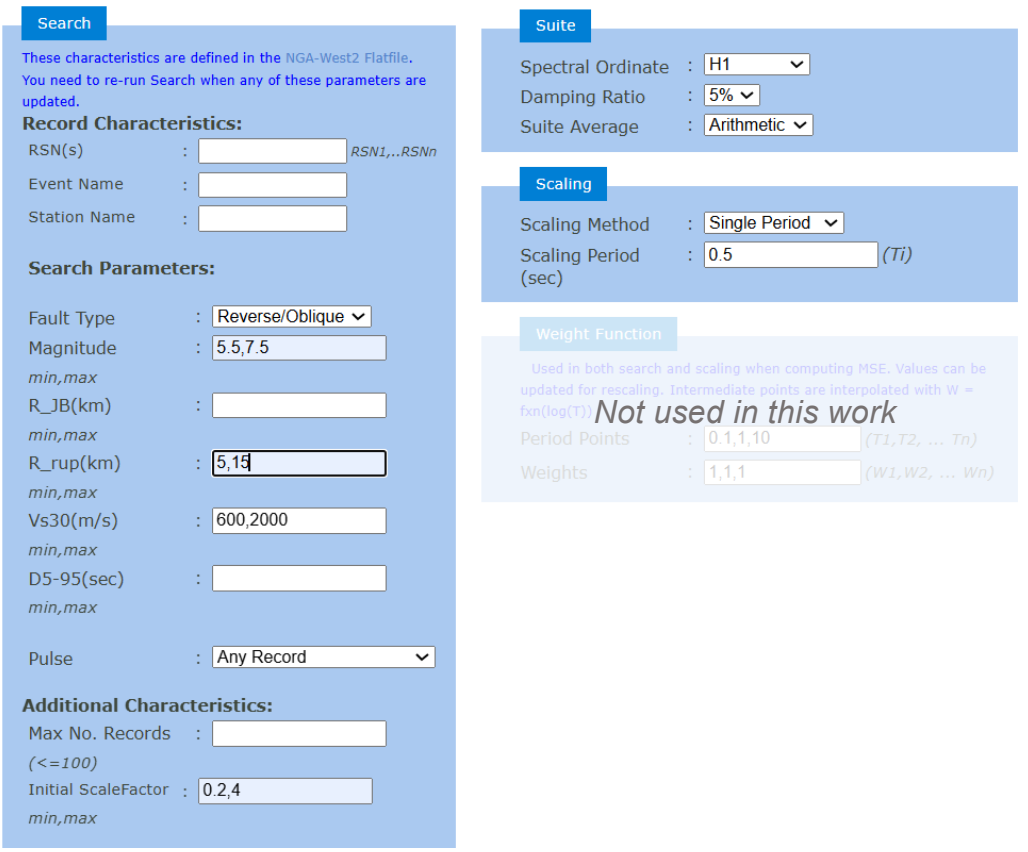


Fig. 5.23: Searching engine of the database of the NGA West 2 project, with three well-defined sections for defining the parameters for searching records, selecting the component, and scaling. The shaded portion corresponds to the definition of a multi-period scaling not used in this work.

A total of 10 ground motions were selected for every return period. The response spectra corresponding to the return period T_R = 2475 y are given in Fig. 5.24 as an example of the results of the record selection process. Moreover, the scale factors and the event and site characteristics of each record are presented in Table 5.7, while Table 5.8 compiles a few selected intensity measures of the scaled ground motions.

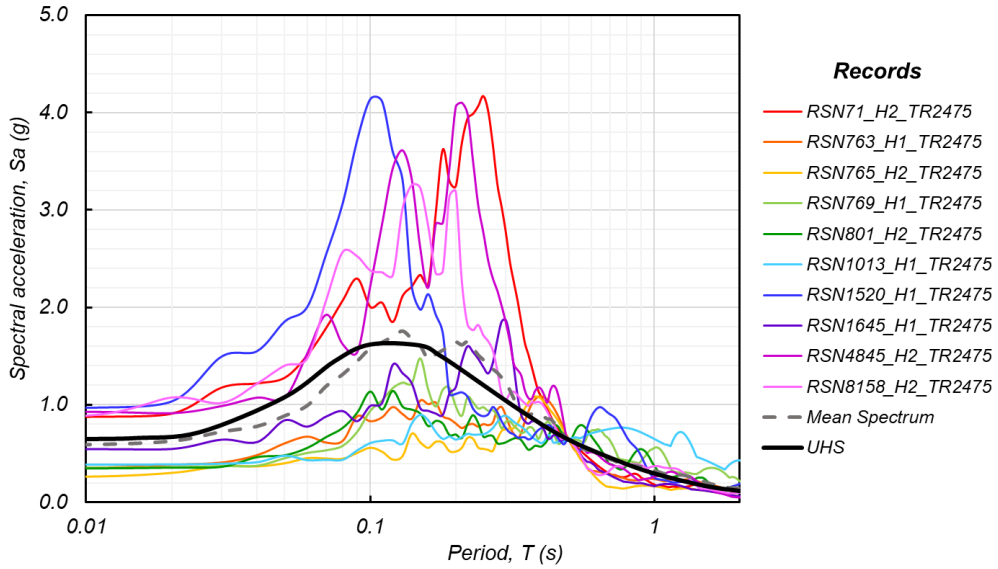


Fig. 5.24: Response spectra for the records selected and scaled for T_R = 2475 y, together with their mean spectrum and respective UHS.

Record Name	Seismic event	Year	Mechanism	M (M_W)	r_{rupt} (km)	Vs_{30}	Scale factor
RSN71_ H2_2475	San Fernando US	1971	Reverse	6.61	19.3	602	0.97
RSN763_ H1_2475	Loma Prieta US	1989	Reverse Oblique	6.93	10.0	730	0.90
RSN765_ H2_2475	Loma Prieta US	1989	Reverse Oblique	6.93	9.6	1428	1.94
RSN769_ H1_2475	Loma Prieta US	1989	Reverse Oblique	6.93	18.3	663	2.80
RSN801_ H2_2475	Loma Prieta US	1989	Reverse Oblique	6.93	14.7	672	0.53
RSN1013_ H1_2475	Northridge US	1994	Reverse	6.69	5.9	629	1.34
RSN1520_ H1_2475	Chi-Chi Taiwan	1999	Reverse Oblique	7.62	18.2	665	0.92
RSN1645_ H1_2475	Sierra Madre US	1991	Reverse	5.61	10.4	680	3.00
RSN4845_ H2_2475	Chuetsu-oki Japan	2007	Reverse	6.80	22.5	610	1.48
RSN8158_ H2_2475	Christchurch New Zealand	2011	Reverse Oblique	6.20	6.1	650	1.84

Table 5.7: Event and site characteristics, and the scaling factor for the records corresponding to the return period T_R = 2475 y.

Record	RSN_71_H2_2475	RSN_763_H1_2475	RSN_765_H2_2475	RSN_769_H1_2475	RSN_801_H2_2475	RSN_1013_H1_2475	RSN_1520_H1_2475	RSN_1645_H1_2475	RSN_4845_H2_2475	RSN_8158_H2_2475
PGA (g)	0.86	0.35	0.26	0.35	0.35	0.38	0.99	0.54	0.90	0.87
PGV (cm/s)	38.3	30.2	17.3	36.6	28.8	67.4	38.4	26.3	30.9	38.0
PGD (cm)	6.6	10.6	8.3	14.2	12.5	17.2	24.9	3.4	7.6	10.7
I_A (m/s)	0.856	1.428	1.552	1.769	0.480	1.785	4.823	7.368	6.219	8.944
CAV (m/s)	5.72	7.97	6.29	11.25	3.93	11.69	11.38	19.69	15.57	25.20
I_H (cm)	104.1	88.7	61.5	147.4	102.5	222.0	126.3	66.7	94.2	100.8
T_P (s)	0.24	0.40	0.38	0.14	0.12	0.30	0.10	0.30	0.20	0.14
$D_{5\text{-}95}$ (s)	12.0	5.0	3.7	13.0	10.1	6.5	9.2	3.2	4.1	3.9

Table 5.8: Selected intensity measures of the scaled ground motions, for T_R = 2475 y.

The last aspect considered in the record selection is related to the vertical input motions, which can be not only significant in the case of thrust faults (Harada et al., 2012) but also influential in the seismic response of embankment dams. The procedures available for scaling vertical ground motions are: include a GMM for vertical ground motions (Gülerce et al., 2017) into the PSHA, or use a vertical-to-horizontal ratio (V/H) model (Bozorgnia & Campbell, 2016) to obtain a spectrum of vertical acceleration and then carry out an independent scaling for the vertical component; or a simpler approach that preserves the amplitude proportions of the recorded ground motion components just scaling the vertical component with the same factor used for the horizontal component.

Even though this latter approach does not explicitly account for the characteristics of the seismic sources and cannot be considered fully consistent with the seismic hazard, it preserves the ratio among components of ground motions associated with seismic scenarios contemplated by the disaggregation. Combined with its simplicity, this justified its adoption in the present work.

The figures with the spectra of scaled ground motions and tables with record information and intensity measures for the remaining return periods are included in Appendix II.

6. Numerical model definition

For the evaluation of the seismic response of the dam, an numerical model will be developed using the finite difference software FLAC2D 9.0 (Itasca Consulting Group, Inc., 2023), based on the information provided in Chapter 3, and following some of the recommendations from Boulanger & Beaty, (2016) and Boulanger & Ziotopoulou, (2018). The assumptions adopted in the construction of the model will aim not only to represent the dam response but also to avoid unnecessary complexity, considering the large number of analyses required to derive the fragility functions. For this last reason, the possibility of using 3D models was declined.

6.1 Geometry for numerical analysis

Given the complex shape of the foundation bedrock and the decision to evaluate the dam response through 2D analysis, the selection of the cross section to be modeled must consider not only the expected worst-case conditions in terms of seismic response, but also the representativeness of the section concerning the overall geometry and behavior of the dam. Fig. 6.1 shows the central cross-sections with respect to the labeling considered for the distribution of the instruments of the monitoring system.

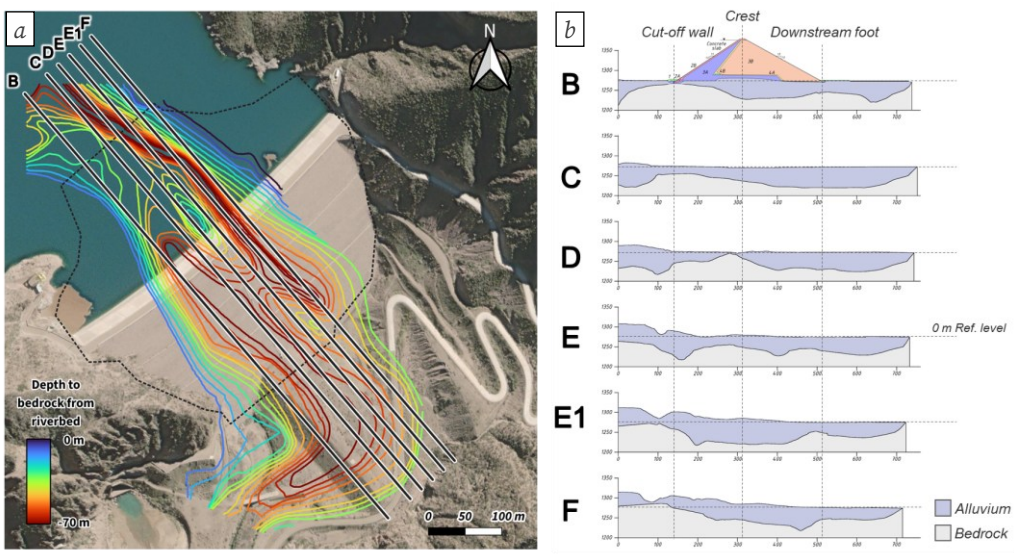


Fig. 6.1: Plan view and central cross sections of the dam, evidencing the variability in geometry of the bedrock.

The variation of geometry among all sections is evident, but can still be grouped with respect to their overall shape in the sections of the right margin (B, C, and D), and left margin (E, E1, and F). In the left margin group, the deepest part of the alluvium is located in cross-section near the dam axis with a tendency toward the upstream side, following the contours of alluvium thickness. This deeper portion of the alluvium is constrained within a narrow valley, which may have limited influence on the response, as the loads from the upper part of the alluvium are expected to transfer primarily toward the bedrock rather than propagating deeper into the alluvium, a response already evidenced in terms of long term permanent settlements (refer to Fig. 3.47).

The group of the right margin instead shows the deeper portion of the alluvial soils towards downstream, and also a wider valley in which it is possible that the whole thickness of the alluvium could be influenced by the loads coming from the dam. This last is evidenced in the largest settlements evaluated by topography in coincidence with Section C (refer to Fig. 3.47). This condition also represents a big portion of the dam center, where the tallest sections are present.

Hence, Section C is then the one selected to follow the analyses, as it is the one that presents the deeper portion of the alluvium, up to almost 70 m beneath the riverbed, and was also the one considered as well for the design of the dam (Barchiesi et al., 2006). In addition, this section contains the accelerometric stations and is located close to the section containing the settlement gauges (Section D), providing two additional reasons to select it, as the parameters derived from the analysis of monitoring records are representative of the response at this specific location.

The numerical model representing the selected section is shown in Fig. 6.2, where each color corresponds to a different block which represents a portion of the soil that due to differences in material properties, or in the case of the dam body due to the representation of construction stages, was divided to be considered divide from the surrounding ones for modeling purposes. The left extreme of the model was reconstructed to respect the outcropping of the bedrock, as the contours of Fig. 6.1 do not reach where the rock outcrops again at the surface.

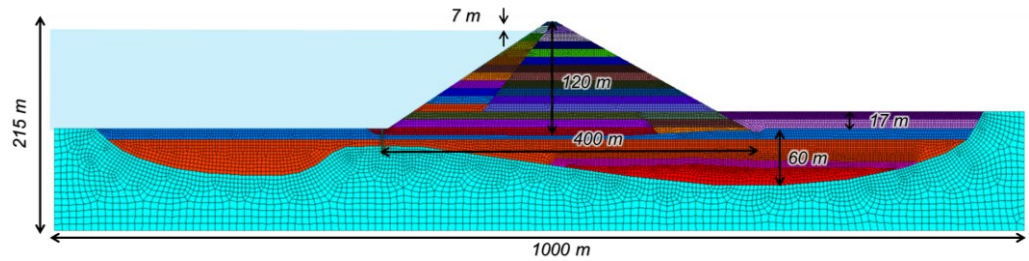


Fig. 6.2: Model of the dam representing Section C, with the identification of the principal dimensions and the color scheme identifying different blocks of the model.

Next, and based on the shear wave velocities obtained from geophysical surveys or estimated from seismic monitoring data, the discretization of the mesh will follow as much as possible the criterion of Kuhlemeyer & Lysmer (1973), contained as well in the manual of FLAC2D, which define the minimum size of the elements of a numerical model in terms of the wavelength fraction that accurately capture the propagation of seismic waves across the continuum media, as presented in Eq. 6.1.

$$\Delta l = \frac{\lambda}{10} = \frac{\mathrm{Vs}}{10 \cdot f_{\max}} \qquad \textit{Eq. 6.1}$$

Where λ stands for the wavelength, Vs is the shear wave velocity of each soil, and $f_{\max}$ is the maximum frequency that is wanted to be captured during the analysis. For applications in geotechnical earthquake engineering, this frequency can be considered around 20 Hz for soil sites, as suggested by Rathje et al. (1998). The fraction of 1/10 of the wavelength is suggested for finite difference by Itasca, when the original work of Kuhlemeyer & Lysmer (1973) suggests 1/6 to 1/8 for finite elements.

By setting a minimum length within the boundaries of each block and manually reviewing conflict areas with poorly conditioned elements, the final mesh was generated. To assess mesh quality, FLAC2D 9.0 provides a tool that evaluates each zone based on four criteria, each rated from 0.0 (poor) to 1.0 (excellent). The lowest score among the four criteria determines the Zone Condition. These criteria quantify how much each element deviates from an ideal square shape, since square elements are better conditioned for the finite difference calculation scheme. The four criteria are:

- Aspect ratio: The ratio between the shortest and the longest edge length.
- 2D shape quality: Establish a relationship between area, perimeter, and maximum length of every triangular zone.

- Orthogonality: Measures of how "well" sides of the zones are inclined to each other, penalizing those elements that tend to be a parallelogram.
- Area Ratio: Ratio of the smallest internal triangular subzone and the averaged triangle in the zone, for unstructured meshes.

The section of the dam with the contours of the Zone condition is presented in Fig. 6.3, evidencing an overall good quality of the mesh.

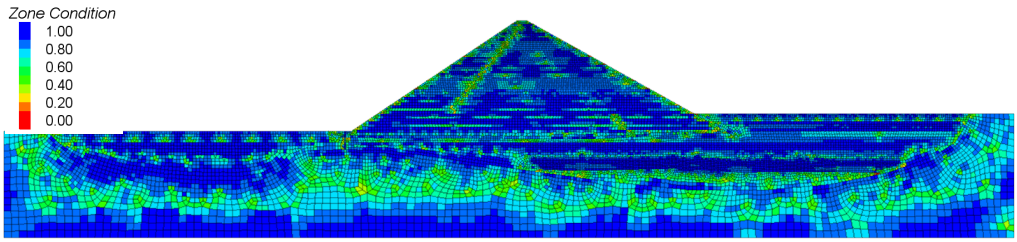


Fig. 6.3: Contours of the zone condition of each element, showing an average good quality of the mesh.

Having defined the mesh, it is time to present the constitutive models considered for every geomaterial present in the dam model, and their further calibration of parameters.

6.2 Selection and calibration of soil constitutive models

The selection of the constitutive models considered in the analysis was focused on the expected response of the soils and the availability of information for their calibration. The constitutive models chosen for every geomaterial and stage, following the color scheme of Fig. 6.4, are presented in Table 6.1.

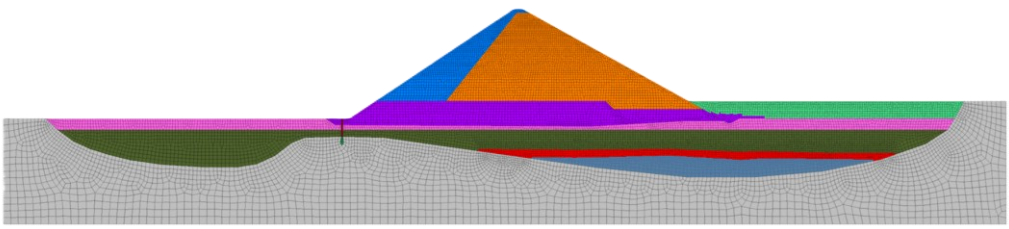


Fig. 6.4: Color scheme to differentiate among different soils considered in the numerical analyses.

Geomaterials		Constitutive model	
Material	Code	Static phase	Dynamic phase
Granite bedrock	BR	Mohr-Coulomb	Elastic
Embankment sand-gravel mixture	3A	Plastic Hardening	UBCHyst
Embankment sand-gravel mixture w/boulders	3B	Plastic Hardening	UBCHyst
Alluvial sand-gravel mixture - Surface	AL_S	Plastic Hardening	PM4Sand
Alluvial sand-gravel mixture - Coarse	AL_C	Plastic Hardening	PM4Sand
Alluvial sand-gravel mixture - Deep	AL_D	Plastic Hardening	PM4Sand
Alluvial sand/silt potentially liquefiable	AL_L	Plastic Hardening	PM4Sand
Saturated part of 3A/3B/SE	3_AS	Plastic Hardening	PM4Sand
Stabilizing embankment – Same as 3A	SE	Plastic Hardening	UBCHyst
Cut-off wall - Concrete	COW	Mohr-Coulomb	Elastic
Grout curtain beneath the cut-off wall	GC	Mohr-Coulomb	Elastic
Reinforced concrete slab and floating plinth	RCS	Elastic	Elastic

Table 6.1: Constitutive models considered for every soil and stage, and the code to distinguish them.

This selection is the consequence of an important work searching for the models that better achieve the expected response of all the soils. A description of the calibration and final parameters adopted for every soil will be detailed below.

6.2.1 Static phase

The calibration of the material models involved in the static phase is supported by a combination of the soil properties identified in Section 3.3 and a few parameters derived from the evaluation of the monitoring records in Section 3.4.

6.2.1.a BR, GC, and COW – Mohr-Coulomb model

Traditionally, in the development of numerical models for dynamic analyses, the bedrock is modeled using an elastic constitutive model, as its influence on the response of the system is more related to stiffness than to strength. An elastic model is generally sufficient to represent the bedrock behavior in this context. However, when the bedrock has a complex geometry, such as in the case under analysis, large spurious tensile stresses may be induced. In such situations, adopting a model capable of releasing these stresses by developing plasticity may be more appropriate. For this reason, a Mohr-Coulomb model was adopted for BR and GC

at least for the static phase, to prevent the development of these excessive tension stresses. On the other hand, the parameters for the COW will be adopted from Ardiaca (2009), considering it as plain concrete of a moderate quality.

The stiffness of the bedrock, in the absence of reliable values from geophysical surveys, is estimated based on the values of RQD and dynamic stiffness of the rock samples, using the empirical relationship from Zhang & Einstein (2004), reproduced in Eq. 6.2.

$$E_{RM} / E_d = 10^{0.0186 \cdot \mathrm{RQD} - 1.91} \qquad \textit{Eq. 6.2}$$

Where E_{RM} is the Young modulus of the rock mass, E_d is the dynamic Young modulus obtained from ultrasonic tests of the three samples reported in Table 3.1, and RQD is the rock quality index calculated in Chapter 3, equal to 60. In this way, and considering the density and Poisson ratio reported in Table 3.1, the elastic parameters G_{BR} and K_{BR} for the rock mass can be easily derived using the equations of the theory of elasticity.

Instead, the definition of the strength parameters of the Mohr-Coulomb model adopted for the rock mass needs a further step. For estimate the friction angle and cohesion of the rock mass was necessary first to adjust a Hoek-Brown model (Hoek & Brown, 2019), based on the already determined value of the GSI = 60, the unconfined compressive strength reported in Table 3.1, adopting a disturbance factor D = 0.25, which can vary between 0-1 and represent the degree of disturbance of the rock mass, and considering the fitting parameter of the model mi = 32 as recommended for Granite.

Once the Hoek-Brown model is defined, it is possible to derive the equivalent Mohr-Coulomb parameters using the procedure presented in Hoek et al. (2002). Finally, the parameters of the Mohr-Coulomb model adopted for BR, GC, and COW are reported in Table 6.2.

Soil	Density (kg/m^3)	Friction angle ϕ (°)	Cohesion c (MPa)	Shear mod. G (MPa)	Bulk mod. K (MPa)
BR & GC	2600	42	8.5	3711	9057
COW	2400	35	0.5	11250	15000

Table 6.2: Parameters adopted for the Mohr-Coulomb model for BR, GC, and COW.

6.2.1.b AL_C, AL_S, AL_D, and AL_L – Plastic hardening

The selection of the parameters for this model was performed in a simplified manner, and regarding that this constitutive model could be considered an evolution of a Mohr-Coulomb model which incorporated the dependence of the stiffness with the confinement and nonlinearity in the unload-reload response, this model can be calibrated in its most simplified form with almost the same information. The minimum set of parameters considered involve the definition of the density, friction angle, an estimation of the secant young modulus E_{50}, and the definition of the parameter m^* that control the increase of the stiffness with the confinement, in a similar way as the m parameter from Dakoulas & Gazetas, (1985).

The friction angle considered is the one evaluated in Chapter 3 based on the results of triaxial tests, and the same for the density adopted, while the Poisson ratio is adopted from De Cicco et al. (2015). For the parameters related to the stiffness of the soil, they will be modified until the model matches the profile of shear wave velocities defined by the cross-hole tests, in a constrained range for E_{50} and m^*.

The inconvenience is that FLAC2D retrieves from the Plastic Hardening soil the parameters G_{UR} and $K_{UR,}$ which are respectively the unload-reload shear modulus and bulk modulus, but not the values at small strains, which are those that can be used to derive Vs. To solve this problem, a relationship to establish the relationship E_0/E_{UR} based on E_{UR} presented in Benz et al. (2009) and the principles of the theory of elasticity were used to convert the values of G_{UR} and K_{UR} to G_0 and $K_{0,}$ and then evaluate the shear wave velocity. Finally, the selected parameters for each one of the soils composing the alluvium are summarized in Table 6.3. The comparison with the profile of shear wave velocity will be presented during the numerical model construction.

Soil	Density (kg/m^3)	Friction angle ϕ (°)	E_{50} MPa	m^*	Poisson ratio ν
AL_S	1800	39.2	160	0.3	0.28
AL_C	1800	39.2	160	0.7	0.28
AL_D	1800	39.2	190	0.6	0.28
AL_L	1800	39.2	75	0.4	0.28

Table 6.3: Parameters from the calibration of the Plastic Hardening model for alluvial soils.

6.2.1.c 3A, 3_AS, 3B, and SE – Plastic hardening

The same approach used for the previous calibration will be used for the soils from the dam body and stabilizing embankment, with the only difference that the value of m^* will be established using the m obtained in Section 3.4 from the analysis of the settlements after the dam construction. Based on the definition of m found in Dakoulas & Gazetas (1985), this parameter is divided in two parts of which one depends on the shape of the dam and oscillate between 0.05-0.2, and the other is exclusive of the material and can range from 0.3-0.9 depending on the kind of soil. Assuming that the part of m that corresponds to the shape of the dam is 0.1, it is possible to separate the part that is exclusive of the soil and consider it equal to m^* in the plastic hardening model.

For the static phase, the parameters for all four soils that compose the dam body and stabilizing embankment will be considered equal, as far as the calibration of E_{50} and m^* will be supported by an average estimation of the stiffness for the whole dam body. Then, assuming the values of the friction angle and density already reported in Chapter 3, and the Poisson ratio reported by De Cicco et al. (2015), the parameters of the plastic hardening model for the soils of the dam body are reported in Table 6.4.

Soil	Density ρ (kg/m^3)	Friction angle ϕ (°)	Young modulus E_{50} (MPa)	m^*	Poisson ratio ν
3A, 3_AS, 3B & SE	2250	39.2	160	0.3	0.26

Table 6.4: Parameters from the calibration of the Plastic Hardening model for the soils of the dam body.

6.2.1.d Reinforced concrete slab (RCS) and interface – Elastic

The concrete slab will be modeled elastic in both static and dynamic phase using a liner structural element available in FLAC2D, while the interface between the slab and the soil will be modeled using a simple link able to reproduce the stiffness in both normal and transverse direction of the slab, and the shear resistance based on a friction angle.

The concrete slab has a variable thickness along the height, with 0.3 m at the top and 0.6 m at the bottom. Then the section properties, cross-section area, and moment of inertia, will vary as well in every element of the slab.

The parameters of the interface model were calibrated based on the vertical stiffness coming from load plate tests and the results from experimental tests made for the concrete slab of Zipingpu dam, reported in Zhang & Zhang (2008). The comparison between experimental information and the calibrated models is presented in Fig. 6.5.

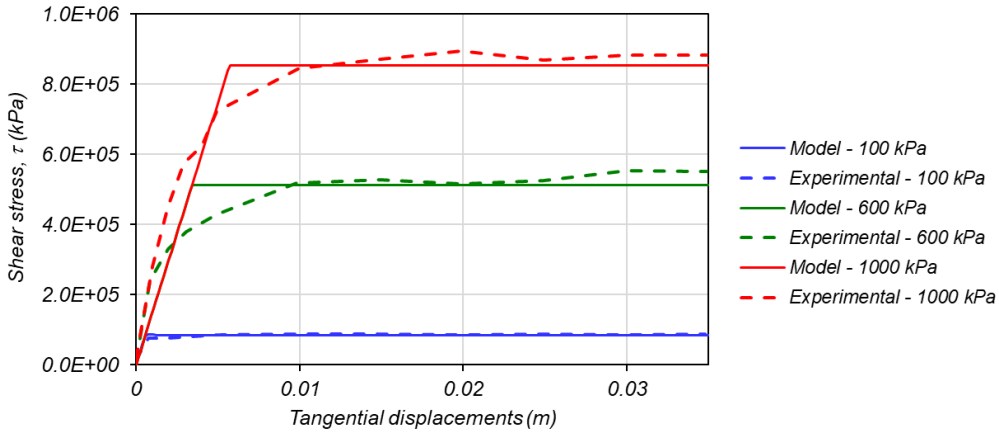


Fig. 6.5: Comparison between the calibrated interface model and the experimental results from Zhang & Zhang (2008) for the interface between concrete slab and soil.

Then, adopting a young modulus and Poisson ratio for the concrete consistent with a characteristic compressive strength f'_c = 30 MPa, it is possible to report in Table 6.4 the parameters needed for modelling the concrete slab in FLAC2D.

Element	Liner structural element			Interface		
	Density (kg/m^3)	Young modulus (MPa)	Poisson ratio ν	Normal stiffness (MPa)	Shear stiffness (MPa)	Friction angle (°)
RCS	2400	25000	0.2	312	140	42

Table 6.5: Parameters from the calibration for the elastic reinforced concrete slab and interface.

6.2.2 Dynamic phase

Part of the soils will change their constitutive model for the dynamic phase, to capture better their cyclic response, assuming beforehand that they will be the ones that control the dynamic response of the dam.

6.2.2.a 3_AS, AL_S, AL_C, AL_D, and AL_L – PM4Sand

The material model selected for capturing the dynamic response of these soils is the sand plasticity model for earthquake engineering applications, PM4Sand version 3.3 (Boulanger & Ziotopoulou, 2024), available as user user-defined model (UDM) in FLAC2D 9.0. This model can reproduce the cyclic response of granular materials, and its calibration is affordable using data from in situ or laboratory tests, notwithstanding that it is an advanced constitutive model.

The model has three primary input properties: the apparent relative density D_R^*, the shear modulus coefficient G_0^*, and the contraction rate parameter h_{p0}. The superscript * is used to distinguish these parameters from the laboratory evaluated relative density D_R and the shear modulus at low strains G_0. The parameters D_R^* and G_0^* can be obtained from correlations with SPT or laboratory tests and geophysical surveys, while h_{p0} have to be calibrated until the cyclic stress ratio (CSR) reaches the cyclic resistance curve (CRR) from a liquefaction triggering correlation or laboratory test, at 15 uniform loading cycles.

The cyclic stress ratio (CSR) is defined as (Eq. 6.3)

$$CSR = \frac{\tau_{cyc}}{\sigma'_{v_0}} \qquad \text{Eq. 6.3}$$

Where τ_{cyc} is the cyclic shear stress and σ'_{v_0} is the consolidation effective vertical stress.

The adjustment of the constitutive model parameters for soils AL_S, AL_C, and AL_D will differ from those used for AL_L, as the latter is based on results from SPT tests, while the firsts will rely on the limited CTX tests available from the upper layers of the alluvium and the geophysical surveys available. Additionally, the calibration of 3_AS will focus on reproducing the expected response of well-compacted soils in the absence of laboratory or in-situ tests for these materials. It must be noted that the calibration performed and its ability to reproduce the expected soil behavior will reflect a balance between the available information and the expected response, and it is likely to improve as more and higher-quality data of the soil properties become available.

Then, the calibration of the layer AL_L is based on the blow count of the SPT identified for the sand material, equal to N =16 at 28 m below the riverbed. This blow count must be further corrected by energy efficiency, whereas corrections because of the diameter of the borehole,

length of the rod length and sampler are not necessary given the test conditions. As mentioned in Chapter 3, the type of hammer and release method of the SPT test widespread in Argentina is the pin-weight free-fall, with a reported energy release of 90% of the potential energy of the falling mass (Leoni et al., 2011). Then, the energy correction factor is (Eq. 6.4):

$$\mathrm{N}_{60} = C_E \cdot \mathrm{N}$$
$$C_E = \frac{E_{released}}{60\,\%} = \frac{90\,\%}{60\,\%} = 1.5 \qquad \textit{Eq. 6.4}$$

Obtaining a value of N_{60} = 24. This number of blow counts has to be further normalized concerning the overburden stresses through the factor C_N, and using the Eq. 6.5 from Boulanger & Idriss (2014), it is possible to obtain the normalized blow count.

$$\left(\mathrm{N}_1\right)_{60} = \mathrm{N}_{60} \cdot C_N$$
$$C_N = \left(\frac{P_a}{\sigma'_v}\right)^m \leq 1.7 \qquad \textit{Eq. 6.5}$$
$$m = 0.784 - 0.0768\sqrt{\left(N_1\right)_{60_{CS}}}$$

Where P_a is the atmospheric pressure equal to P_a = 101.3 kPa, σ'_v is the vertical component of the effective stress, the subscript 1 stands for being the blow count normalized to 1 atmosphere, and the subscript CS refers to "Clean Sand" conditions. Considering the effective stresses at the site, after some iterations, it is possible to obtain the normalized blow count $\left(N_1\right)_{60_{CS}} = 13$. With this value is possible to estimate the D_R^* and G_0^* using the equations provided in the manual of PM4Sand (Boulanger & Ziotopoulou, 2024) and reproduced in Eq. 6.6 and Eq. 6.7.

$$D_R^* = \sqrt{\frac{\left(N_1\right)_{60_{CS}}}{C_d}} \qquad C_c = 46 \qquad \textit{Eq. 6.6}$$

$$G_0^* = 167\sqrt{\left(N_1\right)_{60_{CS}} + 2.5} \qquad \textit{Eq. 6.7}$$

Obtaining respectively D_R^* = 0.53 and G_0^* = 657 for the zone AL_L. It is possible as well to estimate a value of the shear wave velocity Vs and normalized shear wave velocity Vs_1 consistent with the normalized number of blow count, using the relationship find in the

manual of PM4Sand (Boulanger & Ziotopoulou, 2024), slightly adjusted from the original by Andrus & Stokoe (2000), and reported in Eq. 6.8.

$$V_S = V_{S_1} \cdot \left(\frac{\sigma'_v}{P_a} \right)^{0.25}$$
$$V_{S_1} = 85 \cdot \left(\left(N_1 \right)_{60_{CS}} + 2.5 \right)^{0.25} \qquad \textit{Eq. 6.8}$$

Obtaining Vs_1=169 m/s and Vs = 235 m/s. This last value is the one set into the profile of Vs used for the calibration of the plastic hardening model in the static phase, for the stratum of sand. However, this value will be affected during the modeling process by the extra confinement provided by the dam and stabilized embankment, and to take into account these variation of Vs the parameter G_0^* will be set in the model based on the actual shear wave velocity, using the relationships in Eq. 6.9, rearranged from Boulanger & Ziotopoulou (2024) to evaluate shear modulus coefficient G_0^*.

$$G_0^* = \frac{G_0}{P_a} \cdot \sqrt{\frac{P_a}{\sigma'_v}}$$
$$G_0 = \rho \cdot \left(V_S \right)^2 \qquad \textit{Eq. 6.9}$$

Where ρ is the soil density and G_0 is the shear modulus at very low strains.

Before calibrating the remaining parameter $h_{p0,}$ it is necessary to have a reference value of the CRR. Using the liquefaction triggering correlation presented in Boulanger & Idriss (2014), and a reference earthquake magnitude from the disaggregation charts M_w = 6.75, it is possible to evaluate the CRR corresponding to the considered magnitude and overburden conditions using all the relationships contained in Eq. 6.10.

$$CRR_{M,\sigma'_V} = CRR_{M=7.5,\sigma'_V=1} \cdot MSF \cdot K_\sigma$$

$$K_\sigma = 1 - C_\sigma \cdot \ln\left(\frac{\sigma'_v}{P_a}\right) \leq 1.1$$

$$C_\sigma = \frac{1}{18.9 - 2.55\sqrt{(N_1)_{60_{CS}}}} \leq 0.3$$

$$MSF = 1 + (MSF_{\max} - 1) \cdot \frac{\exp(-M/4) - \exp(-7.5/4)}{\exp(-5.25/4) - \exp(-7.5/4)} \qquad \textit{Eq. 6.10}$$

$$MSF_{\max} = 1.09 + \left(\frac{(N_1)_{60_{CS}}}{31.5}\right)^2 \leq 2.2$$

$$CRR_{M=7.5,\sigma'_V=1} = \exp\left(\frac{(N_1)_{60_{CS}}}{14.1} + \left(\frac{(N_1)_{60_{CS}}}{126}\right)^2 - \left(\frac{(N_1)_{60_{CS}}}{23.6}\right)^3 + \left(\frac{(N_1)_{60_{CS}}}{25.4}\right)^4 - 2.8\right)$$

The resulting parameters are then $K_\sigma = 0.871$, $MSF = 1.071$, $CRR_{M=7.5,\sigma'_V=1} = 0.140$ and finally $CRR_{M,\sigma'_V} = 0.131$. This value will be used as the target to be matched when calibrating the contraction rate parameter h_{p0}. Using the driver created by the developers of PM4Sand, and after a few iterations, it was possible to retrieve an $h_{p0} = 0.73$.

The 1-element response based on the previous calibration is then presented in Fig. 6.6 in terms of CRR using $r_u > 95\%$ as liquefaction triggering criteria, CSR-strain curve, normalized stress path, and r_u vs. number of uniform cycles.

The response observed is reasonable for a soil with the characteristics defined for AL_L, which is why the calibration is considered satisfactory for this work.

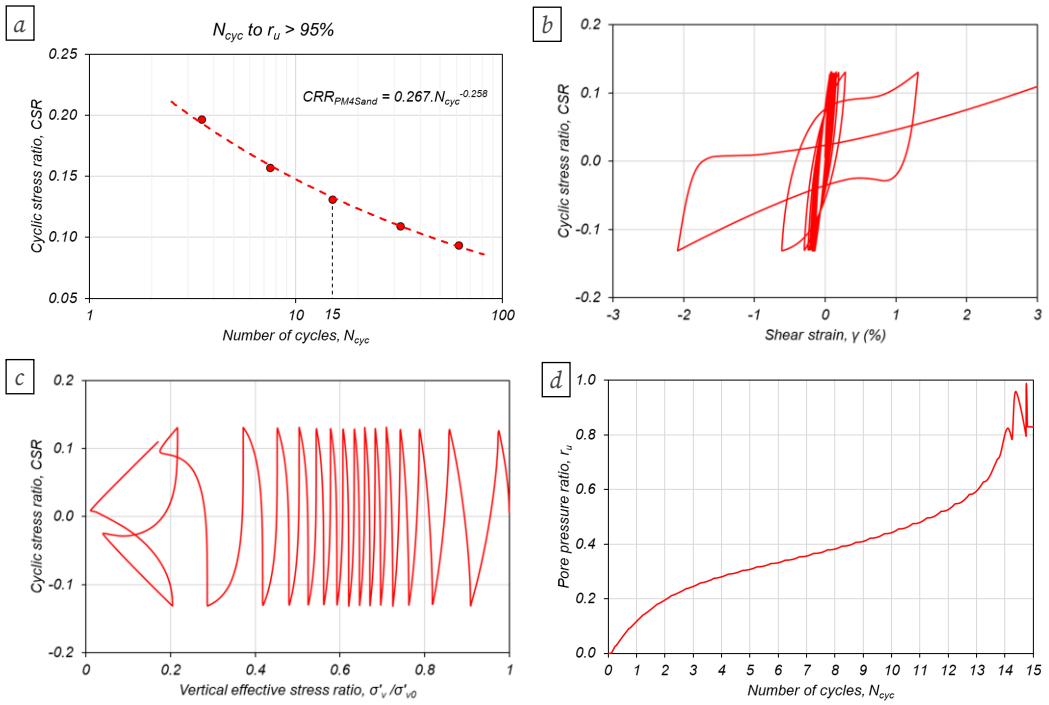


Fig. 6.6: Single element response for the calibration of PM4Sand for AL_L in terms of a) cyclic resistance curve, b) CSR vs. shear strain, c) normalized stress path, and d) r_u vs. number of cycles.

The calibration for the soils AL_C, AL_D, and AL_S will be performed following the same methodology, with the difference that the soils AL_C and AL_D consider the CRR curve from the CTX tests with D_R = 50 % whereas AL_S will use the one with D_R = 60 %, based on the respective values of relative density observed in the test pits.

However, it is worth mentioning that the actual soil may exhibit a different relative density, as the maximum and minimum void ratios (e_{max}, e_{min}) obtained from laboratory tests often exclude a significant portion of the coarse fraction. Additionally, better definitions of the void ratio were proposed to evaluate the liquefaction potential of sand-gravel mixtures (Pokhrel et al., 2024).

The values of CRR from the CTX must be transformed to field values, as the consolidation conditions in both cases can be largely different. For this purpose, Eq. 6.11 reported in Castro (1975) can be used to obtain the values of CRR in field conditions, adopting a K_0 from the field equal to 0.4 based on Jaky's equation and the friction angle evaluated in Chapter 3.

$$\mathrm{CRR}_{field} = \frac{2 \cdot \left(1 + 2\left(K_0\right)_{field}\right)}{3 \cdot \sqrt{3}} \cdot \mathrm{CRR}_{\mathrm{CTX}} \qquad \textit{Eq. 6.11}$$

Then, considering D_R = 0.6 and back-figuring a value for G_0^* = 1210 using the information of the consolidation part of the CTX, empirical relationships (Benz et al., 2009), the theory of elasticity for the conversion between modulus and Eq. 6.9, the calibrated value of h_{p0} = 3.3 obtained by trying to match the CRR at 15 blows from the curves of Fig. 3.26 is presented in Fig. 6.7, together with the CSR vs. strain curve, stress paths, and r_u vs. number of cycles.

It is evident that the response of the model in terms of CRR only matches the experimental curve in the control point used for the calibration, at 15 cycles. A further adjustment can be made by modifying secondary parameters with the aim of getting closer to the experimental curve in a broader range. However, it should also be noted that a more detailed calibration aimed at capturing the response of a reconstructed sample may not significantly improve the representation of the real soil behavior, since the structure of natural soils can differ substantially from that of the reconstructed sample, and fabric plays a critical role in the evaluation of liquefaction (Kramer & Stewart, 2024).

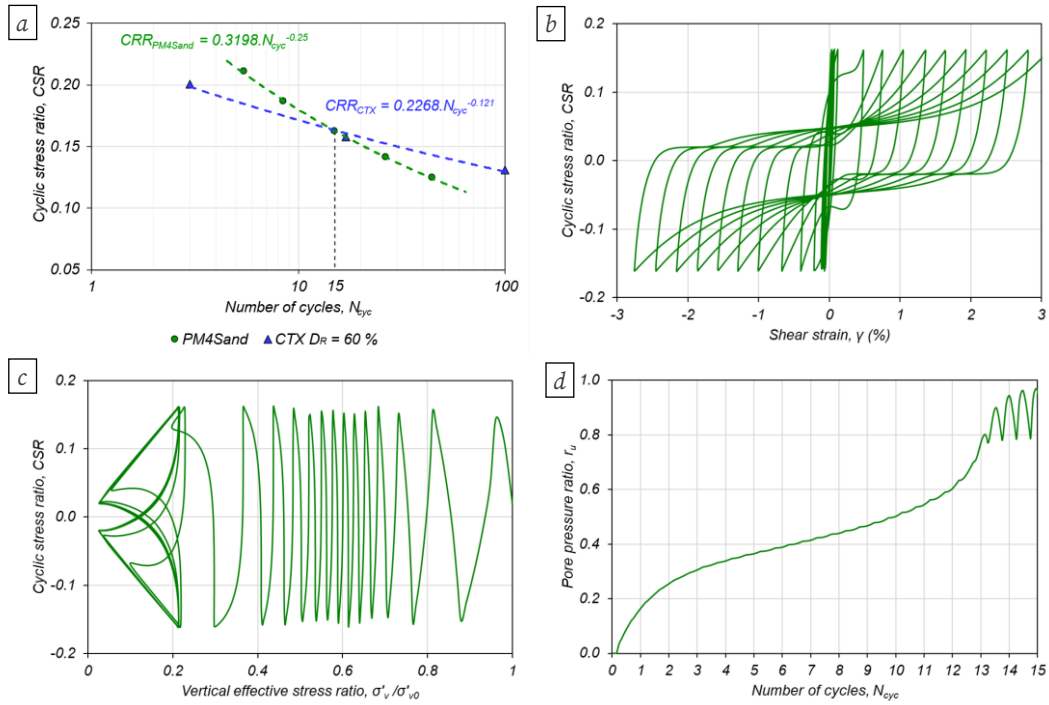


Fig. 6.7: Single element response for the calibration of PM4Sand for AL_S in terms of a) cyclic resistance curve, b) CSR vs. shear strain, c) normalized stress path, and d) r_u vs. number of cycles.

The calibration is then considered acceptable as long as the overall response of the soil remains reasonable and the differences in the number of cycles for values lower than 15, where the CRR_{CTX} is more conservative than the 1-element response, are not significant given all the assumptions involved.

The last soil to be calibrated using PM4Sand is the submerged part of the dam body, immediately below the drains, named 3_AS. The criteria for this calibration will be different from the previous ones. As is not expected an important development of excess of pore water pressure as the soil is a compacted well graded sand-gravel mixture, the condition established as target for the calibration was try to reproduce a reasonable response in terms of the modulus reduction and damping curves G/G_0 vs. γ and D vs. γ using as reference the literature curves for gravel from Rollins et al. (2020) for C_U = 80 and two levels of confinement σ'_0 = 200 MPa and 600 MPa.

The calibration was then carried out considering G_0^* = 2200 in agreement with the values of Vs expected for the zone 3_AS, D_R = 0.9, as the soil from the dam body is a well-graded and well-compacted gravel, and the contraction rate parameter was set as hp_0 = 4.0. With these parameters, the 1-element response in terms of modulus reduction and damping curves is presented in Fig. 6.8.

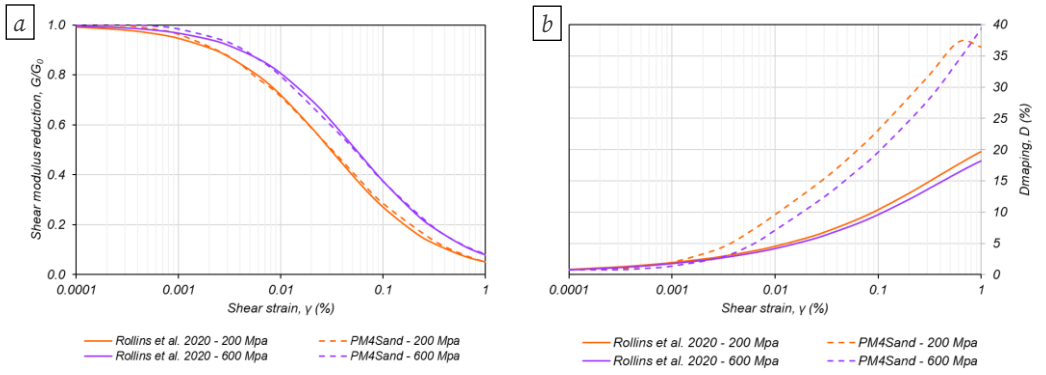


Fig. 6.8: Single element response for the calibration of PM4Sand for 3_AS in terms of a) G/G_0 vs. γ, and b) D vs. γ, for two levels of confinement (200 and 600 MPa), and comparison with the curves from literature for gravel from Rollins et al. (2020).

While the relationship between the curves from literature and the calibration for the modulus reduction curves is very good, the damping shows evident differences for the deformations over 0.01 %. These differences could be reduced with a calibration focused on seeking to fit

the damping curve rather than the modulus reduction curve, but as far as it is expected that the major part of these soils will not be subjected to large deformations, the overdamping should also not be significant.

The table with the calibration parameters for all the soils that use PM4Sand is reported below in Table 6.6. It is important to note that G_0^* is not reported as it will be calculated for each element based on the Vs obtained from the static stage, using Eq. 6.9.

Soil	Relative density D_R	Contraction rate parameter hp_0
AL_L	0.53	0.73
AL_S	0.6	3.3
AL_C	0.5	2.1
AL_D	0.7	2.1
3_AS	0.9	4.0

Table 6.6: Parameters from the calibration of the soils that use the PM4Sand constitutive model.

6.2.2.b 3A, 3B and SE – UBCHyst

The soils that compose the dam body and are over the water table will be modeled using the total stress constitutive model UBCHyst, developed by Naesgaard (2011) and implemented in FLAC2D 9.0 as UDM (Naesgaard et al., 2015). This is a simple hysteretic model with a Mohr-Coulomb cap that showed good performance in applications in seismic analysis of dams (Armstrong et al., 2018).

The calibration of this model will be based using the same densities and friction angles used for the Plastic Hardening soil of the static stage, and the remaining parameters will be modified for reproducing the modulus reduction and damping curves from literature in the same way as done for 3_AS, considering different calibrations for different ranges of confinement levels existing in the dam. The hysteretic response of the model is defined in terms of the tangent shear modulus, which is defined as (Eq. 6.12):

$$G_T = G_0 \cdot \left(1 - R_f \cdot \frac{\eta_1}{\eta_{1_f}} \right)^n \cdot \mathrm{mod}_1 \cdot \mathrm{mod}_2$$

Eq. 6.12

$$\mathrm{mod}_2 = 1 - \left| \frac{h\eta_{\max}}{\eta_f} \right|^{rm} d_{fac} \geq 0.2$$

Where:

- η_1 is the developed stress ratio τ/σ'_v
- $\eta_{1_f} = \sin(\phi_f) + (c/\sigma'_v) \cdot \cos(\phi_f)$
- R_f is the failure ratio, with a default value of 0.9
- n is a calibration parameter of hysteretic behavior, with a default of 2.0
- mod_1 is a virgin loading factor, default between 0.6-0.8
- $h\eta_{\max}$ is the maximum past shear stress ratio
- rm is a calibration factor similar to n
- d_{fac} is a calibration parameter for controlling the permanent modulus reduction
- G_0 is the shear modulus at small strains
- ϕ_f is the peak friction angle, and c is the cohesion

Before the calibration, it is precise to select the modulus degradation and damping curves from the models available in the literature. The selected model from Rollins et al. (2020) is based only on data from laboratory tests made in gravel and sand-gravel mixtures.

This model is defined in terms of the confinement (σ'_0) and the coefficient of uniformity (C_u) of the soils. For the soils in analysis, the range of C_u was already presented in Fig. 3.32, from where it can be observed that for 3A the predominant values range between 20 and 30, whereas for 3B they range between 110 and 120. For the characterization of the degradation curves, the C_u for 3A will be adopted equal to C_u = 20, but for 3B will be adopted in C_u = 80 instead of 120 because the database used for the derivation of the degradation curves only has information from soils with coefficients of uniformity under 80. The curves for different confinement levels expected to take place in every zone are reported in Fig. 6.9.

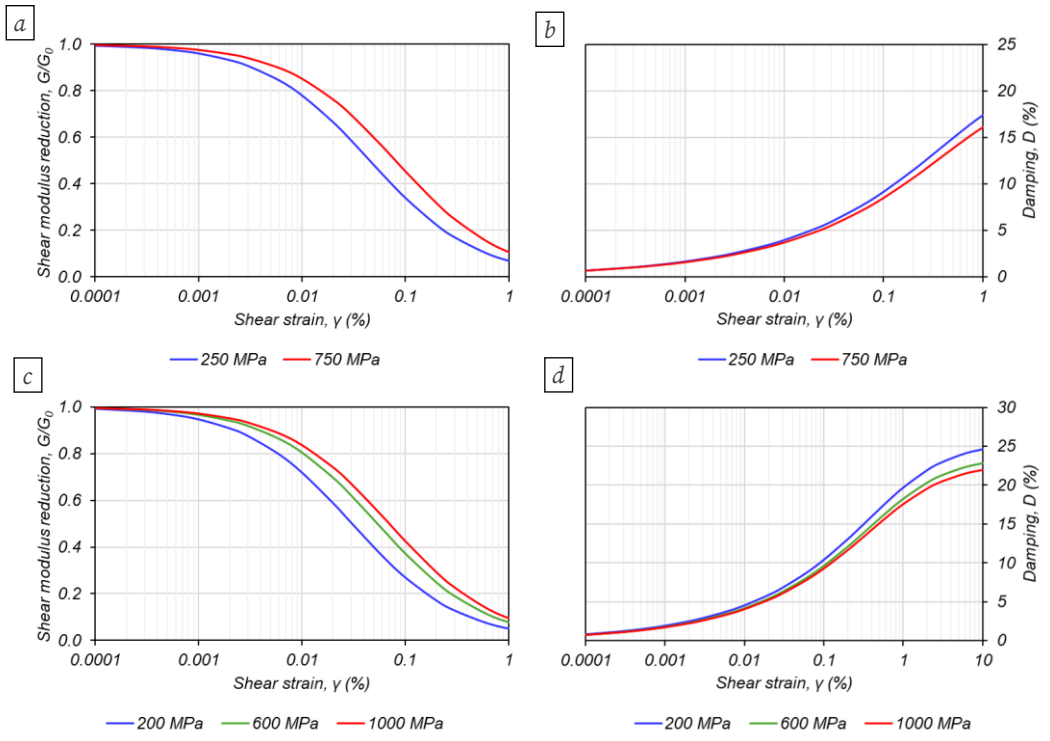


Fig. 6.9: Modulus reduction and damping curves from Rollins et al. (2020) for different levels of confinement. a) G/G_0 vs. γ for 3A, b) D vs. γ for 3A, c) G/G_0 vs. γ for 3B, d) D vs. γ for 3B.

These are de curves that will be set as the target for the calibration of the constitutive model using the UBCHyst constitutive model.

The parameters involved in the calibration are n, mod_1, rm, and d_{fac}, while c = 0 as the soils do not report cohesion in the TXCD tests, and $R_f = 0.98$ as suggested by Armstrong et al. (2018). A driver for the calibration was used to perform 1-element tests in FLAC2D, and the results in terms of modulus reduction and damping curves, as well as the stress-strain curve obtained during the calibration, are presented as an example of the methodology for the case of 3A considering σ'_0 = 250 MPa and 750 MPa, in Fig. 6.10.

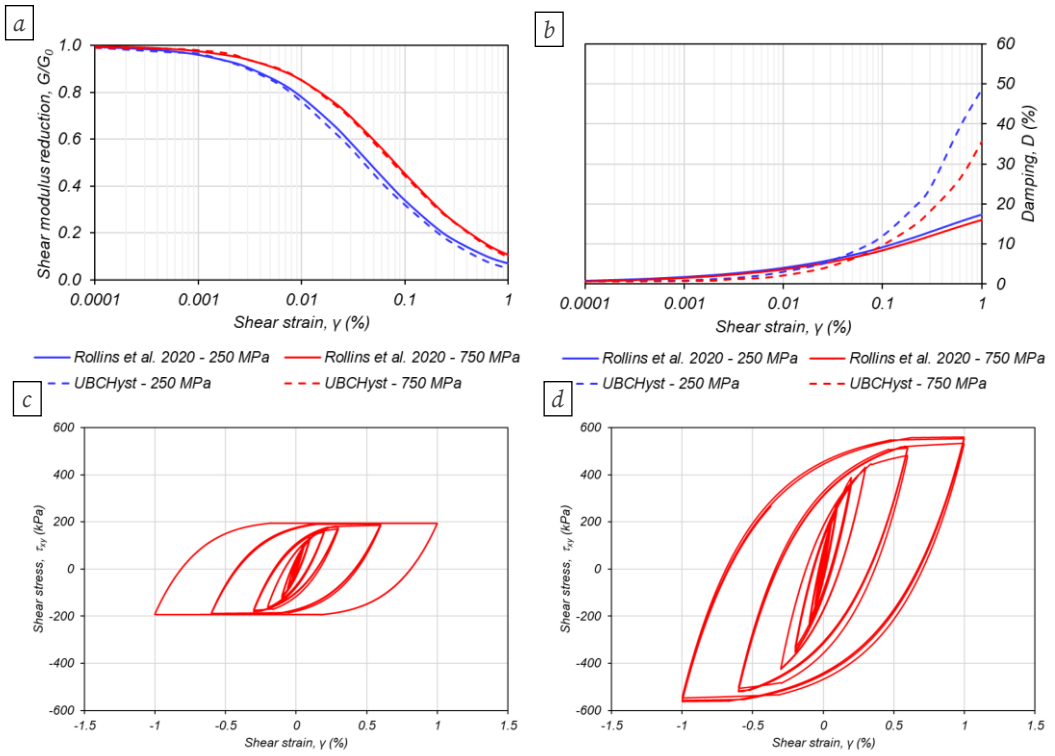


Fig. 6.10: Modulus reduction and damping curves from the calibration 3A using UBCHyst. The curves from the driver are compared with Rollins et al. (2020) for two different confinements. a) G/G_0 vs. γ for 3A, b) D vs. γ for 3A, c) τ_{xy} vs. γ curve for σ'_0 = 250 MPa, d) τ_{xy} vs. γ curve for σ'_0 = 750 MPa.

The figure shows a close agreement between the modulus reduction curves obtained from the calibration and those from the literature, for both levels of confinement. In contrast, the damping curves exhibit overdamping at large strains. This behavior likely results from the use of the Masing rule to represent the unload-reload behavior, which is known to generate wider hysteresis loops and, consequently, higher damping than typically observed in laboratory tests at large strain levels (Phillips & Hashash, 2009).

A summary of the parameters from the calibration done for the soils using UBCHyst is reported in Table 6.7. The stiffness parameter G_0 will be evaluated based on Vs in a similar fashion to what has been done for the soils modeled with PM4Sand, using Eq. 6.9.

Soil	σ'_0 (MPa)	ϕ_f (°)	n	mod_1	rm	d_{fac}
3A	250	41.5	0.9	1.1	0.8	0.55
3A	750	41.5	1.1	1.1	0.8	0.55
3B	200	42.9	1.1	1.1	0.75	0.60
3B	600	42.9	1.4	1.1	0.75	0.65
3B	1000	42.9	1.5	1.1	0.65	0.65
SE	250	41.5	0.9	1.1	0.8	0.55

Table 6.7: Parameters from the calibration of the soils that use the UBCHyst constitutive model.

The curves characterized for every mean effective stress were considered characteristic of a range of stresses centered on the value given by the curve; for example, the curve characteristic of 600 MPa will cover the range 400-800 MPa in the model.

The hydraulic parameters were adopted, except for bedrock that was not reported, from previous works done it the dam and which were based on the laboratory and in-situ tests performed over the dam materials (De Cicco et al., 2015). The permeability corresponding with the sand material was slightly modified from the rest of the alluvium based on their grain size distribution, as no permeability tests were done on this material. The parameters are summarized in Table 6.8 for all the soils considered in the model.

Soil	Vertical permeability k_y (m/s)	Horizontal permeability k_x (m/s)	Porosity n
BR	1.7×10^{-7}		0.02
AL_D & AL_C	1.0×10^{-6}	1.0×10^{-4}	0.38
AL_L	1.0×10^{-5}	1.5×10^{-5}	0.41
AL_S	1.0×10^{-6}	1.0×10^{-4}	0.29
3A, 3_AS & SE	1.0×10^{-5}	1.0×10^{-4}	0.15
3B	1.0×10^{-4}	1.0×10^{-3}	0.12

Table 6.8: Hydraulic conductivity (permeability) and porosity for all the soils considered in the model.

6.3 Numerical model construction and static analysis

Having defined the mesh and calibrated or set the calibration rules of the constitutive models, the following steps in the building of the numerical model can be listed as:

- Bedrock building
- Alluvium building and setting of the river water table
- Staged construction of the dam
- Build the reinforced concrete slab and cut-off wall
- Raising of the reservoir water level
- Switch to the constitutive models used in the dynamic stage
- Definition of the dynamic boundary conditions and damping

The first step does not involve significant complexity. Once the general settings of the model are defined, with gravity set to g = 9.81 m/s^2 and water density ρ_w = 1000 kg/cm^3 and the boundary conditions for the static stage are established as fixed in both horizontal and vertical directions at the bottom of the model and restricted in the horizontal direction only along the lateral boundaries, it is possible to assign the bedrock parameters and perform the initial run.

Once the bedrock is built, the alluvium materials can be introduced into the model, which is then run again. To incorporate the effect of the pore water pressure, the water table must be raised in the model by defining the hydraulic boundary conditions and the pore water pressure distribution. This distribution follows a hydrostatic profile up to the long-term water table verified before construction in the exploratory boreholes. In this step, it is necessary to do a few iterations of the values of E_{50} and m of the Plastic Hardening model for all the soils constituting the alluvium to reproduce the profile of shear wave velocity (Vs) presented in Fig. 3.22, assumed uniform for the whole extension of the alluvium. For AL_L, the shear wave velocity considered is established by the correlation with the SPT values. The resulting profile of shear wave velocities is presented in Fig. 6.11 together with the profiles of Vs from the cross-hole tests, while the contours of shear wave velocity are shown in Fig. 6.12.

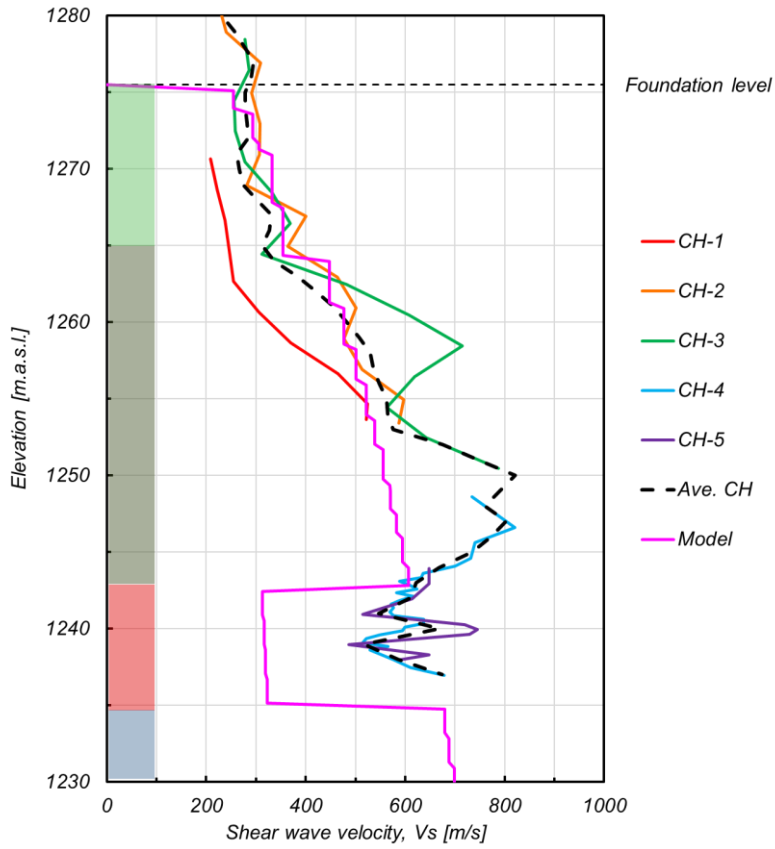


Fig. 6.11: Profile of shear wave velocity into the alluvium, comparing the adjusted model with the Vs profiles obtained from the cross-hole tests, except for the soil AL_L, which adopts the Vs estimated from SPT.

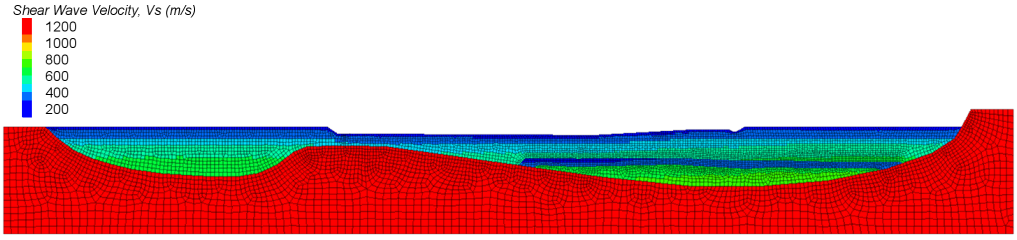


Fig. 6.12: Contours of shear wave velocity for the alluvium and bedrock, before the construction of the dam.

The next step is the construction of the dam body. The embankment is built in 15 layers with a thickness of approximately 8 m each layer, trying to reproduce the state of stresses generated during the construction of the dam. Using a similar approach as the one used for the alluvium, the parameter E_{50} is modified until the profile of shear wave velocity has an average value equal to the Vs =555 m/s estimated from the processing of weak motion records. In this case, the parameter m is not modified as it is adopted from the evaluation of the stiffness distribution

throughout the evaluation of the settlement profiles after construction. The final profile of Vs after the construction of the dam is presented in Fig. 6.13, close to the half-section of the dam, with the layering considered during the construction. The contours of shear wave velocity after construction can be shown in Fig. 6.14.

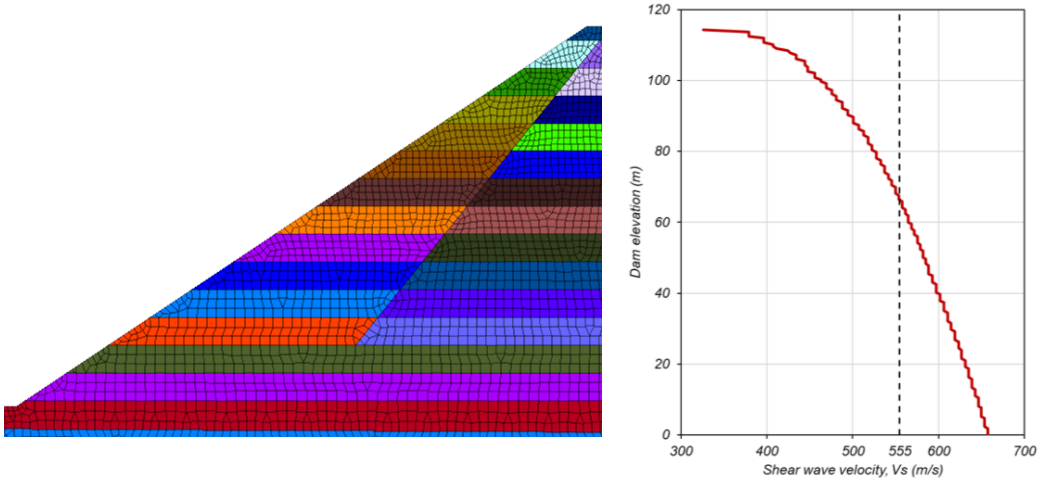


Fig. 6.13: Profile of shear wave velocities at the center of the dam, with the half-section to give the dimension of the height of the dam and show the layering.

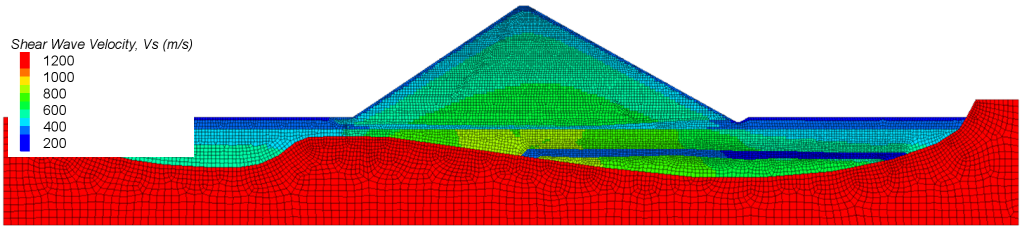


Fig. 6.14: Contours of shear wave velocity after the construction of the dam.

Following the real sequence of the construction, the next step is the construction of the concrete slab and the stabilizing embankment downstream of the dam. This step is done all at once, as the construction of the slab was made only in two stages, and no advantages of modeling in two stages were observed beforehand.

At this point, and before the rising of the water level of the embankment, some contour plots presenting some physical magnitudes and ratios related to the state of stresses and

deformations present into the dam body and foundation follow a reasonable distribution, which is one of the most important reasons of the static phase before a dynamic analysis.

Two ratios that are useful to evaluate the state of stress are also defined. The first is the coefficient of earth pressure at rest, K_0 defined as (Eq. 6.13):

$$K_0 = \frac{\sigma'_H}{\sigma'_V} \qquad \textit{Eq. 6.13}$$

Whereas the second is the alpha coefficient, which is the ratio of the shear stress and the effective vertical stress, as defined by Eq. 6.14:

$$\alpha = \frac{\tau}{\sigma'_V} \qquad \textit{Eq. 6.14}$$

The plots for vertical, horizontal, and mean effective stresses, and K_0 and α are presented in Fig. 6.15 to Fig. 6.19.

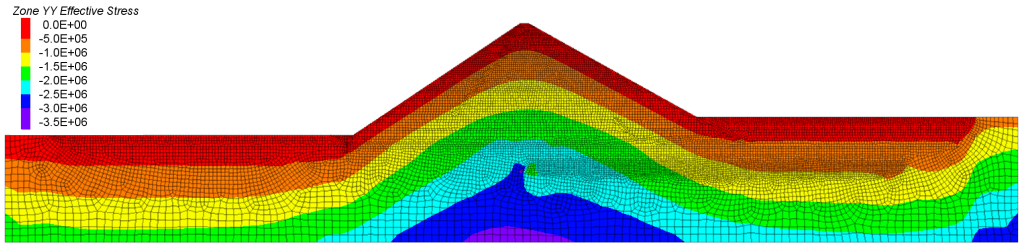


Fig. 6.15: Contours of vertical effective stress after construction, empty reservoir.

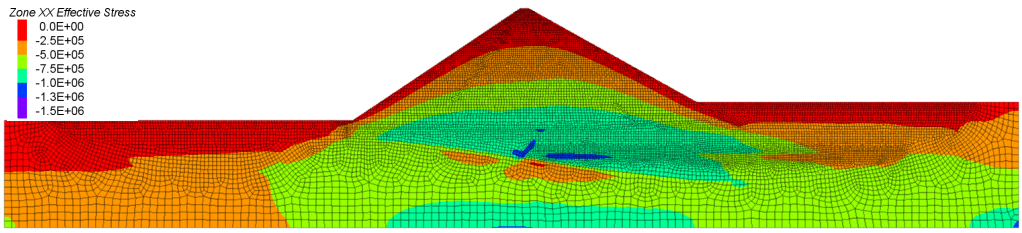


Fig. 6.16: Contour of horizontal effective stress after the construction, empty reservoir.

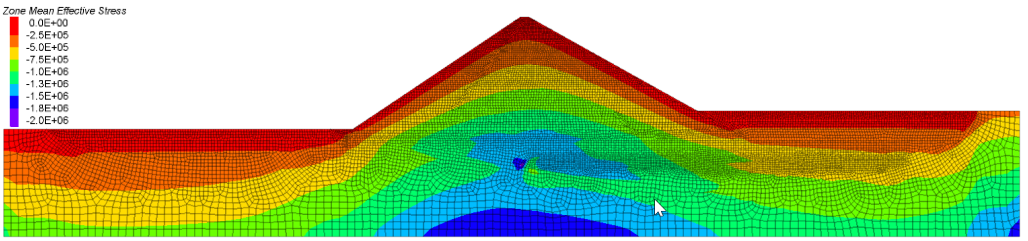


Fig. 6.17: Contours of mean effective stress after the construction, empty reservoir.

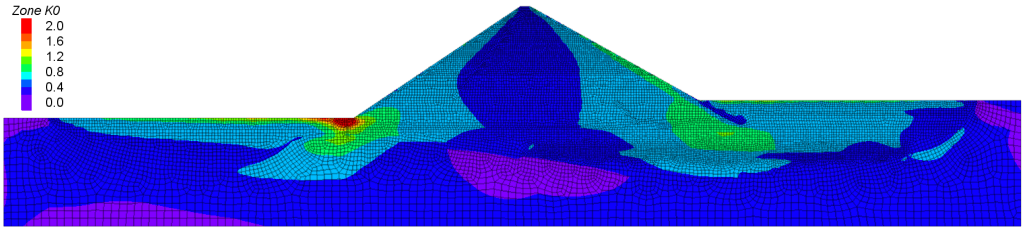


Fig. 6.18: Coefficient of earth pressure at rest K_0 after the construction, empty reservoir.

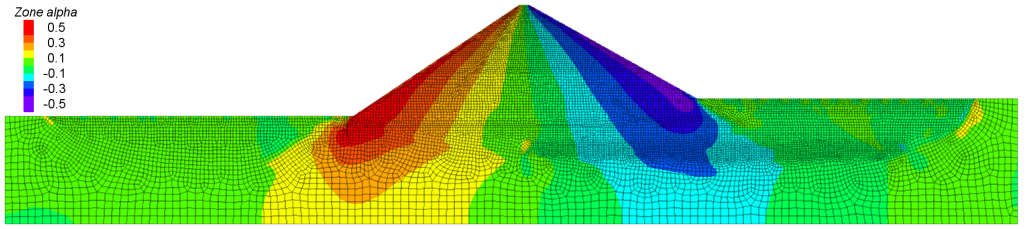


Fig. 6.19: Alpha coefficient α after the construction, empty reservoir.

The distribution of all of them seems to be reasonable, with a small tendency towards downstream in horizontal effective stresses, given the shape of the bedrock sloping in this direction.

In terms of displacements, the contours of vertical and horizontal displacements are presented in Fig. 6.20 and Fig. 6.21.

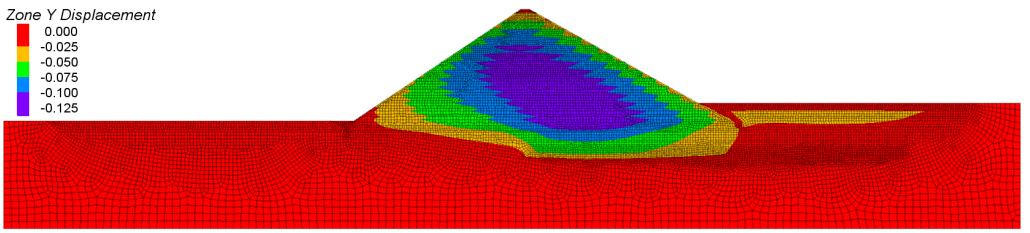


Fig. 6.20: Contours of vertical displacements after the construction, empty reservoir.

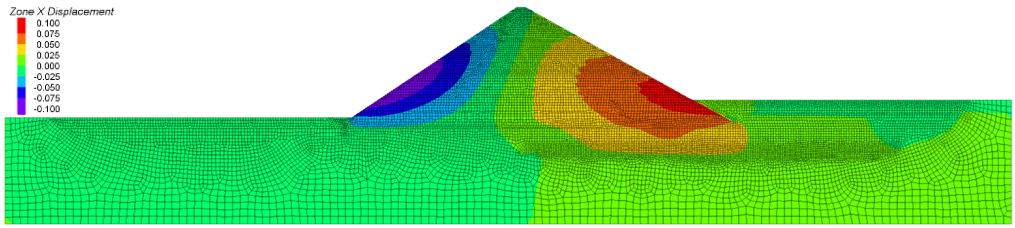


Fig. 6.21: Contours of horizontal displacements after the construction, empty reservoir.

The influence of the inclined bedrock is more evident in terms of displacements, both vertical and horizontal displacements. In the vertical ones, the increase of alluvial thickness is likely the reason because the larger zone of displacements is moving towards downstream, and consistent with the observations of Fig. 3.47. In terms of horizontal displacements, an asymmetric distribution has shifted the point of zero horizontal displacement, which typically coincides with the dam axis, toward the upstream direction. It is evident as well that an important part of the foundation has also significant displacements, indicating that the response of the dam will not be constrained to the embankment.

Following the modelling process, it is the moment to raise the reservoir level, which in terms of the model is supposed to apply the hydrostatic loads in the upstream face of the dam and the upstream part of the foundation, and raise the water table within the foundation and dam. The rising of the reservoir was done in eight stages, and the distribution of pore water pressure was defined within the dam set by constraining it to follow the distribution of pore water pressure defined by the piezometers installed in the dam and foundation, in coincidence with each of the prescribed elevations of the reservoir. The resulting distribution of pore water pressure with the full impoundment is presented in Fig. 6.22.

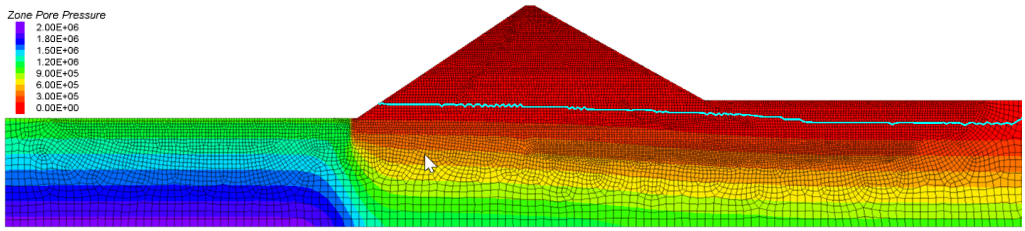


Fig. 6.22: Contours of pore water pressure after the rise of the reservoir.

Finally, the last step of the static phase is to change the material models for those used in the dynamic analysis. In this step, not just the state of stresses and deformations is inherited from the model with the constitutive models used for the static stage, but also the distribution of stiffness is utilized for the new models, as previously commented during the calibration.

Once the materials are changed, a run is performed in static conditions but using the dynamic solver, to guarantee that the new properties do not generate numerical instabilities in the model before the development of dynamic analysis. Once converged, the model is ready to proceed to the dynamic stage.

To run the dynamic analyses is still necessary to set up three important things: reset the displacements from the static stage, set the boundary conditions for dynamic conditions, and set the damping of the model.

The reason for the first is evident; it is important to identify the displacements only produced by the earthquake, as those are representative of the damage to the dam and the ones that will be measured in the field in the case of an earthquake.

To set the dynamic boundary conditions, FLAC2D has many different options available, among which two are the most widespread to define the characteristics of the frontiers of the model to better reproduce the real conditions expected at the site concerning the wave propagation.

The first is to consider the condition of "compliant base" at the bottom of the model, which allows the development of radiation damping that will try to spread the seismic waves generated by the model far away from the modeling domain. For this, the approach developed by Mejia & Dawson (2006) is applied by considering pairs of horizontal and vertical dashpots defined by the criteria of Lysmer & Kuhlemeyer (1969), which link the model to the applied actions (Fig. 6.23). In practice, this is achieved by defining quiet boundary conditions at the bottom of the model and applying the seismic actions in terms of time histories of shear and normal stresses.

These time histories are defined, for horizontal and vertical actions, following Eq. 6.15 and Eq. 6.16, respectively.

$$\tau(t) = \rho_{BR} \cdot \mathrm{V}_{\mathrm{S}_{BR}} \cdot v_x(t) \qquad \textit{Eq. 6.15}$$

$$\sigma_V(t) = \rho_{BR} \cdot \mathrm{V}_{\mathrm{P}_{BR}} \cdot v_y(t) \qquad \textit{Eq. 6.16}$$

Where ρBR is the density of the bedrock, $\mathrm{V}_{\mathrm{S}_{\mathrm{BR}}}$ and $\mathrm{V}_{\mathrm{P}_{\mathrm{BR}}}$ are the shear and pressure wave velocities of the bedrock, and v_x(t) and v_y(t) are the time histories of velocities corresponding with each record selected in Chapter 5.

The lateral boundaries are set up using the Free-field boundary conditions available on FLAC2D, which connect the model with a 1D soil column model that represents the response of the soil conditions outside the model domain, with Lysmer & Kuhlemeyer (1969) dashpots as presented schematically in Fig. 6.23.

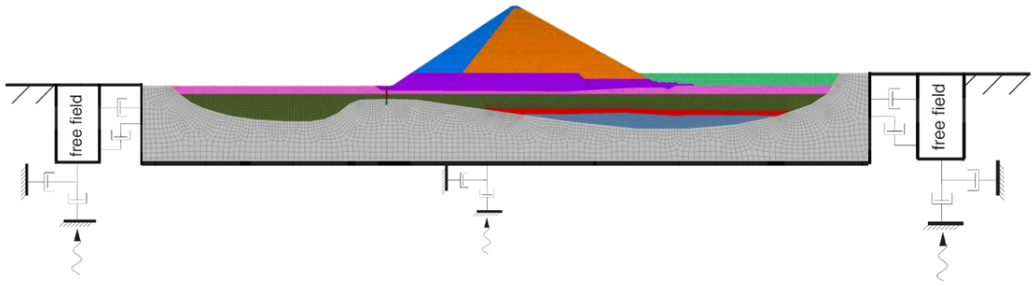


Fig. 6.23: Compliant base and free-field boundary conditions, modified from Itasca software guides (Itasca Consulting Group, Inc., 2023)

The 1D free-field columns are intended to represent the seismic response of a soil profile that extends infinitely in both horizontal directions. By connecting these columns to the model using dashpots, it is possible to account for a portion of the radiation damping along the lateral boundaries of the model as well as the free field response expected in reality.

The last setting is the definition of the complementary damping, which seeks to supplement the hysteretic damping of the material models that often consider a damping at very small strains equal to zero, which is uncommon in real soils.

For this purpose, Rayleigh damping was chosen and calibrated based the double frequency approach and the suggestions presented in Verrucci et al. (2022), which considering the natural frequency of the dam and the predominant frequencies of the ground motions set a frequency for the minimum value of damping equal to $f_{Ray} = 3.46$ Hz, and a fraction of critical damping $\xi_{Ray} = 0.0043$ corresponding to 0.5% of damping.

7. Nonlinear dynamic analyses

With the model ready for performing dynamic analyses, it is now time to carry them out using all the ground motions selected and scaled in Chapter 5 as input motions. The characteristics of the selected input motions are representative of near-field records, generally showing large amplitudes and short durations. This is significant for two aspects that can influence the development of numerical analyses: the effect of the number of loading cycles on the response of saturated soils, and the computational time required to complete the simulations. The first

aspect is addressed by the variability in duration among the selected records, which falls within the expected range for the near-field events characteristics of the sources of the region. The second aspect is itself an advantage, since a large model such as the one considered can be completed in about three hours, considering appropriate time steps.

However, this chapter does not intend to be a summary of all the analyses performed, but to show some particular characteristics of the dynamic response of the dam and the influence of the modeling assumptions on the results obtained. For this reason, the results of only a few selected ground motions will be reported below.

7.1 Evaluation of seismic performance

From the analysis of about 50 nonlinear dynamic analyses carried out, corresponding with five different levels of ground motions, it was possible to distinguish between two main responses of the dam: one response at low intensities and one different at large intensities. The main difference among them relies on the buildup of pore water pressures in the layer AL_L, which generates a weak layer in the alluvium that affects the overall response of the dam.

Starting with the ground motion related to low intensities, the response of the dam, considering the record RSN_4231_H2_TR475, plotted in terms of acceleration time history in Fig. 7.1, is presented in terms of contours of displacements and shear strains in Fig. 7.2 and Fig. 7.3, respectively. This record is one of the largest in terms of *PGA* for this particular intensity level, and even under this condition, the effects generated in the dam were moderate in terms of displacement and shear strains, showing maximum displacements of less than 0.3 m in the upper part of the downstream slope.

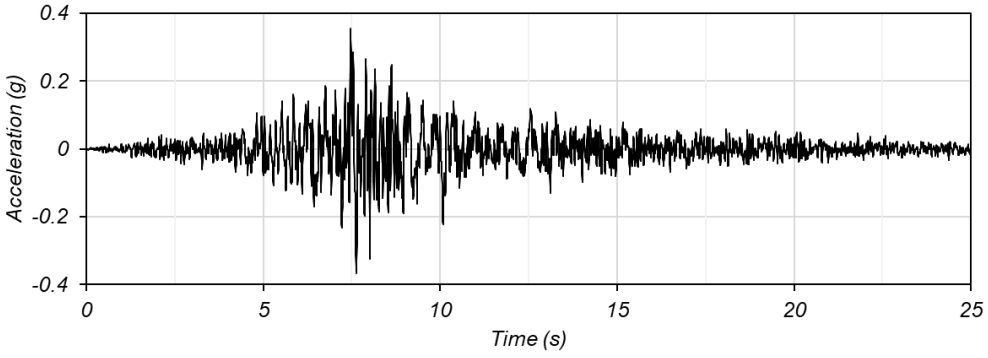


Fig. 7.1: Acceleration time history of the record RSN_4231_H2_TR475.

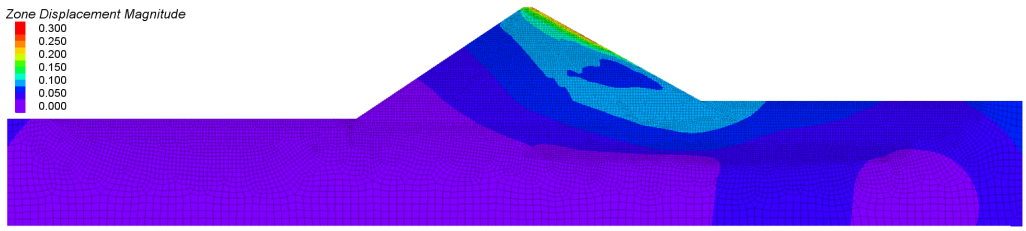


Fig. 7.2: Contour of displacement magnitude for the ground motion RSN_4231_H2_TR475.

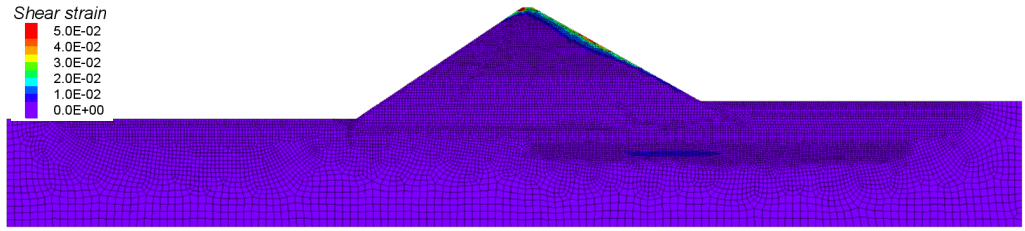


Fig. 7.3: Contour of shear strains for the ground motion RSN_4231_H2_TR475.

In addition, the crest settlements are presented in Fig. 7.4 and the records of r_u in four points located along the layer AL_L in the locations presented in Fig. 7.5, are shown in Fig. 7.6 . The crest settlements confirm what was already discussed about the moderate magnitude of the displacements, with less than 0.2 m of crest settlements, insignificant in comparison with the 7 m of effective freeboard of the dam.

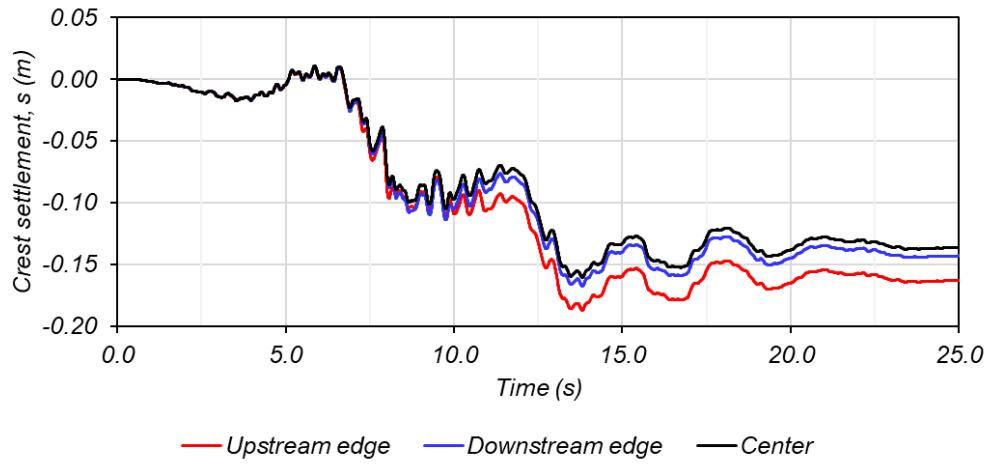


Fig. 7.4: Time history of crest settlements for the ground motion RSN_4231_H2_TR475.

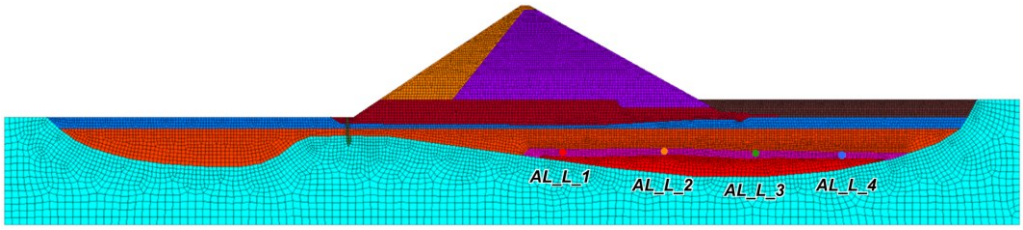


Fig. 7.5: Location of the four points where the pore water pressure was measured, in the soil AL_L.

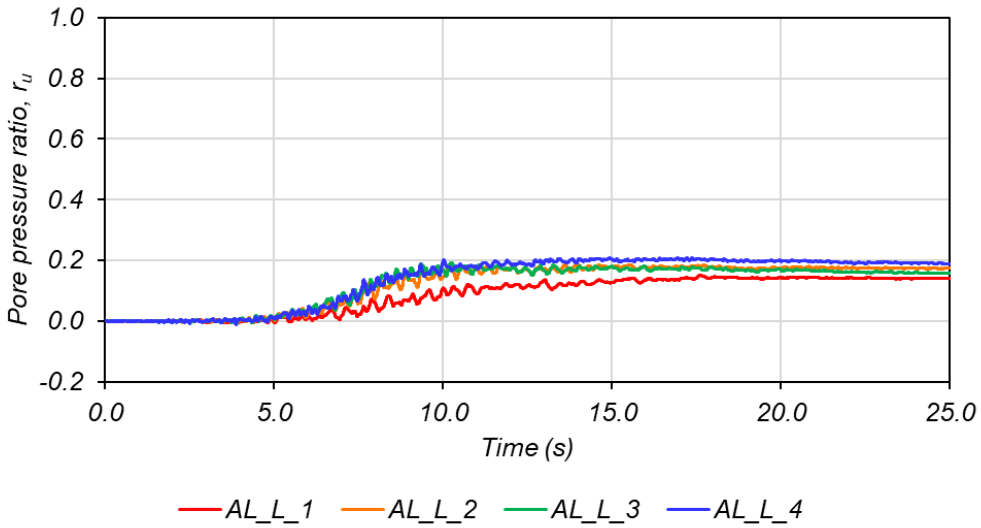


Fig. 7.6: Time history of pore water pressure ratio r_u, for the ground motion RSN_4231_H2_TR475.

The buildup of pore water pressure for these ground motions appears to be light but not negligible, with a maximum r_u value of approximately 0.2. This level of acceleration is not sufficient to reduce the strength of the layer AL_L to the level of inducing the formation of a large sliding mass.

The ground motion selected to represent the large intensities was the ground motion RSN_5618_H2_4975, plotted in terms of acceleration time history in Fig. 7.7.

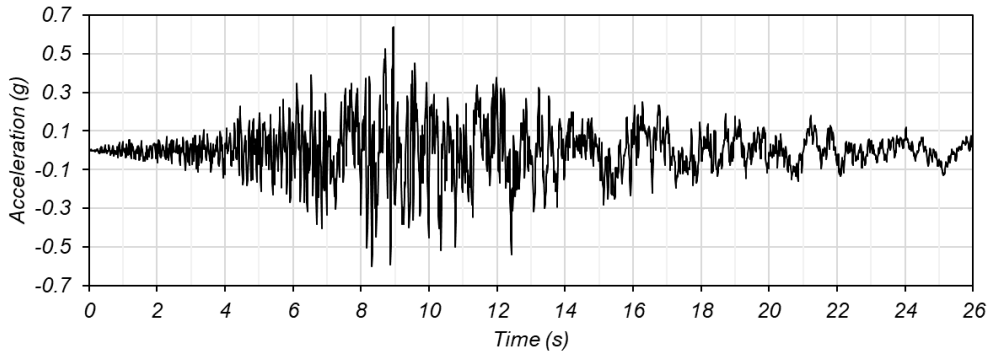


Fig. 7.7: Acceleration time history of the record RSN_5618_H2_TR4975.

The response of the model following the application of this ground motion is presented in terms of contours of displacements (Fig. 7.8) and shear strains in (Fig. 7.9).

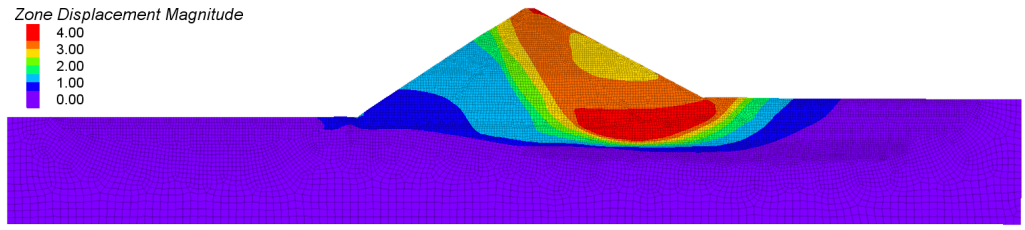


Fig. 7.8: Contour of displacement magnitude for the ground motion RSN_5618_H2_TR4975.

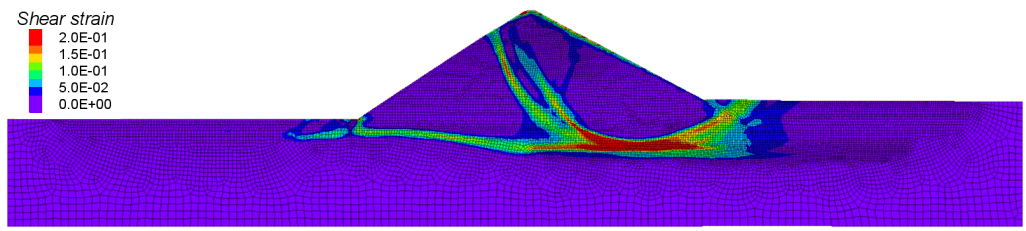


Fig. 7.9: Contour of shear strains for the ground motion RSN_5618_H2_TR4975.

It is evident from the inspection of Fig. 7.8 and Fig. 7.9 that in this case, the influence of the zone AL_L is important in the development of a large sliding mass that involves a large part of the dam and foundation. The consequences can be further described in terms of crest settlements in Fig. 7.10.

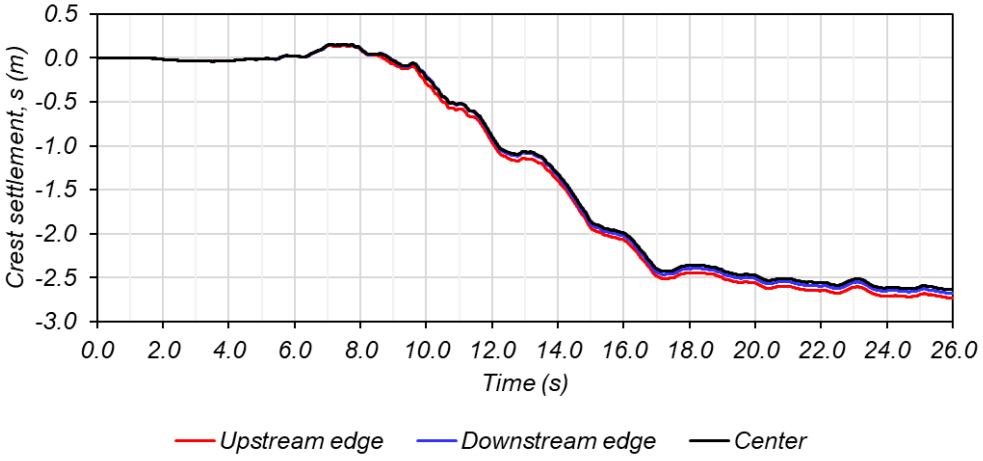


Fig. 7.10 Time history of crest settlements for the ground motion RSN_5618_H2_TR4975.

Even if the crest settlement is important, it is still smaller than 50% of the available freeboard, and considering that this ground motion is related to one of the largest intensity levels of the ground motion and it is related to an extraordinary event, the safety of the dam could be considered not vulnerated in terms of overtopping.

To see the magnitude of the buildup of pore water pressures in the same four positions previously shown in Fig. 7.5, the time histories of the pore water pressure ratio are presented in Fig. 7.11.

From the inspection of the time histories of r_u is evident that the buildup of pore water pressure increases with respect to the case of low intensity ground motion. However, they are still far from the liquefaction, and even if the reduction of strength was large enough to trigger the sliding mechanism observed in Fig. 7.8 and Fig. 7.9, a complete liquefaction was not verified at least in the points where the pore water was measured.

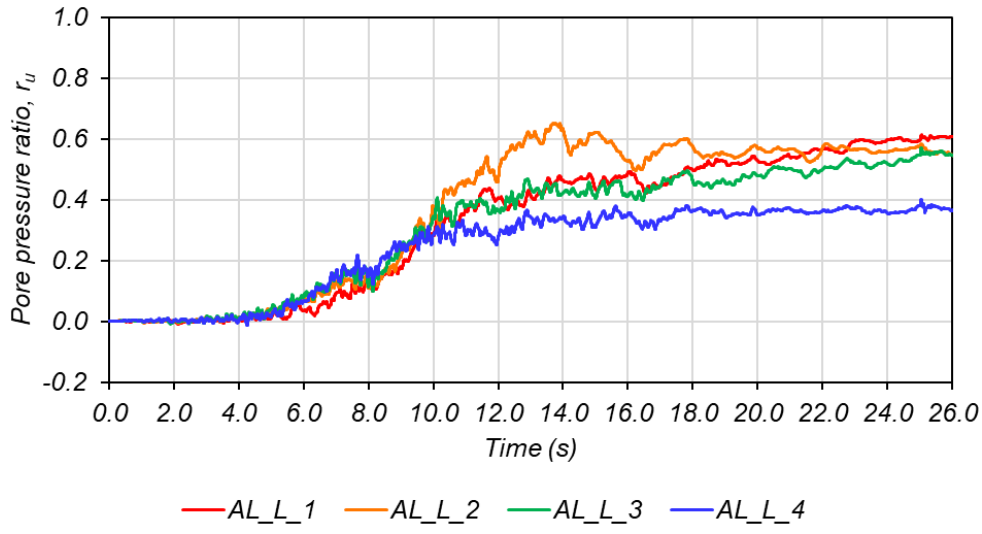


Fig. 7.11: Time history of pore water pressure ratio r_u, for the ground motion RSN_5618_H2_TR4975.

7.2 Influence of the modeling decisions

The conservative assumptions adopted during the calibration of the soils in region AL_L made them highly influential in the dynamic response of the model. Although more detailed information on the actual properties of these soils would improve the assessment, the results already indicate dam performance within the range of the design. Yet under these conservative conditions, the safety margin against overtopping is important, and liquefaction was not observed at the monitoring points within region AL_L. Therefore, it can be concluded that the dam exhibits reasonable behavior under large intensity ground motions, even if the numerical model reflects a pessimistic scenario. The post-shaking evaluation using residual strength of the liquefied soil was not performed, as this work does not aim to be a formal safety evaluation, and the fragility analysis is focused on mainshock effects. However, it is advisable to carry it out under these conditions.

Moreover, it is expected that the response described by the 2D model could be less severe if the adjacent zones of the dam suffer less damage, tending to reduce the overall deformation of the dam body and foundation.

The use of new and better information to characterize the soils from the alluvium will only improve the results of the numerical models and bring more definition to the influence of the soils contained in the region AL_L in the seismic response of the dam.

8. Derivation of seismic fragility functions

The final step to develop case-specific fragility functions for the Potrerillos dam was to fit these functions based on the results of the nonlinear dynamic analyses (NDAs). According to the procedure introduced in Section 3.1, such analyses have been aimed not only at evaluating the seismic performance of the dam but also at supporting the calibration of reliable fragility relationships useful for the evaluation of the seismic safety of the dam.

The steps followed for the derivation of fragility functions were designed to ensure that the resulting relationships provide a feasible and reliable representation of the actual seismic fragility of the dam. Their further application in seismic performance assessment, risk analyses, or early warning systems will depend on their ability to establish a robust relationship between ground motion intensity and the probability of triggering a specific potential failure mode (PFM), reaching a given damage level.

For parametric lognormal fragility functions, the calibration process, regardless of the method applied, involves adjusting the parameters θ and β from the lognormal CDF (Eq. 3.1, retrieved from Section 3), which defines the shape of the fragility curve for an identified PFM and a specific damage level.

$$P\left(EDP \geq DM \mid IM = im\right) = \Phi\left(\frac{\ln\left(im/\theta\right)}{\beta}\right) \qquad \textit{Eq. 3.1}$$

Two calibration methods will be used: Multiple Stripes Analysis (MSA), considering the spectral acceleration at the fundamental period of the dam $Sa(T_1)$ as ground motion intensity measure; and Cloud Analysis (CA), adopting other intensity measures (PGA, PGV, I_A, CAV, and I_H) derived from the same set of ground motions. The pros and cons of each method for this particular case will be briefly discussed along with the results at the end of this section.

Before then, however, a few key variables involved in the derivation of fragility functions should be examined, as they can significantly influence the characteristics of the resulting functions, as the intensity measures (IM) of the ground motions, engineering demand parameters (EDP), and damage measures (DM) considered for every potential failure mode (PFM).

8.1 Intensity measures of the ground motion

The earthquake ground shaking can be quantitatively described throughout ground-motion time histories in terms of accelerations, velocities, displacements, etc. These time-histories can be recorded during real earthquakes by instruments (e.g., accelerometers) placed in specific sites at the ground surface or in borehole arrays, or simply stored at particular locations in the case of numerical simulations.

The time histories contain extensive information about the ground shaking at the recording location, including amplitude, duration, frequency content, and energy content. In certain applications, such as the derivation of fragility functions, it becomes necessary to condense this information into a single parameter capable of representing key aspects of the ground motion (Kazantzi & Vamvatsikos, 2015). These parameters, known as intensity measures (*IMs*), range from simple peak values such as peak ground acceleration (*PGA*) or peak ground velocity (*PGV*), to more complex integrals that aim to capture not only the amplitude but also the frequency content and energy characteristics of the ground motion, as Arias intensity (I_A), or cumulative absolute velocity (*CAV*).

There is no single intensity measure capable of fully capturing all the relevant characteristics of a seismic signal. Moreover, using complex intensity measures that combine multiple ground motion attributes might lead to losing clear physical interpretation. In such cases, it is often preferable to adopt vector-valued approaches that incorporate more than one intensity measure parameter in the definition of fragility surfaces (Derakhshan & Alielahi, 2025).

Moreover, the response of different types of structural or geotechnical civil engineering systems may be more influenced by specific features of the ground motion, which only certain *IMs* can capture efficiently.

This aspect focused the attention of the research community on how to identify the "optimal" *IM* for each particular case, and several metrics have been proposed to identify which is the most suitable *IM* for every civil engineering application. Among the most renowned metrics are the *efficiency* and *sufficiency* (Luco & Cornell, 2007), *predictability* (Kramer & Mitchell, 2006), *practicality* (Mackie & Stojadinović, 2001), *proficiency* (Padgett et al., 2008), *hazard computability* (Giovenale et al., 2004), *scaling robustness* (Tothong & Luco, 2007), and other tools to identify the best *IM* from several points of view. From all the previous metrics, one of the most important is the *efficiency*, which measures the relative variability in the prediction

of a given *EDP* using the *IM* analyzed, corresponding to a smaller uncertainty in the probabilistic predictive model.

In geotechnical systems, the definition of the optimal intensity measures was studied for problems involving liquefaction (Dashti & Karimi, 2017; Karimi & Dashti, 2017; Bullock et al., 2019; Wu et al., 2022), slope stability (Travasarou & Bray, 2003; Cho & Rathje, 2022), tunnels (Huang et al., 2021; Shen et al., 2025), and embankment dams (Armstrong et al., 2021; Regina et al., 2023; Khalid et al., 2023; Derakhshan & Alielahi, 2025). These works showed that the most suitable *IM* for geotechnical systems is not unique; for the case of embankment dams there is not an absolute best intensity measure for all the PFMs or *EDPs*, although the integral intensity measures and those related to the velocity are mostly suited.

As discussed in Section 2.7, the three modern approaches for deriving fragility functions (IDA, MSA, and CA) impose different requirements regarding the selection and scaling of input motions used in the nonlinear dynamic analyses. For MSA, this also affects the choice of the intensity measure, as the scaling must ensure that each stripe is composed of ground motion records with a consistent target value of the selected intensity measure.

In this work, the *IM* selected for the fragility functions obtained via MSA approach is the spectral acceleration at the fundamental period of the dam-foundation system, $Sa(T_1)$, considering $T_1 = 0.5$s as obtained from the evaluation of monitoring records in Section 3.4.3. This choice is directly tied to the selection and scaling of ground motion records for their use as input motions in NDAs, as all spectra were scaled to match the *Sa(0.5s)*, from the UHSs corresponding to each selected return period derived from the PSHA.

For the fragility functions obtained via CA, the selection of *IMs* has no restriction, and they are selected based on recommendations from literature. Therefore, in addition to peak ground acceleration (*PGA),* which is adopted in most of the works summarized in Table 2.2, the intensity measures considered in this study as those more suitable for geotechnical systems are: peak ground velocity (*PGV)* (Saygili & Rathje, 2008), Arias intensity (I_A) (R. Armstrong et al., 2021), cumulative absolute velocity (*CAV)* (Regina et al., 2023), and Housner intensity (I_H) (Silvestri et al., 2024).

8.2 Engineering demand parameters and damage measures

The selection of the engineering demand parameters (*EDPs*) began during the identification of the seismically induced potential failure modes (PFMs) considered in the fragility analyses.

Before selecting the PFMs, the *EDPs* were evaluated not only for their ability to capture the consequences of the physical mechanisms evolving throughout the development of these failure modes, but also for the availability of threshold values (*DMs*) defining distinct damage levels for each particular *EDP*.

This last aspect can strongly influence the selection of the *EDPs*, since the available *DMs* for geotechnical systems are limited in number and often conditioned by the subjective judgment of their developers when defining the thresholds between damage levels.

Moreover, many of the available damage measures are derived from case histories involving different types of dams, introducing an additional source of variability in the evaluation process. It is not completely feasible to directly compare the seismic performance of dams constructed with different materials, in distinct site conditions, or using diverse construction techniques. This is further combined with the reliance on the subjective experience of the developers in identifying different damage levels, which can be based on visual inspections or post-earthquake damage reports. Bearing in mind this possible variability in the definition of the *DMs*, it is expected that different criteria propose different thresholds at diverse damage levels.

8.2.1 EDPs and DMs for the PFM of overtopping

The engineering demand parameters for the overtopping are related to the permanent settlement of the dam's crest after an earthquake. In order to be able to use the available *DMs* based on case histories of dams with different geometrical properties, those settlements were normalized with respect to a particular dimension of the dam-foundation system.

Even though the PFM considered involves overtopping and the subsequent uncontrolled release of reservoir water, most of the *DMs* related to permanent crest settlement were developed to classify the seismic performance observed in case histories, even if only a few collapses of embankment dams after earthquakes were observed to date. It is therefore possible that the "Collapse" damage level defined by some of these criteria corresponds to deformations significantly smaller than the 7 m of freeboard available at Potrerillos dam. This is not only due to the conservative design of the dam, but also because the criteria were often derived from the response of older dams with considerably smaller freeboards, mainly due to hydraulic requirements.

Moreover, an assumption underlying this criterion is that the reservoir is at full impoundment at the time of the earthquake, a condition which, depending on the dam's use and operation, may not be met most of the time. However, for dams with reservoirs dedicated to hydrological control in arid regions, as the case of Potrerillos, water levels remain close to the maximum for a large part of the year, making the hypothesis of a full reservoir reasonable.

8.2.1.a Criterion from Swaisgood (2014)

This criterion is an updated version of the widespread criterion from Swaisgood (2003), which was based on the data from 82 case histories of four different types of dams (earthfill, earth core rockfill dam, hydraulic fill, and CFRD). It establishes 4 damage levels related to the so-called normalized crest settlement NCS_{DH+AT}, defined in Eq. 8.1:

$$NCS_{DH+AT} = \frac{\Delta}{DH + AT} \times 100 \qquad \textit{Eq. 8.1}$$

where Δ is the permanent crest settlement, DH is the height of the dam, and AT is the alluvium thickness just below the dam axis. These variables are sketched in Fig. 8.1.

The damage levels in terms of normalized crest settlement, but also the permanent crest settlement considering $DH + AT$ = 147 m for the cross-section analyzed in Chapter 7, are reported in Table 8.1.

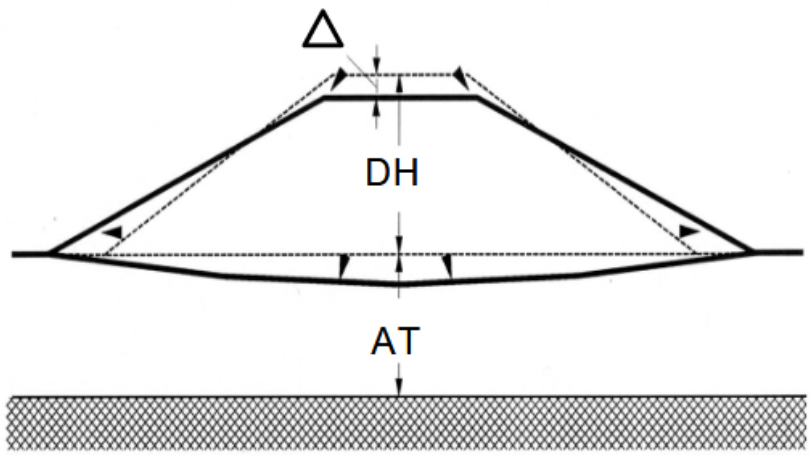


Fig. 8.1: Scheme showing the parameters involved in the calculation of NCS_{DH+AT}*, the settlement* Δ*, dam height DH, and alluvium thickness AT (Swaisgood, 2014).*

It is worth noting that considering the thickness of the alluvium in the evaluation of the settlements is relevant, given that embankment dams are often founded on deep alluvial valleys that may undergo significant deformation during earthquakes and amplify ground motions at the base of the dam. However, this criterion does not account for the complex geometry of the alluvial valley or the spatial variability in the deformation characteristics of alluvial materials that could affect the permanent crest settlement after an earthquake. Yet, given the scope and the way in which this type of criterion was developed, focusing only on the alluvial thickness is reasonable.

Damage level	NCS_{DH+AT} (%)	Crest settlement, Δ (m)
None	0.02	0.03
Minor	0.1	0.15
Moderate	0.5	0.74
Serious	1.0	1.47

Table 8.1: Damage levels in terms of NCS_{DH+AT} *and permanent crest settlement adopting DH+AT=147m, using the criterion from Swaisgood (2014).*

This criterion is one of the most widespread and was used by most of the works reported in Table 2.2 for the fragility functions involving permanent crest settlements.

8.2.1.b Criterion from Pells & Fell (2003)

Slightly different from the previous one, the criterion of Pells & Fell (2003) is based on the normalized crest settlement NCS_{DH}, considers only the height, *DH*. The criterion was also established based on the analysis of several case histories, focused on the impact of seismic cracking and its implications on internal erosion after an earthquake (Pells & Fell, 2002).

The normalized crest settlement used in this analysis is defined by Eq. 8.2. The corresponding damage levels, together with the NCS_{DH} values and permanent crest settlements, are presented in Table 8.2, assuming an embankment height of DH =109.4 m. The difference between this height and that reported in the previous sections lies in their definition: the latter includes the engineered fill placed in the original riverbed, whereas the embankment height refers strictly to the trapezoidal portion of the embankment.

$$NCS_{DH} = \frac{\Delta}{DH} \times 100 \qquad \textit{Eq. 8.2}$$

Damage level	NCS_{DH} (%)	Crest settlement, Δ (m)
None	0.03	0.03
Minor	0.2	0.22
Moderate	0.5	0.55
Major	1.5	1.64
Collapse	5.0	5.47

Table 8.2: Damage levels in terms of NCS_{DH}*, and permanent crest settlement adopting DH =109.4m, using the criterion from Pells & Fell (2003).*

The crest settlement Δ is still the total settlement considering dam and alluvial thickness, which could be questionable as this criterion only considers the height of the dam for normalizing it, whereas also the alluvial thickness could be subject to deformations.

The difference with the criterion proposed by Swaisgood (2014), other than not accounting for the thickness of the alluvium, lies in the introduction of an additional damage level. This aspect highlights the previously discussed subjectivity involved in defining damage states among different references, a tendency that will also become evident in the next criterion.

8.2.1.c Criteria from Pang et al. (2018) and Pang et al. (2019)

The authors of these two criteria have proposed the limits based on their experience in the seismic response of CFRD dams, citing the work of Swaisgood (2014) as a reference for establishing the normalized crest settlement NCS_{DH+AT}. The damage levels and related normalized and permanent crest settlement are presented in Table 8.3 and Table 8.4 for the limits presented in Pang et al. (2018) and Pang et al. (2019), respectively.

Damage level	NCS_{DH+AT} (%)	Crest settlement (m)
Minor	0.2	0.29
Moderate	0.4	0.59
Severe	0.6	0.88

Table 8.3: Damage levels in terms of NCS_{DH+AT}*, and permanent crest settlement adopting DH+AT=147m, established by the criterion from Pang et al. (2018).*

Damage level	NCS_{DH+AT} (%)	Crest settlement (m)
Minor	0.4	0.59
Moderate	0.7	1.03
Severe	1.0	1.47

Table 8.4: Damage levels in terms of NCS_{DH+AT}*, and permanent crest settlement adopting DH+AT=147m, established by the criterion from Pang et al. (2019).*

A comparison of Table 8.3 and Table 8.4 highlights noteworthy differences in the definition of damage levels between the two criteria. The criterion in Table 8.3 is more consistent with that proposed by Swaisgood (2014) for lower damage levels, whereas that in Table 8.4 aligns more closely with higher levels of damage, evidencing the more conservative approach of the first one (Pang et al., 2018) with respect to the second (Pang et al., 2019).

8.2.1.d Criterion from Aliberti et al. (2019)

This criterion can be considered an update of the one proposed by Swaisgood (2014), with the addition of extra case histories to configure a database of 90 case histories subjected to 42 large earthquakes. A re-evaluation of the damage levels and their association to the limit states specified by the Italian seismic standard for dams, furnished the damage levels and related NCS_{DH+AT} presented in Table 8.5.

Damage level	NCS_{DH+AT} (%)	Crest settlement (m)
None	0.1	0.15
Minor	0.4	0.59
Moderate	1.0	1.47
Serious	2.5	3.68

Table 8.5: Damage levels in terms of NCS_{DH+AT} *and permanent crest settlement adopting DH+AT=147 m, using the criterion from Aliberti et al. (2019).*

This criterion seems to be slightly less conservative than Swaisgood (2014), but in light of the better performance of modern dams and the retrofit of old dams to match the requirements of modern standards, it could be considered trustworthy.

8.2.1.e Criterion based on freeboard reduction

This approach, proposed by Regina (2021), sets the damage levels in terms of the reduction of the effective freeboard of the dam. This criterion is the closest to a potential failure mode, as the overtopping will effectively occur once the settlements at the crest of the dam are larger than the available freeboard.

The damage levels presented in Regina (2021) stand for the 50, 65, and 100% of the freeboard reported for the dam. These limits are comparable with the previous criteria when the freeboard is not that large, but when the minimum freeboard is 7 m, as in the case of Potrerillos dam, 50% of freeboard reduction already goes beyond the "Serious" damage level of most of the above-presented criteria. For this reason, another proposal for the limits of freeboard reduction is proposed here. Considering that due to the cracking of the dam close to the crest, 10% of the design freeboard could be lost, the remaining damage levels are evenly distributed as presented in Table 8.6.

Damage level	Freeboard reduction (%)	Crest settlement (m)
Minor	5	0.35
Moderate	30	2.10
Severe	60	4.20
Collapse	90	6.30

Table 8.6: Damage levels in terms of freeboard reduction and permanent crest settlement considering a minimum freeboard of 7 m.

It is evident that this is the least conservative criterion considered so far, but it is also the one most closely related to the actual overtopping of the dam. However, the fact that a large freeboard was defined in the design does not guarantee that the damage associated with a crest settlement smaller than this freeboard cannot be considerable or significantly reduce the overall safety of the dam.

8.2.1.f Statistical definition of *DMs* (He & Rathje, 2024)

An interesting alternative, able to capture the uncertainty in the definition of the damage levels, is the probabilistic definition of damage measures originally proposed by Rathje & He (2022) and further improved in He & Rathje (2024). This criterion, also called capacity or damage models, is based on the statistical analysis of the case histories coming from a harmonized database (He & Rathje, 2023), which combines the cases from Pells & Fell (2002) and Swaisgood (2003) with few modern cases to better populate all the damage levels. The definition of the normalized crest settlement NCS_{DH} used by the capacity models is that of Pells & Fell (2003), already presented in Eq. 8.2.

The damage levels are represented in terms of a lognormal CDF, defining the probability of exceeding a certain damage level by means of Eq. 8.3:

$$P_{DL}\left(\mathrm{NCS}_{\mathrm{DH}}\right)=\Phi\left(\frac{\ln\left(\mathrm{NCS}_{\mathrm{DH}}\right)-\mu_{\ln C}}{\sigma_{\ln C}}\right) \qquad \textit{Eq. 8.3}$$

The parameters $\mu_{\ln C}$ and $\sigma_{\ln C}$ stand for the logarithmic median and standard deviation of the lognormal distribution, and are reported in Table 8.7 for the three defined damage levels,

together with the median value of NCS_{DH} for comparison with the rest of the criteria. The letter "C" in this context refers to a capacity model.

Damage level	$\mu_{\ln C}$	$\sigma_{\ln C}$	Median (NCS_{DH}) (%)
Minor	-3.507	0.94	0.03
Moderate	-0.777	0.99	0.46
Severe	0.833	0.92	2.3

Table 8.7: Parameters of the lognormal distribution defined in Eq. 8.3 to describe the capacity models for the permanent crest settlement of embankment dams, together with the median value for the three damage levels established by He & Rathje (2024).

To better understand the differences between a probabilistic and a deterministic definition of the *DMs*, the criteria of He & Rathje (2024) and Pells & Fell (2003) are plotted together in Fig. 8.2.

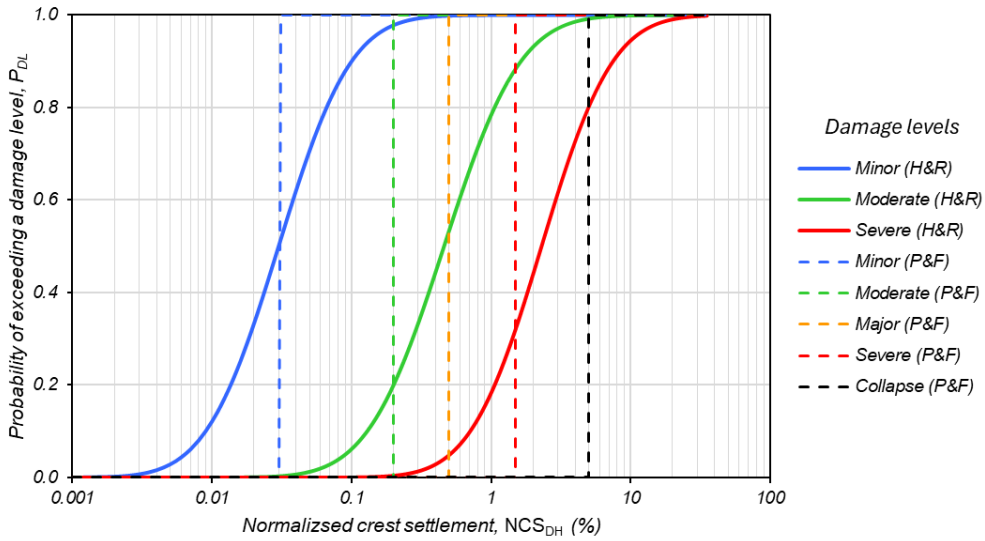


Fig. 8.2: Comparison between the probabilistic and deterministic definitions of DMs, considering the probabilistic models of He & Rathje (2024), and the deterministic limits of Pells & Fell (2003).

Although both models exhibit similarities, such as the median values for "Minor" and "Moderate" damage levels in the probabilistic model closely matching the thresholds for "Minor" and "Major" damage levels in the deterministic model, something also evident from the comparison of the NCS_{DH} from Table 8.7 and Table 8.2, the probabilistic approach accounts for the uncertainty inherent in defining the thresholds that separate the various

damage states, being more adequate for capturing the uncertainties throughout the entire process of developing fragility functions.

However, the use of probabilistic models to define the *DMs* in the most widespread methodologies for deriving fragility functions may not be as straightforward as when using deterministic limits, such as in the cases of IDA or MSA, which require sampling values for the *DMs* and then combining the resulting fragility functions for each sample through statistical analysis. Nonetheless, by adopting a methodology similar in principle to CA, as used in the HAZUS or SYNER-G models, which applies linear regression in the logarithmic domain to establish a relationship *EDP*|*IM*, known as the cloud-based Probabilistic Seismic Demand Model (PSDM), it becomes possible to combine the PSDM with the probabilistic capacity model *DM*|*EDP* to derive the fragility functions, *DM*|*IM* (Porter et al., 2007).

8.2.2 EDPs and DMs for the PFM of global instability

The potential failure mode of global instability, described in Section 4.2.2, is characterized by the presence of large unstable masses that may extend through the dam body and portions of the foundation. The selected *EDP* is the maximum displacement of the well-identified sliding masses (d_{SM}), as also considered by Regina (2021). This parameter can quantify the magnitude and severity of the sliding and provides a reasonable idea of the overall system instability.

The challenges related to this *EDP* arise primarily in defining the thresholds that establish the different *DMs*. Some criteria found in the literature relate the displacement of seismically induced slides to specific damage levels for some geotechnical structures, such as the case of road infrastructure (Silvestri et al., 2006), dikes (Atukorala et al., 2014), or small dams (Darbre, 2004). There are also criteria landslides in natural slopes (Legg & Slosson, 1984; Idriss, 1985; Saygili & Rathje, 2009), but for the case of large embankment dams, only a couple of works (Seed, 1979; Hynes-Griffin & Franklin, 1984) propose a single allowable displacement of 1 m to set a satisfactory dam performance, relying primarily on expert judgment.

Moreover, these limits are set in terms of absolute displacements independently of the size of the geotechnical structure, which is often appropriate for cases involving building or road infrastructure that cannot sustain the prescribed displacements without significant damage or service interruption, but for embankment dams, it is possible to see large dams sustain important displacements without safety concerns (Pagano et al., 2019).

Despite this, and adopting the criteria used by Regina (2021) and Vecchietti et al. (2022) to set the damage measures for displacements in large embankment dams, the two approaches considered in this work are presented below.

8.2.2.a Criterion adopted by Regina (2021) based on Hynes-Griffin & Franklin (1984)

This criterion considers the limit of maximum allowable displacement of 1 m defined by Hynes-Griffin & Franklin (1984) and Seed (1979), coincident with a "Severe" damage level, and then sets the other three smaller levels as presented in Table 8.8.

Damage level	Sliding mass displacement d_{SM} (m)
None	0.15
Minor	0.25
Moderate	0.5
Severe	1.0

Table 8.8: Damage levels considering the displacements of well-defined sliding mass as a damage measure, as adopted by Regina (2021).

These limits carry, as previously mentioned, the shortcoming of being defined in terms of absolute values and not proportional to any dimensions of the dam. This means that while these limits could be reasonable for dams of moderate height, for large dams with heights exceeding 100 or 200 m, greater displacements can be sustained without compromising on their safety, as confirmed by a few modern case histories (Guan, 2009; Lashgari & Moss, 2024).

8.2.2.b Criterion adopted by Vecchietti et al. (2022) based on Idriss (1985)

This criterion was adopted by Vecchietti et al. (2022) for the evaluation of the seismic performance of a large dam, considering the limits of maximum sliding displacement presented by Idriss (1985) and summarized in Table 8.9.

Although the limits of this criterion were originally proposed for landslides on natural slopes, they remain comparable to those previously presented and provide an additional "Collapse" limit deemed reasonable for large dams.

Damage level	Sliding mass displacement d_{SM} (m)
None	0.03
Minor	0.15
Moderate	0.30
Severe	0.90
Collapse	3.0

Table 8.9: Damage levels for the displacement of a well-defined sliding mass, adopted by Vecchietti et al. (2022) from Idriss (1985).

8.2.3 EDP and DMs for the PFM of slab damage leading to internal erosion

This potential failure mode is not as widespread in literature as the prior ones, not just for only affecting a particular type of embankment dam, but also because there is an important assumption behind stating that extensive damage to the concrete slab of a CFRD dam could trigger internal erosion mechanisms within the dam body. However, given the characteristics of Potrerillos Dam, this failure mode is worth considering.

The use of compacted alluvial soils rather than rockfill as the dam's filling material increases the susceptibility to internal erosion due to the presence of sand and fine soils that can be carried by strong seepage flows. If this is combined with an inefficient drainage system as a consequence of the extensive damage to the dam after a powerful earthquake, and the presence of transverse cracks and zones of large deformation within the dam and foundation, the hypothesis of a scouring process becomes a plausible concern.

The remaining component of the scouring process is the entry of a significant volume of water and the induction of large hydraulic gradients within the dam body, an entry that will be controlled by the damage to the impervious barriers. The complete absence of the concrete face has shown that internal erosion processes can take place, as occurred during the construction of the Tokwe-Mukorsi CFRD in Zimbabwe. During an exceptional flood event, the cofferdam was overtopped, and the main dam, still without the concrete slab, was exposed

to the rising reservoir water. Within a few hours, clear signs of backward erosion became evident in the downstream slope, as can be observed in Fig. 8.3 (Fry, 2016).



Fig. 8.3: Backward erosion after a flooding episode during the construction of Tokwe-Mukorsi CFRD, Zimbabwe (Fry, 2016).

On the other hand, the damage to the concrete face during strong earthquakes was verified in some case histories, such as Cogotí (Valenzuela et al., 2020) and Zipingpu (Ishihara, 2010) CFRDs. In both cases, the consequences of the damage in the reinforced concrete slabs did not trigger an internal erosion process, likely because in the first case, the dam was built with highly permeable rockfill not susceptible to scouring, and in the second case the water level at the moment of the earthquake was at its historical minimum of the reservoir, and the largest damage was verified over the impoundment level.

The evidence that internal erosion can occur in a CFRD built with alluvial soils in the absence of an impervious barrier, and the proof of significant damage in the concrete slab of real dams during strong earthquakes, supports the assumption that both phenomena could take place simultaneously and represent a feasible failure mode for the dam under study.

The damage of the concrete slabs of a CFRD during earthquakes has been broadly studied (Kartal et al., 2010; Qu et al., 2020; Saberi et al., 2022), but only a few works, like Pang et al. (2018), have proposed a method to set the overall damage of the slab.

The abovementioned work proposes a unique Slab Damage Index (SDI), based on the hypothesis that most of the damage induced by the earthquake to the concrete slab occurs between 0.4 to 0.9 *DH*, and that it is possible to quantify the damage for each element into which the slab is discretized in numerical analyses. The first hypothesis is supported by studies utilizing plastic constitutive models for the reinforced concrete slab along with advanced representations of the interface and cushion layer (Xu et al., 2017); while the damage of every element of the slab is set by adopting a linear elastic model and applying the criteria based on the relationship between the cumulative overstress duration (COD_S) and demand over capacity ratio (DCR_S) for the slab, widely used in the dynamic analysis of concrete dams (USACE, 2007). The definition of SDI is presented in Eq. 8.4.

$$\mathrm{SDI} = \alpha \cdot \frac{\sum_{i=1}^{n} \left(d_i \cdot S_i \cdot \frac{0.9DH - h_i}{0.25DH} \right)}{\sum_{i=1}^{n} \left(S_i \cdot \frac{0.9DH - h_i}{0.25DH} \right)} \qquad \textit{Eq. 8.4}$$

Where *DH* is the structural height of the dam, n is the number of slab elements in the range 0.4 - 0.9 *DH*, S_i and h_i are the area and elevation with respect to the bottom edge of the slab of the ith element, d_i is the damage factor of the ith element, and α is an influence factor, which can vary between 1.0-2.0, adopting a value α = 1.5 in this case. The damage levels proposed by Pang et al. (2018) for the SDI are shown in Table 8.10.

Damage level	SDI
Minor	0.03
Moderate	0.15
Severe	0.45

Table 8.10: Damage levels proposed by Pang et al. (2018) for the slab damage index (SDI).

The damage factor d_i can vary in the range of $0.0 < d_i < 1.0$ and depends on the relationship between the cumulative overstress duration (COD_S) and demand over capacity ratio (DCR_S). DCR_S is the ratio between the maximum demand verified in a structural element, in terms of stress, force, or bending moment, and its capacity. On the other hand, the COD_S is the accumulated time when the DCR_S is > 1.0. For the case of the concrete slab, Pang et al. (2018) propose considering the tensile stress to evaluate the DCR_S, as shown in Eq. 8.5.

$$\mathrm{DCR}_{S_i} = \frac{\sigma_{t_i}^{\max}}{f_t} \qquad \textit{Eq. 8.5}$$

Where $\sigma_{t_i}^{\max}$ is the maximum elastic tensile stress measured in the ith element during the dynamic analysis, and f_t is the tensile strength of the unreinforced concrete. This last could be considered proportional to the unconfined compressive stress of the concrete, following the criteria from Raphael (1984) for the tensile strength of the concrete in seismic conditions (Eq. 8.6).

$$f_t = 1.2 \cdot f_c'^{2/3} \ (\mathrm{MPa}) \qquad \textit{Eq. 8.6}$$

Adopting f'_c = 35 MPa, a tensile strength of f_t = 12.8 MPa in seismic conditions is obtained. This value of tensile strength seems to be large, but the dynamic tensile strength of the concrete can be several times larger than the static strength for important strain rates (Malvar & Ross, 1998). This large tensile strength is also justified due to the presence of the reinforcement in the slab.

In their original version, the value of d_i is supposed to be set based on Fig. 8.4. This graphic, similar to those used for concrete dams (USACE, 2007), divides the response of the concrete element into three regions based on its $\mathrm{DCR_S}$: if $\mathrm{DCR_S} < 1.0$ there is no damage in the element; if $\mathrm{DCR_S} > 2.0$ the damage is severe, and if $1.0 < \mathrm{DCR_S} < 2.0$ the damage of the element is defined by the position of the pair $\mathrm{DCR_S}$-$\mathrm{COD_S}$ on Fig. 8.4. However, the variation of the damage factor d_i based on $\mathrm{DCR_S}$-$\mathrm{COD_S}$ is not defined in the reference work, and three different options were evaluated in this work to cover this absence.

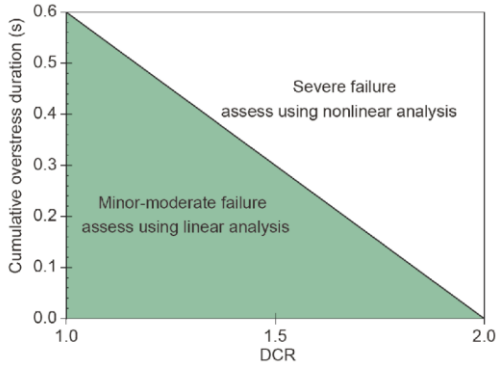


Fig. 8.4: Graphic to set the damage state of a concrete slab element based on the demand over capacity ratio ($\mathrm{DCR_S}$) and the cumulative overstress duration ($\mathrm{COD_S}$) (Pang et al., 2019).

The damage factor intends to represent the transition between the damage states of the concrete element, considering $d = 0$ when $DCR_S < 1.0$ and there is no damage, and $d = 1$ when $DCR_S > 2.0$ and severe damage is expected. For the range $1.0 < DCR_S < 2.0$, d can take values between 0 and 1, as shown in Fig. 8.5 for the two proposed variations of d.

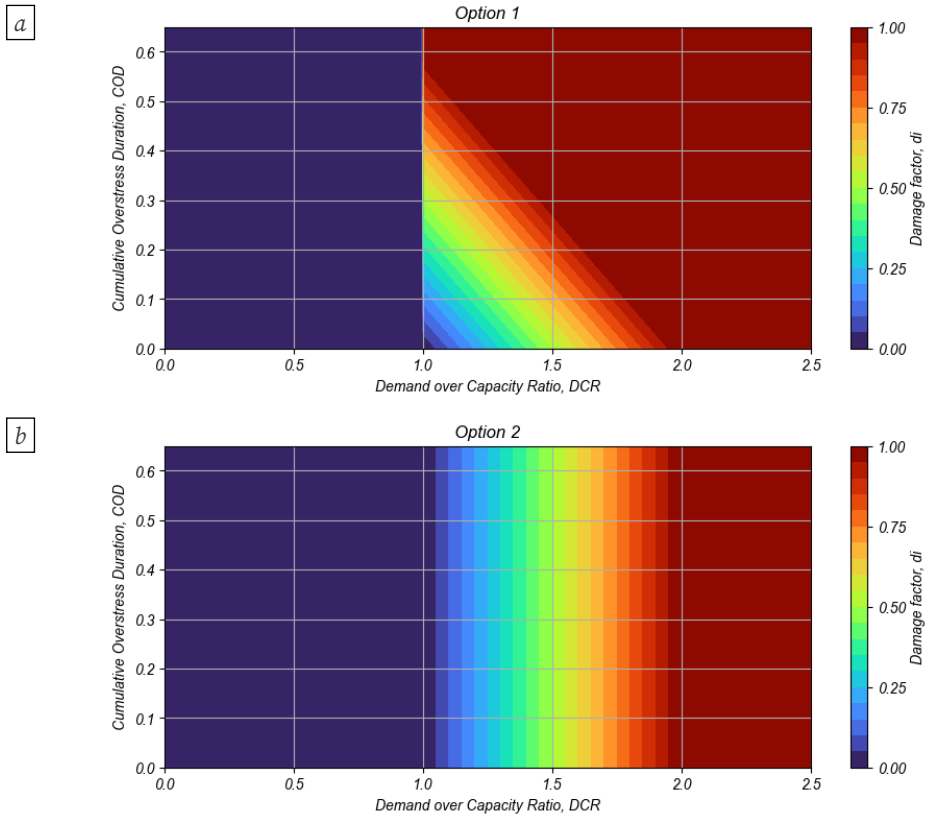


Fig. 8.5: Options for the variation of the damage factor di based on DCR_S-COD_S, a) variation parallel to the limit between severe and moderate damage, and b) variation independent of COD_S.

Option 1 from Fig. 8.5 presents a variation parallel to the limit already set by Fig. 8.4, which could be accurate since for a given DCR_S the damage factor grows with an increasing COD_S, while Option 2 shows a variation independent of the COD_S. To avoid introducing unnecessary complexity to an already intricate *EDP*, and for its inherent simplicity, Option 2 was preferred. The variation of $d(DCR_S)$ is then presented in Eq. 8.7.

$$d\left(DCR_S\right) = \begin{cases} 0.0 & 1.0 > DCR_S \\ DCR_S - 1.0 & 1.0 < DCR_S < 2.0 \\ 1.0 & DCR_S > 2.0 \end{cases} \qquad \textit{Eq. 8.7}$$

A final appraisal of the proposed *EDPs* and *DMs* involves distinguishing between "direct" and "processed" engineering demand parameters, following the classification by Whittaker et al. (2004). The *EDPs* associated with the PFMs of overtopping and global instability are categorized as "direct" *EDPs*, as they are defined in terms of physical quantities that can be directly extracted from numerical analyses. This type of *EDP* is often preferred because it can be observed and measured in real cases, thereby providing valuable input for the development of empirical damage criteria. Nonetheless, the simplicity of "direct" *EDPs* may limit their ability to capture the full range of physical processes involved in the progression of certain PFMs.

In contrast, the slab damage index (SDI) is a "processed" *EDP*, as it incorporates not only a measured physical magnitude (tensile stress) but also the capacity of the structural element (tensile strength). This type of *EDP* aims to represent the response of complex and spatially distributed phenomena that are difficult to characterize using a "direct" *EDP* alone, such as the case of the damage to the concrete face slab of a CFRD. The main shortcoming of processed *EDPs* arises when defining the associated damage measures, since the thresholds between different damage states are often not well established and may involve significant uncertainty.

Finally, the selection of engineering demand parameters and related damage measures should aim to avoid *EDPs* that are unable to capture the global response of the dam or those that are not associated with a feasible potential failure mode.

8.3 Calibration of seismic fragility functions

The process of calibrating the parameters of the lognormal distribution that define the fragility functions is carried out using two methods, with the aim of highlighting their respective advantages and disadvantages in the development of case-specific fragility functions. The objective is not to compare the fragility functions obtained from each method, as this aspect has already been extensively addressed in the literature (Jalayer et al., 2017; Miano et al., 2018), but rather to demonstrate how the same information can be used to derive fragility functions through two different approaches and for several intensity measures, when the record selection process is carefully conducted.

8.3.1 Fitting fragility functions with Multiple Stripes Analysis

The calibration of fragility functions through Multiple Stripes Analysis (MSA) is carried out using the methodology proposed by Baker (2015). In this approach, for each level of intensity measure or "stripe", the numerical analyses provide the maximum values of an *EDP*, which are then compared with the corresponding thresholds (*DMs*) to determine the number of "failures" for each damage level. The number of failures out of the number of analyses for each stripe is considered to evaluate the probability of the *EDP* exceeding the *DM,* adopting a binomial distribution. The pairs $P\,(EDP > DM \mid IM = im)$ vs. *im* for the several intensity levels are then used to fit the lognormal distribution of Eq. 3.1 using the maximum likelihood estimation method. A similar approach available in the code R2R-EU (Baraschino et al., 2020) was used to control the results.

8.3.1.a Fragility functions via MSA for the PFM of overtopping

As already mentioned, for the case of Potrerillos, the *IM* considered for deriving fragility functions using the MSA method is the spectral acceleration at the fundamental period of the dam, *Sa(0.5s)*. This *IM* was used to scale the hazard-consistent input motion utilized during the nonlinear dynamic analyses, following a regular approach for the scaling of ground motion referred to the UHS of a PSHA.

The five levels of intensity measure selected to represent the *Sa(0.5s)* of the UHS for the five return periods initially evaluated in the PSHA are presented in Table 8.11.

Return period, T_R (y)	*Sa(0.5s)* from UHS (g)
144	0.19
475	0.33
975	0.45
2475	0.64
4975	0.81

Table 8.11: Values of Sa(0.5s) for the five stripes considered for the derivation of fragility functions using the MSA approach, coinciding with the initial five T_R of the PSHA.

From the NDAs carried out and presented in Chapter 7, the permanent crest settlements for the 10 analyses corresponding with every intensity level are presented in Fig. 8.6, on a linear scale.

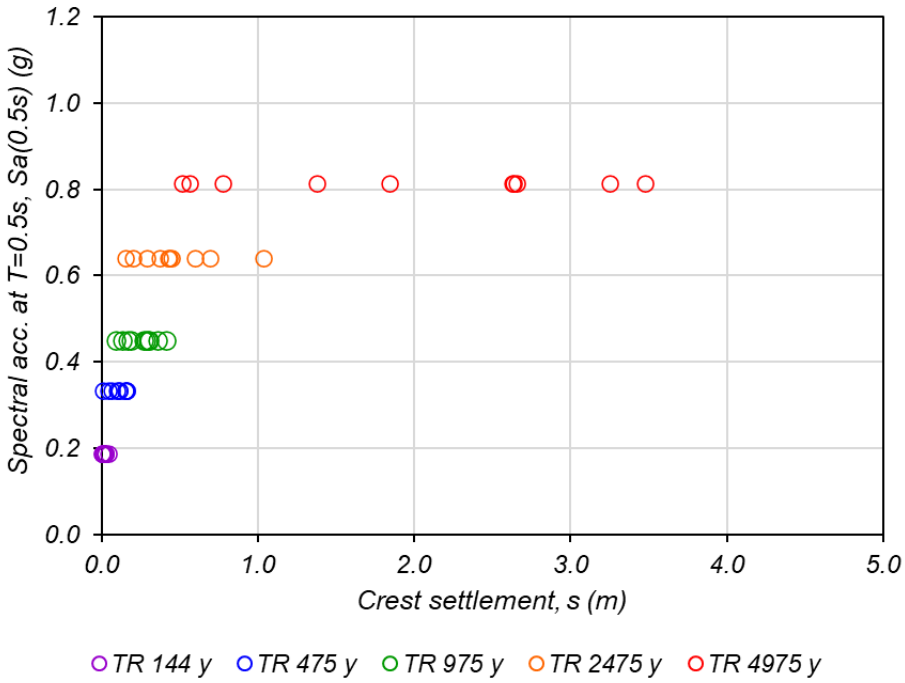


Fig. 8.6: Spectral acceleration at T = 0.5 s, Sa(0.5s), vs. permanent crest settlement for the five initial levels of the intensity measure.

This plot highlights the significant differences in permanent crest settlements observed across various intensity measure levels. To improve the representation and facilitate the comparison among the *IM* levels, it is often useful to employ a semilogarithmic scale, as illustrated in Fig. 8.7. In this figure, the previous data points are also combined with the damage levels defined according to the criterion proposed by Swaisgood (2014), thereby integrating all the necessary components for the derivation of fragility functions via MSA in a single plot: the engineering demand parameters (*EDPs*) corresponding to each *IM* level, and the damage measures (*DMs*) associated to every damage level.

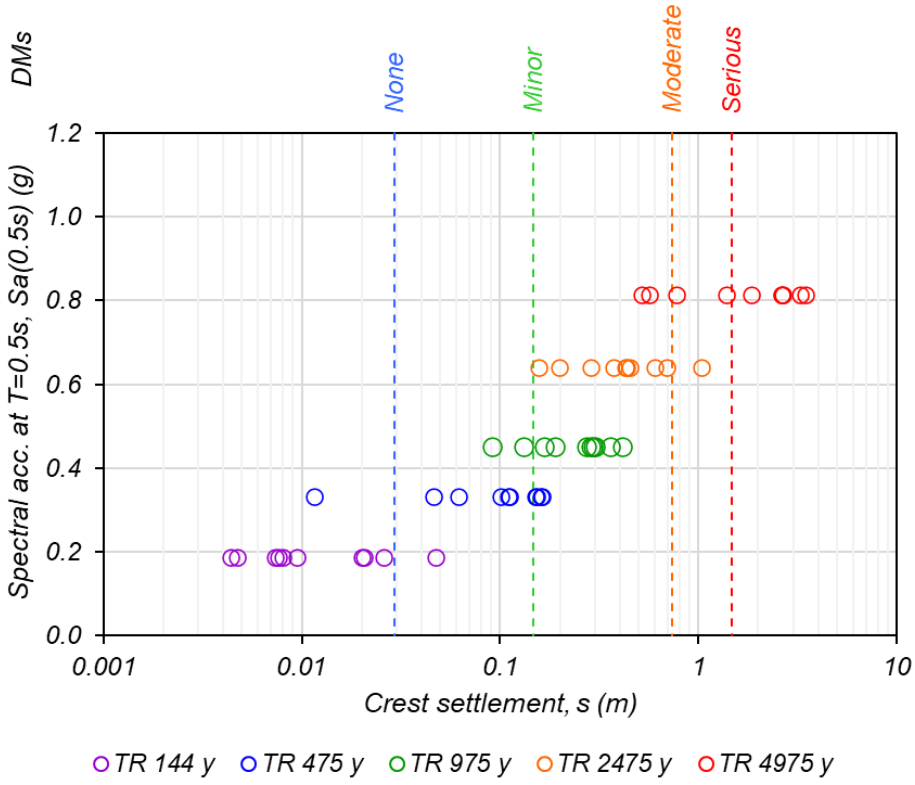


Fig. 8.7: Sa(0.5s) vs. permanent crest settlement, with the DMs from Swaisgood (2014), in semilogarithmic scale.

With this information, it is possible to fit the lognormal CDF representing the parametric fragility function. As an example, in Fig. 8.8 is presented the resulting lognormal fragility curve for the "Minor" damage level is presented, together with the data points corresponding to the pairs $P(EDP>DM \mid IM=im)$ vs. im used for the fitting. The parameters characterizing the fragility function in this case are $\theta = 0.360$ and $\beta = 0.234$, representing the median and the logarithmic standard deviation, respectively.

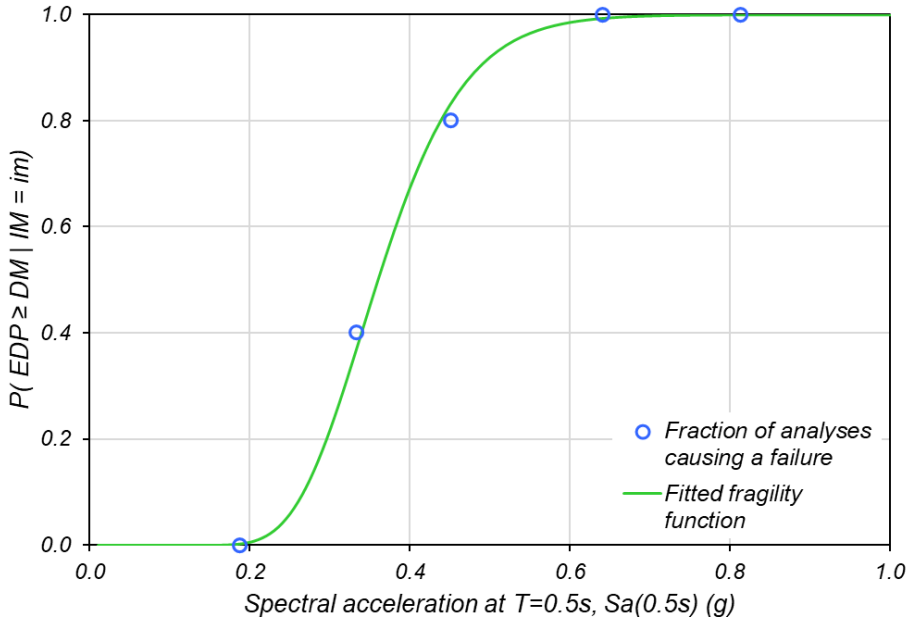


Fig. 8.8: Example of the fragility function fitting using maximum likelihood estimation, showing the points which represent P(EDP >DM | IM = im) vs im, and the adjusted lognormal CDF for the "Minor" damage level of the criterion from Swaisgood (2014).

This process can be repeated for the remaining damage levels, obtaining a first set of fragility functions for the damage criteria of Swaisgood (2014), shown in Fig. 8.9.

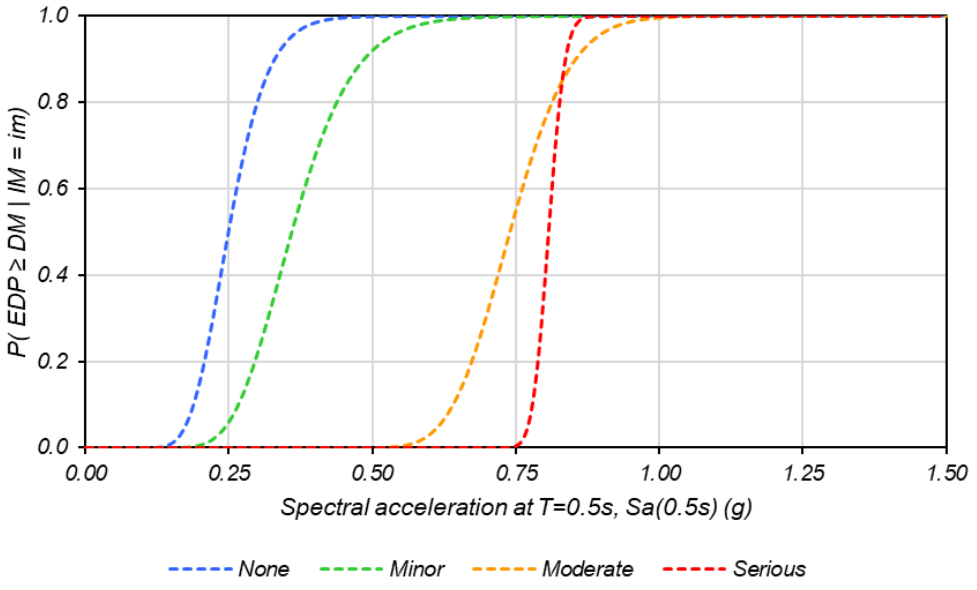


Fig. 8.9: First set of fragility functions for PFM overtopping and DMs set by Swaisgood (2014). It is evident the change in shape and apparent lower dispersion in the curve for the "Serious" damage level.

A preliminary inspection of these curves reveals a noticeable change in shape and an apparently lower dispersion for the fragility curve corresponding to the "Serious" damage level. This case illustrates one of the potential pitfalls that can arise when using the MSA method: fitting the lognormal CDF of the fragility function based on a single non-zero value for the probability of failure. This situation arises at the highest damage levels where failures tend to occur only at the largest intensity level of the *IM* (refer to Fig. 8.7), resulting in a single value of $P(EDP > DM) > 0$ available for the successive fitting.

This condition could be the consequence of a large difference between the intensity levels of the last two stripes or the result of a substantial change in the system's response to large seismic actions. It is important to note that the selection of seismic intensity levels is typically made before the seismic response of the model is known. As a result, setting the ground motion intensity level for each stripe may involve some drawbacks. In the absence of prior studies, intensity levels are often determined using simplified methods, examples from other dams, or professional judgment based on experience.

A feasible and effective solution is to add another intensity level, which increases the number of analyses but ensures a more reliable definition of the fragility for the most hazardous damage levels. This new stripe can be placed between the two highest intensity levels or set higher than the current maximum, in order to guarantee at least two points for fitting the fragility function for the higher damage levels. Simply adding more ground motions at the same intensity level may not yield different results if the response differences between the last two stripes are significant.

For this reason, the return period of 9975 years proposed by ICOLD (2016), which was initially excluded as it is typically reserved for high-risk dams, is adopted as a new intensity level. The ground motions selected for this new stripe consist of a combination of records already chosen for the return periods of 2475 and 4975 years, scaled to match the spectral acceleration at $T = 0.5$ s from the UHS for 9975 y. Table 8.12 presents the main properties of this new return period and the corresponding *Sa(0.5s)*, based on the results of the PSHA performed in Chapter 5.

Return period T_R (y)	Time window (y)	Probability of exceedance (%)	*Sa(0.5s)* from UHS (g)
9975	100	1.0	1.01

Table 8.12: Return period, time window, probability of exceedance, and Sa(0.5s) for T_R = 9975 y.

This approach for selecting the input motion is valid regarding hazard consistency as long as the disaggregation charts for the three return periods are comparable and exhibit similar ranges of mean causal magnitudes and distances. Although a new search would likely be a better option, it would also be considerably more demanding, especially given the constraints on amplitude and seismic scenario characteristics that were already challenging for the previously selected ground motions.

The response spectra for the scaled records, together with the corresponding Uniform Hazard Spectrum (UHS), are presented in Fig. 8.10. Additional information about the seismic hazard and the records for the T_R = 9975 y can be found in Appendix II.

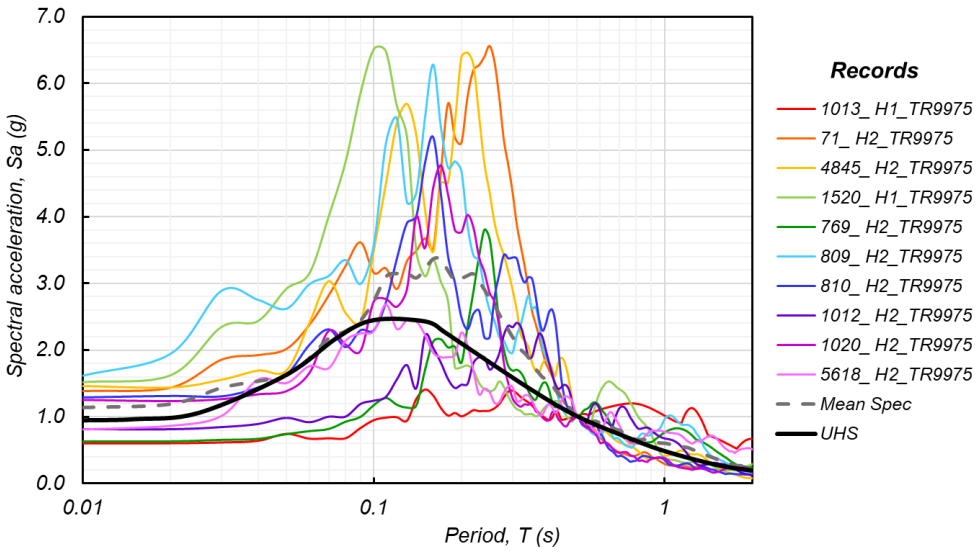


Fig. 8.10: Response spectra for the records selected and scaled for T_R = 9975 y, together with their mean spectrum and respective UHS.

By adding the results of the analyses performed for the new intensity level, the plot combining the permanent crest settlement and the damage levels for the criterion of Swaisgood (2014) is presented in Fig. 8.11.

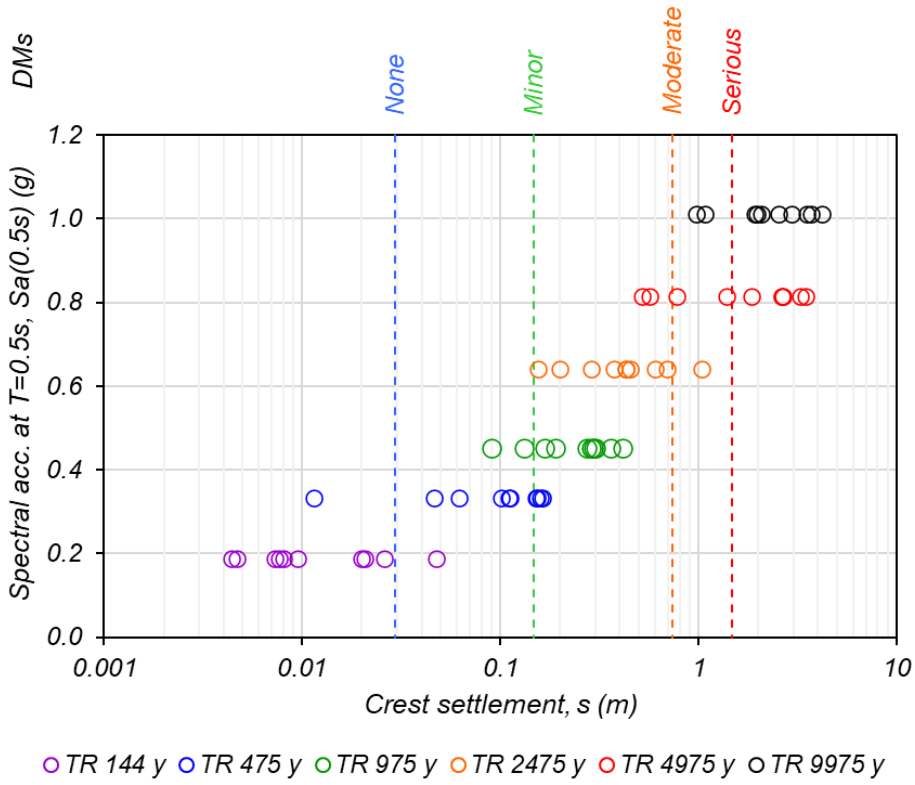


Fig. 8.11: Sa(0.5s) vs. permanent crest settlements including the results from the intensity level corresponding to T_R= 9975 y, together with the DMs from Swaisgood (2014), in semilogarithmic scale.

A second and more accurate group of fragility functions for this criterion can now be derived, as shown in Fig. 8.12, with the corresponding parameters of the lognormal CDF θ and β listed in Table 8.13. In this new set, the curves for the 'Serious' damage level have been calibrated to fit at least two non-zero values of the probability of failure, improving the definition of the fragility for this particular case.

An additional observation from the analysis of the curves in Fig. 8.12 is the presence of a spectral acceleration range around *Sa(0.5s)* ≅ 0.6 g, where the probability of experiencing "Minor" damage is relatively high, while the probability of transitioning to a "Moderate" damage remains very low. This apparent gap in the damage transition may stem from a combination of the specific thresholds defined by the selected *DM* criterion and the response of the system. As illustrated in Fig. 8.11, the permanent crest settlements intercepted by the thresholds of the "Minor" and "Moderate" damage levels correspond to different pairs of intensity levels. This highlights the influence of *DMs* thresholds on the definition of fragility functions.

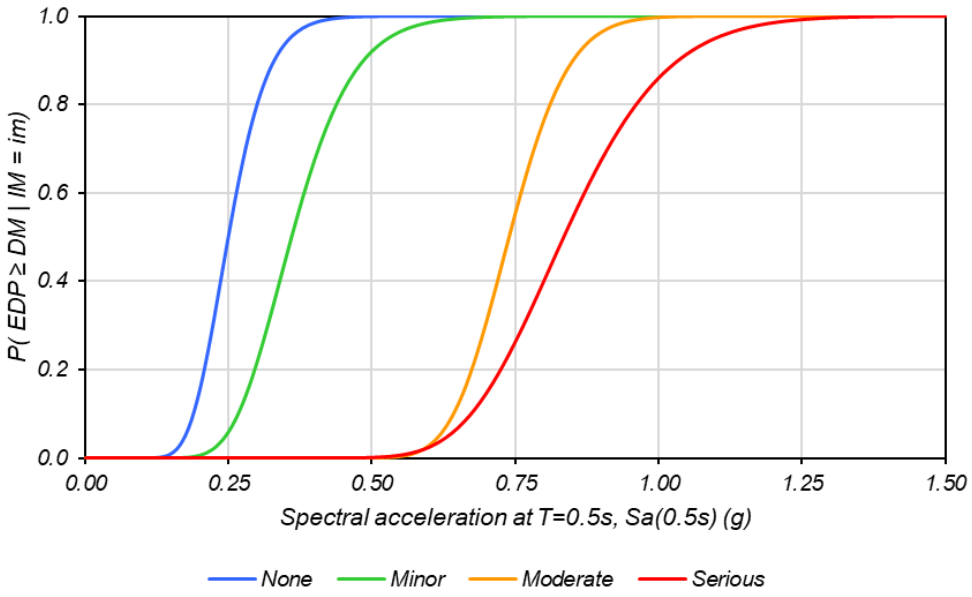


Fig. 8.12: Second group of fragility functions for the DMs proposed by Swaisgood (2014) for the PFM of overtopping, including the results of the new intensity level corresponding to T_R = 9975 y.

Damage level	θ	β
None	0.249	0.218
Minor	0.360	0.234
Moderate	0.739	0.110
Serious	0.835	0.168

Table 8.13: Parameters of the lognormal fragility functions, for the damage levels using the criterion of Swaisgood (2014), for the PFM of overtopping.

Continuing with the next definition of *DMs* for this potential failure mode, the plot containing the permanent crest settlement and damage measures for the criterion of for the criterion of Pells & Fell (2003) is presented in Fig. 8.13, while the fragility functions and their parameters are presented in Fig. 8.14 and Table 8.14 respectively.

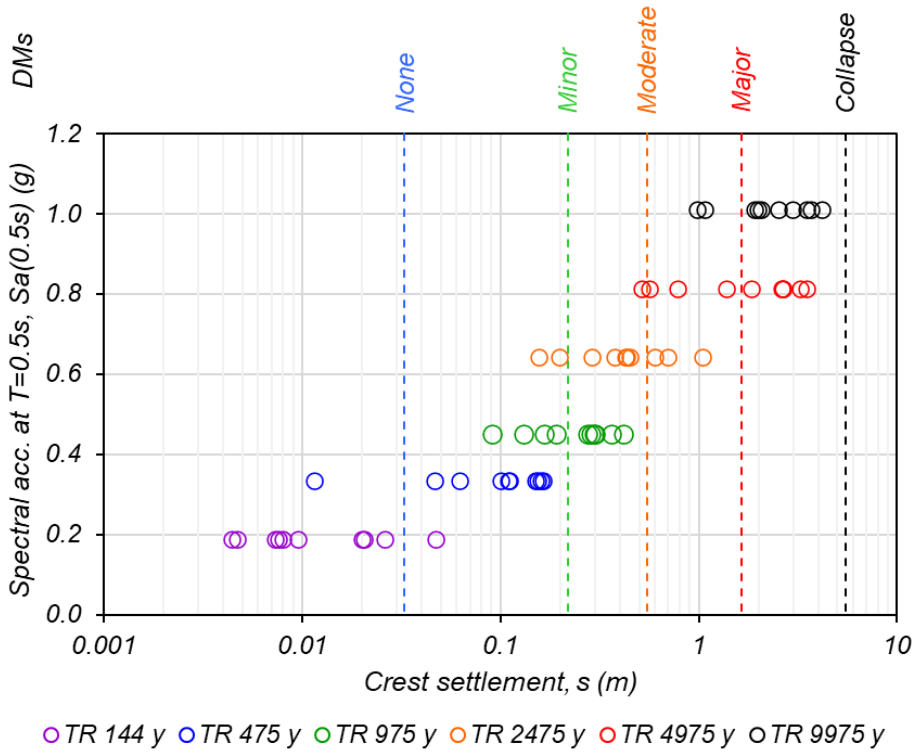


Fig. 8.13: Sa(0.5s) vs. permanent crest settlements, together with the DMs from Pells & Fell (2003), in semilogarithmic scale.

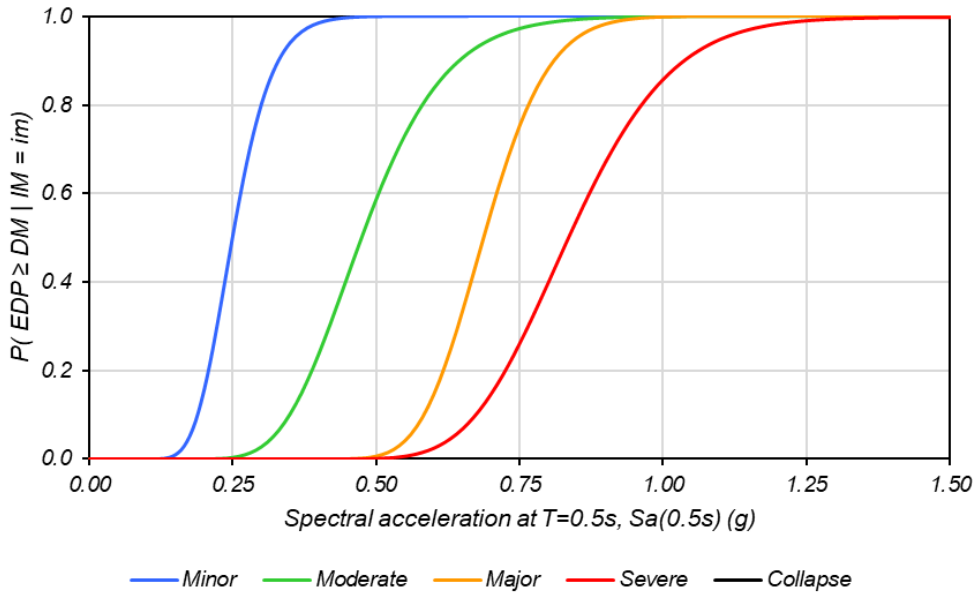


Fig. 8.14: Fragility functions for the DMs proposed by Pells & Fell (2003), for the PFM of overtopping. The "Collapse" damage set by this criterion was not achieved by any ground motion; that is the reason why there is no fragility function defined for this damage state.

Damage level	θ	β
None	0.249	0.218
Minor	0.474	0.240
Moderate	0.687	0.128
Severe	0.835	0.168
Collapse	N/A	N/A

Table 8.14: Parameters of the lognormal fragility functions, for all the damage levels established by the criterion of Pells & Fell (2003), PFM of overtopping.

For this criterion, the "Collapse" damage level is never reached (refer to Fig. 8.13), and for this reason, no fragility can be defined using the MSA approach, as noticed in Fig. 8.14 and Table 8.14. The fragility functions based on this criterion do not show the gap evidenced in the fragility obtained using the Swaisgood (2014) criterion, and this could be associated not just with the differences among damage thresholds in terms of normalized crest settlements, but also with the use of a different definition of the NCS which consider only the height of the dam (Eq. 8.2).

The next criteria evaluated are the two alternative definitions proposed by Pang et al. (2018) and Pang et al. (2019) for CFRD. The figures showing both the permanent crest settlement values and the corresponding damage measures, along with the resulting fragility functions based on the damage thresholds from Pang et al. (2018), are presented in Fig. 8.15 and Fig. 8.16, respectively. The parameters of the lognormal CDF associated with the fragility functions for each damage state are summarized in Table 8.15.

The first impression upon examining the abovementioned figures is that both the smallest and largest intensity levels are above or below the established thresholds, and the two highest damage levels are very close to each other in terms of damage measures and fragilities. This response suggests that the thresholds defined may not be linked to an evident change in seismic performance, or that an important change in response is expected in a small range of normalized crest settlement NCS_{DH+AT}.

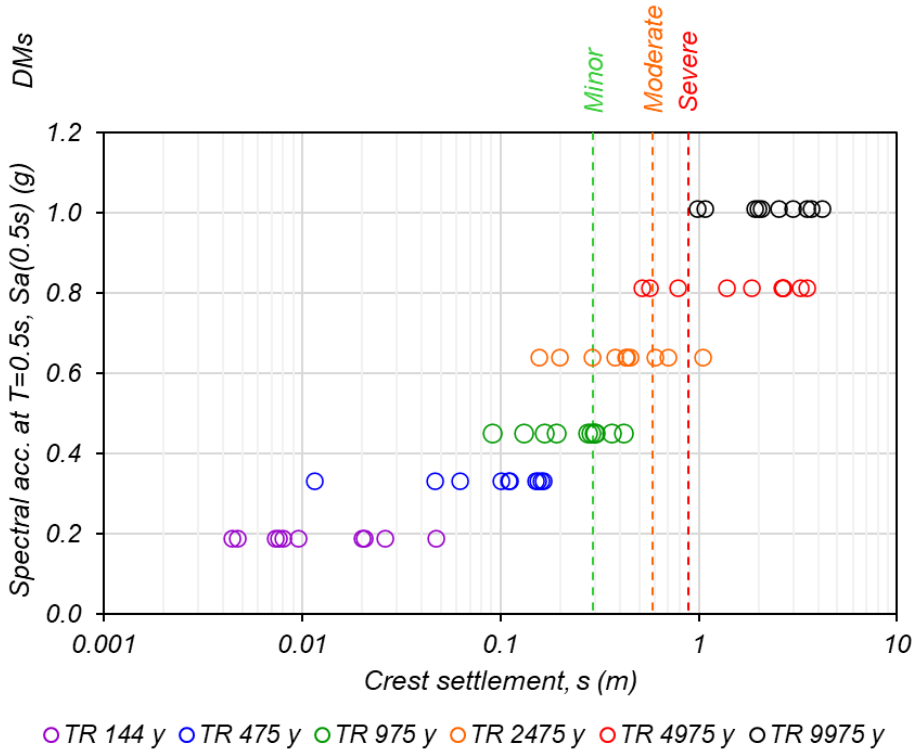


Fig. 8.15: Sa(0.5s) vs. permanent crest settlements, together with the DMs from Pang et al. (2018), in semilogarithmic scale.

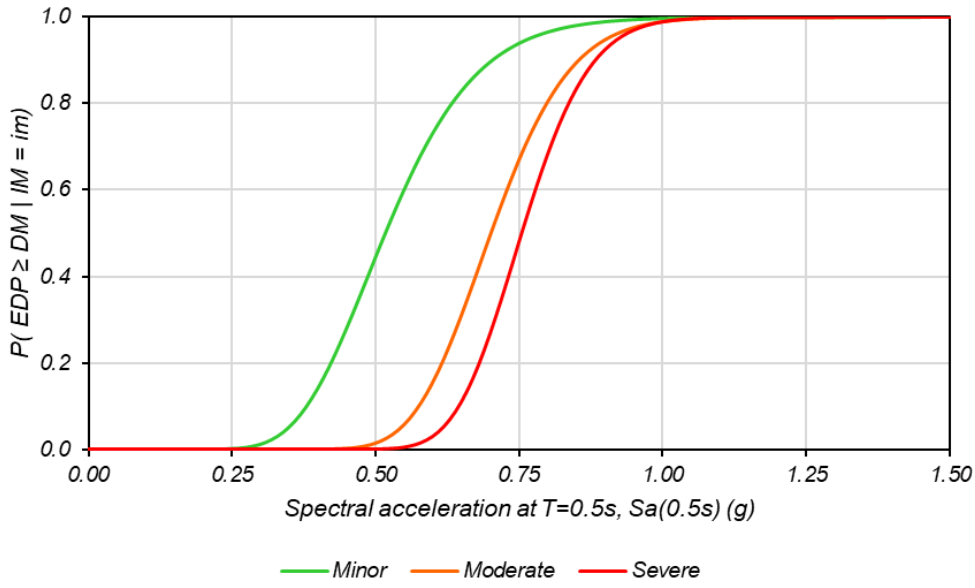


Fig. 8.16: Fragility functions for the DMs proposed by Pang et al. (2018), for the PFM of overtopping.

Damage level	θ	β
Minor	0.518	0.239
Moderate	0.702	0.153
Severe	0.755	0.122

Table 8.15: Parameters of the lognormal fragility functions, for the damage levels set by Pang et al. (2018), PFM of overtopping.

For the damage thresholds established by Pang et al. (2019), the same figures regarding the permanent crest settlements and damage measures, and subsequent fragility functions are reported in Fig. 8.17 and Fig. 8.18. The table containing the parameters θ and β of the lognormal CDF, which define the fragility functions of this criterion is summarized in Table 8.16.

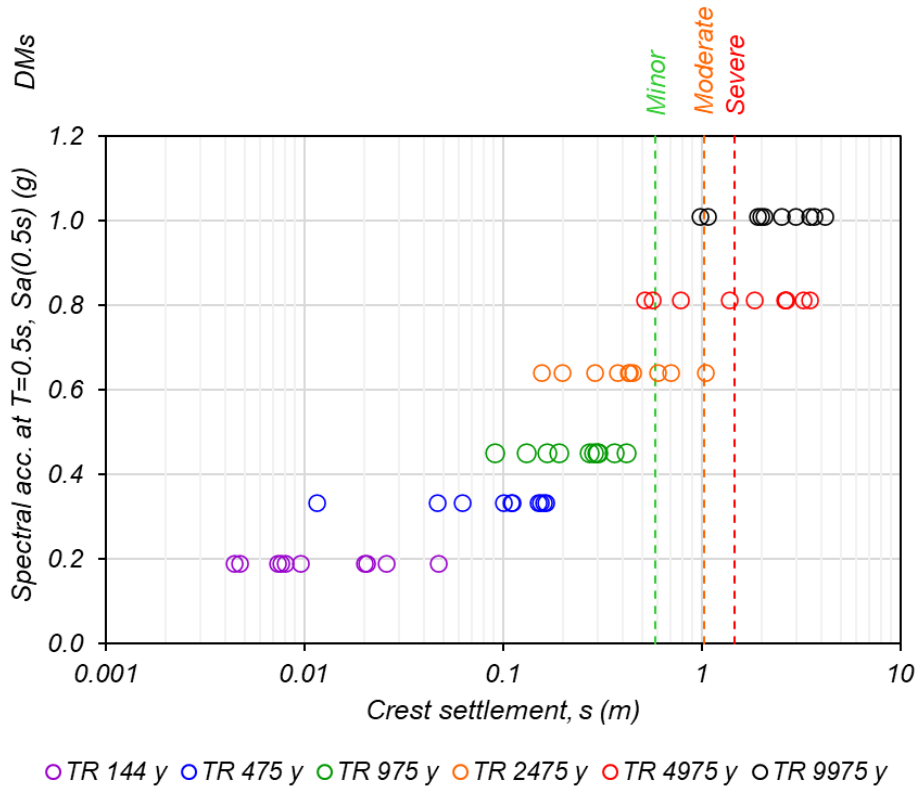


Fig. 8.17: Sa(0.5s) vs. permanent crest settlements, and the DMs set by Pang et al. (2019), in semilogarithmic scale.

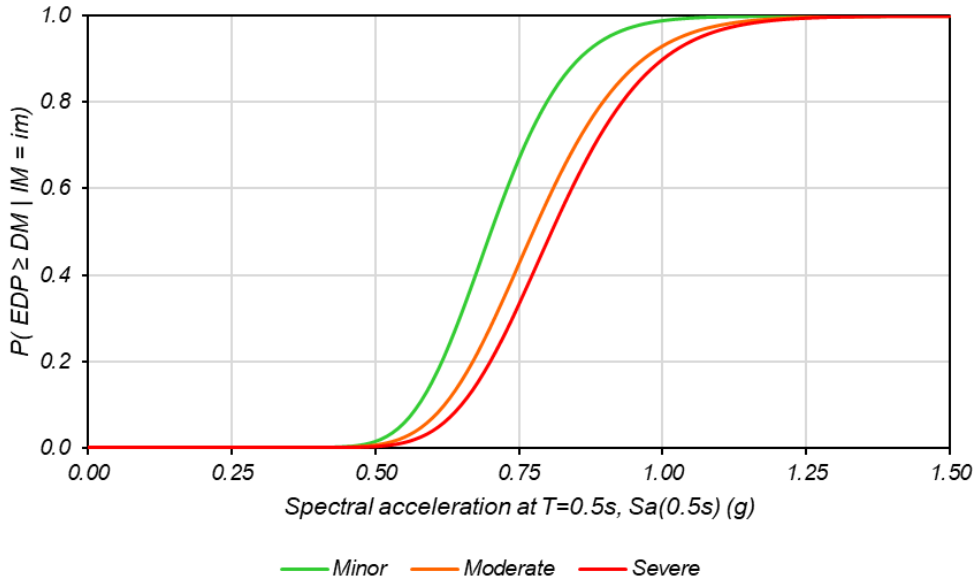


Fig. 8.18: Fragility functions for the DMs proposed by Pang et al. (2019), PFM of overtopping.

Damage level	θ	β
Minor	0.702	0.153
Moderate	0.775	0.172
Severe	0.807	0.168

Table 8.16: Parameters of the lognormal fragility functions, for the damage levels following the criterion of Pang et al. (2019), PFM of overtopping.

It is clear from the observation of Fig. 8.17 that the damage levels were moved toward larger permanent crest settlements, resulting in a displacement of the resulting fragility functions of Fig. 8.18 to larger *Sa(0.5s)*.

However, in comparison to the fragility functions shown in Fig. 8.16, this newer criterion produces fragility functions (Fig. 8.18) that are even closer to each other across the different damage states. This could once again be a consequence of defining the *EDP* threshold for each damage level without considering the expected changes in seismic performance as the seismic intensity increases. In addition, this performance in terms of fragility may reflect a dam response in which the transition from "Minor" to "Severe" damage occurs with only a small

increase in ground-shaking intensity, a response that differs significantly from the behavior expected of a modern dam and is closer to a fragile behavior.

The next criterion related to the PFM of overtopping is the one proposed by Aliberti et al. (2019), which, based on the thresholds set by Swaisgood (2003), included more case histories and re-evaluated the thresholds in terms of NCS_{DH+AT}. The points corresponding to the permanent crest settlement from each nonlinear dynamic analysis are plotted in Fig. 8.19 together with the damage measures established by this criterion.

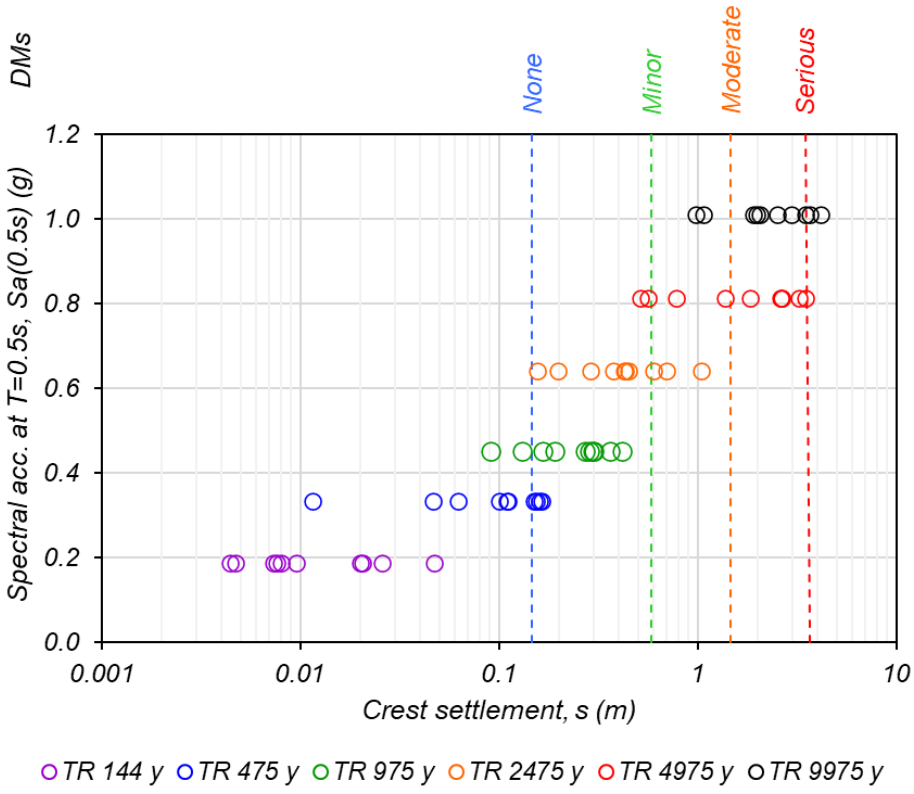


Fig. 8.19: Sa(0.5s) vs. permanent crest settlements, and DMs set by Aliberti et al. (2019), in semilogarithmic scale.

The fragility functions corresponding to these damage thresholds are reported in Fig. 8.20, while the parameters characteristics of every curve are summarized in Table 8.17.

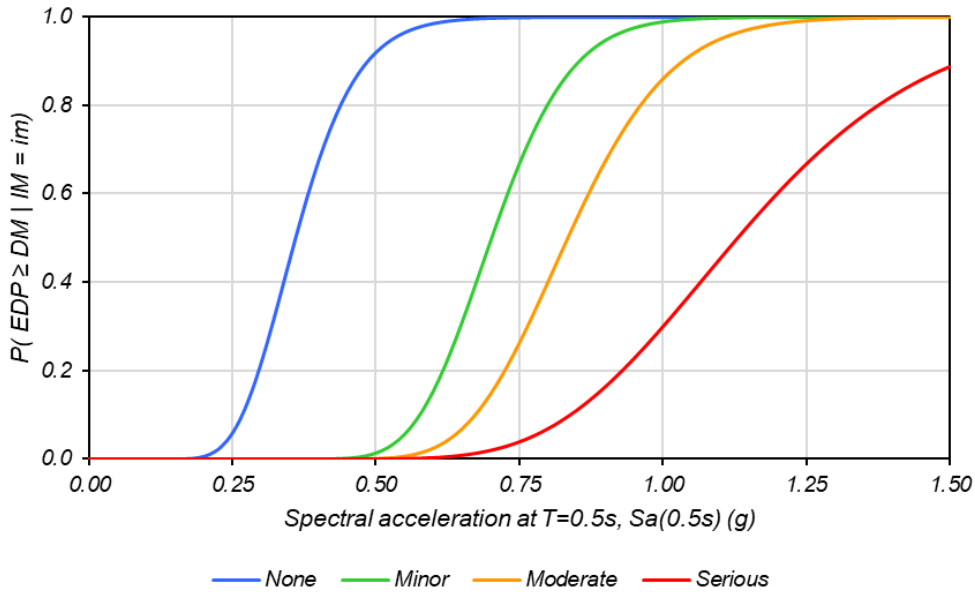


Fig. 8.20: Fragility functions for the DMs given by Aliberti et al. (2019), for the PFM of overtopping.

Damage level	θ	β
None	0.360	0.234
Minor	0.702	0.153
Moderate	0.835	0.168
Serious	1.131	0.233

Table 8.17: Parameters of the lognormal fragility function, for all the damage levels using the criterion of Aliberti et al. (2019), PFM of overtopping.

It is natural to compare the curves reported in Fig. 8.20 with respect to those presented in Fig. 8.12 related to the criterion of Swaisgood (2014), as both correspond to an updated version of the criteria of Swaisgood (2003). From the comparison of these two sets of fragility curves is evident that all the curves following the criterion of Aliberti et al. (2019) are shifted toward larger values of *Sa(0.5s)*, which is consistent with the larger thresholds set for every damage level (refer to Table 8.5).

The last definition of damage measure is based on the reduction of the dam's freeboard, using the limits established in Table 8.6. Given the large freeboard of the dam, of about 7 m, the crest settlements associated with this criterion are the largest among those linked to the PFM

of overtopping. This can also be observed in Fig. 8.21, which shows the damage measures for freeboard reduction along with the points representing the permanent crest settlement vs. *Sa(0.5s)* for each nonlinear dynamic analysis.

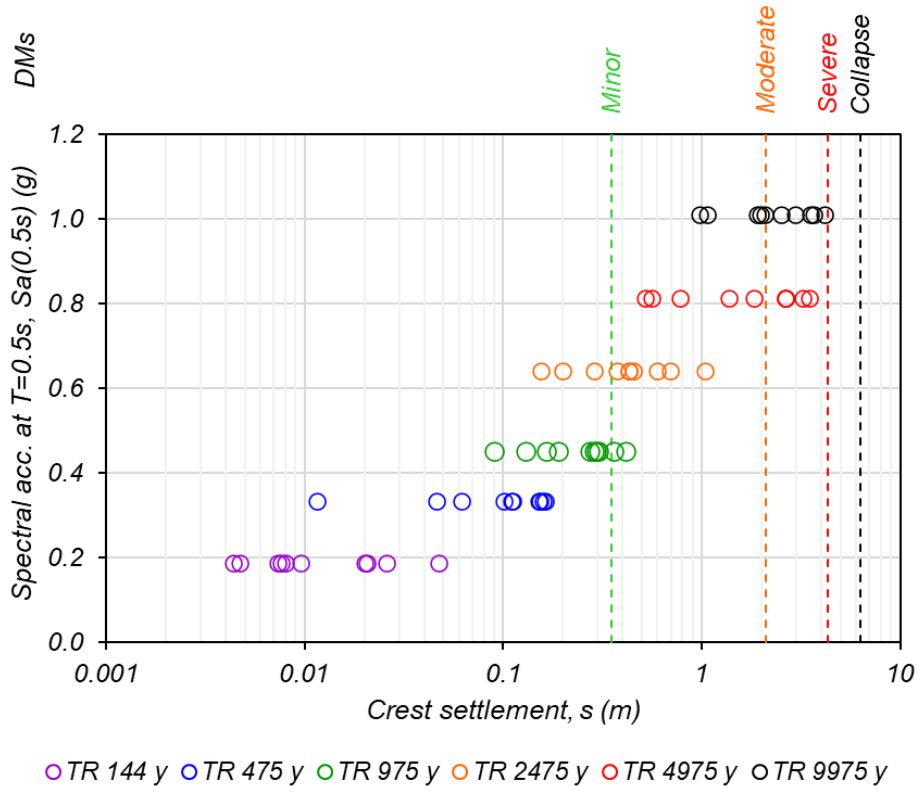


Fig. 8.21: Sa(0.5s) vs. permanent crest settlement, the DMs defined in terms of freeboard reduction, in semilogarithmic scale.

The fragility functions resulting from applying this criterion are shown in Fig. 8.22, while the parameters θ and β corresponding to the lognormal CDF representing each fragility function are reported in Table 8.18.

As could be expected, given the large damage measures set by this criterion, the two most hazardous damage levels were never exceeded, and the definition of fragility functions using the MSA approach was possible only for the “Minor” and Moderate” damage levels.

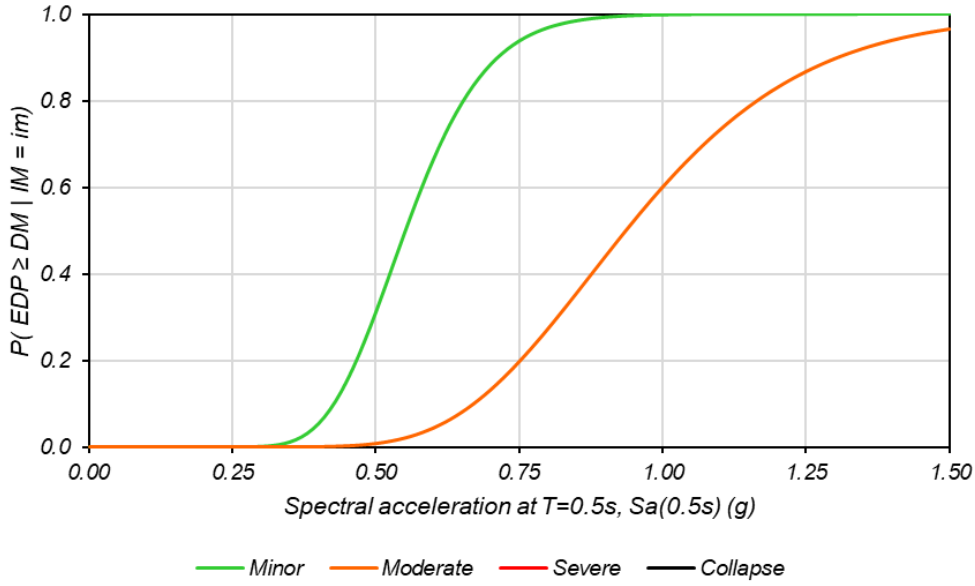


Fig. 8.22: Fragility functions for the DMs based on freeboard reduction, for the PFM of overtopping.

Damage level	θ	β
Minor	0.551	0.200
Moderate	0.936	0.260
Severe	N/A	N/A
Collapse	N/A	N/A

Table 8.18: Parameters of the lognormal fragility function, for all the damage levels using the criterion based on freeboard reduction, for the PFM of overtopping.

The fragility established by this criterion set an upper limit for the fragilities evaluated for this potential failure mode, as can be observed in Fig. 8.23, where a comparison between the fragility functions corresponding to the "Moderate" damage level of all the criteria is presented. From the analysis of Fig. 8.23 is evident the dispersion in what is considered a "Moderate" damage for each criterion, at least for this particular intensity measure.

These differences highlight the inconsistency in how damage levels are defined across the different criteria, and more importantly, the absence of a common procedure for establishing damage measures.

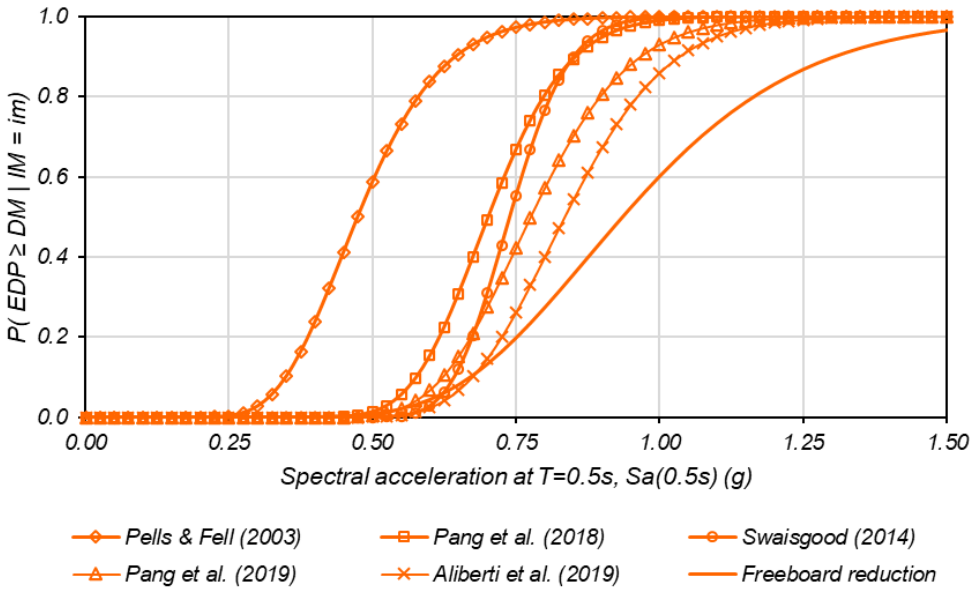


Fig. 8.23: Fragility functions for the "Moderate" damage level, for all the criteria corresponding to the PFM of overtopping.

The probabilistic definition of the *DMs* proposed by He & Rathje (2024) will not be evaluated using the MSA methodology, and will instead be considered for the calibration of fragility functions through Cloud Analysis, where its incorporation is simpler.

8.3.1.b Fragility functions via MSA for the PFM of global instability

The evaluation of fragility functions using the multiple stripe analysis for the potential failure mode of global instability will consider two criteria for defining the damage measures, both of which have already been used in the literature for the fragility assessment of large dams.

Both criteria define the different damage levels in relation to the displacement of a well-defined sliding mass (d_{SM}) that includes the dam body and, depending on site conditions, a portion of the foundation. However, as briefly discussed in Section 8.2.2, the limits established for these criteria in terms of absolute displacement, rather than displacements normalized with respect to the dam's dimensions, could be considered conservative beforehand, given the evidence of larger displacements without significant damage in case histories.

The first criterion, adopted by Regina (2021) and using as a base the allowable displacement proposed by Seed (1979) and Hynes-Griffin & Franklin (1984), is presented in Fig. 8.24 together with the points of displacement of a sliding mass d_{SM} vs. *Sa(0.5s)*.

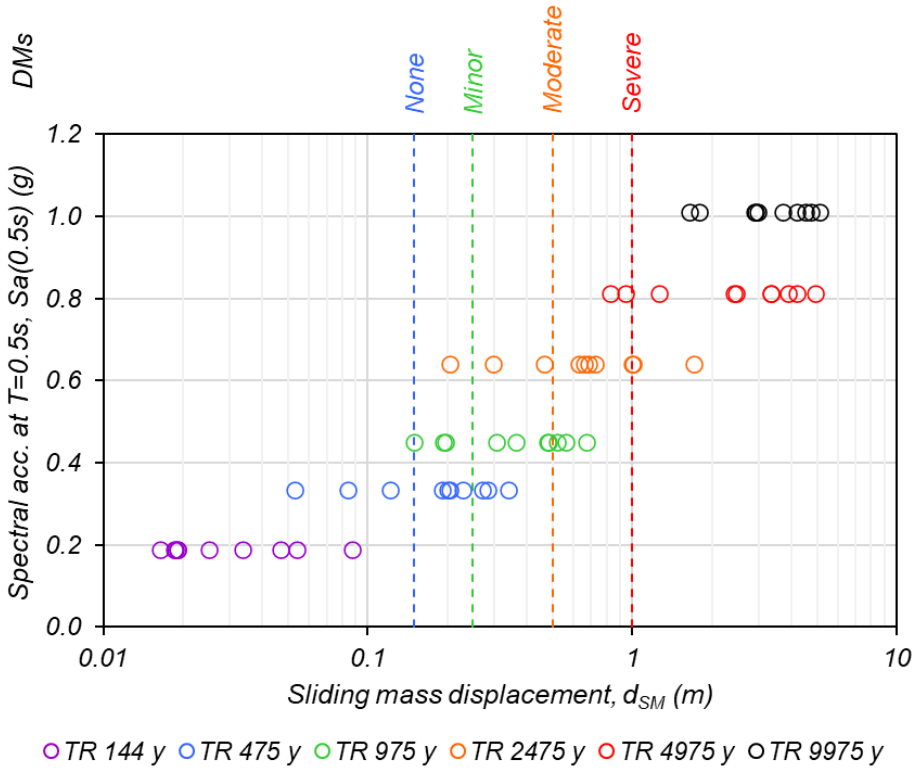


Fig. 8.24: Sa(0.5s) vs. displacement of a well-defined sliding mass, together with the DMs defined in terms of the criteria adopted by Regina (2021), in semilogarithmic scale.

The fragility functions and the parameters of the lognormal CDF that represent them are presented in Fig. 8.25 and Table 8.19, respectively, for the abovementioned criterion.

From the evaluation of Fig. 8.25 can be noticed that the uniform distribution of the thresholds (refer to Table 8.8) is also reflected in the distribution of fragility functions. It is also evident that the abovementioned conservativism is behind this criterion if the fragility functions are compared to the fragility functions for the PFM of overtopping.

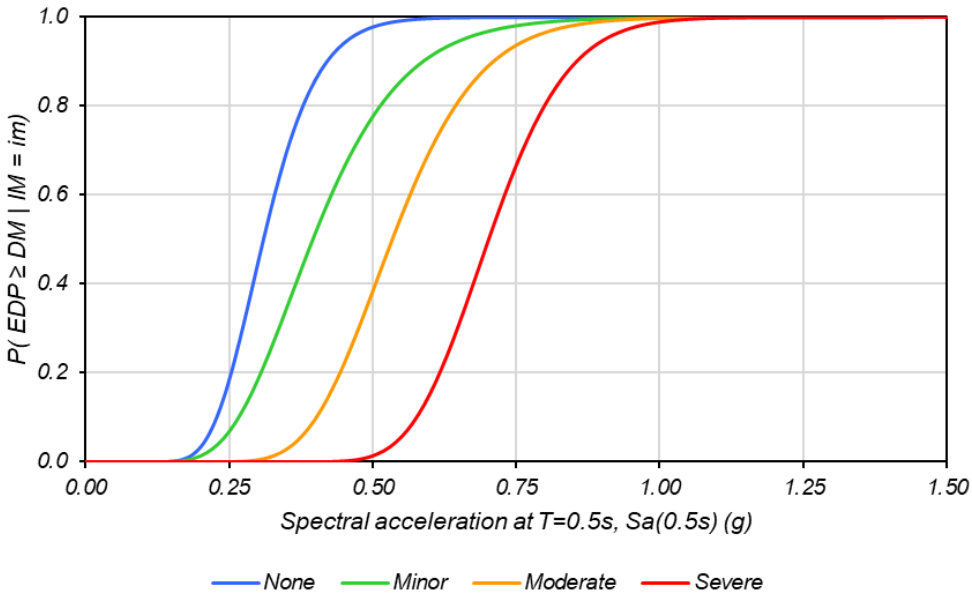


Fig. 8.25: Fragility functions for the DMs based on the criterion adopted by Regina (2021), for the PFM of global instability.

Damage level	θ	β
None	0.310	0.237
Minor	0.396	0.308
Moderate	0.534	0.222
Severe	0.702	0.153

Table 8.19: Parameters of the lognormal fragility function, for all the damage levels using the criterion adopted by Regina (2021), PFM of global instability.

The second criterion considered for the PFM of global instability is the one adopted by Vecchietti et al. (2022) for a large embankment dam, based on the damage thresholds established by Idriss (1985). The displacements of a well-defined sliding mass for every nonlinear analysis carried out are plotted in Fig. 8.26 together with the damage measures previously mentioned. From a simple comparison with Fig. 8.24 is evident that the thresholds for this second criterion cover a wider range of displacements, but the limits for the common damage level are lower than the criterion adopted by Regina (2021). The fragility function resulting from the use of this criterion is presented in Fig. 8.27.

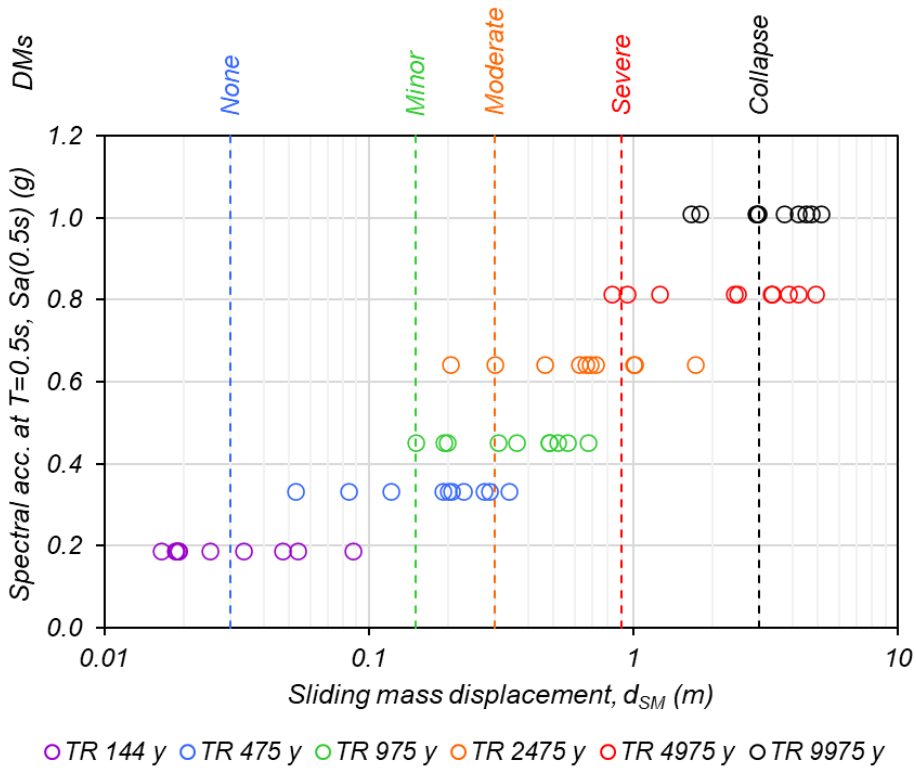


Fig. 8.26: Sa(0.5s) vs. displacement of a well-defined sliding mass, together with the DMs defined in terms of the criteria defined by Idriss (1985), in semilogarithmic scale.

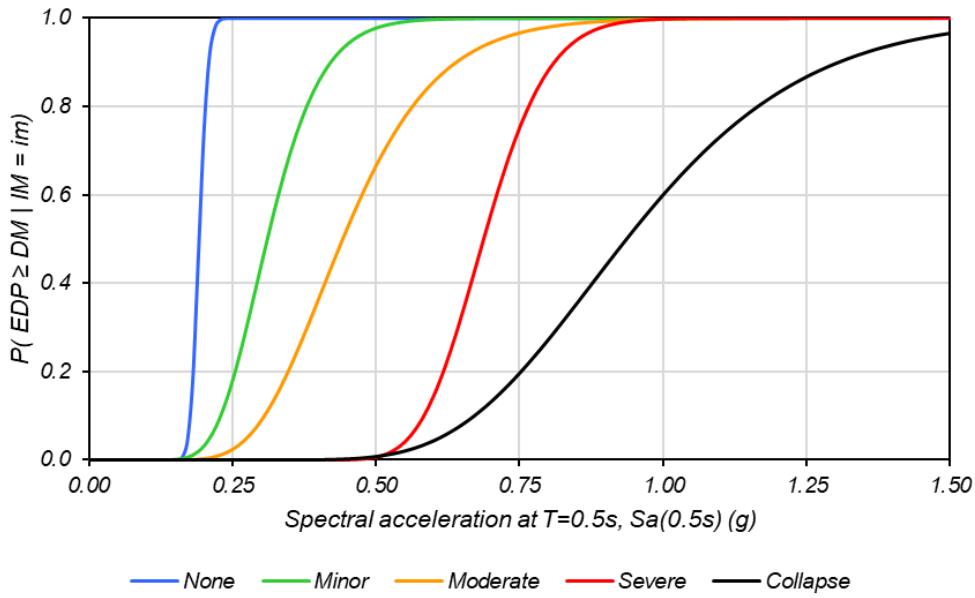


Fig. 8.27: Fragility functions for the DMs defined by Idriss (1985), for the PFM of global instability.

Table 8.20 presents the parameters of the lognormal CDF corresponding to each fragility function from Fig. 8.27.

Damage level	θ	β
None	0.191	0.066
Minor	0.310	0.237
Moderate	0.441	0.289
Severe	0.687	0.128
Collapse	0.936	0.260

Table 8.20: Parameters of the lognormal fragility function, for all the damage levels using the criterion defined by Idriss (1985), for the PFM of global instability.

The curves corresponding to the two groups of *DMs* for the PFM of global instability are then presented in Fig. 8.28. It is evident that the curves constructed following the criterion from Idriss (1985) are more conservative than those following the damage thresholds set by Regina (2021), with the exception of the "Collapse" damage level, only present in the first one.

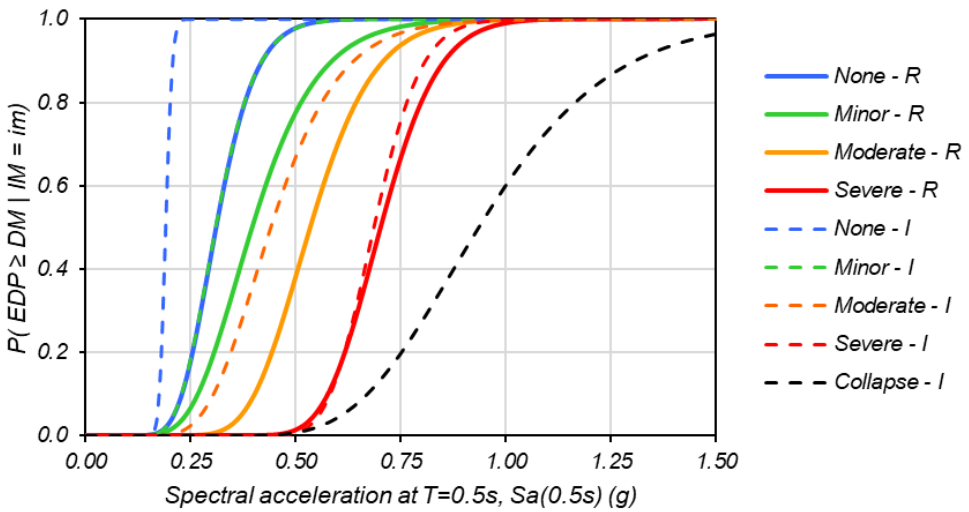


Fig. 8.28: Fragility functions for the two sets of DMs corresponding to the PFM of global instability. "R" stands for Regina (2021) criterion, whereas "I" stands for Idriss (1985) criterion.

8.3.1.c Fragility functions via MSA for the PFM related to slab damage

The last group of fragility functions derived using the MSA approach is those corresponding to the PFM of damage on the reinforced concrete slab, followed by internal erosion. These fragility functions consider the Slab Damage Index (SDI) previously defined in Section 8.2.3 as *EDP*, and the spectral acceleration at the period T=0.5 s as *IM*.

The points representing the values of SDI vs. *Sa(0.5s)* and the DMs proposed by Pang et al. (2018) for the damage thresholds in terms of SDI are reported in Fig. 8.29.

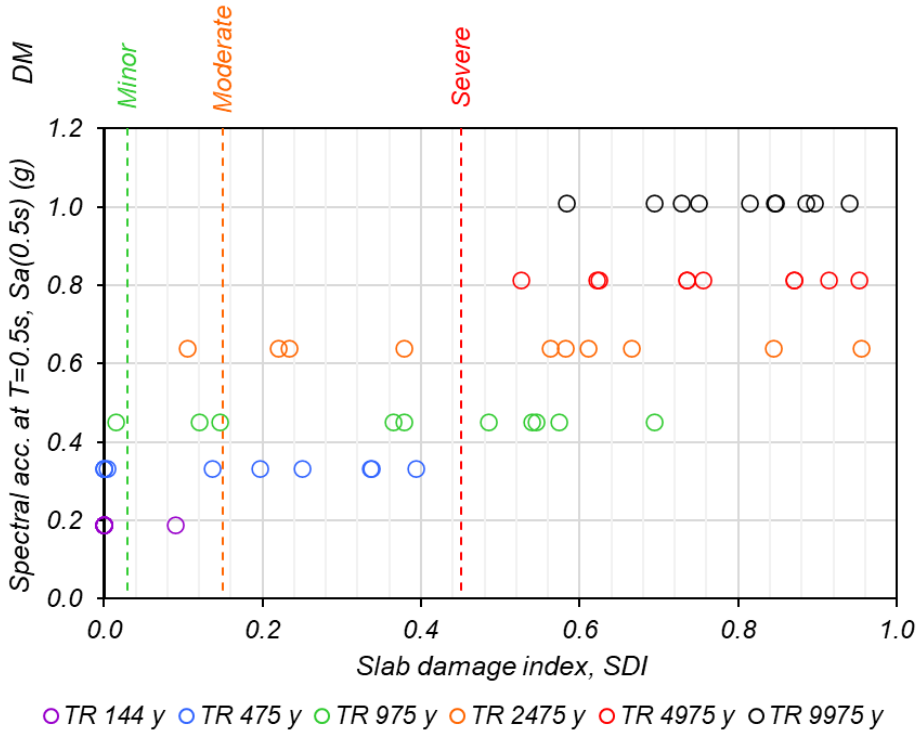


Fig. 8.29: Sa(0.5s) vs. slab damage index (SDI), together with the DMs defined by Pang et al. (2018).

The first impression from examining Fig. 8.29 is that the dispersion of the SDI decreases with increasing ground motion intensity. Additionally, the thresholds proposed by Pang et al. (2018) appear somewhat conservative, as the threshold corresponding to the "Severe" damage level is placed below all the data points for the two highest intensity levels. Moreover, the limits established by similar definitions of the damage index for gravity dams, which were the base for the SDI, report larger thresholds of their respective damage indexes (Hariri-Ardebili & Saouma, 2015; Ansari & Agarwal, 2016)

The fragility functions resulting from applying the abovementioned damage measures are presented in Fig. 8.30, and their characteristic parameter are summarized in Table 8.21.

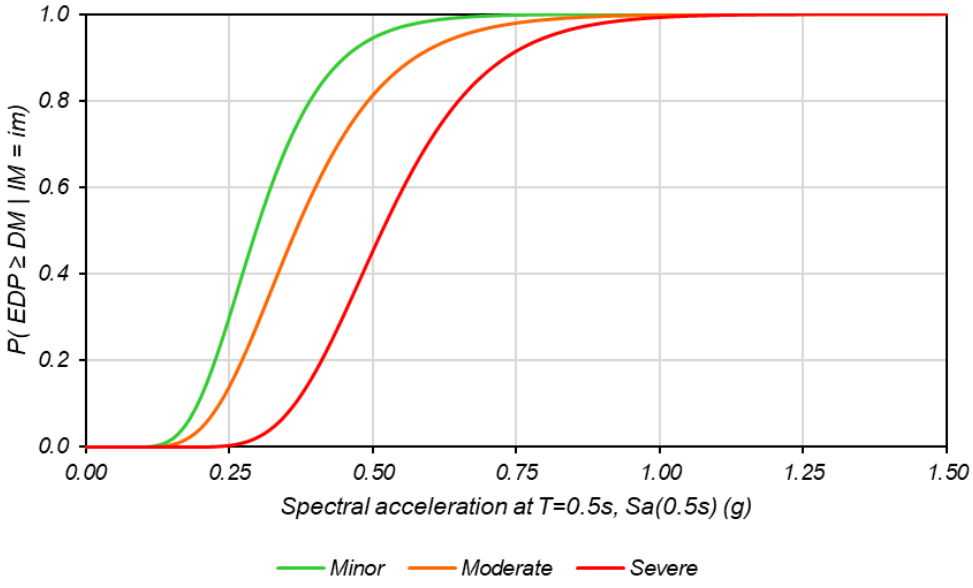


Fig. 8.30: Fragility functions for the PFM of slab damage followed by internal erosion, considering the DMs established by Pang et al. (2018).

Damage level	θ	β
Minor	0.296	0.328
Moderate	0.366	0.353
Severe	0.516	0.273

Table 8.21: Parameters of the lognormal fragility functions, for the PFM slab damage followed by internal erosion, using the DMs set by Pang et al. (2018).

It is evident from a simple inspection of the curves of Fig. 8.30 that the fragility functions related to this PFM are more conservative than for the remaining failure modes. This can be further evidenced by plotting together the fragility functions for the "Severe" damage level from one case of every PFM, as presented in Fig. 8.31.

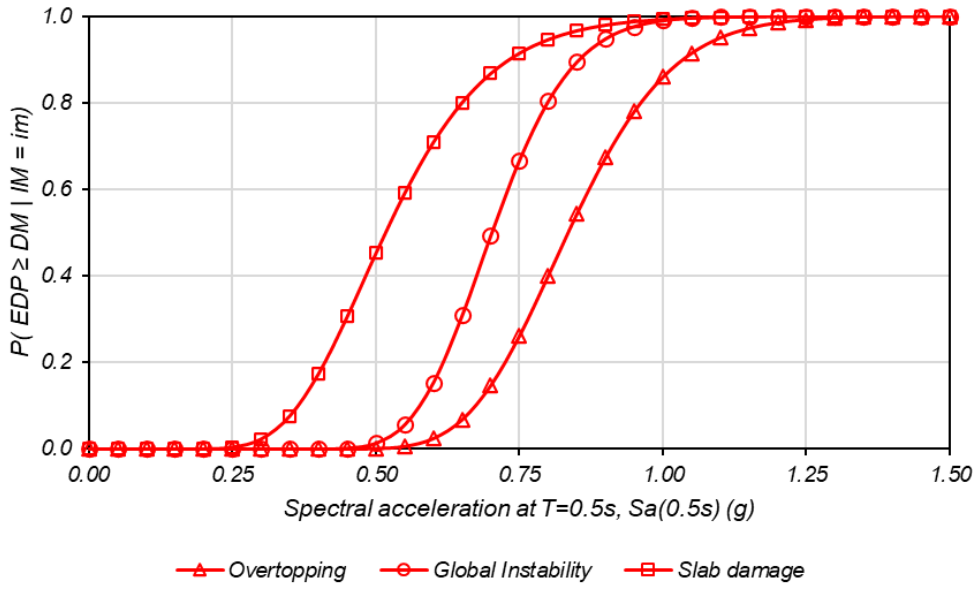


Fig. 8.31: Fragility functions for the "Severe" damage level, for three PFM considering the criteria of Swaisgood (2014) for overtopping, Regina (2021) for global instability, and Pang et al. (2018) for slab damage.

8.3.2 Fitting fragility functions with Cloud Analysis for alternative *IMs*

The second method used to derive fragility functions is the Cloud Analysis (CA), in its variant developed by Jalayer et al. (2015), and further improved (Jalayer et al., 2017) to include a robust approach for deriving the fragility and the possibility of introducing cases of dynamic instability. This method consists, in its most basic formulation, of performing a linear regression in logarithmic space to obtain a probabilistic model for predicting the performance variable, in terms of the demand-to-capacity ratio (DCR_{CA}), given the intensity measure (*IM*) of the ground motion. Following the notation adopted, the DCR_{CA} can be defined as the ratio between the engineering demand parameter (*EDP*) representing the demand, and the damage measure (*DM*) as the capacity (Eq. 8.8).

$$DCR_{CA} = \frac{EDP}{DM} \qquad \textit{Eq. 8.8}$$

The demand-to-capacity ratio formulated in this way represents a "failure" case when $DCR_{CA} \geq 1$. For this reason, this ratio is suitable as a performance variable, and its prediction can be related to the fragility of the structure analyzed. Eq. 8.8 also highlights that this version of Cloud Analysis is suited for the use of deterministic *DMs*. In cases where a probabilistic definition of the damage measures is adopted, it is more appropriate to develop a cloud-based

Probabilistic Seismic Demand Model (PSDM), which can then be combined with a probabilistic capacity model to obtain the resulting fragility curves.

Regarding record selection, CA is convenient for use with unscaled records, since its formulation was developed to address the strong dependence of other methods on ground motion scaling. However, at least three conditions have to be considered when selecting the ground motions:

- The records should be selected to cover a wide range of ground motion intensities, aiming to obtain a well-suited point cloud and a smaller standard error in the estimation of the log-scale regression slope.
- The records should be selected in such a way that a significant portion of the records, ideally more than 30%, have a $DCR_{CA} \geq 1$ in order to prevent extrapolation in regression.
- If possible, avoid selecting the two components of the same ground motion, as well as several records from the same event, in order to prevent low variability in the characteristics of the ground motions (frequency content, duration, etc.).

However, the use of unscaled records attempts to assess the hazard consistency of the ground motions, as the selection can be based on terms of the seismic scenarios defined by the disaggregation charts, but the agreement with the forecasted intensity of the ground shaking is omitted.

In this work, the record selection and scaling were conducted with attention to hazard consistency, both in terms of the seismic scenario and the level of ground shaking. Although records from the same ground motion and seismic event were included, the intention was to scale them to different intensity levels in order to reduce potential similarities in their specific characteristics.

In addition, since the scaling was performed only at *Sa(0.5s),* the amplitude of the remaining ground motion parameters is not constrained, and the resulting distribution of values for alternative *IMs* across all intensity levels is wide enough to support their use in developing fragility functions using CA. Moreover, with the inclusion of the intensity level corresponding to T_R = 9975 y, a significant portion of analyses with $DCR_{CA} \geq 1$ is likely even for the highest damage levels.

Then, the intensity measures considered for the Cloud Analysis will be, other than the peak ground acceleration (*PGA*), those expected to be better suited to capture the dynamic

response of geotechnical systems: peak ground velocity (PGV), Arias intensity (I_A), cumulative absolute velocity (CAV), and Housner intensity (I_H).

On the other hand, just some selected definitions of the *DMs* will be used for deriving fragility using the CA method. For the PFM of overtopping will be adopted the deterministic criteria from Swaisgood (2014), and the probabilistic capacity model from He & Rathje (2024), while for the global instability will be used the criteria adopted by Regina (2021). The PFM of slab damage will not be considered for deriving fragility using CA, as the point cloud data is not structured in a manner suitable for this approach.

To illustrate the calibration procedure using CA, the point cloud corresponding to the pairs PGA vs. DCR_{CA} for the "Moderate" damage level of the criterion of Swaisgood (2014) is presented in logarithmic scale in Fig. 8.32, together with the fitted lognormal CDF that represent the fragility function, considering an interval of confidence of one standard deviation β. The resulting fragility function is plotted in Fig. 8.33.

The procedure by which CA derives fragility functions is not as evident as in the case of MSA, but it is statistically consistent and easy to apply, as it utilizes a simple linear regression. Other than the difficulties guaranteeing hazard consistency in the record selection, one of the shortcomings of the CA method is the assumption of homoscedasticity, that is, assuming constant dispersion in the regression model across the range of IM. Depending on the nonlinear response of the system, this assumption may not be adequate and may bring less reliable fragility functions (Chen, 2025). However, this assumption is reasonable when the point cloud shows limited and uniform dispersion, and when the IM values are uniformly distributed across the whole range of intensity levels. This requires control over the records used as input motions and the results from the analyses before applying the regression, in order to obtain reliable fragility curves.

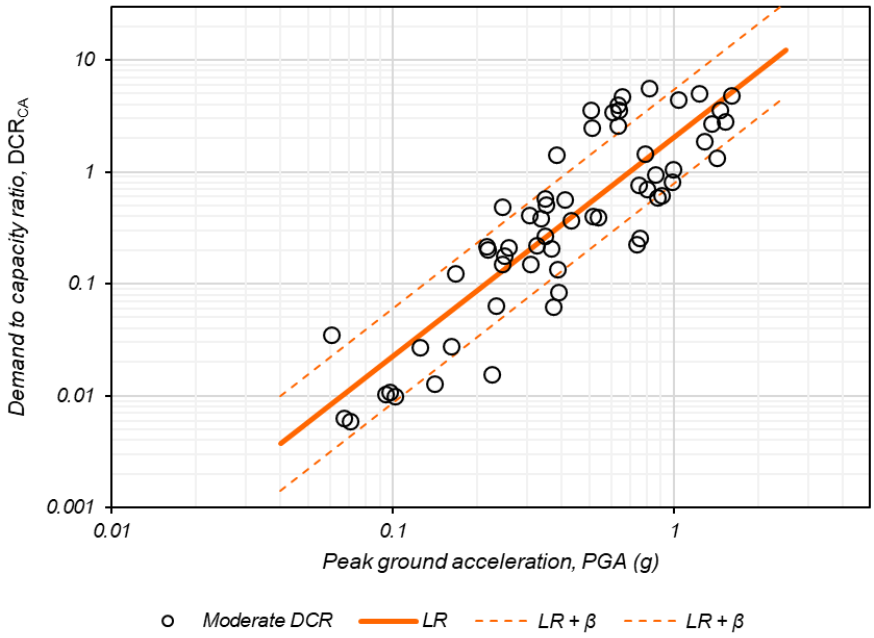


Fig. 8.32: Linear regression in logarithmic space to obtain the fragility function using CA, for the "Moderate" damage level of the criterion of Swaisgood (2014), PFM of overtopping, and PGA as intensity measure. LR stands for Linear Regression, whereas β is the logarithmic standard deviation.

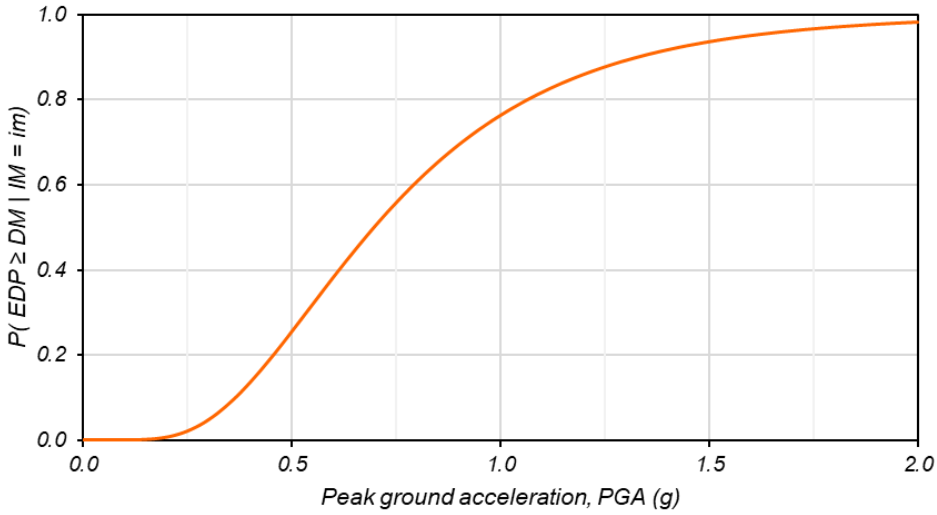


Fig. 8.33: Fragility function via CA for the "Moderate" damage level defined by Swaisgood (2014), PFM of overtopping, and the PGA as intensity measure.

The first group of fragility functions using the CA methodology pertains to the PFM of overtopping using the damage threshold set by Swaisgood (2014). For a better arrangement of the figures, they are split into two groups. Fig. 8.34 contains the fragility functions for the

peak intensity measures *PGA* and *PGV*, whereas Fig. 8.35 presents the fragility curves for the three integral intensity measures I_A, *CAV*, and I_H. The parameters of the lognormal CDF θ and β for every curve are summarized in Table 8.22.

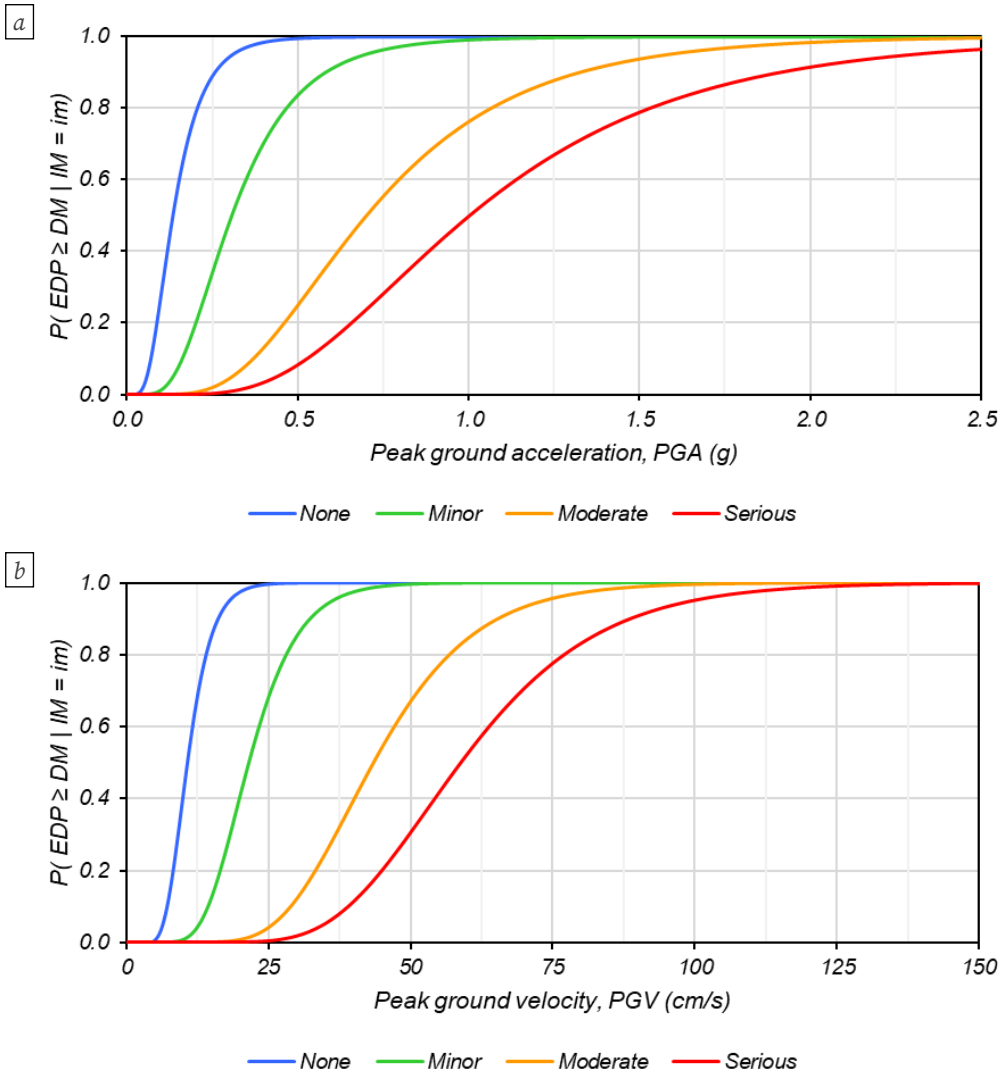


Fig. 8.34: Fragility functions via CA for the PFM of overtopping and DMs defined by Swaisgood (2014), considering two peak intensity measures: a) PGA, and b) PGV.

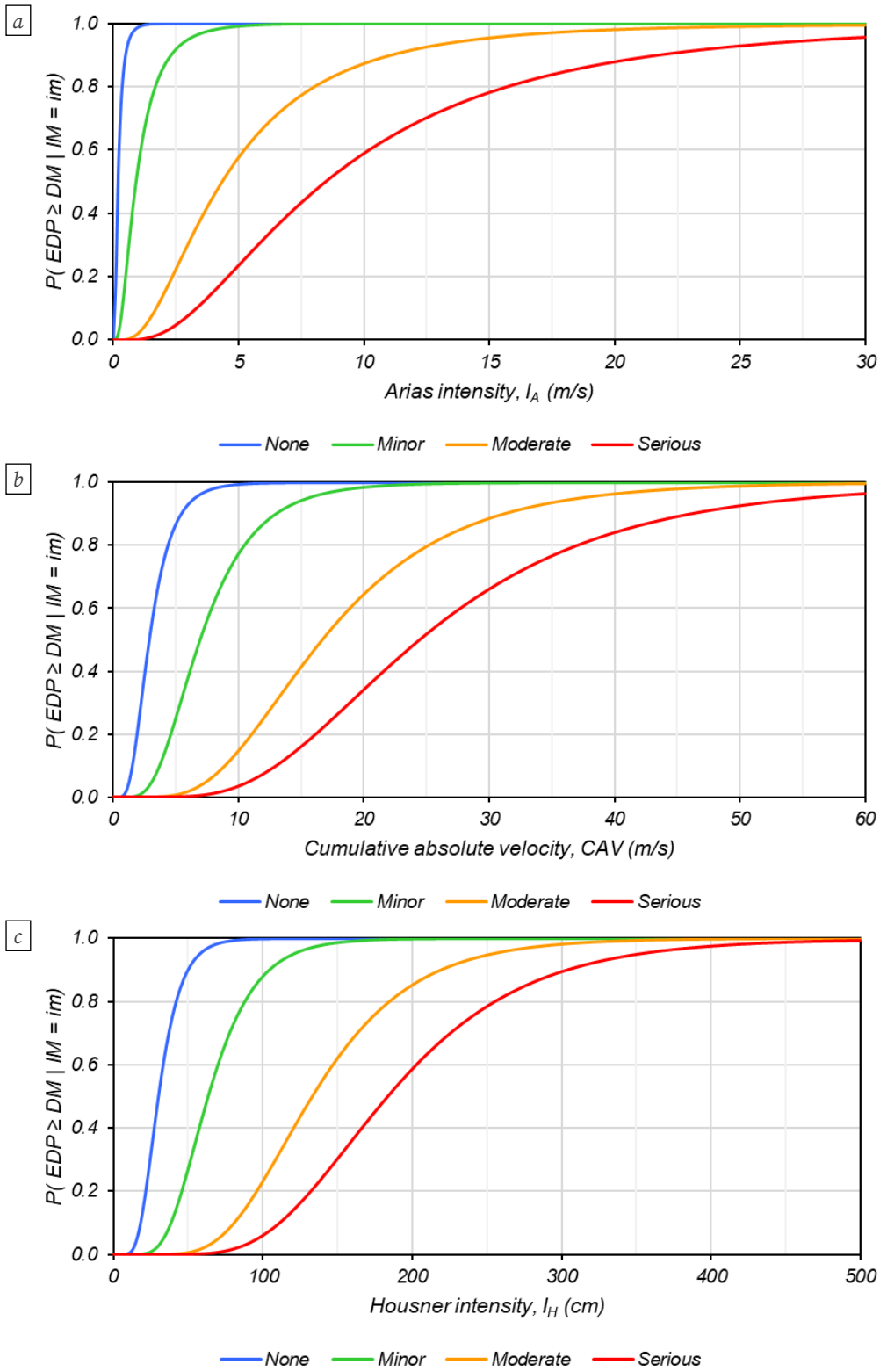


Fig. 8.35: Fragility functions via CA for the PFM of overtopping and the DMs defined by Swaisgood (2014), considering three integral intensity measures: a) I_A, b) CAV, and c) I_H.

IM	None		Minor		Moderate		Serious	
	θ	β	θ	β	θ	β	θ	β
PGA (g)	0.135	0.503	0.308	0.497	0.703	0.499	1.003	0.501
PGV (cm/s)	10.61	0.321	21.44	0.318	43.40	0.319	58.79	0.320
I_A *(m/s)*	0.191	0.735	0.910	0.727	4.334	0.727	8.456	0.731
CAV (m/s)	2.87	0.494	6.92	0.489	16.69	0.489	24.42	0.492
I_H *(cm)*	30.2	0.392	63.5	0.388	133.2	0.389	183.6	0.390

Table 8.22: Parameters of the lognormal fragility functions derived using CA, using the DMs proposed by Swaisgood (2014) for the PFM of overtopping, and several intensity measures (PGA, PGV, I_A, CAV, I_H).

From the initial analysis of the fragility curves obtained through Cloud Analysis, a couple of general trends could be observed, regardless of the selected intensity measure. The first is the relatively uniform shape of all the curves, which is attributed to the fitting of the lognormal CDF based on a larger number of data points. This condition does not necessarily imply that the curves derived from Cloud Analysis are more accurate, but the resulting functional forms tend to be consistently more uniform across all damage levels.

The second is the progressive flattening of the curves with increasing damage states, indicating that higher damage levels are associated with smaller sensitivity to the increase of seismic intensity measures. This behavior reflects a less accentuated nonlinear response and a larger dispersion in the fragility functions as damage levels escalate.

A comparison of the curves in Fig. 8.34 reveals a smaller dispersion for those using *PGV* as the intensity measure, compared to those based on *PGA*. This trend is also reflected in the β values reported in Table 8.22 and supports the idea that *PGV* is a more suitable intensity measure for geotechnical systems.

From the curves in Fig. 8.35, it is worth noting the larger dispersion observed in the fragility functions that use I_A as the intensity measure, compared to those based on *CAV* and I_H, with the latter showing the smallest dispersion among the three *IMs*.

A second set of curves corresponding to the calibration of fragility functions for the PFM of global instability are presented in Fig. 8.36 and Fig. 8.37, with the corresponding parameters of the fitted lognormal CDF summarized in Table 8.23 for all the intensity measures considered.

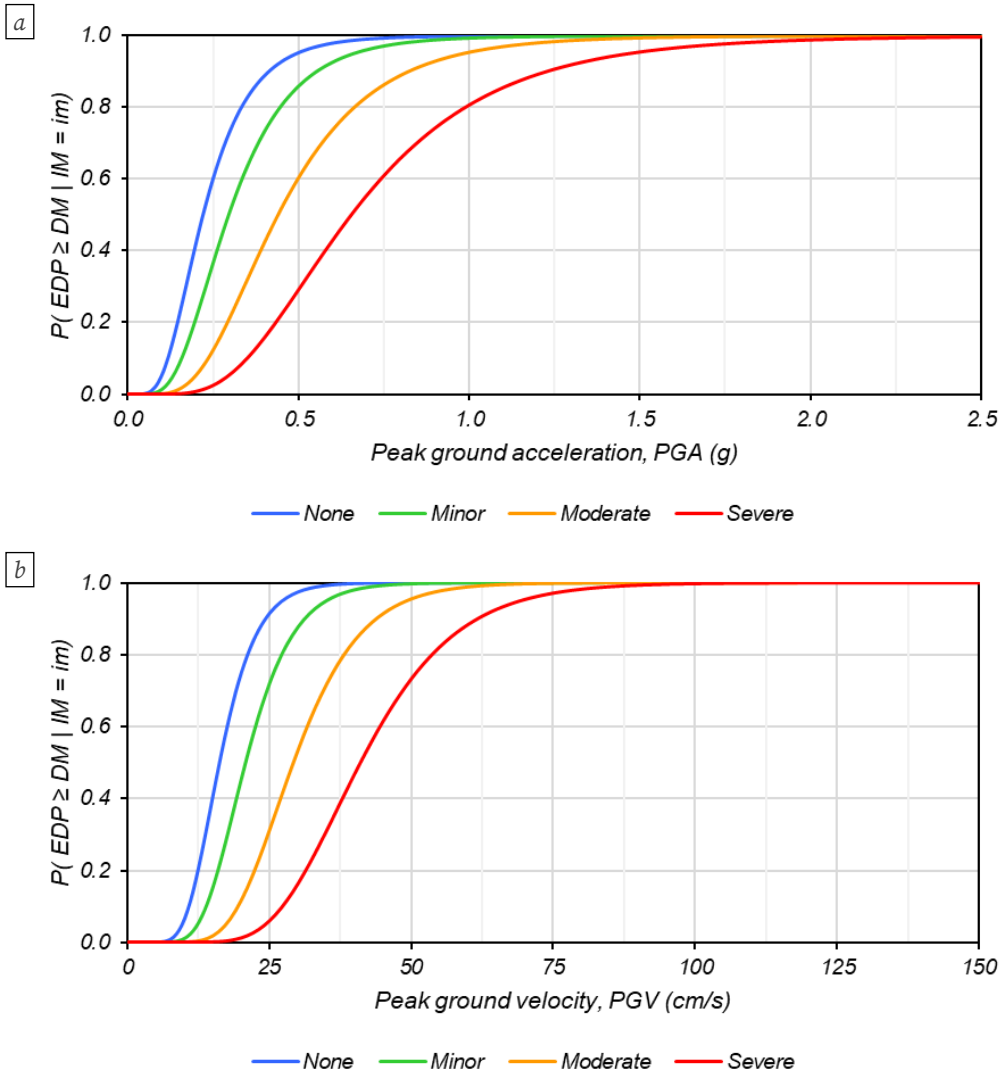


Fig. 8.36: Fragility functions via CA for the PFM of global instability and DMs set by Regina (2021), considering two peak intensity measures: a) PGA, and b) PGV.

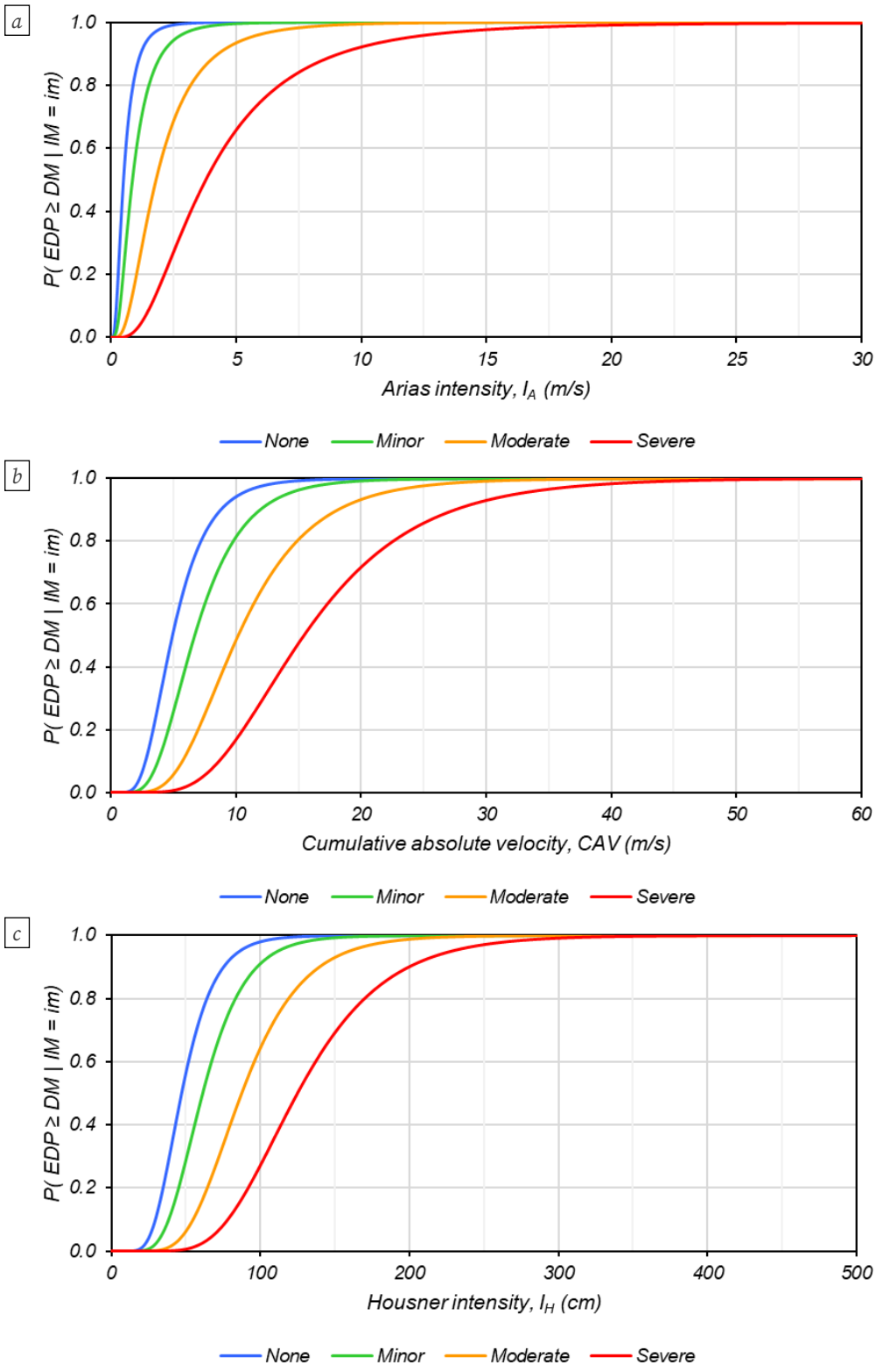


Fig. 8.37: Fragility functions via CA for the PFM of overtopping and the DMs defined by Regina (2021), considering three integral intensity measures: a) I_A, b) CAV, and c) I_H.

IM	None		Minor		Moderate		Serious	
	θ	β	θ	β	θ	β	θ	β
PGA (g)	0.221	0.489	0.296	0.488	0.441	0.487	0.655	0.489
PGV (cm/s)	16.128	0.318	20.726	0.318	29.152	0.317	40.979	0.319
I_A *(m/s)*	0.488	0.684	0.848	0.684	1.790	0.680	3.775	0.683
CAV (m/s)	4.899	0.452	6.674	0.451	10.156	0.451	15.427	0.452
I_H *(cm)*	47.222	0.364	61.367	0.363	87.535	0.364	124.956	0.365

Table 8.23: Parameters of the lognormal fragility functions derived using CA, using the DMs adopted by Regina (2021) for the PFM of global instability, and several intensity measures (PGA, PGV, I_A, CAV, I_H).

The second set of curves representing the failure mode of global instability using Cloud Analysis shows similar trends in terms of standard deviation as those corresponding to the PFM of overtopping, with the curves referred to *PGV* and I_H exhibiting less dispersion.

The fragility functions obtained, in terms of *PGV,* for the PFM of global instability can also be compared to those developed for overtopping, as presented in Fig. 8.38.

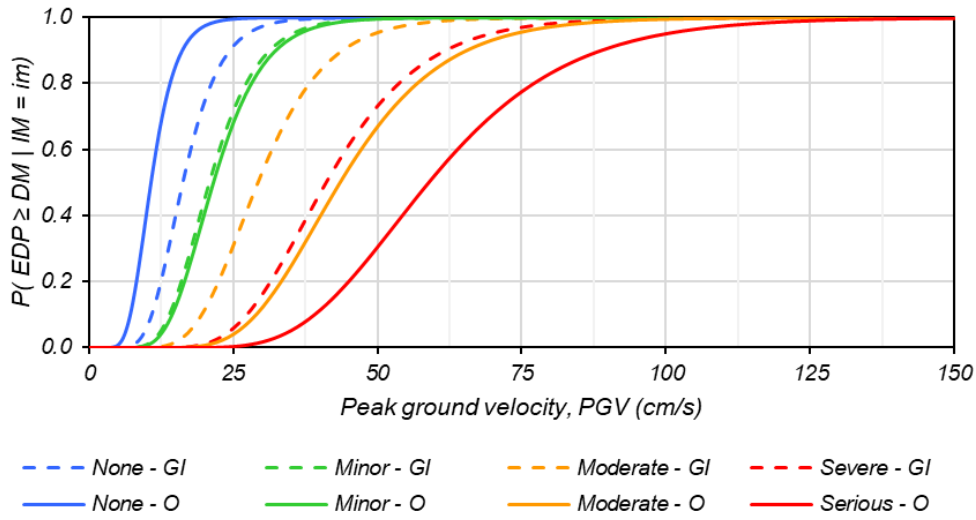


Fig. 8.38: Comparison of fragility function via CA, for the PFM of global instability (GI) and overtopping (O), in terms of PGV.

The comparison shows that for the "None" damage state, overtopping is more likely to occur than global instability at the same *PGV* level. For the "Minor" damage state, the curves are nearly identical, but for the "Moderate" and "Severe" (or "Serious") damage states, the fragility curves corresponding to global instability exhibit a more conservative position compared to those associated with overtopping.

A final group of curves is developed for the potential failure mode of overtopping, using the probabilistic definition of damage measures proposed by He & Rathje (2024). The procedure utilized to derive fragility functions based on this definition of the *DMs* involves the construction of a cloud-based Probabilistic Seismic Demand Model (PSDM), which is essentially a probabilistic model used to predict the value of the *EDP* given a specific value of the intensity measure *IM*. This model is further combined with the capacity model presented in Eq. 8.3 to obtain the fragility function.

The PSDM can be fitted to any probability distribution to better match the data points obtained from numerical analyses. The combination of the PSDM and the capacity model can then be performed through a Monte Carlo simulation. However, if the PSDM follows a power law in terms of *IM*, which in logarithmic space becomes linear and is commonly used to describe the seismic response of structures (Cornell et al., 2002), then the combination of the PSDM and the capacity model proposed by He & Rathje (2024) can be performed in closed form, as presented below.

The relationship between the *EDP* and *IM* following a power law can be established following Eq. 8.9, where the subscript "*D*" stands for "Demand".

$$EDP\left(IM\right) = a_D \cdot IM^{b_D} \qquad \textit{Eq. 8.9}$$

Where a_D and b_D are the parameters adjusted to fit the data points coming from the nonlinear dynamic analyses. By applying natural logarithms to both sides of the equation, it is possible to transform the relationship into its linear form (Eq. 8.10).

$$\ln\left(EDP\right) = \ln\left(a_D\right) + b_D \cdot \ln\left(IM\right) = \mu_{\ln D} \qquad \textit{Eq. 8.10}$$

This functional form assumes that the *EDP* follows a lognormal distribution, with a median value $\mu_{\ln D}$ defined by Eq. 8.10 and a standard deviation obtained as (Eq. 8.11):

$$\sigma_{\ln D} = \sqrt{\frac{\sum_{i=1}^{N}\left[\ln\left(EDP\right) - \mu_{\ln D,i}\right]^2}{N-2}} \qquad \textit{Eq. 8.11}$$

Where N is the number of analyses considered in the definition of the PSDM.

Then, it is possible to derive the coefficients θ and β that define the fragility functions following Eq. 8.12 and Eq. 8.13, reproduced from He & Rathje (2024).

$$\ln\left(\theta\right) = \frac{\mu_{\ln C} - \ln\left(a_D\right)}{b_D} \qquad \textit{Eq. 8.12}$$

$$\beta = \frac{\sqrt{\sigma_{\ln D}{}^2 + \sigma_{\ln C}{}^2}}{b_D} \qquad \textit{Eq. 8.13}$$

Considering the data points *EDP* vs. *IM* from the results of the NDAs, the parameters a_D, b_D, and $\sigma_{\ln D}$ of the PSDM for *PGA*, *PGV*, I_A, *CAV,* and I_H are reported in Table 8.24.

IM	PSDM parameters		
	a_D	b_D	$\sigma_{\ln D}$
PGA (g)	1.463	1.951	0.952
PGV (cm/s)	0.0	2.284	0.714
I_A *(m/s)*	0.162	1.032	0.738
CAV (m/s)	0.004	1.829	0.880
I_H *(cm)*	0.0	2.165	0.827

Table 8.24: Parameters of the adjusted PSDM for the five selected IM (PGA, PGV, I_A, CAV, I_H).

Introducing into the equation Eq. 8.12 and Eq. 8.13 the respective parameters already reported in Table 8.7 for the capacity model, and Table 8.24 for the demand model, it is possible to obtain the fragility functions reported in Fig. 8.39 for the peak intensity measures *PGA* and *PGV*, and Fig. 8.40 for the integral intensity measures I_A, *CAV* and I_H.

The table containing the parameters θ and β of the lognormal CDF corresponding to all fragility functions is summarized in Table 8.25.

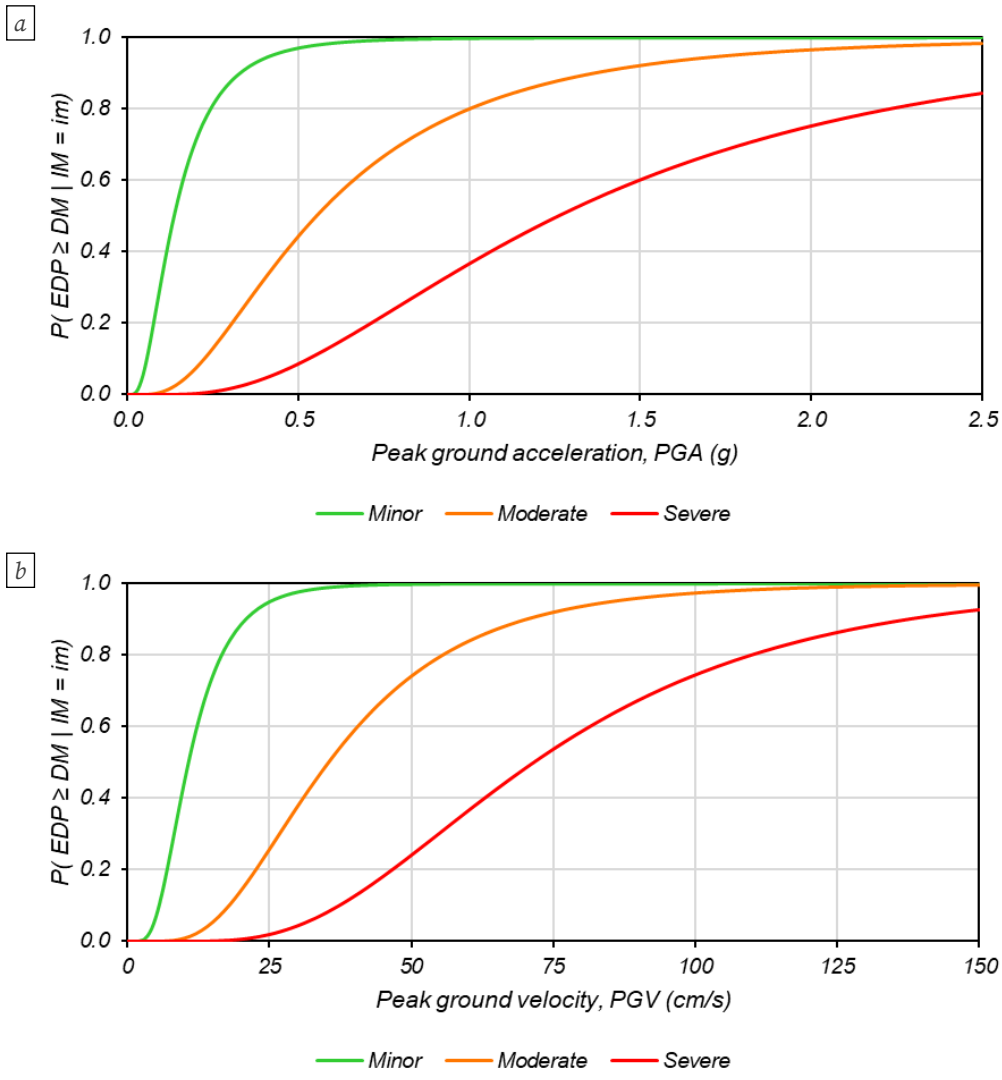


Fig. 8.39: Fragility functions for the PFM of overtopping using the probabilistic capacity model from He & Rathje (2024), considering two peak intensity measures: a) PGA, and b) PGV.

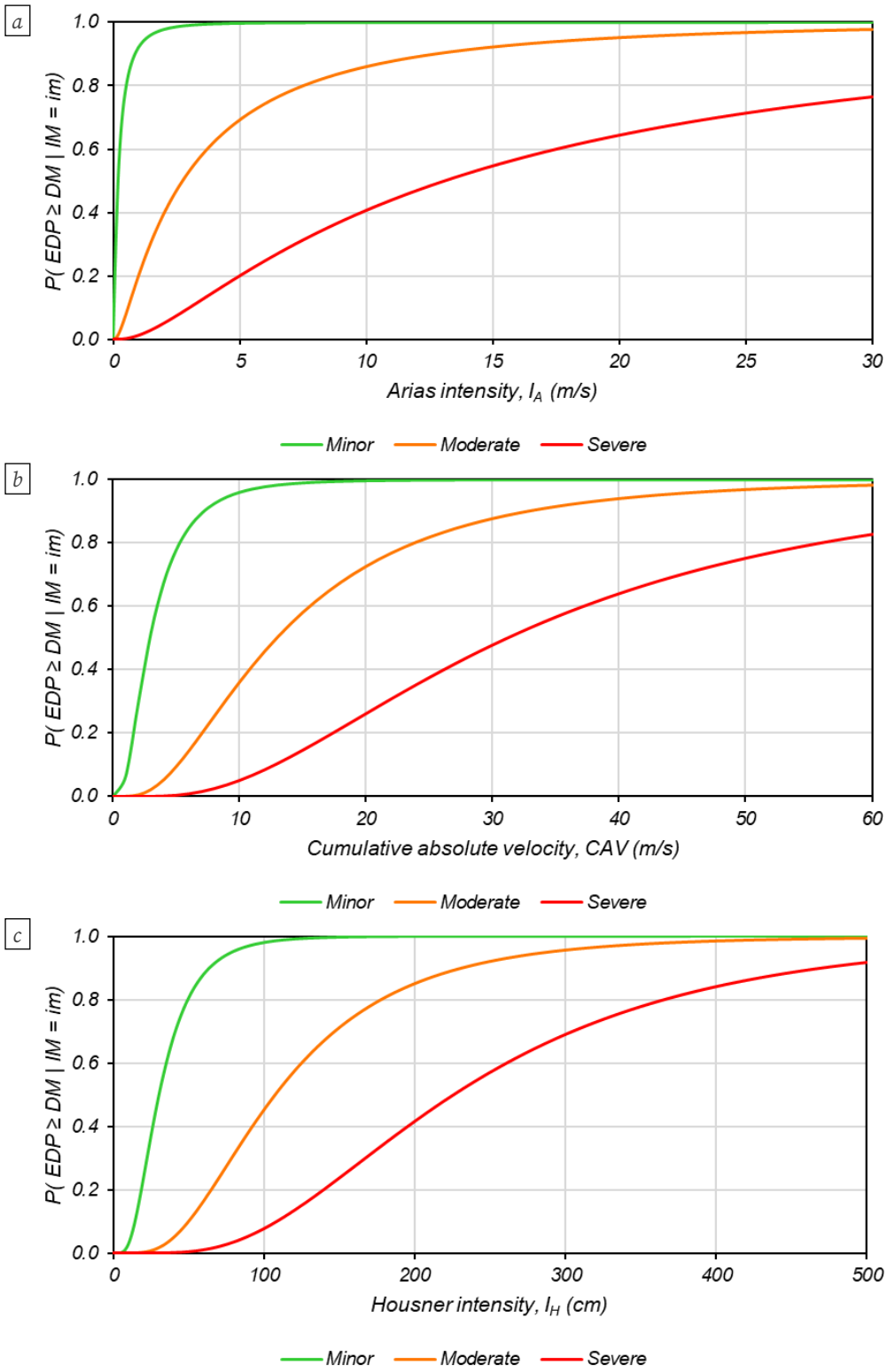


Fig. 8.40: Fragility functions for the PFM of overtopping using the probabilistic capacity model from He & Rathje (2024), considering three integral intensity measures: a) I_A, b) CAV, and c) I_H.

IM	Minor		Moderate		Serious	
	θ	β	θ	β	θ	β
PGA (g)	0.136	0.685	0.553	0.704	1.261	0.678
PGV (cm/s)	10.70	0.517	35.34	0.534	71.51	0.510
I_A *(m/s)*	0.19	1.159	2.75	1.197	13.08	1.144
CAV (m/s)	2.90	0.704	12.92	0.724	31.17	0.696
I_H *(cm)*	30.4	0.578	107.4	0.596	225.9	0.571

Table 8.25: Parameters of the fragility functions derived using the probabilistic capacity model developed by He & Rathje (2024), for the PFM of overtopping and several IMs (PGA, PGV, I_A, CAV, I_H).

It is evident that the flatter shape of this group of fragility functions with respect to those obtained using a deterministic definition of the damage measures, which is a direct consequence of incorporating a definition of the *DMs* that accounts for the uncertainty in establishing the boundaries between different damage states. This larger uncertainty is also reflected in the larger logarithmic standard deviation presented in Table 8.25.

These differences can be further stressed by plotting both sets of curves in the same figure, in terms of *PGA* and I_H, for the “Minor”, “Moderate”, and “Severe” damage states. Then, the curves obtained from the application of the deterministic definition of the *DMs* from Swaisgood (2014) and those using the probabilistic capacity model of He & Rathje (2024) are presented in Fig. 8.41.

It is interesting to note that the curve corresponding to the 'Minor' damage state presents a steeper distribution in the case that considers the probabilistic definition of the DMs, in comparison with the deterministic one, whereas for the two remaining damage states, the curves corresponding to the probabilistic capacity model tend to be flatter. This response is verified for both *IMs* evaluated, showing similar differences among the deterministic and probabilistic definitions of the damage measures.

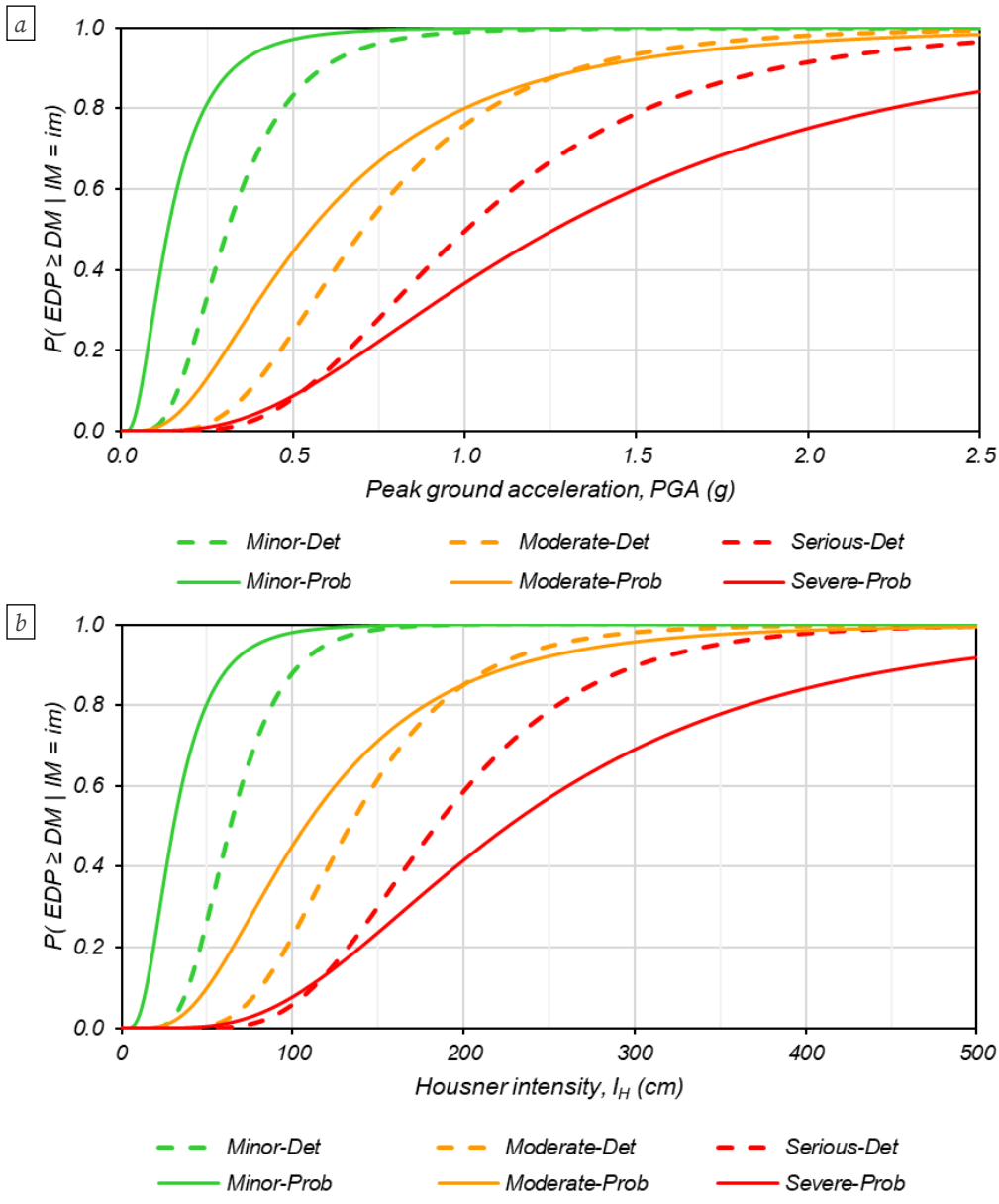


Fig. 8.41: Comparison of fragility functions for the PFM of overtopping using the deterministic definition of the DMs from Swaisgood (2014) and the probabilistic capacity model of He & Rathje (2024), considering two intensity measures: a) PGA, and b) I_H.

A deterministic definition of the *DMs* gives the impression of certainty, as it disregards variability from the outset in the definition of the limits between damage states. However, probabilistic models used to define damage measures may be derived from heterogeneous databases that, in attempting to populate the *DM* slots for all damage states, aggregate data from embankment dams whose responses to strong earthquakes can vary widely. This situation likely increases the variability in the definition of the probabilistic capacity model,

as weaker responses (e.g., hydraulic fill dams) tend to shape the lower tail of the distribution, while stronger-performing dams (e.g., modern dams) define the upper part.

Nonetheless, given the differences among the very few criteria available in the literature for defining the *DMs*, the selection of a particular criterion should be based on an evaluation of the results obtained, as well as on the database and the methodological basis used to define the damage threshold for every damage level. If available, probabilistic models should be preferred, as they account for the uncertainties that deterministic criteria tend to overlook.

8.4 Integration of Fragility Curves into Earthquake Early Warning Systems

Seismic fragility functions are a fundamental component of both probabilistic performance-based earthquake engineering (PBEE) assessments and seismic risk evaluations, but their application can be extended beyond these uses. A possible application of the fragility functions is their insertion into Earthquake Early Warning Systems (EEWS), which are tools designed to reduce seismic risk, enhance the resilience of both infrastructure and the built environment (Satriano et al., 2011), and support post-event emergency management.

In dam management, the most widespread criterion for initiating post-earthquake inspection procedures is primarily based on an estimation of the ground motion at the dam site (ICOLD, 2016b). This estimation can be supported by simplified approaches that rely on the initial assessment of the earthquake's magnitude and distance, such as those illustrated in Fig. 8.42 coming from various agencies or literature works (Tani, 1999; MIT, 2002; ICOLD, 2016b; MIT, 2017), or direct measurements of ground shaking from a local seismic monitoring system can be used when available.

Post-earthquake inspections typically involve activities such as visual inspections, evaluation of monitoring records, assessment of the evolution of critical features, and communication with relevant authorities. However, many of these activities must be carried out by specialists who are not always present at the dam site. As a result, actions that could prevent further damage may be delayed due to the lack of a tool capable of providing a rapid initial estimate of the dam's seismic performance to support immediate decision-making. To address this gap, an EEWS for embankment dams could be introduced to provide real-time information on dam performance and support improved decision-making following a strong earthquake at the dam site.

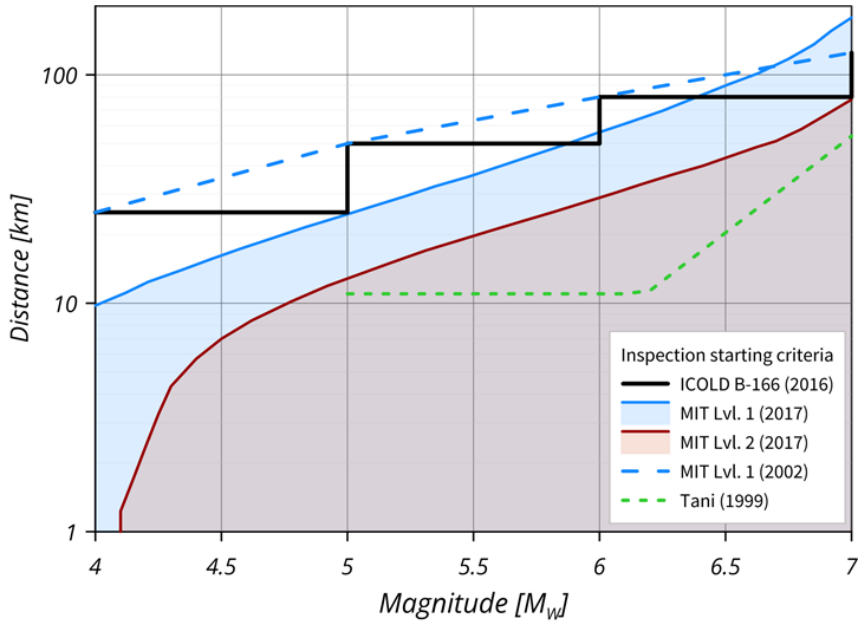


Fig. 8.42: Criteria based on magnitude-distance to start a post-event inspection on dams (Tani, 1999; MIT, 2002; ICOLD, 2016b; MIT, 2017).

Earthquake Early Warning Systems, in their most general implementation, rely on strong-motion networks to provide real-time information about ongoing seismic events, enabling warnings to be issued ahead of the arrival of strong ground shaking. If these systems are developed to assist emergency managers, they can provide rapid first-order estimates of the performance of critical buildings and infrastructure immediately following a seismic event, when they are properly calibrated (Iervolino, 2014; Cremen & Galasso, 2021). Such timely information is vital for effective seismic risk mitigation, as well as for coordinating post-disaster response and resource allocation.

In the field of dams, some approaches have been developed for concrete dams using a combination of seismic monitoring systems deployed at the dam and numerical models (Ariga et al., 2005, 2012; El-Idrissi et al., 2023), while a general framework for embankment dams was proposed by Pagano & Sica (2013). The introduction of generic fragility functions in EEW frameworks was already adopted for lifelines (Lin et al., 2022), bridges (Lin et al., 2022), or roadway retaining walls (Cosentini & Bozzoni, 2022).

Due to the strategic importance of large embankment dams in post-earthquake emergency management and the potentially catastrophic cascading effects of their failure (Tosun, 2024), the development and implementation of case-specific fragility functions for their use within

an EEWS is essential. An accurate definition of its behavior during earthquakes is necessary to ensure a reliable near-real-time assessment of the dam's seismic safety.

This rapid prediction should aim at recognizing the triggering of potential failure modes activated during the shaking phase and provide an initial estimate of structural performance. This, in turn, enables dam operators to enhance standard post-earthquake inspections, prioritizing the monitoring of key physical parameters that can effectively capture the progression of these mechanisms during the post-seismic phase.

To set the differences between traditional EEWS and those involving a rapid estimation of seismic performance of critical infrastructure, in traditional EEWS, the risk mitigation strategies can be implemented by sending alarms alerting people and managers of critical assets before they are reached by the strong ground shaking. This system also utilizes the early ground-shaking estimation, in combination with computational tools, to achieve an initial understanding of the extent and severity of earthquake consequences, helping to ensure better use of the emergency resources and supporting the post-event decision-making associated with short-term earthquake risk management (Wald et al., 2008).

Earthquake early warning systems that include the estimation of the seismic performance of critical infrastructure, such as the Performance Based EEW (Iervolino, 2011) or the Next-Generation Early Warning (Cremen & Galasso, 2020), are in turn designed to provide an initial assessment of infrastructure response based on ground motion estimates from traditional EEWS or recordings from a local seismic monitoring system. These systems aim to deliver a rapid first estimate of the seismic performance of the infrastructure, helping to identify potential safety concerns, evaluate the likelihood of damage, and support the implementation of timely countermeasures to reduce the risks associated with a probable damaged condition of the structure.

This is the case of embankment dams, where the dangerous condition is not the earthquake shaking itself, but the damage that strong ground motions could induce on the dam, which could potentially lead to a drastic decrease in its seismic safety and, eventually, its collapse. This could result from any failure mechanisms that the dam might develop under strong shaking, with the likelihood of developing each failure mode relying on the combination of various conditions, among which the type and characteristics of the dam, the site conditions, and the history of loads and hydraulic conditions, among others, can play a critical role.

Fragility functions constitute a set of tools able to define the probability of exceeding a given damage level for each failure mode, given an intensity measure of the seismic ground motion. Therefore, their integration within EEWS could be greatly beneficial as an interpretative model that directly associates the ground motion with the probability of developing a given damage state.

Based on Pagano & Sica (2013), EEWS for embankment dams comprises:

a) A seismic monitoring system, which typically records earthquake intensity as a time series of acceleration and/or velocity. These time series can then be used to derive earthquake intensity measures such as *PGA* and *PGV*. Ideally, the system should be dedicated exclusively to the dam. However, in the absence of a local seismic monitoring system, such intensity measures can be estimated using data from regional seismic networks in conjunction with GMMs. This approach is valid but less accurate than using direct ground motion recordings at the dam site. Finally, the monitoring variables considered must be consistent with the interpretative model adopted and should be as robust as possible to minimize the risk of errors.
b) An interpretative model that uses the monitored variables for the prediction of the effects of ground shaking on the dam in terms of representative performance parameters, providing insight into the safety margin of the dam. The model could be a direct relationship between variables, a numerical model (or digital twin), or, as proposed in this work, a family of fragility functions.
c) Threshold values of performance parameters related to increasing alert levels, which in turn correspond to different alarm notifications. These limits can be defined based on the tolerable risk.
d) The definition of the actions linked to the different stages of alert, which are usually part of the Emergency Action Plan (EAP) of the dam, where such instrument exists.

Every component should be adapted to the specific case, and different approaches and levels of complexity could be considered along with the EEWS development, seeking a suitable cost-benefit balance while managing uncertainty. The best overall system is that provides the most helpful outcomes in terms of safety assessment and emergency management. An outline of the process is sketched in Fig. 8.43.

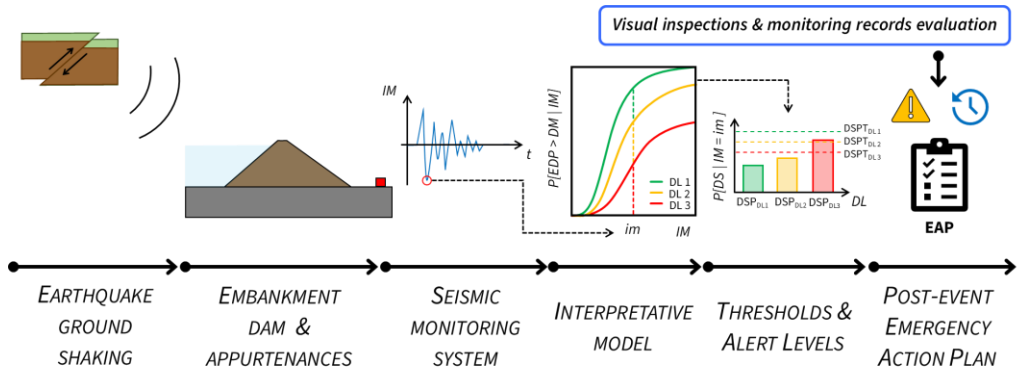


Fig. 8.43: Schematic diagram of the proposed EEWS for an embankment dam with all its components (Barbagelata et al., 2024).

The system becomes active when an earthquake occurs near the dam, producing ground shaking at the site that the seismic monitoring system is capable of recording. The record is then processed in real-time, and a selected *IM*, such as *PGA* or *PGV*, is identified as a representative parameter of the ground shaking intensity. This *IM* is then introduced into the appropriate fragility function to estimate the probability of experiencing a specific damage state of a given PFM, which in practice corresponds to the *EDP* exceeding a defined *DM* or $P(EDP \geq DM \mid IM = im)$. Once the probability of the *EDP* exceeding the *DM* given the *im* recorded is determined for every damage level, the probability of developing a given damage state is evaluated as the difference between the probability for two consecutive damage levels and compared with the corresponding damage state probability threshold value ($DSPT_{DS}$). If the calculated probability exceeds the threshold, the applicable alert level is triggered.

Monitoring activities are conducted over several days following the earthquake to verify the reliability of the predictions and to assess the evolution of suspected damage mechanisms. These assessments often focus on post-earthquake seepage flows, pore water pressure, and displacements. Depending on whether a specific alert level is reached or a combination of alert levels is judged to compromise dam safety, appropriate countermeasures are implemented to reduce the associated risk. During these inspections, the alerts provided by the earthquake early warning system (EEWS) are useful in directing post-event activities toward those parts of the dam that may be more vulnerable or that may provide early indications regarding the current state of safety of the dam.

A description of each component of the proposed procedure is provided below.

8.4.1 Monitoring system and processing of the seismic records

A local monitoring array composed of accelerometers (or velocimeters) is the best tool to record strong ground motions at the dam site. The number of instruments, their location, and the data processing should be carefully addressed to maximize the effectiveness of the system. International guidelines (COSMOS, 2001) suggest a minimum array as the one presented in Fig. 8.44, consisting of at least four stations located at free-field, crest, foundation, and one abutment. Additional stations at the crest, abutments, or within/along the dam body can improve the description of the seismic dam response and the reliability of the array.

Ideally, the free-field station provides the reference input motion only if placed on a flat outcrop of the same rock formation constituting the dam foundation, otherwise, its records should be subjected to a deconvolution analysis down to the underlying seismic bedrock, a process that is not always well suited to the time constraints of an EEWS. Foundation and abutment records can also represent a reliable estimate of the input motions, if not significantly affected by dam-foundation interaction or topographic effects, and serve as a benchmark for the reference motion or a replacement of this latter in case it is not available.

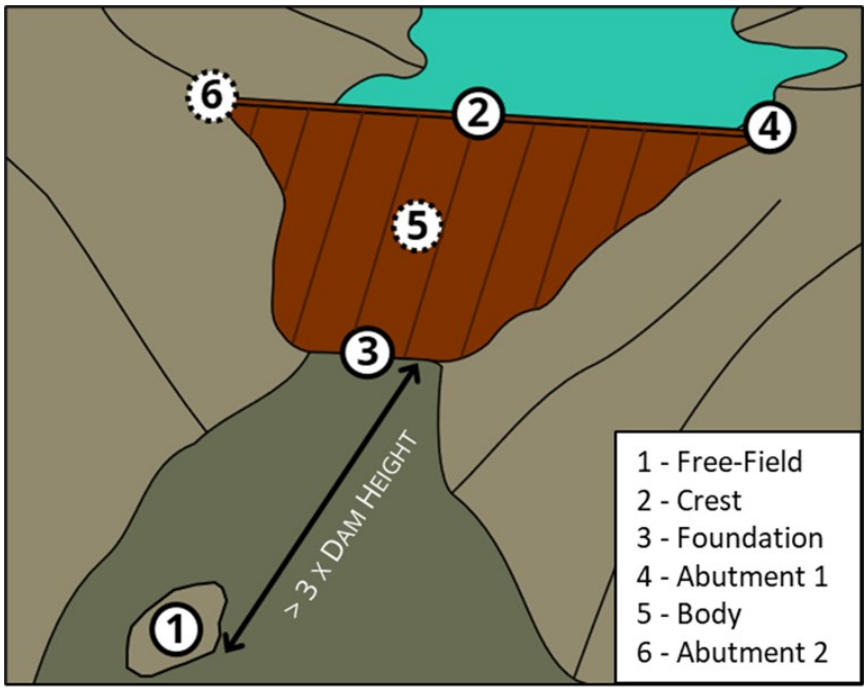


Fig. 8.44: Array of seismic stations for the local dam monitoring, with the minimum (solid) and the recommended (dashed) locations (Barbagelata et al., 2024).

The local monitoring array must be designed to withstand large earthquakes and measure within a broadband range of frequencies. A proper setup of the equipment is crucial to ensure the recorded data is useful for EEWS purposes. Furthermore, connectivity and record management must be guaranteed even during strong shaking. Once the records become available shortly after the event, they should be processed using reliable automatic procedures (Jones et al., 2017), enabling them to characterize the recorded ground motion with the *IM* needed for the use of the fragility functions. It is highly recommended to cross-check *IMs* between free-field and foundation/abutment measurements to identify possible significant discrepancies in shaking intensity, which can lead to detecting station malfunctions.

If the dam is not equipped with a seismic monitoring array, another possibility is to estimate the shaking intensity in terms of the required *IMs* using Shakemaps generated on the basis of a regional seismic network, as illustrated in Fig. 8.45.

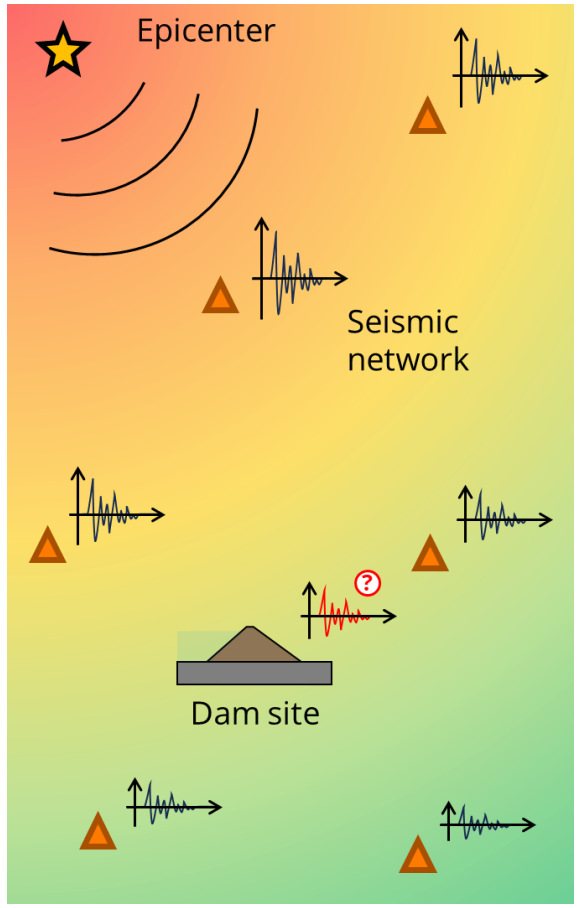


Fig. 8.45: Schematic view of a regional seismic network for the ground motion estimation at the dam (Barbagelata et al., 2024).

As an alternative option, once the earthquake source location and magnitude are determined by an agency (e.g., INGV, USGS, GFZ, EMSC), the magnitude of the ground shaking at the dam site can be estimated using GMMs. It is worth noting that this approach requires an adequate level of accuracy in the prediction of the *IM*, noted as "predictability" (Kramer & Mitchell, 2006), in order to track the uncertainty in the ground motion forecast. In the absence of a local monitoring array, the predictability of a given *IM* is, therefore, an important factor to be considered for the calibration of the fragility functions used in the EEWS, since not all the integral parameters significant for the assessment of a damage mechanism are usually predictable with the selected GMMs.

8.4.2 Interpretative model: case-specific fragility functions

After identifying the magnitude of the ground shaking, the next step is to relate this magnitude to the dam's performance. The tools available for this step range from direct relationships between ground motion and performance parameters (Pagano & Sica, 2013; Nardo et al., 2024) to complex 3D numerical models (Ariga et al., 2012). A good compromise between these approaches is to establish probabilistic relationships between *IM* and performance, such as case-specific fragility functions based on the results of advanced numerical analyses that capture the complex response of the system. From all the types of fragility described in Section 2.7.1, analytical fragility is the most flexible and conceptually straightforward methodology.

The need for case-specific fragility functions is evident in this context, as the closer the interpretative model is to the actual seismic response of the dam, the higher the quality of the forecasting provided by the EEWS and the lower the likelihood of false positive or false negative alert triggers.

To ensure the representativeness of case-specific fragility functions, several requirements already discussed throughout the dissertation must be fulfilled. The most outstanding are:

- Identification of feasible potential failure modes (PFMs) that the dam may develop during earthquakes, taking into account the specific characteristics of the dam and the conditions at the site.
- Assuring the hazard consistency in the selection and scaling of the input ground motions, in order to reduce the epistemic uncertainty regarding the characteristics of the ground shaking that can arise at the dam site. This can be achieved when the

results of a site-specific PSHA are available to set the amplitude of the ground motions (e.g., from UHS) and the seismic scenarios that contribute the most to the seismic hazard (e.g., from disaggregation charts).

- Selection of optimal intensity measures (*IM*) based on relevant metrics such as efficiency, sufficiency, etc., with the aim of identifying the most suitable *IMs* for accurately capturing the seismic response of the dam.
- Use of numerical tools able to reproduce the inelastic response of the dam during earthquakes, based on reliable information or judicious assumptions for the material characteristics, and calibrated using monitoring data if available. The numerical tools utilized should be capable of capturing the diverse damage stages expected during the development of the PFM while the intensity of the ground motion increases.
- Identification of well-suited engineering demand parameters (*EDPs*) that can condense the seismic response of the dam into a single physical magnitude or index. These *EDPs* should be capable of capturing the development of a *PFM* across a wide range of damage levels predictably and reliably, and should also be associated with consistent damage measures (*DMs*), which allow for establishing relationships *EDP|DM* or simply defining thresholds in terms of *EDP* corresponding to different damage levels.

Moreover, one of the major advantages of probabilistic approaches used in deriving fragility functions is the incorporation and management of the uncertainty in the fitting process (Iervolino, 2022). This allows for the consideration of both the epistemic (knowledge-related) and aleatory (random variability) components of uncertainty. Effective uncertainty management is fully addressed in the case that both demand and capacity models are defined as random variables and combined using statistical tools, as the example already presented at the end of Section 8.3.2.

8.4.3 Damage state probability thresholds and countermeasures

The use of fragility functions as interpretative models within the EEWS makes it possible, once the measured or estimated magnitude of the *IM* for the current ground motion is identified, to know the probability of developing a given damage state, or damage state probability (*DSP*), for every PFM. It is evident, then, that to understand the risk or safety concerns associated with this probability, it is necessary to define damage stage probability thresholds for each damage state ($DSPT_{DS}$) and every potential failure mode, as schematically illustrated in Fig. 8.46.

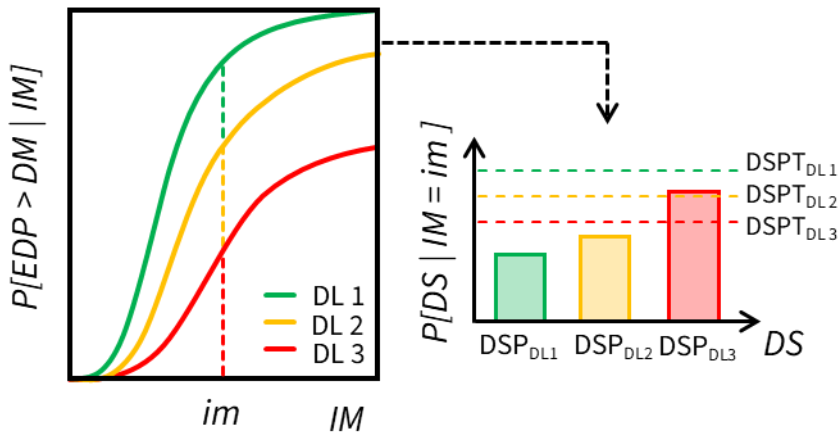


Fig. 8.46: Schematic illustration of the process to obtain the DSP from the fragility functions, knowing the measured value of the intensity measure (im), and comparing it to the respective thresholds.

The definition of these thresholds has to be referred to the particular case under study and could be based on methodologies already adopted in the safety management of other types of infrastructures, such as nuclear or industrial facilities (Melchers, 2001). Some of these methodologies were already introduced by some agencies in the dam field, for both water and tailing dams (FERC, 2016), and principles such as Tolerable Risk, ALARP ("As Low As Reasonable Practicable"), SFAIRP ("So Far As Is Reasonable Practicable"), or CBR ("Cost-Benefit Ratio") are now common terms in the definition of the acceptable dam risk (Fluixá-Sanmartín et al., 2020).

If one or more damage stage probability thresholds are exceeded, appropriate safeguard countermeasures should be implemented to minimize the overall risk. The process begins by tracking the evolution of dam behavior with the dam monitoring system. These actions are outlined in an Emergency Action Plan (EAP), which is expected to be developed for each specific dam. The countermeasures chosen should be the most suitable for the observed damage while minimizing potential losses in terms of costs and human lives.

Additionally, integrating an EEWS into a 'Risk-Informed Decision Making' (RIDM) framework could offer significant advantages, as RIDM is an effective strategy for enhancing the safety of complex systems such as large embankment dams (FERC, 2016; Lacasse et al., 2019)

This procedure exhibits the benefits of adopting analytical fragility functions within an EEWS for embankment dams, highlighting the advantages in managing the uncertainties and

providing results in terms of the probability of failure across multiple damage levels. An accurate interpretative model of the system and the availability of a local seismic monitoring array can significantly enhance the reliability of failure probability assessments.

For embankment dams, this approach represents a substantial improvement in post-event emergency management, complementing and speeding up current procedures primarily based on visual inspections and interpretation of monitoring records. Its straightforward integration into a RIDM framework also presents good opportunities for resource optimization in emergency management and risk mitigation. Finally, the proposed EEWS for embankment dams using fragility functions is a feasible and effective approach to mitigate the seismic risk, easily implementable in both new and existing dams.

9. Discussion and conclusion

The relevant aspects of each part of the dissertation have already been discussed in their respective chapters, but a general discussion that integrates them all will provide a clearer understanding of the overall achievements of this work. Subsequently, the most significant findings will be outlined, and potential research directions related to the addressed topics will be identified to support the ongoing development of the proposed methodologies.

9.1 General discussion

The assessment of the seismic performance of embankment dams in regions of elevated seismicity is a critical concern that requires integrated efforts to ensure the safety of downstream populations and the continuous operation of the facility. Many tools have been developed over the years in the search for better and more efficient methodologies able to capture the complexity around the dynamic response of such a complex geotechnical structure. Since a couple of years, the evaluation of the seismic safety of earth dams have started to migrate to approaches related to risk evaluations in the search for integral evaluation of the safety, the possibility of recognizing complex mechanism of failure, and an explicit introduction of the uncertainty in every step of the assessment of seismic performance, among others advantages. In this context, fragility functions play an essential role in the quantitative evaluation of risk and probabilistic assessments of seismic dam performance, but can also be included in earthquake early warning systems for better decision-making during post-emergency management.

A methodological framework for deriving case-specific fragility functions for embankment dams will not only encourage the use of such tools within the dam engineering community by providing a clear workflow, but also deliver performance and fragility estimations that more accurately reflect the feasible damage scenarios following large seismic events by capturing the sequence of damage mechanisms expected to occur at the dam during strong earthquakes. Moreover, establishing a strong correlation between the identified potential failure modes (PFMs) and the engineering demand parameters (*EDPs*) used in the calculations will further enhance the validity of the fragility functions and the resulting performance assessments. All these aspects were intended to be covered by the proposed methodological framework of Chapter 3.

However, the use of the framework alone does not guarantee reliable results unless each stage of the process is approached with critical thinking and supported by the best available procedures and data. Emphasizing this point highlights the importance of high-quality information in the development of both geotechnical and subsequent numerical models, which serve as the basis for deriving fragility functions. Though it is desirable to use tools that can capture the variability and uncertainty inherent in defining soil properties, informed judgment and careful evaluation of modeling decisions are essential steps toward achieving a more realistic assessment of the dam's seismic performance. While this may sound like general advice, the consequences of failing to conduct a judicious evaluation of the site conditions can be significant, just as relying solely on intuition instead of grounding decisions in sound information can lead to serious misjudgments. In the context of assessing the seismic safety of a large embankment dam, such oversight can lead to completely different outcomes, thereby increasing the uncertainty associated with the safety evaluations.

Potrerillos Dam is a clear example of the previous reflection, as different interpretations of the role of foundation soils in the hydraulic and mechanical response of the dam under both long-term and seismic conditions have led to ongoing discussions. The characterization of the material properties and the analysis of monitoring records presented in Chapter 3, along with the decisions made during the modeling phase in Chapter 6, were focused on providing a better definition of the role of the foundation in the seismic response of the dam, under generally conservative assumptions. However, a carefully planned new campaign of geophysical surveys and geotechnical in situ and laboratory testing could significantly improve the current level of knowledge regarding the characterization of the foundation alluvium and future evaluations of the dam's seismic performance. The same need applies to the characterization of the materials used in the embankment.

On the other hand, one aspect that carries its own uncertainty is the definition of the seismic actions that characterize the seismic hazard at the dam site. Using for the very first time for Potrerillos Dam a methodology that explicitly accounts for this uncertainty, such as probabilistic seismic hazard analysis (PSHA), represents a significant step forward in defining the intensity of the seismic hazard and the characteristics of the seismic scenarios that could take place at the dam site. In combination with adequate record selection and scaling, ensure the hazard consistency necessary for anchoring the seismic actions to the place where the dam is located and reduce the uncertainty on the input motions used for fragility calibration.

The number of ground motions, the levels of scaling, and the guarantees of hazard consistency are closely related to the derivation of case-specific fragility functions. This is not only due to the use of different methodologies for calibrating the probabilistic distributions that define them, but also to ensure case specificity, which has been shown to be an important characteristic to capture in certain applications of fragility curves. This aspect is reflected in Chapter 8, where the MSA and CA approaches show not only different results but also different requirements when it comes to calibrating consistent fragility curves.

Leading to the expected behavior of the dam under seismic actions, a preliminary definition of the potential failure modes makes the derivation of fragility functions based on these PFMs more realistic, as the quantitative evaluation of the probability of failure is linked to a feasible sequence of failure mechanisms that could be triggered in future earthquakes. This step was missing in many of the previous works reported in Table 2.2 and is considered a major advance in the derivation of trustworthy fragility functions.

The building of numerical models based on judicious evaluation of the soils characteristics and advanced constitutive models calibrated focused in the cyclic response expected by the soils of the dam evidenced the importance of using advanced methodologies capable of capturing the complex response of soils during earthquakes, especially for those soils that may be subjected to cyclic softening or liquefaction phenomena. A numerical model that can capture the sequence of events in a potential failure mode across different levels of seismic intensity, and the range of responses the model may exhibit, as confirmed in Chapter 7, the importance of using this kind of tool for the evaluation of seismic performance and fragility.

An important effort was made to highlight the need for a consistent selection of engineering demand parameters (*EDPs*), but above all, to emphasize the importance of better and more reliable definitions of the damage measures (*DMs*) used for both performance and fragility evaluations. These definitions can significantly affect the interpretation of the damage states of the dam and the results in terms of fragility functions, as described in Chapter 8. Differences in derivation procedures and the influence of the experience of the developer in defining the *DMs* criteria, as well as the lack of metrics to evaluate which *EDP* best represents a particular PFM and which *DMs* most accurately describe the expected changes in performance associated with different damage levels, make it difficult to establish clear criteria or quantitatively assess the quality of the chosen parameters. The definition of a framework to consistently define damage measures while considering uncertainty and different

approaches based on case histories and numerical simulations will be a great improvement for future works.

Finally, the integration of fragility functions within an earthquake early warning system (EEWS) for embankment dams is a promising application that could enhance post-event emergency management decision-making, contributing to the mitigation of seismic risk associated with such critical infrastructure.

9.2 Closing remarks

The dissertation aimed to describe and apply a methodological framework for the derivation of case-specific fragility functions, through its implementation for the Potrerillos CFRD. The detailed evaluation of each step in the context of this specific case highlighted the importance of accounting for uncertainty and making judicious modeling decisions throughout the entire process.

The definition of a methodological framework for the derivation of case-specific fragility functions for embankment dams represents one of the most important objectives of this work. Such a framework has been lacking, at least in the extension proposed, in the existing literature. It not only identifies all the necessary steps for deriving reliable fragility functions that can capture the dam's response in terms of the probability of reaching a given damage state for a given ground motion intensity, but also addresses the implications of each decision made throughout the process on the final results.

A rational interpretation of the site conditions and the soil characteristics of both the dam and its foundation was conducted using the information available from the project and construction stages. This analysis, grounded in the existing soil characterization, enabled the identification of the variability in the properties of the geomaterials forming both the dam body and the foundation, with a consistent focus on their incorporation into numerical models developed for seismic performance assessment.

The analysis and interpretation of the long-term hydraulic behavior and stress history of the dam were conducted using records from almost 20 years of continuous monitoring. This effort not only helped to set the baseline static conditions of the dam, but also provided valuable insights about the dynamic response of the dam-foundation system using the recorded weak ground motions, bringing useful information for the calibration of constitutive models during the numerical analyses.

The definition of the seismic hazard at the dam site through the first-ever site-specific probabilistic seismic hazard analysis (PSHA) for Potrerillos Dam was also an important achievement of the thesis. This characterization of the seismic hazard was followed by a suitable selection and scaling of strong motion records, aimed at ensuring the hazard-consistency of the input motions later used in the derivation of seismic fragility functions. Regular methodologies using the UHS and disaggregation charts were applied, with awareness of the need to capture the uncertainty in the characteristics of the ground motions, while maintaining consistency with the seismotectonic environment surrounding the dam.

An advanced numerical model with constitutive models calibrated based on the available information and the expected behavior of the different soils of the dam was constructed for its use in the definition of the seismic performance of Potrerillos. The model was able not just to capture the response of the dam under different levels of seismic actions, but also to provide a better idea of the influence of the foundation on the dam response under the assumptions considered throughout the evaluation of the results from the nonlinear dynamic analyses (NDAs).

The NDAs were able to describe the dynamic response of the dam, as well as capture the development of the PFMs at different damage levels and intensities of the seismic ground shaking. The key aspect highlighted at this stage was that judicious soil characterization and modeling decisions, supported by the best available information, could significantly improve the outcomes of seismic performance evaluations.

The derivation of seismic fragility functions for the main seismically driven PFMs exhibited the pros and cons of the diverse methodologies used for calibrating the parameters of the lognormal CDF used for describing the fragility curves, not just in terms of the fitting procedures but also in relation with the requirements for the scaling of input motions and the quality of the resulting fragility functions.

The evaluation of different types of engineering demand parameters (*EDPs*) as well as diverse criteria for the definition of the damage measures (*DMs*) in the building of the fragility functions was explored, giving a clear overview of the available options and their dispersion in the prescribed damage thresholds and criteria for their derivation. The need for a framework for the better derivation of *DMs* criteria, and some suggestions for the adoption of one or the other, were also reported in the dissertation.

Finally, the integration of the case-specific fragility functions into an earthquake early warning system was illustrated as an alternative application of the curves obtained, with the evaluation of the potential benefits for seismic risk mitigation and post-earthquake emergency management.

9.3 Future developments

As in any research work, many interesting ideas that emerged along the way had to be set aside due to time constraints or the need to maintain a clear scope, and this dissertation is no exception. In addition, potential enhancements to certain components of the work will be addressed, as they also constitute future research opportunities.

A few of these ideas, which could be explored in future developments or parallel projects, are presented here to also serve as motivation for those who reach this stage of the dissertation. In line with the progression of the topics, the prospects are presented below.

The proposed framework for deriving case-specific fragility functions could be enhanced by incorporating it into a structured process for uncertainty characterization, similar to the SSHAC approach used in seismic hazard analysis. Introduction of the uncertainty in every step of the process in a fashion similar to that used for the semi-quantitative risk evaluations, with event trees and a combination of the probability distribution of the models evaluated in every step, could be an interesting improvement for the proposed framework.

The study of variability in soil conditions could be explored through statistical or data driven approaches (Paull et al., 2022), which, when combined with geological constrains (Madsen et al., 2022), and information from new geotechnical in-situ and laboratory tests, could enhance the definition of the geotechnical model, particularly for foundation materials and potentially liquefiable soils. New geophysical surveys could further contribute to a more comprehensive characterization of the current conditions of the dam body and foundation.

An improvement in the PSHA could be made with the introduction of information from new paleoseismological studies, aiming at setting the slip rates of every source in a more reliable manner. Moreover, the introduction of non-ergodic approaches would also benefit the definition of the seismic forecast by introducing the epistemic uncertainty in source, path, and site components of the GMMs (Abrahamson, 2024). The introduction as well of modern tools intended to set the upper boundaries of the expected ground motions, as precariously balanced rocks (PBR), or other fragile geological features (FGF), could be a cap of the

forecasted ground motion for large return periods, as already done in other studies for dams around the world (Rood et al., 2020; M. W. Stirling et al., 2021).

The introduction as well of more advanced record selection techniques as the conditional means spectrum (Baker, 2011), or the combination of the CMS and the UHS (Kwong & Chopra, 2017), and considering all the components of the ground motion at a time, could adjust even more the records selected and scaled to the seismic scenarios identified in the PSHA.

Additionally, other intensity measures beyond those already selected could be considered, and their effectiveness evaluated in terms of how well they correlate with the dam's response across different *EDPs*. Some alternatives related to liquefaction problems (Dashti & Karimi, 2017; Bullock et al., 2021), embankment dams (Nardo et al., 2024), or related to characteristics of near-field ground motions (Dávalos & Miranda, 2019) could be adopted.

Building a three-dimensional model of the entire system focused on seepage analysis could provide valuable insights into the migration of suspended solids through the cut-off wall. This model, complemented by new drillings near the piezometers that show abrupt changes in their records, could help elucidate the likely non-uniform variations in the properties of the foundation soils because of fine soil migration.

Of course, new information about in-situ and laboratory tests over the dam could improve the calibration of the constitutive model, making the model even more reliable at representing the response of the dam during strong earthquakes. Moreover, the calibration of sand-based constitutive models for their use to capture the response of sand-gravel mixtures is a relevant topic (Xu & Athanasopoulos-Zekkos, 2025) that could be further enhanced by the introduction of a new definition of the void ratio for sand-gravel mixtures (Pokhrel et al., 2024). In addition, in order to capture the variability considering modeling decisions, several advanced constitutive models could be calibrated following different strategies and introduced within a logic tree combination, to evaluate the influence in the variation of different strategies to capture the cyclic response of the different soils of the dam.

A more advanced modeling of the concrete slab and its interaction with the cushion layer, with the definition of nonlinear interfaces, could improve the results in terms of slab damage index, allowing for a clearer identification of damage in each element. Moreover, the definition of the demand-to-capacity ratio of the slab, based on the combination of axial

forces and bending moments or rotations, is another possible improvement to be considered in future works.

The need for better criteria to define damage measures is critical not only for the derivation of fragility functions but also for their application in performance-based earthquake engineering assessments for embankment dams. A reevaluation of case histories and the definition of damage levels concerning quantitative estimations, such as risk metrics or repair costs, could lead to significant improvements and provide a foundation for more reliable definitions of performance and fragility. Developing a general procedure for establishing risk or performance-related damage measures for geotechnical systems, based on case histories or numerical modelling, is essential for advancing future work on the seismic performance of geotechnical structures.

Evaluating the quality of the engineering demand parameters (*EDPs*) in relation to the actual damage sustained by the dam during the development of its associated potential failure mode, in a manner like how optimal intensity measures are assessed, could improve the definition of *EDPs* for failure modes where the relationship between the physical parameter and the resulting damage is not evident. The introduction of *EDPs* and *DMs* related to the normalized stretching of the dam, in the presence of potentially liquefiable soils in the foundation, could also be an alternative approach to evaluate the global instability of the dam.

The definition of processed *EDPs* based on conditional probability and empirical or analytical models could also be a valuable approach for investigating complex PFMs, as those related to internal erosion, where a sequence of physical phenomena has to occur to trigger the scouring process. In this context, establishing a relationship between the breach of the impervious barrier and the shearing of dam body materials could be directly translated into the probability of internal erosion failures at varying levels of damage.

The comparison of the results of this work with the outcomes of empirical or semi-empirical models within a uniform framework could provide added value to methodologies that explicitly account for uncertainty in the calculations.

Although the derivation of fragility functions from 3D geotechnical models may still be far from common practice due to complexities in the modelling stages, the integration of fragility functions from multiple 2D models could be an interesting alternative to better capture the overall fragility of dams where 3D features are influential. If the statistical correlation between

the EDPs of the models is established, it may be possible to combine them using statistical methods based on the conditional probability of correlated variables, thereby obtaining a system-level fragility function as a simplified alternative to fragility functions derived from full 3D analysis.

Finally, the evaluation of dam safety through vulnerability curves and quantitative risk assessments should be the natural next step. This will allow for the assessment of dam safety in terms of risk metrics that can support risk-informed decision making related to future retrofits, emergency management, or insurance considerations.

10. References

Abrahamson, N. (2006). Seismic hazard assessment: Problems with current practice and future developments. *First European Conference on Earthquake Engineering and Seismology 2006 (1st ECEES)*. First European Conference on Earthquake Engineering and Seismology 2006 (1st ECEES), Geneva, Switzerland.

Abrahamson, N. (2024). Application of non-ergodic ground-motion models in probabilistic seismic hazard analyses. *Proceedings from the 18th World Conference on Earthquake Engineering*, 4.

Abrahamson, N. A., & Bommer, J. J. (2005). Probability and Uncertainty in Seismic Hazard Analysis. *Earthquake Spectra*, *21*(2), 603–607. https://doi.org/10.1193/1.1899158

Abrahamson, N., Gregor, N., & Addo, K. (2016). BC Hydro Ground Motion Prediction Equations for Subduction Earthquakes. *Earthquake Spectra*, *32*(1), 23–44. https://doi.org/10.1193/051712EQS188MR

Abrahamson, N., Silva, W., & Kamai, R. (2014). Summary of the ASK14 Ground Motion Relation for Active Crustal Regions. *Earthquake Spectra*, *30*(3), 1025–1055. https://doi.org/10.1193/070913EQS198M

Ahmadi, A. A., & Noorzad, A. (2025). Investigating the effects of slope changes of asphaltic concrete core of rockfill dam on the fragility curves. *Discover Civil Engineering*, *2*(1), 153. https://doi.org/10.1007/s44290-025-00312-x

Ahmadi, A. A., Rahbari, E. V., Nejad, S. A., & Khalaj, O. (2025). Seismic responses evaluation of asphaltic concrete core dam through fragility curves—A case study from Meijaran dam. *Soils and Rocks*, *49*(1), e2026001225. https://doi.org/10.28927/SR.2026.001225

Ahmed, T., Alel, M. N. A., & Arsyad, A. (2025). Seismic Fragility Assessment of Earth Dam Using Newmark Deformation Analysis. In *Lecture Notes in Civil Engineering* (pp. 166–177). Springer Nature Singapore. https://doi.org/10.1007/978-981-96-6072-8_14

Aliberti, D., Biondi, G., Cascone, E., & Rampello, S. (2019). Performance indexes for seismic analyses of earth dams. *Earthquake Geotechnical Engineering for Protection and Development of Environment and Constructions*. 7th International Conference on Earthquake Geotechnical Engineering, Rome, Italy.

Alvarado, P., Pardo, M., Gilbert, H., Miranda, S., Anderson, M., Saez, M., & Beck, S. (2009). Flat-slab subduction and crustal models for the seismically active Sierras Pampeanas region of Argentina. In S. M. Kay, V. A. Ramos, & W. R. Dickinson, *Backbone of the Americas: Shallow Subduction, Plateau Uplift, and Ridge and Terrane Collision*. Geological Society of America. https://doi.org/10.1130/2009.1204(12)

Álvarez-Gómez, J. A. (2019). FMC—Earthquake focal mechanisms data management, cluster and classification. *SoftwareX*, *9*, 299–307. https://doi.org/10.1016/j.softx.2019.03.008

Ambraseys, N. (1959). *The Seismic Stability of Earth Dams—Vol. 1* [Imperial College of Science and Technology]. http://hdl.handle.net/10044/1/11968

Amendola, C., Conti, R., & De Silva, F. (2024). Fragility curves for retaining walls in infrastructure road networks. *Japanese Geotechnical Society Special Publication*, *10*(50), 1871–1876. https://doi.org/10.3208/jgssp.v10.OS-39-03

Amendola, C., & Pitilakis, D. (2023). Urban scale risk assessment including SSI and site amplification. *Bulletin of Earthquake Engineering*, *21*(4), 1821–1846. https://doi.org/10.1007/s10518-022-01575-w

Amorosi, A. (2020). The contribution of constitutive modelling to sustainable geotechnical engineering: Examples and open issues. *The Contribution of Constitutive Modelling to Sustainable Geotechnical Engineering: Examples and Open Issues*, *1192*(2), 5–25. https://doi.org/10.19199/2020.2.0557-1405.005

Ancheta, T. D., Darragh, R. B., Stewart, J. P., Seyhan, E., Silva, W. J., Chiou, B. S.-J., Wooddell, K. E., Graves, R. W., Kottke, A. R., Boore, D. M., Kishida, T., & Donahue, J. L. (2014). NGA-West2 Database. *Earthquake Spectra*, *30*(3), 989–1005. https://doi.org/10.1193/070913EQS197M

Andreotti, G., & Lai, C. G. (2019). Use of fragility curves to assess the seismic vulnerability in the risk analysis of mountain tunnels. *Tunnelling and Underground Space Technology*, *91*, 103008. https://doi.org/10.1016/j.tust.2019.103008

Andrianopoulos, K. I., Papadimitriou, A. G., Bouckovalas, G. D., & Karamitros, D. K. (2014). Insight into the seismic response of earth dams with an emphasis on seismic coefficient estimation. *Computers and Geotechnics*, *55*, 195–210. https://doi.org/10.1016/j.compgeo.2013.09.005

Andrus, R. D., & Stokoe Ii, K. H. (2000). Liquefaction Resistance of Soils from Shear-Wave Velocity. *Journal of Geotechnical and Geoenvironmental Engineering*, *126*(11), 1015–1025. https://doi.org/10.1061/(ASCE)1090-0241(2000)126:11(1015)

Ansari, Md. I., & Agarwal, P. (2016). Categorization of Damage Index of Concrete Gravity Dam for the Health Monitoring after Earthquake. *Journal of Earthquake Engineering*, *20*(8), 1222–1238. https://doi.org/10.1080/13632469.2016.1138167

Ardiaca, D. H. (2009). Mohr-Coulomb parameters for modelling of concrete structures. *Plaxis Bulletin*, *Spring issue 2009*, 12–15.

Argyroudis, S., Kaynia, A., & Pitilakis, K. (2013). Development of fragility functions for geotechnical constructions: Application to cantilever retaining walls. *Soil Dynamics and Earthquake Engineering*, *50*, 106–116. https://doi.org/10.1016/j.soildyn.2013.02.014

Ariga, Y., Fujinawa, Y., Kawakami, N., Ohsumi, T., & Nishino, T. (2005). An immediate evaluation method of earthquake damage of dams by utilizing real-time earthquake information. *WIT Transactions on The Built Environment*, *81*.

Ariga, Y., Fujinawa, Y., Ohbo, N., Asaka, H., & Yoda, M. (2012). Rationalization of Emergency Inspection for Hydraulic Structure by combining Earthquake Early Warning and 3D Dynamic Analysis. *WCEE 15*. 15th World Conference on Earthquake Engineering, Lisbon, Portugal.

Armstrong, R. J., Park, D., & Gullen, A. (2018). Cyclic soil behavior of common constitutive models used in non-linear deformation analyses of embankment dams. *Proceedings of the 2018 USSD Annual Conference*, 20.

Armstrong, R., Kishida, T., & Park, D. (2021). Efficiency of ground motion intensity measures with earthquake-induced earth dam deformations. *Earthquake Spectra*, *37*(1), 5–25. https://doi.org/10.1177/8755293020938811

Atukorala, U., Hawson, H., Mylleville, B., & Williams, R. (2014). *Seismic Guidelines for Dikes 2nd Edition*. British Columbia Ministry of Forests, Lands and Natural Resource Operations. https://www2.gov.bc.ca/assets/gov/environment/air-land-water/water/integrated-flood-hazard-mgmt/seismic_guidelines_dikes-2014-2nd_edition.pdf

Ayati Ahmadi, A., Noorzad, A., MohammadNezhad, H., & Mirghasemi, A. A. (2023). Seismic Fragility of Rockfill Dams with Asphaltic Concrete Core. *Iranian Journal of Science and Technology, Transactions of Civil Engineering*, *47*(3), 1585–1598. https://doi.org/10.1007/s40996-022-00993-9

Bakalis, K., & Vamvatsikos, D. (2018). Seismic Fragility Functions via Nonlinear Response History Analysis. *Journal of Structural Engineering*, *144*(10). https://doi.org/10.1061/(ASCE)ST.1943-541X.0002141

Baker, Bradley, & Stafford. (2021). *Seismic Hazard and Risk Analysis*. Cambridge University Press. https://doi.org/10.1017/9781108425056

Baker, J. (2011). Conditional Mean Spectrum: Tool for Ground-Motion Selection. *Journal of Structural Engineering*, *137*(3), 322–331. https://doi.org/10.1061/(ASCE)ST.1943-541X.0000215

Baker, J. (2013). *Introduction to Probabilistic Seismic Hazard Analysis* (p. 79) [White Paper].

Baker, J., Luco, N., Maechling, P., Graves, R., Olsen, K., & Abrahamson, N. (2014). *Engineering uses of physics-based ground motion simulations*. https://doi.org/10.4231/D3QF8JK2C

Baker, J. W. (2015). Efficient Analytical Fragility Function Fitting Using Dynamic Structural Analysis. *Earthquake Spectra*, *31*(1), 579–599. https://doi.org/10.1193/021113EQS025M

Baltzopoulos, G., Baraschino, R., Iervolino, I., & Vamvatsikos, D. (2017). SPO2FRAG: Software for seismic fragility assessment based on static pushover. *Bulletin of Earthquake Engineering*, *15*(10), 4399–4425. https://doi.org/10.1007/s10518-017-0145-3

Baraschino, R., Baltzopoulos, G., & Iervolino, I. (2020). R2R-EU: Software for fragility fitting and evaluation of estimation uncertainty in seismic risk analysis. *Soil Dynamics and Earthquake Engineering*, *132*, 106093. https://doi.org/10.1016/j.soildyn.2020.106093

Barbagelata, J. M., & Barchiesi, A. (2024). Mecanismos de falla en presas de materiales sueltos durante terremotos: Descripción y metodologías de análisis. *Actas del Congreso Argentino de Presas y Aprovechamientos Multipropósito*, 10.

Barbagelata, J. M., d'Onofrio, A., Mingorance, F. A., Pagano, L., & Silvestri, F. (2024). Characterization, processing, and interpretation of weak-motion records of a CFRD dam. *Japanese Geotechnical Society Special Publication*, *10*(38), 1435–1440. https://doi.org/10.3208/jgssp.v10.OS-27-02

Barbagelata, J. M., d'Onofrio, A., & Silvestri, F. (2022). The elastic behavior of two types of embankment dams under seismic loading considering dam-reservoir interaction effects. *Incontro Annuale Dei Ricercatori Geotecnica*. Incontro Annuale dei Ricercatori Geotecnica, Caserta, Italia.

Barbagelata, J. M., Zimmaro, P., d'Onofrio, A., Pagano, L., & Silvestri, F. (2024). *A proposal for earthquake early warning systems for embankment dams using fragility functions*. Incontro Annuale dei Ricercatori di Geotecnica 2024- IARG 2024, Gaeta, Italy.

Barchiesi, A. (2019). *Estudios de verificación de la estabilidad de la presa "Potrerillos"* (p. 164) [Informe Técnico Independiente].

Barchiesi, A., Cazalis, P., & Carrère, A. (2005). Potrerillos Project: Diaphragm wall design. *Proceedings of the 16th International Conference on Soil Mechanics and Geotechnical Engineering*. https://doi.org/10.3233/978-1-61499-656-9-1849

Barchiesi, A., Toso, J., Lara, A., & Carrere, A. (2006). La Fundación y el Diseño Sismorresistente de la Presa Potrerillos. *IV Congreso Argentino de Presas y Aprovechamientos Hidroeléctricos*. IV Congreso Argentino de Presas y Aprovechamientos Hidroeléctricos, Posadas, Argentina.

Baziar, M. H., & Alavi, S. M. (2024). Seismic Assessment of Clayey-Core Earth Fill Dams Using Performance-Based Fragility Curves and Finite Difference Analyses. *Geotechnical and Geological Engineering*, *42*(6), 4581–4608. https://doi.org/10.1007/s10706-024-02800-w

Bazzurro, P., & Cornell, A. (1999). Disaggregation of seismic hazard. *Bulletin of the Seismological Society of America*, *89*(2), 501–520. https://doi.org/10.1785/BSSA0890020501

Benz, T., Schwab, R., & Vermeer, P. (2009). Small-strain stiffness in geotechnical analyses. *Bautechnik*, *86*(S1), 16–27. https://doi.org/10.1002/bate.200910038

Bieniawski, Z. T. (1989). *Engineering rock mass classifications: A complete manual for engineers and geologists in mining, civil, and petroleum engineering*. Wiley.

Bilotta, E., Pagano, L., & Sica, S. (2010). Effect of ground-motion asynchronism on the equivalent acceleration of earth dams. *Soil Dynamics and Earthquake Engineering*, *30*(7), 561–579. https://doi.org/10.1016/j.soildyn.2010.01.014

Bommer, J. (2002). Deterministic vs. Probabilistic Seismic Hazard Assessment: An exaggerated and obstructive dichotomy. *Journal of Earthquake Engineering*, *6*(sup001), 43–73. https://doi.org/10.1080/13632460209350432

Bommer, J. (2022). Earthquake hazard and risk analysis for natural and induced seismicity: Towards objective assessments in the face of uncertainty. *Bulletin of Earthquake Engineering*, *20*(6), 2825–3069. https://doi.org/10.1007/s10518-022-01357-4

Bommer, J., & Acevedo, A. (2004). The use of real earthquake accelerograms as input to dynamic analysis. *Journal of Earthquake Engineering*, *8*(sup001), 43–91. https://doi.org/10.1080/13632460409350521

Bommer, J. J. (2005). On the Use of Logic Trees for Ground-Motion Prediction Equations in Seismic-Hazard Analysis. *Bulletin of the Seismological Society of America*, *95*(2), 377–389. https://doi.org/10.1785/0120040073

Bommer, J. J. (2012). Challenges of Building Logic Trees for Probabilistic Seismic Hazard Analysis. *Earthquake Spectra*, *28*(4), 1723–1735. https://doi.org/10.1193/1.4000079

Bommer, J. J., & Crowley, H. (2017). The Purpose and Definition of the Minimum Magnitude Limit in PSHA Calculations. *Seismological Research Letters*, *88*(4), 1097–1106. https://doi.org/10.1785/0220170015

Bommer, J. J., Douglas, J., Scherbaum, F., Cotton, F., Bungum, H., & Fah, D. (2010). On the Selection of Ground-Motion Prediction Equations for Seismic Hazard Analysis. *Seismological Research Letters*, *81*(5), 783–793. https://doi.org/10.1785/gssrl.81.5.783

Bommer, J. J., Scott, S. G., & Sarma, S. K. (2000). Hazard-consistent earthquake scenarios. *Soil Dynamics and Earthquake Engineering*, *19*(4), 219–231. https://doi.org/10.1016/S0267-7261(00)00012-9

Bommer, J. J., & Stafford, P. J. (2020). Selecting Ground-Motion Models for Site-Specific PSHA: Adaptability versus Applicability. *Bulletin of the Seismological Society of America*, *110*(6), 2801–2815. https://doi.org/10.1785/0120200171

Bommer, J., & Scherbaum, F. (2008). The Use and Misuse of Logic Trees in Probabilistic Seismic Hazard Analysis. *Earthquake Spectra*, *24*(4), 997–1009. https://doi.org/10.1193/1.2977755

Boore, D. M., & Bommer, J. J. (2005). Processing of strong-motion accelerograms: Needs, options and consequences. *Soil Dynamics and Earthquake Engineering*, *25*(2), 93–115. https://doi.org/10.1016/j.soildyn.2004.10.007

Boore, D., Stewart, J., Seyhan, E., & Atkinson, G. (2014). NGA-West2 Equations for Predicting PGA, PGV, and 5% Damped PSA for Shallow Crustal Earthquakes. *Earthquake Spectra*, *30*(3), 1057–1085. https://doi.org/10.1193/070113EQS184M

Boulanger, R. (2022). Nonlinear dynamic analyses involving soil liquefaction or cyclic softening. In *Proceedings of the 20th ICSMGE-State of the art and invited lectures*. Australian Geomechanics Society.

Boulanger, R., & Beaty, M. (2016). Seismic Deformation Analyses of Embankment Dams: A Reviewer's Checklist. *USSD 2016 Annual Meeting and Conference*. https://www.researchgate.net/publication/315615330

Boulanger, R., & Idriss, I. M. (2014). *CPT and SPT based liquefaction triggering procedures* (No. Report No. UCD/CGM-14/01; p. 134). University of California, Davis.

Boulanger, R. W. (2019). Nonlinear Dynamic Analyses of Austrian Dam in the 1989 Loma Prieta Earthquake. *Journal of Geotechnical and Geoenvironmental Engineering*, *145*(11). https://doi.org/10.1061/(ASCE)GT.1943-5606.0002156

Boulanger, R. W., Montgomery, J., & Ziotopoulou, K. (2015). Nonlinear Deformation Analyses of Liquefaction Effects on Embankment Dams. In *Geotechnical, Geological and Earthquake Engineering* (Vol. 37, pp. 247–283). Kluwer Academic Publishers. https://doi.org/10.1007/978-3-319-10786-8_10

Boulanger, R. W., & Ziotopoulou, K. (2018). On NDA Practices for Evaluating Liquefaction Effects. *Geotechnical Earthquake Engineering and Soil Dynamics V*, 1–20. https://doi.org/10.1061/9780784481455.001

Boulanger, R. W., & Ziotopoulou, K. (2024). *PM4Sand (Version 3.3): A sand plasticity model for earthquake engineering applications* (No. UCD/CGM-23/01; p. 122). University of California, Davis.

Bozorgnia, Y., & Campbell, K. W. (2016). Ground Motion Model for the Vertical-to-Horizontal (V/H) Ratios of PGA, PGV, and Response Spectra. *Earthquake Spectra*, *32*(2), 951–978. https://doi.org/10.1193/100614eqs151m

Bray, J. D., & Macedo, J. (2019). Procedure for Estimating Shear-Induced Seismic Slope Displacement for Shallow Crustal Earthquakes. *Journal of Geotechnical and Geoenvironmental Engineering*, *145*(12), 04019106. https://doi.org/10.1061/(ASCE)GT.1943-5606.0002143

Bray, J. D., & Travasarou, T. (2009). Pseudostatic Coefficient for Use in Simplified Seismic Slope Stability Evaluation. *Journal of Geotechnical and Geoenvironmental Engineering*, *135*(9), 1336–1340. https://doi.org/10.1061/(ASCE)GT.1943-5606.0000012

Brooks, B. A., Bevis, M., Smalley, R., Kendrick, E., Manceda, R., Lauría, E., Maturana, R., & Araujo, M. (2003). Crustal motion in the Southern Andes (26°–36°S): Do the Andes behave like a microplate? *Geochemistry, Geophysics, Geosystems*, *4*(10), 2003GC000505. https://doi.org/10.1029/2003GC000505

Bullock, Z., Dashti, S., Liel, A. B., Porter, K. A., & Karimi, Z. (2019). Assessment Supporting the Use of Outcropping Rock Evolutionary Intensity Measures for Prediction of Liquefaction Consequences. *Earthquake Spectra*, *35*(4), 1899–1926. https://doi.org/10.1193/041618EQS094M

Bullock, Z., Liel, A. B., Porter, K. A., & Dashti, S. (2021). Site-specific liquefaction fragility analysis: Cloud, stripe, and incremental approaches. *Earthquake Engineering & Structural Dynamics*, *50*(9), 2529–2550. https://doi.org/10.1002/eqe.3458

Burbank, D. W., & Anderson, R. S. (2011). *Tectonic Geomorphology* (1st ed.). Wiley. https://doi.org/10.1002/9781444345063

Butler, D. K., & Curro, J. R. (1981). Crosshole seismic testing—Procedures and pitfalls. *GEOPHYSICS*, *46*(1), 23–29. https://doi.org/10.1190/1.1441134

Calderón, F., & Cordone, J. P. (2019). Determinación de la frecuencia fundamental de una presa CFRD mediante funciones de transferencia. *XXI Chilean Conference on Seismology and Eartquake Engineering*, 8.

Campbell, K., & Bozorgnia, Y. (2014). NGA-West2 Ground Motion Model for the Average Horizontal Components of PGA, PGV, and 5% Damped Linear Acceleration Response Spectra. *Earthquake Spectra*, *30*(3), 1087–1115. https://doi.org/10.1193/062913EQS175M

Capaldi, T. N., Horton, B. K., McKenzie, N. R., Mackaman-Lofland, C., Stockli, D. F., Ortiz, G., & Alvarado, P. (2020). Neogene Retroarc Foreland Basin Evolution, Sediment Provenance, and Magmatism in Response to Flat Slab Subduction, Western Argentina. *Tectonics*, *39*(7), e2019TC005958. https://doi.org/10.1029/2019TC005958

Carmona, J. S., Carmona, J. M., & Palau, R. (2004). *The Evaluation of the Permanent Seismic Crest Displacement of the CFGD Potrerillos Dam in Argentine by Means of a Tridimensional Limit State Analysis*. 13th World Conference on Earthquake Engineering, Canada.

Casa, A. L., Cortés, J. M., & Borgnia, M. M. (2010). Evidencias de deformación pleistocena en el sistema de falla de La Carrera (32°40'-33°-15'LS), Cordillera Frontal de Mendoza. *Revista de la Asociación Geológica Argentina*, *1*(67), 91–104.

Castro, G. (1975). Liquefaction and Cyclic Mobility of Saturated Sands. *Journal of the Geotechnical Engineering Division*, *101*(6), 551–569. https://doi.org/10.1061/AJGEB6.0000173

Castro, G., Seed, R. B., Keller, T. O., & Seed, H. B. (1992). Steady-State Strength Analysis of Lower San Fernando Dam Slide. *Journal of Geotechnical Engineering*, *118*(3), 406–427. https://doi.org/10.1061/(ASCE)0733-9410(1992)118:3(406)

Castro, R., Ruiz, E., Uribe, A., & Rebollar, C. (2000). Site Response of the Dam El Infiernillo, Guerrero-Michoacan, Mexico. *Bulletin of the Seismological Society of America*, *90*(6), 1446–1453. https://doi.org/10.1785/0119990050

CEMPPSA. (2007). *Manual de Auscultación—Proyecto Potrerillos*. Consorcio de Empresas Mendocinas Para Potrerillos S.A.

Cetin, K., Cuceoglu, F., Ayhan, B. U., Yildirim, S., Aydin, S., Demirdogen, S., Er, Y., Gurbuz, A., & Moss, R. E. S. (2024). Performance of hydraulic structures during 6 February 2023 Kahramanmaraş, Türkiye, earthquake sequence. *Earthquake Spectra*, 87552930241258295. https://doi.org/10.1177/87552930241258295

Chen, K., Pang, R., & Xu, B. (2023). Stochastic dynamic response and seismic fragility analysis for high concrete face rockfill dams considering earthquake and parameter uncertainties. *Soil Dynamics and Earthquake Engineering*, *167*, 107817. https://doi.org/10.1016/j.soildyn.2023.107817

Chen, L. (2025). Improved Probabilistic Seismic Demand–Intensity Relationship: Heteroscedastic Approaches. *ASCE-ASME Journal of Risk and Uncertainty in Engineering Systems, Part A: Civil Engineering*, *11*(1), 04024089. https://doi.org/10.1061/AJRUA6.RUENG-1420

Chiaramonte, L., Ramos, V., & Araujo, M. (2000). Estructura y sismotectónica del anticlinal Barrancas, cuenca Cuyana, provincia de Mendoza. *Revista de la Asociación Geológica Argentina*, *4*(55), 309–336.

Chioccarelli, E., Cito, P., Iervolino, I., & Giorgio, M. (2019). REASSESS V2.0: Software for single- and multi-site probabilistic seismic hazard analysis. *Bulletin of Earthquake Engineering*, *17*(4), 1769–1793. https://doi.org/10.1007/s10518-018-00531-x

Chiou, B. S.-J., & Youngs, R. R. (2014). Update of the Chiou and Youngs NGA Model for the Average Horizontal Component of Peak Ground Motion and Response Spectra. *Earthquake Spectra*, *30*(3), 1117–1153. https://doi.org/10.1193/072813EQS219M

Cho, Y., & Rathje, E. M. (2022). Generic Predictive Model of Earthquake-Induced Slope Displacements Derived from Finite-Element Analysis. *Journal of Geotechnical and Geoenvironmental Engineering*, *148*(4), 04022010. https://doi.org/10.1061/(ASCE)GT.1943-5606.0002757

Choo, Y. W., Shin, D. H., Cho, S. E., Im, E. S., & Kim, D.-S. (2013). Seepage behavior of drainage zoning in a concrete faced gravel-fill dam via centrifuge and numerical modeling. *KSCE Journal of Civil Engineering*, *17*(5), 949–958. https://doi.org/10.1007/s12205-013-0215-2

Chowdhury, I. N., Cabas, A., Kaklamanos, J., Kottke, A., & Gregor, N. (2024). Implications of input ground-motion selection techniques on site response analyses for different tectonic settings. *Earthquake Spectra*, *40*(2), 1521–1551. https://doi.org/10.1177/87552930241230917

Chowdhury, K., Dawson, E., Chitwood, D., Russell, M., Geraci, J., Vu, Q.-H., & Eit, P. (2022). Nonlinear Seismic Deformation Analyses Based Fragility Curves for Risk-Informed Design of Whittier Narrows Dam in California. In USSD (Ed.), *Proceedings of the 2022 USSD Annual Conference* (Issue 1).

Chowdhury, K., Dawson, E., Newman, E., Dober, M., Hazleton, K., Gamblin, A., & Seed, R. B. (2020). Evolution of Seismic Analysis of an Embankment Dam. *Dam Safety 2020*. https://www.researchgate.net/publication/344781151

Chowdhury, K., O'Leary, T., Medley, E., & Serafini, D. (2023). *Assessment of Aging Dams for Seismic Potential Failure Modes: A Delta Approach*. 2023 ASDSO Annual Conference, Palm Springs, California.

Chowdhury, K., Seed, R. B., Hlepas, G., Dawson, E., Alres, M., Zafir, Z., & Finlay, O. (2022). *Considerations for Subsurface Investigations for Seismic Analysis of Embankment Dams and Levees*. 52.

Clements, R. P. (1984). Post-Construction Deformation of Rockfill Dams. *Journal of Geotechnical Engineering*, *110*(7), 821–840. https://doi.org/10.1061/(ASCE)0733-9410(1984)110:7(821)

Consorcio Potrerillos. (1988). *Aprovechamiento Múltiple Potrerillos—Río Mendoza—Materiales para las presas de materiales sueltos* (No. Tomo 9; p. 116).

Cornell, A., & Vanmarcke, E. (1969). The major influences on seismic risk. *Proceedings of the IV World Congress in Earthquake Engineering*, 169–183.

Cornell, A., & Winterstein, S. (1988). Temporal and magnitude dependence in earthquake recurrence models. *Bulletin of the Seismological Society of America*, *78*(4), 1522–1537. https://doi.org/10.1785/BSSA0780041522

Cornell, C. A. (1968). Engineering seismic risk analysis. *Bulletin of the Seismological Society of America*, *58*(5), 1583–1606. https://doi.org/10.1785/BSSA0580051583

Cornell, C. A., Jalayer, F., Hamburger, R. O., & Foutch, D. A. (2002). Probabilistic Basis for 2000 SAC Federal Emergency Management Agency Steel Moment Frame Guidelines. *Journal of Structural Engineering*, *128*(4), 526–533. https://doi.org/10.1061/(ASCE)0733-9445(2002)128:4(526)

Cortés, J. M., Casa, A., Pasini, M., Yamin, M., & Terrizzano, C. (2006). Fajas oblicuas de deformación neotectónica en Precordillera y Cordillera Frontal (31°30'-33°30'LS): Controles paleotectónicos. *Revista de la Asociación Geológica Argentina*, *4*(61), 639–646.

Cosentini, R. M., & Bozzoni, F. (2022). Fragility curves for rapid assessment of earthquake-induced damage to earth-retaining walls starting from optimal seismic intensity measures. *Soil Dynamics and Earthquake Engineering*, *152*, 107017. https://doi.org/10.1016/j.soildyn.2021.107017

COSMOS. (2001). *Instrumental Systems for Diagnostics of Seismic Response of Bridges and Dams—Recommended Guidelines* (p. 105) [Guidelines]. Consortium of Organizations for Strong-Motion Observation Systems.

Costigliola, R. M. (2017). *La rivalutazione della sicurezza sismica delle grandi dighe con manto*.

Costigliola, R. M., Mancuso, C., Pagano, L., & Silvestri, F. (2022). Prediction of permanent settlements of an upstream faced earth dam. *Computers and Geotechnics*, *144*. https://doi.org/10.1016/j.compgeo.2021.104594

Cremen, G., & Galasso, C. (2020). Earthquake early warning: Recent advances and perspectives. *Earth-Science Reviews*, *205*, 103184. https://doi.org/10.1016/j.earscirev.2020.103184

Cremen, G., & Galasso, C. (2021). A decision-making methodology for risk-informed earthquake early warning. *Computer-Aided Civil and Infrastructure Engineering*, *36*(6), 747–761. https://doi.org/10.1111/mice.12670

Cruz, P. T. da, Materón, B., & Freitas, M. de S. (2009). *Concrete face rockfill dams*. CRC Press/Balkema.

Dakoulas, P., & Gazetas, G. (1985). A class of inhomogeneous shear models for seismic response of dams and embankments. *International Journal of Soil Dynamics and Earthquake Engineering*, *4*(4), 166–182. https://doi.org/10.1016/0261-7277(85)90037-3

Dakoulas, P., & Gazetas, G. (1986). Seismic shear vibration of embankment dams in semi-cylindrical valleys. *Earthquake Engineering & Structural Dynamics*, *14*(1), 19–40. https://doi.org/10.1002/eqe.4290140103

Dakoulas, P., & Gazetas, G. (1987). Vibration Characteristics of Dams in Narrow Canyons. *Journal of Geotechnical Engineering*, *113*(8), 899–904. https://doi.org/10.1061/(ASCE)0733-9410(1987)113:8(899)

Darbre, G. (2004). Swiss Guidelines for the Earthquake Safety of Dams. *Proceedings of the 13th World Conference on Earthquake Engineering*. 13th World Conference on Earthquake Engineering, Canada.

Dashti, S., & Karimi, Z. (2017). Ground Motion Intensity Measures to Evaluate I: The Liquefaction Hazard in the Vicinity of Shallow-Founded Structures. *Earthquake Spectra*, *33*(1), 241–276. https://doi.org/10.1193/103015eqs162m

Dávalos, H., & Miranda, E. (2019). Filtered incremental velocity: A novel approach in intensity measures for seismic collapse estimation. *Earthquake Engineering & Structural Dynamics*, *48*(12), 1384–1405. https://doi.org/10.1002/eqe.3205

De Cicco, R., Barchiesi, A., & Silvestri, F. (2015). Metodología y herramientas para el diseño sismorresistente de presas tipo CFRD. *VIII Congreso Argentino de Presas y Aprovechamientos Hidroeléctricos*. VIII Congreso Argentino de Presas y Aprovechamientos Hidroeléctricos, Santa Fe, Argentina.

Deere, D. U., & Deere, D. W. (1988). The Rock Quality Designation (RQD) Index in Practice. In L. Kirkaldie, *Rock Classification Systems for Engineering Purposes* (pp. 91–101). ASTM International100 Barr Harbor Drive, PO Box C700, West Conshohocken, PA 19428-2959. https://doi.org/10.1520/STP48465S

DeJong, J. T., Sturm, A. P., & Ghafghazi, M. (2016). Characterization of gravelly alluvium. *Soil Dynamics and Earthquake Engineering*, *91*, 104–115. https://doi.org/10.1016/j.soildyn.2016.09.032

Derakhshan, A., & Alielahi, H. (2025). Seismic fragility and resilience assessment of instrumented Cogswell concrete-faced rockfill dam using scalar and vector-valued approaches. *Engineering Geology*, *352*, 108090. https://doi.org/10.1016/j.enggeo.2025.108090

DIN. (1993). *DIN 18134:1993-01, Soil; testing procedures and testing equipment; plate load test* (Version 01). DIN Media GmbH. https://doi.org/10.31030/1869979

Donahue, J. L., Amini, Z. A., Hunt, C. E., Rix, G. J., & Umberg, D. R. (2018). Development of a Seismic Risk Screening Tool for Earthen Embankments. *Geotechnical Earthquake Engineering and Soil Dynamics V*, 27–36. https://doi.org/10.1061/9780784481486.004

Dunnicliff, J., Sellers, B., Mikkelsen, E., & Beth, M. (2003). Discussions of "Measurement of Pore Water Pressures in Embankment Dams." *Geotechnical Instrumentation News (GIN)*, *21*(2), 42–51.

Ekström, G., Nettles, M., & Dziewoński, A. M. (2012). The global CMT project 2004–2010: Centroid-moment tensors for 13,017 earthquakes. *Physics of the Earth and Planetary Interiors*, *200–201*, 1–9. https://doi.org/10.1016/j.pepi.2012.04.002

Elgamal, A. M., Abdel-Ghaffar, A. M., & Prevost, J. (1987). 2-D Elastoplastic Seismic Shear Response of Earth Dams: Applications. *Journal of Engineering Mechanics*, *113*(5), 702–719. https://doi.org/10.1061/(ASCE)0733-9399(1987)113:5(702)

Elgamal, A. M., Scott, R. F., Succarieh, M. F., & Yan, L. (1990). La Villita Dam Response during Five Earthquakes including Permanent Deformation. *Journal of Geotechnical Engineering*, *116*(10), 1443–1462. https://doi.org/10.1061/(ASCE)0733-9410(1990)116:10(1443)

El-Idrissi, M., Saifullah, M. K., Ciudad-Real, M., Skolnik, D., & Spassov, E. (2023). Operations and Dam Safety with the KMIDam Platform. In M. P. Limongelli, P. F. Giordano, S. Quqa, C. Gentile, & A. Cigada (Eds.), *Experimental Vibration Analysis for Civil Engineering Structures* (Vol. 432, pp. 314–320). Springer Nature Switzerland. https://doi.org/10.1007/978-3-031-39109-5_32

Espinosa, M., Alvarez, C., & Fuentes, A. (2002). *Presa Potrerillos, descripcion general y aspectos constructivos*. 8.

Espinosa, M. E., Espinosa, G. A., Luquez, G., & Ruiz Freites, S. J. (2010). *Ingeniería de Presas de Escollera*. Facultad de Ingeniería, Universidad Nacional de Cuyo.

Fabbrocino, G., Iervolino, I., Orlando, F., & Salzano, E. (2005). Quantitative risk analysis of oil storage facilities in seismic areas. *Journal of Hazardous Materials*, *123*(1–3), 61–69. https://doi.org/10.1016/j.jhazmat.2005.04.015

Fahlbusch, H. (2009). Early dams. *Proceedings of the ICE - Engineering History and Heritage*, *162*(1), 13–18. https://doi.org/10.1680/ehah.2009.162.1.13

Fell, R., & Fry, J. J. (Eds.). (2007). *Internal erosion of dams and their foundations*. Taylor & Francis.

Fell, R., Macgregor, P., Stapledon, D., Bell, G., & Foster, M. (2014). *Geotechnical Engineering of Dams*. CRC Press/Balkema. https://www.routledge.com/Geotechnical-Engineering-of-Dams/Fell-MacGregor-Stapledon-Bell-Foster/p/book/9781138749344

FEMA. (2011). *Filters for Embankment Dams, best practices for design and construction*. Federal Emergency Management Agency.

FEMA. (2019). *Hazus—MH 2.1 Advanced Engineering Building Module (AEBM) Technical and User's Manual*. Federal Emergency Management Agency.

FERC. (2014). Chapter 13—Evaluation of earthquake ground motions. In *Engineering Guidelines for the Evaluation of Hydropower Projects* (p. 100). Federal Energy Regulatory Commission.

FERC. (2016). *Risk-Informed Decision Making (RIDM)* (No. 4.1; Risk Guidelines for Dam Safety, p. 274). Federal Energy Regulatory Commission.

FERC. (2021). Chapter 17—Potential Failure Mode Analysis. In *Engineering Guidelines for the Evaluation of Hydropower Projects* (p. 134). Federal Energy Regulatory Commission.

Figura, F. (2020). *Comportamento dinamico della diga in terra nel comuni di Briaglia: Definizione delle curve di fragilità* [Master Thesis]. Politectnico di Torino.

Flora, A., & Modoni, G. (1997). Upgrading Equipment and Procedures for Stress Path Triaxial Testing of Coarse-Grained Materials. *Geotechnical Testing Journal*, *20*(4), 459–469. https://doi.org/10.1520/GTJ10412J

Fluixá-Sanmartín, J., Escuder-Bueno, I., Morales-Torres, A., & Castillo-Rodríguez, J. T. (2020). Comprehensive decision-making approach for managing time dependent dam risks. *Reliability Engineering & System Safety*, *203*, 107100. https://doi.org/10.1016/j.ress.2020.107100

Fontanella, E., Pagano, L., & Desideri, A. (2020). Simplified Models for the Interpretation of Total Stress Measurement of Embankment Dams. In *Dam Breach Modelling and Risk Disposal* (pp. 340–344). Springer International Publishing. https://doi.org/10.1007/978-3-030-46351-9_35

Fookes, P. G. (1997). Geology for Engineers: The Geological Model, Prediction and Performance. *Quarterly Journal of Engineering Geology*, *30*(4), 293–424. https://doi.org/10.1144/GSL.QJEG.1997.030.P4.02

Franchin, P., Lupoi, A., Pinto, P., & Schotanus, M. (2004). *Seismic Fragility Analysis of RC Structures: Use of Response Surface for a Realistic Application*. 13th World Conference on Earthquake Engineering, Canada.

Fry, J. (2016). Lessons on internal erosion in embankment dams from failures and physical models. *Scour and Erosion*, 41–58. https://doi.org/10.1201/9781315375045-6

García, V. H., & Casa, A. L. (2015). Quaternary tectonics and seismic potential of the Andean retrowedge at 33–34°S. *Geological Society, London, Special Publications*, *399*(1), 311–327. https://doi.org/10.1144/SP399.11

Gazetas, G. (1981). A New Dynamic Model for Earth Dams Evaluated Through Case Histories. *Soils and Foundations*, *21*(1), 67–78. https://doi.org/10.3208/sandf1972.21.67

Gazetas, G. (1987). Seismic response of earth dams: Some recent developments. *Soil Dynamics and Earthquake Engineering*, *6*(1), 2–47. https://doi.org/10.1016/0267-7261(87)90008-X

Gazetas, G., & Dakoulas, P. (1992). Seismic analysis and design of rockfill dams: State-of-the-art. *Soil Dynamics and Earthquake Engineering*, *11*(1), 27–61. https://doi.org/10.1016/0267-7261(92)90024-8

GCPP. (1998). *Aprovechamiento Integral del Río Mendoza—Proyecto Potrerillos—Fase I - Campaña de investigaciones complementarias*.

GCPP. (1999). *Aprovechamiento Integral del Río Mendoza—Proyecto Potrerillos—Fase II - Proyecto ejecutivo*.

Geomatrix. (2004). *Revisión Técnica de los Estudios de Evaluación de la Seguridad Sísmica de la Presa Potrerillos* (No. 8890; p. 23). Geomatrix Consultants, Inc.

Ghaemi, A., & Konrad, J.-M. (2022). Empirical approaches to estimate the nonlinear dynamic responses of earth-core rockfill dams subjected to earthquake ground motions. *Soils and Foundations*, *62*(2), 101106. https://doi.org/10.1016/j.sandf.2022.101106

Ghaemi, A., & Konrad, J.-M. (2023). Empirical relationships for estimating the crest settlement of earth-core rockfill dams subjected to earthquakes. *Canadian Geotechnical Journal*, *60*(2), 166–181. https://doi.org/10.1139/cgj-2021-0159

Gibson, E. M., & Bensi, M. T. (2023). Bayesian Network Framework to Model Seismic Failure Modes for an Embankment Dam System. *ASCE Inspire 2023*, 650–658. https://doi.org/10.1061/9780784485163.076

Gil, E., Nafá, R. T., & Zamarbide, J. L. (1982). *Microzonificación sísmica del Valle de Tulum—Provincia de San Juan* (Informe Técnico General No. Volumen 1; p. 137). Instituto Nacional de Prevención Sísmica.

Giovenale, P., Cornell, C. A., & Esteva, L. (2004). Comparing the adequacy of alternative ground motion intensity measures for the estimation of structural responses. *Earthquake Engineering & Structural Dynamics*, *33*(8), 951–979. https://doi.org/10.1002/eqe.386

Gregor, N., Abrahamson, N. A., Atkinson, G. M., Boore, D. M., Bozorgnia, Y., Campbell, K. W., Chiou, B. S.-J., Idriss, I. M., Kamai, R., Seyhan, E., Silva, W., Stewart, J. P., & Youngs, R. (2014). Comparison of NGA-West2 GMPEs. *Earthquake Spectra*, *30*(3), 1179–1197. https://doi.org/10.1193/070113EQS186M

Gregori, S. D., & Christiansen, R. (2018). Seismic hazard analysis for central-western Argentina. *Geodesy and Geodynamics*, *9*(1), 25–33. https://doi.org/10.1016/j.geog.2017.07.006

Guan, Z. (2009). Investigation of the 5.12 Wenchuan Earthquake damages to the Zipingpu Water Control Project and an assessment of its safety state. *Science in China Series E: Technological Sciences*, *52*(4), 820–834. https://doi.org/10.1007/s11431-009-0044-1

Gülerce, Z., Kamai, R., Abrahamson, N. A., & Silva, W. J. (2017). Ground Motion Prediction Equations for the Vertical Ground Motion Component Based on the NGA-W2 Database. *Earthquake Spectra*, *33*(2), 499–528. https://doi.org/10.1193/121814EQS213M

Gutenberg, B., & Richter, C. F. (1944). Frequency of earthquakes in California*. *Bulletin of the Seismological Society of America*, *34*(4), 185–188. https://doi.org/10.1785/BSSA0340040185

Guzmán, C. G., & Cristallini, E. O. (2009). Contemporary stress orientations from borehole breakout analysis in the southernmost flat-slab boundary Andean retroarc (32°44′ and 33°40′S). *Journal of Geophysical Research: Solid Earth*, *114*(B2), 2007JB005505. https://doi.org/10.1029/2007JB005505

Hancock, J., Watson-Lamprey, J., Abrahamson, N. A., Bommer∗, J. J., Markatis, A., McCoy, E., & Mendis, R. (2006). An improved method of matching response spectra of recorded earthquake ground motion using wavelets. *Journal of Earthquake Engineering*, *10*(sup001), 67–89. https://doi.org/10.1080/13632460609350629

Harada, T., Nakamura, M., Kanai, N., Nonaka, T., Kodama, Y., & Motohashi, H. (2012). Analysis of Vertical Ground Motion / Phase Motion Near Fault Records in JAPAN and Its Application to Simulation of Vertical Ground Motion. *Proceedings of the 15th World Conference on Earthquake Engineering*, 9.

Harder, L. F., Bray, J. D., Volpe, R. L., & Rodda, K. V. (1998). *Performance of earth dams during the Loma Prieta earthquake* (Professional Paper Nos. 1552-D; The Loma Prieta, California, Earthquake of October 17, 1989: Performance of the Built Environment.). USGS.

Hariri-Ardebili, M. A., & Saouma, V. (2015). Quantitative failure metric for gravity dams. *Earthquake Engineering & Structural Dynamics*, *44*(3), 461–480. https://doi.org/10.1002/eqe.2481

He, J., & Rathje, E. (2023). *Database for the Development of Capacity Relationships for Earth Dam* (Version 1) [Dataset]. Designsafe-CI. https://doi.org/10.17603/DS2-PWTV-P173

He, J., & Rathje, E. M. (2024). Seismic capacity models for earth dams and their use in developing fragility curves. *Earthquake Spectra*, 87552930241243067. https://doi.org/10.1177/87552930241243067

He, K., Fell, R., & Song, C. (2022). Transverse cracking in embankment dams resulting from cross-valley differential settlements. *European Journal of Environmental and Civil Engineering*, *26*(3), 995–1021. https://doi.org/10.1080/19648189.2019.1691663

He, K., Song, C., & Fell, R. (2021). Numerical modelling of transverse cracking in embankment dams. *Computers and Geotechnics*, *132*, 104028. https://doi.org/10.1016/j.compgeo.2021.104028

Hinks, J. L., Spasic-Gril, L., & Palmer, M. J. (2012). Behaviour of embankment dams in earthquakes. *Dams: Engineering in a Social and Environmental Context*. 17th Conference of the British Dam Society, London. https://doi.org/10.1680/dams.57999

Hoek, E., & Brown, E. T. (2019). The Hoek–Brown failure criterion and GSI – 2018 edition. *Journal of Rock Mechanics and Geotechnical Engineering*, *11*(3), 445–463. https://doi.org/10.1016/j.jrmge.2018.08.001

Hoek, E., Carranza-Torres, C., & Corkum, B. (2002). Hoek-Brown failure criterion – 2002 Edition. *Mining and Tunnelling Innovation and Opportunity*, 7.

Hu, H., Bao, Y., Huang, Y., Xiong, M., Mao, W., Zou, B., Han, X., & Wang, W. (2025). Seismic fragility analysis of slopes: Method development, practical application and future prospects. *Soil Dynamics and Earthquake Engineering*, *190*, 109176. https://doi.org/10.1016/j.soildyn.2024.109176

Hu, H., Gan, G., Cui, L., Xia, T., Wang, L., & Han, X. (2023). Nonparametric Representation for Seismic Fragility Assessment of Earth Dams with Spatially Variable Soil Properties. *International Journal of Geomechanics*, *23*(8), 04023108. https://doi.org/10.1061/IJGNAI.GMENG-7266

Huang, Z.-K., Pitilakis, K., Argyroudis, S., Tsinidis, G., & Zhang, D.-M. (2021). Selection of optimal intensity measures for fragility assessment of circular tunnels in soft soil deposits. *Soil Dynamics and Earthquake Engineering*, *145*, 106724. https://doi.org/10.1016/j.soildyn.2021.106724

Hunt, C. E., Umberg, D. R., Rix, G. J., Donahue, J. L., & Amini, Z. (2018). Seismic risk screening of embankment dams. *Proceedings of the 2018 USSD Annual Conference*. 2018 USSD Annual Conference.

Hynes-Griffin, M. E., & Franklin, A. G. (1984). *Rationalizing the Seismic Coefficient Method.* (No. GL-84-13; p. 37). US Army Engineer Waterways Experiment Station, Geotechnical Laboratory.

IAEA. (2022). *Seismic Hazards in Site Evaluation for Nuclear Installations*. INTERNATIONAL ATOMIC ENERGY AGENCY. https://www.iaea.org/publications/14665/seismic-hazards-in-site-evaluation-for-nuclear-installations

Iai, S., Tsuchida, H., & Koizumi, K. (1989). A Liquefaction Criterion Based on Field Performances Around Seismograph Stations. *Soils and Foundations*, *29*(2), 52–68. https://doi.org/10.3208/sandf1972.29.2_52

ICOLD. (2001). *Bulletin 120—Design features of dams to resist seismic ground motion, guidelines and case histories* (p. 199). International Comission on Large Dams.

ICOLD. (2005). *Bulletin 130—Risk Assessment in Dam Safety Management*. International Commission on Large Dams.

ICOLD. (2010). Bulletin 141—Concrete face rockfill dams: Concepts for design and construction. In *Bulletin 141* (p. 408). International Commission on Large Dams.

ICOLD. (2016a). *Bulletin 148—Selecting Seismic Parameters for Large Dams—Guidelines* (p. 42). International Commission on Large Dams.

ICOLD. (2016b). *Bulletin 166—Inspection of dams following earthquakes guidelines*. International Comission on Large Dams.

Idriss, I. (1985). *Evaluating seismic risk in engineering practice*.

Iervolino, I. (2011). Performance-based earthquake early warning. *Soil Dynamics and Earthquake Engineering*, *31*(2), 209–222. https://doi.org/10.1016/j.soildyn.2010.07.010

Iervolino, I. (2014). Engineering Earthquake Early Warning via Regional Networks. In F. Wenzel & J. Zschau (Eds.), *Early Warning for Geological Disasters* (pp. 333–351). Springer Berlin Heidelberg. https://doi.org/10.1007/978-3-642-12233-0_17

Iervolino, I. (2022). Estimation uncertainty for some common seismic fragility curve fitting methods. *Soil Dynamics and Earthquake Engineering*, *152*, 107068. https://doi.org/10.1016/j.soildyn.2021.107068

Iervolino, I., Fabbrocino, G., & Manfredi, G. (2004). Fragility of standard industrial structures by a response surface based method. *Journal of Earthquake Engineering*, *8*(6), 927–945. https://doi.org/10.1080/13632460409350515

INPRES. (1985). *El Terremoto de Mendoza Argentina del 26 de enero de 1985* (p. 137) [Informe general]. Instituto Nacional de Prevención Sísmica.

INPRES. (1986). *Gran Mendoza, el nucleo urbano expuesto al mayor nivel de riesgo sismico en la Republica Argentina* (Publicación técnica No. 10; p. 58). Instituto Nacional de Prevención Sísmica.

INPRES. (2022). *Catálogo sísmico INPRES* [Dataset]. Instituto Nacional de Prevención Sísmica. http://contenidos.inpres.gob.ar/buscar_sismo

ISC. (2022). *ISC Bulletin* [Dataset]. International Seismological Centre. https://doi.org/10.31905/D808B830

Ishihara, K. (2010). Performances of Rockfill Dams During Recent Large Earthquakes. *International Conferences on Recent Advances in Geotechnical Earthquake Engineering and Soil Dynamics. 5.* https://scholarsmine.mst.edu/icrageesdhttps://scholarsmine.mst.edu/icrageesd/05icrageesd/session11/5

Itasca Consulting Group, Inc. (2023). *FLAC3D - Fast Lagrangian Analysis of Continua in Two-Dimensions* (Version 9.0) [Computer software]. Itasca.

Jalayer, F., & Cornell, A. (2003). *A Technical Framework for Probability-Based Demand and Capacity Factor Design (DCFD) Seismic Formats* (No. 2003/08; PEER Reports). Pacific Earthquake Engineering Research Center, University of California, Berkeley, CA. https://peer.berkeley.edu/sites/default/files/0308_f._jalayer_c._allin_cornell.pdf

Jalayer, F., & Cornell, C. A. (2009). Alternative non-linear demand estimation methods for probability-based seismic assessments. *Earthquake Engineering & Structural Dynamics*, *38*(8), 951–972. https://doi.org/10.1002/eqe.876

Jalayer, F., De Risi, R., & Manfredi, G. (2015). Bayesian Cloud Analysis: Efficient structural fragility assessment using linear regression. *Bulletin of Earthquake Engineering*, *13*(4), 1183–1203. https://doi.org/10.1007/s10518-014-9692-z

Jalayer, F., Ebrahimian, H., Miano, A., Manfredi, G., & Sezen, H. (2017). Analytical fragility assessment using unscaled ground motion records. *Earthquake Engineering & Structural Dynamics*, *46*(15), 2639–2663. https://doi.org/10.1002/eqe.2922

Jalayer, F., Ebrahimian, H., Trevlopoulos, K., & Bradley, B. (2023). Empirical tsunami fragility modelling for hierarchical damage levels. *Natural Hazards and Earth System Sciences*, *23*(2), 909–931. https://doi.org/10.5194/nhess-23-909-2023

Jin, C., & Chi, S. (2019). Seismic Fragility Analysis of High Earth-Rockfill Dams considering the Number of Ground Motion Records. *Mathematical Problems in Engineering*, *2019*(1), 6958643. https://doi.org/10.1155/2019/6958643

Jones, J., Kalkan, E., Stephens, C., & Ng, P. (2017). PRISM Software: Processing and Review Interface for Strong-Motion Data. *Seismological Research Letters*, *88*(3), 851–866. https://doi.org/10.1785/0220160200

Jordan, T., Isacks, B., Ramos, V., & Allmendinger, R. W. (1983). Mountain Building in the Central Andes. *Episodes*, *6*(3), 20–26. https://doi.org/10.18814/epiiugs/1983/v6i3/005

Kamalzare, M., & Marquez, H. (2020). Stability Assessment of the Embankment Dam Systems Under Different Seismic Loads in Southern California and Evaluation of the Current Design Criteria. In J.-M. Zhang, L. Zhang, & R. Wang (Eds.), *Dam Breach Modelling and Risk Disposal* (pp. 163–174). Springer International Publishing. https://doi.org/10.1007/978-3-030-46351-9_14

Karimi, Z., & Dashti, S. (2017). Ground Motion Intensity Measures to Evaluate II: The Performance of Shallow-Founded Structures on Liquefiable Ground. *Earthquake Spectra*, *33*(1), 277–298. https://doi.org/10.1193/103015eqs163m

Kartal, M. E., Bayraktar, A., & Başağa, H. B. (2010). Seismic failure probability of concrete slab on CFR dams with welded and friction contacts by response surface method. *Soil Dynamics and Earthquake Engineering*, *30*(11), 1383–1399. https://doi.org/10.1016/j.soildyn.2010.06.013

Kazantzi, A. K., & Vamvatsikos, D. (2015). Intensity measure selection for vulnerability studies of building classes. *Earthquake Engineering & Structural Dynamics*, *44*(15), 2677–2694. https://doi.org/10.1002/eqe.2603

Kennedy, R. P., Cornell, C. A., Campbell, R. D., Kaplan, S., & Perla, H. F. (1980). Probabilistic seismic safety study of an existing nuclear power plant. *Nuclear Engineering and Design*, *59*(2), 315–338. https://doi.org/10.1016/0029-5493(80)90203-4

Kennedy, R. P., & Ravindra, M. K. (1984). Seismic fragilities for nuclear power plant risk studies. *Nuclear Engineering and Design*, *79*(1), 47–68. https://doi.org/10.1016/0029-5493(84)90188-2

Khalid, M., Fei, J., & Chen, X. (2024). Optimal earthquake intensity measures for seismic vulnerability assessment of concrete-faced rockfill dams. *IOP Conference Series: Earth and Environmental Science*, *1334*(1), 012034. https://doi.org/10.1088/1755-1315/1334/1/012034

Khalid, M., Park, D., Fei, J., Nguyen, V.-Q., Nguyen, D.-D., & Chen, X. (2023). Selection of efficient earthquake intensity measures for evaluating seismic fragility of concrete face rockfill dam. *Computers and Geotechnics*, *163*, 105721. https://doi.org/10.1016/j.compgeo.2023.105721

Konno, K., & Ohmachi, T. (1998). Ground-motion characteristics estimated from spectral ratio between horizontal and vertical components of microtremor. *Bulletin of the Seismological Society of America*, *88*(1), 228–241. https://doi.org/10.1785/BSSA0880010228

Kramer, S. (1996). *Geotechnical earthquake engineering*. Prentice Hall.

Kramer, S. (2024). *The evolution of performance-based design in geotechnical earthquake engineering* (International Association for Earthquake Engineering, Vol. 3). Eucentre.

Kramer, S. L., & Mitchell, R. A. (2006). Ground Motion Intensity Measures for Liquefaction Hazard Evaluation. *Earthquake Spectra*, *22*(2), 413–438. https://doi.org/10.1193/1.2194970

Kramer, S. L., & Stewart, J. P. (2024). *Geotechnical Earthquake Engineering* (2nd ed.). CRC Press. https://doi.org/10.1201/9781003512011

Kramer, S., & Stewart, J. (2004). Geotechnical Aspects of Seismic Hazards. In *Earthquake Engineering, From Engineering Seismology to Performance-Based Engineering* (1st ed., p. 85). CRC Press.

Krinitzsky, E., & Hynes, M. (2002). The Bhuj, India, earthquake: Lessons learned for earthquake safety of dams on alluvium. *Engineering Geology*, *66*(3–4), 163–196. https://doi.org/10.1016/S0013-7952(02)00049-2

Krinitzsky, E. L. (2002). How to obtain earthquake ground motions for engineering design. *Engineering Geology*, *65*(1), 1–16. https://doi.org/10.1016/S0013-7952(01)00098-9

Kuhlemeyer, R. L., & Lysmer, J. (1973). Finite Element Method Accuracy for Wave Propagation Problems. *Journal of the Soil Mechanics and Foundations Division*, *99*(5), 421–427. https://doi.org/10.1061/JSFEAQ.0001885

Kwak, D. Y., Stewart, J. P., Brandenberg, S. J., & Mikami, A. (2016a). Characterization of Seismic Levee Fragility Using Field Performance Data. *Earthquake Spectra*, *32*(1), 193–215. https://doi.org/10.1193/030414EQS035M

Kwak, D. Y., Stewart, J. P., Brandenberg, S. J., & Mikami, A. (2016b). Seismic Levee System Fragility considering Spatial Correlation of Demands and Component Fragilities. *Earthquake Spectra*, *32*(4), 2207–2228. https://doi.org/10.1193/083115EQS132M

Kwong, N. S., & Chopra, A. K. (2017). A Generalized Conditional Mean Spectrum and Its Application for Intensity-Based Assessments of Seismic Demands. *Earthquake Spectra*, *33*(1), 123–143. https://doi.org/10.1193/040416eqs050m

Lacasse, S., Nadim, F., Liu, Z. Q., Eidsvig, U. K., Le, T. M. H., & Lin, C. G. (2019). Risk assessment and dams – Recent developments and applications. *Proceedings of the XVII European Conference on Soil Mechanics and Geotechnical Engineering*, *Geotechnical Engineering, foundation of the future*, 5221–5246. https://doi.org/10.32075/17ECSMGE-2019-1110

Lagaros, N. D., Tsompanakis, Y., Psarropoulos, P. N., & Georgopoulos, E. C. (2009). Computationally efficient seismic fragility analysis of geostructures. *Computers & Structures*, *87*(19–20), 1195–1203. https://doi.org/10.1016/j.compstruc.2008.12.001

Lara, A., Toso, J., Barchiesi, A., Silvero, M., & Rosell, L. (2008). *Caverna excavada en un macizo granítico: Particularidades de su funcionamiento evidenciado por la auscultación: Parte I*. 24.

Lashgari, A., & Moss, R. E. S. (2024). Displacement and damage analysis of earth dams during the 2023 Turkiye earthquake sequence. *Earthquake Spectra*, *40*(2), 939–976. https://doi.org/10.1177/87552930231223749

Lee, K. Z.-Z., Gillette, D. R., & Gutierrez, A. (2025). A Comparison of Return Periods of Design Ground Motions for Dams from Different Agencies and Organizations. *Infrastructures*, *10*(5), 105. https://doi.org/10.3390/infrastructures10050105

Legg, M. R., & Slosson, J. E. (1984). Probabilistic approach to earthquake induced landslide hazard mapping. *Proceedings of the Eighth World Conference on Earthquake Engineering*, 445–452.

Leoni, A. J., Guaraglia, D., Bielecki, A., & Cánchero, J. (2011). *Medición de la energía entregada por el impacto del pisón, en la ejecución de los ensayos S.P.T. que se ejecutan en la República Argentina* . 9.

Leyton, F., Ruiz, J., Campos, J., & Kausel, E. (2009). Intraplate and interplate earthquakes in Chilean subduction zone: A theoretical and observational comparison. *Physics of the Earth and Planetary Interiors*, *175*(1–2), 37–46. https://doi.org/10.1016/j.pepi.2008.03.017

Li, J., & Ni, P. (2025). Fragility analysis of buried continuous pipelines under normal faulting through analytical solution combining with machine learning technique. *Canadian Geotechnical Journal*, *62*, 1–18. https://doi.org/10.1139/cgj-2024-0430

Lin, K.-W., Wald, D. J., Slosky, D., Strait, S., Smith, J., Yen, S., & Burmas, N. (2022). Critical ShakeCast Lifeline Users and Their Response Protocols. *Lifelines 2022*, 715–725. https://doi.org/10.1061/9780784484449.065

Lizarraga, H. S., & Lai, C. G. (2012). *Performance-based seismic analysis and design of earthfill dams*. IUSS Press.

Lo, E., & Pelecanos, L. (2018). Comparison of shear-beam and dynamic finite-element modal analysis of earth dams. *Smart Dams and Reservoirs*, 103–111. https://doi.org/10.1680/sdar.64119.103

Loos, P. (1928). El terremoto argentino-chileno del 14 de abril de 1927. *Contribuciones Geofísicas - Observatorio astronómico de la Universidad Nacional de La Plata*, *Tomo 2*(2), 53.

Luco, N., & Bazzurro, P. (2007). Does amplitude scaling of ground motion records result in biased nonlinear structural drift responses? *Earthquake Engineering & Structural Dynamics*, *36*(13), 1813–1835. https://doi.org/10.1002/eqe.695

Luco, N., & Cornell, C. A. (2007). Structure-Specific Scalar Intensity Measures for Near-Source and Ordinary Earthquake Ground Motions. *Earthquake Spectra*, *23*(2), 357–392. https://doi.org/10.1193/1.2723158

Lysmer, J., & Kuhlemeyer, R. L. (1969). Finite Dynamic Model for Infinite Media. *Journal of the Engineering Mechanics Division*, *95*(4), 859–877. https://doi.org/10.1061/JMCEA3.0001144

Mackie, K., & Stojadinović, B. (2001). Probabilistic Seismic Demand Model for California Highway Bridges. *Journal of Bridge Engineering*, *6*(6), 468–481. https://doi.org/10.1061/(ASCE)1084-0702(2001)6:6(468)

Made, P., Curadelli, W., Gutierrez, G., Alvarez, C., & Espinosa, M. (2002). *Presa Potrerillos, sistema de auscultación, primeros resultados*. 7.

Madsen, R. B., Høyer, A.-S., Andersen, L. T., Møller, I., & Hansen, T. M. (2022). Geology-driven modeling: A new probabilistic approach for incorporating uncertain geological interpretations in 3D geological modeling. *Engineering Geology*, *309*, 106833. https://doi.org/10.1016/j.enggeo.2022.106833

Malvar, J., & Ross, A. (1998). Review of Strain Rate Effects for Concrete in Tension. *ACI Materials Journal*, *95*(6). https://doi.org/10.14359/418

Marano, K. D., Hearne, M., Jaiswal, K. S., Thompson, E. M., Bruce Worden, C., & Wald, D. J. (2024). ShakeMap Atlas 4.0 and AtlasCat: An Archive of the Recent and the Historical Earthquake ShakeMaps, and Impacts for Global Hazard Analyses and Loss Model Calibration. *Seismological Research Letters*, *95*(2A), 879–899. https://doi.org/10.1785/0220220324

Marinos, P., & Hoek, E. (2000). *Gsi: A Geologically Friendly Tool For Rock Mass Strength Estimation*. ISRM-IS-2000-035.

Marquez, H., & Kamalzare, M. (2019). Geotechnical risk analyses and evaluation of design criteria of embankment dam systems. *E3S Web of Conferences*, *92*, 16015. https://doi.org/10.1051/e3sconf/20199216015

Marsal, R. J., & Resendiz, D. (1983). *Presas de Tierra y Enrocamiento*. Limusa.

Martin, F., Rojas, F., & Saldi, L. (2010). Domar el agua para gobernar. Concepciones socio-políticas sobre la naturaleza y la sociedad en contextos de consolidación del Estado provincial mendocino hacia finales del

siglo XIX y principios del XX. *Anuario del Centro de Estudios Históricos "Profesor Carlos S. A. Segreti," 10*(10), 159–186. https://doi.org/10.52885/2683-9164.v0.n10.23147

Marzocchi, W., & Sandri, L. (2003). A review and new insights on the estimation of the b-valueand its uncertainty. *Annals of Geophysics*, *46*(6), 1271–1282. https://doi.org/10.4401/ag-3472

McCann, M. W., Benjamin, J. R., Rix, G. J., & Westover, T. (2022). *Potential Failure Mode Screening Analysis*. 10.

McCann, M. W., & Rix, G. J. (2023). A Framework for Quantitative Risk Analysis of Dams. *Geo-Risk 2023*, 312–320. https://doi.org/10.1061/9780784484982.032

McCann, M. W., Ruby, Z., Beaty, M., Westover, T., Castro, G., & Harder, L. (2023). SSHAC Evaluation of the Seismic Fragility for an Embankment Dam. *Geo-Risk 2023*, 318–327. https://doi.org/10.1061/9780784484968.033

McGuire, R. (2001). Deterministic vs. Probabilistic earthquake hazards and risks. *Soil Dynamics and Earthquake Engineering*, *21*(5), 377–384. https://doi.org/10.1016/S0267-7261(01)00019-7

McGuire, R. (2008). Probabilistic seismic hazard analysis: Early history. *Earthquake Engineering & Structural Dynamics*, *37*(3), 329–338. https://doi.org/10.1002/eqe.765

McKenna, G., Argyroudis, S. A., Winter, M. G., & Mitoulis, S. A. (2021). Multiple hazard fragility analysis for granular highway embankments: Moisture ingress and scour. *Transportation Geotechnics*, *26*, 100431. https://doi.org/10.1016/j.trgeo.2020.100431

Mejia, L., & Dawson, E. (2006). *Earthquake Deconvolution for FLAC*. 10.

Mejia, L., & Dawson, E. (2019). Earthquake-induced cracking evaluation of embankment dams. In *Sustainable and Safe Dams Around the World* (1st ed., pp. 2884–2898). CRC Press. https://doi.org/10.1201/9780429319778-258

Mejia, L. H. (2024). The 23rd Ralph B. Peck Lecture: Earthquake Cracking of Embankment Dams. *Journal of Geotechnical and Geoenvironmental Engineering*, *150*(11), 19. https://doi.org/10.1061/JGGEFK.GTENG-12751

Melchers, R. E. (2001). On the ALARP approach to risk management. *Reliability Engineering & System Safety*, *71*(2), 201–208. https://doi.org/10.1016/S0951-8320(00)00096-X

Miano, A., Ebrahimian, H., Jalayer, F., Vamvatsikos, D., & Prota, A. (2024). Propagation of Modelling Uncertainties for Seismic Risk Assessment: The Effect of Sampling Techniques on Low-Rise Non-Ductile RC Frames. *Journal of Earthquake Engineering*, 1–26. https://doi.org/10.1080/13632469.2024.2368159

Miano, A., Jalayer, F., Ebrahimian, H., & Prota, A. (2018). Cloud to IDA: Efficient fragility assessment with limited scaling. *Earthquake Engineering & Structural Dynamics*, *47*(5), 1124–1147. https://doi.org/10.1002/eqe.3009

Mignan, A., & Woessner, J. (2012). Estimating the magnitude of completeness for earthquake catalogs. *Articles from the Community Online Resource for Statistical Seismicity Analysis (CORSSA)*. https://doi.org/10.5078/CORSSA-00180805

Mikami, A., Stewart, J. P., & Kamiyama, M. (2008). Effects of time series analysis protocols on transfer functions calculated from earthquake accelerograms. *Soil Dynamics and Earthquake Engineering*, *28*(9), 695–706. https://doi.org/10.1016/j.soildyn.2007.10.018

Mingorance, F. (2006). Morfometría de la escarpa de falla histórica identificada al norte del cerro La Cal, zona de falla La Cal, Mendoza. *Revista de la Asociación Geológica Argentina*, *4*(61), 620–638.

Mingorance, F. (2024). *Informe Técnico Interno: Características generales de las fuentes sismogénicas potenciales localizadas en la región cercana extendida del Proyecto Potrerillos, Río Mendoza, Provincia de Mendoza, Argentina* (p. 33) [Informe Técnico Interno]. Universidad Nacional de Cuyo, Facultad de Ingeniería, Instituto de Geociencias Aplicadas a la Ingeniería y a los Peligros Naturales (IGAIPEN), Area Geología de Terremotos y Peligro Sísmico.

MIT. (2002). *Controlli straordinari a seguito di eventi sismici* (No. SDI/3536).

MIT. (2017). *Controlli straordinari a seguito di eventi sismici—Aggiornamento procedura ART 6.2.3 del FCEM* (No. 25157). (Italia)

Moehle, J. (2024). *Performance-Based Earthquake Engineering: A Chronicle in Five Easy Pieces* (International Association for Earthquake Engineering, Vol. 4). Eucentre.

Moehle, J., & Deierlein, G. (2004). *A Framework Methodology for Performance-Based Earthquake Engineering*. 13th World Conference on Earthquake Engineering, Canada.

Mononobe, N., Takata, A., & Matumura, M. (1936). Seismic stability of the earth dam. *Proceedings of the 2nd Congress on Large Dams*, *IV*.

Montalva, G., Bastías, N., & Rodriguez-Marek, A. (2017). Ground-Motion Prediction Equation for the Chilean Subduction Zone. *Bulletin of the Seismological Society of America*, *107*(2), 901–911. https://doi.org/10.1785/0120160221

Moreiras, S. M., & Páez, M. S. (2015). Historical damage and earthquake environmental effects related to shallow intraplate seismicity of central western Argentina. *Geological Society, London, Special Publications*, *399*(1), 369–382. https://doi.org/10.1144/SP399.6

Moreiras, S. M., Toural Dapoza, R., Junquera Torrado, S., Gomez, L., Euillades, P., & Lenzano, L. (2021). Deformación cuaternaria en el piedemonte mendocino (32° 50′ S), Argentina. *Boletín de La Sociedad Geológica Mexicana*, *73*(2), A160221. https://doi.org/10.18268/BSGM2021v73n2a160221

Naesgaard, E. (2011). *A hybrid effective stress-total stress procedure for analyzing soil embankments subjected to potential liquefaction and flow* [Ph.D. Thesis]. University of British Columbia.

Naesgaard, E., Byrne, P. M., & Amini, A. (2015). *Hysteretic Model for Non-liquefiable soils (UBCHyst5d)* (p. 9) [Technical report].

Nardo, A., Biondi, G., Casablanca, O., Di Filippo, G., & Cascone, E. (2024). Seismic intensity measures and predictive equations for the evaluation of earthquake—Induced crest settlements of earth dams. *Earthquake Engineering & Structural Dynamics*, *53*(9), 2680–2709. https://doi.org/10.1002/eqe.4135

Navarro, O. (2018). *Informe de la Novena Misión del Consultor Independiente—Aprovechamiento Integral del Río Mendoza—Proyecto "Potrerillos"* [Informe Técnico Independiente].

Newmark, N. M. (1965). Effects of Earthquakes on Dams and Embankments. *Géotechnique*, *15*(2), 139–160. https://doi.org/10.1680/geot.1965.15.2.139

Ni, P., Mangalathu, S., & Yi, Y. (2018). Fragility analysis of continuous pipelines subjected to transverse permanent ground deformation. *Soils and Foundations*, *58*(6), 1400–1413. https://doi.org/10.1016/j.sandf.2018.08.002

Nichols, G. (2010). *Sedimentology and stratigraphy* (2. ed., [Nachdr.]). Wiley-Blackwell.

Nishimura, S., Shibata, T., & Shuku, T. (2021). Reliability-based design for earth-fill dams against severe natural disaster events. *Soils and Foundations*, *61*(2), 271–282. https://doi.org/10.1016/j.sandf.2020.09.004

Nishimura, S., Shuku, T., & Shibata, T. (2016). Reliability-based design of earth-fill dams to mitigate damage due to severe earthquakes. *Georisk: Assessment and Management of Risk for Engineered Systems and Geohazards*, *10*(1), 83–90. https://doi.org/10.1080/17499518.2015.1124123

NTC. (2018). *Norme Tecniche per le Costruzioni (NTC) 2018*.

Núñez, E. (2010). Dos grandes presas CFRD en zonas sísmicas. *XX Congreso Argentino de Mecánica de Suelos e Ingeniería Geotécnica CAMSIG 2010*, 6.

Núñez, E. (2012). Presa Potrerillos. 10 años de discusion. *Congreso Argentino de Mecánica de Suelos e Ingeniería Geotécnica CAMSIG XXI*, 6.

Núñez, E., & Sfriso, A. (2013). Case study of the post-earthquake behavior of a CFRD dam. *Proceedings from the 18th Internatioinal Conference on Soil Mechanics and Geotechnical Engineering*, 4.

Ordaz, M., Martinelli, F., Aguilar, A., Arboleda, J., Meletti, C., & D'Amico, V. (2017). *R-CRISIS. Program and platform for computing seismic hazard.* (Version 20.0) [Computer software].

Padgett, J. E., Nielson, B. G., & DesRoches, R. (2008). Selection of optimal intensity measures in probabilistic seismic demand models of highway bridge portfolios. *Earthquake Engineering & Structural Dynamics*, *37*(5), 711–725. https://doi.org/10.1002/eqe.782

Pagano, L., Desideri, A., & Vinale, F. (1998). Interpreting Settlement Profiles of Earth Dams. *Journal of Geotechnical and Geoenvironmental Engineering*, *124*(10), 923–932. https://doi.org/10.1061/(ASCE)1090-0241(1998)124:10(923)

Pagano, L., Russo, C., Sica, S., & Costigliola, R. M. (2019). Earth dams: Damage mechanisms and limit states in seismic conditions. In F. Silvestri & N. Moraci (Eds.), *Earthquake Geotechnical Engineering for Protection and Development of Environment and Constructions* (pp. 600–616). CRC Press. https://doi.org/10.1201/9780429031274

Pagano, L., & Sica, S. (2013). Earthquake early warning for earth dams: Concepts and objectives. *Natural Hazards*, *66*(2), 303–318. https://doi.org/10.1007/s11069-012-0486-9

Pang, R., Xu, B., Kong, X., & Zou, D. (2018). Seismic fragility for high CFRDs based on deformation and damage index through incremental dynamic analysis. *Soil Dynamics and Earthquake Engineering*, *104*, 432–436. https://doi.org/10.1016/j.soildyn.2017.11.017

Pang, R., Xu, B., Zhou, Y., Zhang, X., & Wang, X. (2020). Fragility analysis of high CFRDs subjected to mainshock-aftershock sequences based on plastic failure. *Engineering Structures*, *206*, 110152. https://doi.org/10.1016/j.engstruct.2019.110152

Pang, R., Xu, B., Zou, D., & Kong, X. (2019). Seismic performance assessment of high CFRDs based on fragility analysis. *Science China Technological Sciences*, *62*(4), 635–648. https://doi.org/10.1007/s11431-017-9220-8

Pang, R., Yao, H., & Xu, B. (2024). Dynamic reliability and seismic fragility analysis for high concrete-faced rockfill dam slopes subjected to stochastic earthquake and parameter excitation via PDEM. *Soil Dynamics and Earthquake Engineering*, *186*, 108915. https://doi.org/10.1016/j.soildyn.2024.108915

Papadimitriou, A. G., Bouckovalas, G. D., & Andrianopoulos, K. I. (2014). Methodology for estimating seismic coefficients for performance-based design of earthdams and tall embankments. *Soil Dynamics and Earthquake Engineering*, *56*, 57–73. https://doi.org/10.1016/j.soildyn.2013.10.006

Park, D., & Kishida, T. (2018). Shear wave velocity profiles of fill dams. *Soil Dynamics and Earthquake Engineering*, *104*, 250–258. https://doi.org/10.1016/j.soildyn.2017.10.013

Paull, N. A., Boulanger, R. W., DeJong, J. T., & Friesen, S. J. (2022). Nonlinear Dynamic Analyses of Perris Dam Using Transition Probability to Model Interbedded Alluvial Strata. *Journal of Geotechnical and Geoenvironmental Engineering*, *148*(1), 05021015. https://doi.org/10.1061/(ASCE)GT.1943-5606.0002663

Pelecanos, L., Kontoe, S., & Zdravković, L. (2020). The Effects of Dam–Reservoir Interaction on the Nonlinear Seismic Response of Earth Dams. *Journal of Earthquake Engineering*, *24*(6), 1034–1056. https://doi.org/10.1080/13632469.2018.1453409

Pells, S., & Fell, R. (2002). *Damage and cracking of embankment dams by earthquakes, and the implications for internal erosion and piping: Vol. R-408*. University of New South Wales.

Pells, S., & Fell, R. (2003). Damage and cracking of embankment dams by earthquake and the implications for internal erosion and piping. *Proceedings 21st International Congress on Large Dams*. 21st International Congress on Large Dams, Montreal, Canada.

Penman, A. (2002). Measurement of Pore Water Pressures in Embankment Dams. *Geotechnical Instrumentation News (GIN)*, *20*(4), 43–49.

Penman, A. D. M., Saxena, K. R., & Sharma, V. M. (2018). *Instrumentation, Monitoring and Surveillance: Embankment Dams* (1st ed.). Routledge. https://doi.org/10.1201/9780203750667

Perucca, L. P., & Moreiras, S. M. (2009). Seismic and Volcanic Hazards in Argentina. In *Developments in Earth Surface Processes* (Vol. 13, pp. 267–300). Elsevier. https://doi.org/10.1016/S0928-2025(08)10014-1

Petala, El., Sotiriadis, D., & Klimis, N. (2024). Assessment of fragility curves of highway embankments due to underlying faults rupture propagation. *Soil Dynamics and Earthquake Engineering*, *184*, 108818. https://doi.org/10.1016/j.soildyn.2024.108818

Phalen, J., Ryan, M., & Wagner, N. (2021). A process for quanitying seismic fragility of an embankment dam. *Proceedings of the 2021 USSD Annual Conference*. 2021 USSD Annual Conference.

Phillips, C., & Hashash, Y. M. A. (2009). Damping formulation for nonlinear 1D site response analyses. *Soil Dynamics and Earthquake Engineering*, *29*(7), 1143–1158. https://doi.org/10.1016/j.soildyn.2009.01.004

Pitilakis, K., Crowley, H., & Kaynia, A. M. (Eds.). (2014). *SYNER-G: Typology Definition and Fragility Functions for Physical Elements at Seismic Risk: Buildings, Lifelines, Transportation Networks and Critical Facilities* (Vol. 27). Springer Netherlands. https://doi.org/10.1007/978-94-007-7872-6

Pokhrel, A., Chiaro, G., Kiyota, T., & Cubrinovski, M. (2024). Liquefaction characteristics of sand-gravel mixtures: Experimental observations and its assessment based on intergranular state concept. *Soils and Foundations*, *64*(2), 101444. https://doi.org/10.1016/j.sandf.2024.101444

Porter, K., Hamburger, R., & Kennedy, R. (2007). Practical Development and Application of Fragility Functions. *Structural Engineering Research Frontiers*, 1–16. https://doi.org/10.1061/40944(249)23

Porter, K., Kennedy, R., & Bachman, R. (2007). Creating Fragility Functions for Performance-Based Earthquake Engineering. *Earthquake Spectra*, *23*(2), 471–489. https://doi.org/10.1193/1.2720892

Potts, D. M., & Zdravković, L. (2001). *Finite element analysis in geotechnical engineering. 2: Application*. Telford.

Poulos, A., Monsalve, M., Zamora, N., & De La Llera, J. C. (2019). An Updated Recurrence Model for Chilean Subduction Seismicity and Statistical Validation of Its Poisson Nature. *Bulletin of the Seismological Society of America*, *109*(1), 66–74. https://doi.org/10.1785/0120170160

Poulos, H. G., Booker, J. R., & Ring, G. J. (1972). Simplified Calculation of Embankment Deformations. *Soils and Foundations*, *12*(4), 1–17. https://doi.org/10.3208/sandf1972.12.4_1

Pretell, R., Ziotopoulou, K., & Abrahamson, N. (2019). Methodology for the development of input motions for nonlinear deformation analyses. In *Earthquake Geotechnical Engineering for Protection and Development of Environment and Constructions* (pp. 4564–4571). CRC Press.

Qiu, Z., Zhou, Y.-G., Prabhakaran, A., & Ebeido, A. (2025). Seismic performance and vulnerability assessment of rockfill dams on liquefiable ground with gravel berms for liquefaction mitigation. *Soil Dynamics and Earthquake Engineering*, *199*, 109690. https://doi.org/10.1016/j.soildyn.2025.109690

Qu, Y., Zou, D., Kong, X., Yu, X., & Chen, K. (2020). Seismic cracking evolution for anti-seepage face slabs in concrete faced rockfill dams based on cohesive zone model in explicit SBFEM-FEM frame. *Soil Dynamics and Earthquake Engineering*, *133*, 106106. https://doi.org/10.1016/j.soildyn.2020.106106

Quinteros, J., Strollo, A., Evans, P., Hanka, W., Heinloo, A., Hemmleb, S., Hillmann, L., Jaeckel, K.-H., Kind, R., Saul, J., Zieke, T., & Tilmann, F. (2021). The GEOFON Program in 2020. *Seismological Research Letters*, *92*(3), 1610–1622. https://doi.org/10.1785/0220200415

Ramos, V. A., & Folguera, A. (2009). Andean flat-slab subduction through time. *Geological Society, London, Special Publications*, *327*(1), 31–54. https://doi.org/10.1144/SP327.3

Ramos, V., Cristallini, E., & Pérez, D. (2002). The Pampean flat-slab of the Central Andes. *Journal of South American Earth Sciences*, *15*(1), 59–78. https://doi.org/10.1016/S0895-9811(02)00006-8

Raphael, J. M. (1984). Tensile Strength of Concrete. *ACI Journal Proceedings*, *81*(2), 158–165. https://doi.org/10.14359/10653

Rathje, E. M., Abrahamson, N. A., & Bray, J. D. (1998). Simplified Frequency Content Estimates of Earthquake Ground Motions. *Journal of Geotechnical and Geoenvironmental Engineering*, *124*(2), 150–159. https://doi.org/10.1061/(ASCE)1090-0241(1998)124:2(150)

Rathje, E. M., & He, J. (2022). A Seismic Fragility Framework for Earth Dams. *Lifelines 2022*, 405–415. https://doi.org/10.1061/9780784484432.036

Reasenberg, P. (1985). Second-order moment of central California seismicity, 1969–1982. *Journal of Geophysical Research: Solid Earth*, *90*(B7), 5479–5495. https://doi.org/10.1029/JB090iB07p05479

Regina, G. (2021). *Probabilistic assessment of the seismic performance of two earth dams in Southern Italy using simplified and advanced constitutive models* [PhD Thesis]. Università della Calabria.

Regina, G., Zimmaro, P., Ziotopoulou, K., & Cairo, R. (2022). *Seismic Fragility Analysis of Two Earth Dams in Southern Italy Using Simplified and Advanced Constitutive Models* (pp. 1968–1975). https://doi.org/10.1007/978-3-031-11898-2_180

Regina, G., Zimmaro, P., Ziotopoulou, K., & Cairo, R. (2023). Evaluation of the optimal ground motion intensity measure in the prediction of the seismic vulnerability of earth dams. *Earthquake Spectra*, *39*(4), 2352–2378. https://doi.org/10.1177/87552930231170894

Remy, N., Boucher, A., & Wu, J. (2009). *Applied Geostatistics with SGeMS: A User's Guide* (1st ed.). Cambridge University Press. https://doi.org/10.1017/CBO9781139150019

Rix, G. J., Luettich, A. L., & Hunt, C. (2019). Seismic fragility relationships for embankment dams from empirical performance data. *Proceedings of the 2019 USSD Annual Conference*. 2019 USSD Annual Conference, Chicago.

Rix, G. J., McCann, M., Hasan, H., Zimmerman, P., & Huebner, M. (2023). Quantitative risk analysis of blue ridge hydroelectric project. *Proceedings of the 2023 USSD Annual Conference*. 2023 USSD Annual Conference.

Rollins, K. M., Singh, M., & Roy, J. (2020). Simplified Equations for Shear-Modulus Degradation and Damping of Gravels. *Journal of Geotechnical and Geoenvironmental Engineering*, *146*(9), 04020076. https://doi.org/10.1061/(ASCE)GT.1943-5606.0002300

Rood, A. H., Rood, D. H., Stirling, M. W., Madugo, C. M., Abrahamson, N. A., Wilcken, K. M., Gonzalez, T., Kottke, A., Whittaker, A. C., Page, W. D., & Stafford, P. J. (2020). Earthquake Hazard Uncertainties Improved Using Precariously Balanced Rocks. *AGU Advances*, *1*(4), e2020AV000182. https://doi.org/10.1029/2020AV000182

Rosti, A., Del Gaudio, C., Rota, M., Ricci, P., Di Ludovico, M., Penna, A., & Verderame, G. M. (2021). Empirical fragility curves for Italian residential RC buildings. *Bulletin of Earthquake Engineering*, *19*(8), 3165–3183. https://doi.org/10.1007/s10518-020-00971-4

Rosti, A., Smerzini, C., Paolucci, R., Penna, A., & Rota, M. (2023). Validation of physics-based ground shaking scenarios for empirical fragility studies: The case of the 2009 L'Aquila earthquake. *Bulletin of Earthquake Engineering*, *21*(1), 95–123. https://doi.org/10.1007/s10518-022-01554-1

Ruegg, J. C., Rudloff, A., Vigny, C., Madariaga, R., De Chabalier, J. B., Campos, J., Kausel, E., Barrientos, S., & Dimitrov, D. (2009). Interseismic strain accumulation measured by GPS in the seismic gap between Constitución and Concepción in Chile. *Physics of the Earth and Planetary Interiors*, *175*(1–2), 78–85. https://doi.org/10.1016/j.pepi.2008.02.015

Saberi, M., Annan, C.-D., & Konrad, J. M. (2022). Seismic response analysis of face slabs in concrete face rockfill dams. *Journal of Earthquake Engineering*, *26*(1), 192–220. https://doi.org/10.1080/13632469.2019.1666756

Sainov, M. (2020). Theoretical Basis for Designing Seepage-Control Walls in Dam Foundations. *IOP Conference Series: Materials Science and Engineering*, *753*(5), 052017. https://doi.org/10.1088/1757-899X/753/5/052017

Salomon, E., Schmidt, S., Hetzel, R., Mingorance, F., & Hampel, A. (2013). Repeated Folding during Late Holocene Earthquakes on the La Cal Thrust Fault near Mendoza City (Argentina). *Bulletin of the Seismological Society of America*, *103*(2A), 936–949. https://doi.org/10.1785/0120110335

Sasaki, T., Ohmachi, T., & Matsumoto, N. (2018). Analysis on acceleration data of dams collected by JCOLD. In *Validation of Dynamic Analyses of Dams and Their Equipment* (1st ed., pp. 3–30). CRC Press. https://doi.org/10.1201/9780429491160-1

Satriano, C., Wu, Y.-M., Zollo, A., & Kanamori, H. (2011). Earthquake early warning: Concepts, methods and physical grounds. *Soil Dynamics and Earthquake Engineering*, *31*(2), 106–118. https://doi.org/10.1016/j.soildyn.2010.07.007

Saygili, G., & Rathje, E. M. (2008). Empirical Predictive Models for Earthquake-Induced Sliding Displacements of Slopes. *Journal of Geotechnical and Geoenvironmental Engineering*, *134*(6), 790–803. https://doi.org/10.1061/(ASCE)1090-0241(2008)134:6(790)

Saygili, G., & Rathje, E. M. (2009). Probabilistically based seismic landslide hazard maps: An application in Southern California. *Engineering Geology*, *109*(3–4), 183–194. https://doi.org/10.1016/j.enggeo.2009.08.004

Schumm, S. A., Dumont, J. F., Holbrook, J. M., & Holbrook, J. M. (2002). *Active tectonics and alluvial rivers* (1. paperback ed). Cambridge University Press.

Seed, H. B. (1979). Considerations in the earthquake-resistant design of earth and rockfill dams. *Géotechnique*, *29*(3), 215–263. https://doi.org/10.1680/geot.1979.29.3.215

Seed, H. B., Idriss, I. M., Lee, K. L., & Makdisi, F. I. (1975). Dynamic Analysis of the Slide in the Lower San Fernando Dam during the Earthquake of February 9, 1971. *Journal of the Geotechnical Engineering Division*, *101*(9), 889–911. https://doi.org/10.1061/AJGEB6.0000195

Seed, H. B., Seed, R. B., Harder, L. F., Jong, H. L., H. Bolton Seed, I., Engineers, U. S. A. C. of, & Station, U. S. A. E. W. E. (1989). *Re-evaluation of the Lower San Fernando Dam: Examination of the post-earthquake slide of February 9, 1971. Report 2* (Contract Report No. 2). U.S. Army Engineer Waterways Experiment Station. https://books.google.it/books?id=d_Z3pIfdaIEC

Shen, Y., Hesham El Naggar, M., Zhang, D., Huang, Z., & Du, X. (2025). Optimal intensity measure for seismic performance assessment of shield tunnels in liquefiable and non-liquefiable soils. *Underground Space*, *21*, 149–163. https://doi.org/10.1016/j.undsp.2024.03.008

Shinoda, M., Nakajima, S., Watanabe, K., Nakamura, S., Yoshida, I., & Miyata, Y. (2022). Practical seismic fragility estimation of Japanese railway embankments using three seismic intensity measures. *Soils and Foundations*, *62*(4), 101160. https://doi.org/10.1016/j.sandf.2022.101160

Shuku, T., & Phoon, K.-K. (2023). Data-driven subsurface modelling using a Markov random field model. *Georisk: Assessment and Management of Risk for Engineered Systems and Geohazards*, *17*(1), 41–63. https://doi.org/10.1080/17499518.2023.2181973

Sica, S., & Pagano, L. (2009). Performance-Based Analysis of Earth Dams: Procedures and Application to a Sample Case. *Soils and Foundations*, *49*(6), 921–939. https://doi.org/10.3208/sandf.49.921

Sica, S., & Pagano, L. (2020). On the Role of Weak-Motion Earthquakes Recorded on Earth Dams. In J.-M. Zhang, L. Zhang, & R. Wang (Eds.), *Dam Breach Modelling and Risk Disposal* (pp. 345–356). Springer International Publishing. https://doi.org/10.1007/978-3-030-46351-9_36

Sica, S., Pagano, L., & Modaressi, A. (2008). Influence of past loading history on the seismic response of earth dams. *Computers and Geotechnics*, *35*(1), 61–85. https://doi.org/10.1016/j.compgeo.2007.03.004

Sica, S., Pagano, L., & Rotili, F. (2019). Rapid drawdown on earth dam stability after a strong earthquake. *Computers and Geotechnics*, *116*, 103187. https://doi.org/10.1016/j.compgeo.2019.103187

Sica, S., Pagano, L., & Vinale, F. (2008). Interpretazione dei segnali sismici registrati sulla diga di Camastra. *Rivista Italiana di Geotecnica*, *4*(4/2008), 15.

Silvestri, F., Aiello, V., Barile, A., Costanzo, A., Puglia, R., Pescatore, T., Lo Russo, E., Pinto, F., & Tornesello, D. (2006). *Analisi e zonazione della stabilità dei pendii in condizioni sismiche: Applicazioni di metodi tradizionali ed avanzati ad un'area di studio* (Questioni di Ingegneria Geotecnica – Scritti in onore di Arturo Pellegrino). Hevelius. http://www.hevelius.it/download/Silvestri.pdf

Silvestri, F., De Silva, F., Piro, A., & Parisi, F. (2024). Soil-structure interaction effects on out-of-plane seismic response and damage of masonry buildings with shallow foundations. *Soil Dynamics and Earthquake Engineering*, *177*, 108403. https://doi.org/10.1016/j.soildyn.2023.108403

Singh, R., Roy, D., & Jain, S. K. (2005). Analysis of earth dams affected by the 2001 Bhuj Earthquake. *Engineering Geology*, *80*(3–4), 282–291. https://doi.org/10.1016/j.enggeo.2005.06.002

Smalley, R. F., & Isacks, B. L. (1987). A high-resolution local network study of the Nazca Plate Wadati-Benioff Zone under western Argentina. *Journal of Geophysical Research: Solid Earth*, *92*(B13), 13903–13912. https://doi.org/10.1029/JB092iB13p13903

Somerville, P., & Moriwaki, Y. (2003). Seismic hazards and risk assessment in engineering practice. In *International Handbook of Earthquake & Engineering Seismology: Vol. Part B* (pp. 1065–1080). https://doi.org/10.1016/S0074-6142(03)80179-1

Somerville, P., Skarlatoudis, A., Bayless, J., & Thio, H. (2015). *Assessment of Seismic Design Motions in Areas of Low Seismicity: Comparing Australia and New Zealand*. 8.

Sousa, L., Marques, M., Silva, V., & Varum, H. (2017). Hazard Disaggregation and Record Selection for Fragility Analysis and Earthquake Loss Estimation. *Earthquake Spectra*, *33*(2), 529–549. https://doi.org/10.1193/062016EQS101M

SPANCOLD. (2012). *Risk analysis applied to managament of dam safety*. Cómite Nacional Español de Grandes Presas.

Stiphout, T. V., Marsan, D., & Zhuang, J. (2012). Seismicity declustering. *Articles from the Community Online Resource for Statistical Seismicity Analysis (CORSSA)*. https://doi.org/10.5078/corssa-52382934

Stirling, M., Rhoades, D., & Berryman, K. (2002). Comparison of Earthquake Scaling Relations Derived from Data of the Instrumental and Preinstrumental Era. *Bulletin of the Seismological Society of America*, *92*(2), 812–830. https://doi.org/10.1785/0120000221

Stirling, M. W., Abbott, E. R., Rood, D. H., McVerry, G. H., Abrahamson, N. A., Barrell, D. J. A., Huso, R., Litchfield, N. J., Luna, L., Rhoades, D. A., Silvester, P., Van Dissen, R. J., Van Houtte, C., & Zondervan, A. (2021). First Use of Fragile Geologic Features to Set the Design Motions for a Major Existing Engineered Structure. *Bulletin of the Seismological Society of America*. https://doi.org/10.1785/0120210026

Su, Z., Xiao, X., Tong, D., Wang, X., Zhong, Z., Zhao, P., & Yu, J. (2025). Seismic fragility of earth-rock dams with heterogeneous compacted materials using deep learning-aided intensity measure. *Structures*, *73*, 108373. https://doi.org/10.1016/j.istruc.2025.108373

Subsecretaría de Recursos Hídricos. (2022). *Sistema Nacional de Información Hídrica* (Version 2022) [Información hidrológica].

Sukkarak, R., Jongpradist, P., & Pramthawee, P. (2019). A modified valley shape factor for the estimation of rockfill dam settlement. *Computers and Geotechnics*, *108*, 244–256. https://doi.org/10.1016/j.compgeo.2019.01.001

Swaisgood, J. (2014). Behavior of Embankment Dams during Earthquake. *The Journal of Dam Safety*, *12*(2), 35–44.

Swaisgood, J. R. (2003). Embankment Dam Deformations Caused by Earthquakes. *Handbook from the 7th Pacific Conference on Earthquake Engineering*. 7th Pacific Conference on Earthquake Engineering, Christchurch, New Zealand.

Taborda, R., & Roten, D. (2015). Physics-Based Ground-Motion Simulation. In M. Beer, I. A. Kougioumtzoglou, E. Patelli, & I. S.-K. Au (Eds.), *Encyclopedia of Earthquake Engineering* (pp. 1–33). Springer Berlin Heidelberg. https://doi.org/10.1007/978-3-642-36197-5_240-1

Talbot, L. E. D., Given, J., Tjung, E. Y. S., Liang, Y., Chowdhury, K., Seed, R., & Soga, K. (2024). Modeling large-deformation features of the Lower San Fernando Dam failure with the Material Point Method. *Computers and Geotechnics*, *165*, 105881. https://doi.org/10.1016/j.compgeo.2023.105881

Tani, S. (1999). Behavior of large fill dams during earthquake and earthquake damage. *Soil Dynamics and Earthquake Engineering*, *20*(1–4), 223–229. https://doi.org/10.1016/S0267-7261(00)00055-5

Tatsuoka, F., & Gomes Correia, A. (2018). Importance of controlling the degree of saturation in soil compaction linked to soil structure design. *Transportation Geotechnics*, *17*, 3–23. https://doi.org/10.1016/j.trgeo.2018.06.004

Thomann, T., Goldberg, A., & Napolitano, R. (2003). Are those pore pressure readings correct? *Geotechnical Instrumentation News (GIN)*, *21*(1), 50–53.

THYA & Coyne et Bellier. (2005). *Proyecto Potrerillos—Terraplén—Decreto 745/04—Informes de investigaciones*.

Toso, J., & Barchiesi, A. (2013). *Presa potrerillos: Fin del conflicto con definición judicial nitidamente favorable al concesionario y al diseño ejecutivo*. 9.

Tosun, H. (2024). Risk Management of Large Dams under Operation Stage and Case Studies for Cascade System. In H. Tosun, N. Gürsakal, & A. Sebatli-Saglam (Eds.), *Civil Engineering* (Vol. 2). IntechOpen. https://doi.org/10.5772/intechopen.113342

Tothong, P., & Luco, N. (2007). Probabilistic seismic demand analysis using advanced ground motion intensity measures. *Earthquake Engineering & Structural Dynamics*, *36*(13), 1837–1860. https://doi.org/10.1002/eqe.696

Toum, E., Villalba, R., & Masiokas, M. H. (2024). *Snow and glacier contributions to the Mendoza River in the semiarid Central Andes of Argentina*. Preprints. https://doi.org/10.22541/au.173153012.29166108/v1

Travasarou, T., & Bray, J. D. (2003). Optimal Ground Motion Intensity Measures for Assessment of Seismic Slope Displacements. *Handbook from the 7th Pacific Conference on Earthquake Engineering*. 7th Pacific Conference on Earthquake Engineering, Christchurch, New Zealand.

Tretola, M., & Sica, S. (2023). *Fragility curves for a small zoned earth dam*. 4133–4143. https://doi.org/10.7712/120123.10707.20857

Tropeano, G., Silvestri, F., & Ausilio, E. (2017). An uncoupled procedure for performance assessment of slopes in seismic conditions. *Bulletin of Earthquake Engineering*, *15*(9), 3611–3637. https://doi.org/10.1007/s10518-017-0113-y

Tsinidis, G., Stefanidou, S., & Karatzetzou, A. (2024). New limit states for the seismic fragility assessment of circular tunnels: Application in case of tunnels in clayey soil deposits. *Tunnelling and Underground Space Technology*, *154*, 106129. https://doi.org/10.1016/j.tust.2024.106129

USACE. (2007). *Earthquake Design and Evaluation of Concrete Hydraulic Structures* (Engineering Manual Nos. 1110-2–6053; p. 247). US Army Corps of Engineers.

USBR. (2014). *Chapter 15: Foundation Grouting* (Design Standards No. 13 - Embankment Dams, p. 175). United States Department of the Interior Bureau of Reclamation.

USBR, & USACE. (2019). *Best practices in dam and levee safety risk analysis* (Guidelines No. 4.1; p. 1300). United States Department of the Interior Bureau of Reclamation & United States Army Corps of Engineers.

USGS. (2017). *Advanced National Seismic System (ANSS) Comprehensive Catalog* [Dataset]. U.S. Geological Survey. https://doi.org/10.5066/F7MS3QZH

USNRC. (2018). *Updated Implementation Guidelines for SSHAC Hazard Studies* (No. NUREG-2213; NUREG Series, p. 145). US Nuclear Regulatory Commission.

USSD. (1992). *Observed Performance of Dams During Earthquakes Volume I*. United States Socity on Dams. www.ussdams.org

USSD. (2014). *Observed Performance of Dams During Earthquakes Volume III: Vol. III*. United States Socity on Dams. www.ussdams.org

Vahedifard, F., Jasim, F. H., Tracy, F. T., Abdollahi, M., Alborzi, A., & AghaKouchak, A. (2020). Levee Fragility Behavior under Projected Future Flooding in a Warming Climate. *Journal of Geotechnical and Geoenvironmental Engineering*, *146*(12), 04020139. https://doi.org/10.1061/(ASCE)GT.1943-5606.0002399

Valentini, A., Visini, F., Boncio, P., Scotti, O., & Baize, S. (2025). Twenty-Five Years of Probabilistic Fault Displacement Hazard Assessment. *Reviews of Geophysics*, *63*(3), e2024RG000875. https://doi.org/10.1029/2024RG000875

Valenzuela, L. (2015). Tailings Dams and Hydraulic Fills: The 2015 Casagrande Lecture. In *Advances in Soil Mechanics and Geotechnical Engineering*. IOS Press. https://doi.org/10.3233/978-1-61499-599-9-5

Valenzuela, L., Verdugo, R., Vampaña, J., & Opazo, C. (2020). *Safety performance of dams in Chile highly seismic environment*. 32.

Vamvatsikos, D., & Cornell, C. A. (2002). Incremental dynamic analysis. *Earthquake Engineering & Structural Dynamics*, *31*(3), 491–514. https://doi.org/10.1002/eqe.141

Vamvatsikos, D., & Cornell, C. A. (2004). Applied Incremental Dynamic Analysis. *Earthquake Spectra*, *20*(2), 523–553. https://doi.org/10.1193/1.1737737

Vaskou, P., De Quadros, E. F., Kanji, M. A., Johnson, T., & Ekmekci, M. (2019). ISRM Suggested Method for the Lugeon Test. *Rock Mechanics and Rock Engineering*, *52*(10), 4155–4174. https://doi.org/10.1007/s00603-019-01954-x

Vecchietti, A., Cecconi, M., Russo, G., & Pane, V. (2022). Seismic Vulnerability of a Rockfill Dam through Different Displacement-based Approaches. *Journal of Earthquake Engineering*, *26*(1), 113–139. https://doi.org/10.1080/13632469.2019.1662346

Verdugo, & Peters. (2009). Observed seismic behavior of three Chilean large dams. In T. Kokusho (Ed.), *Earthquake Geotechnical Case Histories for Performance-Based Design* (pp. 409–430). CRC Press. https://doi.org/10.1201/NOE0415804844.ch25

Verret, D., LeBœuf, D., & Péloquin, É. (2021). Site effects of the Denis-Perron dam (SM-3): A case study in Eastern North America. *Earthquake Spectra*, *37*(1_suppl), 1602–1625. https://doi.org/10.1177/87552930211019439

Verrucci, L., Pagliaroli, A., Lanzo, G., Di Buccio, F., Biasco, A. P., & Cucci, C. (2022). Damping formulations for finite difference linear dynamic analyses: Performance and practical recommendations. *Computers and Geotechnics*, *142*, 104568. https://doi.org/10.1016/j.compgeo.2021.104568

Wald, D., Lin, K.-W., Porter, K., & Turner, L. (2008). ShakeCast: Automating and Improving the Use of ShakeMap for Post-Earthquake Decision-Making and Response. *Earthquake Spectra*, *24*(2), 533–553. https://doi.org/10.1193/1.2923924

Wang, W., Li, D.-Q., Tang, X.-S., & Du, W. (2023). Seismic fragility and demand hazard analyses for earth slopes incorporating soil property variability. *Soil Dynamics and Earthquake Engineering*, *173*, 108088. https://doi.org/10.1016/j.soildyn.2023.108088

Wang, Z., Peng, W., Zhang, J.-M., & Wang, R. (2025). Seismic performance assessment for high CFRD on thick layered deposit considering various reinforcement measures. *Soil Dynamics and Earthquake Engineering*, *197*, 109550. https://doi.org/10.1016/j.soildyn.2025.109550

Watson-Lamprey, J., & Abrahamson, N. (2006). Selection of ground motion time series and limits on scaling. *Soil Dynamics and Earthquake Engineering*, *26*(5), 477–482. https://doi.org/10.1016/j.soildyn.2005.07.001

Wei, J., Chen, K., Gao, M., Zhou, J., Wang, Y., & Cai, Y. (2025). A Fault Sources-Based Probabilistic Seismic Hazard Analysis for Next-Generation Seismic Ground Motion Parameters Zonation Map of China. *International Journal of Disaster Risk Science*, *16*(2), 248–261. https://doi.org/10.1007/s13753-025-00632-7

Wells, D. L., & Coppersmith, K. J. (1994). New empirical relationships among magnitude, rupture length, rupture width, rupture area, and surface displacement. *Bulletin of the Seismological Society of America*, *84*(4), 974–1002. https://doi.org/10.1785/BSSA0840040974

Wen, L., Wu, L., Li, Y., Liu, Y., Zhou, H., & Li, B. (2022). Quantitative Study on the Influence of Alluvium Foundation on the Behavior of Concrete Face Rockfill Dam. *International Journal of Geomechanics*, *22*(9), 04022145. https://doi.org/10.1061/(ASCE)GM.1943-5622.0002501

Whittaker, A., Deierlein, G., Hooper, J., & Merovich, A. (2004). *Engineering Demand Parameters for Structural Framing Systems* (No. Task 2.2; ATC-58 Project, p. 20). Applied Technology Council.

Wieland, M. (2019). *Limitations of risk and probabilistic safety analyses for large storage dams*. International Dam Safety Conference, Bhubaneswar, India.

Wiemer, S. (2001). A Software Package to Analyze Seismicity: ZMAP. *Seismological Research Letters*, *72*(3), 373–382. https://doi.org/10.1785/gssrl.72.3.373

Williams, R. A., Stephenson, W. J., Frankel, A. D., & Odum, J. K. (1999). Surface Seismic Measurements of Near-Surface P- and S-Wave Seismic Velocities at Earthquake Recording Stations, Seattle, Washington. *Earthquake Spectra*, *15*(3), 565–584. https://doi.org/10.1193/1.1586059

Woessner, J., & Wiemer, S. (2005). Assessing the Quality of Earthquake Catalogues: Estimating the Magnitude of Completeness and Its Uncertainty. *Bulletin of the Seismological Society of America*, *95*(2), 684–698. https://doi.org/10.1785/0120040007

Wu, Q., Li, D.-Q., & Du, W. (2022). Identification of optimal ground-motion intensity measures for assessing liquefaction triggering and lateral displacement of liquefiable sloping grounds. *Earthquake Spectra*, *38*(4), 2707–2730. https://doi.org/10.1177/87552930221094344

Xu, B., & Athanasopoulos-Zekkos, A. (2025). Calibration and assessment of sand-based constitutive models for gravel cyclic response via numerical single element analyses. *Soil Dynamics and Earthquake Engineering*, *196*, 109461. https://doi.org/10.1016/j.soildyn.2025.109461

Xu, B., & Pang, R. (2025). *Stochastic Dynamic Response Analysis and Performance-Based Seismic Safety Evaluation for High Concrete Faced Rockfill Dams*. Springer Nature Singapore. https://doi.org/10.1007/978-981-97-7198-1

Xu, B., Wang, X., Pang, R., & Zhou, Y. (2023). Effect of Multi-Components Strong Motion Duration on Seismic Performance of High CFRDs Based on Fragility Analysis. *Journal of Earthquake Engineering*, *27*(9), 2587–2605. https://doi.org/10.1080/13632469.2022.2121335

Xu, B., Zou, D., Kong, X., Zhou, Y., & Liu, X. (2017). Concrete Slab Dynamic Damage Analysis of CFRD Based on Concrete Nonuniformity. *International Journal of Geomechanics*, *17*(9), 04017055. https://doi.org/10.1061/(ASCE)GM.1943-5622.0000939

Youngs, R. R., & Coppersmith, K. J. (1985). *Implications of fault slip rates and earthquake recurrence models to probabilistic seismic hazard estimates*. *75*(4), 939–964. https://doi.org/10.1785/BSSA0750040939

Zamarbide, J. L., & Castano, J. C. (1993). Analysis of the January 26th, 1985, Mendoza (Argentina) earthquake effects and of their possible correlation with the recorded accelerograms and soil conditions. *Tectonophysics*, *218*(1–3), 221–235. https://doi.org/10.1016/0040-1951(93)90269-P

Zareian, F., Ibarra, L., & Krawinkler, H. (2004). *Seismic Demands and Capacities of Single-Story and Low-Rise Multi-Story Woodframe Structures*. 13th World Conference on Earthquake Engineering, Canada.

Zhang, G., & Zhang, J.-M. (2008). Unified Modeling of Monotonic and Cyclic Behavior of Interface Between Structure and Gravelly Soil. *Soils and Foundations*, *48*(2), 231–245. https://doi.org/10.3208/sandf.48.231

Zhang, J.-M., Yang, Z., Gao, X., & Zhang, J. (2015). Geotechnical aspects and seismic damage of the 156-m-high Zipingpu concrete-faced rockfill dam following the Ms 8.0 Wenchuan earthquake. *Soil Dynamics and Earthquake Engineering*, *76*, 145–156. https://doi.org/10.1016/j.soildyn.2015.03.014

Zhang, L., & Einstein, H. H. (2004). Using RQD to estimate the deformation modulus of rock masses. *International Journal of Rock Mechanics and Mining Sciences*, *41*(2), 337–341. https://doi.org/10.1016/S1365-1609(03)00100-X

Zhou, Y., Zhang, Y., Pang, R., & Xu, B. (2021). Seismic fragility analysis of high concrete faced rockfill dams based on plastic failure with support vector machine. *Soil Dynamics and Earthquake Engineering*, *144*. https://doi.org/10.1016/j.soildyn.2021.106587

Zimmaro, P., & Ausilio, E. (2020). Numerical Evaluation of Natural Periods and Mode Shapes of Earth Dams for Probabilistic Seismic Hazard Analysis Applications. *Geosciences*, *10*(12), 499. https://doi.org/10.3390/geosciences10120499

Zou, D., Zhou, Y., Ling, H. I., Kong, X., & Xu, B. (2012). Dislocation of face-slabs of Zipingpu concrete face rockfill dam during Wenchuan earthquake. *Journal of Earthquake and Tsunami*, *6*(2). https://doi.org/10.1142/S1793431112500078

11. Appendixes

11.1 Appendix I

This appendix contains the graphics of the records from all the piezometers from the monitoring system, which were evaluated in order to evaluate the long-term hydraulic conditions of the dam and foundation.

For better identification of each instrument, they are labeled using a notation that reflects their relative position within the dam, as shown in Fig. 11.1. Additionally, instruments with no available records are highlighted by enclosing them within a gray dashed-line square.

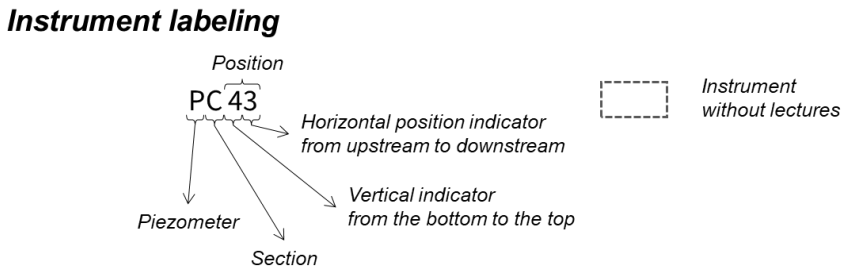


Fig. 11.1: Labeling used for the identification of the instruments.

In addition, the sections with a large number of instruments were split into two or three different graphics identified with the suffix i, ii, or iii. The referenced graphics are presented below.

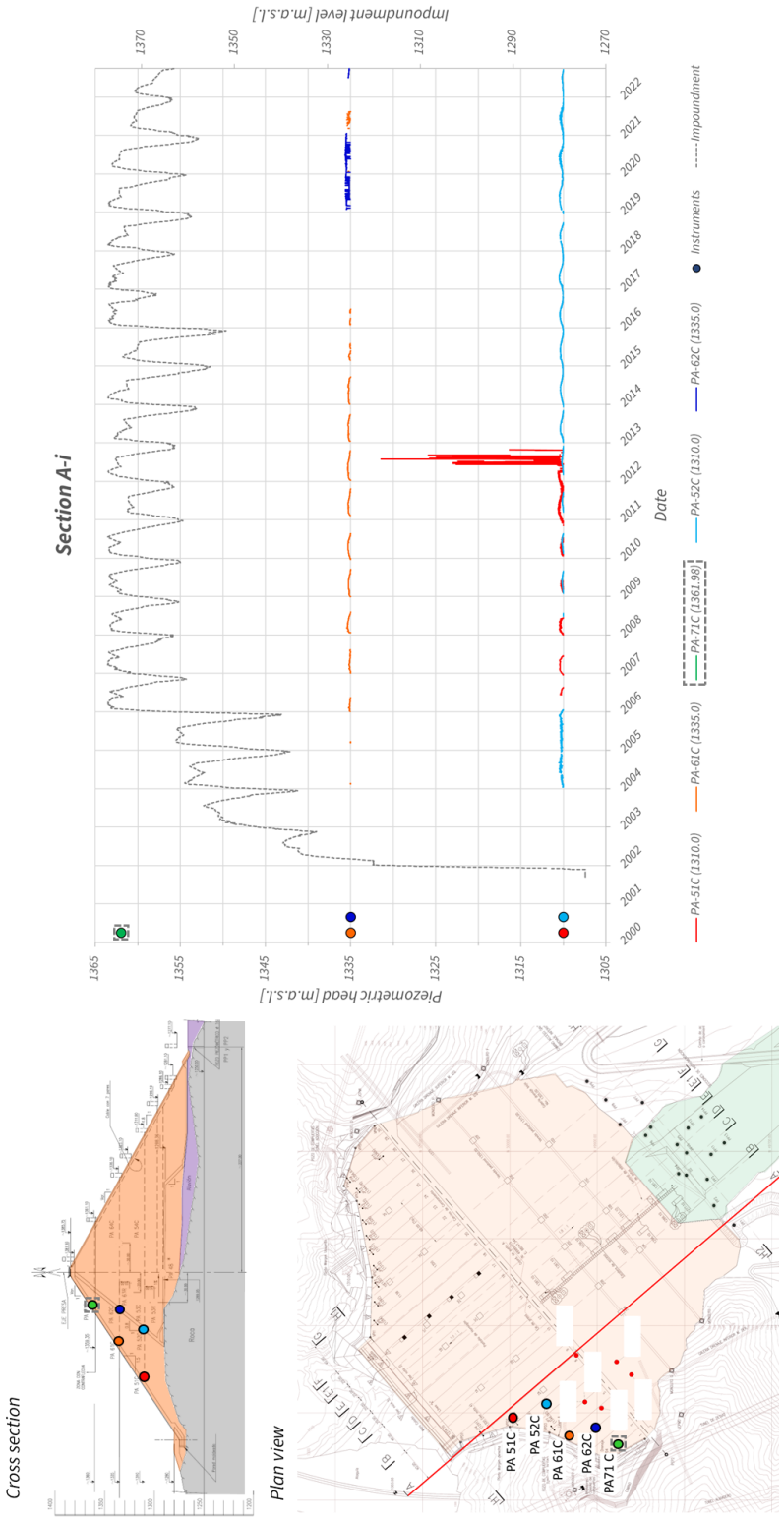


Fig. 11.2: Location and records of piezometers of Section A-i.

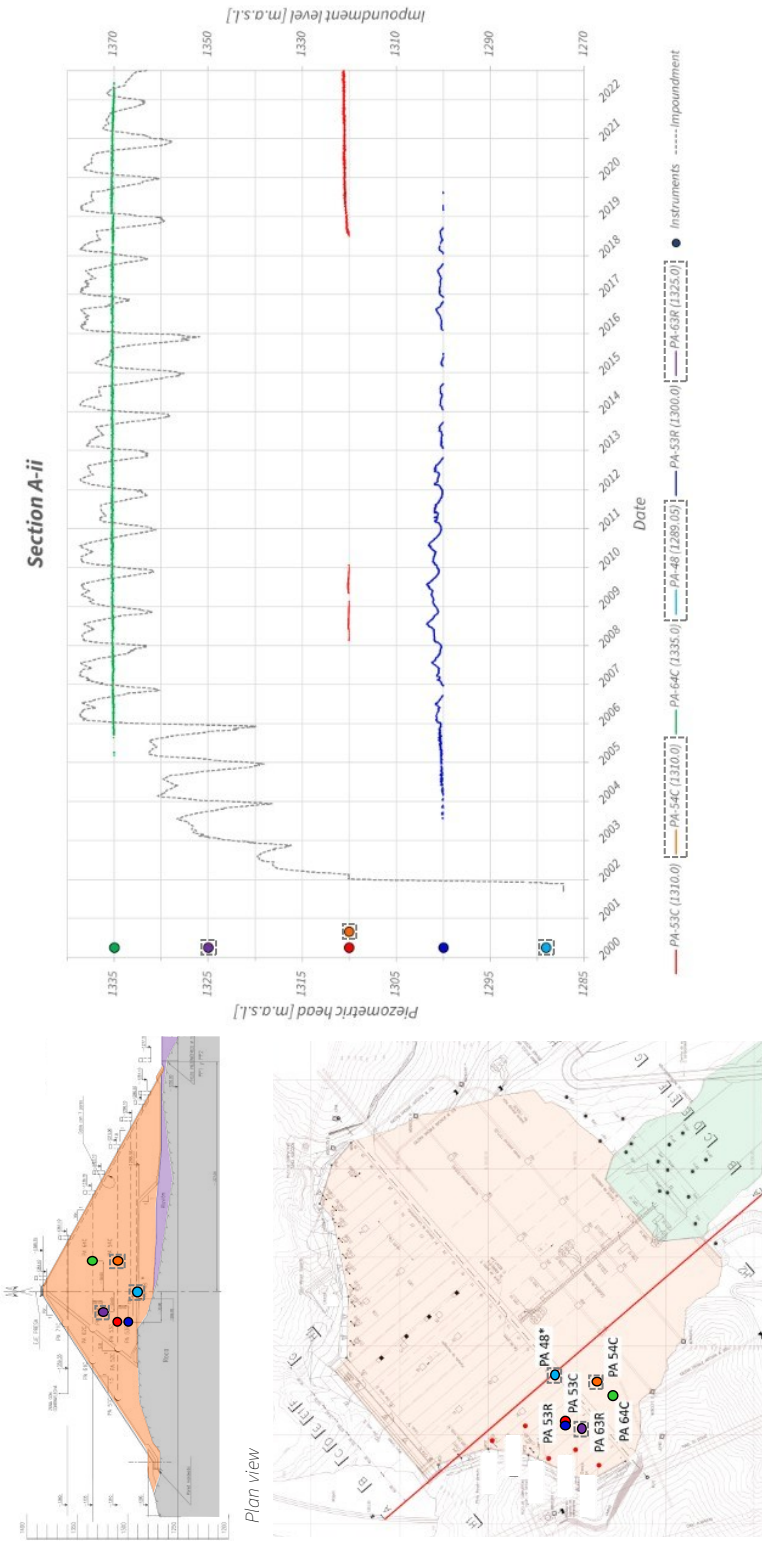


Fig. 11.3: Location and records of piezometers of Section A-ii.

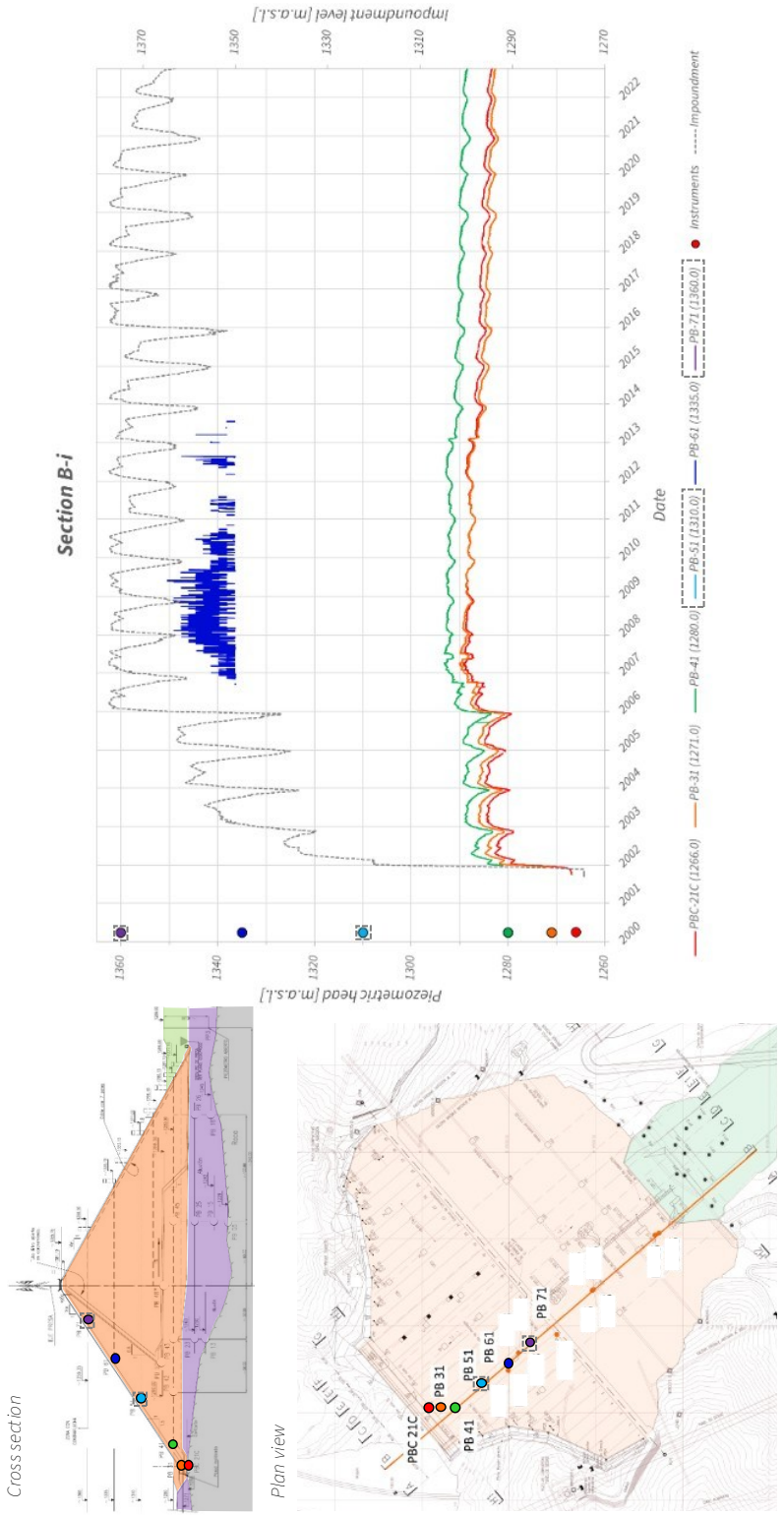


Fig. 11.4: Location and records of piezometers of Section B-i.

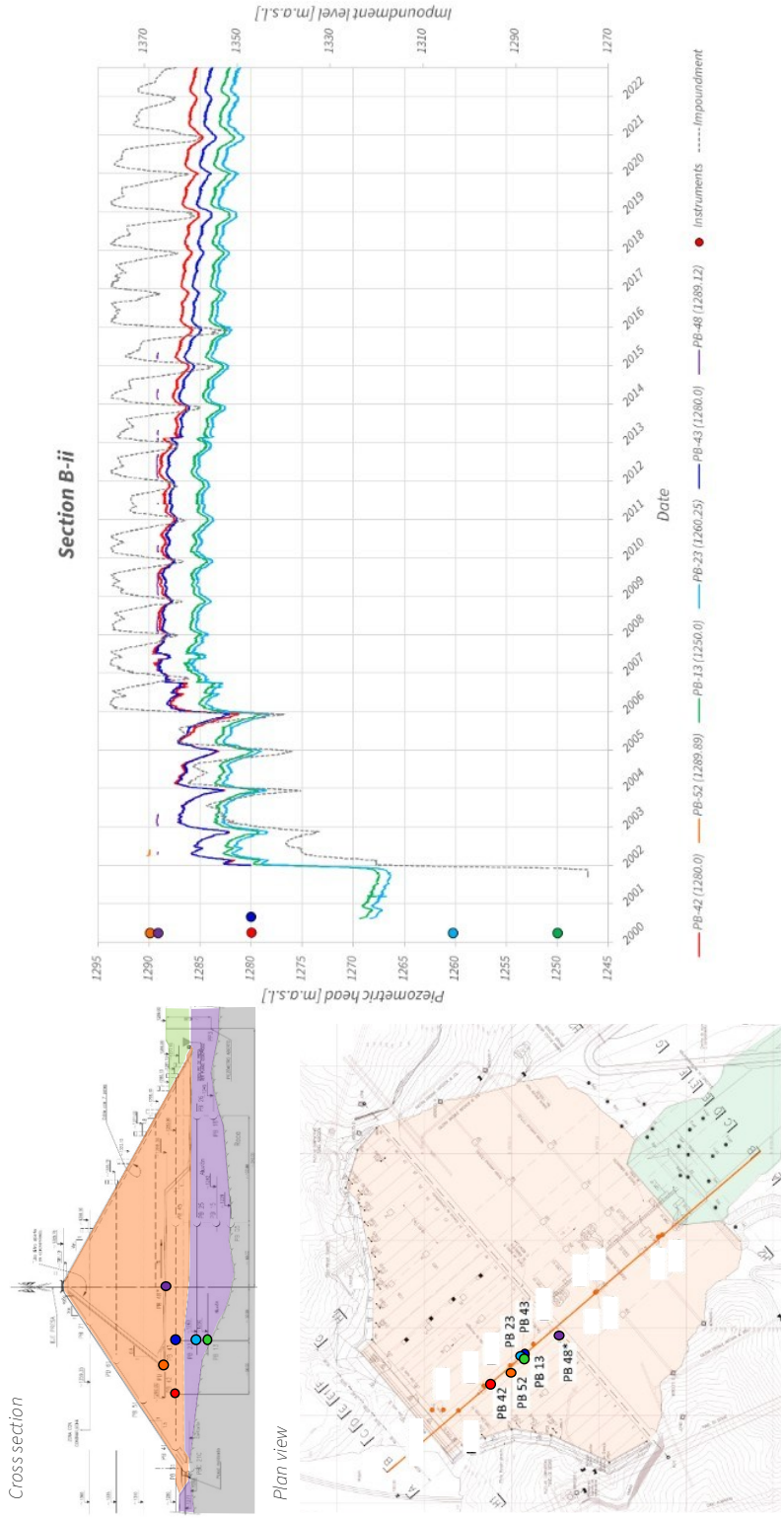


Fig. 11.5: Location and records of piezometers of Section B-ii.

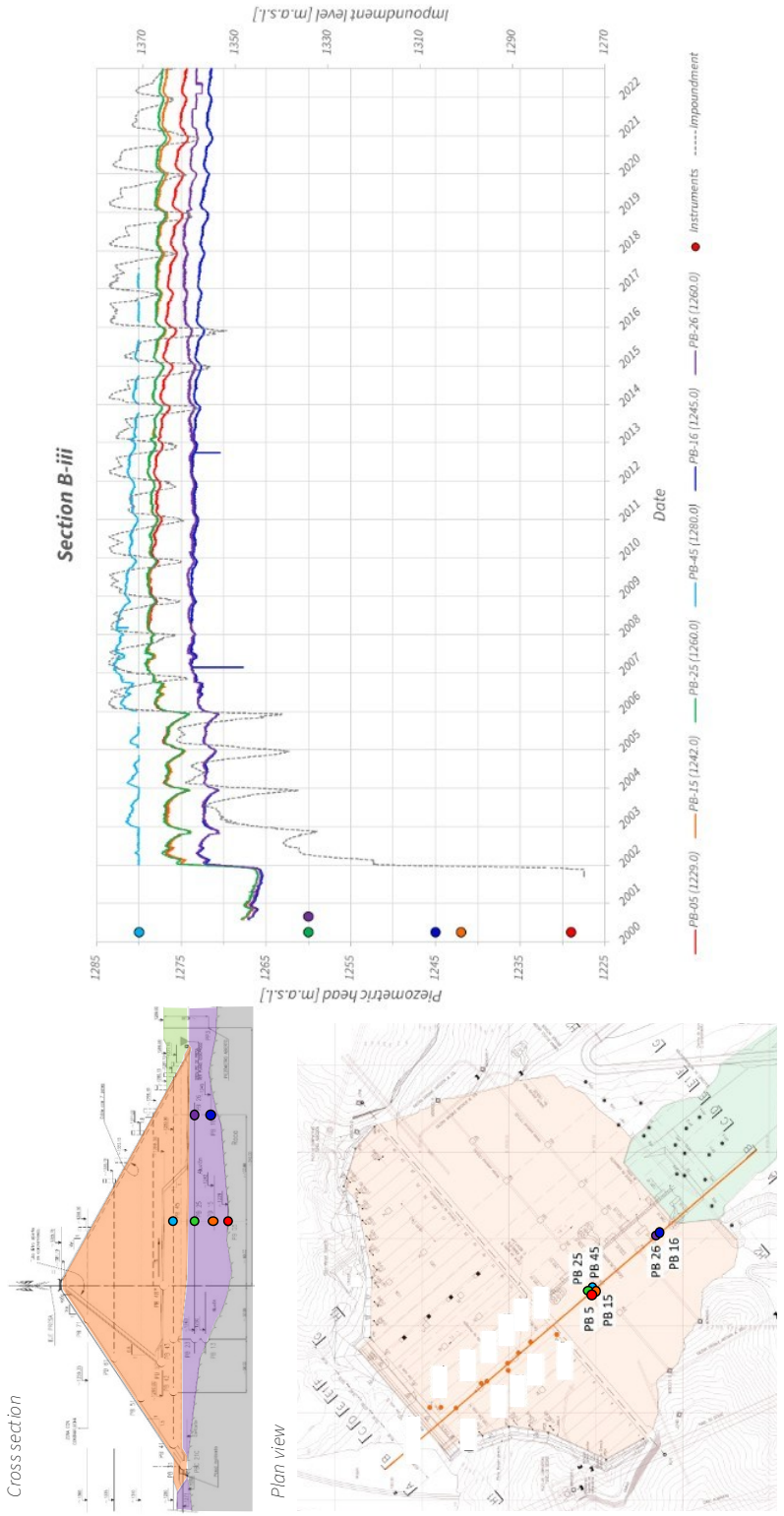


Fig. 11.6: Location and records of piezometers of Section B-iIi.

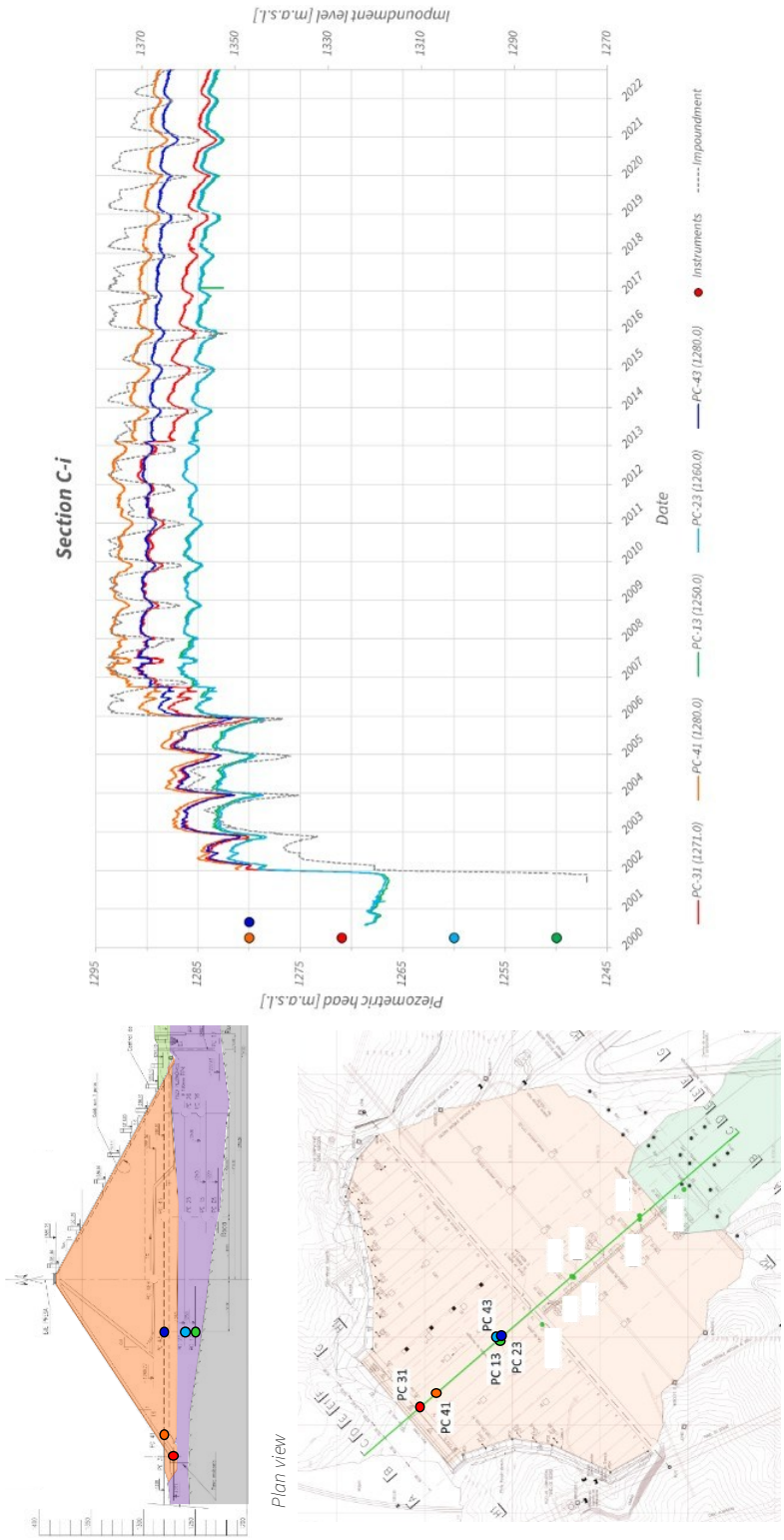


Fig. 11.7: Location and records of piezometers of Section C-i.

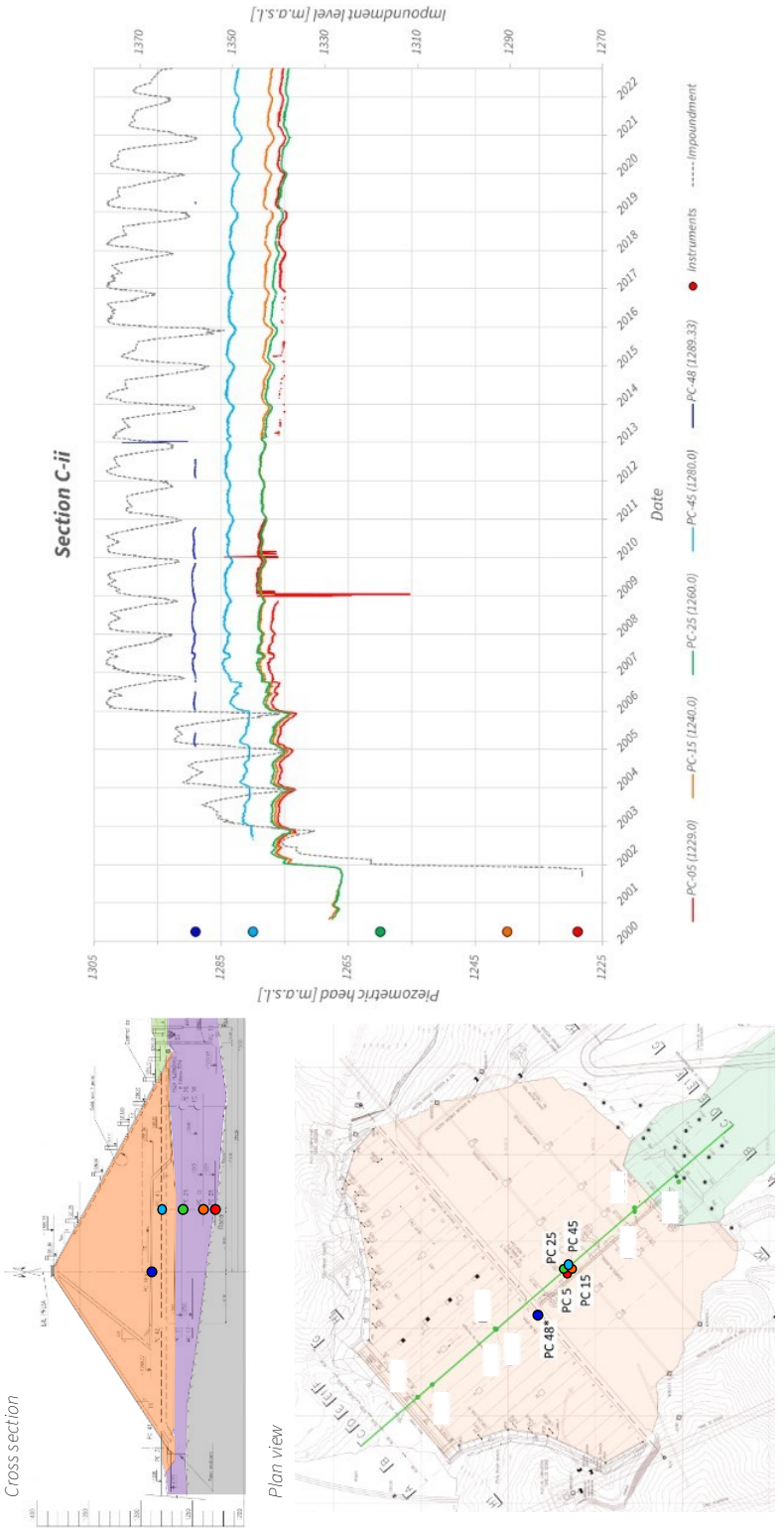


Fig. 11.8: Location and records of piezometers of Section C-ii.

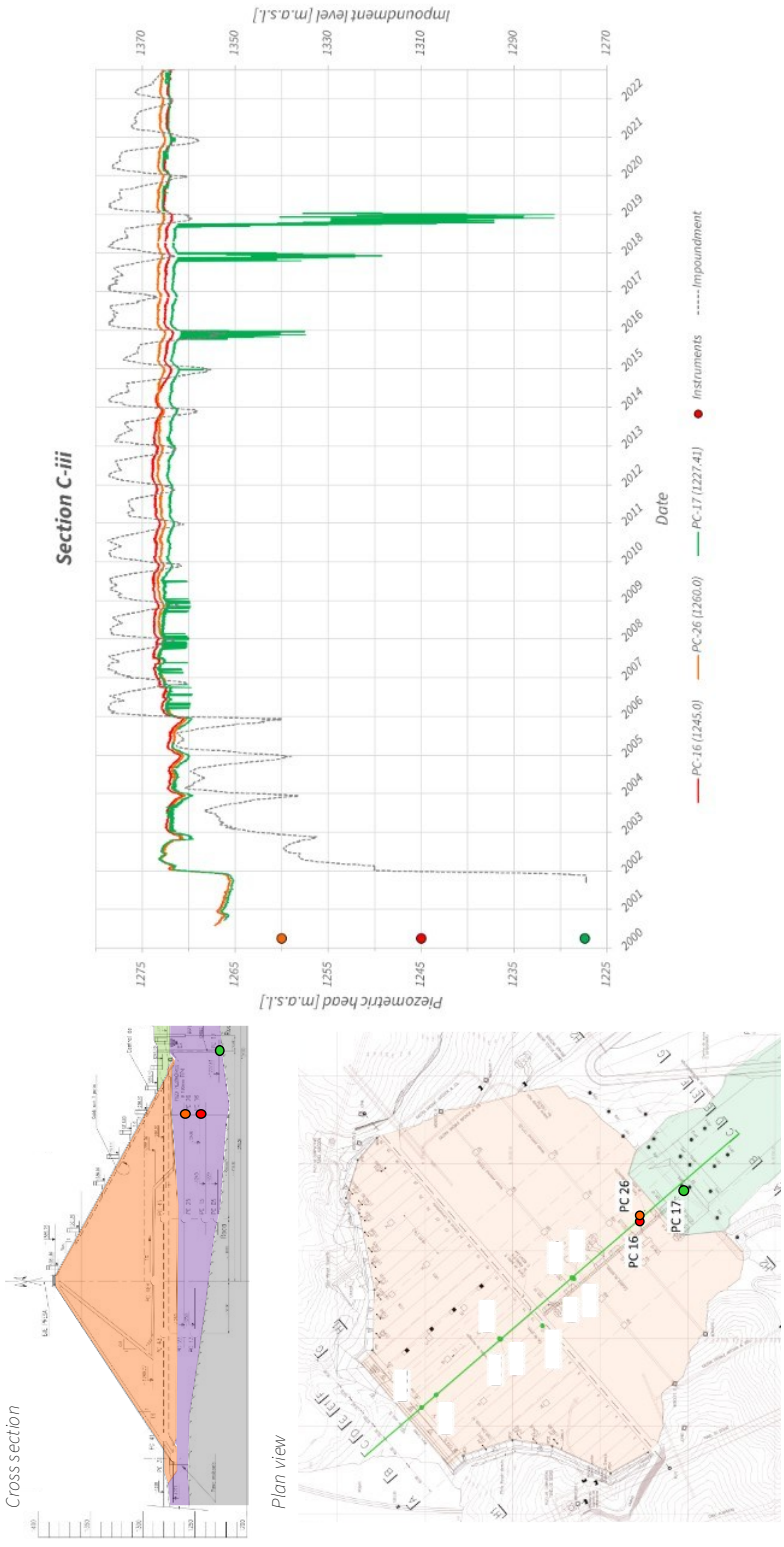


Fig. 11.9: Location and records of piezometers of Section C-iii.

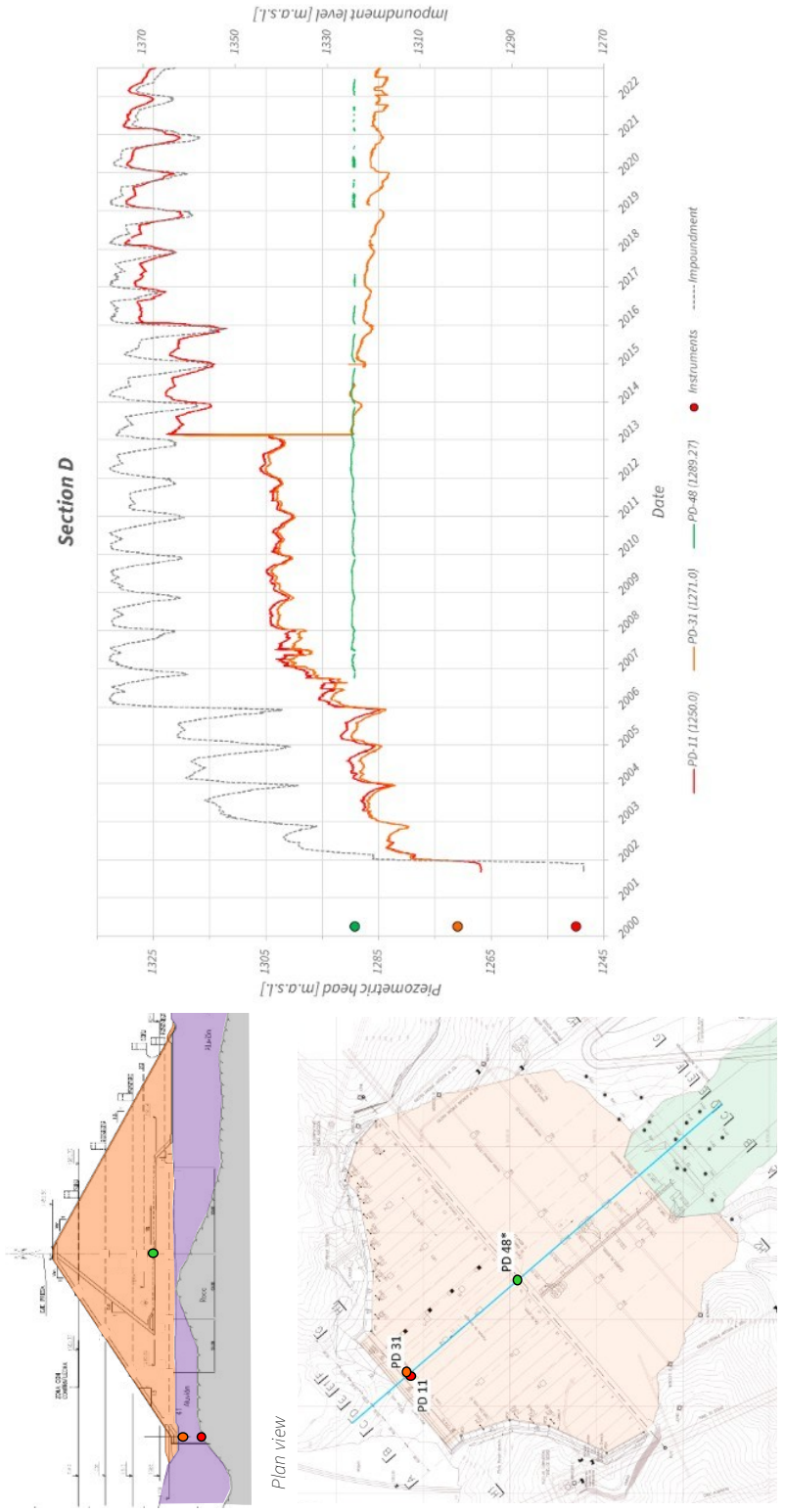


Fig. 11.10: Location and records of piezometers of Section D.

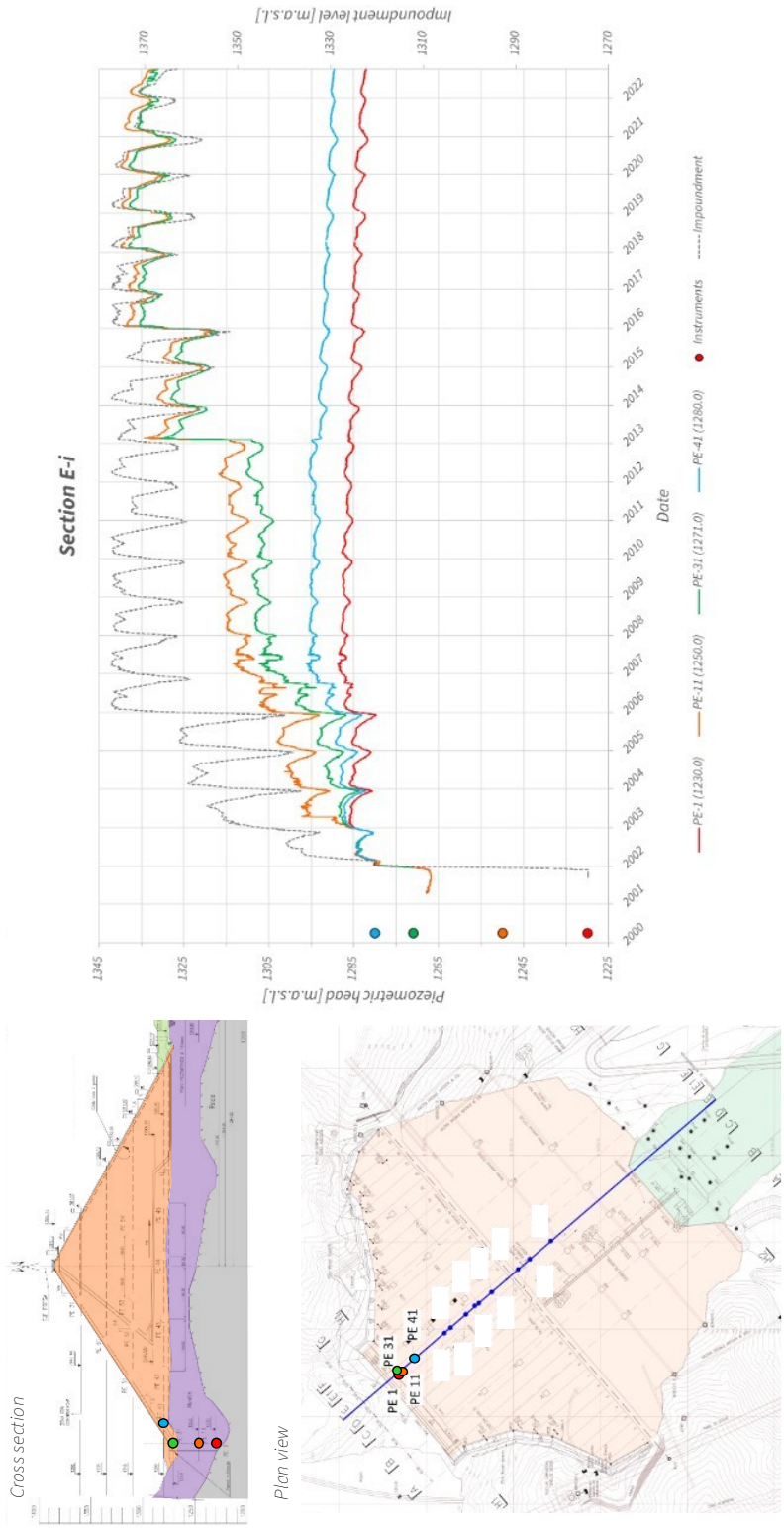


Fig. 11.11: Location and records of piezometers of Section E-i.

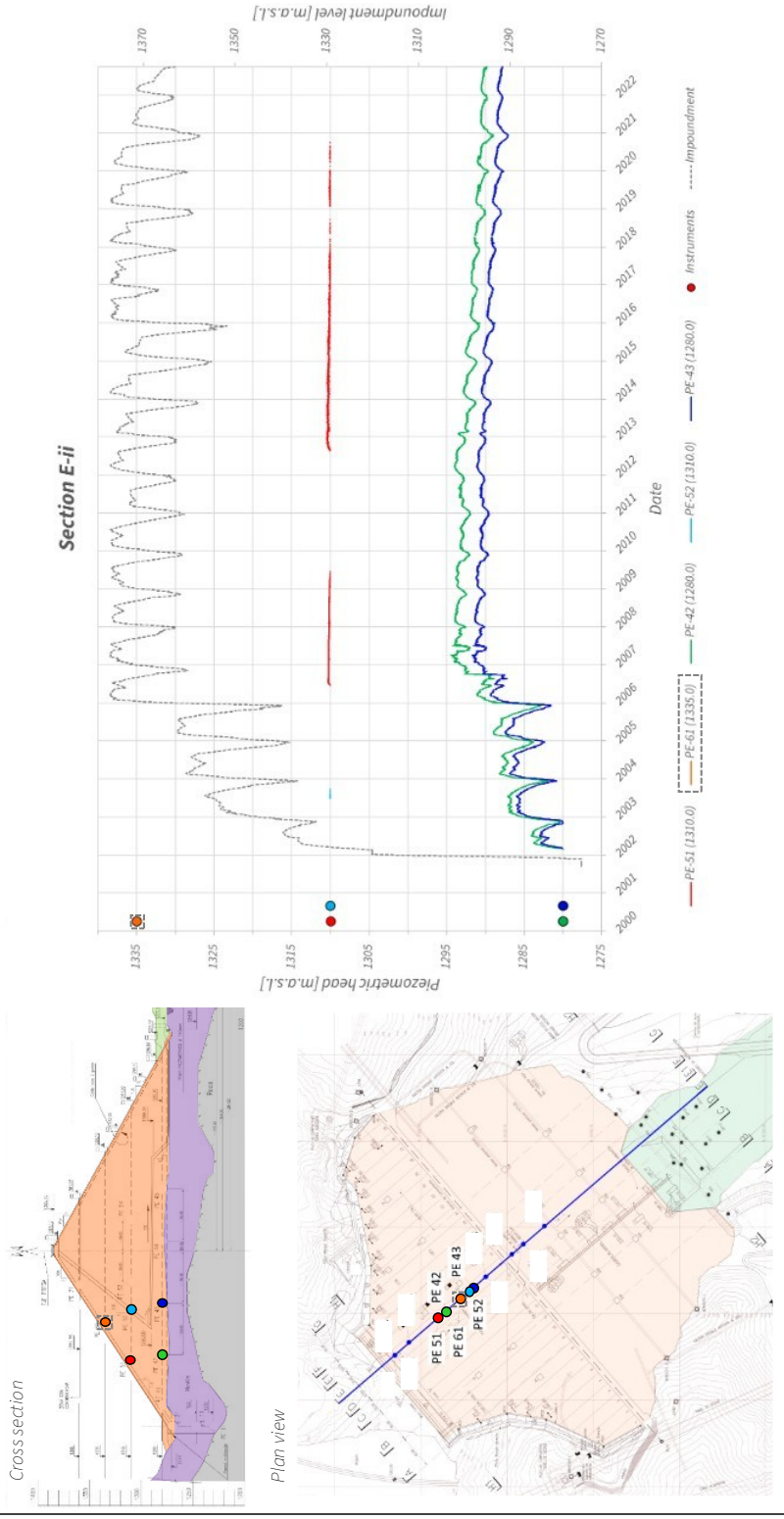


Fig. 11.12: Location and records of piezometers of Section E-ii.

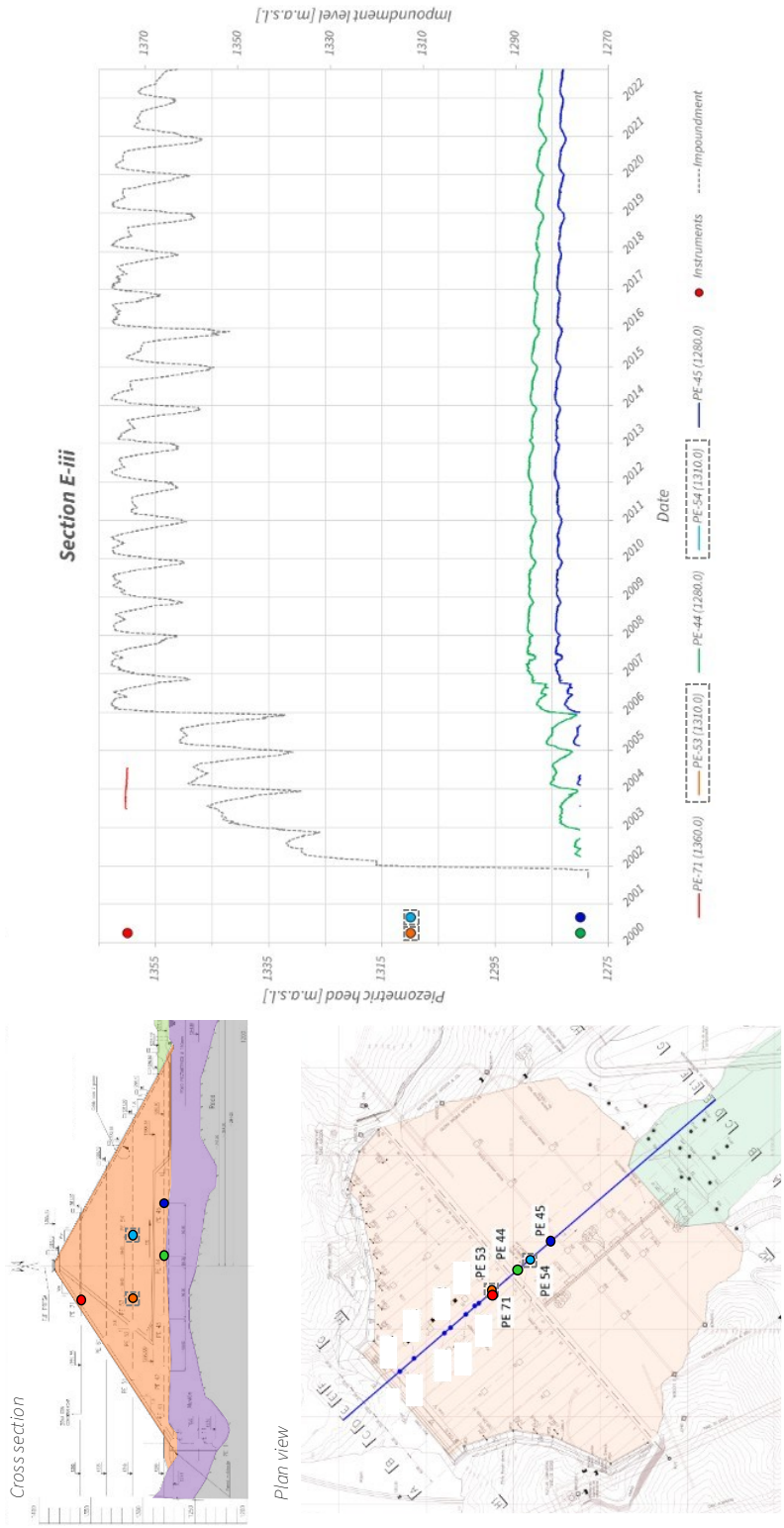


Fig. 11.13: Location and records of piezometers of Section E-iii.

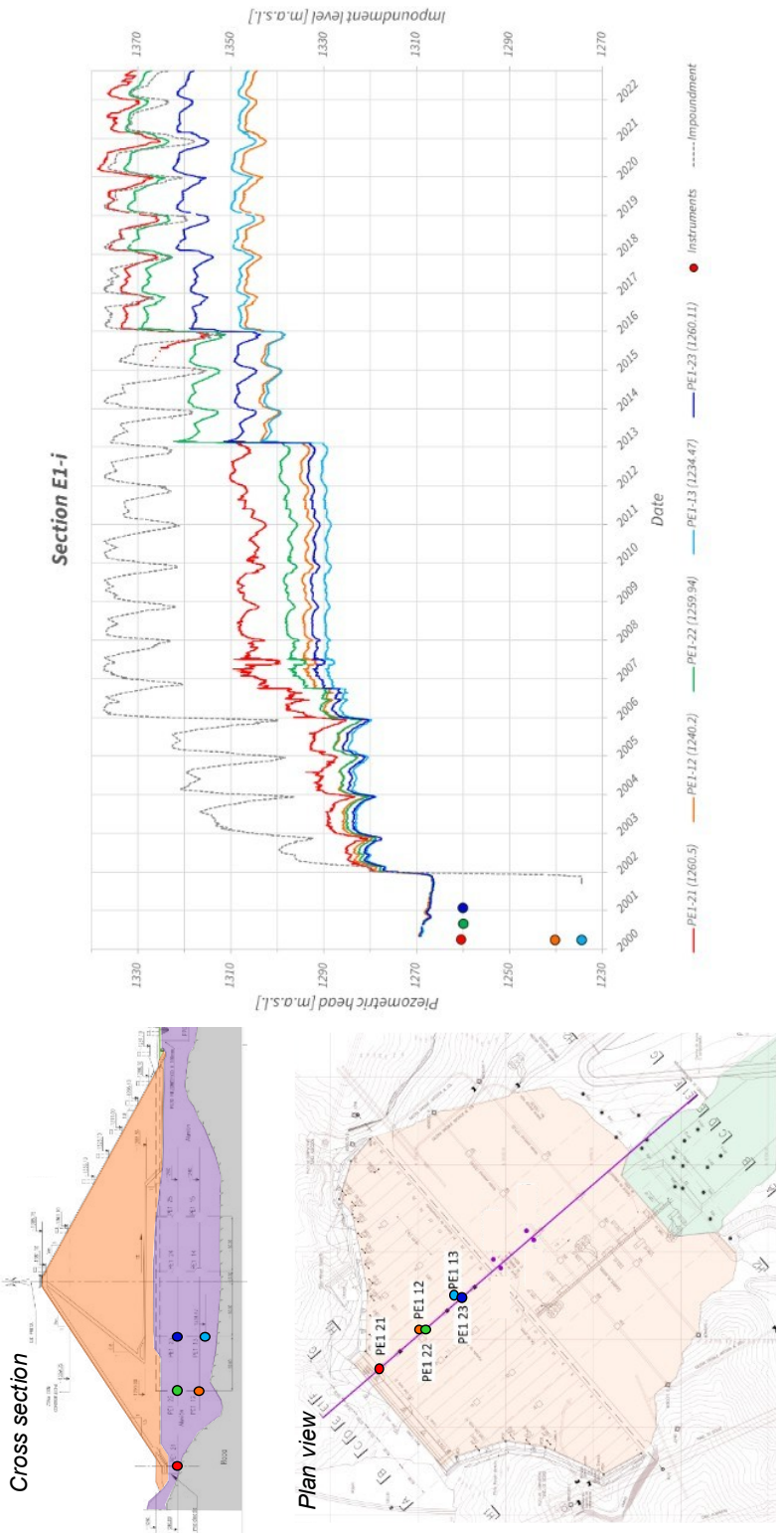


Fig. 11.14: Location and records of piezometers of Section E1-i.

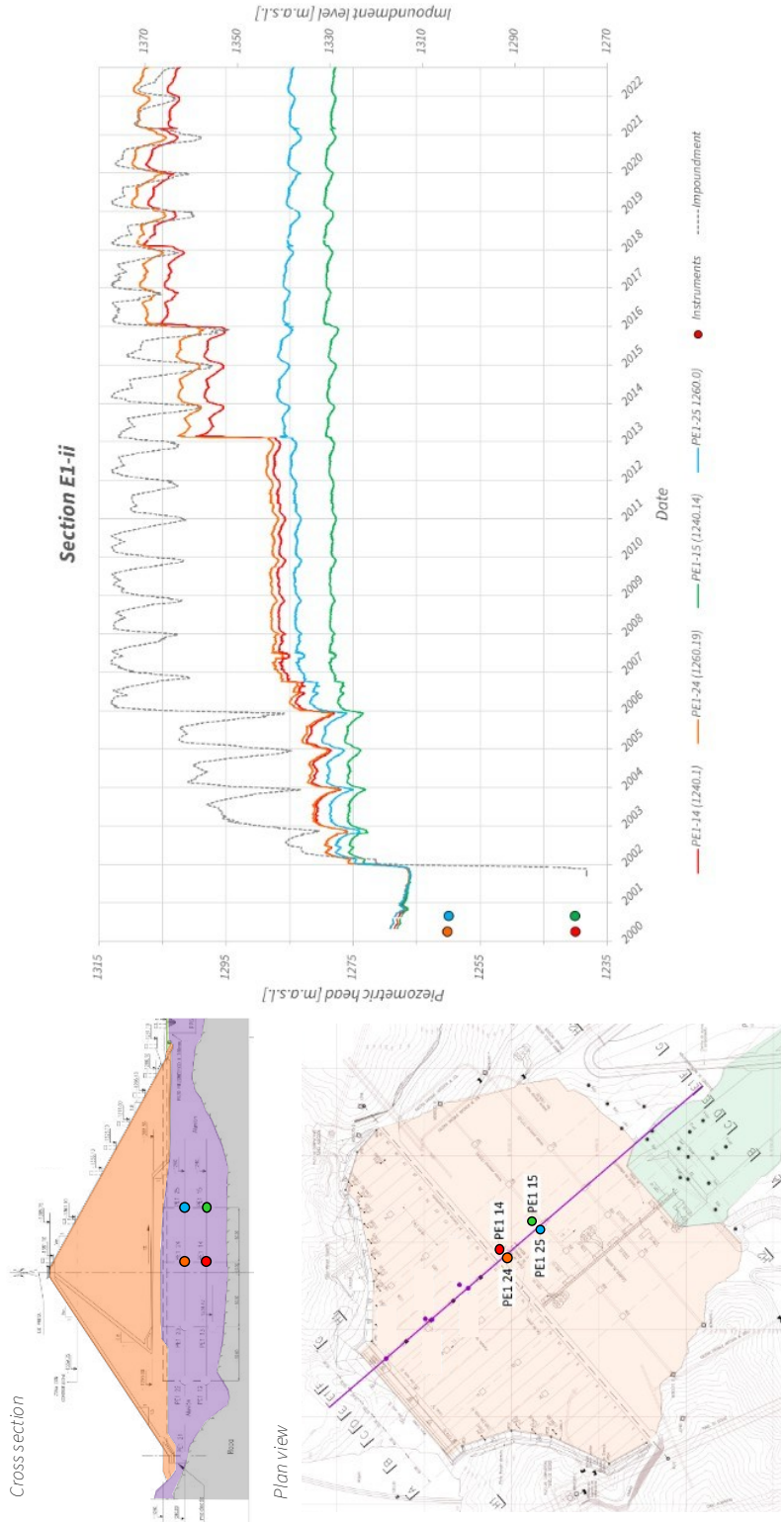


Fig. 11.15: Location and records of piezometers of Section E1-ii.

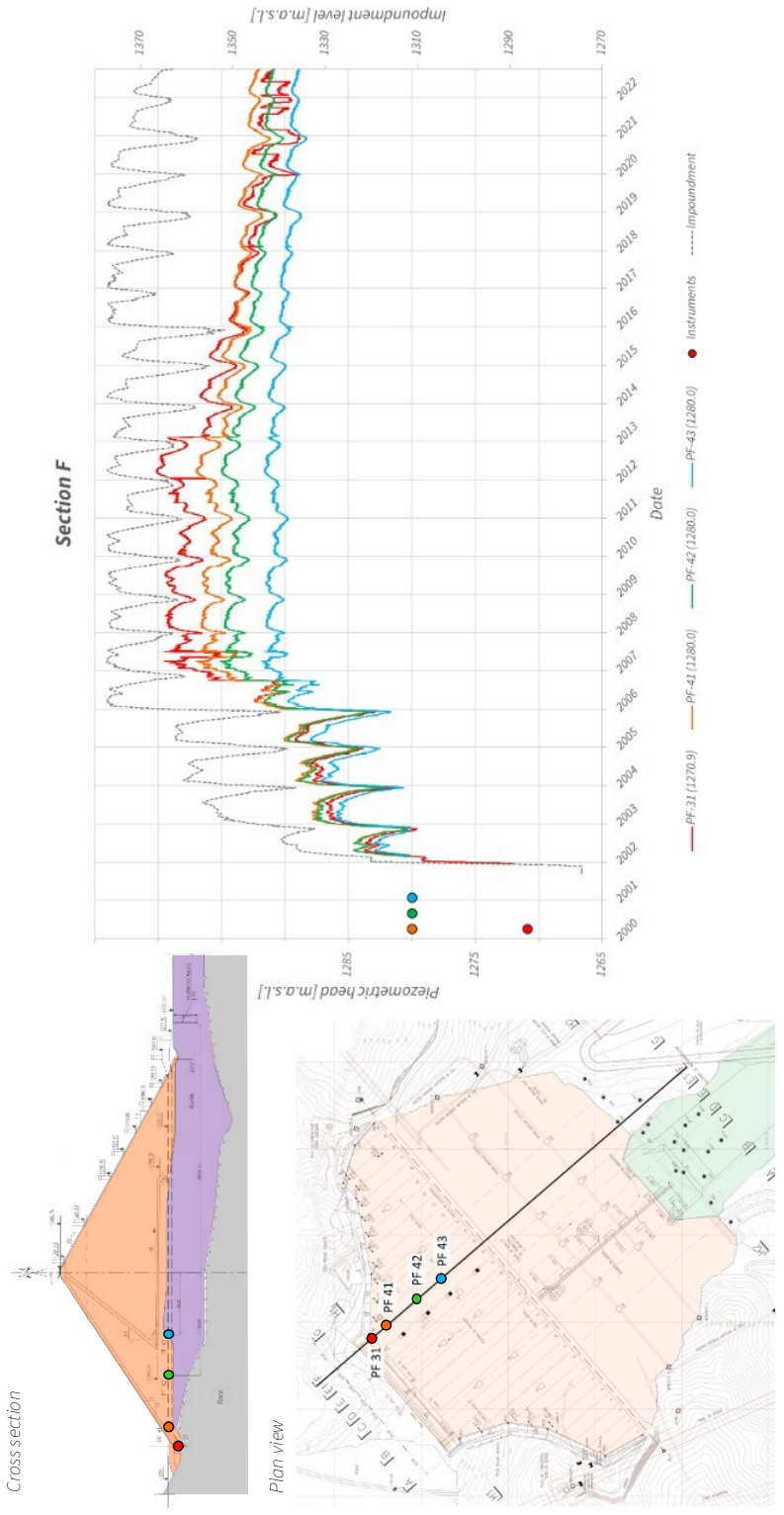


Fig. 11.16: Location and records of piezometers of Section F.

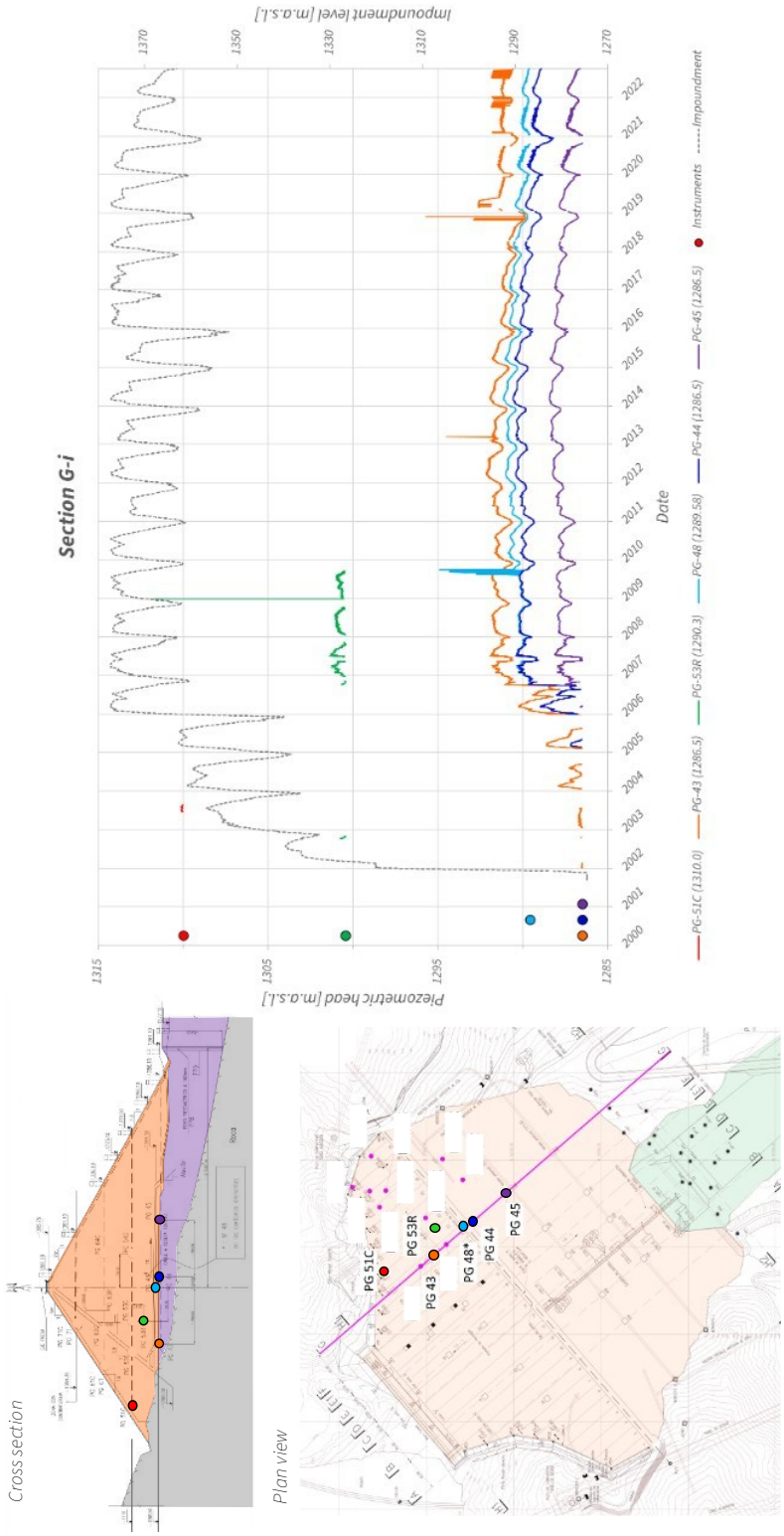


Fig. 11.17: Location and records of piezometers of Section G-i.

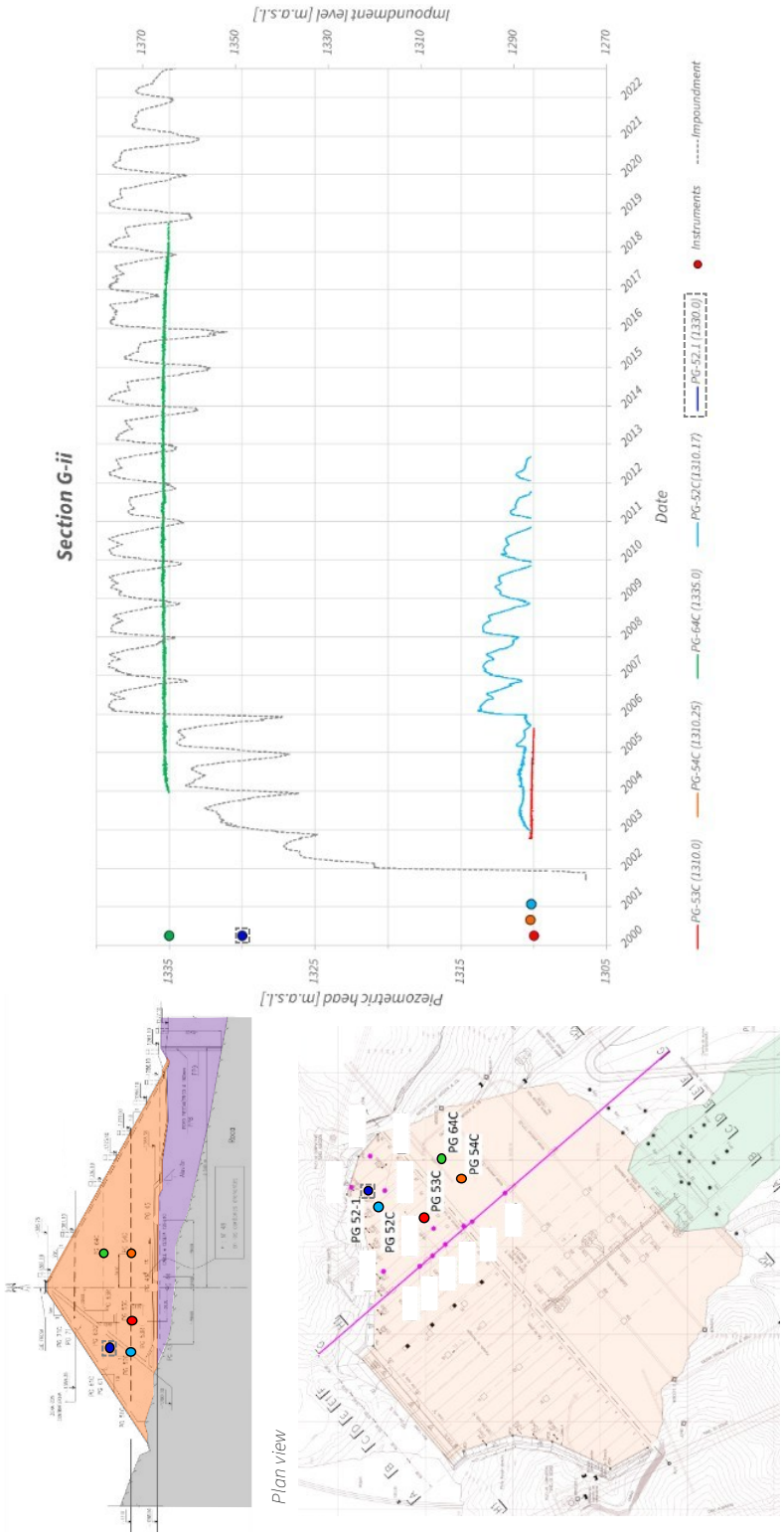


Fig. 11.18: Location and records of piezometers of Section G-ii.

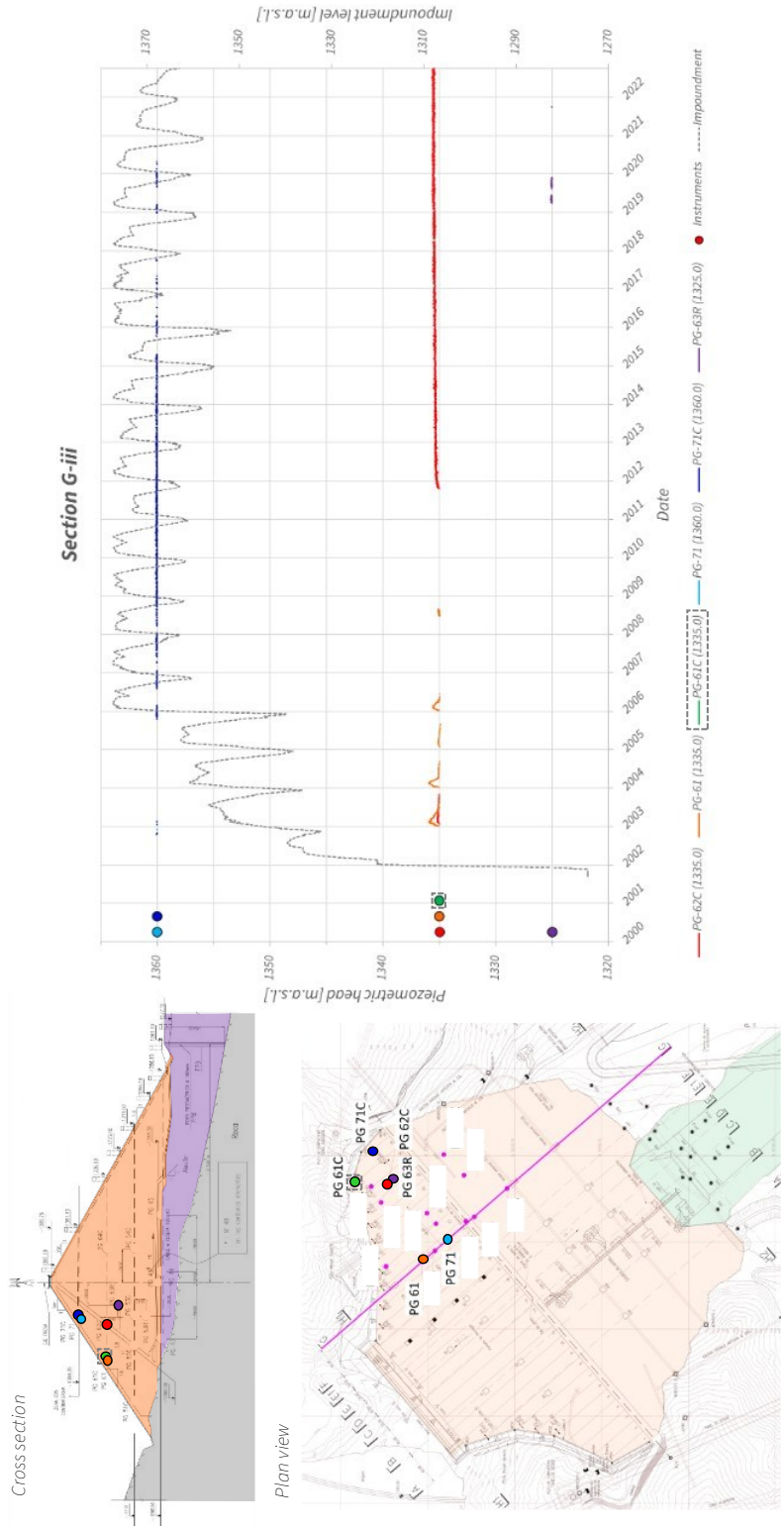


Fig. 11.19: Location and records of piezometers of Section G-iii.

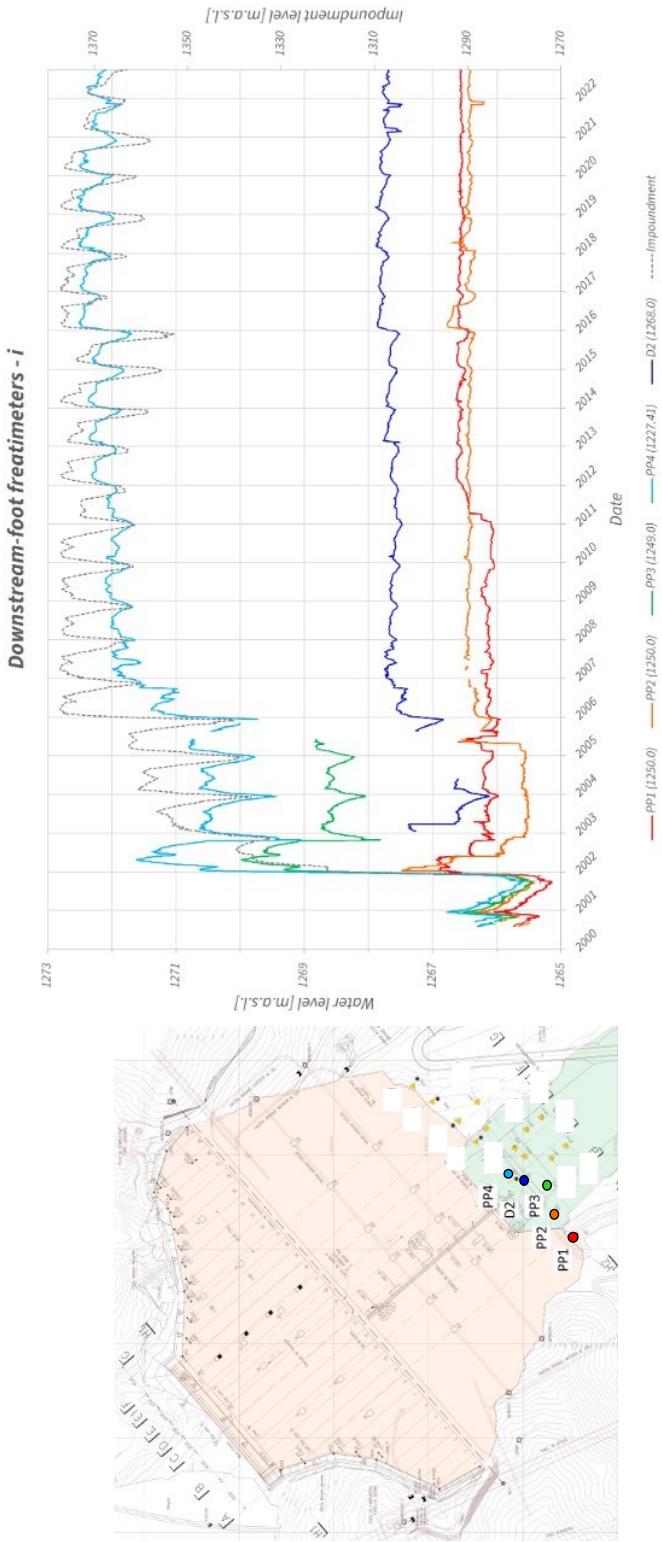


Fig. 11.20: Location and records of standpipe piezometers (freatimeters) of the downstream foot -i.

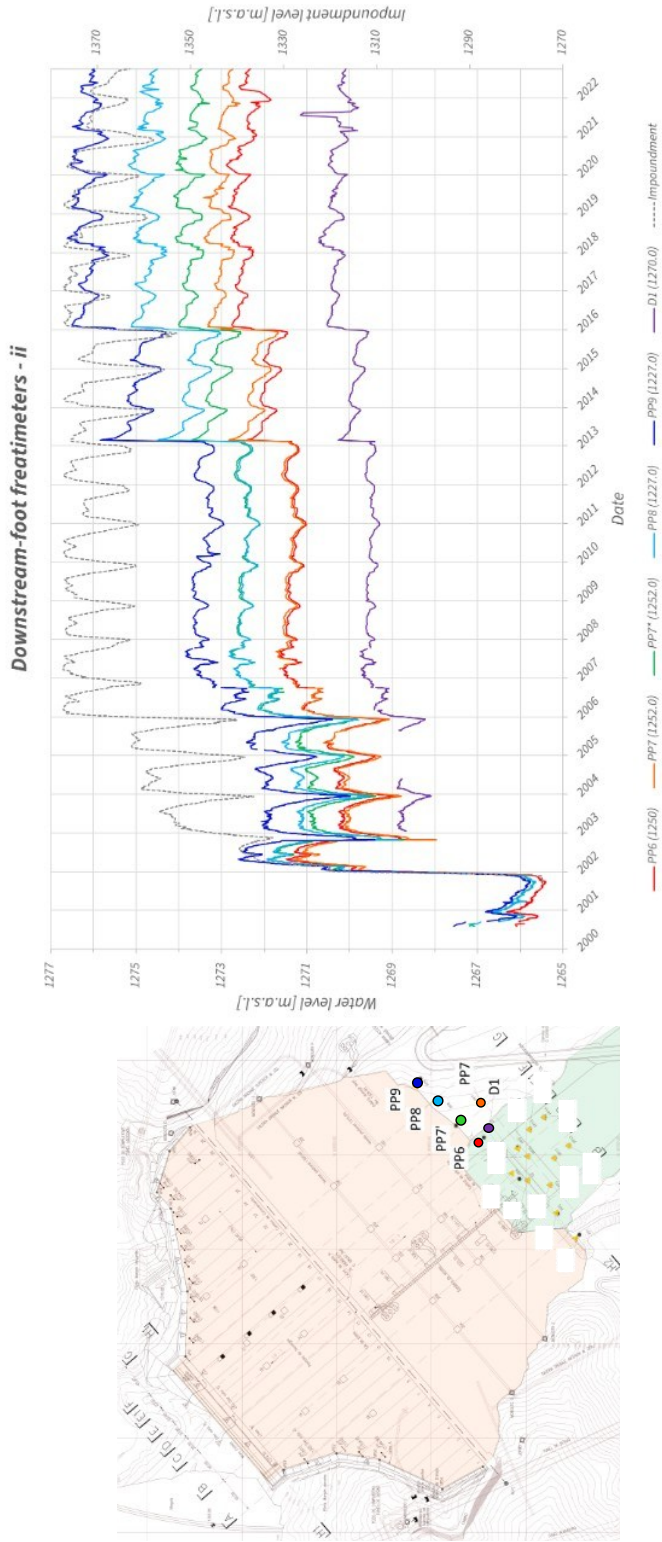


Fig. 11.21: Location and records of standpipe piezometers (freatimeters) of the downstream foot -ii.

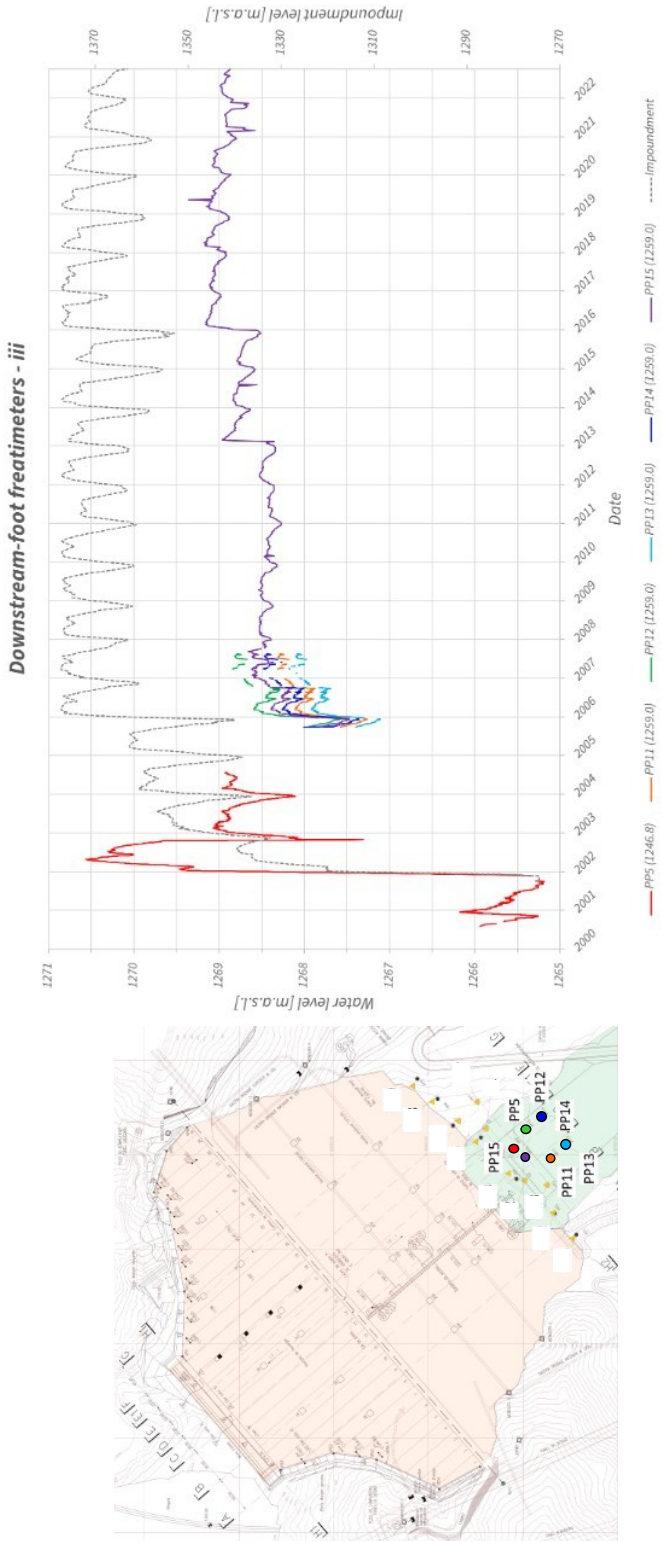


Fig. 11.22: Location and records of standpipe piezometers (freatimeters) of the downstream foot -iii.

11.2 Appendix II

This appendix contains information related to the seismic hazard assessment that was not presented in the main body of the dissertation.

Are included the hazard curves for three different values of the structural period T (0.0, 0.5, and 1.0 s), the plot and table of the Uniform Hazard Spectra, the disaggregation charts for all the combinations of return periods (144y, 475y, 975y, 2475y, 4975y, and 9975y) and intensity measures (*PGA* and *Sa(0.5s)*), and the plots and tables containing the ground motion parameters of the scaled records.

11.2.1 Hazard curves

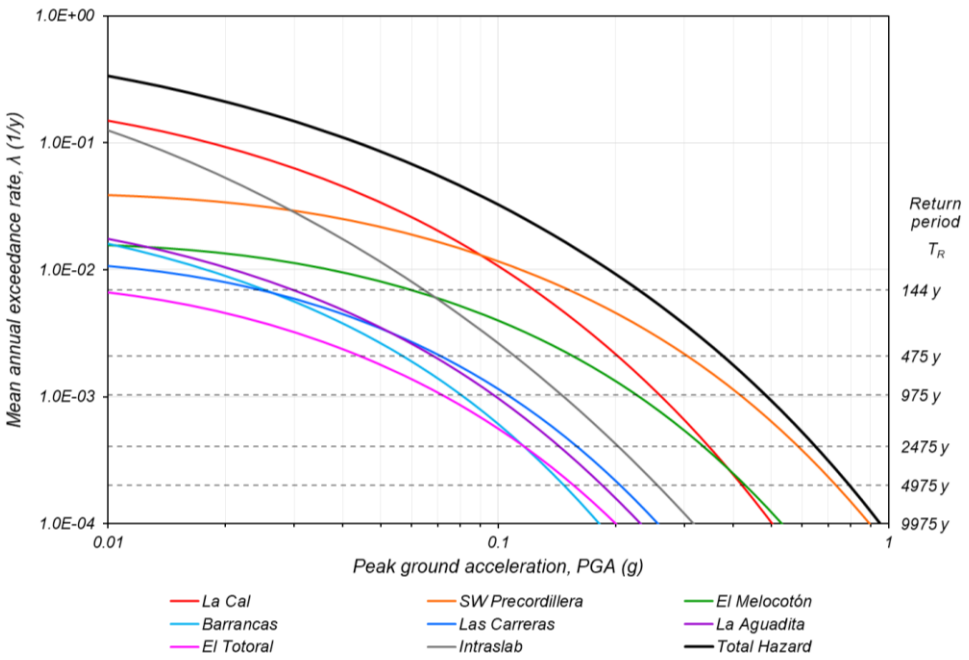


Fig. 11.23: Hazard curves in terms of PGA for all the seismic sources, and their combination (Total Hazard). Evidenced the return periods for every level of the ground shaking selected.

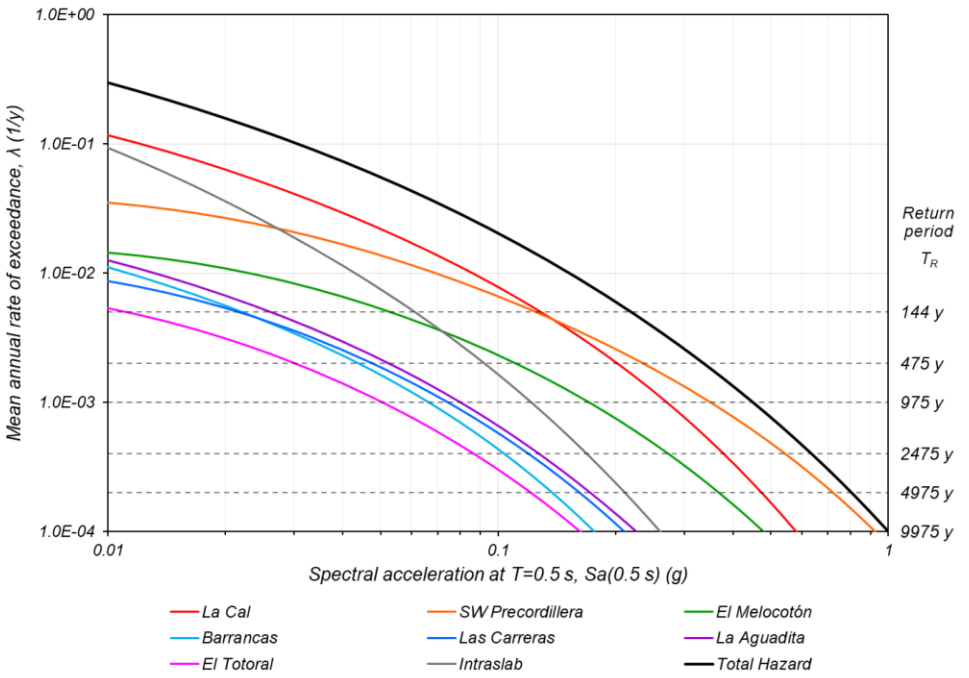


Fig. 11.24: Hazard curves in terms of Sa(0.5s) for all the seismic sources, and their combination (Total Hazard). Evidenced the return periods for every level of the ground shaking selected.

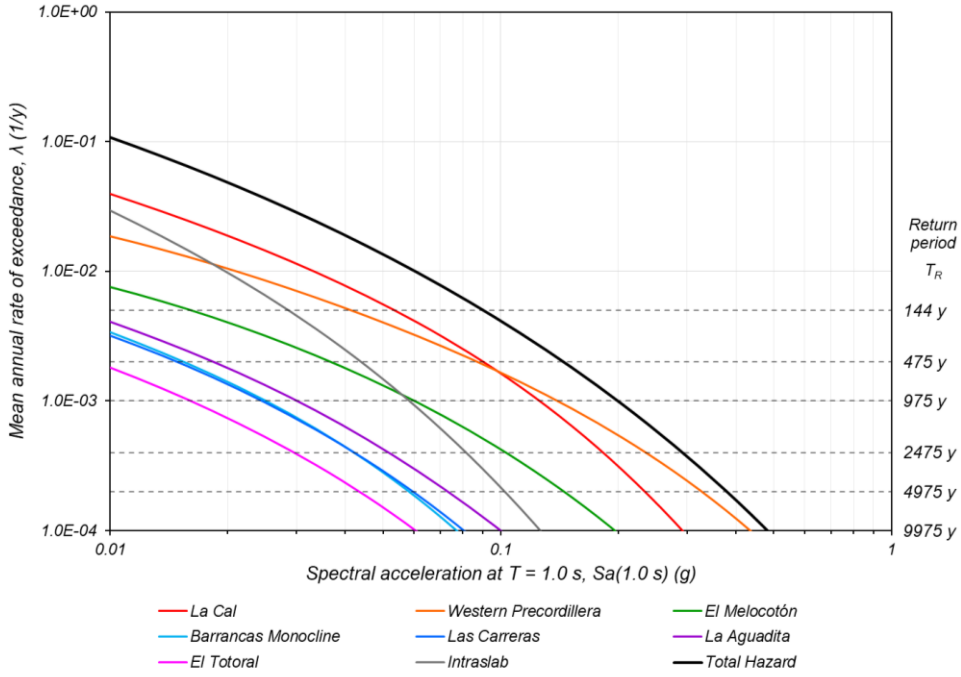


Fig. 11.25: Hazard curves in terms of Sa(1.0s) for all the seismic sources, and their combination (Total Hazard). Evidenced the return periods for every level of the ground shaking selected.

11.2.2 Uniform Hazard Spectra (UHSs)

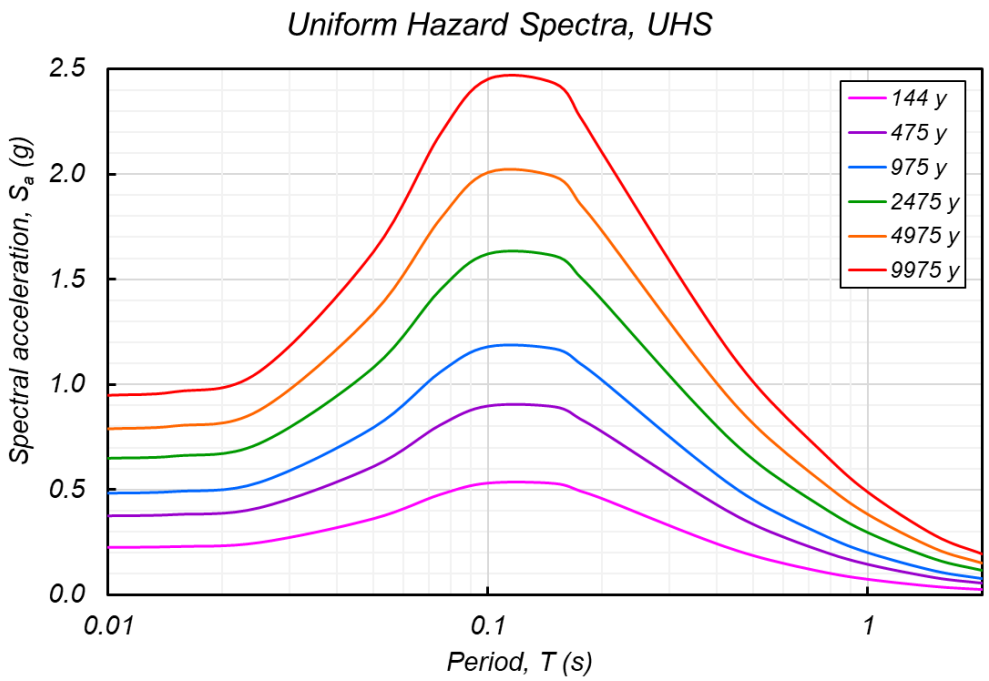


Fig. 11.26: Uniform hazard spectra (UHSs) for the six return periods considered.

Period, T (s)	Spectral acceleration, $Sa(T)$ (g)					
	144 y	475 y	975 y	2475 y	4975 y	9975 y
0.0	0.23	0.37	0.48	0.65	0.79	0.95
0.02	0.23	0.38	0.49	0.66	0.80	0.97
0.03	0.25	0.41	0.53	0.72	0.88	1.06
0.05	0.36	0.61	0.80	1.08	1.34	1.63
0.08	0.48	0.81	1.06	1.45	1.79	2.19
0.10	0.53	0.90	1.18	1.62	2.01	2.45
0.15	0.53	0.89	1.17	1.61	1.99	2.43
0.18	0.50	0.84	1.10	1.51	1.86	2.27
0.20	0.46	0.77	1.02	1.40	1.73	2.10
0.35	0.28	0.49	0.65	0.91	1.14	1.40
0.50	0.19	0.33	0.45	0.64	0.81	1.01
0.75	0.11	0.21	0.29	0.42	0.54	0.69
1.00	0.08	0.14	0.20	0.30	0.38	0.49
1.50	0.04	0.08	0.11	0.17	0.22	0.28
2.00	0.03	0.05	0.08	0.12	0.15	0.19

Table 11.1: Table with the values of spectral acceleration Sa(T) of the UHSs.

11.2.3 Disaggregation charts

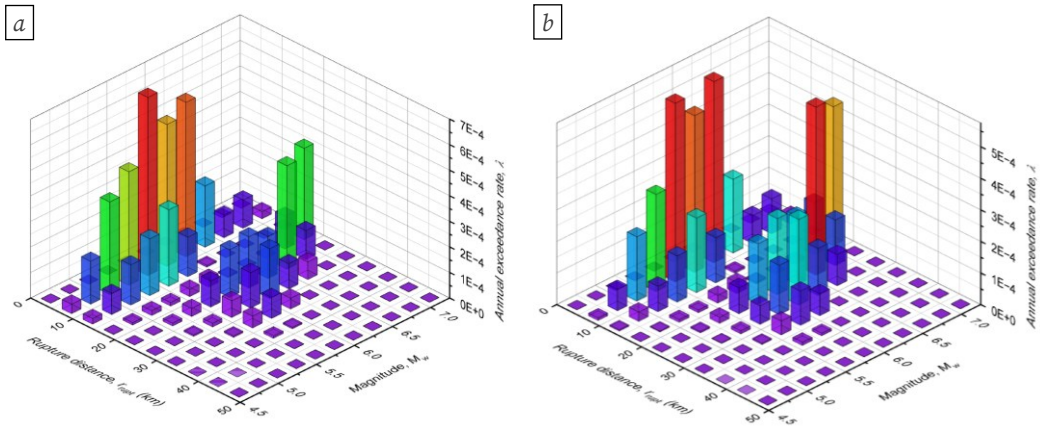


Fig. 11.27: Disaggregation charts for T_R = 144 y, for a) PGA, and b) Sa(0.5s).

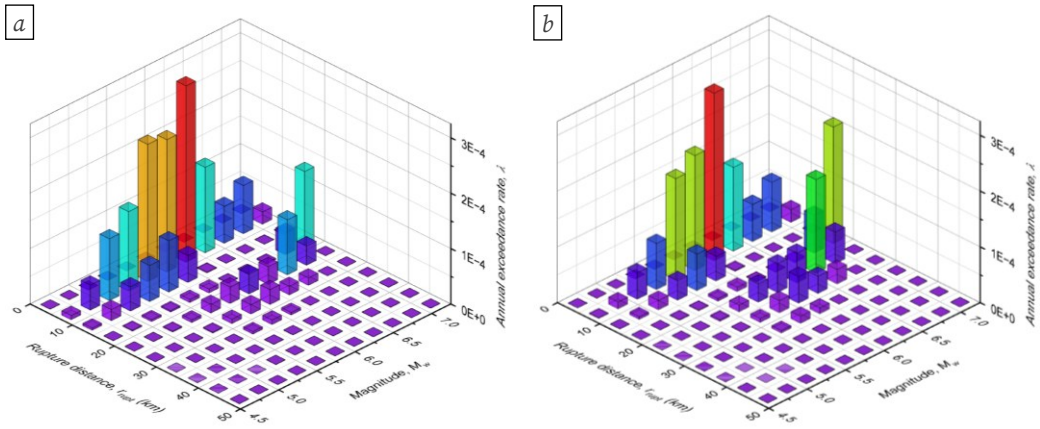


Fig. 11.28: Disaggregation charts for T_R = 475 y, for a) PGA, and b) Sa(0.5s).

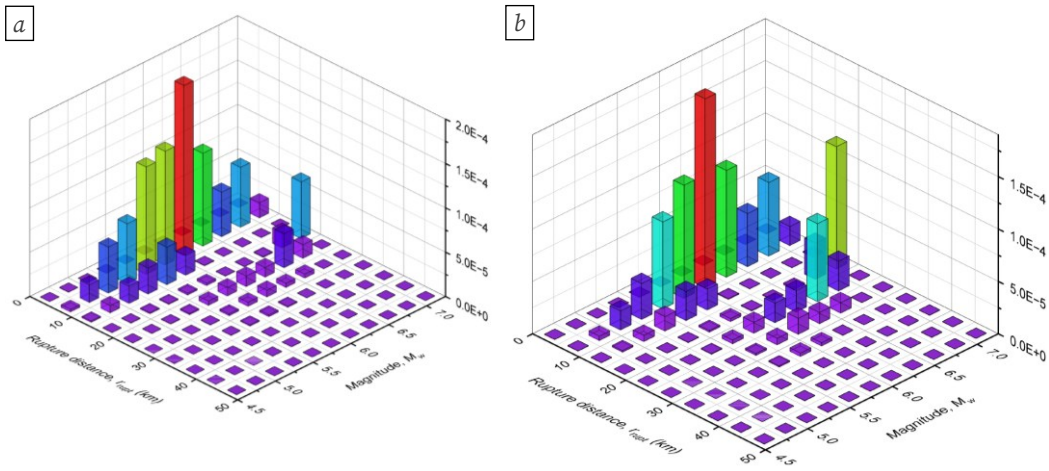


Fig. 11.29: Disaggregation charts for T_R = 975 y, for a) PGA, and b) Sa(0.5s).

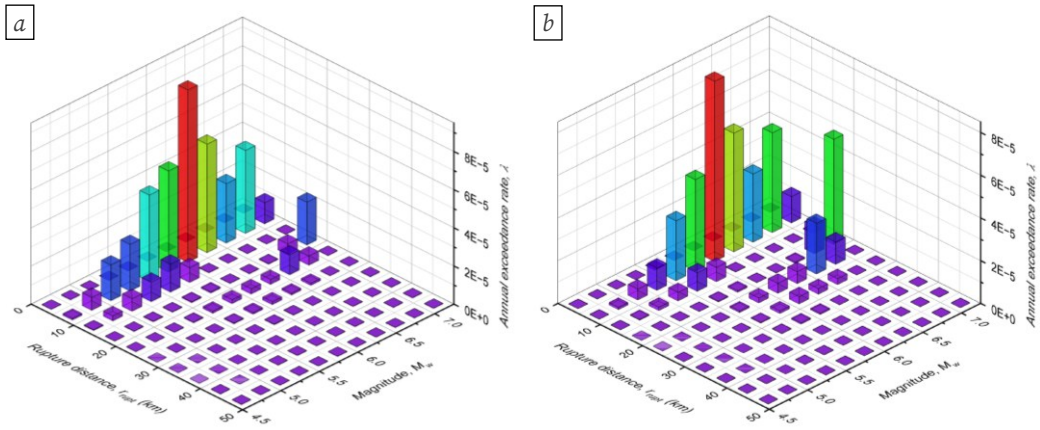


Fig. 11.30: Disaggregation charts for T_R = 2475 y, for a) PGA, and b) Sa(0.5s).

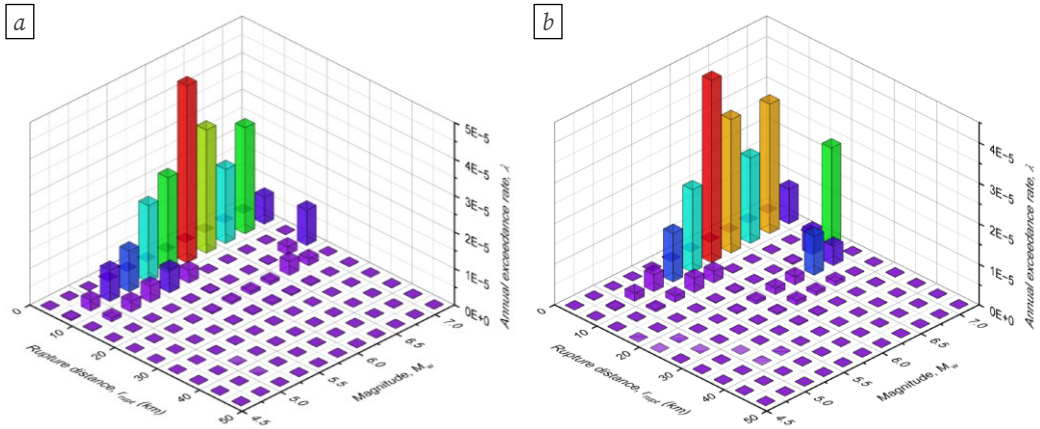


Fig. 11.31: Disaggregation charts for T_R = 4975 y, for a) PGA, and b) Sa(0.5s).

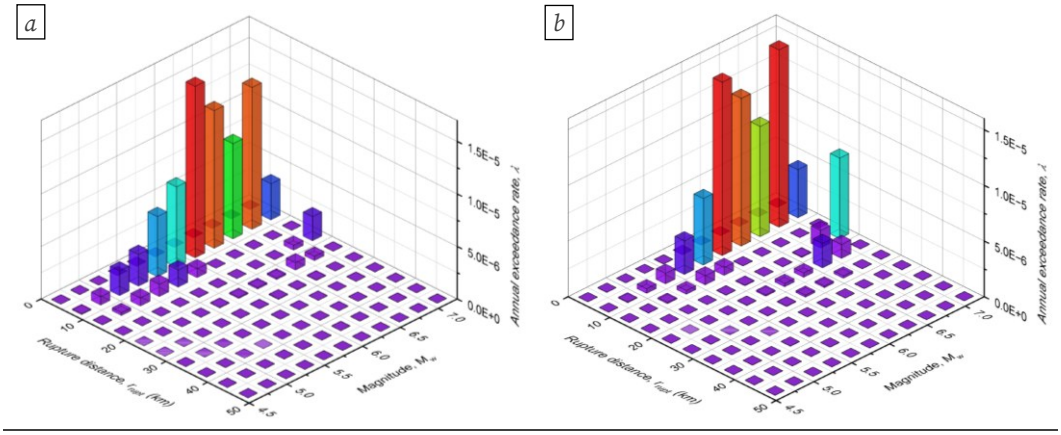


Fig. 11.32: Disaggregation charts for T_R = 9975 y, for a) PGA, and b) Sa(0.5s).

11.2.4 Selected records, scaled response spectra, and ground motion parameters

11.2.4.a Return period T_R = 144 y

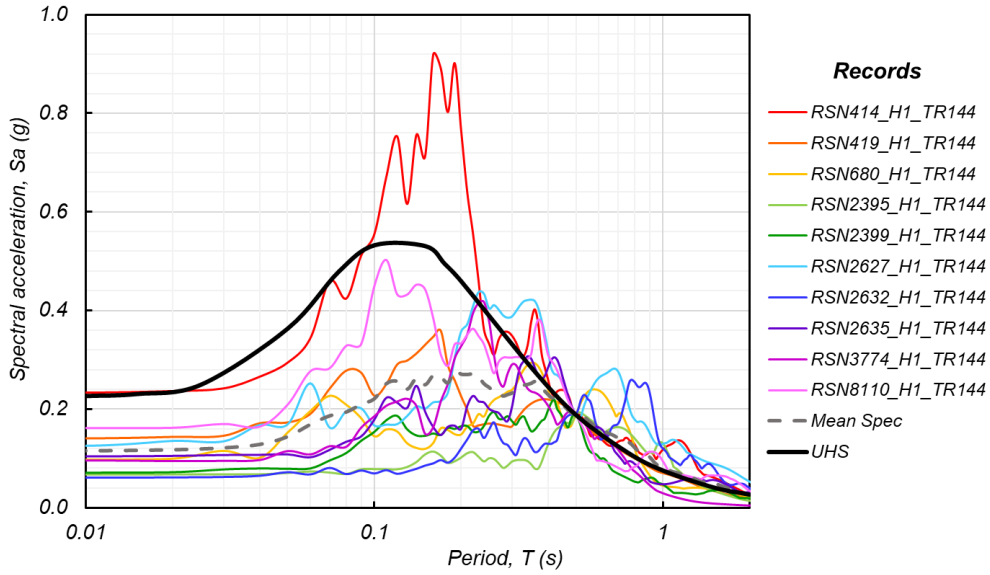


Fig. 11.33: Response spectra for the records selected and scaled for T_R = 144 y, together with their mean spectrum and respective UHS.

Record Name	Seismic event	Year	Mechanism	M (M_W)	r_{rupt} (km)	Vs_{30}	Scale factor
RSN414_ H1_144	Coalinga US	1983	Reverse	5.77	11.4	617	1.88
RSN419_ H1_144	Coalinga US	1983	Reverse	5.21	12.1	617	0.98
RSN680_ H1_144	Whittier Narrows US	1987	Reverse Oblique	5.99	18.1	969	0.87
RSN2395_ H1_144	Chi-Chi Taiwan	1999	Reverse	5.9	8.6	665	0.71
RSN2399_ H1_144	Chi-Chi Taiwan	1999	Reverse	5.9	12.0	672	1.81
RSN2627_ H1_144	Chi-Chi Taiwan	1999	Reverse	6.2	14.7	615	0.78
RSN2632_ H1_144	Chi-Chi Taiwan	1999	Reverse	6.2	9.3	665	0.91
RSN2635_ H1_144	Chi-Chi Taiwan	1999	Reverse	6.2	9.8	672	1.18
RSN3774_ H1_144	Northridge US	1994	Reverse	5.28	17.0	740	1.15
RSN8110_ H1_144	Christchurch New Zealand	2011	Reverse Oblique	6.2	16.1	650	1.09

Table 11.2: Event and site characteristics, and the scaling factor of the records for T_R = 144 y.

Record	RSN_414_H1_144	RSN_419_H1_144	RSN_2395_H1_144	RSN_2399_H1_144	RSN_2627_H1_144	RSN_2632_H1_144	RSN_2635_H1_144	RSN_3774_H1_144	RSN_8110_H1_144	RSN_414_H1_144
PGA (g)	0.23	0.14	0.10	0.07	0.07	0.12	0.06	0.10	0.09	0.16
PGV (cm/s)	10.0	8.9	9.0	6.1	5.1	16.2	12.3	6.9	5.7	7.7
PGD (cm)	2.1	1.5	1.2	1.2	0.8	7.7	7.0	1.9	0.4	2.6
I_A (m/s)	0.356	0.059	0.066	0.046	0.052	0.124	0.109	0.069	0.055	0.185
CAV (m/s)	4.28	1.53	1.51	1.89	1.71	2.68	3.12	1.63	1.00	3.03
I_H (cm)	34.9	21.5	23.1	21.4	17.8	44.9	36.2	24.3	12.3	29.1
T_P (s)	0.16	0.16	0.36	0.52	0.42	0.24	0.78	0.34	0.24	0.14
$D_{5\text{-}95}$ (s)	10.4	5.7	3.5	11.8	8.4	12.5	15.6	7.3	2.8	7.9

Table 11.3: Selected intensity measures of the scaled ground motions, for T_R = 144 y.

11.2.4.b Return period T_R = 475 y

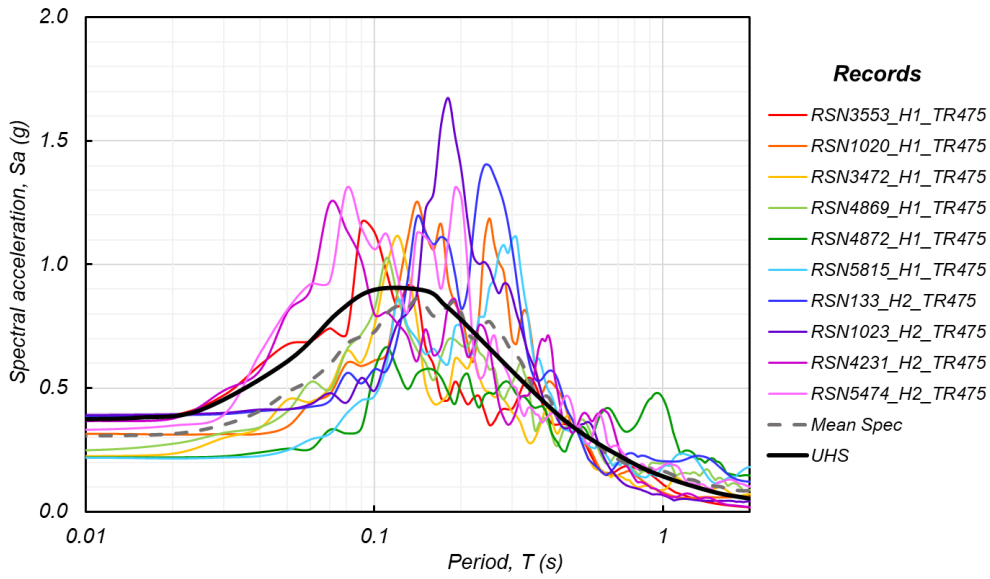


Fig. 11.34: Response spectra for the records selected and scaled for T_R = 475 y, together with their mean spectrum and respective UHS.

Record Name	Seismic event	Year	Mechanism	M (M_W)	r_{rupt} (km)	Vs_{30}	Scale factor
RSN3553_ H1_475	Friuli Italy	1976	Reverse	5.5	6.3	629	1.76
RSN1020_ H1_475	Northridge US	1994	Reverse	6.69	21.4	602	1.77
RSN3472_ H1_475	Chi-Chi Taiwan	1999	Reverse	6.3	25.9	615	1.96
RSN4869_ H1_475	Chuetsu-oki Japan	2007	Reverse	6.8	29.3	640	1.67
RSN4872_ H1_475	Chuetsu-oki Japan	2007	Reverse	6.8	27.3	640	1.49
RSN5815_ H1_475	Iwate Japan	2008	Reverse	6.9	25.6	655	1.11
RSN133_ H2_475	Friuli Italy	1976	Reverse	5.91	14.5	650	2.87
RSN1023_ H2_475	Northridge US	1994	Reverse	6.69	25.4	671	1.79
RSN4231_ H2_475	Niigata Japan	2004	Reverse	6.63	22.1	686	2.00
RSN5474_ H2_475	Iwate Japan	2008	Reverse	6.9	28.8	640	1.83

Table 11.4: Event and site characteristics, and the scaling factor of the records for T_R = 475 y.

Record	RSN_3553_H1_475	RSN_1020_H1_475	RSN_3472_H1_475	RSN_4872_H1_475	RSN_5815_H1_475	RSN_133_H2_475	RSN_1023_H2_475	RSN_4231_H2_475	RSN_5474_H2_475	RSN_3553_H1_475
PGA (g)	0.37	0.31	0.23	0.24	0.22	0.22	0.38	0.39	0.37	0.33
PGV (cm/s)	14.3	20.8	12.8	12.6	34.5	22.3	22.4	17.6	18.0	24.5
PGD (cm)	1.4	8.1	6.1	7.1	10.7	5.8	5.7	4.9	8.2	17.5
I_A (m/s)	0.34	1.05	0.46	0.94	0.69	1.14	0.73	0.75	1.04	2.68
CAV (m/s)	2.71	8.25	6.40	10.31	8.73	10.90	4.41	5.96	9.90	18.69
I_H (cm)	29.4	46.0	47.2	66.1	99.7	91.6	90.6	39.3	34.3	69.2
T_P (s)	0.1	0.14	0.12	0.12	0.1	0.3	0.24	0.18	0.08	0.08
$D_{5\text{-}95}$ (s)	3.2	9.8	17.6	22.5	22.7	12.7	5.0	7.9	11.7	17.3

Table 11.5: Selected intensity measures of the scaled ground motions, for T_R = 475 y.

11.2.4.c Return period T_R = 975 y

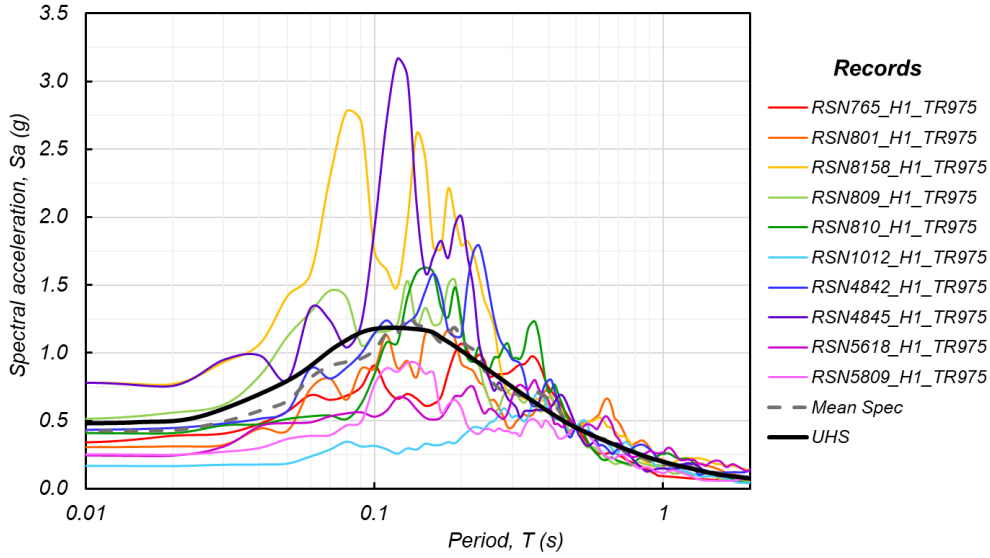


Fig. 11.35: Response spectra for the records selected and scaled for T_R = 975 y, together with their mean spectrum and respective UHS.

Record Name	Seismic event	Year	Mechanism	M (M_W)	r_{rupt} (km)	Vs_{30}	Scale factor
RSN765_ H1_975	Loma Prieta US	1989	Reverse Oblique	6.93	9.6	1428	0.81
RSN801_ H1_975	Loma Prieta US	1989	Reverse Oblique	6.93	14.7	672	1.10
RSN8158_ H1_975	Christchurch New Zealand	2011	Reverse Oblique	6.2	6.1	650	0.81
RSN809_ H1_975	Loma Prieta US	1989	Reverse Oblique	6.93	18.5	714	1.65
RSN810_ H1_975	Loma Prieta US	1989	Reverse Oblique	6.93	18.4	714	0.89
RSN1012_ H1_975	Northridge US	1994	Reverse	6.69	19.1	706	0.64
RSN4842_ H1_975	Chuetsu-oki Japan	2007	Reverse	6.8	22.7	655	1.67
RSN4845_ H1_975	Chuetsu-oki Japan	2007	Reverse	6.8	22.5	610	1.16
RSN5618_ H1_975	Iwate Japan	2008	Reverse	6.9	16.3	826	1.09
RSN5809_ H1_975	Iwate Japan	2008	Reverse	6.9	21.3	655	1.02

Table 11.6: Event and site characteristics, and the scaling factor of the records for T_R = 975 y.

Record	RSN_765_H1_975	RSN_801_H1_975	RSN_8158_H1_975	RSN_809_H1_975	RSN_810_H1_975	RSN_1012_H1_975	RSN_4842_H1_975	RSN_4845_H1_975	RSN_5618_H1_975	RSN_5809_H1_975
PGA (g)	0.34	0.30	0.74	0.52	0.41	0.17	0.43	0.76	0.24	0.25
PGV (cm/s)	27.3	31.1	32.4	17.1	20.2	16.5	36.2	24.3	23.7	17.2
PGD (cm)	6.5	25.6	13.4	4.7	7.3	3.8	12.4	7.4	8.6	4.4
I_A (m/s)	0.70	1.59	3.16	2.32	2.10	0.40	1.64	2.31	1.54	0.98
CAV (m/s)	5.40	10.78	9.46	11.20	11.66	5.07	10.71	9.88	15.55	9.16
I_H (cm)	49.8	73.2	95.0	51.7	63.2	52.8	83.7	69.0	106.0	57.8
T_P (s)	0.2	0.18	0.08	0.18	0.16	0.38	0.22	0.12	0.36	0.14
$D_{5\text{-}95}$ (s)	6.6	10.1	4.1	8.9	9.5	8.0	12.5	4.8	19.7	11.5

Table 11.7: Selected intensity measures of the scaled ground motions, for T_R = 975 y.

11.2.4.d Return period T_R = 2475 y

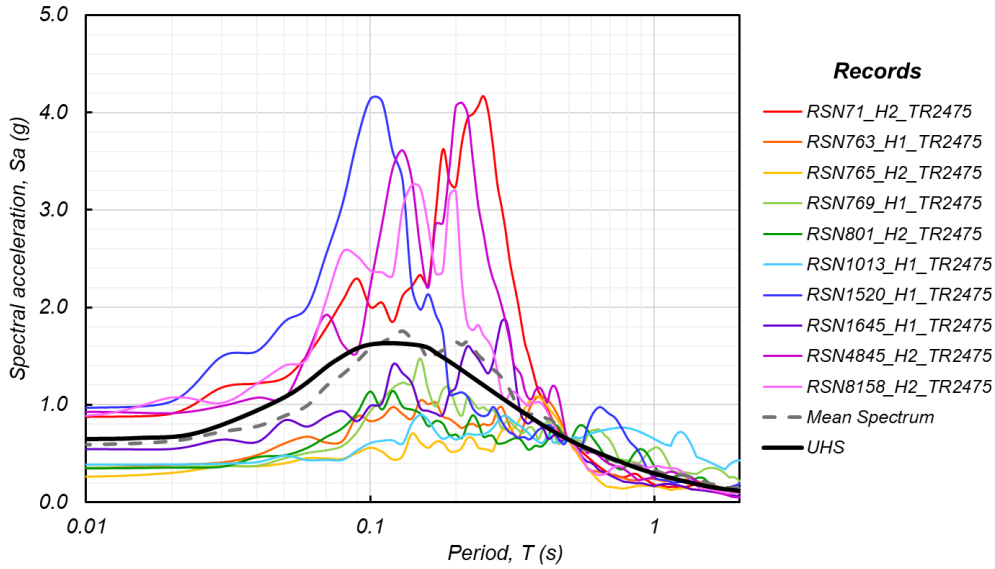


Fig. 11.36: Response spectra for the records selected and scaled for T_R = 2475 y, together with their mean spectrum and respective UHS.

Record Name	Seismic event	Year	Mechanism	M (M_W)	r_{rupt} (km)	Vs_{30}	Scale factor
RSN71_ H2_2475	San Fernando US	1971	Reverse	6.61	19.3	602	0.97
RSN763_ H1_2475	Loma Prieta US	1989	Reverse Oblique	6.93	10.0	730	0.90
RSN765_ H2_2475	Loma Prieta US	1989	Reverse Oblique	6.93	9.6	1428	1.94
RSN769_ H1_2475	Loma Prieta US	1989	Reverse Oblique	6.93	18.3	663	2.80
RSN801_ H2_2475	Loma Prieta US	1989	Reverse Oblique	6.93	14.7	672	0.53
RSN1013_ H1_2475	Northridge US	1994	Reverse	6.69	5.9	629	1.34
RSN1520_ H1_2475	Chi-Chi Taiwan	1999	Reverse Oblique	7.62	18.2	665	0.92
RSN1645_ H1_2475	Sierra Madre US	1991	Reverse	5.61	10.4	680	3.00
RSN4845_ H2_2475	Chuetsu-oki Japan	2007	Reverse	6.80	22.5	610	1.48
RSN8158_ H2_2475	Christchurch New Zealand	2011	Reverse Oblique	6.20	6.1	650	1.84

Table 11.8: Event and site characteristics, and the scaling factor for the records corresponding to the return period T_R = 2475 y.

Record	RSN_71_H2_2475	RSN_763_H1_2475	RSN_765_H2_2475	RSN_769_H1_2475	RSN_801_H2_2475	RSN_1013_H1_2475	RSN_1520_H1_2475	RSN_1645_H1_2475	RSN_4845_H2_2475	RSN_8158_H2_2475
PGA (g)	0.86	0.35	0.26	0.35	0.35	0.38	0.99	0.54	0.90	0.87
PGV (cm/s)	38.3	30.2	17.3	36.6	28.8	67.4	38.4	26.3	30.9	38.0
PGD (cm)	6.6	10.6	8.3	14.2	12.5	17.2	24.9	3.4	7.6	10.7
I_A (m/s)	0.856	1.428	1.552	1.769	0.480	1.785	4.823	7.368	6.219	8.944
CAV (m/s)	5.72	7.97	6.29	11.25	3.93	11.69	11.38	19.69	15.57	25.20
I_H (cm)	104.1	88.7	61.5	147.4	102.5	222.0	126.3	66.7	94.2	100.8
T_P (s)	0.24	0.40	0.38	0.14	0.12	0.30	0.10	0.30	0.20	0.14
$D_{5\text{-}95}$ (s)	12.0	5.0	3.7	13.0	10.1	6.5	9.2	3.2	4.1	3.9

Table 11.9: Selected intensity measures of the scaled ground motions, for T_R = 2475 y.

11.2.4.e Return period T_R = 4975 y

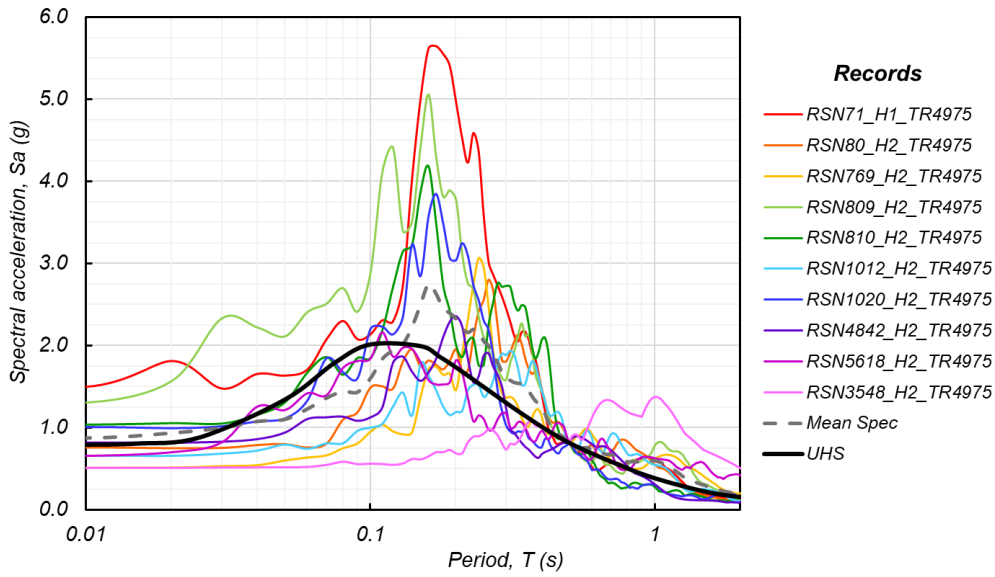


Fig. 11.37: Response spectra for the records selected and scaled for T_R = 4975 y, together with their mean spectrum and respective UHS.

Record Name	Seismic event	Year	Mechanism	M (M_W)	r_{rupt} (km)	Vs_{30}	Scale factor
RSN71_ H1_4975	San Fernando US	1971	Reverse	6.61	19.3	602	3.82
RSN80_ H2_4975	San Fernando US	1971	Reverse	6.61	21.5	969	3.65
RSN769_ H2_4975	Loma Prieta US	1989	Reverse Oblique	6.93	18.3	663	2.99
RSN809_ H2_4975	Loma Prieta US	1989	Reverse Oblique	6.93	18.5	714	3.16
RSN810_ H2_4975	Loma Prieta US	1989	Reverse Oblique	6.93	18.4	714	2.48
RSN1012_ H2_4975	Northridge US	1994	Reverse	6.69	19.1	706	1.72
RSN1020_ H2_4975	Northridge US	1994	Reverse	6.69	21.4	602	3.86
RSN4842_ H2_4975	Chuetsu-oki Japan	2007	Reverse	6.8	22.7	655	1.42
RSN5618_ H2_4975	Iwate Japan	2008	Reverse	6.9	16.3	826	2.21
RSN3548_ H2_4975	Loma Prieta US	1989	Reverse Oblique	6.93	5.0	1070	1.23

Table 11.10: Event and site characteristics, and the scaling factor of the records for T_R = 4975 y.

Record	RSN_71_H1_4975	RSN_80_H2_4975	RSN_769_H2_4975	RSN_809_H2_4975	RSN_810_H2_4975	RSN_1012_H2_4975	RSN_1020_H2_4975	RSN_4842_H2_4975	RSN_5618_H2_4975	RSN_3548_H2_4975
PGA (g)	1.46	0.75	0.51	1.28	0.81	0.66	0.99	0.80	0.64	0.51
PGV (cm/s)	62.6	46.8	41.7	41.7	80.9	65.1	34.2	40.6	58.0	118.3
PGD (cm)	5.9	4.9	13.1	7.3	7.6	6.1	15.9	12.1	38.1	37.4
I_A (m/s)	13.6	4.6	4.0	15.8	4.8	3.1	7.0	2.8	6.7	2.7
CAV (m/s)	26.7	17.0	16.7	29.4	16.6	13.4	20.7	11.8	32.6	9.9
I_H (cm)	144.8	131.0	175.3	171.6	174.1	140.2	112.0	97.3	253.3	332.6
T_P (s)	0.16	0.26	0.24	0.16	0.16	0.32	0.16	0.2	0.14	1.0
$D_{5\text{-}95}$ (s)	10.7	6.9	12.7	8.6	8.0	8.0	9.8	6.3	22.8	4.1

Table 11.11: Selected intensity measures of the scaled ground motions, for T_R = 4975 y.

11.2.4.f Return period T_R = 9975 y

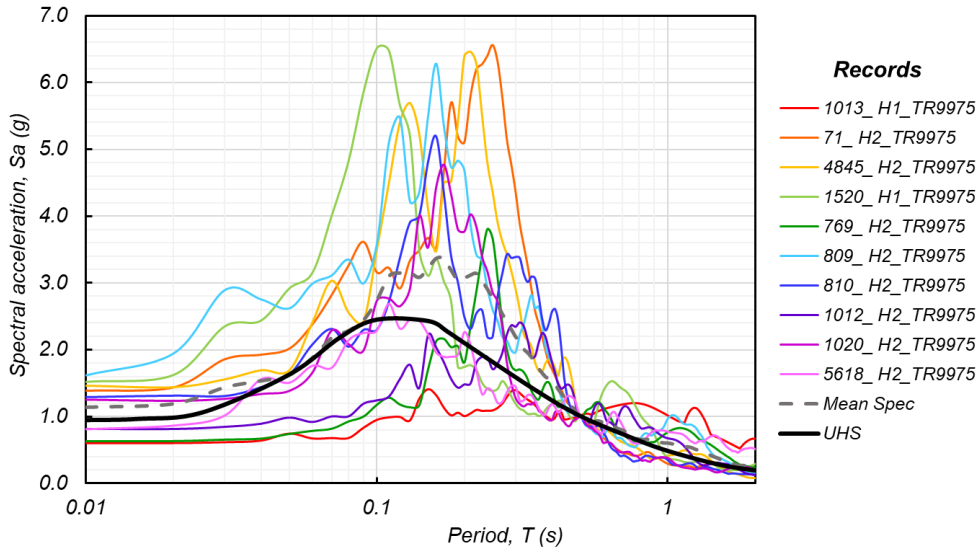


Fig. 11.38: Response spectra for the records selected and scaled for T_R = 9975 y, together with their mean spectrum and respective UHS.

Record Name	Seismic event	Year	Mechanism	M (M_W)	r_{rupt} (km)	Vs_{30}	Scale factor
RSN1013_ H1_9975	Northridge US	1994	Reverse	6.69	5.9	629	1.42
RSN71_ H2_9975	San Fernando US	1971	Reverse	6.61	19.3	602	4.82
RSN4845_ H2_9975	Chuetsu-oki Japan	2007	Reverse	6.8	22.5	610	2.33
RSN1520_ H1_9975	Chi-Chi Taiwan	1999	Reverse Oblique	7.62	18.2	665	2.89
RSN769_ H2_9975	Loma Prieta US	1989	Reverse Oblique	6.93	18.3	663	3.71
RSN809_ H2_9975	Loma Prieta US	1989	Reverse Oblique	6.93	18.5	714	3.93
RSN810_ H2_9975	Loma Prieta US	1989	Reverse Oblique	6.93	18.4	714	3.08
RSN1012_ H2_9975	Northridge US	1994	Reverse	6.69	19.1	706	2.13
RSN1020_ H2_9975	Northridge US	1994	Reverse	6.69	21.4	602	4.79
RSN5618_ H2_9975	Iwate Japan	2008	Reverse	6.9	16.3	826	2.75

Table 11.12: Event and site characteristics, and the scaling factor of the records for T_R = 9975 y.

Record	RSN_1013_H1_9975	RSN_71_H2_9975	RSN_4845_H2_9975	RSN_1520_H1_9975	RSN_769_H2_9975	RSN_809_H2_9975	RSN_810_H2_9975	RSN_1012_H2_9975	RSN_1020_H2_9975	RSN_5618_H2_9975
PGA (g)	0.60	1.36	1.42	1.52	0.63	1.60	1.03	1.23	0.79	0.63
PGV (cm/s)	106.1	60.3	48.7	100.6	51.8	51.8	51.7	42.5	72.1	146.9
PGD (cm)	27.0	10.4	11.9	84.0	16.2	9.0	15.3	19.8	47.4	46.5
I_A (m/s)	3.5	18.3	15.4	22.9	6.1	24.4	12.6	10.7	10.3	4.1
CAV (m/s)	12.6	31.0	24.5	40.2	20.7	36.5	29.0	25.8	40.5	12.2
I_H (cm)	349.7	164.0	148.4	201.9	217.8	213.1	107.1	139.1	314.6	413.2
T_P (s)	0.3	0.24	0.2	0.1	0.24	0.16	0.32	0.16	0.14	1.0
$D_{5\text{-}95}$ (s)	6.5	12.0	4.1	9.2	12.7	8.6	9.7	9.8	22.8	4.1

Table 11.13: Selected intensity measures of the scaled ground motions, for T_R = 9975 y.